

北海道大学  
エネルギー先端工学研究センター

年 報 第 2 号

Annual Report of CARET, No. 2

CARET

*Hokkaido University*

*Center for Advanced Research of Energy Technology*

*Hokkaido University*

NEDO 図書・資料室

1996



010017782-3

北海道大学  
エネルギー先端工学研究センター

年 報 第 2 号

**Annual Report of CARET, No. 2**

*CARET*

*Hokkaido University*

*Center for Advanced Research of Energy Technology*

*Hokkaido University*

1996

# エネルギー先端工学研究センター 年報第2号の刊行にあたって

北海道大学エネルギー先端工学研究センター  
センター長 吉田 宏

エネルギー先端工学研究センターが平成6年度に北海道大学の学内共同利用研究施設として10年の時限をもって設置されてから早くも2年が経過しました。センターは、石炭を中心とする化石燃料資源の高効率エネルギー転換と新エネルギー源を確保することを目指した技術開発に必要とされる化学、物理、ならびに材料工学の研究を行うことを目的としています。

本センターは、炭素系資源転換反応分野、炭素系資源評価分野、エネルギー転換制御分野、極限材料工学分野の4グループからなっています。炭素系資源転換反応分野は、石炭転換反応における熱及び物質移動過程や反応機構の解明を、炭素系資源評価分野は、石炭転換反応のための高効率触媒の探索を、エネルギー転換制御分野は、石炭燃焼高温プラズマから電磁エネルギーへの直接変換を、極限材料工学分野は、エネルギー変換などの過酷条件下で用いる材料の開発を、それぞれ研究の中心課題として研究に取り組んできました。

平成6年度末に、本センターの設置に力を尽くされた前センター長で炭素系資源転換反応分野担当の真田雄三教授と同分野の横山晋助教授が定年で去られました。センターの研究推進にとって大きな痛手でしたが、幸いにして、本年度より同分野担当に北海道大学工学部より千葉忠俊教授を迎えることができ、これで10年時限の本センターの目標を達成するための陣容が整いました。

本センターは、もとをたどれば、工学部附属の金属化学研究施設、石炭資源実験施設、先端電磁流体実験施設が改組拡充してできあがったものですが、各分野の間の研究協力も次第に進展し、各大学・研究所から多数ご参加を得て各分野が一体となった「96エネルギー先端工学シンポジウム」を開催するまでになりました。今後、各分野固有の研究の進展はもちろんのこと、「21世紀の文明社会を支えるエネルギー研究」に対して貢献するというセンター共通の目標に向けても前途が見えてきたように思います。1995年度には、センター全体として、学術論文を33編、総説評論等を5編の成果を世に問うことができました。

ここに、1995年度のセンターの活動状況と研究成果とをまとめてご報告します。各方面のご批評とご教示をいただければ幸いです。本センターに対するご支援をあわせてお願いいたします。

1996年3月

# 目 次

1. エネルギー先端工学研究センターの機構・組織	1
2. センターの研究内容	2
3. 研 究 報 告	5
3. 1 学術論文	5
3. 2 総説, 解説, 評論等	10
3. 3 著 書	11
3. 4 学術講演	12

## 学術論文

### [炭素系資源転換反応分野]

Formation of Free Radicals during Drying and Oxidation of a Lignite and a Bituminous Coal	21
--	----

R. M. Carr, H. Kumagai, B. M. Peake, B. H. Robinson, A. H. Clemens  
and T. W. Matheson

Fuel, 74(3): 389-394(1995)

ベンチスケール石炭直接液化反応器の反応解析	27
-----------------------	----

井戸川清, 佐々木正秀, 池上真志樹, 永石博志, 成田英夫, 佐々木皇美  
小谷川毅, 福田隆至, 山本光義, 吉田忠, 前河涌典, 千葉忠俊  
日本エネルギー学会誌, 74(3): 161-169(1995)

A Model Structure of Zao Zhuang Bituminous Coal	36
---	----

K. Nakamura, T. Takanohashi, M. Iino, H. Kumagai, M. Sato, S. Yokoyama  
and Y. Sanada

Energy & Fuels, 9(6): 1003-1010(1995)

An Additional Carbon Layer over the Surface of C/C Composite Substrate with the Aid of Polyvinyl Chloride	44
--	----

T. Ueda, T. Morimoto, H. Kumagai and Y. Sanada

Carbon, 33(1): 73-78(1995)



Carbonization of Pitches in Air Blowing Batch Reactor J. H. Choi, H. Kumagai, T. Chiba and Y. Sanada Carbon, 33(2): 109-114(1995)	50
Air-Blowing Reactions of Pitch: Oxidation of Aromatic Hydrocarbons C. Yamaguchi, J. Mondori, A. Matsumoto, H. Honma, H. Kumagai and Y. Sanada Carbon, 33(2): 193-201(1995)	56
2. 4ton/day 石炭直接水添液化 PDUスラリー予熱器におけるスラリー 粘度変化の推算 山口宏, 横山敬, 真田雄三, 千葉忠俊 化学工学論文集, 21(4): 707-714(1995)	65
Surface Chemistry of Carbon Black through Curing Process of Epoxy Resin M. Nakahara, T. Takada, H. Kumagai and Y. Sanada Carbon, 33(11): 1537-1540(1995)	73
ESRを用いたエアープロンピッチの特性評価 崔 在薫, 熊谷治夫, 真田雄三 炭素, No. 167: 108-115(1995)	77
[炭素系資源評価分野]	
Formation of Protonic Acid Sites from Hydrogen Molecules and Their Roles in Acid-Catalyzed Reactions H. Hattori, T. Shishido, J. Tsuji, T. Nagase, H. Kita Proc. Science and Technology in Catalysis 1994, Kodansha-Elsevier, 93-98(1995)	85
Highly Active Absorbent for SO <sub>2</sub> Removal Prepared from Coal Fly Ash Tsuchiai, T. Ishizuka, T. Ueno, H. Hattori and H. Kita Ind. Eng. Chem. Res., 34: 1404-1411(1995)	91

<sup>29</sup> Si-NMR study of the absorbent for flue gas desulfurization H. Hattori, N. Kanuka and R. Kanai Coal ScienceI&II., 1875-1878(1995)	99
Reduction of NO on Au single-crystal electrodes in alkaline solution <sup>1</sup> S. Suzuki, T. Nakato, H. Hattori and H. Kita Journal of Electroanalytical Chemistry, 396: 143-150(1995)	103
Thermal Activation of KF/Alumina Catalyst for Double Bond Isomerization and Michael Addition H. Tsuji, H. Kabashima, H. Kita and H. Hattori React. Kinet. Catal. Lett., 56(2), 363-369(1995)	111
The State of Platinum in a Pt/SO <sub>4</sub> <sup>2-</sup> /ZrO <sub>2</sub> Super Acid Catalyst T. Tanaka, T. Shishido, H. Hattori, K. Ebitani and S. Yoshida Physica B 208 & 209, 649-650(1995)	118
Cationic Mobility in MgX Zeolite: An FTIR Study G. Martra, N. Damilano, S. Coluccia, H. Tsuji and H. Hattori J. Chem. Soc. Faraday Trans., 91(17), 2961-2964(1995)	120
Chemical Structure of Organic Sulfur Compounds in Extracted Oils and Hydrogenated Oils Derived from Coals Examined by Means of GC-FPD and GC-LVEI MS S. Yokoyama, A. Ohtani, M. Muraji, H. Sugibuchi, M. M. Y. Bakr, M. Satou and Y. Sanada 石油学会誌, 38(2): 97-104(1995)	124
石炭水素化分解生成オイルのGC-MS/MS分析 横山 晋, 中村久志, 伊藤好江, 佐藤正昭, 真田雄三 鈴木 優, 野原 勉 日本エネルギー学会誌 74(8): 722-730(1995)	132

Vapor Pressure Estimation for Hydrocarbons in a Coal Derived Liquid S. Harikae, M. Satou, T.Chiba, S. Yokoyama and Y. Sanada Coal Science and Technology Vol.24, Coal Science Volume II, J. A. Pajares and J. M. D. Tascon, Eds., ELsevier, Amsterdam, The Netherlands, 1451-1454(1995)	141
Refining of Coal Liquid - Structural Analysis of Hydrogenated SRC-II distillates with HPLC-GC/MS - K. Tanabe, M. Satou, S. Yokoyama and Y. Sanada 石油学会誌, 38(5): 333-344(1995)	145
[エネルギー転換制御分野] アルカリ添加燃焼ガスの輻射吸収計測法における新しい関係式 粥川尚之, 山崎康男 日本機械学会論文集(B), 61(585):1921-1927(1995)	157
The Effects of Plasma Fluctuation in MHD Generators (Studies with a Numerical Turbulence Model) N. Kayukawa JSME Int. J., 38(3(B)):366-373(1995)	164
流体変動を伴う弱電離プラズマの相関電流の評価 及川俊一, 三井恒明, 粥川尚之, 青木義明, 榎戸武揚 電気学会論文誌B (電力・エネルギー部門誌) , 115-B(9):1116-1122(1995)	172
On Applicability of Optical Depth-Atomic Absorption Relationship to Measurements of Alkali-Seeded Combustion Flames N. Kayukawa Thermochemica Acta(Special issue), 267(7):107-115(1995)	179
Plasma Diagnostics of Magnetohydrodynamic Generators N. Okinaka, S. Oikawa, S. Yatsu, Y. Aoki and N. Kayukawa Int. J. of Applied Electromagnetics and Mechanics, 6:207-220(1995)	188

Consideration of Optimal Magnet Coil Design Using Nb-Ti Superconductor for 200 MWe Magnetohydrodynamic Generator R. Nishimura, Y. Aoki and N. Kayukawa Jpn. J. Appl. Phys., 34:2504-2512(1995)	202
[極限材料工学分野]	
Facilities for in situ ion beam studies in transmission electron microscopes C. W. Allen, S. Ohnuki and H. Takahashi Trans. Mat. Res. Soc. Jpn. ,17:93-96(1994)	211
Microchemical change and grain boundary migration due to excess defects flow under irradiation H. Takahashi, N. Hashimoto and S. Watanabe Materials for Advanced Energy Systems & Fission and Fusion Engineering '94, edited by A. Kohyama et al., JCSTE 7 Series Symposium, 386-391(1994)	215
Solid transmutation effect in fusion reactor materials S. Ohnuki, H. Kinoshita and H. Takahashi ibid., 413-416(1994)	221
Mechanical properties of neutron-irradiated lower activated Fe-Cr-Mn alloys H. Takahashi, S. Ohnuki and H. Kinoshita Sci. Rep. RITU, A40(1):63-67(1994)	225
Concentration dependence of radiation induced segregation S. Watanabe, N. Sakaguchi, H. Kinoshita and H. Takahashi J. Nucl. Mater., 226:330-331(1995)	230
Quantitative studies of irradiation-induced segregation and grain boundary migration in Fe-Cr-Ni alloy S. Watanabe, N. Sakaguchi, N. Hashimoto and H. Takahashi J. Nucl. Mater., 224:158-168(1995)	232

Grain Boundary Segregation Under Irradiation in a HVEM	243
H. Takahashi, T. Kato, S. Watanabe and N. Sakaguchi	
Annales De Physique 20:C3-109 -C3-116(1995)	
Phase transformation induced by irradiating an $\text{Al}_{62}\text{Cu}_{25.5}\text{Fe}_{12.5}$ icosahedral quasicrystal	251
R. Wang, X. Yang, H. Takahashi and S. Ohnuki	
J. Phys., Condens. Matter 7:2105-2114(1995)	
Influence of transmutation on microstructure, density change, and embrittlement of vanadium and vanadium alloys irradiated in HFIR	261
S. Ohnuki, H. Takahashi, K. Shiba, A. Hishinuma, J. E. Pawel and F. A. Garner	
J. Nucl. Mater., 218:217-223(1995)	
総説, 解説, 評論等	
[炭素系資源転換反応分野]	
(総説) 計算機化学の石炭構造研究への応用	269
村田 聡, 三浦雅博, 野村正勝, 鷹觜利公, 飯野 雅, 熊谷治夫, 真田雄三, 中村和夫	
日本エネルギー学会誌, 74(6): 342-351(1995)	
(総説) 炭素のふしぎ	279
真田雄三	
ペトロテック, 18(12): 1000-1002(1995)	
[炭素系資源評価分野]	
(総説) ファインケミカルズと固体塩基触媒	282
服部 英, 辻 秀人	
触媒誌, 37: 2-9(1995)	
(総説) 塩基性触媒としてのゼオライトによる新しい反応	290
服部 英	
ゼオライト, 12: 2-7(1995)	

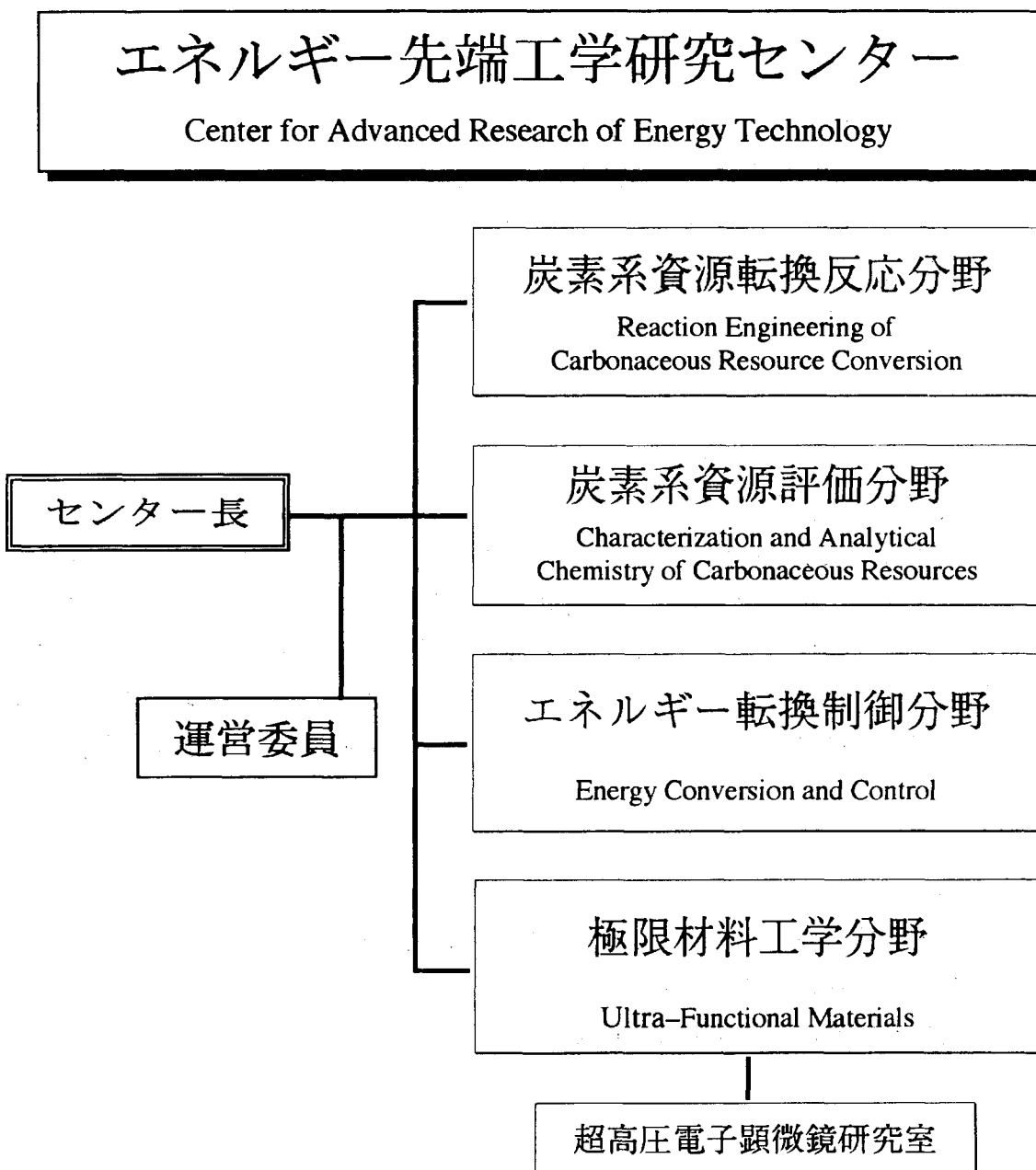
(総説) Heterogeneous Basic Catalysis H. Hattori Chem. Rev., 95(3): 537-558(1995)	296
(総説) 固体塩基触媒による有機合成 服部 英 PETROTECH, 18(6): 473-478(1995)	318
(総説) トルエンの側鎖アルキル化 服部 英 PETROTECH, 18(10): 842-843(1995)	324
[極限材料工学分野]	
(解説) 高エネルギー粒子線照射による核変換反応を利用した 組成制御と新材料 高橋平七郎, 野田哲二 まてりあ, 34(8):966-968(1995)	326
4. 共同研究者ならびに研究テーマ一覧	329
5. 指導学生研究テーマ一覧	331
6. 科学研究費等一覧	333
7. 国際会議出席一覧	334
8. 学会賞受賞一覧	336
9. 平成7年度センター職員名簿	337
10. 平成7年度運営委員会委員名簿	338

**1. エネルギー先端工学研究センターの  
機構・組織**

**2. センターの研究内容**

## 1. エネルギー先端工学研究センターの機構・組織

エネルギー先端工学研究センターは図1に示すように、4分野から組織されている。学部の教授会に相当する議決機関として運営委員会がありセンターの教授、助教授の他、工学部をはじめ学内の関連部局選出の教授から構成されている。エネルギー転換制御分野には客員制度が附設され、他大学より専門家が任命され、研究体制を敷いている。





## 2. センターの研究内容

### 炭素系資源転換反応分野

複雑な固体高分子である石炭をはじめとする炭素系資源を、高効率でクリーンなエネルギーへ転換するプロセスに関する物理化学、反応工学ならびに化学工学的研究を炭素系資源評価分野と協力して実施している。主要な研究分野は、高分子凝集構造、熱分解・炭化、着火、他資源との複合転換、環境適合型流動層燃焼および石炭灰の有効利用である。

#### 研究課題

- 1 高分子凝集構造の評価と改質
- 2 熱分解・炭化反応における熱物性と生成物の制御
- 3 石炭単一粒子の熱分解・着火挙動の解明
- 4 石炭灰の改質と有用物質の回収
- 5 石炭-重質油コプロセッシング

### 炭素系資源評価分野

炭素系資源転換反応分野とともに、炭素系資源を有効利用するために触媒化学、有機化学、物理化学および分析化学的な研究を行っている。主要な研究分野は、石炭転換反応システムにおける高効率触媒の探索・開発、石炭や液化油の物理・化学構造の解明ならびに物性との関連、さらに、環境調和型触媒プロセスの開発と環境保全のための $\text{SO}_x$ ・ $\text{NO}_x$ 除去吸収剤の基礎研究も行っている。

#### 研究課題

- 1 石炭転換用触媒の基礎となる固体酸塩基触媒の開発
- 2 石炭燃焼排煙のクリーン化
- 3 石炭液化油の化学構造と物性推算

## エネルギー転換制御分野

環境と調和した石炭等各種炭素系資源の利用の基本として、高温熱エネルギーの生成と電磁エネルギーへの変換に関する研究を行っている。熱エネルギーの質を高め電磁エネルギーへの直接変換を可能とするために、各種燃料の純酸素燃焼炎とアルカリ金属化合物添加による燃焼プラズマの生成、これを対象とした新計測法の開発、高速熱プラズマ現象の解析、高熱流束・高電流に耐える材料の実験解析、MHD発電を主とする電磁エネルギーへの転換と新しい高効率複合エネルギーシステムの研究を行っている。

### 研究課題

- 1 炭素系燃料の超高温燃焼と燃焼プラズマの生成
- 2 燃焼プラズマの新しい計測法
- 3 高速熱プラズマ現象の解析
- 4 耐高熱流束・高電流材料の実験解析
- 5 高効率MHD複合エネルギーシステム

## 極限材料工学分野（超高压電子顕微鏡研究室）

新エネルギー源として期待されている核融合炉、原子炉ならびに燃焼プラズマなど、非常に苛酷な使用環境に耐える材料の研究開発を主に行っている。超高压電子顕微鏡(1300kV)をはじめ各種の電子顕微鏡やイオン加速器を活用して、極限状況下での材料の研究を進めている。高分解能電子顕微鏡の使用により、原子レベルでの解析・評価を行っており、半導体材料などの高機能材料の構造物性研究にも着手している。

### 研究課題

- 1 材料開発基礎 ―高熱負荷材料の損傷解析―
- 2 合金における照射誘起偏析挙動の解明
- 3 合金及び半導体のイオン注入による表面改質
- 4 半導体界面の(原子)構造解析及び評価
- 5 固体物性を対象としたコンピューターシミュレーション

(平成7年度)

3. 研究報告

3. 1 学術論文

3. 2 総説, 解説, 評論等

3. 3 著書

3. 4 学術講演

### 3. 研 究 報 告

#### 3. 1 学術論文

##### 3. 1 - 1 学術論文

[炭素系資源転換反応分野]

- 1) Formation of Free Radicals during Drying and Oxidation of a Lignite and a Bituminous Coal  
R. M. Carr, H. Kumagai, B. M. Peake, B. H. Robinson, A. H. Clemens and T. W. Matheson  
Fuel, 74(3): 389-394(1995)
- 2) ベンチスケール石炭直接液化反応器の反応解析  
井戸川清, 佐々木正秀, 池上真志樹, 永石博志, 成田英夫, 佐々木皇美  
小谷川毅, 福田隆至, 山本光義, 吉田忠, 前河涌典, 千葉忠俊  
日本エネルギー学会誌, 74(3): 161-169(1995)
- 3) A Model Structure of Zao Zhuang Bituminous Coal  
K. Nakamura, T. Takanohashi, M. Iino, H. Kumagai, M. Sato, S. Yokoyama and Y. Sanada  
Energy & Fuels, 9(6): 1003-1010(1995)
- 4) An Additional Carbon Layer over the Surface of C/C Composite Substrate with the Aid of Polyvinyl Chloride  
T. Ueda, T. Morimoto, H. Kumagai and Y. Sanada  
Carbon, 33(1): 73-78(1995)
- 5) Carbonization of Pitches in Air Blowing Batch Reactor  
J. H. Choi, H. Kumagai, T. Chiba and Y. Sanada  
Carbon, 33(2): 109-114(1995)
- 6) Air-Blowing Reactions of Pitch: Oxidation of Aromatic Hydrocarbons  
C. Yamaguchi, J. Mondori, A. Matsumoto, H. Honma, H. Kumagai and Y. Sanada  
Carbon, 33(2): 193-201(1995)
- 7) 2. 4ton/day 石炭直接水添液化 PDUスラリー予熱器におけるスラリー粘度変化の推算  
山口宏, 横山敬, 真田雄三, 千葉忠俊  
化学工学論文集, 21(4): 707-714(1995)
- 8) Surface Chemistry of Carbon Black through Curing Process of Epoxy Resin  
M. Nakahara, T. Takada, H. Kumagai and Y. Sanada  
Carbon, 33(11): 1537-1540(1995)

- 9) ESRを用いたエアープロンピッチの特性評価  
崔 在薫, 熊谷治夫, 真田雄三  
炭素, No. 167: 108-115(1995)

[炭素系資源評価分野]

- 1) Formation of Protonic Acid Sites from Hydrogen Molecules and Their Roles in Acid-Catalyzed Reactions  
H. Hattori, T. Shishido, J. Tsuji, T. Nagase, H. Kita  
Proc. Science and Technology in Catalysis 1994, Kodansha-Elsevier, 93-98(1995)
- 2) Highly Active Absorbent for SO<sub>2</sub> Removal Prepared from Coal Fly Ash  
Tsuchiai, T. Ishizuka, T. Ueno, H. Hattori and H. Kita  
Ind. Eng. Chem. Res., 34: 1404-1411(1995)
- 3) <sup>29</sup>Si-NMR study of the absorbent for flue gas desulfurization  
H. Hattori, N. Kanuka and R. Kanai  
Coal Science I&II., 1875-1878(1995)
- 4) Reduction of NO on Au single-crystal electrodes in alkaline solution<sup>1</sup>  
S. Suzuki, T. Nakato, H. Hattori and H. Kita  
Journal of Electroanalytical Chemistry, 396: 143-150(1995)
- 5) Thermal Activation of KF/Alumina Catalyst for Double Bond Isomerization and Michael Addition  
H. Tsuji, H. Kabashima, H. Kita and H. Hattori  
React. Kinet. Catal. Lett., 56(2), 363-369(1995)
- 6) The State of Platinum in a Pt/SO<sub>4</sub><sup>2-</sup>/ZrO<sub>2</sub> Super Acid Catalyst  
T. Tanaka, T. Shishido, H. Hattori, K. Ebitani and S. Yoshida  
Physica B 208 & 209, 649-650(1995)
- 7) Cationic Mobility in MgX Zeolite: An FTIR Study  
G. Martra, N. Damilano, S. Coluccia, H. Tsuji and H. Hattori  
J. Chem. Soc. Faraday Trans., 91(17), 2961-2964(1995)
- 8) Chemical Structure of Organic Sulfur Compounds in Extracted Oils and Hydrogenated Oils Derived from Coals Examined by Means of GC-FPD and GC-LVEI MS  
S. Yokoyama, A. Ohtani, M. Muraji, H. Sugibuchi, M. M. Y. Bakr, M. Satou and Y. Sanada  
石油学会誌, 38(2): 97-104(1995)
- 9) 石炭水素化分解生成オイルのGC-MS/MS分析  
横山 晋, 中村久志, 伊藤好江, 佐藤正昭, 真田雄三, 鈴木 優, 野原 勉  
日本エネルギー学会誌 74(8): 722-730(1995)

- 10) Vapor Pressure Estimation for Hydrocarbons in a Coal Derived Liquid  
S. Harikae, M. Satou, T.Chiba, S. Yokoyama and Y. Sanada  
Coal Science and Technology Vol.24, Coal Science Volume II,  
J. A. Pajares and J. M. D. Tascon, Eds., Elsevier, Amsterdam,  
The Netherlands, 1451-1454(1995)
- 11) Refining of Coal Liquid - Structural Analysis of Hydrogenated SRC-II distillates with  
HPLC-GC/MS -  
K. Tanabe, M. Satou, S. Yokoyama and Y. Sanada  
石油学会誌, 38(5): 333-344(1995)

[エネルギー転換制御分野]

- 1) アルカリ添加燃焼ガスの輻射吸収計測法における新しい関係式  
粥川尚之, 山崎康男  
日本機械学会論文集(B), 61(585):1921-1927(1995)
- 2) The Effects of Plasma Fluctuation in MHD Generators (Studies with a Numerical  
Turbulence Model)  
N. Kayukawa  
JSME Int. J., 38(3(B)):366-373(1995)
- 3) 流体変動を伴う弱電離プラズマの相関電流の評価  
及川俊一, 三井恒明, 粥川尚之, 青木義明, 榎戸武揚  
電気学会論文誌B (電力・エネルギー部門誌) ,  
115-B(9):1116-1122(1995)
- 4) On Applicability of Optical Depth-Atomic Absorption Relationship to Measurements of  
Alkali-Seeded Combustion Flames  
N. Kayukawa  
Thermochemica Acta(Special issue), 267(7):107-115(1995)
- 5) Plasma Diagnostics of Magnetohydrodynamic Generators  
N. Okinaka, S. Oikawa, S. Yatsu, Y. Aoki and N. Kayukawa  
Int. J. of Applied Electromagnetics and Mechanics, 6:207-220(1995)
- 6) Consideration of Optimal Magnet Coil Design Using Nb-Ti Superconductor for 200  
MWe Magnetohydrodynamic Generator  
R. Nishimura, Y. Aoki and N. Kayukawa  
Jpn. J. Appl. Phys., 34:2504-2512(1995)
- 7) Intermittent Plasma Chaos Generated by Forced Oscillating Magnetic Field  
S. Yatsu, A. Iobe, Y. Abe and N. Kayukawa  
Proc. of the International Conference on Dynamical Systems and Chaos,  
World Scientific, Vol.2(Physics), 308-311(1995)

[極限材料工学分野]

- 1) Facilities for in situ ion beam studies in transmission electron microscopes  
C. W. Allen, S. Ohnuki and H. Takahashi  
Trans. Mat. Res. Soc. Jpn. ,17:93-96(1994)
- 2) Microchemical change and grain boundary migration due to excess defects flow under irradiation  
H. Takahashi, N. Hashimoto and S. Watanabe  
Materials for Advanced Energy Systems & Fission and Fusion Engineering '94,  
edited by A. Kohyama et al., JCSTEA 7 Series Symposium, 386-391(1994)
- 3) Solid transmutation effect in fusion reactor materials  
S. Ohnuki, H. Kinoshita and H. Takahashi  
ibid., 413-416(1994)
- 4) Mechanical properties of neutron-irradiated lower activated Fe-Cr-Mn alloys  
H. Takahashi, S. Ohnuki and H. Kinoshita  
Sci. Rep. RITU, A40(1):63-67(1994)
- 5) Concentration dependence of radiation induced segregation  
S. Watanabe, N. Sakaguchi, H. Kinoshita and H. Takahashi  
J. Nucl. Mater., 226:330-331(1995)
- 6) Quantitative studies of irradiation-induced segregation and grain boundary migration in Fe-Cr-Ni alloy  
S. Watanabe, N. Sakaguchi, N. Hashimoto and H. Takahashi  
J. Nucl. Mater., 224:158-168(1995)
- 7) Grain Boundary Segregation Under Irradiation in a HVEM  
H. Takahashi, T. Kato, S. Watanabe and N. Sakaguchi  
Annales De Physique 20:C3-109 -C3-116(1995)
- 8) Phase transformation induced by irradiating an  $\text{Al}_{62}\text{Cu}_{25.5}\text{Fe}_{12.5}$  icosahedral quasicrystal  
R. Wang, X. Yang, H. Takahashi and S. Ohnuki  
J. Phys., Condens. Matter 7:2105-2114(1995)
- 9) Influence of transmutation on microstructure, density change, and embrittlement of vanadium and vanadium alloys irradiated in HFIR  
S. Ohnuki, H. Takahashi, K. Shiba, A. Hishinuma, J. E. Pawel and F. A. Garner  
J. Nucl. Mater., 218:217-223(1995)
- 10) 酸化物分散強化フェライト鋼の電子線照射挙動  
万 発栄, 黄 学牢, 孔 峰, 緒 武揚, 肖 紀美, 高橋平七郎  
Acta Metallurgica Sinica, 30(10) :448-452(1994)

### 3. 1-2 その他の学術論文

#### [エネルギー転換制御分野]

- 1) 石炭ガス化MHD-ブレイトン複合サイクルの基礎的検討  
粥川尚之, 青木義明, 沖中憲之, 谷津茂男  
平成7年度電気学会電力・エネルギー部門大会論文集II, 219-220(1995)
- 2) 画像処理用非対称アーベル変換の精度  
大山裕之, 谷津茂男, 青木義明, 粥川尚之  
第26回画像工学コンファレンス論文集, 137-140(1995)

#### [極限材料工学分野]

- 1) 照射下における粒界移動ならびに偏析に及ぼす結晶方位の影響  
橋本直幸, 高橋平七郎, 木下博嗣  
北海道大学工学部研究報告, No. 172:33-38(1995)
- 2) Influence of transmutation on microstructure, density change, and embrittlement of vanadium and vanadium alloys irradiated in HFIR  
S. Ohnuki, H. Takahashi, K. Shiba, A. Hishinuma, J. Pawel and F. A. Garner  
Fusion Materials, DOE/ER-0313/16:293-302(1994)



### 3. 2 総説, 解説, 評論等

#### [炭素系資源転換反応分野]

- 1) (総説) 計算機化学の石炭構造研究への応用  
村田 聡, 三浦雅博, 野村正勝, 鷹觜利公, 飯野 雅, 熊谷治夫,  
真田雄三, 中村和夫  
日本エネルギー学会誌, 74(6): 342-351(1995)
- 2) (総説) 炭素のふしぎ  
真田雄三  
ペトロテック, 18(12): 1000-1002(1995)

#### [炭素系資源評価分野]

- 1) (総説) ファインケミカルズと固体塩基触媒  
服部 英, 辻 秀人  
触媒誌, 37: 2-9(1995)
- 2) (総説) 塩基性触媒としてのゼオライトによる新しい反応  
服部 英  
ゼオライト, 12: 2-7(1995)
- 3) (総説) Heterogeneous Basic Catalysis  
H. Hattori  
Chem. Rev., 95(3): 537-558(1995)
- 4) (総説) 固体塩基触媒による有機合成  
服部 英  
PETROTECH, 18(6): 473-478(1995)
- 5) (総説) トルエンの側鎖アルキル化  
服部 英  
PETROTECH, 18(10): 842-843(1995)

#### [極限材料工学分野]

- 1) (解説) 高エネルギー粒子線照射による核変換反応を利用した組成制御と  
新材料  
高橋平七郎, 野田哲二  
まてりあ, 34(8):966-968(1995)

### 3. 3 著 書

#### 3. 3－2 共 著

[エネルギー転換制御分野]

1) プラズマダイナミクス, 1-160

粥川尚之, 青木義明

プラズマダイナミクス (翻訳), 講談社サイエンティフィック, 東京  
(1995)

### 3. 4 学術講演

#### 3. 4 - 1 学術講演

[炭素系資源評価分野]

- 1) Hydrogen Effects on the Catalytic Cracking for Liquid Fuel  
H. Hattori, T. Shishido, T. Nagase and K. Higo  
17th Symposium on Efficient Use of Energy and Direct Electrical Power  
Generation, Sapporo (1995)
- 2) Mechanistic Study of the Flue Gas Desulfurization by Absorbent Prepared from Coal  
Fly Ash  
服部 英  
An International Workshop on Environmental Catalysis Technology, 浦項市,  
韓国(1995)

[エネルギー転換制御分野]

- 1) 2 波長輻射吸収法における燃焼プラズマ温度・発光原子数密度の新測定式  
粥川尚之  
平成 7 年度宇宙輸送シンポジウム, 相模原 (1995)

[極限材料工学分野]

- 1) Effect of He on microstructural development during ion/electron dual irradiation of 1st  
wall candidate alloy  
H. Takahashi, Y. Hidaka and S. Watanabe  
17th Symposium on Efficient Use of Energy and Direct Electrical Power  
Generation, Center for Advanced Research of Energy Technology,  
Hokkaido University, 8-17(1995)
- 2) 点欠陥のクラスターリング過程の観察と解析  
大貫惣明, 高橋平七郎, 日高康善  
日本電子顕微鏡学会第40回シンポジウム, 札幌 (1995)

### 3. 4 - 2 その他の学術講演

[炭素系資源転換反応分野]

- 1) 非・微粘結炭の性状評価に関する研究  
竹村佳朗, 熊谷治夫, 真田雄三  
日本化学会第69回春季年会, 京都(1995)
- 2) 水の脱離に伴う褐炭の高次構造変化  
則永行庸, 熊谷治夫, 真田雄三, 佐々木正秀, 小谷川毅  
日本化学会第69回春季年会, 京都(1995)
- 3)  $\text{MoSi}_2$ -SiC 複合材料の高温酸化挙動  
黒川一哉, 宇部誠, 真田雄三  
金属学会春期大会, 東京 (1995)
- 4) Effect of Riser Height and Downcomer Solids Inventory on Dense-Bed Height in a CFB Riser  
T. Hirama, K. Kuramoto and T. Chiba  
Engineering Foundation Conference on Fluidization, Tours, France (1995)
- 5) 石炭ペレット炭化反応中のガス発生速度  
松岡浩一, 川井仁, 熊谷剛彦, 千葉忠俊  
化学工学会新潟大会, 新潟(1995)
- 6) 塩化揮発処理による石炭灰物性変化  
嶋田太平, 千葉忠俊, 熊谷剛彦, 鶴江孝, 中田善徳, 奥谷猛, 武田詔平  
化学工学会新潟大会, 新潟(1995)
- 7) Change in the Conformation of Lignite Molecule during Moisture Release Process  
K. Norinaga, H. Kumagai, Y. Sanada, M. Sasaki and T. Kotanigawa  
8th International Conference on Coal Science, Oviedo, Spain(1995)
- 8) A Model Structure of Zao Zhuang Bituminous Coal  
T. Takanohashi, M. Iino, H. Kumagai, Y. Sanada and K. Nakamura  
8th International Conference on Coal Science, Oviedo, Spain (1995)
- 9) Interaction Between Coal and Mixed Solvent System by Means of L-band EPR  
K. Matsuoka, H. Kumagai and Y. Sanada  
8th International Conference on Coal Science, Oviedo, Spain (1995)
- 10) ヨウ化リチウム添加による褐炭の熱分解特性の変化  
村岡淳一, 熊谷治夫, 千葉忠俊, 真田雄三  
日本エネルギー学会第32回石炭科学会議, 東京(1995)
- 11) 混合溶媒中での石炭の高次構造変化  
松岡献二郎, 熊谷治夫, 千葉忠俊, 真田雄三  
日本エネルギー学会第32回石炭科学会議, 東京(1995)

- 12) Chlorination Characteristics of Minerals in Coal Ashes  
T. Shimada, T. Kumagai, S. Takeda and T. Chiba  
45th Canadian Chemical Engineering Conference, Quebec, Canada (1995)

- 13) ピッチ類の凝集構造と炭化特性の関係  
吉田憲博, 熊谷治夫, 千葉忠俊, 真田雄三, 齊藤恒夫  
第22回炭素材料学会年会, 長崎(1995)

[炭素系資源評価分野]

- 1) チオフェン類の沸点推算  
三国真紀, 佐藤正昭, 横山 晋, 真田雄三  
日本化学会第69春季年会, 京都(1995)
- 2) 固体塩基触媒を用いたニトロメタンのマイケル付加  
渋谷 忠, 桃島 一, 喜多英明, 服部 英  
日本化学会第69春季年会, 京都 (1995)
- 3) Cs添加ゼオライトの塩基触媒反応特性と反応選択性  
八木冬樹, 喜多英明, 服部 英  
日本化学会第69春季年会, 京都 (1995)
- 4)  $\text{CaCO}_3$  を利用した排煙脱硫・脱硝反応の研究  
町田崇一郎, 金井隆一, 喜多英明, 服部 英  
日本化学会第69春季年会, 京都 (1995)
- 5)  $\text{MgO}$ ,  $\text{CaO}$  表面上に吸着した  $\text{CO}_2$  の昇温過程における挙動  
岡村明恵, 辻 秀人, 喜多英明, 服部 英  
日本化学会第69春季年会, 京都 (1995)
- 6) Al 修飾メソポーラスシリケートの固体酸特性  
濱口光一, 八木冬樹, 中戸晃之, 服部 英  
第38回石油学会年会, 東京 (1995)
- 7) Pt 担持  $\text{Al}_2\text{O}_3$  系触媒を用いたヘプタンの異性化における共存水素の効果  
肥後健太郎, 辻 純平, 長瀬宇弘, 宍戸哲也, 服部 英  
第38回石油学会年会, 東京 (1995)
- 8)  $^{29}\text{Si}$ -NMR Study of the Absorbent for Flue Gas Desulfurization  
H. Hattori, N. Kanuka, R. Kanai  
8th International Conference on Coal Science, Oviedo, Spain (1995)
- 9) Vapor Pressure Estimation for Hydrocarbons in a Coal Derived Liquid  
S. Harikae, M. Satou, T. Chiba, S. Yokoyama and Y. Sanada  
8th International Conference on Coal Science, Oviedo, Spain (1995)

- 10)  $\text{MoO}_3/\text{Al}_2\text{O}_3$  参照触媒の  $\text{NH}_3$ -TPD, TPRによる評価  
 穴戸哲也, 服部 英  
 第76回触媒討論会, 室蘭 (1995)
- 11)  $^{29}\text{Si}$ -NMR Study of the Absorbent for Flue Gas Desulfurization  
 H. Hattori  
 環境触媒フォーラム国際特別シンポジウム, 東京 (1995)
- 12) 石炭液化油オイル分の蒸気圧推算 (3) ヘテロ化合物の蒸気圧推算および熱力学的考察  
 小野俊哉, 佐藤正昭, 張替伸也, 真田雄三, 千葉忠俊  
 石油学会第25回石油・石油化学討論会, 伊勢 (1995)

[エネルギー転換制御分野]

- 1) Reconstructing Local Plasma Intensity Profile by Asymmetric Abel Inversion  
 H. Oyama, S. Yatsu, Y. Aoki, N. Kayukawa and T. Okuo  
 The 33rd Symposium on Engineering Aspects of MHD, Tennessee (1995)
- 2) Functionally Gradient Material Electrodes for a Coal-fired MHD Channel  
 H. Usami, Y. Aoki, N. Kayukawa and T. Okuo  
 ibid., Tennessee (1995)
- 3) On the MHD-Braiton Combined Cycle with Coal-Gasification  
 N. Kayukawa, Y. Aoki, N. Okinaka and S. Yatsu  
 The 17th Symposium on Efficient Use of Energy and Direct Electrical Power Generation, Sapporo (1995)
- 4) Research on Tungsten/Copper - FGM Electrodes  
 H. Usami, Y. Aoki, N. Kayukawa and T. Okuo  
 ibid., Sapporo (1995)
- 5) Reconstructing Local Plasma Intensity Profile  
 H. Oyama, S. Yatsu, Y. Aoki and N. Kayukawa  
 ibid., Sapporo (1995)
- 6) Investigation of the NPG on the Effects of Oxygen Dissociation / Recombination and Condensed Light Metal Oxide  
 S. Oikawa, N. Kayukawa, Y. Aoki and T. Enoto  
 ibid., Sapporo (1995)
- 7) 10MWth級MHD発電チャネルの3次元数値解析  
 西山正人, 青木義明, 沖中憲之, 谷津茂男, 粥川尚之  
 電気学会 新・省エネルギー研究会, 東京 (1995)
- 8) 石炭燃料MHD発電チャネル用 $\text{Y}_2\text{O}_3$ -W電極の実験研究  
 宇佐見英明, 青木義明, 粥川尚之, 奥尾隆保  
 同上, 東京 (1995)

- 9) 画像データのAbel変換処理におけるノイズの影響評価  
大山裕之, 谷津茂男, 青木義明, 粥川尚之  
同 上, 東京 (1995)
- 10) MHDプラズマゆらぎのスペクトル解析  
沖中憲之, 谷津茂男, 青木義明, 粥川尚之  
同 上, 東京 (1995)
- 11) EPI法による流速測定における高速化の検討  
三橋健治, 沖中憲之, 谷津茂男, 青木義明, 粥川尚之  
同 上, 東京 (1995)
- 12) MRIによるMHDプラズマ流れの可視化の検討  
水沢英男, 沖中憲之, 谷津茂男, 青木義明, 粥川尚之  
同 上, 東京 (1995)
- 13) MHD発電チャンネル内の3次元電磁流体数値解析  
西山正人, 青木義明, 沖中憲之, 谷津茂男, 粥川尚之  
平成7年度電気関係学会北海道支部連合大会, 札幌 (1995)
- 14) MHDプラズマ中のカリウムスペクトルの測定  
小野照幸, 沖中憲之, 谷津茂男, 青木義明, 粥川尚之  
同 上, 札幌 (1995)
- 15) Abel変換を用いた画像処理でのノイズの影響評価  
大山裕之, 谷津茂男, 青木義明, 粥川尚之  
同 上, 札幌 (1995)
- 16) EPI法を用いたMHDプラズマ流速測定における高速化の試案  
三橋健治, 沖中憲之, 谷津茂男, 青木義明, 粥川尚之  
同 上, 札幌 (1995)
- 17) EPI法によるMHDチャンネル内2次流れ分布の計測  
水沢英男, 沖中憲之, 谷津茂男, 青木義明, 粥川尚之  
同 上, 札幌 (1995)
- 18) MHD発電機内アーク現象の時間一周波数解析  
沖中憲之, 谷津茂男, 青木義明, 粥川尚之  
同 上, 札幌 (1995)
- 19) W-Cu傾斜組成材のMHD発電用電極への適用  
青池 聡, 沖中憲之, 谷津茂男, 青木義明, 粥川尚之  
同 上, 札幌 (1995)
- 20) 石炭燃焼MHD発電チャンネル用改良型タングステン電極  
宇佐見英明, 青木義明, 粥川尚之, 奥尾隆保  
同 上, 札幌 (1995)

- 21) 高効率- $\text{CO}_2$ 循環MHD-気力複合発電システムの検討  
大石 茂, 沖中憲之, 谷津茂男, 青木義明, 粥川尚之, 及川俊一, 石川本雄  
同 上, 札幌 (1995)
- 22) 石炭ガス化MHD複合サイクルの基礎的検討  
富山みゆき, 粥川尚之, 沖中憲之, 谷津茂男, 青木義明  
同 上, 札幌 (1995)
- 23)  $\theta$  ピンチプラズマ振動モードの時間一周波数スペクトル解析  
新美大伸, 赤木憲二, 谷津茂男, 沖中憲之, 青木義明, 粥川尚之  
同 上, 札幌 (1995)
- 24) 小振幅振動磁場印加によるピンチプラズマ挙動の解析  
赤木憲二, 新美大伸, 谷津茂男, 沖中憲之, 青木義明, 粥川尚之  
同 上, 札幌 (1995)
- 25) MHD燃焼プラズマ画像からの温度分布測定  
大山裕之, 谷津茂男, 青木義明, 粥川尚之  
日本原子力学会北海道支部第13回研究発表会, 札幌 (1995)
- 26) 石炭燃焼MHD発電用電極の実験研究  
宇佐見英明, 青木義明, 沖中憲之, 粥川尚之, 奥尾隆保  
同 上, 札幌 (1995)

[極限材料工学分野]

- 1) Theoretical and experimental studies of irradiation-induced grain boundary migration depending on orientation  
H. Takahashi, N. Sakaguchi, N. Hashimoto and S. Watanabe  
7th International Conference Intergranular and Interphase Boundaries in Materials, Lisbon (1995)
- 2) Grain boundary segregation under irradiation in a HVEM  
H. Takahashi, S. Watanabe and N. Hashimoto  
The 4th Japan-France Materials Science Seminar on Structural Evolution in Materials: The Dependence on Atomistic Phenomena, Fontainebleau (1995)
- 3) Effect of additional minor elements on void nucleation in stainless steels under simultaneous irradiation with Helium ions and electrons  
H. Takahashi, Y. Hidaka, S. Watanabe, H. Tsuchida, N. Sakaguchi and S. Ohnuki  
7th International Conference on Fusion Reactor Materials, Obninsk (1995)
- 4) Unusual Response of the binary V-2Si Alloy to Neutron Irradiation in FFTF at 430-600 °C  
S. Ohnuki, H. Kinoshita, F. A. Garner and H. Takahashi  
ibid., Obninsk (1995)



- 5) Transmutation-induced embrittlement of V-Ti-Ni and V-Ni alloys in HFIR  
S. Ohnuki, F. A. Garner, J. E. Pawel, H. Takahashi, K. Shiba and A. Hishinuma  
ibid., Obninsk (1995)
- 6) Effect of W, V on irradiation swelling resistance and phase stability in a Fe-Cr-Mn austenitic steel  
H. Benfu and H. Takahashi  
The 3rd Sino-Japanese Symposium on Materials for Advanced Energy Systems and Fission and Fusion Engineering, Chengdu (1995)
- 7) Irradiation behaviors of Fe-Cr-Ni-xP-yTi alloy under electrons /He ions dual irradiation  
H. Takahashi, H. Tsuchida, Y. Hidaka, H. Kinoshita and S. Watanabe  
ibid., Chengdu (1995)
- 8) Effect of crystal orientation on grain boundary migration and radiation-induced segregation  
N. Hashimoto, Y. Eda and H. Takahashi  
The 117th Meeting of JIM on International Symposia on Advanced Materials and Technology for the 21st Century, Honolulu (1995)
- 9) In-situ observation of austenitic stainless steel during dual beam irradiation  
H. Tsuchida, S. Mochizuki, Y. Hidaka, S. Watanabe and H. Takahashi  
ibid., Honolulu (1995)
- 10) A computational study of RIS at grain boundary  
N. Sakaguchi, S. Watanabe and H. Takahashi  
ibid., Honolulu (1995)
- 11) The defect cluster formation and stability of oxide particles in austenitic ODS steel during electron irradiation  
H. Sasaki, H. Kato, S. Ohnuki, H. Takahashi, K. Okada, S. Ukai, N. Akasaka and I. Shibahara  
ibid., Honolulu (1995)
- 12) In-situ observation of defect cluster formation in metals and semiconductors by means of HVEM  
S. Ohnuki, T. Suda, N. Kawakami and H. Takahashi  
ibid., Honolulu (1995)
- 13) Role of Mn on decrease of Cr depletion at grain boundary in austenitic alloy irradiated with electrons  
S. Kasahara, K. Nakata and H. Takahashi  
ibid., Honolulu (1995)
- 14) RIS at grain boundary in Fe-Cr-Ni alloys system: Effect of temperature variation  
S. Watanabe, J. Satou, H. Kinoshita, N. Sakaguchi and H. Takahashi  
ibid., Honolulu (1995)
- 15) Effect of Ni and Cr concentration on grain boundary segregation in Fe-Cr-Ni alloys  
H. Kinoshita, S. Watanabe, and H. Takahashi

ibid., Honolulu (1995)

- 16) Computational study of grain boundary segregation under irradiation in stainless steels  
S. Watanabe and H. Takahashi  
International Symposium on Plant Aging and Life Prediction of Corrodible Structures, Sapporo (1995)
- 17) Modeling radiation-induced segregation  
S. Watanabe  
US/Japan Workshop on Theory and Modeling of Irradiation Effects in Materials for Fusion Energy System, Livermore (1995)
- 18) 分散強化型合金中の微粒子の電子顕微鏡観察  
大貫惣明, 佐々木仁, 高橋平七郎  
平成6年度第36回日本電子顕微鏡学会北海道支部学術講演会,  
旭川 (1995)
- 19) 転位ループ内部の空孔型欠陥形成に及ぼすHeの影響  
日高康善, 高橋平七郎  
同上, 旭川 (1995)
- 20) ODS316鋼の熱処理挙動と電子線照射効果  
佐々木仁, 加藤 元, 大貫惣明, 高橋平七郎, 岡田浩一, 鶴飼重治,  
赤坂尚昭, 柴原 格  
日本金属学会1995年春期(第116回)大会, 東京 (1995)
- 21) Fe-Cr-Ni-xP-yTi系合金の電子線/Heイオン同時照射効果  
土田博思, 日高康善, 渡辺精一, 高橋平七郎  
同上, 東京 (1995)
- 22) 電子線照射したFe-Cr-Ni-Mn合金におけるCrの照射誘起粒界偏析挙動  
笠原茂樹, 仲田清智, 大貫惣明, 高橋平七郎  
同上, 東京 (1995)
- 23) Fe-Cr-Ni合金の粒界偏析に及ぼすNi濃度の影響  
木下博嗣, 渡辺精一, 高橋平七郎  
同上, 東京 (1995)
- 24) 照射下における粒界移動に及ぼす冷間加工の影響  
橋本直幸, 江田陽一, 高橋平七郎  
同上, 東京 (1995)
- 25) 粒界移動を伴う照射誘起偏析の定量的解析  
坂口紀史, 渡辺精一, 橋本直幸, 高橋平七郎  
同上, 東京 (1995)
- 26) Gibbsian偏析の照射誘起偏析に及ぼす影響  
渡辺精一, 坂口紀史, 高橋平七郎  
同上, 東京 (1995)

- 27) HFIR照射したV合金の核変換効果 (Ⅱ)  
大貫惣明, 高橋平七郎, 芝 清之, 菱沼章道, F. A. Garner  
同上, 東京 (1995)
- 28) イオン注入したSi中の二次欠陥分布  
石田秀幸, 横山拓也, 高橋平七郎, 大貫惣明, 阿部征吾, 木村幸治, 成瀬宏,  
阿部正泰  
日本電子顕微鏡学会第51回学術講演会, 堺(1995)
- 29) オーステナイト系モデル合金における照射誘起粒界移動に及ぼす冷間加工の影響  
江田陽一, 橋本直幸, 高橋平七郎  
平成7年度日本鉄鋼協会日本金属学会両支部合同夏季講演大会,  
室蘭(1995)
- 30) 鋼の繰り返し急速加熱・冷却による表面亀裂発生について  
相沢大器, 渡辺精一, 高橋平七郎, 吉永 泰, 正田満志, 石坂淳二  
同上, 室蘭 (1995)
- 31) TEM-EDS分析における濃度分布評価に及ぼすプローブ径の影響  
黒目和也, 渡辺精一, 坂口紀史, 木下博嗣, 高橋平七郎  
同上, 室蘭(1995)
- 32) SiO<sub>2</sub> 基板上の多結晶Siの形成挙動  
川上奈緒美, 須田孝徳, 大貫惣明, 高橋平七郎  
同上, 室蘭(1995)
- 33) イオン注入したSi中の二次欠陥分布  
石田秀幸, 高橋平七郎, 阿部征善, 木村幸治, 成瀬宏, 阿部正泰  
同上, 室蘭(1995)
- 34) 酸化物分散合金の分散相界面の微細構造解析  
神田北斗, 高橋平七郎, 池田省三, 井形直弘  
同上, 室蘭(1995)
- 35) SUS316L鋼の照射損傷挙動に及ぼすSi, Ti, Zrの複合添加効果  
金田潤也, 青野泰久, 加藤隆彦, 高橋平七郎  
(社)日本原子力学会「1995年秋の大会」, 東海村(1995)
- 36) Fe-Cr-Ni合金の粒界偏析に及ぼす組成および内部シンクの影響  
木下博嗣, 渡辺精一, 高橋平七郎  
同上, 東海村(1995)
- 37) 照射誘起粒界偏析に及ぼす組成および内部シンクの影響  
木下博嗣, 渡辺精一, 高橋平七郎  
第1回核融合エネルギー連合講演会, 京都(1995)

# 学 術 論 文

## Formation of free radicals during drying and oxidation of a lignite and a bituminous coal

R. Melville Carr, Haruo Kumagai, Barrie M. Peake, Brian H. Robinson, Anthony H. Clemens\* and Trevor W. Matheson\*

Chemistry Department, University of Otago, Box 56, Dunedin, New Zealand

\* Coal Research Association of New Zealand Inc., PO Box 31-244, Lower Hutt, New Zealand

(Received 20 August 1993; revised 5 May 1994)

The changes in radical concentrations and species brought about by vacuum and gas flow drying of New Vale lignite and Stockton bituminous coal samples were studied. Vacuum drying produces a sudden increase in concentration, flow drying a more gradual but ultimately greater one. For both coals the changes depend on a balance between decarboxylation, which produces new radical sites, and removal of moisture from heteroatomic sites within the coal macrostructure. This balance is influenced by the drying method used. Exposure of dried samples to dry air produces changes in radical concentration consistent with the findings of previous oxidation studies of these coals.

(Keywords: coal; drying; free radicals)

Since the first reports of the use of electron paramagnetic resonance (e.p.r.) to detect free radicals in coals<sup>1,2</sup>, the technique has been applied to a wide variety of coals and become a well-established coal research tool. The main interest has been in the organic free radical signal ( $g$ -value  $\sim 2.00$ ) and there have been many reports of changes in  $g$ -value, linewidth and intensity of this signal in relation to coal characteristics such as chemical composition and rank<sup>3–6</sup>. There have also been many attempts to establish links between e.p.r. parameters and coal liquefaction<sup>4,7</sup>, carbonization<sup>4,8</sup> and oxidation<sup>9–16</sup>.

E.p.r. studies of the coal drying process are comparatively few, even though drying is often a prerequisite to subsequent utilization and may significantly alter coal properties, the increased susceptibility of dried low-rank coals to spontaneous combustion being a notable example. Dack *et al.*<sup>9</sup> have reported that the spin concentration of an Australian brown coal is increased on vacuum drying, and similar results have been reported for both vacuum and nitrogen-flow drying of a Wyoming subbituminous coal<sup>17</sup>. More recent studies have used selective spin probe techniques to observe the effect of vacuum drying, weathering and oxidation on the spin concentrations in coals of widely differing rank<sup>18–21</sup>. It was found that even in higher-rank coals, the removal of water is accompanied by an increase in active sites.

These studies show that the removal of water has a profound effect on the concentration and nature of the radicals present in coals. They also imply that the method used to remove the moisture influences the outcome. To establish whether or not this is so, the present e.p.r. study of the involvement of free radicals in vacuum and nitrogen flow drying of a lignite and a bituminous coal was undertaken. Changes in spin concentration,  $g$ -values, linewidths and microwave power saturation responses<sup>22</sup>

were monitored during the drying process. Through parallel studies, differences produced by the two drying methods were highlighted, as was the different drying behaviour of the two samples. The effect of oxidation on the radical concentrations in the predried coals was also examined.

### EXPERIMENTAL

Two New Zealand coals were used: New Vale lignite and Stockton No. 2 bituminous coal, some properties of which are shown in Table 1. The samples were obtained fresh from the mine and stored as lumps under nitrogen. Before use, the lumps were reduced in size and ground to 150–300  $\mu\text{m}$  under water using a mortar and pestle. About 40 mg of ground wet coal was placed in the bottom of a 2.5 mm i.d. cylindrical quartz e.p.r. sample tube and glass wool was packed tightly on top of the coal to minimize sample loss, particularly during vacuum operations, and to maintain an approximately constant sample volume and shape. The quartz tube was fitted to a tap assembly

Table 1 Analyses of fresh coals (wt%)

	Newvale	Stockton
Moisture	27.4	1.1
Ash <sup>a</sup>	5.4	0.5
Carbon <sup>b</sup>	68.6	85.4
Hydrogen <sup>b</sup>	5.7	5.7
Nitrogen <sup>b</sup>	0.7	1.5
Sulfur <sup>b</sup>	0.4	1.2
Oxygen (diff.) <sup>b</sup>	24.6	6.2

<sup>a</sup> db

<sup>b</sup> dmmf

which allowed for easy connection to a vacuum or gas line as well as isolating the sample from the atmosphere during cooling and any subsequent e.p.r. measurements. The sample was purged with nitrogen, then cooled to  $-100^{\circ}\text{C}$  so that the e.p.r. spectrum could be measured without the difficulties associated with mobile water<sup>17</sup>.

Flow drying was carried out using a stream ( $\sim 20\text{ ml min}^{-1}$ ) of oxygen-free ( $<10\text{ ppm}$ ) nitrogen in a tube furnace preset to  $105$  or  $150^{\circ}\text{C}$  for preselected periods up to 72 h. Vacuum drying was performed at room temperature ( $\sim 18^{\circ}\text{C}$ ) and at  $105$  and  $150^{\circ}\text{C}$  by evacuating the e.p.r. tube containing the wet coal to a final pressure of  $<0.1\text{ Pa}$ . Samples were heated to drying temperature for the desired time interval then cooled to  $-100^{\circ}\text{C}$  for e.p.r. measurement. This procedure was repeated at regular intervals throughout 72 h. Equilibration for heating or cooling took  $\sim 5\text{ min}$ .

Samples selected for oxidation were predried at  $105^{\circ}\text{C}$  by a nitrogen flow for 15 h. The e.p.r. spectrum of the dried sample was measured and the sample returned to the tube furnace set to the temperature required for oxidation ( $30, 105, 150^{\circ}\text{C}$ ). The gas flow was then switched to dry air ( $20\text{ ml min}^{-1}$ ). At selected times, the gas flow was switched back to nitrogen and the sample was withdrawn from the tube furnace, cooled to  $-100^{\circ}\text{C}$  for e.p.r. measurement and then returned to the furnace for further oxidation. Oxidation was continued for 10 days.

E.p.r. spectra were recorded using a Varian E-104 X-band spectrometer with  $100\text{ kHz}$  modulation and a  $\text{TE}_{102}$  cavity. Low sample temperatures were obtained using the Varian E-254 variable-temperature unit and a thermocouple for temperature monitoring. The microwave power was determined directly from the microwave bridge console dial and was varied over the range  $0.2\text{--}200\text{ mW}$ . The microwave frequency was determined with a microwave counter. Magnetic field values, measured with a proton gaussmeter when the first-derivative e.p.r. signal changed sign, were used in the calculation of  $g$ -values. Varian strong pitch sample (no. 904550-01) with a  $g$ -value of  $2.0028$  was used as a  $g$ -value standard. Typical e.p.r. spectrometer settings were: scan  $324.0 \pm 0.2\text{ mT}$  in 4 min; time constant  $0.128\text{ s}$ ; modulation amplitude  $0.05\text{ mT}$ ; receiver gain  $2.5 \times 10^2$ ; microwave power  $1\text{ mW}$ .

The relative spin concentration ( $S$ ) was calculated using the simplified formula

$$S = I_{pp} \times B_{pp}^2$$

where  $I_{pp}$  and  $B_{pp}$  represent the intensity and peak-to-peak linewidth respectively of a given line. The relative spin concentration calculated for each sample was normalized with respect to sample weight. Selected e.p.r. spectra were resolved into several isotropic components using a VAX version of the ESRSIM program<sup>23</sup>. Each component was assumed to have a Lorentzian lineshape<sup>24</sup>.

## RESULTS AND DISCUSSION

### Drying of New Vale lignite

The e.p.r. spectrum observed at  $-100^{\circ}\text{C}$  for fresh New Vale lignite was a single broad signal with a linewidth of  $\sim 0.8\text{ mT}$  (Figure 1a). Drying under all conditions increased the intensity of this peak; the resulting changes

in relative spin concentration with time of drying are shown in Figure 2a. For vacuum drying at  $105$  and  $150^{\circ}\text{C}$  there was a rapid increase in spin concentration, reaching a maximum after  $\sim 12\text{ h}$  and then levelling off or even decreasing slightly. The increase in spin concentration was less rapid for room temperature vacuum drying but eventually reached levels similar to those at the higher temperatures.

For nitrogen flow drying ( $105, 150^{\circ}\text{C}$ ) the increase was more gradual, but the levels eventually reached, especially at  $150^{\circ}\text{C}$ , were somewhat higher than those for vacuum drying. The extremely variable percentage increase in spin concentration ( $11\text{--}218\%$ ) previously reported for vacuum drying of Victorian brown coal<sup>9</sup> was not observed in the present study.

Similar trends were observed for linewidths and  $g$ -values in that increases occurred predominantly during the initial drying stages and were more rapid for vacuum drying (Figures 2b and c).

Computer simulation of the e.p.r. spectrum of New Vale lignite indicated the presence of at least two component signals (Figure 1a). The changes in their peak intensities, linewidths and  $g$ -values on both nitrogen-flow and vacuum drying at  $150^{\circ}\text{C}$  are listed in Table 2. Vacuum drying led to doubling of the intensity of both signals, whereas nitrogen flow drying gave more than threefold increases in both. The data show that flow drying generates radicals with the same  $g$ -values as those obtained by vacuum drying, but eventually produces more of them.

Microwave power saturation measurements for drying New Vale lignite at  $150^{\circ}\text{C}$  (Figure 3) showed that the saturation curves for vacuum drying became quite similar after 4 h, consistent with a system undergoing little change after this short time. However, those obtained for flow drying continued to increase in intensity

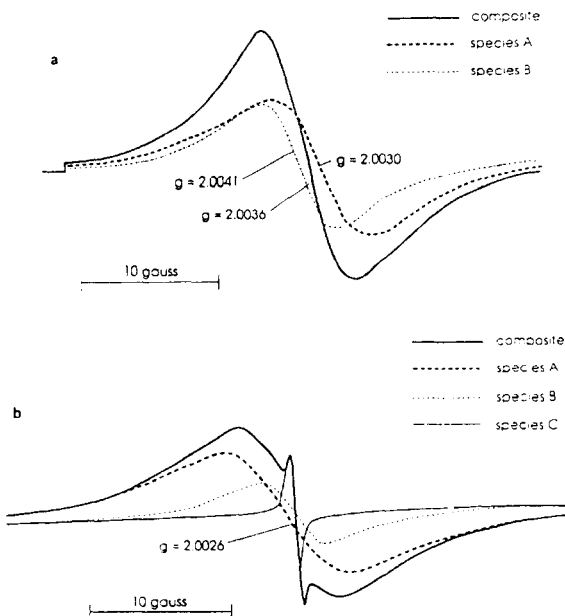


Figure 1 Observed and simulated component e.p.r. spectra at  $-100^{\circ}\text{C}$  for fresh samples of (a) New Vale lignite. (b) Stockton No. 2 bituminous coal.  $10\text{ gauss} = 1\text{ mT}$

throughout the 72 h experiment. In both cases the curves appeared to reach saturation at  $\sim 50$  mW, but it was not possible to determine whether the intensity subsequently decreased with increasing power (indicative of a homogeneously broadened signal<sup>25</sup>) or levelled off (due to non-homogeneous broadening<sup>25</sup>).

These results suggest that free radicals are present in

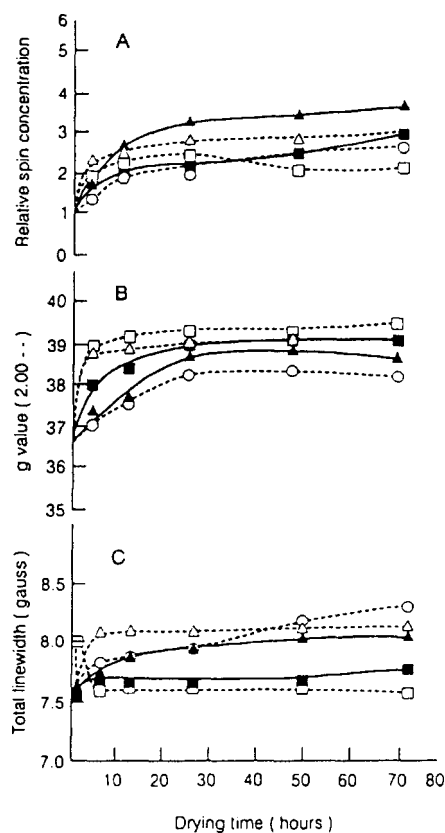


Figure 2 Variation in (A) spin concentration relative to initial wet sample, (B)  $g$ -value, (C) linewidth for New Vale lignite under different drying conditions:  $\circ$ , vacuum at room temperature;  $\triangle$ , vacuum at  $105^\circ\text{C}$ ;  $\square$ , vacuum at  $150^\circ\text{C}$ ;  $\bullet$ , nitrogen flow at  $105^\circ\text{C}$ ;  $\blacktriangle$ , nitrogen flow at  $150^\circ\text{C}$ . 10 gauss = 1 mT

the initial wet New Vale lignite and that drying under vacuum or nitrogen flow at temperatures from ambient to  $150^\circ\text{C}$  leads to increased free radical concentrations. This increased radical concentration is probably responsible, at least in part, for the increased susceptibility of dried coals to attack by oxygen<sup>9</sup>.

Similar results were obtained in previous drying studies on Victorian brown coal<sup>9</sup> and a range of North American coals<sup>14,17,19,26</sup>. The increase in radical concentration can be attributed to several factors, including the desorption of oxygen — which may lead to previously broadened signals becoming narrower and more readily observed — and to low temperature decarboxylation reactions, of which many have been reported for a variety of coals<sup>27–30</sup>. *In situ* FT-i.r. monitoring<sup>31</sup> did not indicate any decarboxylation when samples of this particular New Vale lignite were dried by nitrogen flow at  $105^\circ\text{C}$ , and subsequent heating of the dried coals to  $180^\circ\text{C}$  under argon gave only small amounts of  $\text{CO}_2$  in the off-gas<sup>32</sup>. However, the extent of decarboxylation required to produce doubling of the free radical concentration is very low<sup>9</sup>, and the possibility remains that such reactions are responsible.

Decarboxylation does not account for the accompanying  $g$ -value increases. It is known that heat-treating low-rank coals at temperatures at which  $\text{CO}_2$  evolution occurs leads to lower  $g$ -values<sup>33</sup> as heteroatomic centres are

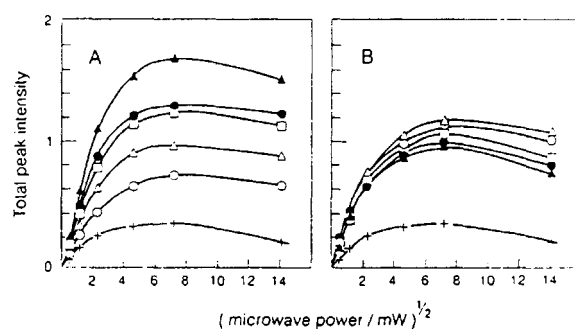


Figure 3 Microwave power saturation curves for New Vale lignite on drying at  $150^\circ\text{C}$  under (A) nitrogen flow, (B) vacuum: +, wet sample;  $\circ$ , dried 4 h;  $\triangle$ , dried 12 h;  $\square$ , dried 24 h;  $\bullet$ , dried 48 h;  $\blacktriangle$ , dried 72 h

Table 2 Simulation of e.p.r. spectra of Stockton and Newvale samples on drying at  $150^\circ\text{C}$

Sample	Drying method	Time (h)	Species A			Species B			Species C		
			Intensity	Linewidth (mT)	$g$ -value	Intensity	Linewidth (mT)	$g$ -value	Intensity	Linewidth (mT)	$g$ -value
Stockton	Vacuum	0	0.65	0.650	2.0029	0.69	0.780	2.0027	0.17	0.050	2.0026
		72	0.78	0.650	2.0030	0.81	0.780	2.0028	0.16	0.050	2.0026
	Flow	0	0.64	0.650	2.0029	0.64	0.780	2.0027	0.15	0.050	2.0026
		72	0.65	0.680	2.0031	1.51	0.800	2.0029	0.15	0.050	2.0026
Newvale	Vacuum	0	0.09	0.800	2.0030	0.08	0.600	2.0041	—	—	—
		12	0.24	0.780	2.0033	0.23	0.590	2.0044	—	—	—
		72	0.18	0.740	2.0033	0.19	0.560	2.0044	—	—	—
	Flow	0	0.10	0.800	2.0030	0.09	0.600	2.0041	—	—	—
		12	0.21	0.800	2.0033	0.21	0.615	2.0044	—	—	—
		72	0.32	0.800	2.0033	0.31	0.630	2.0044	—	—	—

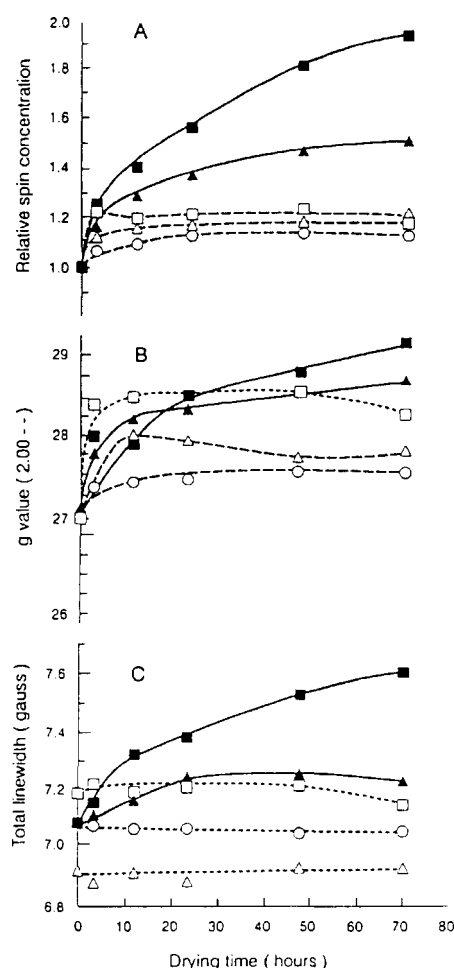


Figure 4 Variation in (A) spin concentration relative to initial wet sample, (B)  $g$ -value and (C) linewidth for the broad Stockton signal under different drying conditions. Symbols as in Figure 2

removed with the off-gases. Neither is it likely that oxygen desorption alone would account for the higher  $g$ -values observed upon drying. The  $g$ -value recorded for wet New Vale lignite (2.0036) indicates considerable interaction between unpaired electrons and heteroatomic (nitrogen or oxygen) centres<sup>34,35</sup>, in keeping with the high concentration of oxygen in this sample (Table 1). The increase in  $g$ -value (to 2.0040) shows that this interaction is considerably enhanced in the radicals formed on drying. The most likely cause of this enhancement under drying conditions is the removal of water molecules associated with oxygen sites in the coal macrostructure, allowing greater interaction between unpaired electrons and the heteroatom.

#### Drying of Stockton No. 2 bituminous coal

The e.p.r. spectrum of wet Stockton No. 2 bituminous coal (Figure 1b) contained a broad signal (linewidth  $\sim 0.8$  mT) together with a superimposed narrow signal (linewidth  $\sim 0.05$  mT,  $g = 2.0026$ ). The narrow signal showed no significant changes under any drying conditions. Changes in relative spin concentration, linewidth and  $g$ -value for the broad signal are shown in Figures 4a-c.

The trends are similar to those for the New Vale lignite, in that drying increased the spin concentration and  $g$ -value, most of the change occurring in the initial stages and flow drying, especially at 150°C, leading eventually to significantly larger increases than those associated with vacuum drying. The overall increases were much smaller than those accompanying drying of New Vale lignite, and the  $g$ -values were all significantly lower (wet 2.0027, dry 2.0028). This can be attributed to aromatic and/or aliphatic hydrocarbon free radicals and is consistent with the low nitrogen and oxygen contents of this coal (Table 1). On drying, relatively little decarboxylation occurs and relatively few heteroatomic centres are available to interact with unpaired electrons and become incorporated into new radicals.

Computer simulation of the Stockton e.p.r. spectrum indicated the presence of two components (A and B) in the broad signal, with a third narrow signal (C) superimposed as shown in Figure 1b. The changes in peak intensities, linewidths and  $g$ -values with time under both drying regimes at 150°C are listed in Table 2. For this coal, vacuum drying led to an increase by a factor of 1.2 in the intensities of both signals A and B forming the broad peak, whereas nitrogen flow drying did not change the intensity of signal A but resulted in an increase by a factor of 2.4 in the intensity of signal B. The radicals responsible for the narrow peak (C) were not affected by either drying process. As observed in experiments with New Vale lignite, flow drying generates radicals with the same  $g$ -values as those obtained by vacuum drying, but in this case it introduces a definite bias in favour of the radical species with the (slightly) lower  $g$ -value (species B in Table 2).

Microwave power saturation curves for drying Stockton coal at 150°C are shown in Figure 5. As in the corresponding experiment with New Vale lignite, the vacuum drying curves converged quickly and remained superimposable, whereas those for flow drying continued to increase in intensity as drying proceeded. In addition, the curves were indicative of homogeneous broadening, and for nitrogen flow drying the power at maximum intensity ( $P_{\max}$ ) increased steadily from 1.0 mW for wet coal to  $\sim 8$  mW after drying for 72 h. The narrow Stockton signal was not saturated at 200 mW, and no assignment of line broadening could be made for it. A similar narrow line in the 35 GHz spectrum of a high-rank Pittsburgh coal which showed no saturation up to 100 mW was attributed to an exchange narrowed species due to a high localized radical concentration<sup>36</sup>.

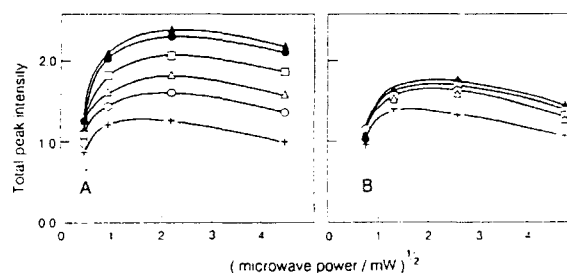


Figure 5 Microwave power saturation curves for Stockton No. 2 bituminous coal on drying at 150°C under (A) nitrogen flow, (B) vacuum. Symbols as in Figure 3



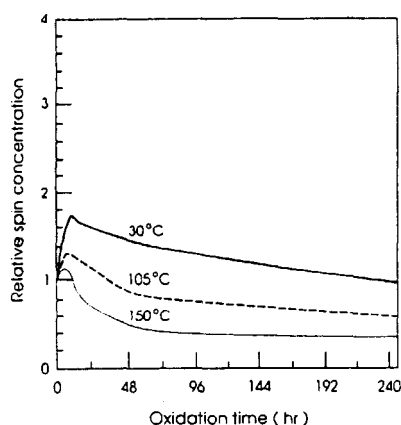


Figure 6 Changes in spin concentration on exposure of nitrogen-flow-dried New Vale lignite to dry air at various temperatures

#### Drying: general remarks

The above results show for both the lignite and the bituminous coal that different drying methods may lead to different outcomes in terms of increase in radical concentration. They also suggest that a major factor in determining the outcome is the balance between the rate at which new radical centres are formed, possibly by decarboxylation, and the availability of heteroatomic sites to interact with the newly generated unpaired electron density. The distribution of radical sites, which previous workers<sup>14,22</sup> have concluded are clustered rather than evenly spread throughout the coal, is also likely to influence the outcome of a drying process. With these factors in mind, it may be expected that the initial rapid increase in radical concentrations and subsequent levelling-off during vacuum drying are due to initial rapid removal of water leading to high concentrations of 'non-hydrated' radical clusters, followed by coupling reactions to form non-radical diamagnetic species. In contrast, during flow drying, when water loss is more gradual<sup>37</sup>, rapid increases in the concentrations of 'non-hydrated' radical clusters and associated coupling reactions become less likely. Newly generated radical sites remain in the system and lead eventually to a greater increase in radical concentration. If water removal is slow and heteroatomic sites are not freed up, unpaired electrons may instead be delocalized into polycondensed aromatic ring systems if these are available. The preference shown for a radical species with a lower  $g$ -value on drying of the bituminous coal under nitrogen flow conditions illustrates this point.

#### Oxidation effects

Oxidation of dried New Vale lignite at all temperatures caused an initial slight increase in radical concentration followed by a steady decrease over the ensuing 10 days. After this time the radical concentration for oxidation at 30°C had returned to approximately the same level as before exposure, but it had fallen significantly below this level for oxidation at the higher temperatures (Figure 6).

When dried Stockton coal was exposed to dry air, the narrow signal disappeared within minutes, regardless of oxidation temperature. Oxidation at 30 and 105°C caused a steady increase in radical concentration throughout the

10 days experiment, whereas at 150°C there was a quite rapid increase during the first 24 h followed by a fairly pronounced decrease until the end of the experiment (Figure 7).

The changes in radical concentration observed on exposure of dried New Vale lignite to dry air at 30°C are similar to those reported by Dack *et al.*<sup>9,38</sup> for room temperature oxidation of predried Victorian brown coal. They are also consistent with the oxidation mechanism proposed<sup>31</sup> on the basis of the chemical and thermal responses of this New Vale sample on exposure to dry oxygen. This involves the generation of new radical species through the formation and breakdown of hydroperoxy radical species and subsequent conversion of the radicals into non-radical products. At 30°C the reaction is sufficiently slow to allow the increase in radical concentration accompanying hydroperoxy formation and breakdown to be observed, whereas at higher temperatures the reaction quickly reaches the stage at which the formation of non-radical products predominates.

The rapid disappearance of the narrow Stockton signal probably results from formation of a complex between oxygen and the highly aromatized Stockton coal macrostructure. Similar results have been reported by others and assigned to complex formation between oxygen and structures containing delocalized unpaired electrons<sup>35,39</sup>.

As may be expected for this unresponsive coal<sup>31</sup>, the broad component of the Stockton signal is not significantly altered after the coal has been exposed to air for 10 days at 30°C. Even after 10 days at 105°C it appears that reaction has not advanced to the stage at which formation of non-radical products is predominant. This stage is not reached until 150°C.

#### CONCLUSIONS

Drying of New Vale lignite and Stockton No. 2 bituminous coal increases the radical concentrations in both, the increase being greater for the lignite. For both samples the increase in radical concentration is accompanied by increases in  $g$ -values. Vacuum drying produces rapid change, whereas the increase in radical

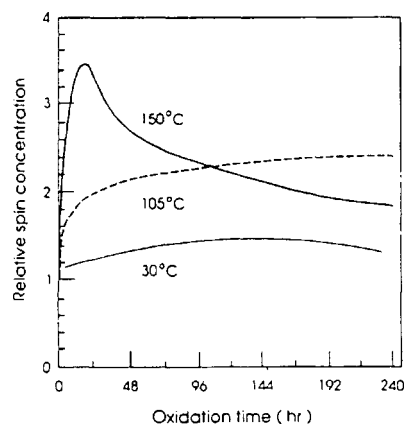


Figure 7 Changes in spin concentration on exposure of nitrogen-flow-dried Stockton No. 2 bituminous coal to dry air at various temperatures

concentration during flow drying is more gradual but greater overall. The changes depend on the balance between two processes. One is a small amount of decarboxylation to generate new radicals; the other is the removal of water from heteroatomic sites within the coal macrostructure to allow increased interaction between the unpaired electrons of these radicals and the heteroatoms. The balance is influenced by many factors, including the rate at which water is removed (and hence the drying method) and the distribution of radicals within the coal.

Exposure of dried New Vale lignite to dry air leads to an initial increase and subsequent decrease in radical concentrations. This trend is observed for oxidation at 30, 105 and 150°C, the onset of the decrease becoming more rapid at higher temperatures. The initial increase in radicals arises from the formation and breakdown of hydroperoxy species, and the decrease is the result of their subsequent conversion to non-radical products. Stockton bituminous coal behaves similarly but is far less reactive.

#### ACKNOWLEDGEMENTS

The authors thank the Minister of Science and Technology and the University Grants Committee for their financial support of this work.

#### REFERENCES

- 1 Uebersfeld, J., Etienne, A. and Combrisson, J. *Nature* 1954, **174**, 614
- 2 Ingram, D. J. E., Tapley, G. G., Jackson, R., Bond, R. L. and Murnaghan, A. R. *Nature* 1954, **174**, 797
- 3 Retcofsky, H. L. In 'Coal Science' (Eds M. L. Gorbaty, J. W. Larsen and I. Wender), Vol. 1, Academic Press, New York, 1982, p. 51
- 4 Petrakis, L. and Grandy, D. W. 'Free Radicals in Coals and Synthetic Fuels', Coal Science and Technology, Vol. 5, Elsevier, Amsterdam, 1983
- 5 Kwan, C. I. and Yen, T. F. *Anal. Chem.* 1979, **51**, 1225
- 6 Jeunet, A., Nickel, B. and Rassat, A. *Fuel* 1989, **68**, 883
- 7 Yokono, T., Iyama, S., Sanada, Y., Shimokawa, S. and Yamada, E. *Fuel* 1986, **65**, 1701
- 8 Obara, T., Yokono, T. and Sanada, Y. *Liquid Fuels Technol.* 1983, **1**, 59
- 9 Dack, S. W., Hobday, M. D., Smith, T. D. and Pilbrow, J. R. *Fuel* 1984, **63**, 39
- 10 Seki, H., Ito, O. and Iino, M. *Fuel* 1990, **69**, 317
- 11 Kudynska, J., Buckmaster, H. A., Duczmal, J., Bachelor, F. W. and Majumdar, A. *Fuel* 1992, **71**, 1127
- 12 Buckmaster, H. A. and Kudynska, J. *Fuel* 1992, **71**, 1137
- 13 Kudynska, J. and Buckmaster, H. A. *Fuel* 1992, **71**, 1141
- 14 Buckmaster, H. A. and Kudynska, J. *Fuel* 1992, **71**, 1147
- 15 Kudynska, J. and Buckmaster, H. A. *Fuel* 1993, **72**, 1733
- 16 Kudynska, J. and Buckmaster, H. A. *Fuel* 1994, **73**, 526
- 17 Goldberg, I. B., McKinney, T. M., Chung, K. E. and Galli, R. *Fuel* 1986, **65**, 241
- 18 Sady, W., Kispert, L. D. and Spears, D. R. *Am. Chem. Soc. Div. Fuel Chem. Preprints* 1992, **37**, 1151
- 19 Sady, W., Tucker, D., Kispert, L. and Spears, D. R. *Am. Chem. Soc. Div. Fuel Chem. Preprints* 1993, **38**, 1323
- 20 Tucker, D., Kispert, L. and Sady, W. *Am. Chem. Soc. Div. Fuel Chem. Preprints* 1993, **38**, 1330
- 21 Tucker, D. and Kispert, L. *Am. Chem. Soc. Div. Fuel Chem. Preprints* 1993, **38**, 1335
- 22 Dack, S. W., Hobday, M. D., Smith, T. D. and Pilbrow, J. R. *Fuel* 1985, **64**, 219
- 23 Peake, B. M. Ph.D. Thesis, Canterbury University, Christchurch, New Zealand, 1971
- 24 Duber, S. and Wieckowski, A. B. *Fuel* 1982, **61**, 433
- 25 Poole, C. P. 'Electron Spin Resonance', 2nd Edn, Wiley, New York, 1983, Ch. 13
- 26 Fowler, T. G., Kandiyoti, R. and Bartle, K. D. *Fuel* 1988, **67**, 1711
- 27 Fowles, W. W., Hoepfner, J. S. and McMurtrie, R. *Fuel* 1957, **36**, 469
- 28 Allardice, D. J. and Evans, D. G. *Fuel* 1971, **50**, 201
- 29 Schafer, H. N. S. *Fuel* 1979, **58**, 673
- 30 Gethner, J. S. *Fuel* 1985, **64**, 1443
- 31 Clemens, A. H., Matheson, T. W. and Rogers, D. E. *Fuel* 1991, **70**, 215
- 32 Matheson, T. W. and Rogers, D. E. New Zealand Energy Research and Development Committee, Publication P135, July 1988
- 33 Ref. 3, p. 61
- 34 Ref. 3, pp. 56-64
- 35 Goldberg, I. B., Crowe, H. R., Ratto, J., Skowronski, R. P. and Heredy, L. A. *Fuel* 1980, **59**, 133
- 36 Schick, S., Narayana, M. and Kevan, L. *Fuel* 1983, **62**, 1250
- 37 Kumagai, H., Grigor, B. A. and Howe, R. F. New Zealand Energy Research and Development Committee, Report RD 8828, 1989
- 38 Dack, S. W., Hobday, M. D., Smith, T. D. and Pilbrow, J. R. *Fuel* 1983, **62**, 1510
- 39 Duber, S. and Wieckowski, A. B. *Fuel* 1982, **61**, 433

## 論文

## ベンチスケール石炭直接液化反応器の反応解析

(キーワード 石炭液化, 液化反応器, 予熱器, 反応速度定数, 石炭転化率, ガスホルドアップ)

— 1994. 8. 22 受理 —

北海道工業技術研究所\*<sup>1</sup> 井戸川 清, 佐々木正秀, 池上真志樹\*<sup>2</sup>  
 永石 博志, 成田 英夫, 佐々木皇美  
 小谷川 毅, 福田 隆至, 山本 光義  
 吉田 忠, 前河 涌典  
 北海道大学\*<sup>3</sup> 千葉 忠俊

## 1. 緒言

ベンチあるいはパイロット規模の石炭液化連続式反応器による反応実験は, 工業規模の反応器へのスケールアップに不可欠である。とくに, その操作性およびオートクレーブ等の実験室的規模の研究との対応について知ることは, 連続式反応器における反応特性を理解するうえできわめて重要である。さらに, 連続式反応器での液化反応に及ぼす滞留時間, 混合の影響などに関するデータの集積は, 反応器の研究開発の進展に寄与する。このような状況を反映して, 石炭の液化反応に関する研究は, 近年, 回分式反応器によるものばかりでなく, 連続式反応器によるもの<sup>1)~17)</sup>も増えている。守富ら<sup>18)</sup>は回分式反応器における石炭粒子の昇温速度を連続式反応器の場合と同等にすれば, 前者から決定した反応速度データを用いて後者の定常状態反応率を予測できることを示した。

他方, 石炭液化反応では, 反応物である石炭ばかりでなく生成物である液化油も非常に多くの複雑な成分から構成されるので, これらをすべて把握し, 反応過程を記述することは不可能に近い。したがって, 通常液化生成物は溶解力の異なった数種の溶剤によって順次抽出, 分別した成分に基づいて評価されている<sup>19)20)</sup>。そのため, 現在まで提出されている石炭の反応速度モデルはすべて, この巨視的分類に基づいた成分によって表現されている。千葉ら<sup>21)</sup>はこの分類

に基づいてそれまで公表されている反応速度データを統一的に説明するために, 石炭を液化反応性が異なる2成分の反応種と考えた反応モデルを提案した。さらにNagaishiら<sup>20)</sup>は同様のモデルにおいて, 石炭は液化によって反応しない不活性成分,  $I_0$ , 気相および溶媒からの外部水素の消費なしに直接油やガスに転化する成分,  $C_{A2}$  およびプレアスファルテン, アスファルテンを経由してオイルあるいはガスに転化する成分,  $C_{A1}$  の反応性の異なる三種類の成分から成っているとする液化反応モデルを提案し, 各成分の比率を示した。このように, 液化反応機構については次第に明らかになり, これに基づく2反応種モデルが反応速度の解析に適用されるようになった。しかし, それらの研究は溶媒にテトラリンやナフタレンなどのモデル物質を使用しているものが大部分である。

そこで, 本研究では, 太平洋炭の液化反応を, 溶媒に脱晶アントラセン油, 触媒に赤泥/硫黄を用い, 急速昇温操作の回分式反応器で行い, 得られた結果を2反応種モデルで解析し, 反応速度定数を得た。さらに, 連続式液化反応装置の予熱器を用いた実験によっても速度定数を求め, 両者の結果から連続装置の反応解析に適用可能な, 液化反応速度定数を得た。つぎにこの反応速度定数を用い, ベンチスケール液化反応器の石炭転化率についてシミュレーションを行い, 実測値との比較検討を行った。

## 2. 実験装置および方法

## 2.1 試料

試料炭は100メッシュ以下に粉碎した太平洋炭で,

\*<sup>1</sup> 資源エネルギー基礎工学部\*<sup>2</sup> 極限環境材料部 札幌市豊平区月寒東2-17-2-1\*<sup>3</sup> 工学部金属工学科 札幌市北区北13条西8

Table 1 Properties of Taiheiyo coal and DAO used

	Ultimate analysis [wt%, d.a.f. base]				
	C	H	O	S	N
Taiheiyo	72.55	6.57	18.05	0.32	1.58
DAO	91.22	5.95	1.41	N.D.	0.61

	Proximate analysis [wt%, wet base]			
	Moisture	Ash	Volatile Matter	Fixed Carbon
Taiheiyo	5.90	12.55	44.64	36.91

Table 2 Elements of red mud catalyst used

[wt%, dry base]							
Al	Si	S	Cl	P	Ca	Ti	Fe
14.05	7.71	0.32	2.81	0.32	2.20	7.67	64.92

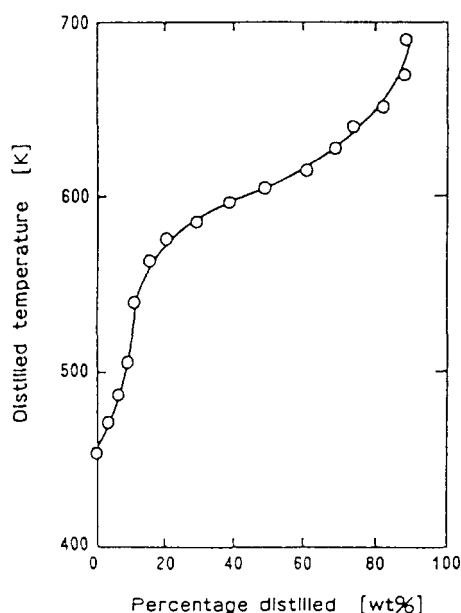


Fig. 1 Distillation curve for decrystallized anthracene oil

その元素および工業分析結果を Table 1 に示す。使用溶媒は脱晶アントラセン油 (DAO) であり、石炭スラリーは石炭 : DAO が重量比で 4 : 6 になるように調製した。DAO の元素分析結果は Table 1 に、蒸留曲線を Fig. 1 に示す。また、100メッシュ以下に粉碎した赤泥と市販粉末硫黄を、石炭重量基準でそれぞれ 5 wt% および 0.5wt% 触媒として加えた。Table 2 に赤泥の性状を示す。

## 2.2 液化実験

回分式反応器には内容積が 50cm<sup>3</sup> の電磁攪拌式オートクレーブを用い、太平洋炭 4 g、脱晶アントラセン油 6 g および赤泥/硫黄触媒 0.2 g を充填した。水素初

圧を 10MPa として昇温し、所定温度に達してから 0 ~ 90 分間保持した。攪拌器の回転数は毎分 600 回転、昇温速度はベンチプラントの予熱器では、80 ~ 100K/min なので 100K/min とした。また、反応中の圧力は圧力緩衝用の 500cm<sup>3</sup> オートクレーブを接続することにより、ほぼ一定に保った。

0.1t/d 石炭液化ベンチプラントの概要とその操作法は前報<sup>22)</sup> とほぼ同様である。液化反応部は内径が 4 cm、高さが 100cm の予熱器と内径が 8 cm、高さが 100cm の反応器とから成る。ただし、本実験では反応器のスラリー抜き出し高さは、底部から 80cm とした。高圧水素ガスとスラリーは予熱器下部入口直前で合流し、所定反応温度近くまで加熱後、反応器に送入した。流通式反応器による液化反応速度の測定は、液化反応部から反応器を分離し、予熱器のみを用いて行った。予熱器および反応器内の温度は、高さ方向の 3 ケ所 (塔底部からそれぞれ 19, 49, 79cm) に挿入した熱電対により測定した。また、予熱器入口の温度は水素、スラリーの合流点での温度とした。予熱器と反応器の温度はそれぞれ 673K と 723K に設定し、オートクレーブ実験に用いたスラリーと同一成分、同一比率のスラリーの滞留時間を変数として石炭の反応率を求めた。ガス状生成物の収率は、オフガス流量とガスクロマトグラフによる組成分析によって求めた。水素消費量は入口水素流量とオフガス中の水素流量の差として算出した。

反応後の試料の分別は溶剤にトルエンとテトラヒドロフラン (THF) あるいはピリジンをを用いた溶剤沸点抽出分別法<sup>20)</sup> によった。トルエン不溶成分, TI, THF 不溶成分, THFI, ピリジン不溶成分, PI は触媒、灰分を含んだまま測定し、各成分の収率は残存する触

媒, 灰分分率で重量減少率を補正して無水無灰基準で求めた。

石炭の転化率は原炭中と TI 中の灰分および添加触媒重量割合から次式によって求めた。

$$\text{Conv.} = (a_r - a_0) / a_r (1 - a_0) \quad (1)$$

ここで,  $a_0 = W_{\text{Ash}} / W_0$

$$a_r = (W_{\text{Ash}} - W_{\text{Cat.}}) / (W_{\text{TI}} - W_{\text{Cat.}})$$

### 3. 結果と考察

#### 3.1 回分式反応器による反応速度解析

Fig. 2 にピリジン可溶分収率,  $y_{\text{PS}}$  の経時変化を示す。これをみると,  $y_{\text{PS}}$  は反応の初期の段階で急激に増加するが, その後はあまり増加しない。比較のために, 溶媒に水素供与性のテトラリンと水素非供与性のナフタレンを用いたときの  $y_{\text{PS}}^{20)}$  も示したが, 溶媒に脱晶アントラセン油 (DAO) を用いた本結果は, 両者の中間にあることがわかる。

未反応石炭をトルエン不溶成分とし, それと無水無灰の原炭との比,  $C_A$  を反応時間,  $\theta$  に対して片対数プロットしたのが Fig. 3 である。各温度において太平洋炭の水素化分解反応は, 直線にならないことが明らかである。なお, 図には吉田ら<sup>23)</sup>の673Kにおける未反応炭をベンゼン不溶分とした結果も合わせて示す。かれらの結果は本実験とは異なり, おおよそ直線で表すことができる。これは昇温速度の違いに起因しており, かれらの昇温速度は3 K/min と遅いので, 易反

応成分の反応 (石炭  $\rightarrow$  O & G) は昇温過程で終了し, 難反応成分の反応 (石炭  $\rightarrow$  PA  $\rightarrow$  A  $\rightarrow$  O & G) のみが実測されたものと考えられる。以上の結果から, 本実験系の液化反応は, 反応性の異なる二つの成分の併発反応とみなせるので, 液化反応速度定数は, 2 反応種モデル<sup>21)</sup>に基づき, 無水無灰の原炭基準のトルエン不溶分 (未反応炭割合) の減少速度から算出した。2 反応種モデルでは, 難反応性成分,  $C_{A1}$  と易反応性成分,  $C_{A2}$  の併発反応を仮定する。両者の液化反応速度定数  $k_1, k_2$  を千葉ら<sup>21)</sup>の方法で求め, これらの Arrhenius プロットを Fig. 4 に示す。データにばらつきはあるが, 直線とみなせるので, 次式から  $k_1, k_2$  の活性化エネルギーと頻度因子を得ることができる。

$$k_i = k_{i0} \exp(-E_i / RT), \quad i = 1, 2 \quad (2)$$

図より DAO を用いたときの  $k_1$  は  $k_2$  に比べて約1桁小さい。比較のためにテトラリンを用いたときの結果<sup>20)</sup>も示したが, その場合の  $k_2$  は本結果とほぼ一致

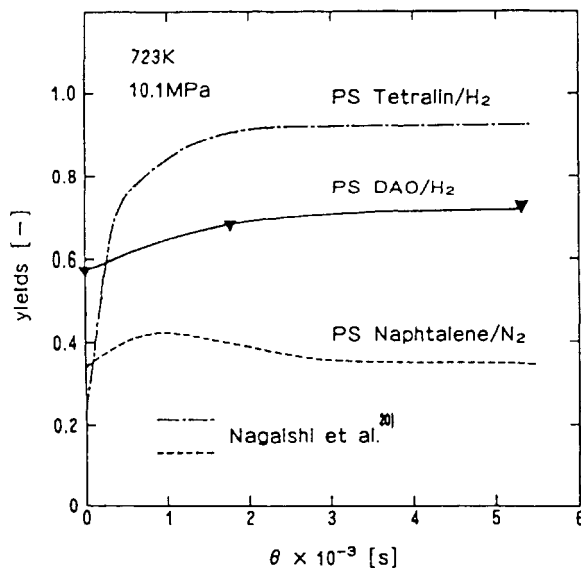


Fig.2 Change with time of pyridine soluble yields for Taiheiyo coal with DAO and red mud/sulfur

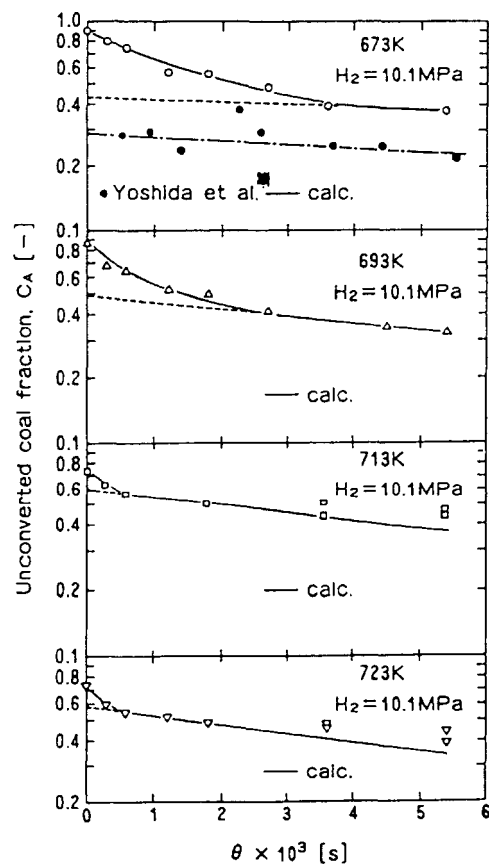


Fig.3 Changes of organic toluene-insolubles remained with time for Taiheiyo coal with DAO and red mud/sulfur

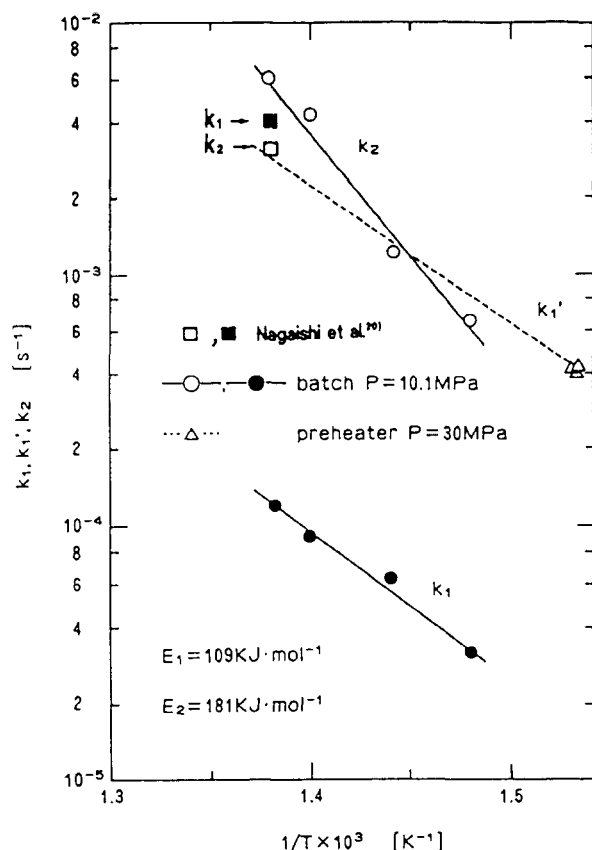


Fig.4 Arrhenius plots of rate constants for Taiheiyo coal with DAO and red mud/sulfur catalyst

している。しかし、テトラリンの水素供与能はDAOに比べて大きいので、前者の $k_1$ が後者に比べて大きくなり、 $k_2$ と同程度になる。すなわち、 $k_1$ は溶媒の水素供与能に強く依存するが、 $k_2$ は依存しないことが明らかである。さらに、触媒存在下では、気相水素による溶媒の水素化を経由した石炭への間接的な水素移動が主反応として起こる<sup>24)</sup>ので、DAOのようにそれ自身が一旦水素化されてから液化反応に関与する溶媒の水素供与能は、溶媒の水素化の程度に大きく依存すると考えられる。以上の2点を考慮すれば $k_1$ 、 $k_2$ は次式のように表すことができる。

$$k_1 = f(T, CH_2) = k_{1T} CH_2^m \quad (3)$$

$$k_2 = f(T) \quad (4)$$

ここで、 $k_1$ は見かけの速度定数であり、真の速度定数と水素供与性溶剤濃度（溶媒から石炭への移行可能な水素濃度）の積で表される。

### 3.2 連続式液化反応装置における液化反応

#### 3.2.1 予熱器による反応速度解析

回分式反応器で得られた $k_1$ 、 $k_2$ が流通式反応器の

反応解析に対しどの程度有用であるかを検証するため、予熱器出口の未反応炭濃度を後述の方法で推算したが、推算値は測定値に比べて10-12%大きい。したがって、この結果とEqs.(3), (4)を考慮すれば、回分式反応器で得られた $k_1$ は流通式反応器の反応解析に対し、そのままでは適用できないことが明らかである。

そこで、本項ではベンチスケール予熱器による反応速度解析を行う。

$k_1$ が同一温度において圧力によって変化するのはEq.(3)から明らかのように、水素供与性溶剤濃度が変化するためであり、反応の本質は変わらない。さらに、温度が低い場合も高い場合と同種の反応が起こると考えられるので、予熱器における $C_A$ を計算するにあたり、 $k_1$ の活性化エネルギーは回分式反応器の場合と同じと仮定する。すなわち、 $k_1$ において圧力にともない変化するのは頻度因子のみであり、予熱器の $k_1$ を $k_1'$ 、その頻度因子を $k_{10}'$ とすると、

$$k_1' = k_{10}' \exp(-E_1/RT_x) \quad (5)$$

となる。ここで、 $T_x$ は予熱器高さ方向の温度である。

他方、予熱器内のスラリー滞留時間は次式で与えられる。

$$\theta_R = V_1(1 - \epsilon_g)/(W_{sl}/\rho_{sl}) \quad (6)$$

ここで、 $V_1$ は予熱器体積、 $\epsilon_g$ はガスホールドアップ、 $W_{sl}/\rho_{sl}$ はスラリーの体積流量である。本予熱器と反応器におけるガスホールドアップの実測結果は前報<sup>22)</sup>で報告した。 $\epsilon_g$ および $\theta_R$ をTable 3に示す。

石炭液化反応のように、反応速度定数の小さい場合、反応率は混合状態に依存しない<sup>25)</sup>ので、本研究では非等温反応器である予熱器の反応解析に、取扱が簡便な完全混合槽列モデルを適用した。その基礎式は次式で表される。

$$C_{A1} = C_{A10} / \{1 + k_1'(\theta_R/N)\}^N \quad (7)$$

$$C_{A2} = C_{A20} / \{1 + k_2(\theta_R/N)\}^N \quad (8)$$

$$C_A = C_{A1} + C_{A2} \quad (9)$$

体積 $V_1$ の予熱器は、温度の異なる体積 $V_1/N$ の完全混合槽が直列に $N$ 個連結されているものと想定し、 $N=10$ とした。予熱器高さ方向の平均温度は、温度分布を図積分して求めた。また、 $C_{A10}$ 、 $C_{A20}$ は石炭に固有の難および易反応成分の割合であり、太平洋炭では以下のようなものである<sup>20)</sup>。

$$C_{A10} = 0.61, C_{A20} = 0.31 \quad (10)$$

Table 3 Experimental conditions for measurements of the kinetics of Taiheiyo coal hydrogenation using the preheater

RUN number		RUN-1	RUN-2	RUN-3
<u>Experimental conditions</u>				
Temperature*	[K]	655	655	655
Pressure	[MPa]	30	30	30
Recycle gas rate	[Ncm <sup>3</sup> /s]	6555	8361	11667
Slurry feed rate	[g/s]	2.26	2.26	2.28
$\epsilon_{gl}$	[-]	0.43	0.45	0.50
$\theta_{R1}$	[s]	353	341	308
<u>Yield [wt%, d.a.f. base]</u>				
Gas		1.78	1.80	1.95
Water		1.45	1.82	2.33
TI** (=C <sub>A</sub> )		76.40	77.00	78.60
TS***		24.60	23.00	21.40
Total		104.20	103.60	104.30
H <sub>2</sub> consumption		3.66	3.59	3.42
<u>[wt%, d.a.f. base]</u>				

\* averaged values of temperature in the longitudinal direction at the preheater

\*\* Toluene insolubles

\*\*\* Toluene solubles

Table 3, 4 にベンチプラントの実験条件と物質収支を, Table 5 に予熱器の高さ方向の温度分布を示す。予熱器高さ方向の未反応炭濃度,  $C_A$  はこの温度分布に基づいて, 第1槽より Eq.(2), (5)-(10) を順次適用して非定常計算を行い, 予熱器出口 ( $N=10$ ) における  $C_A$  の値が Table 3 に示した実測値と最もよく一致するときの  $k_{10}'$  を決定した。Fig. 4 にはこのようにして求めた  $k_{10}'$  と高さ方向の平均温度から求めた  $k_1'$  もプロットした。また,  $k_{10}'$  に基づく各温度の  $k_1'$  の推算値を点線で示す。これを見ると  $k_1'$  は  $k_1$  に比べて約1桁大きく,  $k_2$  に近い値になることがわかる。 $k_1$ ,  $k_1'$  のこのような差は Eq.(3) から推察できるように, 予熱器の水素圧力が回分式反応器に比べて約3倍大きいことによる水素供与性溶剤濃度の相違に起因すると考えられるが, これについての定量的な議論は, 現在のこの分野の研究レベルでは困難である。しかし, 定性的には次のように説明できる。石炭は液化条件下で熱分解し, ガスを生成するとともに, 熱分解したフラグメントは溶媒や気相からの水素により水添されて安定化し, プレアスファルテン, アスファルテン, オイルへと次第に低分子化していき<sup>26)</sup>, 高圧になるほど液化油収率は増加する<sup>27)</sup>。さらに水素を放出し, 非水素供与性溶剤となった溶媒を触媒上で気相からの溶

存水素により再生させる<sup>26)</sup>。また, 水素化反応は高温になるほど, 脱水素側に平衡を移行する傾向にあるが, 高圧になるとこれを抑制してガス状生成物を少なく, 液収率を増加させる<sup>27)</sup>。本結果は, このような圧力効果の重畳により生じたものと考えられる。Table 6 に本反応系の  $k_1'$ ,  $k_2$  の頻度因子と活性化エネルギーを示す。

Fig. 5 に予熱器高さ方向の温度分布および未反応炭濃度,  $C_A$  の分布を示す。Table 6 の頻度因子と活性化エネルギーを用いて計算した  $C_A$  は実測値とよく一致している。

次に上記速度定数を用いてベンチスケール液化反応器の石炭転化率のシミュレーションを行う。

### 3.2.2 連続式液化反応装置の反応解析

0.1t/d 連続式液化反応装置の反応部は予熱器と反応器とから構成されており, 実験で得られた石炭転化率は両者の値を含んでいる。したがって, 液化反応器における石炭転化率,  $Conv._2$  は実測値,  $Conv._T$  と Table 5 に示した高さ方向の温度分布に基づき, 上述の手順で計算した予熱器中の石炭転化率,  $Conv._1$  から次式で求めた。

$$Conv._2 = \frac{\{(1 - Conv._1) - (1 - Conv._T)\}}{(1 - Conv._1)} \quad (11)$$

Table 4 Experimental conditions for the experiments of coal liquefaction

RUN number		RUN-4	RUN-5	RUN-6
<u>Experimental conditions</u>				
Temperature*	[K]	720	729	724
Pressure	[MPa]	30	30	30
Recycle gas rate	[Ncm <sup>3</sup> /s]	5639	8611	11250
Slurry feed rate	[g/s]	2.36	2.28	2.36
$\epsilon_{g1}$	[-]	0.38	0.46	0.52
$\epsilon_{g2}$	[-]	0.11	0.16	0.20
$\theta_{R1}$	[s]	368	332	284
$\theta_{R2}$	[s]	1835	1799	1656
<u>Yield [wt%, d.a.f. base]</u>				
Gas		6.69	6.48	6.09
Water		12.09	9.38	10.86
Oil**		35.31	44.97	38.08
Residue***		47.46	40.14	42.14
Total		101.50	101.00	108.60
H <sub>2</sub> consumption		4.96	5.99	6.08
<u>[wt%, d.a.f. base]</u>				

\* averaged values of temperature in the longitudinal direction at the reactor

\*\* IBP-811K

\*\*\* Unreacted coal+Toluene solubles(811K-)

Table 5 Axial distribution of temperature at the preheater

X*	RUN No.	Temperature				
		RUN-1	RUN-2	RUN-3	RUN-4	RUN-5
[-]						
0		463	488	503	473	478
0.1		560	570	590	600	605
0.2		642	647	652	643	649
0.3		651	654	657	646	653
0.4		658	661	662	649	656
0.5		665	666	666	652	658
0.6		670	669	669	654	660
0.7		674	672	671	656	661
0.8		676	674	672	656	661
0.9		676	674	673	656	661
1.0		676	674	673	656	661

\* dimensionless length from bottom of the preheater

Table 6 Observed frequency factors and activation energies of Taiheiyo coal with DAO and red mud/sulphur

Frequency factor [s <sup>-1</sup> ]		Activation energy [KJ/mol]	
k <sub>10</sub> '	k <sub>20</sub>	E <sub>1</sub>	E <sub>2</sub>
2.33×10 <sup>5</sup>	7.04×10 <sup>10</sup>	109.0	181.0



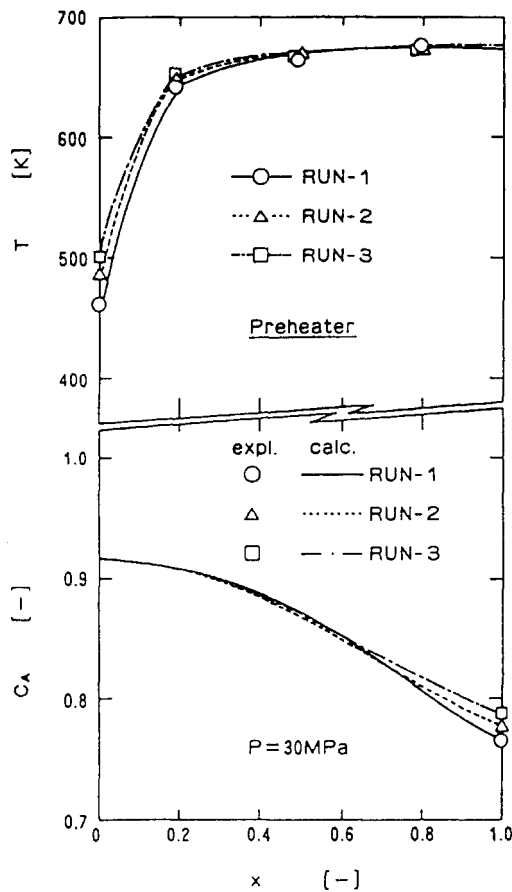


Fig. 5 Longitudinal distribution of temperature and dimensionless concentration of unconverted coal at the preheater

Conv. 2 の推算値は次のようにして求めた。すなわち、予熱器出口の  $C_A$  が反応器入口の  $C_A$  とみなすことができるから、この値を用いて反応器出口の  $C_A$  を計算し、石炭転化率を求めた。なお、反応器は高さ方向の温度分布がほぼ均一なので、完全混合槽型反応器として取り扱った。反応器のスラリー滞留時間、 $\theta_R$  は Eq.(6) から求めた。 $\epsilon_g$  および  $\theta_R$  を Table 4 に示す。

Fig. 6 に石炭転化率と  $\theta_R$  との関係を示す。これを見ると、計算値は実測値とほぼ一致している。したがって、 $k_1'$  の活性化エネルギーは圧力および反応器種には依存しないとした仮定は妥当であることがわかる。なお、スラリー滞留時間、 $\theta_R$  は、溶媒の蒸発量を測定していないので、ガスホールドアップのみから算出した。上述の結果から、スラリー滞留時間に対する溶媒蒸発の影響は、本実験では無視できる。以上の結果から、石炭中の難反応成分の速度定数は圧力や反応器種に依存することが明らかになったが、今後、反応前後の DAO 中での水素の挙動を検討し、本結果と

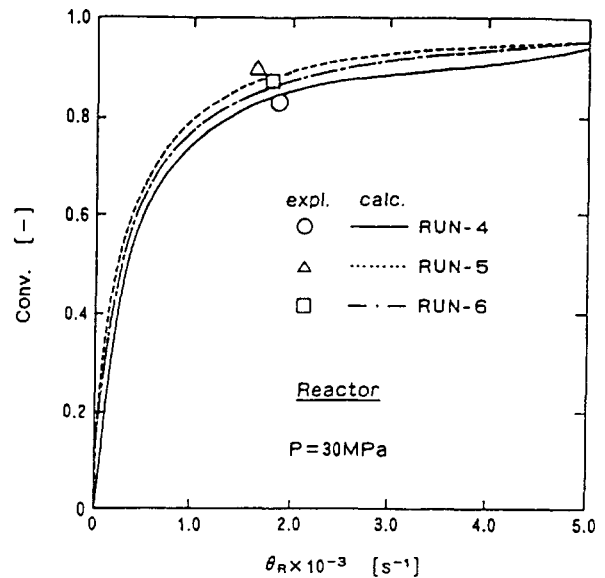


Fig. 6 Effect of residence time of slurry on coal conversion for Taiheiy coal at the reactor

の関連を調べる必要がある。

#### 4. 結論

太平洋炭の液化反応を、溶媒に脱晶アントラセン油、触媒に赤泥／硫黄を用い、急速昇温操作の回分式反応器で行い、得られた結果を 2 反応種モデルで解析し、反応速度定数を得た。さらに、連続式液化反応装置の予熱器を用いた実験によっても速度定数を求め、両者の比較から連続装置の反応解析に適用可能な、液化反応速度定数を得た。つぎに 0.1t/d 連続石炭液化反応器を運転して得られた石炭転化率が、連続式反応器の石炭スラリーの滞留時間と反応速度の実測値からどの程度予測できるかについて、完全混合槽モデルを用いて検討した。

1. 溶媒に脱晶アントラセン油を用いた場合、石炭中の難反応成分の反応速度は回分式反応器と流通式反応器では異なった。これは両反応器の圧力が 3 倍異なることによる溶媒中の水素供与性溶剤濃度の相違に起因するものと考えられる。
2. 石炭転化率の計算値は実測値とほぼ一致した。したがって、難反応性成分の液化反応速度定数において頻度因子は圧力や反応器種に依存し変化するが、活性化エネルギーは変化しないことがわかった。また、本反応条件下では、スラリー滞留時間は、ガスホールドアップのみから算出した値で代替でき、溶媒蒸発の影響は無視できる。

[使用記号]

$a_0$  = ash fraction of coal

[-]

$a_r$	= ash fraction of toluene insolubles	[-]
$C_{A1}$	= unreacted coal fraction of less active coal component	[-]
$C_{A2}$	= unreacted coal fraction of active coal component	[-]
$C_{H2}$	= dimensionless concentration of hydrogen in the bulk slurry	[-]
Conv.	= coal conversion	[-]
$E_1$	= activation energy of $k_1$	[J · mol <sup>-1</sup> ]
$E_2$	= activation energy of $k_2$	[J · mol <sup>-1</sup> ]
$I_0$	= inactive fraction of coal	[-]
$k_1$	= reaction rate constant for less active coal component	[s <sup>-1</sup> ]
$k_{1T}$	= true reaction rate constant for less active coal component	[s <sup>-1</sup> ]
$k_1'$	= reaction rate constant for less active coal obtained using a continuous reactor	[s <sup>-1</sup> ]
$k_2$	= reaction rate constant for active coal component	[s <sup>-1</sup> ]
$k_{10}$	= frequency factor of $k_1$	[s <sup>-1</sup> ]
$k_{10}'$	= frequency factor of $k_1'$	[s <sup>-1</sup> ]
$k_{20}$	= frequency factor of $k_2$	[s <sup>-1</sup> ]
$m$	= reaction order	[-]
$N$	= number of mixed reactors in series	[-]
$R$	= gas constant	[J · mol <sup>-1</sup> · K <sup>-1</sup> ]
$T$	= temperature	[K]
$T_x$	= temperature at the height of the preheater	[K]
$V$	= volume of reactor	[m <sup>3</sup> ]
$W_{Ash}$	= weight of ash	[g]
$W_{cat.}$	= weight of catalyst	[g]
$W_{sl}$	= mass flow rate of slurry	[kg · s <sup>-1</sup> ]
$w_0$	= weight of coal load	[g]
$w_{TI}$	= weight of toluene insolubles fraction	[g]
$x$	= dimensionless axial distance from nozzle	[-]
$y_{PS}$	= yields of pyridine-soluble fraction	[-]
$\epsilon_g$	= gas holdup	[-]
$\theta$	= time	[s]
$\theta_R$	= residence time of slurry	[s]
$\rho_{sl}$	= density of slurry	[kg · m <sup>-3</sup> ]

&lt;添字&gt;

0 = initial conditions 1 = preheater 2 = reactor

## 文 献

- 1) Kang, C. C., Norgbri, G. and Stewert, N., *ACS Div. Fuel Chem. Prep.*, 21, 19 (1976)
- 2) Han, K. W., Dixit, V. B. and Wen, C. Y. *Ind. Eng. Chem. Process Des. Dev.*, 17, 16 (1978)
- 3) 大嶋 哲, 湯村守雄, 島田和夫, 武松敏式, 鈴木守夫, 吉留 浩, 栗木安則, 第18回石炭科学会議論文集, 138 (1981)
- 4) idem: 第19回石炭科学会議論文集, 247 (1982)
- 5) 前河涌典, 上田 成, 長谷川義久, 吉田諒一, 横山慎一, 中田善徳, 吉田 忠, 成田英夫, 三枝等, 原 祥夫, 酒井直秀, 小野重好, 第18回石炭科学会議論文集, 187 (1981)
- 6) 角南好彦, 早川恵一, 白藤民雄, 高橋幸司, 南良平, 第21回石炭科学会議論文集, 68 (1984)
- 7) 矢内俊一, 大隅 修, 村越浩二, 前 一広, 齊藤海三郎, 中子敬夫, 第21回石炭科学会議論文集, 60 (1984)
- 8) 上田幹夫, 村田勝英, 福寿芳雄, 橋本孝雄, 角誠之, 第21回石炭科学会議論文集, 77 (1984)
- 9) 伊藤秀伸, 三上公一, 汐崎真之佑, 村田勝英, 上田幹夫, 第21回石炭科学会議論文集, 171 (1984)
- 10) Exxon Research and Engineering Co., "EDS Coal Liquefaction Process Development Phase V 1982", EPRI AP-3128, Annual Report, p.212-216 (1983)
- 11) 稲葉 敦, 三木啓司, 佐藤芳樹, 山川敏雄, 燃協誌, 63, 877 (1984)
- 12) 大嶋 哲, 栗木安則, 湯村守雄, 大森隆夫, 河村光隆, 第24回石炭科学会議論文集, 175 (1987)
- 13) 三枝 等, 橋本孝雄, 津久井裕, 松尾和芳, 第24回石炭科学会議論文集, 194 (1987)
- 14) 矢内俊一, 大隅 修, 平野龍夫, 齊藤海三郎, 松村哲夫, 第25回石炭科学会議論文集, 64 (1988)
- 15) 碓 秀文, 早川恵一, 越後格之, 山田健彦, 第25回石炭科学会議論文集, 72 (1988)
- 16) 山浦純治, 井口憲二, 山本久敬, 佐藤孝志, 望月通晴, 小林正俊, 第27回石炭科学会議論文集, 72 (1990)
- 17) 吉田祥治, 野上義信, 山浦純治, 井口憲二, 山本久敬, 望月通晴, 寺下靖司, 小林正俊, 第28回石炭科学会議論文集, 113 (1991)
- 18) 守富 寛, 黒氏昭仁, 真田雄三, 千葉忠俊, 燃協誌, 62, 199 (1983)
- 19) 千葉忠俊, 燃協誌, 63, 156 (1984)
- 20) Nagaishi, H., Moritomi, H., Sanada, Y. and Chiba, T., *Energy & Fuels*, 2, 522 (1988)
- 21) 千葉忠俊, 真田雄三, 燃協誌, 57, 259 (1978)

- 22) Idogawa, K., Nagaishi, H., Narita, H., Fukuda, T.,  
Kotanigawa, T., Yoshida, R., Yoshida, T.,  
Yokoyama, S., Yamamoto, M., Sasaki, A., Sasaki,  
M., Hirama, T., Maekawa, Y., Ueda, S., and Chi-  
ba, T., *J. Chem. Eng. Japan*, 27, (6), 95 (1994)
- 23) 吉田諒一, 前河涌典, 石井忠雄, 武谷 愿, 日化  
誌, 1885 (1972)
- 24) 守富 寛, 永石博志, 成瀬雅彦, 真田雄三, 千葉  
忠俊, 燃協誌, 62, 254 (1983)
- 25) Levenspiel, O., "Chemical Reaction Engineering",  
p.136-137, Wiley-International Edition (1972)
- 26) Han, K. W. and Wen, C. Y., *Fuel*, 58, 779  
(1979)
- 27) 伊藤博徳, 大内公耳, 燃協誌, 58, 158 (1979)

~~~~~

## AnaLysis of Coal Liquefaction Reaction in a Bench-Scale Direct Coal Liquefaction Reactor

Kiyoshi IDOGAWA, Masahide SASAKI, Hiroshi NAGAISHI, Hideo NARITA,  
Akiyoshi SASAKI, Takeshi KOTANIGAWA, Takashi FUKUDA,  
Mituyoshi YAMAMOTO, Tadashi YOSHIDA and Yosuke MAEKAWA

(Resources and Energy Division, Hokkaido National Industrial Research Institute)

Mashiki Ikegami

(Materials Division, Hokkaido National Industrial Research Institute)

Tadatoshi Chiba

(Dept. of Metallurgical Eng., Hokkaido University)

**SYNOPSIS :**— Coal liquefaction experiments for Taiheiyo coal with decrystallized anthracene oil as the solvent and red-mud/sulfur as the catalyst were conducted by a batch reactor with rapid heating operation and, a bench-scale continuous preheater. Rate constants were obtained from analysis of the experimental results by two reactants model. Moreover, the coal conversion in a continuous liquefier was estimated with these rate constants by the perfect mixed reactor model.

The coal liquefaction rates of the less active component for Taiheiyo coal were different between the batch reactor and the continuous reactor, with decrystallized anthracene oil as the solvent. It was considered that the reason was due to the differences in the donor hydrogen concentration of the two reactors.

The observed values of the coal conversion were approximately coincided with the calculated values. Therefore, it was found that the frequency factor of the reaction rate of the less active coal components varied with both the pressure and the reactor types, but the activation energy did not change. Effect of vaporization of the solvent on the values of the residence time of slurry could be neglected in these experimental conditions (30 MPa, 723 K), and they were represented by the values calculated using only the gas holdup.

Key Words

Coal liquefaction, Liquefier, Preheater, Reaction rate constant, Coal conversion,  
Gas holdup

# A Model Structure of Zao Zhuang Bituminous Coal

Kazuo Nakamura

Fundamental Research Laboratories, Osaka Gas Co., Ltd.,  
19-9, 6-chome Torishima, Konohana-ku, Osaka 554, Japan

Toshimasa Takanohashi\* and Masashi Iino

Institute for Chemical Reaction Science, Tohoku University,  
2-1-1, Katahira, Aoba-ku, Sendai 980-77, Japan

Haruo Kumagai, Masaaki Sato, Susumu Yokoyama, and Yuzo Sanada

Center for Advanced Research of Energy Technology, Hokkaido University,  
Kita-ku, Sapporo 060, Japan

Received May 16, 1995. Revised Manuscript Received August 8, 1995\*

A model structure of Zao Zhuang bituminous coal (Shan Tong province in China, 86.9 wt % C) based on the structural analyses and the computer simulation was constructed. The coal was extracted with pyridine or carbon disulfide-*N*-methyl-2-pyrrolidinone (CS<sub>2</sub>-NMP) mixed solvent, and the extracts obtained were further fractionated. The extract fractions were hydrogenated using Adkins catalyst under mild condition at 430 °C for 1 h. The structure of the oil (*n*-hexane solubles) obtained from each extract fraction was analyzed by mass spectrometry after column separation and the molecular models of the fractions including the extraction residue were constructed assuming associated structure of coal molecules. Finally, a model structure of Zao Zhuang coal which consists of a huge associate of coal molecules was constructed three-dimensionally using computer-aided molecular design (CAMD) by assuming an anisotropic model structure formed from a periodic boundary cell. Good agreement of the physical density (1.22 g/cm<sup>3</sup>) of the constructed model with that (1.29 g/cm<sup>3</sup>) observed experimentally suggests that Zao Zhuang coal has a possibility to have associated structure of coal molecules having a continuous distribution of molecular weight from the lighter fraction to the solvent-insoluble residue.

## Introduction

The nature of macromolecular structure of coals has not been fully understood. Shinn<sup>1</sup> has constructed a model structure of Illinois No. 6 bituminous coal based on analytical data on the coal and its liquefaction products and showed various structural components. Shinn described that considerations of the secondary structure such as hydrogen bonding interaction and the three-dimensional nature of the coal would be necessary. Spiro<sup>2,3</sup> has constructed three-dimensional coal models proposed by Given,<sup>4</sup> Wiser,<sup>5</sup> Solomon,<sup>6</sup> and Heredy,<sup>7</sup> using space-filling models. The three models of them were found to include spatially or sterically inaccessible moieties. Carlson<sup>8</sup> has determined three-dimensional minimum-energy conformations of coal models suggested by Given,<sup>4</sup> Wiser,<sup>5</sup> Solomon,<sup>6</sup> and Shinn<sup>1</sup> and

found that secondary bondings, in particular, van der Waals interactions and hydrogen bonding, are strong driving forces to form and to maintain the three-dimensional structure of coals. Nomura et al. has constructed a bituminous coal structural model based on the data of pyrolysis GC/MS and CP/MAS <sup>13</sup>C NMR.<sup>9</sup> Faulon and co-workers<sup>10,11</sup> developed a new simulation technique including CASE (computer-aided structure elucidation) and CAMD and calculated statistically structural, energetic, and physical characteristics for five coal models with different cross-linking densities. Takanohashi and co-workers<sup>12,13</sup> determined the minimum-energy structure of solvent-soluble molecules by the computer-aided molecular design (CAMD) and reported that the most stable conformation was an associated structure of several coal molecules through noncovalent interactions and these molecules seemed to form a three-dimensional cross-link structure which mainly consists of physical cross-links. The solvent-

\* To whom correspondence should be addressed.

† Abstract published in *Advance ACS Abstracts*, October 1, 1995.

- (1) Shinn, J. H. *Fuel* 1984, 63, 1187.
- (2) Spiro, C. L.; Kosky, P. G. *Fuel* 1981, 60, 1121.
- (3) Spiro, C. L. *Fuel* 1982, 61, 1080.
- (4) Given, P. H. *Fuel* 1960, 39, 147.
- (5) Wiser, W. H. *NATO ASI Ser. C* 1984, 124, 325.
- (6) Solomon, P. R. *New Approaches in Coal Chemistry*; ACS Symp. Ser. 169; American Chemical Society: Washington, DC, 1981; p 61.
- (7) Heredy, L. A.; Wender, I. *Prepr. Pap.-Am. Chem. Soc., Div. Fuel Chem.* 1980, 28, 38.
- (8) Carlson, G. A. *Energy Fuels* 1992, 6, 771.

(9) Nomura, M.; Matsubayashi, K.; Ida, T.; Murata, S. *Fuel Process. Technol.* 1992, 31, 169.

(10) Faulon, J.-L.; Carlson, G. A.; Hatcher, P. G. *Energy Fuels* 1993, 7, 1062.

(11) Faulon, J.-L.; Mathews, J. P.; Carlson, G. A.; Hatcher, P. G. *Energy Fuels* 1994, 8, 408.

(12) Takanohashi, T.; Iino, M.; Nakamura, K. *Energy Fuels* 1994, 8, 395.

(13) Takanohashi, T.; Iino, M.; Nakamura, K. *Kagaku Kogaku Ronbunshu* 1994, 20, 959.

soluble molecules after extraction seem to have the minimum-energy conformation, since the strained structure of coal has been relaxed and stabilized during extraction and fractionation. The structure of raw coal is considered to be anisotropic with increasing rank of coal. The understanding of the macromolecular structure of coals seems to be a key factor in coal handling and reactivities of coal conversion processes, such as liquefaction and pyrolysis.

A concept of "two-phase (component) structure" of coal, i.e., a main three-dimensional covalently cross-linked network and a small amount of low-molecular weight components trapped in the network, has been widely accepted.<sup>14,15</sup> Significant contributions of non-covalent interactions among coal molecules to coal structure, such as hydrogen bondings,<sup>16</sup>  $\pi$ - $\pi$  interactions,<sup>17,18</sup> and charge transfer interactions,<sup>19-21</sup> have been recently reported. It has been found that carbon disulfide-*N*-methyl-2-pyrrolidinone (CS<sub>2</sub>-NMP) mixed solvent gave very high extraction yields more than 50% (daf) for some bituminous coals even at room temperature<sup>22,23</sup> and that the addition of a small amount of tetracyanoethylene or *p*-phenylenediamine greatly increased the extraction yield, suggesting that a large part of coals is composed of associates of solvent-soluble molecules which are dissociated by the reagents above.<sup>20,24</sup> Physical cross-links by locally cooperative noncovalent interactions for the formation of three-dimensional cross-linked structure have been indicated in synthetic and biological polymers. Cody et al.<sup>25,26</sup> have reported that a pyridine-swollen coal shows viscoelastic properties and that it behaves like an entangled network unlike a covalently cross-linked macromolecular network.

In the present paper, Zao Zhuang coal (Chinese bituminous coal) was extracted with pyridine in a Soxhlet extractor, or with CS<sub>2</sub>-NMP mixed solvent at room temperature. For the fractions obtained by solvent fractionation after the extraction, structural analyses were carried out. A molecular model of the raw coal which consists of a huge associate of coal molecules was constructed three-dimensionally using the CAMD method.

## Experimental Section

**Extraction and Fractionation.** Zao Zhuang coal (Shan Tong province in China, 86.9 wt % C, <250  $\mu$ m,) was extracted

(14) Derbyshire, F.; Marzec, A.; Schulten, H.-R.; Wilson, M. A.; Davis, A.; Tekely, P.; Delpuech, J.-J.; Jurkiewicz, A.; Bronnimann, C. E.; Wind, R. A.; Maciel, G. E.; Narayan, R.; Bartle, K.; Snape, C. *Fuel* **1989**, *68*, 1091.

(15) Given, P. H.; Marzec, A.; Barton, W. A.; Lynch, L. J.; Gerstein, B. C. *Fuel* **1986**, *65*, 155.

(16) Larsen, J. W.; Green, T. K.; Kovac, J. J. *Org. Chem.* **1985**, *50*, 4729.

(17) Quinga, E. M.; Larsen, J. W.; Stock, L. M. *Energy Fuels* **1987**, *1*, 300.

(18) Miyake, M.; Stock, L. M. *Energy Fuels* **1988**, *2*, 815.

(19) Sanokawa, Y.; Takanohashi, T.; Iino, M. *Fuel* **1990**, *69*, 1577.

(20) Liu, H.-T.; Ishizuka, T.; Takanohashi, T.; Iino, M. *Energy Fuels* **1993**, *7*, 1108.

(21) Flowers, II, R. A.; Gebhard, L.; Larsen, J. W.; Sanada, Y.; Sasaki, M.; Silbernagel, B. *Energy Fuels* **1994**, *6*, 1524.

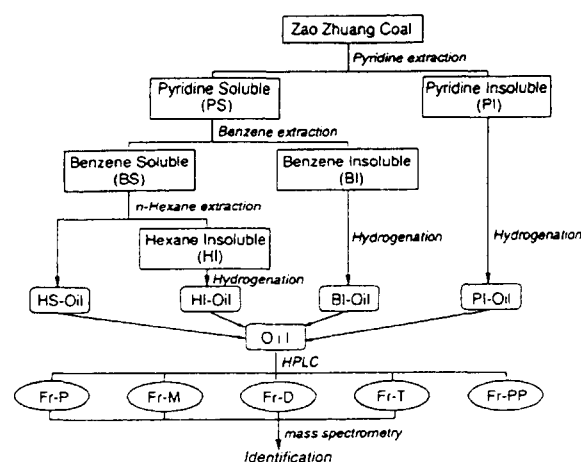
(22) Iino, M.; Takanohashi, T.; Ohsuga, H.; Toda, K. *Fuel* **1988**, *67*, 1639.

(23) Takanohashi, T.; Iino, M. *Energy Fuels* **1990**, *4*, 452.

(24) Ishizuka, T.; Takanohashi, T.; Ito, O.; Iino, M. *Fuel* **1993**, *72*, 579.

(25) Cody, G. D.; Davis, A.; Hatcher, P. G. *Energy Fuels* **1993**, *7*, 455.

(26) Cody, G. D.; Davis, A.; Hatcher, P. G. *Energy Fuels* **1993**, *7*, 463.



**Figure 1.** Solvent extraction and fractionation procedures of Zao Zhuang coal.

**Table 1.** Fraction Distribution of Zao Zhuang Coal

| extraction yield, <sup>a</sup><br>wt % (daf) | extract fraction, wt % (daf) |     |      |      |      |
|----------------------------------------------|------------------------------|-----|------|------|------|
|                                              | HS                           | BS  | PS   | MS   | MI   |
| 63.0                                         | 1.7                          | 4.5 | 24.6 | 28.7 | 37.0 |

<sup>a</sup> The yield with CS<sub>2</sub>-NMP mixed solvent at room temperature.

with pyridine in a Soxhlet extractor and then fractionated with benzene and *n*-hexane into *n*-hexane-soluble (HS), hexane-insoluble, and benzene-soluble (BS), benzene-insoluble, pyridine-soluble (PS), and pyridine-insoluble (PI) fraction as shown in Figure 1. The raw coal was also extracted with the CS<sub>2</sub>-NMP mixed solvent (1:1 by volume) which gives a heavier extract fraction than the PS, i.e., pyridine-insoluble and the mixed solvent-soluble (MS) fraction, and the mixed solvent-insoluble (MI) fraction. A detailed description of the mixed solvent extraction is shown elsewhere.<sup>22</sup>

**Hydrogenation.** The BS, PS, and PI fractions were hydrogenated under mild condition using Adkins catalyst under 10 MPa of hydrogen at 430 °C for 1 h.<sup>27,28</sup> The products were Soxhlet-extracted with *n*-hexane and the oils (*n*-hexane solubles) from each fraction, i.e., BS-oil, PS-oil, and PI-oil, were obtained as shown in Figure 1.

**Structural Analysis of Oil.** The oils were separated into alkanes (Fr-P), monoaromatics (Fr-M), diaromatics (Fr-D), tri- and tetraaromatics (Fr-T), and polyaromatic and polar compounds (Fr-PP) by HPLC with a Zorbax BP-NH<sub>2</sub> column (Du Pont), respectively, using *n*-hexane as an eluent.<sup>29</sup> The structure of the fractions obtained above was analyzed by mass spectrometry. A JEOL JMS-01 SG-2 Series mass spectrometry with field desorption was used for obtaining mass spectra for each fraction. The density of raw coal was measured in water with a gravity bottle and corrected for the content of ash.

## Construction of Molecular Model for Each Fraction

A molecular model with molecular weight of around 10 000 for the raw coal is constructed. The extraction yield and the fraction distribution are shown in Table 1. The ultimate analysis for each fraction is shown in Table 2, together with the molecular formulas of each fraction. The oil yield after hydrogenation for each fraction is shown in Table 3. The oil yield for HS-oil, BS-oil, and PS-oil was 1–3%. Katoh and Ouchi have

(27) Katoh, T.; Ouchi, K. *Fuel* **1985**, *64*, 1260.

(28) Katoh, T.; Ouchi, K. *Fuel* **1987**, *66*, 58.

(29) Satou, M.; Tanimoto, M.; Yokoyama, S.; Sanada, Y. *J. Chem. Soc. Jpn.* **1987**, *1*, 67.

Table 2. Molecular Formulas of Each Fraction

| fraction        |          | ultimate analysis (wt %, daf) |     |     |     |                  | molecular formula                                                                | $\bar{M}_n$        | H/C  | O/C   | N/C   | S/C   | $f_a$             |
|-----------------|----------|-------------------------------|-----|-----|-----|------------------|----------------------------------------------------------------------------------|--------------------|------|-------|-------|-------|-------------------|
|                 |          | C                             | H   | N   | S   | O                |                                                                                  |                    |      |       |       |       |                   |
| HS              | observed | 86.5                          | 7.7 | 1.1 |     | 4.7 <sup>a</sup> |                                                                                  | 380 <sup>b</sup>   | 1.07 |       | 0.011 |       | 0.62 <sup>c</sup> |
|                 | model    | 87.6                          | 7.9 | 0.0 | 0.0 | 4.5              | C <sub>26</sub> H <sub>28</sub> O <sub>1</sub>                                   | 356                | 1.08 | 0.038 | 0.000 | 0.000 | 0.62              |
| BS <sup>d</sup> | observed | 89.1                          | 6.8 | 1.2 | 1.1 | 1.8              |                                                                                  | 705 <sup>b</sup>   | 0.92 | 0.015 | 0.012 | 0.005 | 0.68 <sup>c</sup> |
|                 | model    | 88.1                          | 6.8 | 2.3 | 0.0 | 2.7              | C <sub>44</sub> H <sub>41</sub> O <sub>1</sub> N <sub>1</sub>                    | 599                | 0.93 | 0.023 | 0.023 | 0.000 | 0.68              |
| PS              | observed | 85.9                          | 5.3 | 1.7 | 1.8 | 5.3              |                                                                                  | 1990 <sup>b</sup>  | 0.74 | 0.046 | 0.017 | 0.008 | 0.74 <sup>c</sup> |
|                 | model    | 86.0                          | 5.3 | 1.8 | 1.4 | 5.5              | C <sub>167</sub> H <sub>123</sub> O <sub>8</sub> N <sub>3</sub> S <sub>1</sub>   | 776                | 0.75 | 0.048 | 0.018 | 0.006 | 0.83              |
| MS              | observed | 85.5                          | 5.1 | 1.8 | 1.7 | 5.9              |                                                                                  | 3080 <sup>b</sup>  | 0.71 | 0.052 | 0.019 | 0.007 | 0.82 <sup>c</sup> |
|                 | model    | 85.3                          | 5.0 | 1.8 | 2.1 | 5.8              | C <sub>216</sub> H <sub>152</sub> O <sub>11</sub> N <sub>4</sub> S <sub>2</sub>  | 1013               | 0.70 | 0.051 | 0.019 | 0.009 | 0.85              |
| MI              | observed | 85.3                          | 4.7 | 1.6 | 2.1 | 6.3              |                                                                                  | 1419               | 0.66 | 0.055 | 0.016 | 0.009 |                   |
|                 | model    | 85.4                          | 4.7 | 1.6 | 2.3 | 6.0              | C <sub>303</sub> H <sub>198</sub> O <sub>16</sub> N <sub>5</sub> S <sub>3</sub>  | 1419               | 0.65 | 0.053 | 0.017 | 0.010 | 0.87              |
| raw coal        | observed | 86.9                          | 5.1 | 1.5 | 1.6 | 4.9              |                                                                                  | 10580 <sup>e</sup> | 0.70 | 0.042 | 0.015 | 0.007 |                   |
|                 | model    | 85.8                          | 5.1 | 1.7 | 1.8 | 5.6              | C <sub>756</sub> H <sub>542</sub> O <sub>37</sub> N <sub>13</sub> S <sub>6</sub> | 10580 <sup>e</sup> | 0.72 | 0.049 | 0.017 | 0.008 | 0.85              |

<sup>a</sup> By difference (S + O). <sup>b</sup> SEC.<sup>12</sup> <sup>c</sup> <sup>1</sup>H NMR.<sup>30</sup> <sup>d</sup> Acetone-soluble fraction. <sup>e</sup> Total molecular weight.

Table 3. Yield of Oil Obtained from Each Fraction

|                                | HS-oil <sup>a</sup> | BS-oil <sup>b</sup> | PS-oil <sup>b</sup> | PI-oil <sup>b</sup> |
|--------------------------------|---------------------|---------------------|---------------------|---------------------|
| oil yield, wt % raw coal basis | 1.7                 | 0.97                | 2.9                 | 13                  |

<sup>a</sup> Obtained from extraction and fractionation. <sup>b</sup> Obtained from the hydrogenation of each fraction.

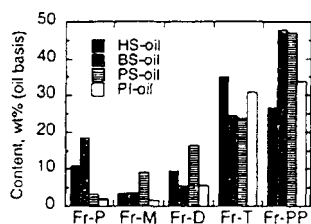


Figure 2. Fraction distribution of each oil separated by HPLC.

conducted<sup>27,28</sup> the same mild hydrogenation for Taiheiyao coal (77.0 wt % C) using Adkins catalysis at 360–430 °C, and extracted *n*-hexane solubles (oil), and then the residue (*n*-hexane insolubles) obtained was again hydrogenated and extracted, and this hydrogenation procedure was repeated six times. Total oil yield was up to 68.8%. The aromatic structure of each oil fraction from the Taiheiyao coal was very similar and mono- and diaromatics were main components, regardless of the number of hydrogenation. Iino et al. have reported<sup>30</sup> that three extract fractions obtained from the CS<sub>2</sub>-NMP extraction showed a similar degree of aromatic condensation independent of the heaviness of fractions, although the aromaticity ( $f_a$ ) increased with the fractions heavier. These results indicate that the structures of aromatic moieties in coal are similar throughout the entire fractions from the lighter fraction to the heavy one including the residue. Therefore, the structure of aromatic ring for the oils from each fraction is assumed to be that for the each fraction itself.

The fraction distribution of each oil (HS-oil, BS-oil, PS-oil, PI-oil) by HPLC separation is shown in Figure 2. Fr-T and Fr-PP were abundant in all oils. The distribution of aromatic rings of models for HS-PI was determined from the fraction distribution in Figure 2. The distribution of MI was assumed to be similar to that

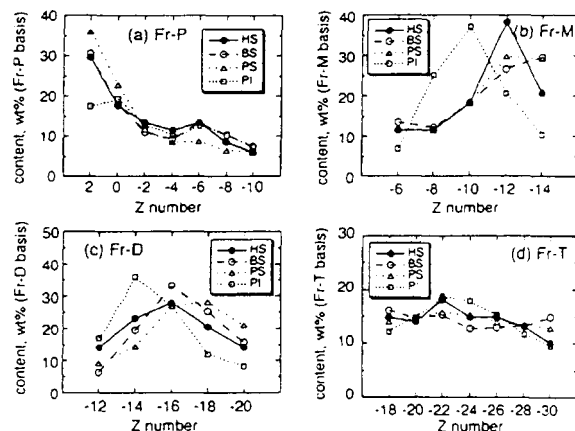



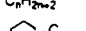

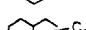

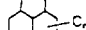



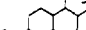

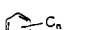
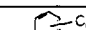
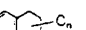
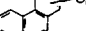
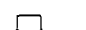


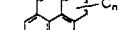
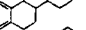
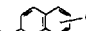

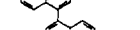
Figure 3. Distribution of compound type of each fraction classified with Z number: (a) Fr-P, (b) Fr-M, (c) Fr-D, (d) Fr-T.

of PI. The structural parameters for extract fractions of Zao Zhuang coal have been reported,<sup>30</sup> and the average number of aromatic rings for all fractions was 3–4 independent of the heaviness of fractions. Ultimate analysis of all fractions shown in Table 2 also indicates that H/C decreased and O/C increased continuously from the lighter fraction to the heavier one including the residue. The aromaticity of MI was estimated ( $f_a = 0.87$ ) from the extrapolation of the line connecting HS ( $f_a = 0.62$ ), BS ( $f_a = 0.68$ ), PS ( $f_a = 0.83$ ), and MS ( $f_a = 0.85$ ).

Figure 3a–d shows distributions of compound type which was classified with the Z number ( $C_nH_{2n+2}$ ), for Fr-P, Fr-M, Fr-D, and Fr-T, respectively. Typical compound types classified with the Z number are shown in Table 4. Fr-PP is polyaromatic and polar components and it was impossible to analyze the Fr-PP. The aromatic structure of Fr-PP is considered to be similar to that of Fr-P–Fr-T, since all oils from each fraction contained Fr-PP to a similar extent. Therefore, the amount of Fr-P–Fr-PP in HS–MI was determined from the distribution of fractions (in Figure 2), and then compound types with larger content in Figure 3 were selected for HS–MI, respectively. The structural elements for all fractions (HS, BS, PS, MS, and MI) are shown in Figure 4. The tri- and tetraaromatics were

(30) Iino, M.; Takanohashi, T.; Obara, S.; Tsueta, H.; Sanokawa, Y. *Fuel* 1989, 68, 1588.

Table 4. Typical Compound Type Classified with Z Number

|      | Z   | Comp. type                                                                        |      | Z                                                                                 | Comp. type                                                                        |
|------|-----|-----------------------------------------------------------------------------------|------|-----------------------------------------------------------------------------------|-----------------------------------------------------------------------------------|
| Fr-P | +2  | $C_nH_{2n+2}$                                                                     | Fr-D | -12                                                                               |  |
|      | 0   |  |      | -14                                                                               |  |
|      | -2  |  |      | -16                                                                               |  |
|      | -4  |  |      | -18                                                                               |  |
|      | -6  |  |      | -20                                                                               |  |
|      | -8  |  |      |                                                                                   |                                                                                   |
|      |     | -10                                                                               |      |  |                                                                                   |
| Fr-M | -6  |  | Fr-T | -18                                                                               |  |
|      | -8  |  |      | -20                                                                               |  |
|      | -10 |  |      | -22                                                                               |  |
|      | -12 |  |      | -24                                                                               |  |
|      | -14 |  |      | -26                                                                               |  |
|      |     |                                                                                   | -28  |  |                                                                                   |
|      |     |                                                                                   | -30  |  |                                                                                   |

$^{\circ} C_nH_{2n+2}$

 $C_nH_{2n+2}$ 

the main components independent of the heaviness of fractions. Functional types of oxygen were assumed to be hydroxyl and ether groups. The content of hydroxyl groups was determined previously.<sup>30</sup> It was assumed that the bonding types of nitrogen and sulfur are pyridinic and pyrrolic groups<sup>31,32</sup> and thiophenic and thioether groups,<sup>33</sup> respectively.

The aromatic rings for HS and BS in Figure 4 were connected with a methylene bridge. The aliphatic carbons which are side chains or naphthenic types were attached to fit the H/C atomic ratio of each fraction. The molecular models for HS and BS are shown in Figure 5.

It has been reported<sup>12</sup> that the structures in the energy-minimum state for PS or PI fraction were associates among several coal molecules. Molecular weight distributions of PS and PI have been found<sup>12</sup> to change by using the eluent solvent containing a small amount of lithium bromide or anthracene, i.e., the region in high molecular weight ( $10^5$ – $10^6$ ) was shifted to that in lower molecular weight ( $10^2$ – $10^3$ ), suggesting that these additives could dissociate the associates of coal molecules and make their apparent molecular weight lower. Acetone-soluble fraction (AS) from the  $CS_2$ –NMP extraction of Zao Zhuang coal showed the distribution of molecular weight with one peak in the

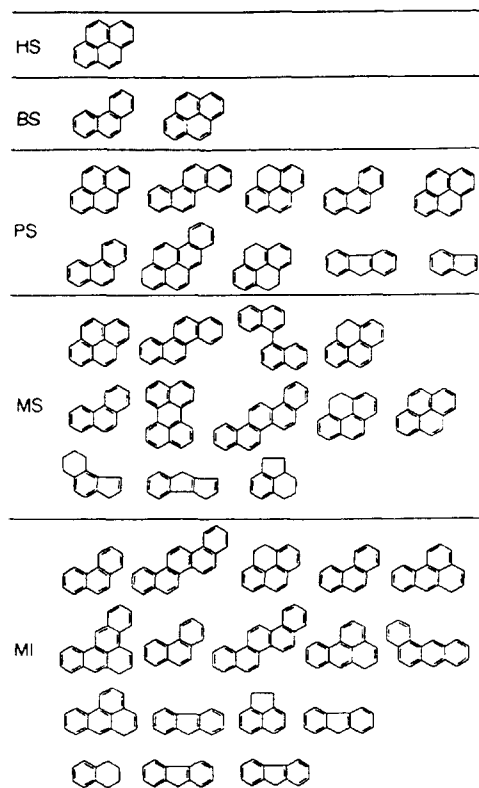


Figure 4. Aromatic structural elements for each fraction (HS, BS, PS, MS, MI).

low molecular weight region (around  $10^2$ – $10^3$ ), and no change in molecular weight distribution by the additives was observed, indicating AS does not so much associate in the mixed solvent. If all associates in PS and PI are dissociated, their fractions may show a similar distribution of molecular weight to AS fraction. The average molecular weight of one molecule for PS and PI should be lower than the data obtained from size exclusion chromatography (SEC), although it is difficult to determine the true molecular weight. In this study the average molecular weight for HS and BS was determined from the SEC measurement since their fractions do not so much associate in the mixed solvent, while the average number weight for PS, MS, and MI was assumed in the range of 776–1419, as described below.

The addition of a small amount of tetracyanoethylene (TCNE) to the carbon disulfide–*N*-methyl-2-pyrrolidone mixed solvent greatly increased the extraction yield of coals at room temperature,<sup>20,24</sup> suggesting that the MI (residue) still includes associates of a considerable amount of solvent-soluble components and TCNE dissociates them. The increased solvent-solubles from the MI was almost MS fraction. Thus, the structure of MI is also considered to be association of coal molecules, not a covalently bound three-dimensionally developed cross-linked network as generally accepted. Molecular models for PS, MS, and MI were constructed in the same way as HS and BS, and are shown in Figure 5. The model for PS, MS, and MI consists of three molecules, respectively. The average molecular weight for the model structures is 356, 599, 776, 1013, 1419, for HS, BS, PS, MS, and MI, respectively. So, the raw coal is composed of the 11 molecules from HS (oil) to MI

(31) Kelemen, S. R.; Gorbaty, M. L.; Kwiatak, P. J. *Energy Fuels* 1994, 8, 896.

(32) George, G. N.; Gorbaty, M. L.; Kelemen, S. R.; Sansone, M. *Energy Fuels* 1991, 5, 93.

(33) Huffman, G. P.; Mitra, S.; Huggins, F. E.; Shah, N.; Vaidya, S.; Lu, F. *Energy Fuels* 1991, 5, 574.

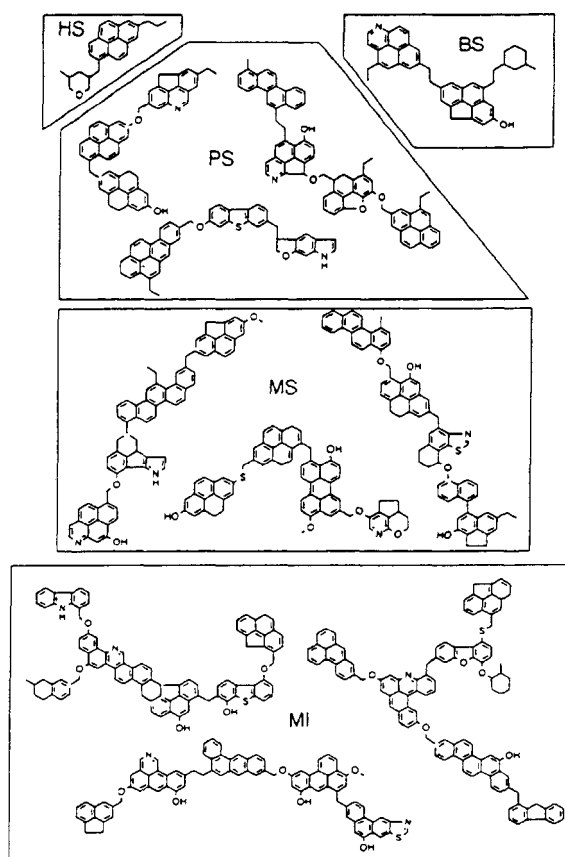


Figure 5. Model structure for each fraction (HS, BS, PS, MS, MI).

(residue), and the total molecular weight is 10 580. It is noted that the model structure of the raw coal is a huge associate of coal molecules which have a continuous distribution of molecular weight, from HS to MI. The distinctions of heaviness among fractions separated by solvent fractionation are explained by the average molecular weight and the content of polar functional groups which are related to a tendency to form associates. In the previous paper, molecular models for PS and PI were constructed<sup>12</sup> using structural parameters calculated from <sup>1</sup>H NMR data. The present model structures were similar to previous ones.

### Simulation Methods

**Computer and Software.** TITAN 750V graphic workstation (Kubota Computer Inc.) and Polygraf (version 3.21, Molecular Simulation Inc.) were used as the hardware on computer and the software program for the CAMD, respectively. The DREIDING method<sup>34</sup> was used for the force field calculation. Polygraf also allows the use of periodic boundary conditions, in which model molecules are placed in a basic cell surrounded by the same cells in all directions. If a molecular segment exits on the one surface of the cell, the same segment enters from the opposite surface. Molecular segments in the cell can interact with others in the neighboring cells as well as in the same cell. Using these periodic boundary

conditions, the estimation of the physical density of model molecules was carried out.<sup>35-37</sup> The densities estimated for styrene oligomer and coal models have been found to agree with the observed ones.

**Potential Functions.** The energy for model molecules was evaluated from forces of bonded interactions (bond ( $E_b$ ), angle ( $E_\theta$ ), torsion ( $E_\phi$ ), inversion ( $E_i$ )), and forces of nonbonded interactions (van der Waals ( $E_{vdW}$ ), electrostatic ( $E_{el}$ ), hydrogen bond ( $E_{hb}$ )), as shown in eq 1.

$$E = E_b + E_\theta + E_\phi + E_i + E_{vdW} + E_{el} + E_{hb} \quad (1)$$

### Construction of Molecular Model for Raw Coal

All coal molecules of HS, BS, PS, MS, and MI were randomly placed in a rectangular cell. It is not required to connect between coal molecules by covalent bonds, because their fractions were obtained from the mild extraction and fractionation and no bond scission has been indicated.<sup>22</sup> Thus, the associated structure of coal molecules having a continuous molecular weight distribution from HS to MI was considered for the model structure of Zao Zhuang bituminous coal, which is different from the two-phase model structure which consists of a covalently bound cross-linked network (immobile phase) and a small amount of low-molecular weight component (mobile phase) trapped in the network, which was widely accepted.<sup>14,15</sup> The model after enclosing into the cell is shown in Figure 6. The size of cell is 72.9 Å × 79.9 Å × 12.9 Å. Cody et al.<sup>38</sup> have reported anisotropic swelling behaviors of raw coals. The swelling was greater perpendicular to the bedding plane than parallel to it. This result suggests that raw coals possess originally anisotropic structures, i.e., orientation of aromatic rings parallel to the bedding plane. Aromatic rings can interact with other aromatic ring systems through  $\pi$ - $\pi$  and van der Waals interactions and hydrogen bonding. Coal underground would have been pressurized to a great extent and would have a strained structure. Then, the coal mined would have been relaxed to some extent; however, significant strains still remain because of less mobility of coal molecules. Such strained structure for raw coal can be fully relaxed in good solvents or by thermal treatments. It was found<sup>39</sup> that treatment with pyridine decreased the extraction yield of bituminous coals, indicating that the structure relaxed in the solvent has formed more stable conformation through noncovalent interactions. Yun and Suuberg<sup>40</sup> also have found that the thermal structural relaxation of coal macromolecules occurred at 350–430 °C. Therefore, the rectangular cell (72.9 Å × 79.9 Å × 12.9 Å) as shown in Figure 6 was used to make the raw coal have such anisotropic macromolecular structure.

Figure 7 shows the flow chart of the calculation procedure. The molecular mechanics (MM) and molecular dynamics (MD) calculations were carried out for model molecules in a basic cell. The size of cell was

(35) Nakamura, K.; Murata, S.; Nomura, M. *Energy Fuels* 1993, 7, 347.

(36) Murata, S.; Nomura, M.; Nakamura, K.; Kumagai, H.; Sanada, Y. *Energy Fuels* 1993, 7, 469.

(37) Dong, T.; Murata, S.; Miura, M.; Nomura, M.; Nakamura, K. *Energy Fuels* 1993, 7, 1123.

(38) Cody, G. D. Jr.; Larsen, J. W.; Siskin, M. *Energy Fuels* 1988, 2, 340.

(39) Takanohashi, T.; Iino, M. *Energy Fuels* 1991, 5, 708.

(40) Yun, Y.; Suuberg, E. M. *Fuel* 1993, 72, 1245.

(34) Mayo, S. L.; Olafson, B. D.; Goddard III, W. A. *J. Phys. Chem.* 1990, 94, 8897.



for the extract fractions from Zao Zhuang coal also have agreed with the observed one.<sup>12</sup> So, the associated model structure suggested here seems to be appropriate for the Zao Zhuang coal.

### Conclusions

Zao Zhuang coal was extracted and fractionated, and the extract fractions obtained were hydrogenated under mild conditions. Structural analyses for the oils obtained showed that the main components of oils were aromatics with 3–4 rings independent of the heaviness of fraction. Associated structure of coal molecules having a continuous molecular weight distribution from the lighter fraction to the extraction residue was assumed for the model structure of the coal. The periodic boundary condition was used for modeling of structure

of the raw coal, to make the coal have the anisotropic structure. The estimated density for the model structure was in agreement with the observed one. Finally, the associated model structure suggested here seems to be appropriate for the Zao Zhuang coal.

**Acknowledgment.** This work was supported by the Ministry of Education, Science and Culture, Japan (Japan–USA Joint Research Program). The simulation of the density performed in this paper was developed by Dr. M. Nomura and Dr. S. Murata of the Faculty of Engineering of Osaka University, and Dr. K. Nakamura of Osaka Gas Co., Ltd. We are grateful to Dr. M. Nomura and Dr. S. Murata for discussions on the simulation.

EF950094B



0008-6223(94)00114-6

## AN ADDITIONAL CARBON LAYER OVER THE SURFACE OF C/C COMPOSITE SUBSTRATE WITH THE AID OF POLYVINYL CHLORIDE

T. UEDA and T. MORIMOTO

Advanced Technology Research Center, Mitsubishi, Heavy Industries, Ltd.,  
Kanazawa-ku, Yokohama 236 Japan

H. KUMAGAI and Y. SANADA

Faculty of Engineering, Hokkaido University, Kita-ku, Sapporo, 060 Japan

(Received 14 January 1994; accepted in revised form 30 August 1994)

**Abstract**—The novel bonding of an additional carbon layer over a C/C composite substrate surface was studied. Furan resin was selected for the additional carbon layer precursor. Molding was performed using a hot press apparatus. Polyvinyl chloride resin (PVC) was used as the bonding agent. The bonding mechanisms were studied with thermal gravity analysis, thermal gravity-mass spectroscopy, and high-temperature electron paramagnetic resonance spectroscopy. No peel-off was observed at the boundary between the carbon layer derived from furan resin/graphite powder and the C/C composite after loading by an external stress. The spins in thin carbon derived from PVC are recombined and are erased by the particular sites of graphite surface as one of roles of enhancement of adhesion.

**Key Words**—C/C composite, polyvinyl chloride resin, chemical bonding.

### 1. INTRODUCTION

Carbon fiber-reinforced carbon (C/C) composites have potential for use as high-temperature structural materials, despite drawbacks such as high cost and low oxidation resistivity[1–2]. A protection system against high-temperature oxidation is required to use C/C composites on aerospace vehicles. A silicone carbide (SiC) surface coating is one of the most promising systems[3–4]; however, a decrease in strength of the underlying C/C composite occurs during the high-temperature surface modification process. Additionally, uniform coating by an SiC film is difficult to achieve because of the non-uniform structure of a C/C composite surface. These difficulties have been overcome by the use of an additional carbon layer bonded with the aid of PVC over the surface of the C/C composite[5–6]. After processing, the carbon layer has an SiC concentration gradient, and the interlayer is strongly bonded to the C/C composite[7].

In this paper we describe the results of the interfacial bonding mechanisms between the carbon layer and the C/C composite.

### 2. EXPERIMENTAL

A C/C composite of 2D type was used as a substrate. Commercially available furan resin (Hitachi Kasei Inc., Hitafuran 302) was selected for the carbon layer precursor. This furan resin gives low carbonization yields; therefore, fine graphite powder (Wako Pure Chemical Industries, Ltd., grain size under 45  $\mu\text{m}$ ) was added. Polyvinyl chloride resin (Sunarrow Chemical Corporation, Sunar SA 400L) was used for the inter-

layer between the carbon layer precursor and the surface of the C/C composite. Epoxy resin (Refinetic Ltd., Epomount) and phenol formaldehyde resin (Dainippon Inc. & Chemicals Inc., Phenolite) were also tested as references to polyvinyl chloride resin.

The materials were hot pressed, as shown in Fig. 1. The interlayer resin, including graphite powder, was placed between the carbon layer precursor resin and the C/C composite. The molding pressure was 200 kgf/cm<sup>2</sup> at 200°C. After molding, the test materials were baked at 1000°C for 5 h in an argon gas atmosphere.

The carbon layer microstructure was observed by a scanning electron microscope (SEM) to evaluate and monitor the bonding processes. The apparent density of the carbon layer was measured by a liquid replacement method. Ethanol was selected as the substitution medium.

The bond strength between the carbon layer and the C/C composite was determined by the short-beam, three-point bending method described in the ASTM D2344. The short beam specimens contained a middle carbon layer, derived from furan/graphite and bonded with carbon interlayer derived from PVC/graphite films to top and bottom C/C composite plates. Specimens without PVC interlayer films were also tested for comparison.

Thermal gravity analysis (TGA), thermal gravity-mass spectroscopy (TG-MS), and high-temperature electron paramagnetic resonance spectroscopy (EPR) were performed to clarify the bonding mechanisms. TGA data were obtained under a nitrogen gas atmosphere up to 600°C with a heating rate of 10°C/min. The differential TGA curve (DTGA) was measured under the same condition as TGA and evolved gases

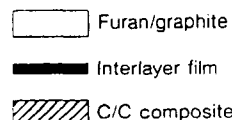
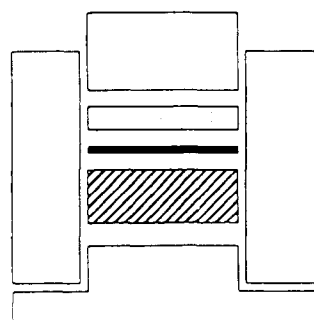


Fig. 1. Hot-press apparatus.

were sampled and analysed by MS at a temperature interval of 50°C. The detail of EPR measurement is described elsewhere[8]. The maximum EPR analysis temperature was 600°C.

The instruments used for each analysis were as follows: Rigaku Corporation TG-810 (TGA), Shimadzu Corporation TG-QP 1000 EX (TG-MS), and Varian Instruments Ltd. E-109 (EPR).

### 3. RESULTS AND DISCUSSION

Figure 2 shows the change of apparent density of the furan/graphite derived carbon layer vs carbonization temperature. The apparent density of the carbon layer was approximately 2 g/cc after a 1000°C carbon-

Table 1. Mechanical test data of furan-derived carbon layer over the surface of C/C composite

| Furan/graphite <sup>b</sup><br>C/C composite | Furan/graphite <sup>b</sup> -C/C composite<br>PVC film as an interlayer |
|----------------------------------------------|-------------------------------------------------------------------------|
| peel-off                                     | 6.7 MPa <sup>a</sup>                                                    |

<sup>a</sup>Shear stress.

<sup>b</sup>Furan/graphite weight ratio: 1/4.

ization treatment; this value then increased gradually to 2.2 g/cc after a 2000°C carbonization treatment. The carbon layer after the 1000°C carbonization treatment is adequate to protect the C/C composite.

The carbon layer derived from furan/graphite is not able to bond to the C/C composite without interlayer films. The carbon layer also easily peeled off from the surface of C/C composite in the presence of the carbon layer derived from epoxy resin/graphite and phenol-formaldehyde resin/graphite films. No bonding on the surface of the C/C composite is evidenced by SEM, as shown in Fig. 3a and b. These results indicate that the association was slight between the carbon layer and the surface of the C/C composite in these cases. Figure 3c shows an SEM photograph of the bonding site of a specimen that used a PVC/graphite interlayer. The interlayer film of PVC/graphite powder (weight ratio 1/4) is sandwiched in between the carbon layer derived from furan/graphite powder (weight ratio 1/4) and the surface of C/C composite. The carbon layer adheres well to the surface of C/C composite. Table 1 shows the results of a mechanical test of the specimens. The specimen with PVC interlayer film peeled off under a 6.7 MPa shear stress. The adhesion is high enough for practical use.

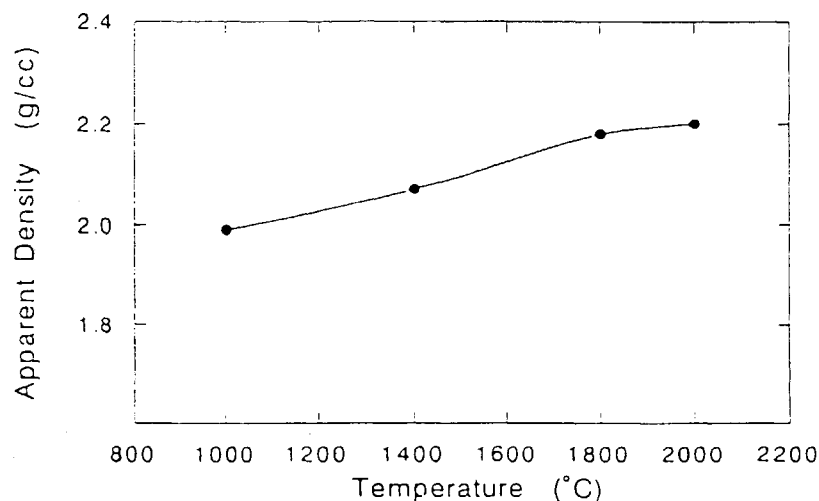


Fig. 2. Change of apparent density of the carbon derived from furan/graphite vs carbonization temperature.

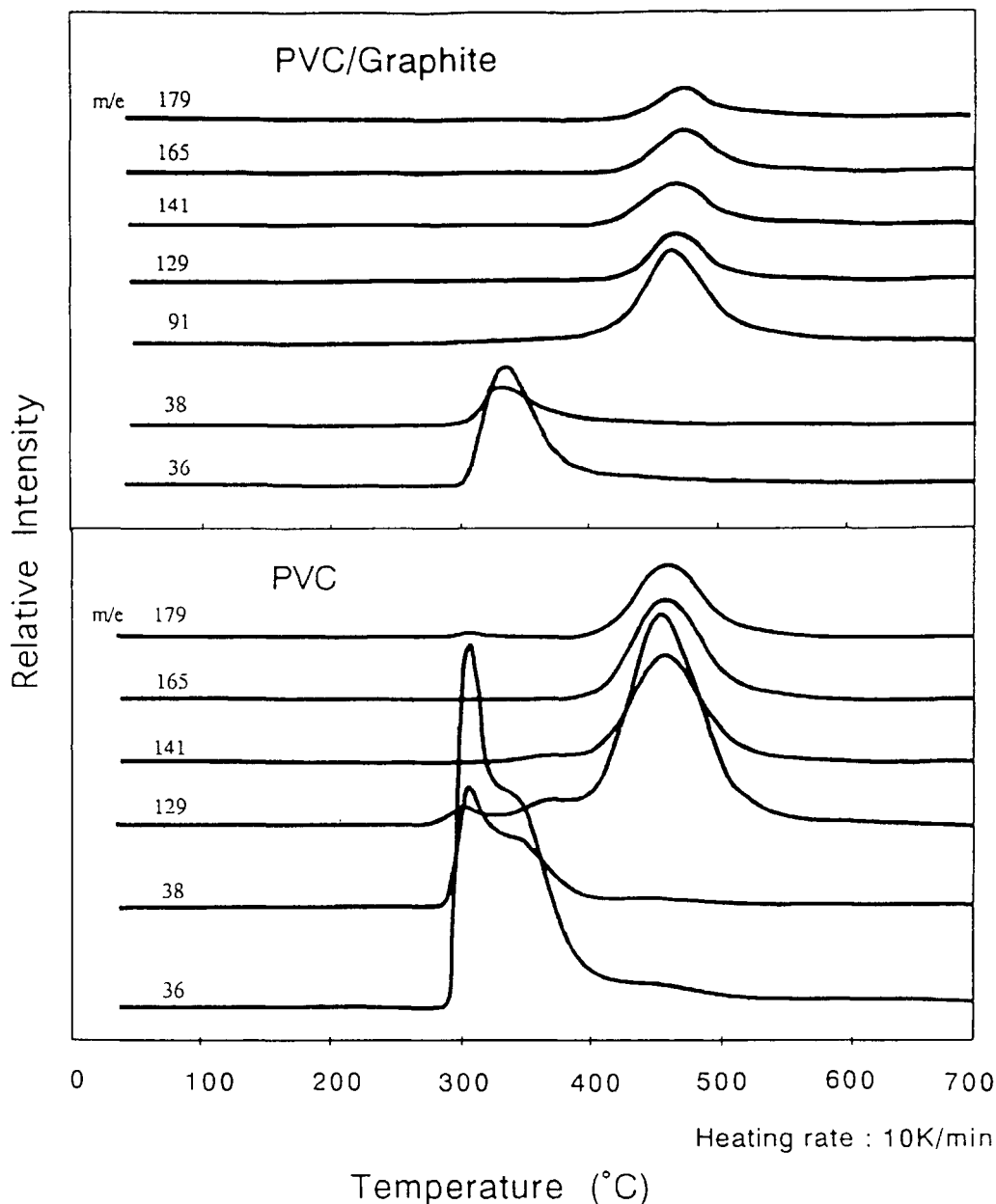


Fig. 5. TG-MS curve for PCV samples.

crease of spin concentration for co-carbonized products[14]. They suggest that the increase of the spin concentration in the presence of carbon black is probably due to (a) increase of delocalized unpaired electrons due to the development of aromatic lamellae, (b) reducing the rate of recombination reaction of free radicals, and (c) lack of transferable hydrogen in the pitch. The hydrogens have a role stabilizing the free radicals created by pyrolysis of pitch. This is because the transferable hydrogens consume functional groups on the carbon black surface. Therefore, oxygen con-

taining functional groups on the surface of carbon will play an important role in the carbonization reaction.

Our special attention is focused on a difference of the temperature dependency of PVC thermal decomposition. That is, weight decreases of PVC with and without graphite powder at 300°C, at which HCl starts to evolve, were tabulated in Table 2. From the results, it is presumed that evolution of HCl gas become restricted and/or is retarded chemically or catalytically with the existence of functional groups over the surface of graphite powder.

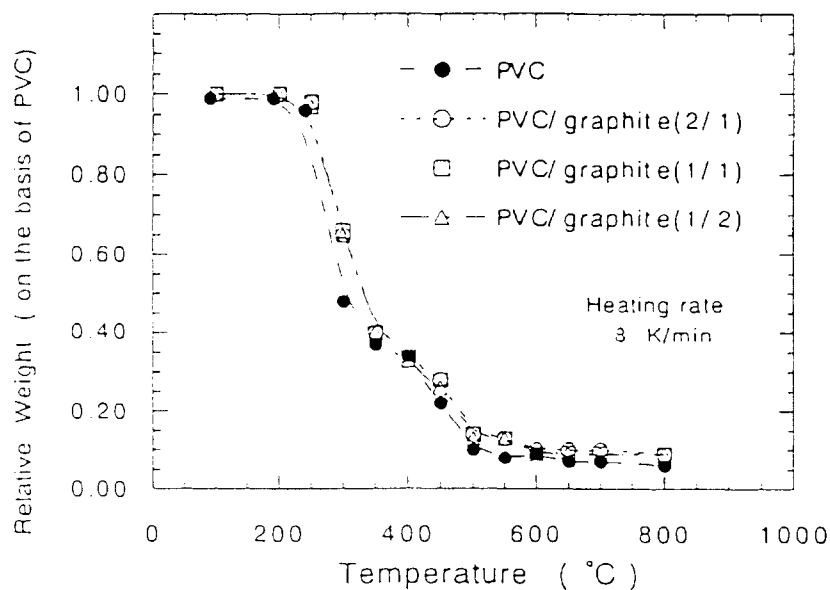


Fig. 6. TGA curve of PVC samples.

Figure 8 shows a model describing the phenomena during heating. In the absence of graphite, PVC decomposes to generate pitch-like material with spins accompanied by evolution of HCl. As the spins in the pitch recombine partially, the ampoule amount of spins will survive during heating. On the other hand, in the presence of graphite, evolved HCl from PVC

reacts with oxygen-containing functional groups on the surfaces of graphite particles to generate active spins. Thus, the total amount of spins will increase compared to the case of PVC alone at the temperature 250–500°C. At higher temperatures (~500°C), the spins in the pitch recombine and are erased by the particular sites of graphite surface. This is a probable rea-

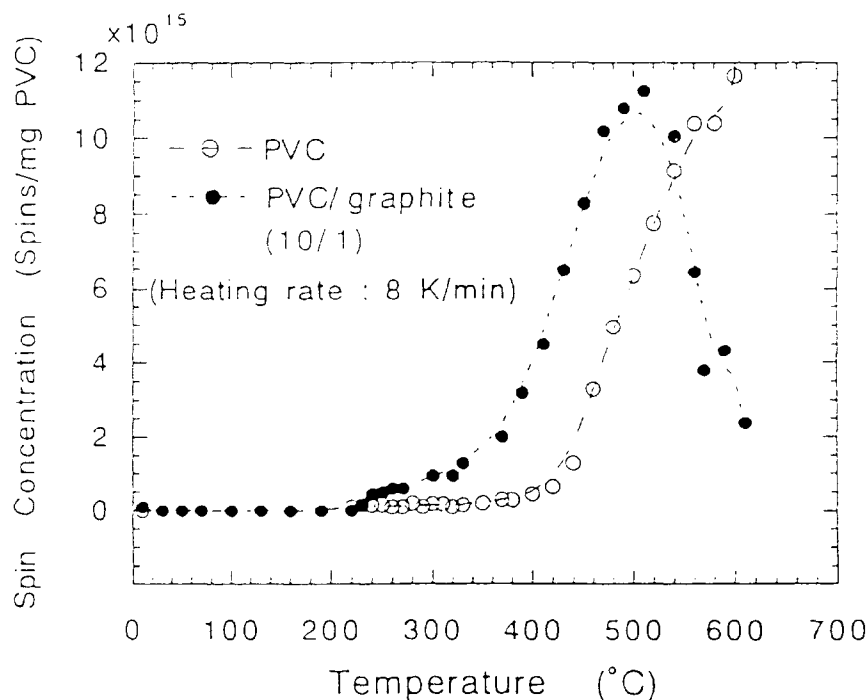


Fig. 7. High-temperature EPR data of PVC.

Table 2. Weight changes of PVC with graphite powder at 300°C

|                              | PVC alone | PVC with graphite<br>(wt ratio) |      |      |
|------------------------------|-----------|---------------------------------|------|------|
|                              |           | 2:1                             | 1:1  | 1:2  |
| Weight decrease <sup>a</sup> | 0.48      | 0.65                            | 0.66 | 0.65 |

<sup>a</sup>Weight of residue after heat treatment (on basis of PVC).

son why the carbon layer derived from PVC/graphite precursor associates strongly with the C/C composite substrate.

Currently we are studying the interaction of PVC

with oxygen-containing functional groups bonded to the edge carbon of graphite crystals.

#### 4. CONCLUSIVE REMARKS

We have demonstrated the feasibility of chemical bonding between carbon blocks (C/C composite and carbon layer) using polyvinyl chloride resin (PVC) as an interlayer material. It was found that thermal decomposition of PVC and the subsequent interaction between evolved gas components and the surface of carbon were effective in producing a strong chemical bond.

*Acknowledgements*—The authors thank Toray Research Center, Inc. for help in TG-MS analysis.

#### REFERENCES

1. E. Fitzer, A. Gkogkidis, and M. Heine, *High Temp-High Pres.* **16**, 363 (1984).
2. J. D. Buckley, *Ceramic Bulletin* **67**, 364 (1988).
3. J. R. Strife and J. E. Sheehan, *Ceramic Bulletin* **67**, 369 (1988).
4. D. W. McKee, *Carbon* **25**, 510 (1987).
5. T. Ueda, T. Morimoto, and Y. Sanada, *Preprint of 19th Annual Meeting of Carbon Soc. Japan*, p. 172 (1992).
6. T. Ueda, T. Morimoto, H. Kumagai, and Y. Sanada, *Preprint of 20th Annual Meeting of Carbon Soc. Japan*, p. 188 (1993).
7. M. Kondo, T. Morimoto, A. Kohyama, and H. Tsunakawa, In *Proc. 9th Intern. Conf. Composite Materials*, Vol. 3, p. 703. Madrid, Spain (1993).
8. M. Oshikiri, T. Yokono, and Y. Sanada, *Tanso* **140**, 306 (1989).
9. D. Owen, In *Degradation and stabilization of PVC*, p. 21. Elsevier Applied Science Publishers, Oxford (1984).
10. S. A. Liebman, J. F. Reuwer, Jr., K. A. Gollatz, and C. D. Nauman, *J. Polym. Sci.* **9**, 1823 (1971).
11. M. Carenza, Y. V. Moiseev, and G. Palma, *J. Polym. Sci.* **17**, 2685 (1973).
12. K. P. Nolan and J. S. Shapiro, *J. Polym. Sci. Symposium* **55**, 201 (1976).
13. S. Otani, *J. Chem. Soc. Jpn.* **61**, 1324 (1958).
14. K. Murakami, T. Yokono, and Y. Sanada, In *Proc. 18th Bienn. Conf. on Carbon*, p. 207, Worcester, MA (1987).

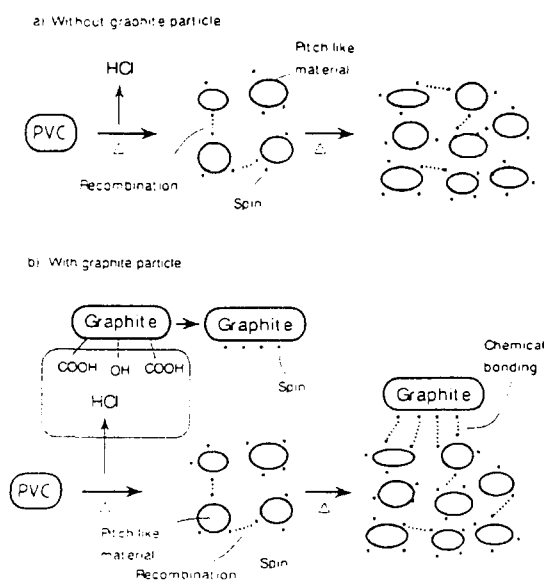


Fig. 8. Phenomena of chemical bonding between graphite and PVC carbon.



0008-6223(94)00112-X

## CARBONIZATION OF PITCHES IN AIR BLOWING BATCH REACTOR

J. H. CHOI,<sup>1</sup> H. KUMAGAI,<sup>1</sup> T. CHIBA,<sup>2</sup> and Y. SANADA<sup>1</sup><sup>1</sup>Center for Advanced Research of Energy Technology and <sup>2</sup>Faculty of Engineering, Hokkaido University, Sapporo 060, Japan

(Received 5 April 1994; accepted in revised form 16 September 1994)

**Abstract**—Carbonization of petroleum and coal tar pitches to toluene insoluble fraction (*TI*) was investigated under air and nitrogen gas blowing systems. The *TI* yield was evaluated on the basis of the weight of pitch loaded. Changes of the yield with the reaction time were analyzed by a kinetic model of carbonization. The model assumes that pitch as a reactant contains a reactive component,  $P_1$ , which converts to active thermal fragment,  $P^*$ , and gas and tar,  $G$ , more quickly than the residual component,  $P_2$ , exhibiting a nonlinear decrease of pitch in semi-logarithmic plot against the reaction time in an early stage of the reaction. The activation energies for  $P_1$  and  $P_2$  conversions depended on pitch and gas atmosphere. In particular, activation energies for  $P_1$  conversion in the air blowing system was found to be appreciably smaller than those in the nitrogen blowing system. This less temperature-sensitive carbonization in the former system may be attributed to pitch reactivity improved by oxygen in air.

**Key Words**—Air blowing, kinetics, toluene insoluble, coal tar pitch, petroleum pitch.

### 1. INTRODUCTION

Air blowing is known to be one of the methods to raise the softening point of pitches and to produce precursors preferable to general-purpose carbon fiber (GPCF)[1]. A great feature of the air blowing is oxidative polymerization reaction, which participates to complicated reactions such as dehydrogenation, condensation, and aromatization, usually accompanied with heat treatment of carbonaceous materials under inert gas atmosphere. Many researchers have studied chemical properties and carbonization behavior of pitches produced with air blowing[2–8]. Mochida *et al.*[1–3] reported that the carbonization mechanism of pitches under air blowing was different from the types of the pitches, and the softening point of a pitch was effectively increased by air blowing and the product pitch was easily converted to carbon fiber with fully developed anisotropic texture by conventional heat treatment under inert gas atmosphere.

In spite of numerous investigations on the kinetics of mesophase formation in an inert gas blowing system[9–11], few have been reported for those in an air blowing system. Recently, Hüttinger *et al.*[12–14] investigated the kinetics of mesophase formation under several kinds of atmospheric gases such as hydrogen, argon, and carbon dioxide. They found that the activation energy depends on gas atmosphere as well as raw materials, reflecting different reactivities among them.

In a gas blowing carbonization system, formation of pyridine or toluene insoluble fraction and mesophase from pitch would be affected not only by chemical properties of raw materials and gas atmosphere, but also more or less inevitably by physical factors such as the heat treatment temperature, the gas flow rate, and the initial load of pitch through a change in

production and/or removal rates of light hydrocarbon components in the pitch.

In the present study, kinetics of *TI* formation from a coal tar and a petroleum pitch was investigated under various conditions of air blowing. Before analyzing rates and deducing a kinetic model, influence of the air flow rate and the initial load of pitch on *TI* formation was examined as a function of the reaction temperature and time to clarify the effect above mentioned. The results are compared to some extent with those obtained in a nitrogen gas blowing system.

### 2. EXPERIMENTAL

#### 2.1 Raw materials

Raw pitches used in the present experiments were coal tar pitch (KCTP) and petroleum pitch (PP). Results of solvent fractionation and C/H atomic ratio of the pitches are shown in Table 1. *TI* contents of KCTP and PP are 19.5 and 17.9 wt%, respectively.

#### 2.2 Carbonization

The pitches were carbonized by blowing air or nitrogen gas through a gas inlet into a pyrex glass tube having an inner diameter of 30 mm and a length of 300 mm. A thermocouple was directly immersed into the liquid pitch for exact measurement of the pitch temperature. The blowing gases were introduced through a 3 mm i.d. tube into the bed of pitch particles at room temperature at a calibrated flow rate. For air blowing, the reactor was heated immediately after initiation of the blowing; for nitrogen blowing, the heating was commenced about 20 min after purging air in the reactor without any loss of the pitch particles by entrainment. In all the present experimental runs, the heating rate was steady and about 80 K/min.

Table I. Characteristics of raw pitches

| Sample            | SP <sup>a</sup><br>(°C) | Solubility (wt%) |                    |                 | Elemental analysis |     |     |                |                  |  |
|-------------------|-------------------------|------------------|--------------------|-----------------|--------------------|-----|-----|----------------|------------------|--|
|                   |                         | HS <sup>b</sup>  | HI-TS <sup>c</sup> | TI <sup>d</sup> | C                  | H   | N   | O <sup>e</sup> | C/H <sup>f</sup> |  |
| KCTP <sup>g</sup> | 80                      | 28.1             | 52.4               | 19.5            | 93.3               | 4.4 | 1.1 | 1.2            | 1.78             |  |
| PP <sup>h</sup>   | 116                     | 29.6             | 52.5               | 17.9            | 92.0               | 5.3 | 0.6 | 2.1            | 1.44             |  |

<sup>a</sup>softening point,<sup>b</sup>n-hexane-soluble,<sup>c</sup>n-hexane-insoluble/toluene-soluble,<sup>d</sup>toluene-insoluble,<sup>e</sup>100-(C + H + N),<sup>f</sup>atomic ratio,<sup>g</sup>coal tar pitch,<sup>h</sup>petroleum pitch.

In experiments for examination of effects of physical factors on the yield of *TI* fraction, the temperature of the reactor contents was held at 633 K for the air blowing system and at 713 K for the nitrogen blowing system for a fixed time of 60 minutes, while the gas flow rate and the initial load of pitch were varied in a range, respectively, of 5 to 15 g and 20 to 200 cm<sup>3</sup> min<sup>-1</sup> g<sup>-1</sup>. Kinetic data were obtained at a fixed condition of the gas flow rate of 50 cm<sup>3</sup> min<sup>-1</sup> g<sup>-1</sup> and in a temperature range of 613 to 693 K in the air-blowing system and 653 to 733 K in the nitrogen-blowing system for various holding times.

### 2.3 Extraction of heat-treated pitch by toluene

The heat-treated pitches were ground to a size less than 0.150 mm before subjecting them to extraction by toluene. About 1 g of the ground pitch was mixed with about 50 cm<sup>3</sup> of toluene and dissolved in an ultrasonic bath for 10 min and then stirred for 1 hour at 333 K. The suspension was filtered with filter paper (pore size 1 µm) under reduced pressure, and solid residue was washed with additional toluene and n-hexane. Then, *TI* fraction, thus obtained, was dried overnight in a vacuum oven at 333 K. The *TI* fraction was quantified as the *TI* yield,  $Y_{TI}$ , which indicates the weight percentage of *TI* fraction in the pitch initially loaded.

## 3. RESULTS AND DISCUSSION

### 3.1 Effects of gas flow rate and initial pitch load

Preliminary experiments were carried out on effects of the volumetric gas flow rate,  $F$ , and the initial pitch load,  $W_0$ , on the yield of *TI* fraction,  $Y_{TI}$ . As a result, no appreciable dependency of  $Y_{TI}$  on  $F$  was observed for a range of  $F$  from 100 to 1000 cm<sup>3</sup> min<sup>-1</sup>. On the other hand, a slight dependency of  $Y_{TI}$  on  $W_0$  was detected, with  $Y_{TI}$  decreasing with increasing  $W_0$  from 5 to 15 g. From visual observation through the transparent reactor wall, the dependency was attributed to loss of light fractions of pitch due to entrainment by gas blowing out from carbonizing pitch in the

liquid phase. In the present experiments, gas supplied into the reactor passes as a number of tiny bubbles, which erupt at the upper surface of the liquid-phase pitch. The bubbles hardly grew along the reactor height within the present experimental conditions, which might result in entrainment invariable with  $W_0$ . In addition, no essential change of the bubble size with  $W_0$  was observed, and the decrease of the height of liquid-phase pitch was almost independent of  $W_0$ .

Thus, in Fig. 1,  $Y_{TI}$ s for KCTP blown by air at 633 K and by nitrogen at 713 K with different  $W_0$ s are plotted against  $F/W_0$ , which is considered a measure of effective gas flow rate. As expected, variations of the yields with the gas flow rate are correlated as single curves for both nitrogen- and air-blowing systems. It is also seen that  $Y_{TI}$ s for the air system are about 20% higher than those for the nitrogen system, in spite of the lower reaction temperature for the former. In addition, the yields for the latter are almost independent of  $F/W_0$ , whereas a slight maximum in the yield appears for the former at  $F/W_0 = 50$  cm<sup>3</sup> min<sup>-1</sup> g<sup>-1</sup>.

These variations of  $Y_{TI}$  with  $F/W_0$  seem to correspond to a change of the oxygen content in the residual pitch with  $F/W_0$ , as shown in Fig. 2 for  $W_0 = 5$  g. Here, the oxygen content was calculated as a percentage difference: 100 - (C + H + N), assuming a negligible sulfur content within the pitch. As can be seen in the figure, a maximum oxygen content appears at nearly the same effective gas flow rate as above. Also, a difference amounting up 1.5% can be seen between the oxygen content in air and nitrogen systems. This

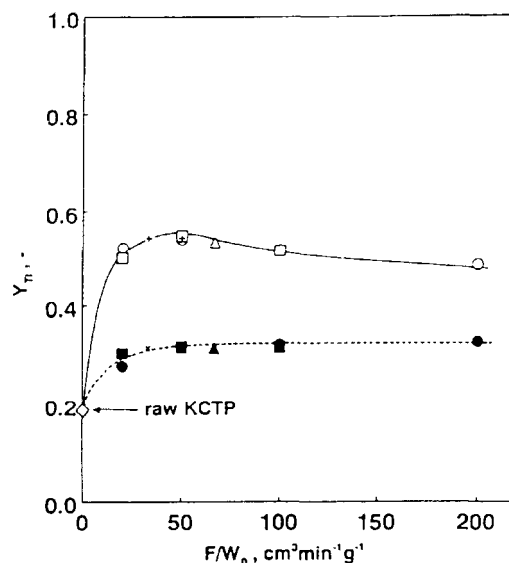


Fig. 1. Dependency of *TI* yields from KCTP on effective gas flow rate in air- (633 K, 60 min) and N<sub>2</sub>- (713 K, 60 min) blowing systems with different initial pitch load:

| gas            | initial pitch load |      |       |       |
|----------------|--------------------|------|-------|-------|
|                | 5.0g               | 7.5g | 10.0g | 15.0g |
| air            | ○                  | △    | □     | +     |
| N <sub>2</sub> | ●                  | ▲    | ■     | x     |



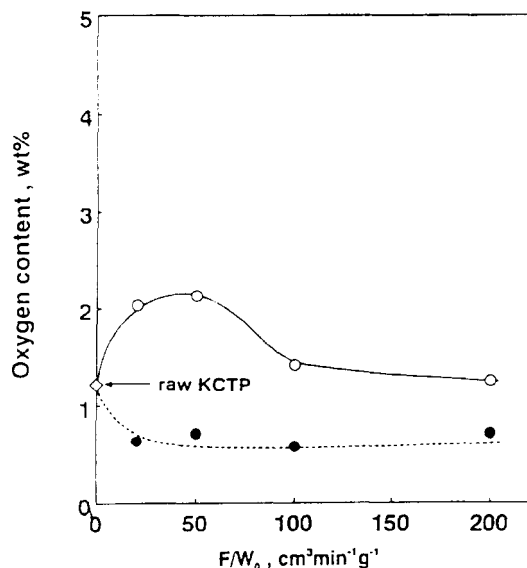


Fig. 2. Dependency of oxygen contents in raw (○) and blown KCTP pitches (○, ●) on effective gas flow rate with initial pitch load of 5.0 g. ○: air blowing system at 633 K for 60 min; ●: N<sub>2</sub> blowing system at 713 K for 60 min.

implies that for the air system the oxygen content in the pitch changes in a balance of volatilization of oxygen-containing gas and tar into the gas phase and polymerization through substitution of hydrocarbon side-chains by oxygen[2,15], whereas for the nitrogen system only the volatilization proceeds without any oxygen supply into the liquid-phase pitch.

### 3.2 Rates of *TI* formation

For kinetic analysis of the present air- or nitrogen-blowing carbonization, a systematic series of experiments were carried out on change of  $Y_{TI}$  with time,  $t$ , at different temperatures under conditions where  $W_0 = 5$  g and  $F = 250$  cm<sup>3</sup>min<sup>-1</sup>. Figure 3 shows changes of  $Y_{TI}$  with time,  $t$ , for KCTP blown by air and nitrogen at different temperatures. In the air-blowing system,  $Y_{TI}$  increases sharply with  $t$  less than 15 min, followed by a comparatively slow increase for  $t > 30$  min. The rates of increase of  $Y_{TI}$  for the N<sub>2</sub> systems are much lower even at higher temperatures (i.e., 713 and 733 K) than those in the air systems at temperatures below 693 K.

These characteristic change of  $Y_{TI}$  with  $t$  were analyzed on the basis of simple reaction models. First, an  $n$ th order irreversible reaction kinetics of the pitch remaining in the liquid phase was applied to the changes by plotting  $\ln(-dY_{TI}/dt)$  against  $\ln Y_{TI}$  at a given temperature for each gas. However, no straight line was obtained for all cases, implying that *TI* fraction consists of multi-component reactants. Figure 4 shows a typical result of analysis where logarithms of  $Y_{TI}$  are plotted against  $t$  assuming a first-order irreversible reaction.

Along with the progress of *TI* formation was observed an appreciable decrease in the weight of liquid-

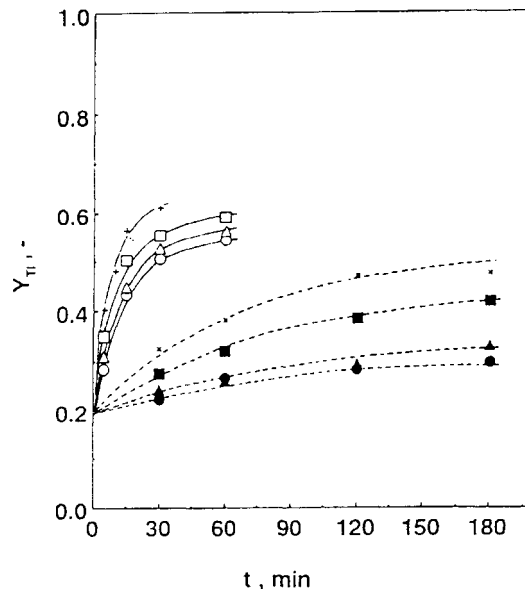


Fig. 3. Variation of *TI* yields with reaction time for KCTP at different temperatures with gas flow rate of 250 cm<sup>3</sup>/min and initial pitch load of 5.0 g:

| gas            | 633K | 653K | 673K | 693K |
|----------------|------|------|------|------|
| air            | ○    | △    | □    | +    |
| N <sub>2</sub> | ●    | ▲    | ■    | x    |

phase pitch due to release of gas and tar into gas phase. In Figure 5 changes of the gas and tar yield with time,  $t$ , for (a) KCTP and (b) PP are evaluated in terms of  $1 - Y_p$  where  $Y_p$  denotes the weight fraction

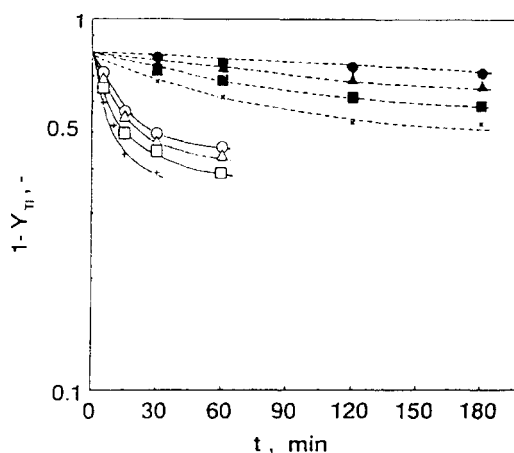


Fig. 4. Semi-logarithmic plots of *TI* yield against reaction time for (a) KCTP and (b) PP at different temperatures with gas flow rate of 250 cm<sup>3</sup>/min and initial pitch load of 5.0 g:

| gas            | 633K | 653K | 673K | 693K |
|----------------|------|------|------|------|
| air            | ○    | △    | □    | +    |
| N <sub>2</sub> | ●    | ▲    | ■    | x    |

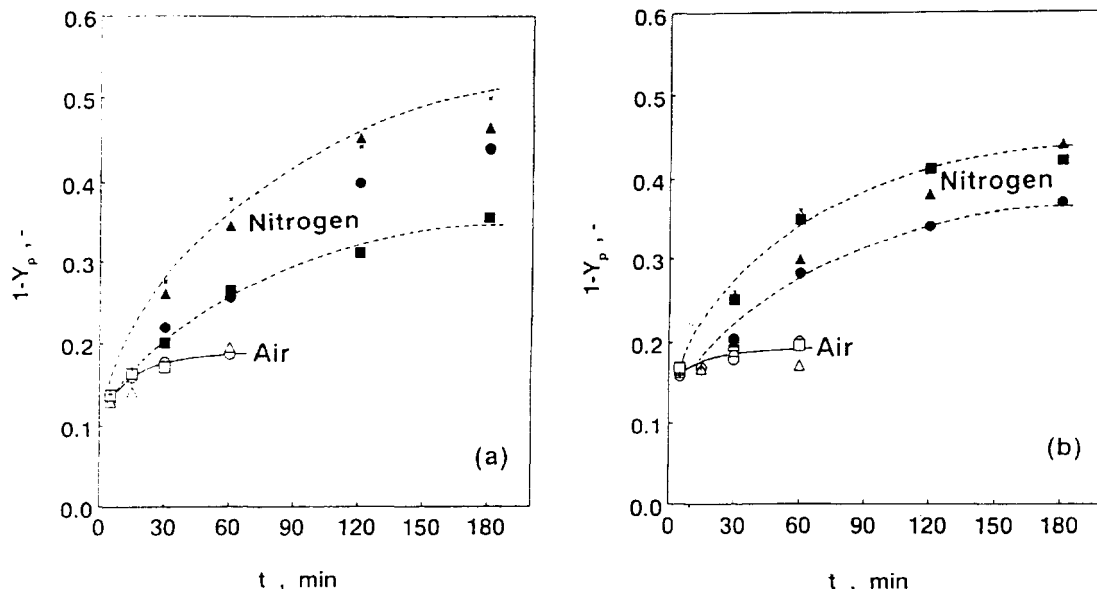


Fig. 5. Variation of gas and tar yields with reaction time for (a) KCTP and (b) PP at different temperatures with gas flow rate of 250 cm<sup>3</sup>/min and initial pitch load of 5.0 g:

| gas            | temperature |      |      |      |
|----------------|-------------|------|------|------|
|                | 633K        | 653K | 673K | 693K |
| air            | ○           | △    | □    | +    |
| N <sub>2</sub> | ●           | ▲    | ■    | x    |

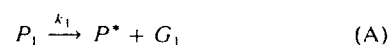
of the residual pitch based on the weight of initially loaded pitch. For both pitches, the gas and tar yields in the air-blowing system are clearly shown to be less temperature dependent compared to those in the N<sub>2</sub> blowing system. Also, the former yield is shown to increase very rapidly within 10 min. The rate of increase then reduces very quickly, giving  $1 - Y_p$  less than 0.2. On the other hand, the latter yield increases over  $t$  up to 60 min. As a result, the yields in the former system are lower than in the latter for  $t$  shorter than ca. 10 to 25 min while being higher for longer  $t$ .

### 3.3 Kinetic reaction model of gas-blowing carbonization

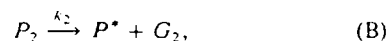
The kinetic nonlinearity in the above semi-logarithmic plot of  $1 - Y_{TI}$  vs  $t$  in Fig. 4 is a feature not only for pitch carbonization, but also for direct coal liquefaction and mesophase formation during pitch carbonization. In our previous papers [16–18] we developed a kinetic model for coal liquefaction that assumes two competitive first-order irreversible reactions of reactive and less reactive portions of coal. Hüttinger *et al.* [14] also modeled mesophase formation during carbonization by including evolution of volatile fractions as inactive components. Hence, a new reaction model is developed here to explain the above-described features of gas-blowing carbonization on the basis of the following assumptions for simplification.

1. Considering the appreciable and rapid release of gas and tar,  $G$ , as shown in Fig. 5, in the early stage of the reaction, raw pitch,  $P$ , is assumed to consist of  $P_1$  and  $P_2$  where  $P_1$  is a portion of  $P$  to produce

thermal fragment,  $P^*$ , and gas and tar,  $G_1$ , at a rate faster than the residual portion of  $P$ ,  $P_2$ , to produce  $P^*$  and gas and tar,  $G_2$ :

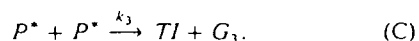


$$k_1 > k_2$$



where  $k_1$  and  $k_2$  are the first-order reaction rate constants for reaction (A) and (B), respectively.

2. Toluene-insoluble fraction,  $TI$ , is produced by recombination of  $P^*$ s with the second-order reaction rate constant  $k_3$ , which is accompanied by evolution of gas and tar,  $G_3$ :



3. Weight gain of the liquid-phase pitch due to oxygen uptake is ignored because of its negligible contribution, as shown in Fig. 2.

Applying the steady-state approximation to  $P^*$  in reactions (A) and (B), the rate of decrease in the yield of the  $TI$  fraction is expressed as

$$\frac{d(1 - Y_{TI})}{dt} = k_1(1 - Y_{TI1}) + k_2(1 - Y_{TI2}), \quad (1)$$

where  $Y_{TI1}$  and  $Y_{TI2}$ , respectively, represent the yields of  $TI$  fraction from  $P_1$  and  $P_2$ . According to the above

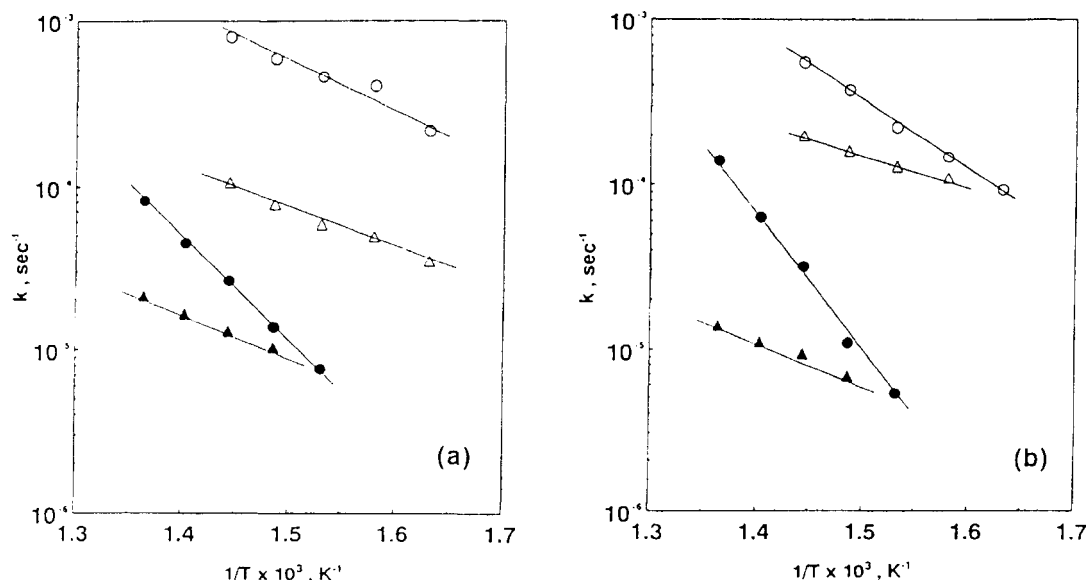


Fig. 6. Arrhenius plots of  $T/I$  formation rate constants for (a) KCTP and (b) PP with gas flow rate of 250  $\text{cm}^3/\text{min}$  and initial pitch load of 5.0 g:

| gas          | $k_1$ | $k_2$ |
|--------------|-------|-------|
| air          | ○     | △     |
| $\text{N}_2$ | ●     | ▲     |

assumptions and eqn (1), both reactions (A) and (B) occur in the early stage of carbonization, which would result in the nonlinear decrease of  $\ln(1 - Y_{TI})$  with  $t$ , as shown in Fig. 4. As the reactions proceed,  $P_1$  disappears much faster than  $P_2$ , and only a decrease of  $P_2$  with  $t$  is observed in the latter carbonization stage, which is described as a straight line in  $\ln(1 - Y_{TI2})$  vs the  $t$  plot.

Hence, by the same method as adopted in our previous paper[17],  $k_1$  and  $k_2$  were obtained analyzing data of  $Y_{TI}$  at different times and temperatures for pitches KCTP and PP, blown by  $\text{N}_2$  or air. The Arrhenius plots of these reaction rate constants for (a) KCTP and for (b) PP are shown in Fig. 6. It is seen for both pitches that  $k_1$  for conversion of  $P_1$  is higher than  $k_2$  for  $P_2$  within the present range of the reaction temperature, and that  $k_1$  and  $k_2$  are considerably higher in the air-blowing system than in the  $\text{N}_2$ -blowing system, reflecting the promotion of carbonization reactions by oxygen. The activation energies,  $E_1$  and  $E_2$ ,

respectively, for  $k_1$  and  $k_2$ , obtained from the plots are listed in Table 2. As can be seen,  $E_1$ s are larger than  $E_2$ s for all cases of pitch and gas atmosphere, and  $E_1$ s for KCTP are smaller than those for PP. Moreover, it is clearly shown that oxygen results in a drastic decrease of  $E_1$  for both pitches.

#### 4. CONCLUSION

Carbonization of petroleum and coal tar pitches to toluene insoluble fraction ( $T/I$ ) was investigated under air and nitrogen gas-blowing systems. The following are concluded within the present experimental conditions:

1. Changes of the  $T/I$  yield with the reaction time are not described by simple first-order kinetics, but fairly well by a model that assumes that pitch,  $P$ , as a reactant contains a reactive component,  $P_1$ , to convert to active thermal fragment,  $P^*$ , and gas and tar,  $G$ , more quickly than the residual component,  $P_2$ .

2. The activation energies for  $P_1$  and  $P_2$  conversions depend on pitch and gas atmosphere. In particular, activation energies for  $P_1$  conversion in an air-blowing system are appreciably smaller than those in the nitrogen-blowing system. This less temperature-sensitive carbonization in the former system may be attributed to pitch reactivity improved by oxygen in air.

Table 2. Activation energies for  $P_1$  and  $P_2$  carbonization

| Sample            | Gas          | $E_1^a$<br>(kcal/mol) | $E_2^b$<br>(kcal/mol) |
|-------------------|--------------|-----------------------|-----------------------|
| KCTP <sup>c</sup> | Air          | 13                    | 10                    |
|                   | $\text{N}_2$ | 30                    | 12                    |
| PP <sup>d</sup>   | Air          | 19                    | 8                     |
|                   | $\text{N}_2$ | 40                    | 11                    |

<sup>a</sup>activation energies for  $P_1$ .

<sup>b</sup>activation energies for  $P_2$ .

<sup>c</sup>coal tar pitch.

<sup>d</sup>petroleum pitch.

#### REFERENCES

1. T. Maeda, S. M. Zeng, K. Tokumitsu, J. Mondori, and I. Mochida, *Carbon* 31, 407 (1993).

2. S. M. Zeng, T. Maeda, K. Tokumitsu, J. Mondori, and I. Mochida, *Carbon* 31, 413 (1993).
3. S. M. Zeng *et al.*, *Carbon* 31, 421 (1993).
4. J. B. Barr and I. C. Lewis, *Carbon* 16, 439 (1978).
5. T. Maeda, K. Tokumitsu, H. Morita, and I. Mochida, *19th Biennial Conf. on Carbon*, Penn State, Univ. Extended Abstracts (American Carbon Society), p. 162 (1989).
6. T. Maeda *et al.*, *19th Biennial Conf. on Carbon*, Extended Abstracts (American Carbon Society), p. 164 (1989).
7. I. Mochida, T. Inaba, Y. Korai, H. Fujitsu, and K. Takeshida, *Carbon* 21, 543 (1983).
8. K. Yanagisawa and T. Suzuki, *Fuel* 72, 25 (1993).
9. J. D. Brooks and G. H. Taylor, In *Chemistry and Physics of Carbon*, (P. L. Walker Jr, Ed.) Vol. 4, p. 243. Dekker, New York (1968).
10. H. Honda, H. Kimura, Y. Sanada, S. Sugawara, and T. Furuta, *Carbon* 8, 181 (1970).
11. S. Eser and R. G. Jenkins, *16th Biennial Conf. on Carbon*, San Diego, CA, Extended Abstracts (American Carbon Society), p. 98 (1983).
12. K. J. Hüttinger and J. P. Wang, *Carbon* 29, 439 (1991).
13. K. J. Hüttinger, M. Bernhauer, K. Christ, and A. Gschwindt, *Carbon* 30, 931 (1992).
14. M. Bernhauer, K. Christ, A. Gschwindt, and K. J. Hüttinger, *Carbon '92*, Essen, (German Ceramic Soc.), p. 39 (1992).
15. S. Otani, K. Okuda, and H. S. Matsuda, *Carbon Fibre*, p. 153. Kindai Henshu Ltd., Tokyo (1983).
16. H. Moritomi, T. Chiba, and Y. Sanada, *J. Japan Petro. Inst.* 25, 32 (1982).
17. T. Chiba and Y. Sanada, *J. Fuel Soc. Japan* 57, 259 (1978).
18. T. Chiba, *J. Fuel Soc. Japan* 63, 156 (1984).

## NOMENCLATURE

- $F$ : volumetric gas flow rate,  $\text{cm}^3\text{min}^{-1}$   
 $k_t$ : apparent reaction rate constant,  $\text{sec}^{-1}$   
 $t$ : reaction time, min  
 $W_0$ : weight of pitch loaded, g  
 $Y_i$ : yield based on weight of pitch loaded, -

## Subscripts

- $G$ : gas and tar  
 $P$ : raw pitch  
 $P_1$ : reactive portion of  $P$   
 $P_2$ : less reactive portion of  $P$   
 $P^*$ : active thermal fragment produced from  $P$   
 $TI$ : toluene-insoluble fraction



## AIR-BLOWING REACTIONS OF PITCH: I. OXIDATION OF AROMATIC HYDROCARBONS

CHIHARU YAMAGUCHI,<sup>1</sup> JUJI MONDORI,<sup>2</sup> AKIRA MATSUMOTO,<sup>2</sup> HIDEKAZU HONMA,<sup>2</sup>

HARUO KUMAGAI,<sup>3</sup> and YUZO SANADA<sup>3</sup>

<sup>1</sup>Osaka Gas Co., Ltd. Torishima Plant, 5-11-151 Torishima, Konohana-ku, Osaka 554, Japan

<sup>2</sup>Osaka Gas Co., Ltd., 6-19-9 Torishima, Konohana-ku, Osaka 554, Japan

<sup>3</sup>Faculty of Engineering, Hokkaido University, Kita 13-joh,  
Nishi 8-chome, Kita-ku, Sapporo 060, Japan

(Received 24 January 1994; accepted in revised form 31 October 1994)

**Abstract**—In order to deepen our understanding of the air-blowing reaction of pitch as a precursor of carbon fiber, aromatic hydrocarbons having 2 to 3 rings were selected as pitch models, and structural analyses of their air-blown products were conducted using FD-MS, GC-MS, NMR, and FT-IR spectroscopies.

Alkyl-substituted aromatic compounds polymerized with methylene, biphenyl-type, and ether bonding, leading the methylene to partially change into carbonyl during the air-blowing reaction. Therefore, the pitches containing alkyl-substituted compounds are the most effective source materials for raising the softening point, increasing molecular weight, and suppressing anisotropic texture. The properties of the air-blown products were characterized by, and dependent mainly upon, the crosslinked carbon and the condensed aromatic carbon formed by the air-blowing reaction.

**Key Words**—Air-blowing reaction, aromatic hydrocarbon, structural analysis, isotropic pitch.

### 1. INTRODUCTION

Raising the softening point of petroleum- and coal-based pitches has been achieved by air-blowing, an extremely important reaction in industry. Paving asphalts[1], precursors for isotropic carbon materials[2], as well as pitch precursors used for general-purpose carbon fibers[3,4] are prepared on an industrial scale because the air-blowing reaction more effectively increases coke yield than heat treatment, distillation, or other methods.<sup>5,6</sup> The air-blowing reaction shows every indication of raising the softening point, and increasing the insolubles for solvent and the C/H ratio [6–11]. Also, the air-blowing reaction suppresses the growth of mesophase spheres in the isotropic matrix[4].

Structural changes in pitch during the air-blowing reaction have been reported, based on NMR, IR and other measurements, where carbon in the  $\alpha$ -position of alkyl aromatic compounds in source-material pitch is attacked by oxygen. This results in crosslinkings, such as ether bonding, as well as condensation reactions mainly involving dehydrogenation by oxygen[5–15]. Air-blowing reactions at high temperatures involving dehydrogenation reactions in the source pitch by oxygen have also been reported[16–19]. Polymerization is accelerated by the biphenyl-type condensation reaction. It is believed that the air-blowing reaction proceeds via the radical reaction mechanism [12–15,20–22]. The autooxidation of alkylbenzene and other compounds are typical examples[17–19]. Unfortunately, the details of the mechanisms in the air-blowing reaction of pitch accompanying the rise of softening point, molecular weight, and suppression of anisotropic texture are still unclear.

The present study aims to clarify the paths of air-

blowing reactions for various model compounds in order to improve the preparation pitch for carbon fiber precursor. Model compounds with 2–3 rings of aromatic hydrocarbons were selected as starting materials. FD-MS, GC-MS, NMR, and FT-IR analytic methods were employed for the structural analysis of the reaction products.

### 2. EXPERIMENTAL

#### 2.1 Materials

As representatives of the major compounds in pitch, the following 2–3 ring aromatic hydrocarbons were selected and tested: Naphthalene (N) and biphenyl (B) as unsubstituted compounds, quinoline (Q) as a heterocyclic compound, 1-methylnaphthalene (1-MN) and 2-methylnaphthalene (2-MN) as aromatics with alkyl side chains, diphenylmethane (DPM) and diphenylethane (DPE) as models of crosslinking between aromatic rings, 9, 10-dihydroanthracene (DA) and tetralin (T) as naphthene compounds. Reagent grade compounds were used without further purification. The physical properties of the aromatic compounds selected are shown in Table 1[23].

#### 2.2 Air-blowing

For the air-blowing reactions, a 100-ml autoclave was used. An initial 40 g of the material was heated at 330°C under a pressure of 2.1 MPa at a dried air flow rate of 0.27 Nl/min. In the course of air-blowing, samplings were carried out at intervals of 90, 180, and 280 minutes for 1-MN, DPE, and T, but at 280 minutes for the other materials. The residual products in the reaction vessel were also analysed.

Table I. General properties of the raw materials and the air-blown residual products<sup>a</sup>

|      | Raw materials |              | Air-blown residual products |                |                |           |           |            |              |                                   |
|------|---------------|--------------|-----------------------------|----------------|----------------|-----------|-----------|------------|--------------|-----------------------------------|
|      | Mw<br>(—)     | m.p.<br>(°C) | Run no.                     | Yield<br>(wt%) | SP<br>(°C)     | AP<br>(%) | BI<br>(%) | H/C<br>(—) | Odif.<br>(%) | SC<br>( $\times 10^{19}$ spins/g) |
| N    | 128           | 81           | N-280                       | 56.8           | m.p.<br>(69.0) | 0         | 0         | 0.66       | 5.3          | 0.64                              |
| B    | 154           | 70           | B-280                       | 79.2           | 70.8           | 0         | 0.1       | 0.76       | 1.3          | — <sup>b</sup>                    |
| Q    | 129           | —23          | Q-280                       | 62.8           | — <sup>b</sup> | 0         | 13.9      | 0.69       | 6.0          | — <sup>b</sup>                    |
| 1-MN | 142           | —22          | 1-MN-280                    | 64.3           | 87.8           | 0         | 1.3       | 0.62       | 6.6          | 0.31                              |
| 2-MN | 142           | 35           | 2-MN-280                    | 71.5           | 113.0          | 0         | 15.3      | 0.6        | 7.6          | 0.26                              |
| DPM  | 168           | 26           | DPM-280                     | 73.8           | — <sup>b</sup> | 0         | 3.1       | 0.63       | 10.1         | — <sup>b</sup>                    |
| DPE  | 182           | 52           | DPE-280                     | 56.5           | 49.3           | 0         | 9.6       | 0.65       | 9.3          | 0.15                              |
| DA   | 180           | 109          | DA-280                      | 93.5           | 197.5          | 35        | 22.6      | 0.56       | 7.2          | 0.89                              |
| T    | 132           | —36          | T-280                       | 51.2           | 104.2          | 1         | 26.9      | 0.56       | 11.0         | 3.0                               |

m.p.: melting point; Run no.: raw material-air-blowing time (min); Yield: residual product yield; SP: softening point by Mettler FP800; AP: Percent of anisotropy; BI: Benzene insoluble; Odif.:  $100-(C+H+N)$ ; SC: Spin concentration.

<sup>a</sup>Reaction time is 280 mins.

<sup>b</sup>Not measured.

### 2.3 Structural characterization of the air-blown residual products

Softening point analysis (Mettler EP800 apparatus), polarized-light microscopic observation (Leitz Orthoplan), solvent fractionation analysis, elemental analysis (Perkin-Elmer's 2400CHN coder) were conducted by routine methods. Bruker's ESP300E spectrometer was used to measure ESR. For radical concentrations, DPPH was used as a standard material and the g-value was determined by a frequency counter and a Gaussmeter. For FD-MS, GC-MS spectroscopies, JEOL, JMS-DX300 and JMA-DA6000 data processing systems were employed. Also, JEOL, GX-270 spectrometer was used to measure NMR[24,25]. The respective spectra signals were assigned to the references of the various organic compounds[26–28]. FT-IR was measured with a Nicolet 740 spectrophotometer. Differences in the spectrum between the raw material and the air-blown residual product were calculated and evaluated for the reaction mechanism.

## 3. RESULTS

### 3.1 General properties of the air-blown residual products

The general properties of the air-blown residual products are shown in Table I.

The air-blowing of the aromatic hydrocarbons for 280 minutes yielded a range of 51.2 to 93.5%, depending on the materials used. The softening points of the residual products derived from 1-MN, 2-MN, T, and DA were higher than the melting points of the original materials, that is, 1-MN-280: 87.8°C; 2-MN-280: 113°C; T-280: 104.2°C; DA-280: 197.5°C, respectively. However, hardly any rise in the softening point was realized with the other products. The formation of an anisotropic texture was observed only with DA-280

and T-280. The development of anisotropic texture in DA-280 was remarkable. The increase of the fraction of benzene-insoluble (BI) was also as much as 22.6% and 26.9% for DA-280 and T-280, respectively. Oxygen taken up in the residual products through air-blowing occurs clearly for DPM-280, DPE-280, and T-280, as much as 9 to 11%. The generation of organic free radicals from the air-blowing reaction was observed. ESR recorded at room temperature were  $0.15 \times 10^{19}$  to  $3.0 \times 10^{19}$  spins/g of the radical concentration and 2.0027 to 2.0031 of the g-value. These results suggest that polymerization is occurring during the air-blowing.

### 3.2 Structural characterization of the air-blown residual products

**3.2.1 Analysis of FD-MS and GC-MS.** Figure 1 illustrates the results of FD-MS for the fraction of benzene-soluble (BS) of the air-blown residual products. Little reaction was promoted on unsubstituted compounds (N,B) and the heterocyclic compound (Q). The main peak was related to dimer in these cases. From the results of GC-MS,  $M/Z = 254$  in N-280,  $M/Z = 306$  in B-280 and  $M/Z = 256$  in Q-280, confirmed as the respective dimers with direct bonding of two aromatic rings.

Aromatics with alkyl side chains were more reactive than unsubstituted ones. The BS fractions in 1-MN-280 and 2-MN-280 display peaks corresponding from monomer to heptamer. High resolution analysis of FD-MS indicated that crosslinking has occurred by means of a combination of carbonyl (+154), methylene (+140), and biphenyl-type bonding (+126). Ether bonding was also confirmed to some extent. Furthermore,  $M/Z = 172$  for 1-MN-280 was found and assigned as 1-naphthalenecarboxylic acid.

FD-MS results for DPM-280 and DPE-280 were less regular than 1-MN-280 and 2-MN-280, as shown

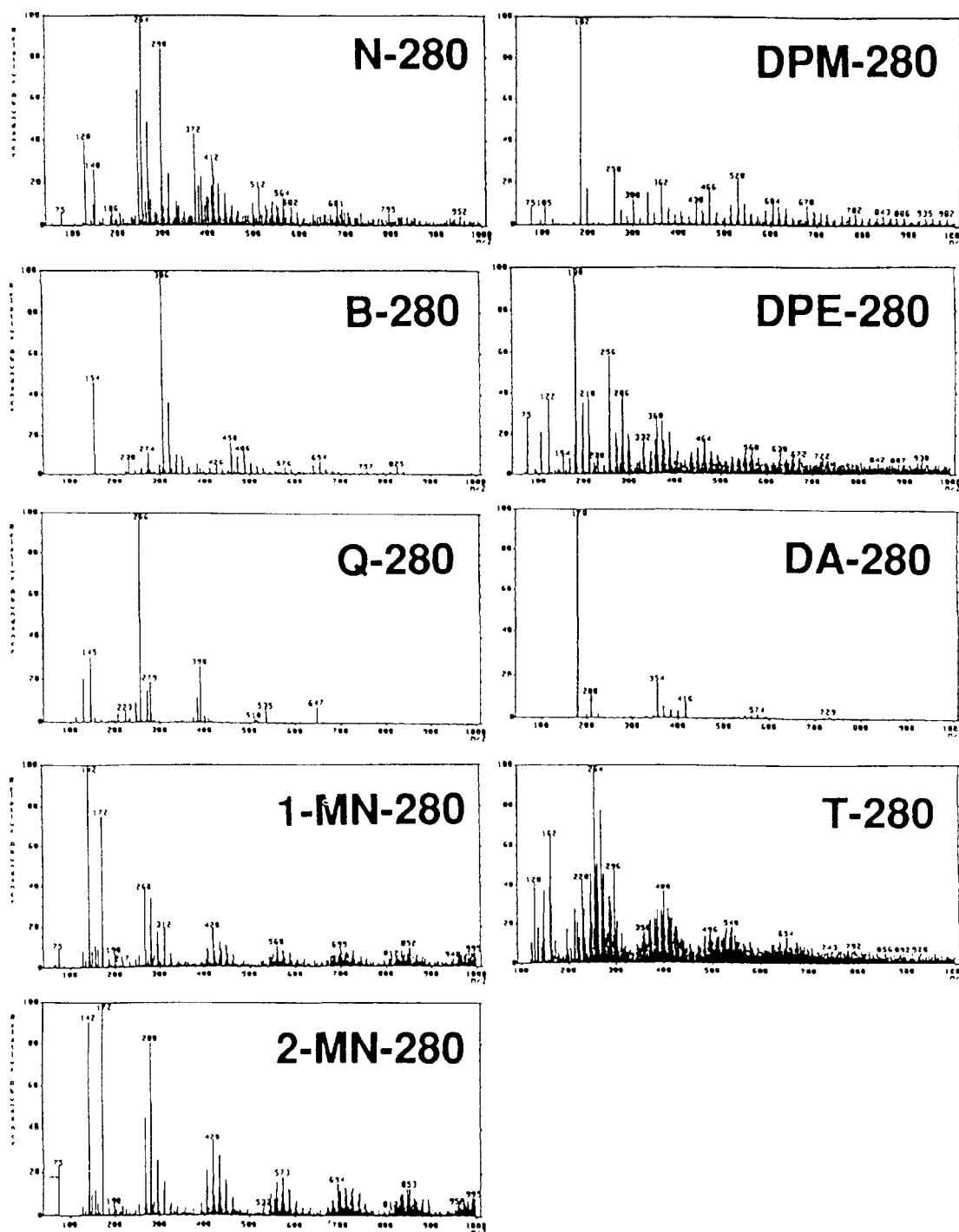
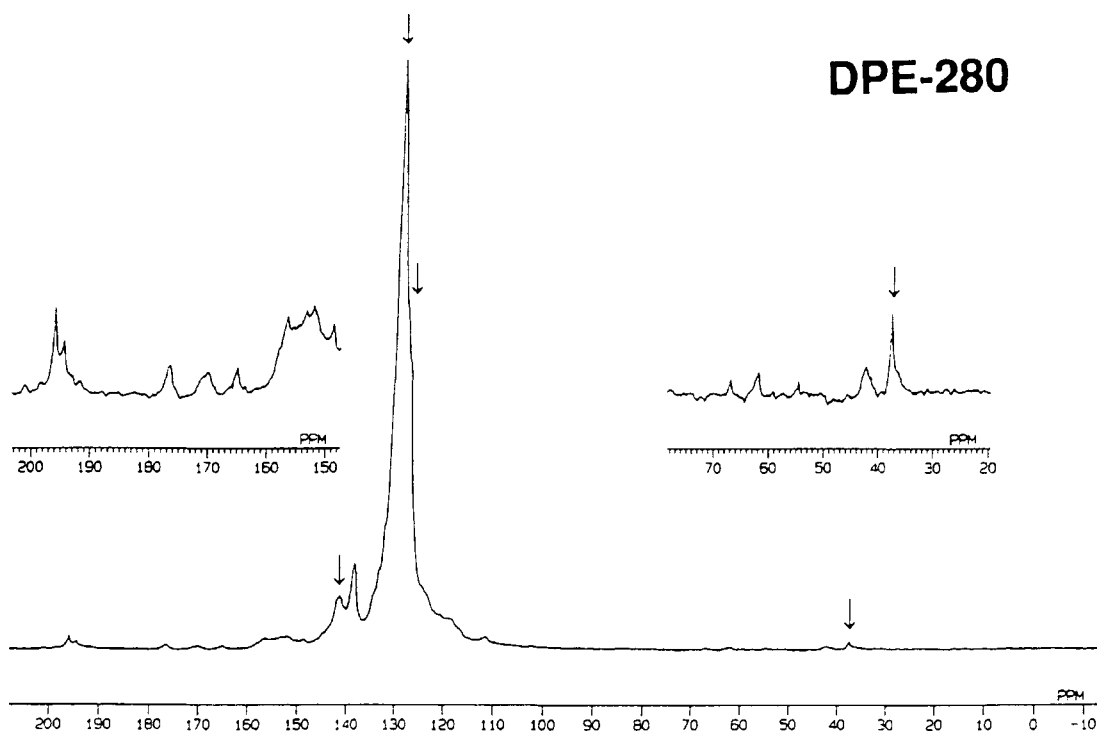


Fig. 1. FD-MS spectra of the BS fractions in the air-blown residual products.

in Fig. 1. This could be explained by the occurrence of decomposition reaction at the site of bridge and polymerizing reaction together with the crosslinked bonding mentioned above. However, there was a clear increase in molecular weight. It is conceivable from the result of GC-MS that  $M/Z = 180$  for DPE-280 is stilbene and/or 9, 10-dihydrophenanthrene.

From FD-MS measurements of DA-280, the main air-blowing reaction of DA is aromatization due to dehydrogenation. The termination of the reaction might be generation of the anthracene monomer ( $M/Z = 178$ ). Concerning T-280, it is clear that a number of reactions are simultaneously promoted, although the material has the same naphthene group as DA. This

Fig. 2.  $^{13}\text{C}$ -NMR spectra of the air-blown residual products DPE-280.

is thought to be caused by a decomposition reaction, together with the resultant aromatization due to dehydrogenation, with respect to the results of GC-MS and  $^{13}\text{C}$ -NMR. It was also found out from GC-MS that the values of  $M/Z = 128$  and  $M/Z = 254$  for T-280 were the monomer and dimer of naphthalene, respectively. In summary, it was learned that a variety of reaction mechanisms contribute to the increase of molecular weight by air-blowing.

**3.2.2  $^{13}\text{C}$ -NMR analysis.**  $^{13}\text{C}$ -NMR spectrum of DPE-280 is shown in Fig. 2. The measurement was done under melting conditions at  $170^\circ\text{C}$ . In addition

to the parent peaks marked by the arrows, various new peaks were observed. Assignment of the chemical shift ranges in the  $^{13}\text{C}$ -NMR spectra are summarized in Table 2[26-28]. Table 3 summarizes the results of the various materials and air-blown residual products.

In the reaction process, it was clear that the effective polymerization occurred according to desubstitution and/or dehydrogenation of the methyl group (Cal 1) for 1-MN and 2-MN, crosslinked methylene group (Cal 2.1) for DPM and DPE, and naphthene group (Cal 2.2) for DA and T. Aliphatic carbons, namely, Cal 2.1 and Co 1 for 1-MN and 2-MN, Co 1

Table 2. Ranges of chemical shift assigned to various bonding type carbon on  $^{13}\text{C}$ -NMR spectra

| Notation             | Co 1           | Car 4·1 | Car 4·2                 | Car 3               | Co 2                    | Cal 2·1                   | Cal 2·2                      | Cal 1          |
|----------------------|----------------|---------|-------------------------|---------------------|-------------------------|---------------------------|------------------------------|----------------|
| Shift range (ppm)    | 200-160        | 160-136 | 136-130                 | 130-100             | 70-45                   | 45-33                     | 33-22                        | 22-8.5         |
|                      | $\text{:C=O}$  |         | outer quaternary carbon | C-H aromatic carbon | $-\text{CH}_2\text{OH}$ | $-\text{CH}_2-$ (bridged) | $-\text{CH}_2-$ (naphthenic) | $-\text{CH}_3$ |
|                      | $-\text{CHO}$  |         |                         |                     | $-\text{OCH}_3$         |                           |                              |                |
| Possible carbon type | $-\text{COOH}$ |         |                         |                     |                         |                           |                              |                |
|                      |                |         |                         |                     |                         |                           |                              |                |
|                      |                |         |                         |                     |                         |                           |                              |                |



Table 3. Carbon distribution of the raw materials and the air-blown residual products by  $^{13}\text{C}$ -NMR

| Run no.            | Carbon (%) |                          |                          |      |     |        |        |      |
|--------------------|------------|--------------------------|--------------------------|------|-----|--------|--------|------|
|                    | Co1        | Car4.1                   | Car4.2                   | Car3 | Co2 | Cal2.1 | Cal2.2 | Cal1 |
| N-0 <sup>a</sup>   | 0          | 0                        | 20                       | 80   | 0   | 0      | 0      | 0    |
| N-280 <sup>b</sup> | 0.4        | 2.7                      | 19.5                     | 77.8 | 0   | 0      | 0      | 0    |
| B-0                | 0          | 16.7                     | 0                        | 83.3 | 0   | 0      | 0      | 0    |
| B-280              | 0          | 15.9                     | 0                        | 84.1 | 0   | 0      | 0      | 0    |
| Q-0                | 0          | 22.2                     | 11.1                     | 66.7 | 0   | 0      | 0      | 0    |
| Q-280              | 0          | 24.0                     | 12.2                     | 63.8 | 0   | 0      | 0      | 0    |
| 1-MN-0             | 0          | 0                        | 27.3 (18.2) <sup>d</sup> | 63.6 | 0   | 0      | 0      | 9.1  |
| 1-MN-280           | 0.8        | 7.7                      | 24.0 (21.7) <sup>d</sup> | 64.9 | 0   | 0.3    | 0      | 2.3  |
| 2-MN-0             | 0          | 0                        | 27.3 (18.2) <sup>d</sup> | 63.6 | 0   | 0      | 0      | 9.1  |
| 2-MN-280           | 0.9        | 12.1                     | 21.3 (19.4) <sup>d</sup> | 63.9 | 0   | 0.4    | 0      | 1.9  |
| DPM-0              | 0          | 15.4 (0) <sup>c</sup>    | 0                        | 76.9 | 0   | 7.7    | 0      | 0    |
| DPM-280            | 2.9        | 21.8 (21.8) <sup>c</sup> | 14.4                     | 59.2 | 1.6 | 0      | 0      | 0    |
| DPE-0              | 0          | 14.3 (0) <sup>c</sup>    | 0                        | 71.4 | 0   | 14.3   | 0      | 0    |
| DPE-280            | 1.8        | 13.1 (12.5) <sup>c</sup> | 15.4                     | 68.5 | 0.5 | 0.6    | 0      | 0    |
| DA-0               | 0          | 28.6 (0) <sup>c</sup>    | 0                        | 57.1 | 0   | 0      | 14.3   | 0    |
| DA-280             | 4.1        | 5.4 (5.4) <sup>c</sup>   | 36.1                     | 54.4 | 0   | 0      | 0      | 0    |
| T-0                | 0          | 20.0 (0) <sup>c</sup>    | 0 (0) <sup>d</sup>       | 40.0 | 0   | 0      | 40.1   | 0    |
| T-280              | 0.9        | 13.6 (13.0) <sup>c</sup> | 20.3 (19.8) <sup>d</sup> | 63.2 | 0   | 0.6    | 1.1    | 0.5  |

<sup>a</sup>Raw material.<sup>b</sup>Air-blown residual product.<sup>c</sup>Cross-linked aromatic carbon produced by air-blowing reaction.<sup>d</sup>Condensed aromatic carbon.

and Co 2 for DPM and DPE, Co 1 for DA, Co 1 and Cal 2.1 and Cal 1 for T, were newly produced. From the results, it is plausible that in the air-blowing reaction of substituted material, new bonds with cross-linking and oxygen-containing functional groups were generated along with the desubstitution reaction.

Figure 3 shows the changes in the  $^{13}\text{C}$ -NMR spectra of DPE caused by the air-blowing reaction. It is clear that, as the reaction proceeds, the aromatic carbon (142 ppm) bonded with a crosslinked methylene group (the parent peak marked by the arrow) decreases. On the other hand, an increase is seen in aromatic carbon bonded with carbonyl groups (138 ppm), ether group (145 to 160 ppm), and outer quaternary aromatic or vinyl group-bonded aromatic carbons (130 to 136 ppm).

Car4.1 in Table 3 indicates the intensity ratio of the crosslinked aromatic carbon. However, Car4.1 of DPM, DPE, DA, and T include the crosslinked aromatic carbon produced by the air-blowing reaction, as well as that derived from the material itself. To obtain the intensity ratio of the crosslinked carbon produced by the air-blowing reaction, the intensity ratio of the crosslinked aromatic carbon derived from the material, which is calculated from the signal intensity of aliphatic group, must be deducted from the intensity ratio of Car4.1. The results of the calculations are shown in brackets in Table 3.

Car4.2 in Table 3 shows the intensity ratio related to the condensed aromatic carbon. By comparing the intensity ratios of the material and air-blown residual product, the intensity ratio of the condensed aromatic

carbon produced by the air-blowing reaction can be obtained. However, Car4.2 of 1-MN, 2-MN, and T include not only the condensed aromatic carbon, but also the aromatic carbon bonded with the methyl group. In order to obtain the intensity ratio of the condensed aromatic carbon only, the intensity ratio of the aromatic carbon bonded with the methyl group, which is calculated from the signal intensity of the aliphatic group, must be deducted from the intensity ratio of Car4.2. The results of the calculations are shown in brackets in Table 3.

In N-280, B-280, and Q-280 very little crosslinked and condensed carbon appeared. The formation of crosslinked carbon was observed, but that of condensed carbon was found to be very little for 1-MN-280 and 2-MN-280. However, remarkable increases both in crosslinked and condensed carbons occurred for DPM-280, DPE-280, and T-280. The generation of condensed carbon was seen in DA-280 but there was little crosslinked carbon. The increases of condensed carbon in DA-280 and T-280 are thought to be mainly due to the aromatization caused by the dehydrogenation of the naphthene rings. This confirms that the pattern of bonding made by the air-blowing reaction is dependent on the structure of the raw materials.

**3.2.3 FT-IR analysis.** Figure 4 shows a typical FT-IR spectrum representing the difference between the spectra of the reaction product and the original one for 1-MN. The differences in the spectra of 1-MN-90, 1-MN-180, and 1-MN-280 shown in Fig. 4 suggest clearly increases in the out-of-plane deformation vibra-

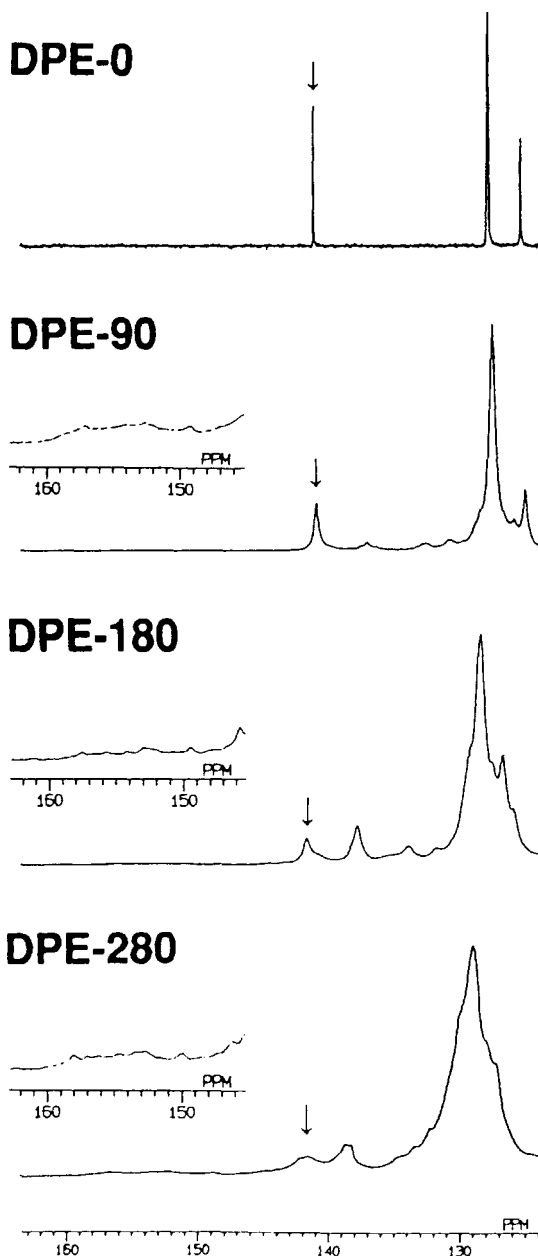


Fig. 3.  $^{13}\text{C}$ -NMR spectra of the raw material and the air-blown residual products of DPE.

tion of aromatic group C—H ( $770\text{ cm}^{-1}$ – $790\text{ cm}^{-1}$ ), in the aromatic ether or phenol ( $1260\text{ cm}^{-1}$ ), in the stretching vibration of carbonyl ( $1690\text{ cm}^{-1}$ ) and aromatic esters ( $1720\text{ cm}^{-1}$ – $1770\text{ cm}^{-1}$ ). This is in addition to the decrease of the absorption of aliphatic C—H stretching vibration due to methyl groups with  $2800\text{ cm}^{-1}$  to  $3000\text{ cm}^{-1}$ . The sharp absorption of the out-of-plane deformation vibration of aromatic group C—H indicate the generation of ortho- or para-positioned two substituted aromatic components. This means that the reaction with air-blowing is marked by

crosslinked bonding. However, hardly any increase in the peak due to the C=C stretching vibration of aromatic rings near  $1600\text{ cm}^{-1}$  was observed.

In DPM-280, DPE-280, DA-280, and T-280, the increase of the peak due to aromatic ring C=C stretching vibration at  $1600\text{ cm}^{-1}$  was clearly observed, together with a decrease in the peak due to aliphatic methylene. In DPE, the  $1600\text{ cm}^{-1}$  peak increased as the reaction time increased. Also, in DA-280 and T-280, new peaks appeared at  $881\text{ cm}^{-1}$  and  $754\text{ cm}^{-1}$ , respectively. These are due to benzene's four- and two-substituted components, which are caused by the appearance of anthracene and naphthalene rings due to the dehydrogenated naphthene ring.

#### 4. DISCUSSION

The results reported in 3.1 and 3.2 are helpful for the preparation of the pitches because air-blowing makes it possible to control the values of softening point, molecular weight, and generation of anisotropic texture.

##### 4.1 Softening point change

The temperature of softening for 1-MN-280, 2-MN-280, and T-280 is almost the same as the melting temperature of naphthalene. The softening point of DA-280 is near the melting point of anthracene. Accordingly, the dealkylation of the methyl group in 1-MN-280 and 2-MN-280 and aromatization due to dehydrogenation in T-280 and DA-280, respectively, have been confirmed. The softening point of DA-280 reached  $197.5^\circ\text{C}$ , even though the reaction product consists mainly of anthracene monomer. It is reported that the rates of dealkylation and aromatization due to the dehydrogenation of the naphthene ring in oxidizing conditions (i.e., air-blowing) are faster than those occurring in thermal reactions[29]. Oxidative dehydrogenation is generally more advantageous than dehydrogenation in thermodynamic consideration. From these facts, it can be said that the reasons that the air-blowing reaction is effective in raising the softening point are: (1) the dealkylation of the methyl group; and (2) aromatization caused by dehydrogenation of the naphthene group. The reason that the softening points in DPM-280 and DPE-280 are almost unchanged, while the molecular weight increased to the equivalent value of heptamer with several cross-linked bondings, might be that the decomposition reaction occurred simultaneously.

##### 4.2 Changes in molecular weight increase

Polymerization products up to heptamers for 1-MN-280, 2-MN-280, DPM-280, DPE-280, and T-280 were evident, while N-280, B-280, Q-280, and DA-280 mainly yielded dimers. The generation of crosslinking confirmed with  $^{13}\text{C}$ -NMR was remarkable for 1-MN-280, 2-MN-280, DPM-280, DPE-280, and T-280, but was negligible in the cases of N-280, B-280, Q-280, and DA-280. From these findings, obtained by  $^{13}\text{C}$ -NMR

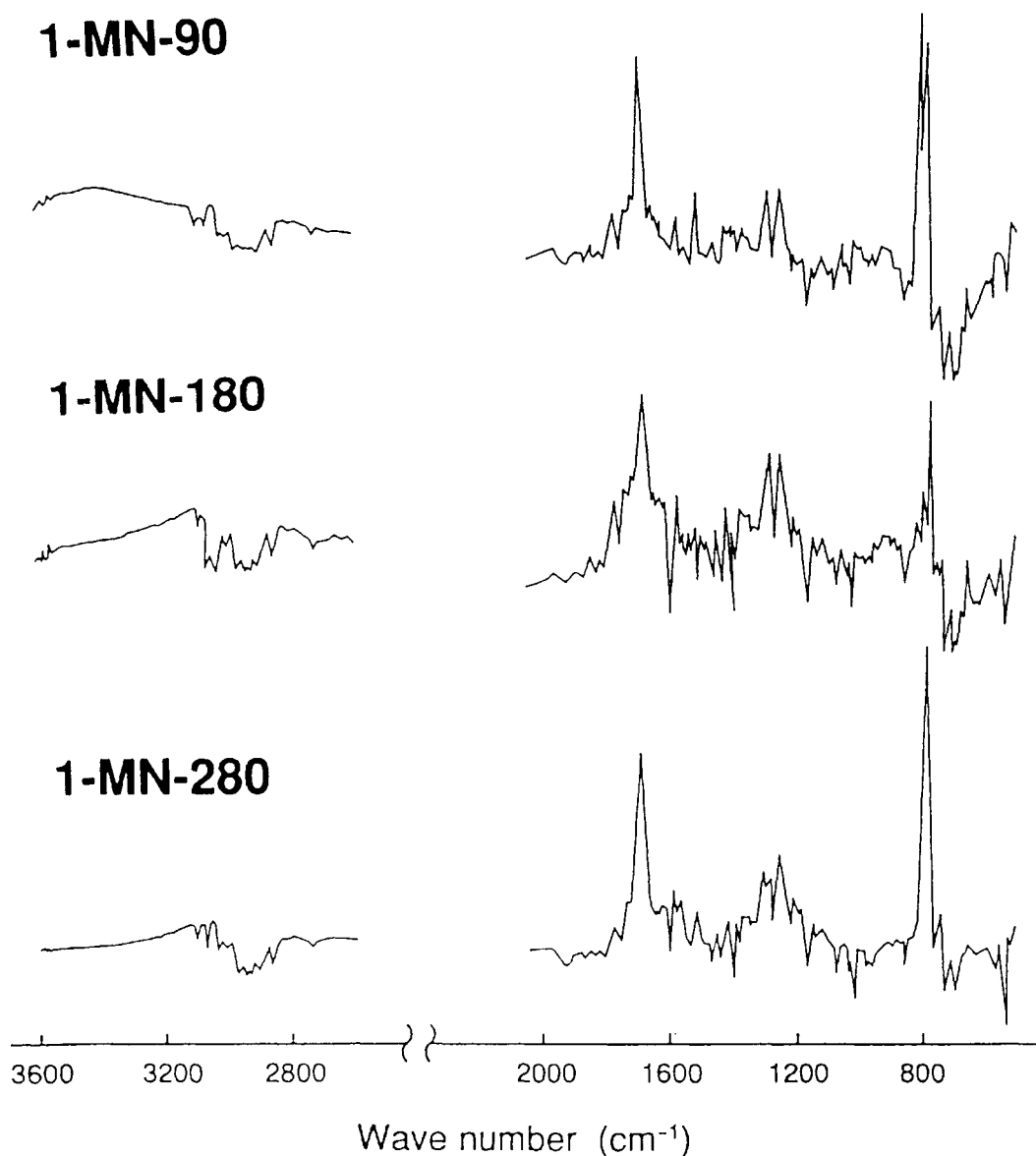


Fig. 4. FT-IR spectra of the air-blown residual products of 1-MN.

and FD-MS measurements, the air-blowing reaction remarkably accelerates an increase in molecular weight, mainly due to the generation of crosslinked bonds. These crosslinked bonds were specified as methylene, biphenyl-type, carbonyl and, to some extent, ether, respectively.

#### 4.3 Development of anisotropic texture

Polymerization with crosslinked bonding generally proceeds to the formation of three-dimensional molecular conformation, which suppresses the development of anisotropic texture in the mesophase. Polymerization by condensation proceeds to the formation of a planar molecular structure, which promotes the development of anisotropic texture. The development

of anisotropy is dependent mainly upon the type of bonding formed by the air-blowing reaction.

The outer quaternary aromatic carbon at the band of Car4.2 assessed by  $^{13}\text{C}$ -NMR can be regarded as one of the parameters relevant to the degree of condensation of the aromatic structure. The band of Car4.2 hardly increases at all for N, B, and Q, and only a little for 1-MN and 2-MN during the air-blowing process. On the other hand, there was a remarkable increase of this band for DPM and DPE. This is mainly due to the formation of vinyl polymer, rather than the condensing reaction of aromatic rings, which will be discussed later in section 4.4. It is confirmed for DA-280 and T-280 not only that the naphthene group decreased, but the condensed aromatic

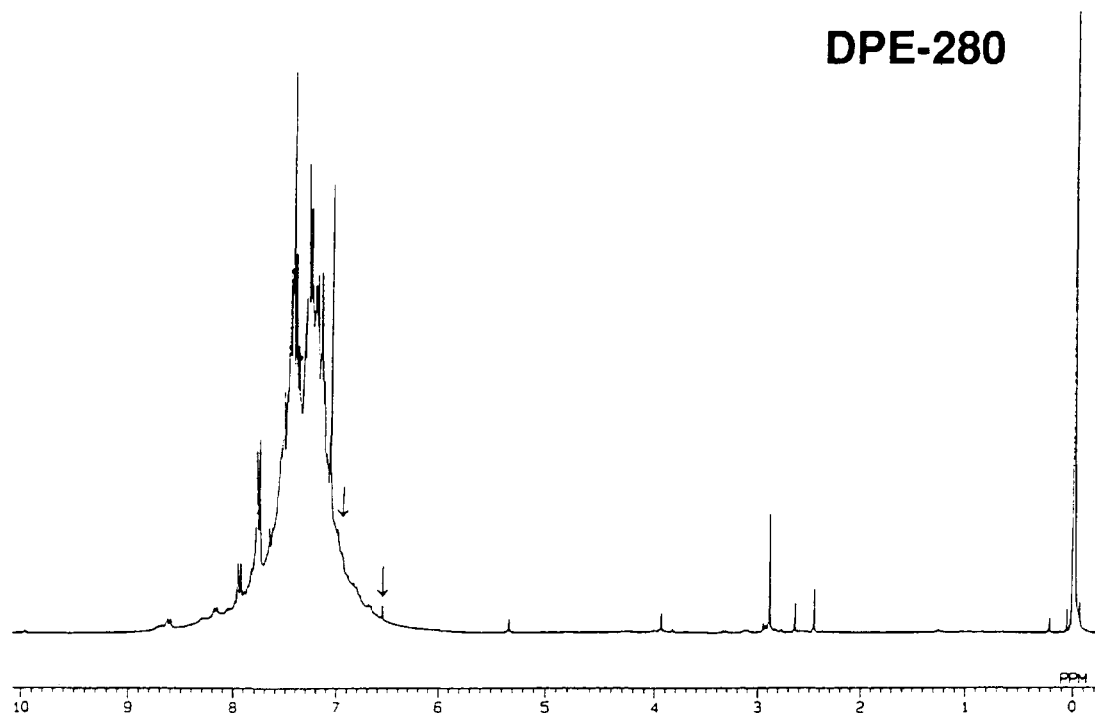


Fig. 5.  $^1\text{H}$ -NMR spectra of the air-blown residual product DPE-280.

carbon and development of anisotropic texture increased. The fraction of the naphthene group in pitch is relatively low[29], which implies that it is hard to develop anisotropic texture with the air-blowing reaction. On the other hand, naphthene groups in hydrogenated pitch could work to form anisotropic texture.

#### 4.4 Air-blowing reaction mechanism

It is generally conceivable that the air-blowing reactions of pitch are analogous with the oxidation of aromatic hydrocarbons. As mentioned in 3.2, the air-blowing reaction of aromatic hydrocarbons occurs through the intermediates with radicals[17,18,30,31]. The rate of the oxidation at high temperatures (330°C) is determined by the diffusion control of oxygen[19]. Since the aromatic hydrocarbons are viscous liquids during the reaction, it is suggested that the reaction system is under the condition of oxygen shortage. The ESR results support the radical reaction mechanisms under the condition of oxygen shortage. Namely, the crosslinked methylene bonding, biphenyl-type bonding, and ether bonding are formed through the termination reaction of the species with radicals. Carbonyl bonding is thought to be generated by the subsequent oxidation of crosslinked methylene groups.

$M/Z = 180$  in the DPE's air-blown residual product is assigned as stilbene and/or 9,10-dihydrophenanthrene. To confirm this, the spectrum of  $^1\text{H}$ -NMR (in  $\text{CDCl}_3$ ) for DPE-280 was taken and is shown in Fig. 5. Absorptions at 6.5 and 7.0 ppm can be assigned to vinyl-group hydrogen of *cis*- and *trans*-stilbene, re-

spectively. This evidence is also supported by the thermodynamic consideration that stilbene is more stable than 9,10-dihydrophenanthrene.\* Accordingly, the DPE's air-blowing does not proceed by the condensation of aromatic rings, but promotes the polymerization of vinyl groups.

#### 5. CONCLUSION

When subjected to oxidation in air at 330°C, alkyl-substituted aromatic compounds polymerized with methylene, biphenyl-type, and ether bonding, leading the methylene to partially change into carbonyl during the air-blowing reaction. Therefore, it was learned that the pitches containing alkyl-substituted compounds are the most effective source materials for raising the softening point, increasing molecular weight, and suppressing anisotropic texture. Furthermore, it was also learned that the properties of the air-blown products were characterized by, and dependent mainly upon, the crosslinked carbon and the condensed aromatic carbon formed by the air-blowing reaction.

*Acknowledgement*—The authors would like to express their deepest appreciation to Dr. Keiji Hashimoto, Osaka Municipal Research Institute, for his valuable advice and comments. Thanks are due to Osaka Gas Co., Ltd. for permission for publication.

\*The standard Gibbs free energies of *cis*- and *trans*-stilbene are 150.1 KJ/mol and 149.4 KJ/mol, respectively, while that of 9,10-dihydrophenanthrene is 207.3 KJ/mol[32].

## REFERENCES

1. E. J. Barth, *Asphalt Science and Technology*, p. 386. Gordon & Breach, New York (1962).
2. S. Otani, *Carbon* **3**, 31 (1965).
3. Y. Matsumura, *Sekiyu Gakkaishi* (in Japanese) **30**, 291 (1987).
4. T. Maeda, S. M. Zeng, K. Tokumitsu, J. Mondori, and I. Mochida, *Carbon* **31**, 407 (1993).
5. I. Mochida, T. Inaba, Y. Korai, H. Fujitsu, and K. Takeshita, *Carbon* **21**, 543 (1983).
6. I. Mochida, T. Inaba, Y. Korai, H. Fujitsu, and K. Takeshita, *Carbon* **21**, 553 (1983).
7. I. Mochida, Y. Korai, Y. Matsumura, and T. Maeda, *Sekiyu Gakkaishi* (in Japanese) **28**, 1 (1985).
8. J. B. Barr and I. C. Lewis, *Carbon* **16**, 439 (1978).
9. Y. Fukui, T. Hosoi, H. Mukaida, H. Makita, and J. Nishimura, *Sekiyu Gakkaishi* (in Japanese) **21**, 35 (1978).
10. S. M. Zeng, T. Maeda, K. Tokumitsu, J. Mondori, and I. Mochida, *Carbon* **31**, 413 (1993).
11. J. H. Choi, H. Kumagai, S. Yokoyama, and Y. Sanada, *19th Annual Meeting of Tansozairyo* (in Japanese) (1992) p. 40.
12. H. Seki, O. Ito, and M. Iino, *Fuel* **69**, 317 (1990).
13. J. L. Shultz, A. G. Sharkey, and R. A. Friedel, *J. Appl. Chem.* **20**, 126 (1970).
14. M. Hein and H. Weber, *Extended Abstracts, Conference on Carbon*, The University of Newcastle upon Tyne, UK (1988) p. 404.
15. L. C. Ling, L. Liu, and M. Z. Wang, *Extended Abstracts, Conference on Carbon*, Paris (1990) p. 294.
16. I. Mochida, *Tansozai no Kagaku to Kougaku* (in Japanese), Asakura Shoten (1990) p. 169.
17. Y. Kamiya, *Nenryo Kyokaishi* (in Japanese) **47**, 498 (1968).
18. E. Niki and Y. Kamiya, *Nenryo Kyokaishi* (in Japanese) **48**, 136 (1969).
19. Y. Kamiya, *Organic Oxidation Reaction* (in Japanese), GIHODO, Tokyo (1973).
20. E. Fitzer, K. Mueller, and W. Schaefer, *Chemistry and Physics of Carbon* (Edited by P. L. Walker, Jr.) Vol. 7, p. 305, Marcel Dekker, New York (1971).
21. I. C. Lewis and L. S. Singer, *J. Phys. Chem.* **85**, 354 (1981).
22. F. Goodarzi, G. Hermon, M. Iley, and H. Marsh, *Fuel* **54**, 105 (1975).
23. *The Merck Index*, seventh edition, Merck & Co., Inc., NJ (1960).
24. C. Yamaguchi, J. Mondori, S. Baba, H. Kumagai, and Y. Sanada, *Aromatics* (in Japanese) **44**, 17 (1992).
25. M. Hamaguchi and T. Nishizawa, *15th Annual Meeting of Tansozairyo* (in Japanese) (1988) p. 12.
26. T. Yoshida, Y. Nakata, R. Yoshida, S. Ueda, N. Kanda, and Y. Maekawa, *Fuel* **61**, 824 (1982).
27. Y. Maekawa, T. Yoshida, and Y. Yoshida, *Fuel* **58**, 864 (1979).
28. S. Baba, H. Matsui, and T. Nakamura, *Nenryo Kyokaishi* (in Japanese) **70**, 1151 (1991).
29. C. Yamaguchi, H. Matsuyoshi, J. Mondori, S. Baba, H. Kumagai, and Y. Sanada, *Tanso* (in Japanese) [No. 162], 78 (1994).
30. Y. Yokono, K. Murakami, and Y. Sanada, *Tanso* (in Japanese) [No. 125], 53 (1986).
31. D. C. Cronauer, R. G. Ruberto, R. G. Jenkins, A. Davis, P. C. Painter, D. S. Hoover, M. E. Starsinic, and D. Schlyer, *Fuel* **62**, 1124 (1983).
32. R. C. Reid, J. M. Prausnitz, and T. K. Sherwood, *The Properties of Gases and Liquids*, McGraw-Hill, New York (1977).

## 2.4 ton/day 石炭直接水添液化 PDU スラリー 予熱器におけるスラリー粘度変化の推算<sup>†</sup>

山口 宏

日本鋼管(株) エンジニアリング研究所<sup>††</sup>

横山 敬

日本鋼管(株) エネルギーエンジニアリング本部<sup>†††</sup>

真田雄三・千葉忠俊

北海道大学 工学部<sup>††††</sup>

2.4 ton/day 石炭直接水添液化プロセスにおいて、イリノイ No. 6 炭スラリーと水素が主成分のガスによる液化運転時の予熱器加熱管内スラリー粘度変化を差圧計と温度計による測定結果から推定した。すなわち、まず高圧下における粘度が既知の冷油および熱油運転結果に基づいて気液二相流の圧力損失に関する Lockhart-Martinelli 法 (L-M 法) を高温高圧下へ適用できるように修正し、これにより液化運転時の加熱管各部のスラリー温度と圧損の測定値を解析してスラリー粘度を推算した。修正 L-M 法によるスラリー粘度は石炭粒子初期濃度が小さい場合は濃度および温度とともに単調に増大するが、濃度が高い場合には最大値を示した。スラリー粘度の温度変化は、回分式粘度計の測定結果とは異なった。既往の著者らの回分式粘度計による検討結果から、両装置の結果の違いはスラリーの昇温速度に起因し、予熱器におけるスラリー粘度は膨潤に起因して変化すると推察した。

### 緒 言

石炭直接水添液化プロセスのスラリー予熱器では、水素を主成分とするガスと予め混合した石炭スラリーを気液固三相流の状態では液化反応温度付近まで急速昇温するが、この過程で石炭スラリーの粘度は複雑に変化する<sup>1)</sup>。このようなスラリー粘度変化を定量的に把握することは、流動および伝熱特性に基づいた予熱器の最適設計を図る上で重要である<sup>1)</sup>。著者らは、これまで回分式粘度計により昇温過程のスラリー粘度変化を系統的に測定し、粘度変化の主原因が石炭粒子の溶剤吸収による膨潤や液化反応により生成した粘着性液化生成物による凝集であることを明らかにした<sup>1)</sup>。しかし、これらの回分系における知見を工業操業条件下での流通式予熱器の場合にも拡張

できるかどうかは不明である。また、米国のパイロットプラント<sup>6,7)</sup>や毛細管による測定<sup>19)</sup>を除き、流通式予熱器で取得したデータを解析してスラリー粘度を推定した報告はなく、流通式予熱器の設計に提供できるスラリー粘度データは数少ない。

NKK 2.4 ton/day 石炭直接水添液化 PDU では予熱器加熱管の軸方向に熱電対と差圧計を取り付け、スラリー昇温過程における加熱管各部の圧損を測定した。既存の円管内気液二相流に関する圧力損失式を高温高圧気液固三相流に適用できるように修正し、これにより上述の圧損測定データを解析してスラリー粘度を逆算し、回分式高温高圧粘度計による測定値と比較した。

### 1. 実 験

#### 1.1 圧損の測定とスラリー粘度の推算

**実験装置** 予熱器は円筒対流型で、らせん状加熱管は外径 35 mm、内径 15 mm、長さ 68.1 m、らせん径 1.5 m である。加熱管の平均熱流束は外表面積基準で約

† 1994 年 11 月 22 日受理  
†† 〒210 川崎市川崎区南渡田町 1-1  
††† 〒230 横浜市鶴見区末広町 2-1  
†††† 〒060 札幌市北区 13 条西 8 丁目

Table 1 Experimental conditions and observed pressure-drop for room-temperature hydrogen gas/creosote oil system

|                                                   |        |        |        |       |       |       |       |        |
|---------------------------------------------------|--------|--------|--------|-------|-------|-------|-------|--------|
| Liquid feed rate, $\text{kg} \cdot \text{h}^{-1}$ | 247    | 236    | 229    | 236   | 349   | 347   | 360   | 349    |
| Gas feed rate, $\text{Nm}^3 \cdot \text{h}^{-1}$  | 95.5   | 72.0   | 149    | 259   | 254   | 158   | 96.0  | 74.0   |
| Pressure drop*, MPa                               | 0.0637 | 0.0515 | 0.0896 | 0.158 | 0.221 | 0.148 | 0.109 | 0.0969 |

\* the sum of pressure drops for PdR-271, -272 & -273

Table 2 Experimental conditions, observed pressure-drop and temperature for high-temperature hydrogen gas/anthracene oil system

|                                                   |     |       |       |       |       |       |
|---------------------------------------------------|-----|-------|-------|-------|-------|-------|
| Liquid feed rate, $\text{kg} \cdot \text{h}^{-1}$ | 275 | 275   | 275   | 275   | 275   | 275   |
| Gas feed rate, $\text{Nm}^3 \cdot \text{h}^{-1}$  | 50  | 155   | 253   | 297   | 392   | 490   |
| Pressure drop, MPa                                |     |       |       |       |       |       |
| PdR-272                                           | 0   | 0.033 | 0.077 | 0.082 | 0.116 | 0.174 |
| PdR-273                                           | 0   | 0.033 | 0.077 | 0.080 | 0.116 | 0.175 |
| Fluid temperature, K                              |     |       |       |       |       |       |
| TR-250                                            | 400 | 463   | 503   | 483   | 494   | 511   |
| TR-251                                            | 469 | 508   | 537   | 503   | 510   | 519   |
| TR-252                                            | 541 | 563   | 582   | 534   | 533   | 536   |
| TR-253                                            | 588 | 603   | 621   | 563   | 557   | 552   |
| TR-254                                            | 614 | 630   | 649   | 586   | 580   | 573   |
| Average temperature, K                            |     |       |       |       |       |       |
| PdR-272                                           | 553 | 573   | 593   | 542   | 540   | 542   |
| PdR-273                                           | 595 | 610   | 628   | 569   | 563   | 560   |

$5500 \text{ kcal} \cdot \text{m}^{-2} \cdot \text{h}^{-1}$ , 総括伝熱係数は約  $50 \text{ kcal} \cdot \text{m}^{-2} \cdot \text{h}^{-1} \cdot \text{K}^{-1}$  である。差圧計と内部流体温度測定用熱電対の取り付け位置を Fig. 1 に示す。加熱管には 24 個の外表面温度用熱電対, 5 個の内部流体温度用熱電対および 18.85 m 間隔で 3 台の差圧計 (PdR-271, PdR-272 および PdR-273) を図のように設置した。

**スラリー粘度推算方法** スラリー粘度の推算は直管中の気液二相流の圧損の解析に広く用いられている Lockhart-Martinelli 法 (以下, L-M 法)<sup>10)</sup> による。この方法で用いる圧力損失式と粘度推算法については Appendix を参照されたい。本実験のようならせん状管内での気液二相流や気液固三相流の圧損は, 一般にはわん曲流れの遠心力による二次流れの発生や乱れの増大により, 直管の場合よりも大きくなる<sup>11)</sup>。そこで, この点をまず粘度が既知のクレオソート油/水素ガス系の常温高圧の冷油運転結果と, 気液平衡状態や粘度が推算できるアントラセン油/水素ガス系の高圧高圧の熱油運転結果について検討した。冷油および熱油運転条件を圧損の測定値とともに Tables 1 & 2 に, クレオソート油とアントラセン油の性状を Table 3 に示す。冷油運転では流体の温度が約 300 K と一定であるため, 3 箇所の差圧計で測定した圧損の合計を示した。また, 表には熱油運転中に故障した差圧計 PdR-271 を除いた PdR-272 および PdR-273 による測定値を示した。アントラセン油には沸点範囲が IBP~493 K, 493~623 K およ

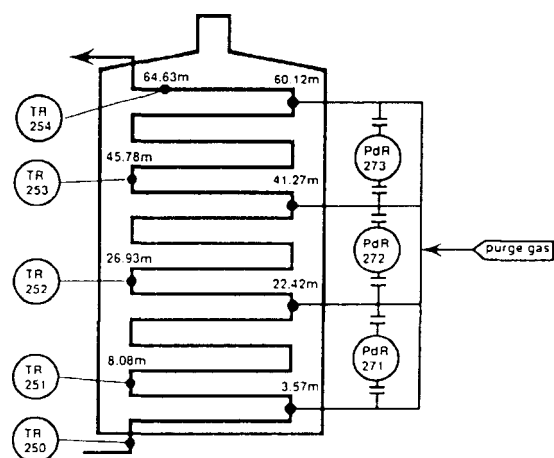


Fig. 1 Positions of thermocouple and of differential-pressure cell in preheater

び 623 K 以上の留分がそれぞれ 3.6, 44.4 および 52.0 wt% 含まれる。また, 熱油運転におけるアントラセン油の気液平衡状態は, GC-MS 分析結果から液相の組成を Table 4 のように仮定し, Grayson-Streed 法により計算した。クレオソート油の密度と粘度はそれぞれ  $1050 \text{ kg} \cdot \text{m}^{-3}$  および  $9.4 \times 10^{-3} \text{ kg} \cdot \text{m}^{-1} \cdot \text{s}^{-1}$  と常圧における測定値と同一であり, 水素ガスは密度と粘度がそれぞれ  $16.7 \text{ kg} \cdot \text{m}^{-3}$  および  $9.4 \times 10^{-6} \text{ kg} \cdot \text{m}^{-1} \cdot \text{s}^{-1}$  の理想気体<sup>9)</sup>であるとした。以上のデータより求めたらせん状管と直管の圧損比は, 加熱管内径に対してらせん径が大き

いため、ほぼ1.00であった。したがって、本実験ではらせん状加熱管を用いているが、圧損の推算には近似的に直管の場合の推算式を適用できると考えた。

L-M 法の高圧高温気液固三相流への適用は以下の手順によった。まず、クレオソート油/水素ガス系の冷油運転とアントラセン油/水素ガス系の熱油運転で測定した圧損とクレオソート油およびアントラセン油の粘度を用いて L-M 法により推算した圧損を比較した。その結果、L-M 法は常圧での圧損推算には十分適用できるが、高温高圧系には適用に限界があるので、後述のように、この方法に含まれる気相の流動パラメーター  $X$  と比例定数  $\phi_s$  の関係式を両系の測定結果を満足するように修正した。石炭液化反応系では石炭粒子は液相と同一に挙動し、液相の質量速度、密度および粘度の代わりにスラリーの質量速度、密度および粘度を用いれば L-M 法は三相流へ適用できる<sup>12)</sup>ことから、本研究でもこれと同じ手法と修正した  $X$  と  $\phi_s$  の関係式を用いて高温高圧気液固三相流状態下のスラリー粘度を推算することにした。

液化運転は、石炭試料として 95 wt% 以上が 100

Table 3 Result of ultimate analysis of solvents

| Solvent        | C                | H   | N   | S   | O*  |
|----------------|------------------|-----|-----|-----|-----|
|                | [d. a. f.** wt%] |     |     |     |     |
| Creosote oil   | 90.1             | 6.8 | 1.5 | 0.4 | 1.2 |
| Anthracene oil | 90.9             | 5.9 | 1.1 | 0.5 | 1.6 |

\* by difference \*\* dry ash free

mesh 以下のイリノイ No. 6 炭粒子および溶剤としてアントラセン油を用いて行った。また、触媒にはパイライト系合成硫化鉄触媒<sup>21)</sup>を用いた。運転条件と圧損の測定結果を Table 5 に、石炭粒子の関連性状および供給ガス組成を Tables 6 & 7 に示す。Table 5 から、スラリーの加熱管内滞留時間は空塔線速度基準で約 170 s、ガスホールドアップは 0.5 程度であると予想され<sup>12)</sup>、液化初期反応の起こる温度以上の領域に滞留する時間は上

Table 4 Input data of anthracene oil composition for calculation of gas-liquid equilibrium

| Compounds                | Boiling-point temperature [K] | Weight fraction [-] |
|--------------------------|-------------------------------|---------------------|
| Phenol                   | 435                           | 0.015               |
| Naphthalene              | 491                           | 0.021               |
| Methylnaphthalene        | 516                           | 0.013               |
| Dimethylnaphthalene      | 539                           | 0.019               |
| Acenaphthene             | 511                           | 0.041               |
| Fluorene                 | 569                           | 0.062               |
| Methylfluorene           | 591                           | 0.086               |
| Phenanthrene             | 613                           | 0.223               |
| Methylphenanthrene       | 634                           | 0.133               |
| C <sub>20</sub> paraffin | 653                           | 0.034               |
| Fluoranthene             | 656                           | 0.097               |
| Pyrene                   | 666                           | 0.077               |
| C <sub>24</sub> paraffin | 693                           | 0.061               |
| C <sub>26</sub> paraffin | 723                           | 0.060               |
| C <sub>28</sub> paraffin | 756                           | 0.058               |

Table 5 Experimental conditions, observed pressure-drop and fluid temperature for hydrogen rich gas/Illinois No. 6 coal slurry system

|                                                 |                    |                    |                    |                    |                    |
|-------------------------------------------------|--------------------|--------------------|--------------------|--------------------|--------------------|
| TI* in slurry, wt%                              | 26                 | 29                 | 33                 | 35                 | 37                 |
| Liquid feed rate, kg·h <sup>-1</sup>            | 275                | 275                | 280                | 280                | 285                |
| Gas feed rate, Nm <sup>3</sup> ·h <sup>-1</sup> | 107                | 104                | 113                | 111                | 108                |
| Pressure drop, MPa                              |                    |                    |                    |                    |                    |
| PdR-271                                         | 0.0343             | 0.0441             | 0.0883             | 0.136              | 0.253              |
| PdR-272                                         | 0.0490             | 0.0981             | 0.186              | 0.313              | 0.464              |
| PdR-273                                         | 0.132              | 0.186              | 0.294              | 0.314              | 0.254              |
| Fluid temperature, K                            |                    |                    |                    |                    |                    |
| TR-250                                          | 420                | 423                | 426                | 429                | 427                |
| TR-251                                          | 479                | 481                | 485                | 489                | 487                |
| TR-252                                          | 546                | 545                | 547                | 547                | 543                |
| TR-253                                          | 603                | 601                | 601                | 601                | 597                |
| TR-254                                          | 645                | 643                | 643                | 642                | 642                |
| PdR-271                                         | 449-531<br>(490**) | 452-531<br>(492**) | 459-532<br>(495**) | 462-533<br>(498**) | 461-531<br>(496**) |
| PdR-272                                         | 531-589<br>(560**) | 531-589<br>(560**) | 532-589<br>(561**) | 533-589<br>(561**) | 531-585<br>(558**) |
| PdR-273                                         | 589-635<br>(612**) | 589-633<br>(611**) | 589-634<br>(612**) | 589-633<br>(611**) | 585-631<br>(608**) |

\* Toluene Insoluble \*\* Average temperature



Table 6 Properties of Illinois No. 6 coal

| Ultimate analysis (d. a. f.* wt%) |     |                  |     |              | Proximate analysis (d. b.** wt%) |      |      |
|-----------------------------------|-----|------------------|-----|--------------|----------------------------------|------|------|
| C                                 | H   | N                | S   | O**          | VM*                              | FC*  | Ash  |
| 77.4                              | 5.4 | 1.4              | 3.7 | 12.1         | 37.8                             | 50.9 | 11.3 |
| * dry ash free                    |     | ** by difference |     | *** dry base |                                  |      |      |
| * volatile matter                 |     | * fixed carbon   |     |              |                                  |      |      |

Table 7 Feed gas composition at preheater inlet for hydrogen-rich gas/Illinois No. 6 coal slurry system

| component       | weight fraction [—] |
|-----------------|---------------------|
| hydrogen        | 0.5054              |
| methane         | 0.1749              |
| ethane          | 0.1230              |
| propane         | 0.0601              |
| carbon monoxide | 0.0765              |
| carbon dioxide  | 0.0601              |

記滞留時間の25%以下、すなわち、約43 s以下であるが、このような条件下でも液化初期反応は進行し、粘度以外のスラリー物性も変化する<sup>3,18)</sup>可能性がある。既往の研究<sup>18)</sup>によれば、石炭の溶解は570 K以上で観測され、約650 Kまでスラリーを加熱したときのトルエン不溶成分量の減少は7 wt%程度、高沸点留分のプレアスファルテン（テトラヒドロフラン可溶-トルエン不溶成分）の生成率は10 wt%程度と推定される。これらの値は石炭粒子初期濃度40 wt%スラリーを想定すると、溶剂量がトルエン可溶成分量で5 wt%、プレアスファルテン量で7 wt%、計12 wt%程度増加するにすぎない。さらに、石炭の熱分解により生成するガス量は供給ガス量に比べてきわめて少量である<sup>13)</sup>。そこで、ここでは解析の簡略化のため、まず気液固各相の成分および組成は加熱管内の570 K以上の領域で起こる反応により変化しないものと見なし、石炭粒子/アントラセン油/供給ガス系の気液平衡状態を計算し、得られたスラリーの密度 $\rho_s$ 、質量速度 $W_s$ 、ガスの密度 $\rho_g$ 、粘度 $\mu_g$ 、空塔基準線速度 $U_0$ と圧損の実測値から、Appendixに示した手順によりスラリー粘度を決定した。

#### 1.2 高温高圧粘度計によるスラリー粘度の測定

用いた装置は内容積750 cm<sup>3</sup>の同心二重円筒回転式<sup>19)</sup>の粘度計（外筒42 mm $\phi$ ×104 mmL、内筒38 mm $\phi$ ×50 mmL）である。用いたスラリー試料は液化運転で使ったものと同じ石炭粒子、溶剤および触媒を使用した。石炭/溶剤重量比がそれぞれ25/75、30/70、35/65、40/60の各スラリー試料210 cm<sup>3</sup>を粘度計に仕込み、水素を初圧10 MPaで充填した後、200 rpmで回転しながら、約620 Kまで3 K $\cdot$ min<sup>-1</sup>の速度で昇温し、昇温

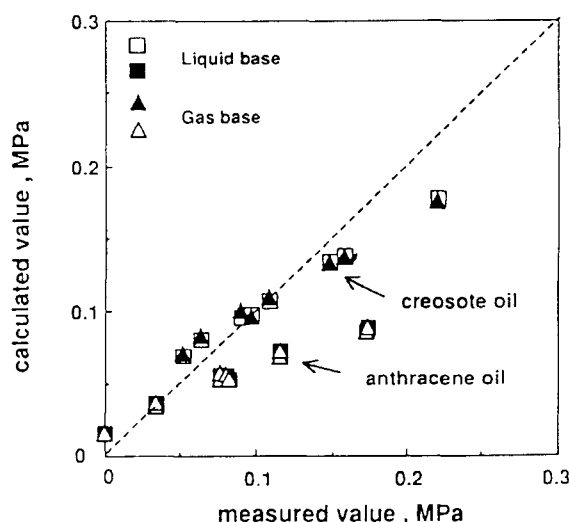


Fig. 2 Comparison between calculated and measured values of pressure drop obtained by L-M method for creosote oil/hydrogen and anthracene oil/hydrogen systems

過程のスラリー粘度変化を測定した。

## 2. 結果および考察

### 2.1 冷油運転および熱油運転

Fig. 2に、冷油運転および熱油運転時における加熱管各部圧損の測定値と推算値を示す。冷油の場合、推算値は測定値と比較的良く一致しているが、熱油運転の場合には測定値と推算値との差がかなり大きい。これは、ガスホールドアップが常温常圧下よりも高温高圧下のほうが高くなる<sup>8,20)</sup>にもかかわらず、L-M法が常温常圧で得られた流動パラメーター $X$ と比例定数 $\phi_s$ との関係<sup>10)</sup>を用いるためと考え、以下のように、この関係を圧損の推算値が冷油および熱油の高圧運転の場合の測定値とできるだけ合致するように修正した。まず、熱油運転条件と物性値から、 $X$ と気相だけによる圧損 $\Delta P_g$ を算出し、つぎに二相流の圧損の測定値と $\Delta P_g$ から $\phi_s$ を求め、次式のような $\phi_s$ と $X$ の関係を得た。

$$\phi_s = 4.01 + 1.12X \quad (1)$$

この式を用いたときの冷油および熱油運転における圧損の測定値と推算値を再プロットしたのがFig. 3である。両運転の場合とも、測定値と推算値は満足すべき一致を

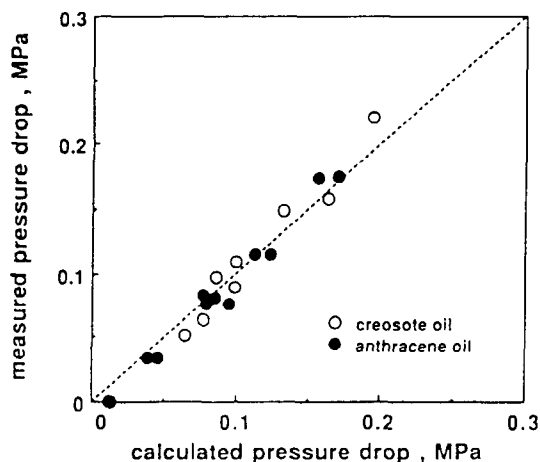


Fig. 3 Comparison of measured pressure drops with those estimated by L-M method using Eq. (1)

示している。

## 2.2 液化運転時の圧損データ解析とスラリー粘度推算

加熱中のスラリーの粘度増加は石炭粒子の膨潤やブレアスファルテンの生成、減少は温度上昇による溶剤粘度の低下や液化反応生成物の溶剤への溶解による<sup>3-5)</sup>。Fig. 4に、スラリー中の石炭粒子の初期濃度が25, 30, 35および40 wt%の場合のスラリー粘度を回分式粘度計により測定した結果を示す。これをみると、粒子濃度とともに粘度が大きくなるのがわかる。さらに、25および30 wt%と濃度が低い場合は、570～600 Kの高温領域で鋭い粘度ピークが見られるのに対し、35および40 wt%と濃度が高くなると、上記のピークに加えて450～520 Kの低温領域にもピークが現れる。この結果を既往の研究に基づいて考えると、低温領域のピークは膨潤による石炭粒子体積濃度の増加と膨潤が止まり体積濃度が一定となった状態での溶剤粘度のみの低下に対応し、高温領域のピークは粘性の高いブレアスファルテンの生成と溶解に対応するものと言えよう。

Fig. 5は、Table 5に示した粒子初期濃度が26, 29, 33, 35および37 wt%のスラリーの液化運転で測定した加熱管各部の圧損からスラリー粘度を推算し、温度に対してプロットしたものである。図から、粘度は粒子濃度とともに増加するが、温度による変化は粒子濃度により異なることがわかる。すなわち、濃度が33 wt%以下では粘度は濃度および温度とともに単調に増加するが、35および37 wt%の場合には540～560 Kと比較的低い温度域で最大となり、濃度が37 wt%の場合の最大値は約240 cpである。また、図には、各粒子濃度のスラリーについて圧損を測定した時の加熱管各部の温度域に対応した粘度の平均値を、回分式粘度計による測定結果 (Fig. 4) から読み取り、破線で示してある。ここで、

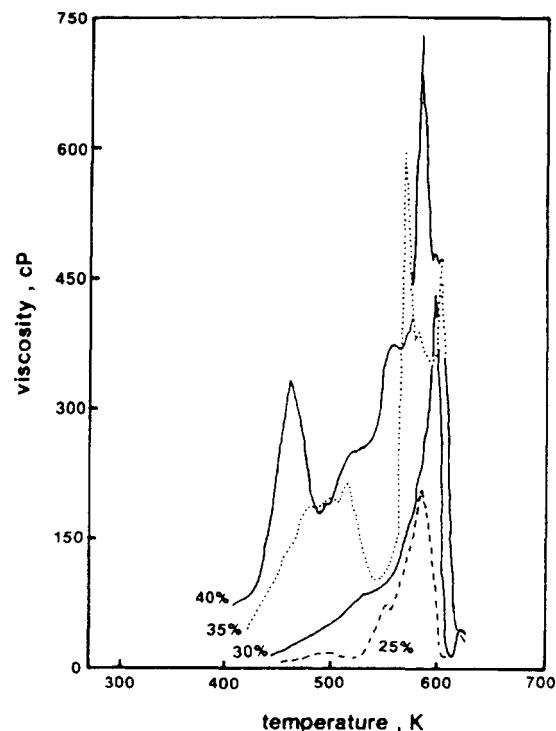


Fig. 4 Viscosities of Illinois No. 6 coal slurry measured by batch high-temperature and high-pressure viscometer

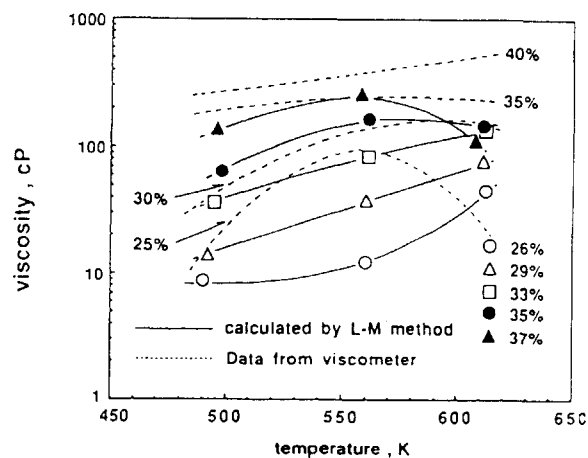


Fig. 5 Comparison of slurry viscosities in preheater with those in batch high-temperature and high-pressure viscometer

圧損を測定しなかった40 wt%スラリーについては、上述の加熱管各部の温度域をそれぞれ461～531 K, 531～585 K, 585～631 Kとして推定した。図から明らかなように、圧損の測定から推算した粘度と回分式粘度計の測定値および両装置の粘度の温度変化プロフィールは必ずしも一致しない。

上記の両装置における粘度の差はつぎのような運転条

件の違いに起因すると思われる。すなわち、予熱器加熱管ではスラリーの昇温速度が約  $180 \text{ K} \cdot \text{min}^{-1}$ 、入口圧力が  $20 \sim 21 \text{ MPa}$ 、剪断速度が  $50 \text{ s}^{-1}$  であるのに対し、回分式粘度計では昇温速度が  $3 \text{ K} \cdot \text{min}^{-1}$ 、圧力が  $11 \sim 20 \text{ MPa}$ 、剪断速度が  $300 \text{ s}^{-1}$  であり、両装置の昇温速度と剪断速度はかなり異なる。まず、石炭スラリーは非ニュートン性流体であり<sup>16)</sup>、剪断速度が大きいほど測定される粘度は小さくなるが、粘度ピークが現れる温度域はほとんど変わらない<sup>2)</sup>。したがって、本実験で予熱器と回分式粘度計の剪断速度を同一としても、両装置の粘度ピークの大きさの差は拡大するが、ピークが現れる温度域の違いは変わらないはずであるので、石炭スラリーの非ニュートン性により両装置における結果の差は説明できない。他方、昇温速度が大きくなれば、膨潤に起因する粘度ピークを与える温度は高温側にシフトすると同時に、ピーク高さも小さくなる<sup>3)</sup>。これに基づいて考えると、本実験の場合、例えば回分式粘度計により低温度域で観測された膨潤に対応した粘度ピークは、予熱器ではこれより高い温度域に小さなピークとしてシフトするはずである。また、高温度域で観測されたプレアスファルテンの生成・溶解に対応した粘度ピークも大半は予熱器出口温度の  $650 \text{ K}$  よりも高温度域に移行するか、石炭やプレアスファルテンの溶解が急速に進む  $600 \text{ K}$  以上の温度域に移行し、粘度は顕著に減少するはずであるので、昇温速度が同じであれば両装置の粘度変化は同じようになると推察される。以上のことから、本実験において予熱器で観測された粘度ピークは膨潤に起因すると考えられ、回分式粘度計により測定した粘度変化にスラリーの昇温速度、剪断速度の影響を考慮すれば、流通式予熱器における粘度ピークが現れる温度域を概略推定できると推察されるが、この点については今後の検討を要する。さらに、流通式予熱器における粘度ピークの高さは、剪断速度や昇温速度に加えて圧力損失の測定間隔にも依存するはずである。すなわち、本実験のように低感度の検出器により圧力損失を長い間隔で測定した場合には、平均粘度は低めに算出されることになり、これも両装置による結果の差の一因と考えられる。

## 結 論

NKK 2.4 ton/day 石炭直接水添液化 PDU のスラリー予熱器の液化運転において加熱管各部のスラリー温度と圧損を測定し、結果を常温、常圧における気液二相流の圧力損失推算に用いられる Lockhart-Martinelli 法 (L-M 法) を高温高压の石炭液化系へ拡張、適用できるように修正した方法により解析し、スラリーの粘度を推算した。また、推算結果を回分式粘度計による測定結果と

比較し、本実験範囲で以下のことを明らかにした。

1) 推算した予熱器におけるスラリー粘度の変化は、石炭粒子の膨潤に起因し、スラリー中の石炭粒子初期濃度が小さい場合は濃度および温度とともに単調に増大するが、濃度が高い場合には最大値を示した。

2) 上記の粘度ピークを与える温度域は流通式予熱器と回分式粘度計の場合では異なった。これは、両装置のスラリーの昇温速度が異なるためと推察した。

## Appendix

### Lockhart-Martinelli法<sup>10)</sup>

直管内の気液二相流が層流あるいは乱流の場合、圧力損失  $\Delta P_{\text{m}} [\text{MPa}]$  は気相と液相それぞれの均相流の圧力損失を  $\Delta P_g [\text{MPa}]$  および  $\Delta P_l [\text{MPa}]$  とすると、

$$\Delta P_{\text{m}} = \phi_g^2 \Delta P_g = \phi_l^2 \Delta P_l \quad (\text{a-1})$$

と与えられ、比例定数  $\phi_g [-]$ 、 $\phi_l [-]$  と均相流圧力損失、 $\Delta P_g$  および  $\Delta P_l$  がわかれば  $\Delta P_{\text{m}}$  を推算できる。いま、気液各均相流の圧力損失を  $\Delta P_i [\text{MPa}]$  ( $i$  は気相の場合  $g$ 、液相の場合  $l$ 、スラリーの場合  $sl$  (以下、同じ)) とすると、これらは空塔基準線速度を  $U_m [\text{m} \cdot \text{s}^{-1}]$ 、密度を  $\rho_i [\text{kg} \cdot \text{m}^{-3}]$ 、摩擦係数を  $f_i [-]$ 、管径を  $D [\text{m}]$ 、管長を  $L [\text{m}]$  として次式で与えられる。

$$\Delta P_i = 2 \times 10^{-6} f_i \rho_i U_m^2 L / D \quad (\text{a-2})$$

さらに、上式中の  $f_i$  は粘度を  $\mu_i [\text{kg} \cdot \text{m}^{-1} \cdot \text{s}^{-1}]$  とするとレイノルズ数  $Re_i (= \rho_i U_m D / \mu_i)$  の関数であり、以下のように与えられる。

$$Re_i < 1000 \text{ (層流)}; f_i = 16 / Re_i \quad (\text{a-3})$$

$$Re_i > 2000 \text{ (乱流)}; f_i = 0.046 / Re_i^{0.2} \quad (\text{a-4})$$

他方、気液二相流の流動状態は各均相流についてのレイノルズ数、 $Re_g$  および  $Re_l$  により、以下のように与えられる流動パラメータ  $X [-]$  により評価できるものとする<sup>10)</sup>。すなわち、気相および液相の質量速度をそれぞれ  $W_g [\text{kg} \cdot \text{s}^{-1}]$ 、 $W_l [\text{kg} \cdot \text{s}^{-1}]$  とすると、

①熱油運転のように気相および液相がともに乱流 ( $Re_g > 2000$  および  $Re_l > 2000$ ) の場合:

$$X = (W_l / W_g)^{0.5} (\rho_g / \rho_l)^{0.5} \times (\mu_l / \mu_g)^{0.1} \quad (\text{a-5})$$

②冷油運転や液化運転のように気相が乱流、液相 (あるいはスラリー相) が層流 ( $Re_g > 2000$  および  $Re_l$  (あるいは  $Re_{sl}) < 1000$ ) の場合:

$$X = 18.7 Re_l^{0.4} (W_l / W_g)^{0.5} (\rho_g / \rho_l)^{0.5} \times (\mu_l / \mu_g)^{0.5} \quad (\text{a-6})$$

(スラリー相の場合、上式中の  $Re_l$ 、 $W_l$ 、 $\rho_l$ 、 $\mu_l$  がそれぞれ  $Re_{sl}$ 、 $W_{sl}$ 、 $\rho_{sl}$ 、 $\mu_{sl}$  となる)

ここで、冷油および熱油運転の場合には、 $\mu_l$  が既知であるので、Eqs. (a-2) ~ (a-4) から  $Re_i$ 、 $f_i$  および  $\Delta P_i$  を求め、さらに  $\phi_l$  と  $X$  の関係<sup>10)</sup> および Eq. (a-1) より  $\Delta P_{\text{m}}$  を計算し、測定値と比較する。

スラリーの場合の液化運転では上記の  $\mu_l$  に相当するスラリー粘度、 $\mu_{sl}$  をつぎのようにして推定できる。すなわち、Eq. (a-6) 中の  $W_l$ 、 $\rho_l$ 、 $\mu_l$  をそれぞれに  $W_{sl}$ 、 $\rho_{sl}$ 、 $\mu_{sl}$  に置き換え、まず、 $\rho_{sl}$ 、 $\rho_g$ 、 $\mu_g$ 、 $W_{sl}$  および  $U_m$  を気液平衡計算結果に基づいて推算して  $Re_{sl}$ 、 $f_{sl}$  および  $\Delta P_{sl}$  を求め、ついで、 $\Delta P_{sl}$  と  $\Delta P_{\text{m}}$  の測定値から比例定数  $\phi_g$  を計算した。冷油、熱油の各運転で圧損の推算値と測定値が合致するように求め直した  $\phi_g$  と

$X$  の関係式 (Eq. (1)) が、液化運転でも変わらないと仮定し、Eq. (1) から流動パラメータ  $X$  を算出すると、Eq. (a-6) より  $X$  に含まれる  $\mu_u$  を決定することができる。

【謝 辞】 本研究は新エネルギー・産業技術総合開発機構 (NEDO) の委託により実施した。ここに謝意を表する。

# Nomenclature

|                 |                                                                                          |                                        |
|-----------------|------------------------------------------------------------------------------------------|----------------------------------------|
| $D$             | = pipe diameter                                                                          | [m]                                    |
| $f_i$           | = friction factor defined by Eq. (a-3)<br>or Eq. (a-4)                                   | [—]                                    |
| $L$             | = pipe length                                                                            | [m]                                    |
| $\Delta P_{mu}$ | = pressure drop for gas-liquid or -slurry<br>flow                                        | [MPa]                                  |
| $\Delta P_i$    | = pressure drop for gas, liquid or slurry<br>flow                                        | [MPa]                                  |
| $Re_i$          | = Reynolds number for gas, liquid or slurry<br>( $\rho_i \cdot U_{oi} \cdot D / \mu_i$ ) | [—]                                    |
| $U_{oi}$        | = superficial gas, liquid or slurry velocity                                             | [m·s <sup>-1</sup> ]                   |
| $W_i$           | = mass flow rate of gas, liquid or slurry                                                | [kg·s <sup>-1</sup> ]                  |
| $X$             | = Lockhart-Martinelli parameter                                                          | [—]                                    |
| $\mu_i$         | = viscosity of gas, liquid or slurry                                                     | [kg·m <sup>-1</sup> ·s <sup>-1</sup> ] |
| $\rho_i$        | = density of gas, liquid or slurry                                                       | [kg·m <sup>-3</sup> ]                  |
| $\phi_i$        | = square root of pressure drop ratio<br>defined by Eq. (a-1)                             | [—]                                    |
| <Subscripts>    |                                                                                          |                                        |
| $g$             | = gas                                                                                    |                                        |
| $l$             | = liquid                                                                                 |                                        |
| $sl$            | = slurry                                                                                 |                                        |

# Literature cited

- 1) Akagawa, K., T. Sakaguchi and M. Ueda: "Rasen-Kantyu no Kieki-Nisoryu no Ryudo ni Kansuru Kenkyu", *Nihon Kikai Gakkai Ronbunshu*, **36**, 1712 - 1718 (1970)
- 2) Cohen, A. and D. Richon: "Rheological Properties of Coal Powder+Solvent+Nitrogen to 653 K for Two Different Coals", *Fuel*, **65**, 117 - 121 (1986)
- 3) Deng, C. -R., H. Moritomi, Y. Sanada and T. Chiba: "Change of Apparent Viscosity of Coal Slurry during Liquefaction", *J. Fuel Soc. Japan*, **65**, 265 - 272 (1986)
- 4) idem: "Change of Apparent Viscosity of Coal/ Tetralin Slurry during Liquefaction", *ibid.*, **66**, 114 - 120 (1987)

- 5) Deng, C. -R., T. Nio, Y. Sanada and T. Chiba: "Relationship between Swelling of Coal Particles and Apparent Viscosity of Slurry during Coal Liquefaction for Akabira Coal/Creosote Oil Slurry System", *Fuel*, **68**, 1134 - 1139 (1989)
- 6) Pittsburg & Midway Coal Mining Co.: "Solvent Refined Coal Process", DOE Report, DOE/ET/ 1010: - 46 (Vols. 1 & 2) (1982)
- 7) Fluor Engineers and Constructors, Inc.: "Coal Liquefaction Design Practice Manual", PB- 2575-11
- 8) Idogawa, K., K. Ikeda, T. Fukuda and S. Morooka: "Formation and Flow of Gas Bubbles in a Pressurized Bubble Column with a Single Orifice or Nozzle Gas Distributor", *Chem. Eng. Comm.*, **59**, 201 - 212 (1987)
- 9) Kagaku Kogaku Kyokai (ed.): "Bussei-Josu Suisanh-o", Vol. 2, Maruzen, p.14 (1964)
- 10) Lockhart, R.W. and R. C. Martinelli: "Proposed Correlation of Data for Isothermal Two-Phase, Two-Component Flow in Pipes", *Chem. Eng. Prog.*, **45**, 39 - 48 (1949)
- 11) Mehta, D.C.: "Full Scale Cold-Flow Modelling of the SRC-I Slurry Fired Heater at Creare, Inc.", DOE Report, DOE/OR/ 03054 - 58 (1985)
- 12) Morooka, S., T. Kago, K. Kusakabe and Y. Kato: "Flow Properties in Liquefier and Preheater of Direct Coal Liquefaction Process", *J. Fuel Soc. Japan*, **66**, 338 - 347 (1987)
- 13) Neavel, R.C.: "Liquefaction of Coal in Hydrogen-Donor and Non-Donor Vehicles", *Fuel*, **55**, 237 - 242 (1976)
- 14) Nishida, F., M. Takayasu and N. Nishida: "Sekitan-Ekika-Hanno-Sochi no Kaihatsu", *Kagaku Kōgaku*, **45**, 567 - 573 (1981)
- 15) Okutani, T., S. Yokoyama and Y. Maekawa: "Viscosity Changes in Coal Paste During Hydrogenation", *Fuel*, **63**, 164 - 168 (1984)
- 16) Sakaki, T., M. Shibata and S. Arita: "Change of Rheological Behavior in Wandoan Coal-Anthracene Oil Slurry by Heating", *J. Fuel Soc. Japan*, **66**, 365 - 372 (1987)
- 17) Shah, Y.T., S. J. Parulekar and N. L. Carr: "Reaction Engineering in Direct Coal Liquefaction", Ed. Y.T. Shah, Addison-Wesley, pp.221 - 227 (1981)
- 18) Shibata, M., T. Sakaki, Y. Adachi, T. Miki and S. Arita: "Initial Stage Liquefaction of Coal in the Process of Rising Temperature (1) —Effects of heating patterns—", *J. Fuel Soc. Japan*, **68**, 55 - 62 (1989)
- 19) Tsutsumi, A. and K. Yoshida: "Rheological Behaviour of Coal-Solvent Slurries", *Fuel*, **65**, 906 - 909 (1986)
- 20) Yamaguchi, H., T. Ogawa and K. Yokoyama: "Gas Hold-Up in a High Pressure and Temperature Reactor of 2.4 ton/day Direct Coal Liquefaction Process", *J. Fuel Soc. Japan*, **70**, 1143 - 1150 (1991)
- 21) Yamaguchi, H., S. Moriguchi, K. Matsubara, T. Fukuyama and M. Yanagiuchi: "Sekitan-Surari-Yonetsuki ni Okeru Ryukatetsu no Futuyaku", Proc. 52th Annual Meeting of Chem. Eng. Soc. Japan, 154 (1987)

# Estimation of Slurry Viscosity in Preheater of 2.4 ton/day Direct Coal Liquefaction Process

Hiroshi Yamaguchi

Eng. Res. Center., NKK, Kawasaki 210

Kei Yokoyama

Energy Ind. Eng. Div., NKK, Yokohama 230

Yuzo Sanada and Tadatoshi Chiba

Faculty of Engineering, Hokkaido Univ., Sapporo 060

**Key Words:** Coal, Liquefaction, Preheater, Slurry Viscosity

Slurry viscosity in the preheater of the NKK 2.4 ton/day direct coal liquefaction process was estimated from observed results of pressure-drop and temperature distributions through the preheater. The estimation of slurry viscosity was performed by utilizing the modified Lockhart-Martinelli (L-M) method for gas-liquid two-phase flow at normal temperature and pressure. In this method, the relationship between the fluid parameter,  $X$ , and the square root of the pressure drop ratio,  $\phi_g$ , for the gas phase was modified for estimated results to fit those observed for a cold hydrogen-gas/creosote oil system and for a hot hydrogen-gas/anthracene oil system. On the basis of the modified relationship, the slurry viscosities were estimated for hydrogen rich gas/Illinois No. 6 coal particles-anthracene oil slurry system under liquefaction conditions. The estimated slurry viscosity was found to increase with the initial volume concentration of coal particles in the slurry. The viscosity also increased monotonously with temperature for slurries having lower coal concentrations, while exhibiting a maximum for those with higher coal concentrations, implying that the viscosity change was caused by swelling of coal particles. The difference of temperature ranges for viscosity peak appearance in the preheater and in a batch viscometer was recognized and attributed to differences in the slurry heating rates between the two apparatus.

---



## SURFACE CHEMISTRY OF CARBON BLACK THROUGH CURING PROCESS OF EPOXY RESIN

M. NAKAHARA,<sup>a</sup> T. TAKADA,<sup>b</sup> H. KUMAGAI,<sup>c</sup> and Y. SANADA<sup>c</sup>

<sup>a</sup>Faculty of Engineering, Gunma University, Kiryu, Gunma 376, Japan

<sup>b</sup>Process Research and Product Evaluation Department, Japan Energy Corporation, 2-1 Ushiodori, Kurashiki, Okayama 712, Japan

<sup>c</sup>Center for Advanced Research of Energy Technology, Hokkaido University, N-13, W-8, Sapporo 060, Japan

(Received 13 February 1995; accepted in revised form 25 May 1995)

**Abstract**—The effects of oxidized carbon black surfaces on the epoxy resin curing process were examined by differential scanning calorimetry (DSC). The addition of oxidized carbon black accelerated the initial cure reaction of the epoxy-amine system. Peak temperature in DSC exotherm of the resin system falls in proportion to the ratio of surface ester groups on carbon black added. Results obtained from model compounds confirmed that COOH groups on the carbon black surface play an important role in promoting the initial cure reaction of the system. The degree of enthalpy change associated with the cure reaction was found to be almost independent of the chemical structure of the carbon black surface.

**Key Words**—Carbon black, epoxy resin, oxygen-containing functional groups, cure reaction, enthalpy, differential scanning calorimetry.

### 1. INTRODUCTION

The interfacial strength between carbon materials and epoxy resin matrices varies with the surface chemical structure of carbon materials[1]. As a result, the chemical structure affects many important properties such as interlaminar shear strength and impact behavior of composite materials with carbon fiber[2 and 3]. Moreover, oxidized carbon surfaces affect the cure behavior of epoxy resin systems[4]. The relationships between surface functionalities on the oxidized carbon materials and cure behaviors of epoxy resin matrices are important in understanding and controlling the carbon/epoxy composite interfaces. However, few detailed studies have been reported on the relationships mentioned above.

We have reported on the surface chemical structure of carbon black in the previous paper[5]. In this paper we describe the effects of the chemical structure of carbon black surface concerning the curing behavior of the epoxy resin system. Moreover, we will discuss the effects of the surface oxygen-containing functional groups introduced onto the carbon surface concerning the curing behavior, using model compounds as authentic species for oxidized carbon black surfaces.

### 2. EXPERIMENTAL

The epoxy resin system used in this study consisted of a diglycidyl ether of bisphenol A (DGEBA) type epoxy resin (Ep828, Shell), and its hardener, meta-phenylene diamine (MPDA, Aldrich). The molecular structures of Ep828 and MPDA are shown in Fig. 1. MPDA was used by pulverizing under 200 mesh. The

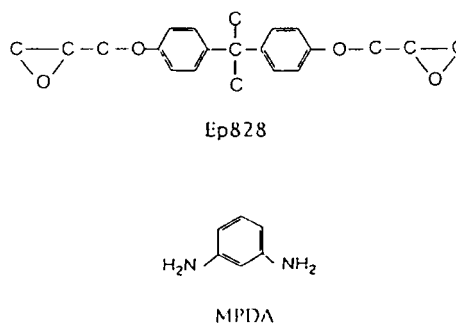


Fig. 1. Molecular structures of DGEBA and MPDA.

resin system was composed of Ep828, 100 parts by weight, and MPDA, 14 parts by weight.

The carbon blacks treated by oxygen plasma in the previous paper[5] were used as samples in the present study. We have already reported the surface chemical structure of the carbon blacks in the preceding paper[5]. The carbon blacks treated with oxygen plasma were mixed with the Ep828+MPDA resin system in the ratio by weight 1:10.

Aromatic compounds having different oxygen-containing functional groups, as model surfaces for the carbon blacks, were utilized to characterize the influence of carbon black surface on the curing behavior of the resin system. The aromatic compounds used were 9-phenanthrol, anthracenemethanol, anthraquinone, anthracenecarboxylic acid and anthracene. Molecular structures of the aromatic compounds are shown in Fig. 2. Each compound was mixed with Ep828+MPDA resin system, in which the molar fraction of functional group of the model compound varied from  $1.5 \times 10^{-3}$  to  $5.0 \times 10^{-3}$ .

The enthalpy changes occurring during the cure

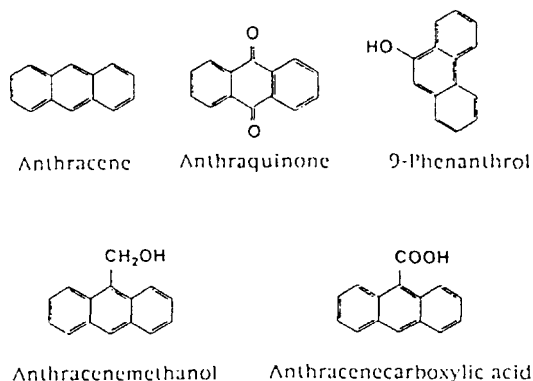


Fig. 2. Molecular structures of model compounds.

reactions of the resin system, the carbon black/resin system and the aromatic compound/resin system were quantitatively determined by differential scanning calorimetry (DSC120, Seiko). The heating rate was  $8^{\circ}\text{C min}^{-1}$ . The data analysis of DSC exotherms associated with the cure reactions was performed with SSC5020 Disc Station (Seiko).

### 3. RESULTS AND DISCUSSION

#### 3.1 DSC exotherm

Representative DSC scans from the epoxy resin system (Ep828 + MPDA) and the carbon black/epoxy resin system are shown in Fig. 3. The DSC exotherm of the epoxy resin system shows a maximum at  $162.2^{\circ}\text{C}$ . On addition of carbon black, which was treated at 20 W for 240 minutes under oxygen plasma[5], the temperature of the exotherm maximum ( $T_{\text{ExM}}$ , see Fig. 3) shifts from  $162.2$  to  $142.8^{\circ}\text{C}$ . The drop in  $T_{\text{ExM}}$  due to the addition of the carbon black tends to increase with the oxygen plasma treatment time, as shown in Fig. 4. This tendency is

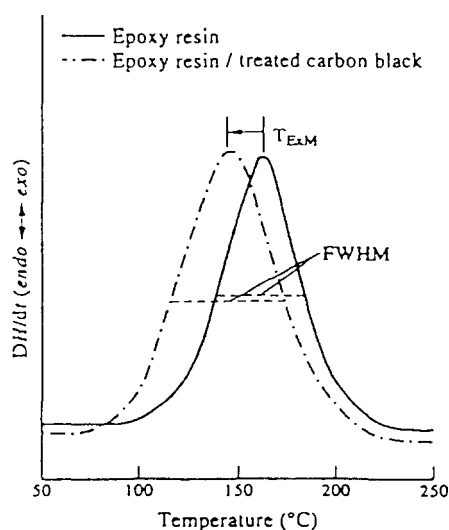
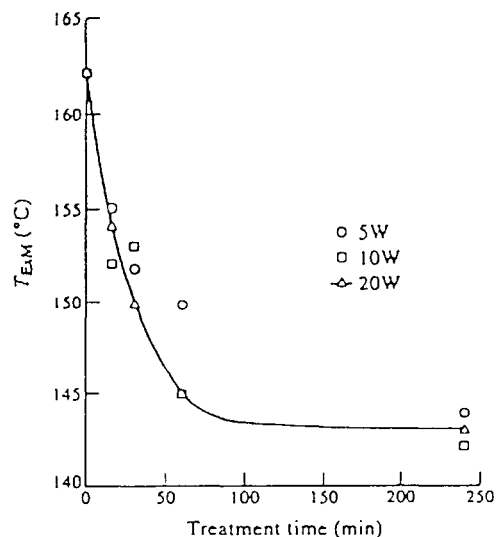
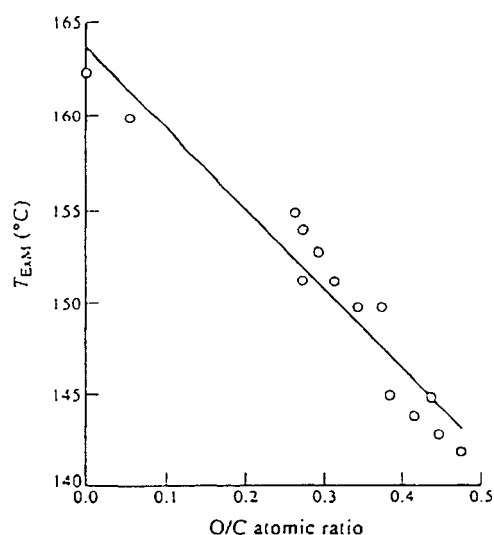


Fig. 3. DSC exotherm scans.

Fig. 4. Effect of plasma treatment time on the temperature of exotherm maximum ( $T_{\text{ExM}}$ ).

observed for each input power. It is found that the plasma-treated carbon blacks significantly promote the cure reaction of the epoxy resin system.

The cure reaction of the epoxy resin system is expected to be influenced by the surface chemical structure of carbon black. XPS O/C atomic ratio on the carbon black surface increases due to oxygen plasma treatment and the values have been reported in the previous paper[5].  $T_{\text{ExM}}$  is shown as a function of the O/C atomic ratio in Fig. 5. The O/C atomic ratio gives a good correlation for  $T_{\text{ExM}}$ . That is,  $T_{\text{ExM}}$  decreases linearly with the increase of the O/C atomic ratio. This indicates that the oxygen-containing functional groups introduced onto the carbon black surface induce the acceleration of the cure reaction of the epoxy resin system.

Fig. 5. The relation between  $T_{\text{ExM}}$  and XPS O/C atomic ratio.

### 3.2 Evaluation by model aromatic compounds

In order to clarify the contribution of oxygen-containing functional groups to the cure reaction of the epoxy resin system, the model aromatic compound instead of carbon black was mixed with the epoxy resin system. The relationship between the molar fraction of oxygen-containing functional group of model compound and  $T_{EAM}$  is shown in Fig. 6. Anthracene with no functional groups did not change  $T_{EAM}$ . As can be seen from Fig. 6, anthraquinone with carbonyl groups and anthracenemethanol with an alcoholic hydroxyl group hardly alter  $T_{EAM}$ . It is clear that carbonyl and alcoholic hydroxyl groups scarcely affect the cure reaction of the epoxy resin system. On the other hand, phenanthrol with a phenolic hydroxyl group and anthracenecarboxylic acid with a carboxyl group lower the  $T_{EAM}$ . Particularly, carboxyl groups depress the  $T_{EAM}$  markedly and the values of  $T_{EAM}$  decrease in proportion to the molar fraction of carboxyl group. It is noted that the initial cure reaction of the epoxy resin system depends on the type of functional groups added, and acidic groups, in particular the carboxyl group, play an important role in stimulating the cure reaction. The authors have demonstrated that both phenolic hydroxyl and carboxyl groups react with epoxy groups[6]. Two cure processes would actually take place in the model compound/epoxy resin system. One is associated with the chemical reaction of Ep828 with phenolic hydroxyl and/or carboxyl groups, and the other is involved in the cross-linking in the resin system itself, that is, the reaction of epoxy groups with amino groups. However, since the molar fraction of the phenolic hydroxyl or carboxyl group in the epoxy resin system itself is negligibly small, contribution of the former process to DSC exotherms may be almost neglected, compared with the case of the latter process. Therefore, the acidic groups would act mainly

as a catalysis, accelerating the cure reaction of the epoxy resin system.

On the basis of the result described above, we have focused on the relation between  $T_{EAM}$  and ester groups on the carbon black surface, which has been reported in the previous paper[5]. Figure 7 shows  $T_{EAM}$  as a function of the ratio of ester groups on the carbon black surface.  $T_{EAM}$  decreases corresponding to the increase of ester groups. It is suggested in comparison between both good correlations in Figs 6 and 7 that COOH groups are present on the carbon black surface and strongly affect the shift of  $T_{EAM}$ . The molar fraction of COOH group in the carbon black (ester groups = 16%)/the epoxy resin system is also found to be smaller than  $4.5 \times 10^{-3}$ . Therefore, the amount of COOH group present in the carbon black/epoxy resin system is negligibly small. Nevertheless, the oxidized carbon black surface affects amine-cured epoxies, which must be due to acceleration of the primary reaction by catalytic action of the carboxyl groups on the surface.

Moreover, from a comparison of Figs 6 and 7, one can obtain the following empirical formula:

$$[\text{molar fraction of COOH}] = 0.2 \times 10^{-3} \times [\text{the ratio of ester groups}]$$

The amount of COOH groups on the carbon black surface can be estimated by use of this formula.

Figure 8 shows the relation between full-width at half-maximum of DSC exothermic curve (FWHM, see Fig. 3) and  $T_{EAM}$ . For the treated carbon black/epoxy resin system, FWHM increases with decreasing  $T_{EAM}$ , or with increasing O/C atomic ratio from the result of Fig. 5. This means that the initial cure reaction of the epoxy resin system is significantly facilitated by the oxygen-containing functional groups on the carbon black surface. This is consistent with the results of air- or  $\text{HNO}_3$ -oxidized carbon

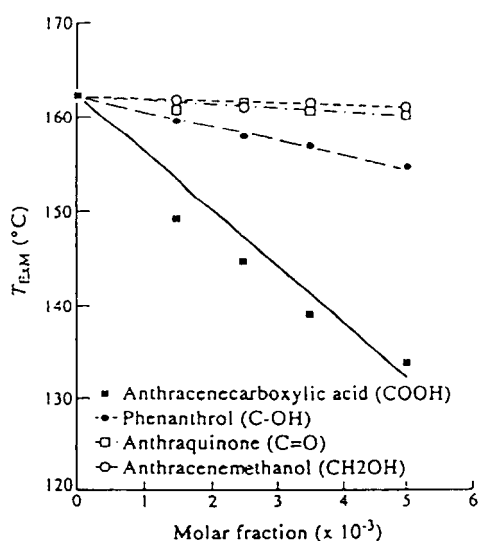


Fig. 6. Effect of oxygen-containing functional groups on  $T_{EAM}$ .

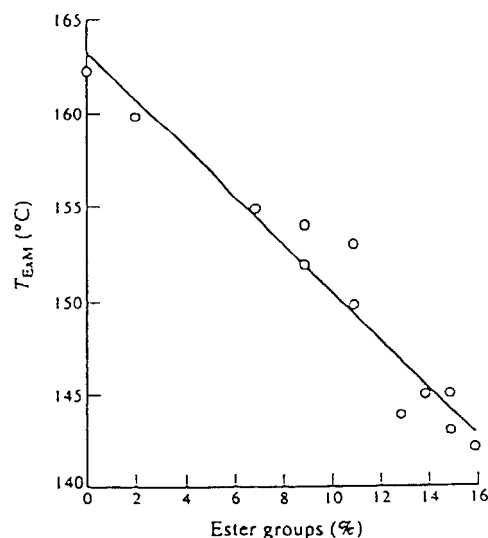
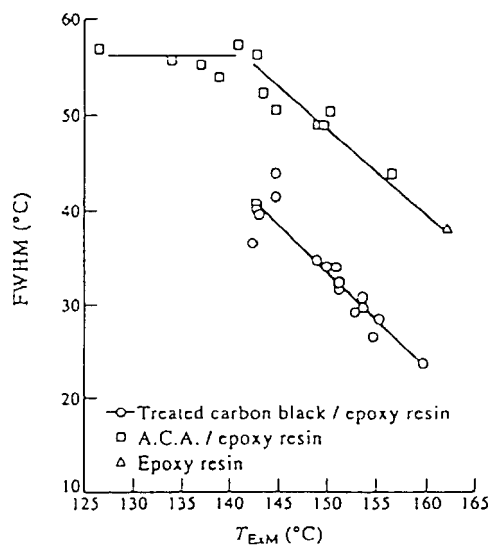
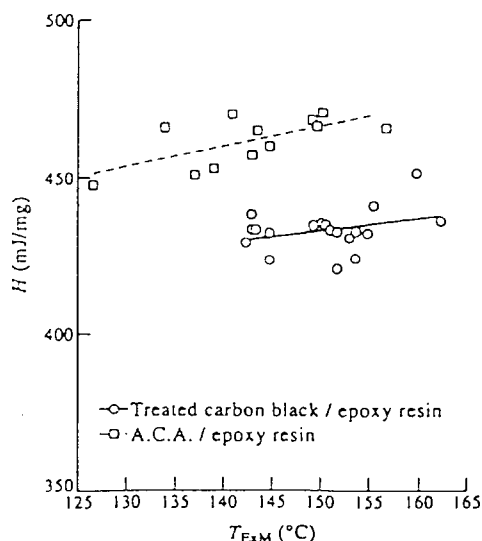


Fig. 7. The relationship between the ratio of ester groups present on the carbon black surface and  $T_{EAM}$ .



Fig. 8. FWHM as a function of  $T_{EAM}$ .Fig. 9. Enthalpy change ( $\Delta H$ ) vs  $T_{EAM}$ .

black reported by Garton *et al.*[4]. On the other hand, a plot of  $T_{EAM}$  vs FWHM gives a straight line above 140°C of  $T_{EAM}$  for the anthracenecarboxylic acid (ACA)/epoxy resin. In the case of the treated carbon/epoxy resin system, the plot also gives the slope and the linear correlation of the same kind (see Fig. 8). This supports the idea that carboxyl groups contribute to the progress of the initial cure reaction of the epoxy resin system. However, the value of FWHM against the same  $T_{EAM}$  is much larger in the ACA/epoxy resin, compared with the treated carbon

black/epoxy resin. The secondary structure of the carbon black could act to hinder the initial cure acceleration for the epoxy-amine system, unlike the case of fragment-like ACA. In the temperature below 140°C of  $T_{EAM}$ , FWHM for the ACA/epoxy resin is almost constant, irrespective of  $T_{EAM}$ . The reason for the behavior is not understood at the moment.

Enthalpy changes,  $\Delta H$ , obtained from DSC exotherm scans as a function of  $T_{EAM}$  are shown in Fig. 9. The  $\Delta H$  tends to increase slightly with  $T_{EAM}$  for both treated carbon black/epoxy resin and ACA/epoxy resin. The faint increase demonstrates that the degree of cross-linking due to the cure reaction of the epoxy resin system is little affected by the carboxyl groups on the carbon black surface. The values of  $\Delta H$  for the treated carbon black/epoxy resin and the ACA/epoxy resin are around 435 and 460 mJ mg<sup>-1</sup>, respectively. The lower value for the treated carbon black/epoxy resin could also be related to the secondary structure of the carbon black as described above. It is found that the addition of oxidized carbon black is effective only for a lowering of curing temperature almost without altering the degree of cross-linking for the epoxy-amine system.

#### 4. CONCLUSIONS

The effect of surface functionality of carbon black on the cure reaction of the epoxy-amine system has been investigated. The addition of acidic groups attached to aromatic model compounds affects the acceleration of the initial cure reaction of the resin system. The amount of ester groups on the carbon black surface significantly influences the degree of the promotion of the initial cure reaction. Moreover, the amount of enthalpy change due to the cure reaction is little influenced by the surface chemical structure of oxygen plasma treated carbon black.

#### REFERENCES

1. K. Shimizu, M. Nakahara and K. Noguchi, *J. Mater. Sci.* 27, 6134 (1992).
2. T. Norita, J. Matsui and H. S. Matsuda, In *Composite Interfaces* (Edited by H. Ishida and J. L. Koenig). Elsevier, New York, pp. 123-132 (1986).
3. J. Matsui, *Critical Reviews in Surface Chemistry*, Vol. 1, CRC Press, Boca Raton, Florida, pp. 71-130 (1990).
4. A. Garton, W. T. K. Stevenson and S. Wang, *British Polym. J.* 19, 459 (1987).
5. T. Takada, M. Nakahara, K. Kumagai and Y. Sanada, *Carbon* (in press).
6. M. Nakahara, Y. Nakayama, G. Katagiri and K. Shimizu, *J. Mater. Sci.* 26, 861 (1991).



## ESR を用いたエアブロンピッチの特性評価

崔 在薫, 熊谷治夫, 真田雄三

(平成6年10月31日受理)

### Characterization of Air Blown Pitches with ESR

Jae Hoon Choi, Haruo Kumagai and Yuzo Sanada

Center for Advanced Research of Energy Technology,  
Hokkaido University, N-13, W-8, Sapporo 060, Japan

Reactions of coal tar and petroleum pitches with air blowing process for carbon fiber precursors were investigated. Air and nitrogen blown pitches were divided into several fractions with solvent extraction. The fractions were characterized with electron spin resonance (ESR). Structural features of the pitches were well represented by the ESR parameters, such as spin concentration ( $N_s$ ), shapes of spectra, and peak-to-peak linewidth ( $\Delta H_{pp}$ ) which had good relationships with molecular weight, the size of condensed aromatic ring, and hydrogen contents. It is supposed that coal tar pitch was much sensitive to air blowing process rather than that of petroleum pitch. Development of polycondensed structure at the stage of mesophase transformation was restricted in the air blowing process.

**KEYWORDS** : Air-blowing reaction, Coal tar pitch, Petroleum pitch, ESR (electron spin resonance)

#### 1. 序 論

汎用炭素繊維 (GPCF) 用のプリカーサーピッチの調製にはエアブローイング反応が応用されている。これは通常の蒸留法に比べ軟化点が高いピッチが高収率で製造できるからである。さらに得られたエアブロンピッチは光学的に等方性組織のみから成っている<sup>1),2)</sup>。炭化水素化合物の混合物であるピッチ類を熱処理すると脱水素, 脱アルキル化, 重合, 芳香族化等の極めて複雑な化学反応が同時に起きている。エアブローイング反応は上記の反応に加え, 酸素の導入によりピッチの脱水素化反応が促進され高分子化が加速される特徴がある<sup>3)</sup>。著者らはエアブローイング反応におけるピッチ中のトルエン不溶分 (TI) の生成速度が同一条件下での窒素ブローイング反応に比べ極めて速いことを報告した<sup>4)</sup>。

エアブローイングにおけるピッチの高分子化反応機構および化学構造の変化に関する研究も行われてきた。LewisらはESRを用い種々の多環芳香族化合物の酸化機構を検討した結果, 反応中間体としてのAryloxyラジカルが存在すること, この中間体が高分子化反応の進行に主な役割をすることを報告している<sup>5)</sup>。また, Zengらは<sup>13</sup>C-NMRを用いた研究の結果より, 原料ピッチの化学構造によってエアブロンピッチ中のラジカルの重合反応機構が相違することを明らかにしている<sup>6)</sup>。一般に, エアブローイングによるピッチの化学構造変化の特徴として<sup>1</sup>H-NMRから $\alpha$ 位水素量の減少が著しいこと<sup>1),7)</sup>, IRからはカルボニル基のピーク ( $C=O$ ) が新しく現れることなどが知られている<sup>6),7)</sup>。しかし, 元素分析によるエアブロンピッチ中の酸素量の増加値はごくわずかであることから, 反応中に導入される酸素はピッチ構成分子の高分子化を促進させるがピッチ分子と結合しないといわれている<sup>3)</sup>。

一方, ESRスペクトルは高分子量で溶剤不溶の成分を含む

北海道大学エネルギー先端工学研究センター: 〒060 札幌市北区北13条西8丁目

ピッチに関して有用な情報を与える。室温および高温 ESR から求められるスピンの濃度、スペクトルのピーク間幅 ( $\Delta H_{pp}$ ) および飽和現象などのパラメータを用い、直接にピッチ類をキャラクタリゼーションしようとする試みが多く行われている<sup>8)-15)</sup>。しかし、エアブロンピッチに関する研究は極めて少ない<sup>2)</sup>。本研究ではピッチ中の TI を用いて熱処理に伴うピッチの高分子化程度の尺度として設定し、ピッチ中の TI 含量が同程度になるように原料ピッチを空気または窒素ブローイングした。得られたピッチを溶剤分別した後、各々の溶剤分別物について ESR を測定し、エアブローイングにおけるピッチ類の化学構造変化の特徴を検討した。

## 2. 実 験

### 2.1 原料ピッチ

用いた原料ピッチは一次 QI (キノリン不溶分) を取り除いたコールタールピッチ (KCTP) および石油ピッチ (PP) である。両ピッチの分析値を Table 1 に示した。

### 2.2 ブロンピッチの調製

5g の原料ピッチをパイレックス製ガラスチューブに入れ、昇温速度 80K/min、反応温度 633K の条件で空気または窒素流量 500ml/min で吹き込み、エアーおよび窒素ブロンピッチをそれぞれ調製した。ブロンピッチ中の TI 含量が約 65wt % 位になるように保持時間を調節した。反応器の概略

および詳細実験手法は既報<sup>16)</sup> に準じた。

### 2.3 溶剤分別および平均分子量の測定

原料および生成ピッチは *n*-ヘキサン、トルエン、ピリジンを用いて溶媒分別し、ヘキサン不溶分-トルエン可溶分 (HI-TS)、トルエン不溶分-ピリジン可溶分 (TI-PS)、ピリジン不溶分 (PI) の各フラクションを求めた。溶剤分別法の詳細は既報<sup>16)</sup> に準じ、各溶剤分別物中の HI-TS と TI-PS 成分はピリジンを溶媒とし VPO 法により平均分子量を求めた。

### 2.4 分析

各溶剤分別物の化学構造の特徴は FT-IR (Nicolet 社製, 5DX-S) を用い拡散反射法で評価した。ESR (Varian 社製, E-109B) の測定は、試料を 1.3 ~ 0.13mPa に減圧し室温で行った。測定条件は共鳴周波数 9.3GHz、マイクロ波パワー 0.2mW、掃引時間 2min であり、スピン濃度 (Ns/g)、スペクトルのピーク間幅 ( $\Delta H_{pp}$ ) を求めた。スピン濃度を求めるにあたっては標準物質である DPPH (1,1-diphenyl-2-picrylhydrazyl) を用いた。Ns/g 値と平均分子量より 1 モル当たりのスピン量、モルスピン濃度 (Ns/mol) を求めた。

## 3. 結 果

### 3.1 エアーおよび窒素ブロンピッチの調製特性

各反応後に得られたピッチの重量変化、すなわちピッチ

Table 1 Properties of raw pitches.

| Items<br>Sample       | C/H<br>ratio | Ns <sup>a</sup><br>(10 <sup>18</sup> spins/g) | Solubilities (wt%) |                    |                    |                 |
|-----------------------|--------------|-----------------------------------------------|--------------------|--------------------|--------------------|-----------------|
|                       |              |                                               | HS <sup>b</sup>    | HI-TS <sup>c</sup> | TI-PS <sup>d</sup> | PI <sup>e</sup> |
| KCTP (K) <sup>f</sup> | 1.78         | 3.10                                          | 28.1               | 52.4               | 17.5               |                 |
| PP (P) <sup>g</sup>   | 1.44         | 2.10                                          | 29.6               | 52.5               | 14.9               | 3.0             |

a) spin concentration of whole pitch, b) *n*-hexane soluble,  
c) *n*-hexane insoluble-toluene soluble, d) toluene insoluble-pyridine soluble,  
e) pyridine insoluble, f) coal tar pitch, g) petroleum pitch

Table 2 Preparation conditions and TI contents of the air and nitrogen blown pitches.

| Sample <sup>a</sup> | Gas            | HTT <sup>b</sup><br>(K) | Soaking<br>Time (min) | Yield<br>(wt%) | Texture <sup>c</sup> | TI <sup>d</sup><br>(wt%) | PI <sup>e</sup><br>(wt%) | YTI <sup>f</sup><br>(wt%) |
|---------------------|----------------|-------------------------|-----------------------|----------------|----------------------|--------------------------|--------------------------|---------------------------|
| KA                  | Air            | 633                     | 30                    | 79.4           | I                    | 67.5                     | 49.6                     | 53.6                      |
| KN                  | N <sub>2</sub> | 633                     | 540                   | 45.2           | A                    | 66.5                     | 41.2                     | 30.1                      |
| PA                  | Air            | 633                     | 60                    | 72.8           | I                    | 65.2                     | 46.2                     | 47.5                      |
| PN                  | N <sub>2</sub> | 633                     | 1800                  | 50.6           | A                    | 60.2                     | 36.6                     | 30.5                      |

a) KA : air blown KCTP, KN : nitrogen blown KCTP, PA : air blown PP, PN : nitrogen blown PP, b) heat treatment temperature, c) optical texture : 'I' denotes isotropic and 'A' indicates anisotropic mesophase spheres are contained. d) toluene insoluble on the basis of the blown pitch, e) pyridine insoluble on the basis of the blown pitch, f) yield of toluene insoluble on the basis of raw pitch

Table 3 Molecular weight distribution<sup>a</sup> of the fractionated pitches for raw and the blown pitches.

| Sample <sup>b</sup><br>Fraction | KR   | KA365 | KN365 | PR   | PA365 |     |
|---------------------------------|------|-------|-------|------|-------|-----|
| HI-TS (A) <sup>c</sup>          | 510  | 470   | 620   | 810  | 760   | 890 |
| TI-PS (B) <sup>d</sup>          | 1940 | 1080  | 1380  | 4220 | 1960  |     |
| B/A ratio                       | 3.8  | 2.3   | 2.3   | 5.2  | 2.5   | 2.4 |

a) measured by VPO with pyridine solution, b) KR : raw KCTP, KA : air blown KCTP, KN : nitrogen blown KCTP, PR : raw PP, PA : air blown PP, PN : nitrogen blown PP, c) n-hexane insoluble-toluene soluble, d) toluene insoluble-pyridine soluble

の収率とTI, PI含量をTable 2に示した。全体的にピッチ中のTI含量は約65~67wt%に揃えてある。PIに関してはエアブロンピッチが窒素ブロンピッチよりも大きな値を有している。しかし、TI生成速度を表す保持時間には大きな差があり、熱反応の効果のみの窒素ブロイングに比べエアブロイングの方がさらに短時間でTI含量が高くなることがわかる。また、原料ピッチからTIの調製収率(Y<sub>TI</sub>)もエアブロイングの方が窒素より20wt%位高い値を示している。エアブロイング反応ではピッチ中の低分子成分の高分子化が促進され高い調製収率を示していると考えられる。

同一のTI含有量のピッチを調製するにあたってコールタールピッチが石油ピッチより保持時間が短かくてすむことは前者は後者に比べて高分子化反応が容易に進行する構造を有しているからといえよう。Table 1に示したように両ピッチ間の溶剤分別物の割合分布の差はほとんどないが、コールタールピッチは石油ピッチよりスピンの濃度が高い。スピン濃度は芳香族環構造の発達の程度と関連していると考えられるので、ピッチの反応性の一指標として表示することができる。Table 2に示すようにエアブロンピッチはすべて光学的等方性で、窒素ブロンピッチは3~5 $\mu$ mの大きさの異方性の球体が生成されているのが偏光顕微鏡観察で確認された。

### 3.2 溶剤分別したフラクションの平均分子量の変化

Table 3に各反応から得られたピッチの溶剤分別物の平均分子量の変化を示した。HI-TSとTI-PSの両フラクションの平均分子量については、コールタールピッチの分子量は石油ピッチより小さく、また同ピッチ種ではエアブロンピッチの分子量の方が窒素ブロンピッチのそれより常に小さい。特に、TI-PSフラクションは、エアまたは窒素ブロンピッチともに、原料ピッチに比べ分子量が約半減している。原料ピッチ中のTI-PSはミセル構造を形成し見掛けの分子量が大きく求められる<sup>17)</sup>。このミセル構造が熱処理中に破壊されることによって分子量が減少した可能性がある<sup>14)</sup>。同時に、各熱処理反応に伴いピッチ中の低分子成分が重合して高分子成分に転換する動的変化、つまりHI-TS成分の重合生成物がTI-PSに、またTI-PSはPI成分になる逐次的な

反応も起こっていることを考慮する必要がある。表中のB/A比から各ピッチのTI-PS成分は、HI-TS分子がほぼ2~3量体重合して新しく形成されることと推測される。

### 3.3 FT-IRによる構造分析

Fig.1は各ピッチの溶剤分別物の中で代表的にHI-TS成分の赤外線吸収スペクトルを示す。コールタールピッチは芳香族CHの伸縮振動によるピーク(3050 $\text{cm}^{-1}$ )の強度に比べ脂肪族CHの伸縮振動によるピーク(2920 $\text{cm}^{-1}$ )の強度が極めて低い(a)。また、芳香族CHの面外変角振動を表すピークの中で4個の隣接した水素によるピーク(752 $\text{cm}^{-1}$ )の強度が孤立した水素によるもの(876 $\text{cm}^{-1}$ )よりかなり大きい。石油ピッチの場合は脂肪族CHの伸縮振動ピークの強度がかなり大きく、芳香族CHの面外変角振動ピークの中で孤立した水素によるピークも相対的に大きくなっていることから芳香族環に脂肪族側鎖がより多く付いていることが推測できる(d)。

エアブロイングによって両ピッチともにカルボニル基(C=O)の伸縮振動ピーク(1700 $\text{cm}^{-1}$ )が新しく表れている(b, e)。また、コールタールピッチ(b)は窒素ブロンピッチ(c)より脂肪族CHのピーク強度減少が顕著である。エアブロンした石油ピッチ(e)も窒素ブロイングしたもの(f)より脂肪族CHのピーク強度がやや小さくなっているものの相当のアルキル側鎖が残存している。これはエアブロイングによる両ピッチの脱アルキル化反応に違いがあるのではないかと考えられる。コールタールピッチ、石油ピッチの芳香族CHの面外変角振動のピーク強度差は特徴的であるが脱アルキル化に伴う芳香族環構造の変化が(a~c), (d~f)でそれぞれ大きい変化が認められないことから重合反応機構を議論することは困難である。

### 3.4 ESRパラメータの変化

#### 3.4.1 スピン濃度

Fig.2は各フラクションの平均分子量に対してESRスペクトルから求めたスピン濃度の変化を示したものである。Fig.2(a)に示したように各フラクションの1グラム当たりのスピン濃度Ns/g値は平均分子量の増加に伴い増加している。各ピッチのHI-TSフラクションがNs $\approx 10^{18}$ のオーダー

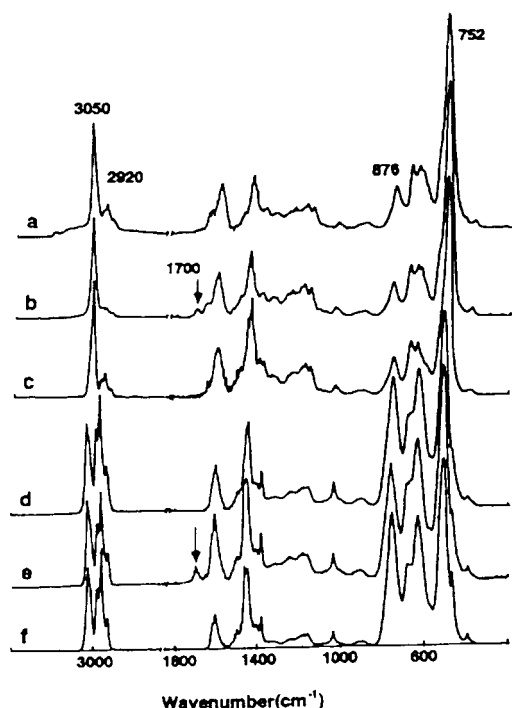


Fig.1 FT-IR spectra for the HI-TS fractions of the raw, air and nitrogen blown pitches prepared from coal tar and petroleum pitches;  
a : KR, b : KA, c : KN, d : PR, e : PA, f : PN

であるがTI-PSフラクションでは $N_s \approx 10^{19}$ とスピン濃度の1桁の上昇が見られる。

本実験では平均分子量の測定が可能なHI-TSおよびTI-PSフラクションに対しては、各フラクションのモル質量当たりのスピン濃度、モルスピン濃度 ( $N_s/\text{mol}$ ) を算出した。その結果をFig.2 (b) に示す。ここでは高分子量成分は低分子量の方よりモルスピン濃度が一層高くなっており\*、全体的な変化傾向にはFig.2 (a) と同じようにモルスピン濃度も平均分子量と高い相関性を持っている。分子量の増加に対するスピン濃度の変化を $N_s/g$  または  $N_s/\text{mol}$  で表した場合、コールタールピッチは同分子量の石油ピッチよりスピン濃度が大きい。一般にピッチ中のスピン濃度はピッチの分子量と分子構造に依存し、分子量が大きく多環芳香族構造が発達するほどスピンは共鳴安定し易くなるからその存在確率も高くなる<sup>9), 13)</sup>。つまり、Fig.1のIRスペクトル結果から述べたようにコールタールピッチは石油ピッチより芳香族性が高い化学構造をもっているのでスピン濃度も高い状態で比較的安定に存在することができるのであろう。

[注] \* : 一般に石炭、有機溶剤に対して不溶成分の占める割合が高いピッチでは分子量の測定は不可能なので、試料中のスピン濃度 ( $N_s$ ) を1g当たりのスピン濃度 ( $N_s/g$ ) で表さざるを得ない。この場合、高分子量成分について、 $N_s/g$  による表示では低分子量成分に比べ見掛けの値は小さくなることもあり得る。

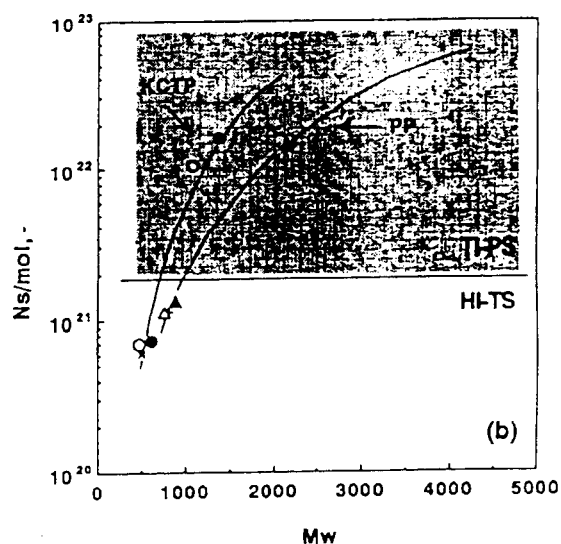
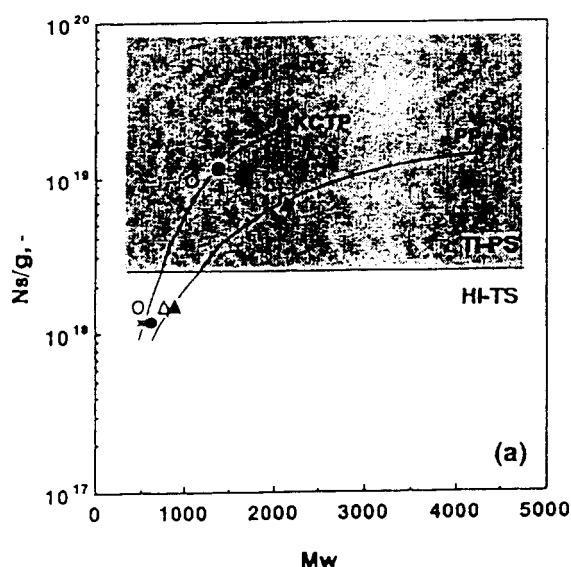


Fig.2 Relationships between average molecular weight ( $M_w$ ) and spin concentration ( $N_s/g$  : a), and mol spin concentration ( $N_s/\text{mol}$  : b) for the fractionated pitches;  
KR :  $\times$ , KA :  $\circ$ , KN :  $\bullet$ , PR :  $+$ , PA :  $\triangle$ , PN :  $\blacktriangle$

Fig.3はブロンピッチのNs/gとC/H比との関係を示したものである。一般にC/H比の高いKCTPでも、C/H比の低いPPについてもPIフラクションのNsは $2 \times 10^{19}$ 以上、HI-TSは $3 \times 10^{18}$ 以下であり、TI-PSはその中間にプロットされている。Nsは溶剤分別特性と深く関わりあっていると云えよう。

### 3.4.2 スペクトルのピーク間幅 ( $\Delta H_{pp}$ )

ESRの測定は十分な減圧状態で、スピン濃度が最も低いHI-TSフラクションについてもスペクトルが飽和の危険性のないマイクロ波の出力条件で行ったので、吸着酸素または飽和によるスペクトルの広幅化の影響はないと思われる。 $\Delta H_{pp}$ は測定対象のスピンとその周辺の環境との相互作用を表す因子であり、 $\Delta H_{pp}$ 値の変化からスピンの周りの化学種と構造に関する情報が得られる。一般に $\Delta H_{pp}$ の値より、スピンの緩和機構の影響が論ぜられる<sup>18), 19)</sup>。ピッチ類の場合は、(1) スピンと周りの芳香族水素および脂肪族水素との相互作用、(2) スピン同士の相互作用、(3) スピンまたはスピンを持つ分子の運動性などが $\Delta H_{pp}$ 変化に寄与する主な因子として挙げられる<sup>20, 21)</sup>。

Fig.4 (a) には $\Delta H_{pp}$ を分子量に対してプロットした。HI-TSの分子量は1000以下、TI-PSのそれは1000以上とみられるが $\Delta H_{pp}$ とMwとの間には後述のようにC/H比のような明確な相関はみられなかった。Fig.4 (b) は各フラクションのC/H原子比に対するESRスペクトルのピーク間

幅 ( $\Delta H_{pp}$ ) の変化を表したものである。分子量が小さいHI-TSフラクションが最も大きい $\Delta H_{pp}$ を与えている。溶剤分別した各フラクションの $\Delta H_{pp}$ 値とC/H比との関係は、コールタールピッチと石油ピッチ、各々の原料ピッチ毎に

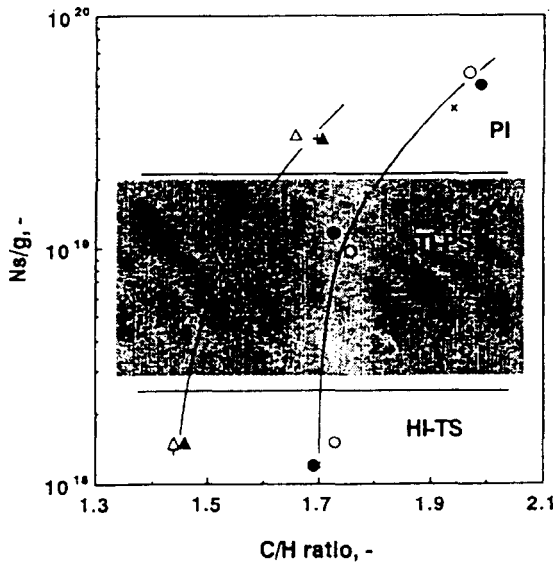


Fig.3 Relationships between C/H atomic ratio and spin concentration (Ns/g) for the fractionated pitches; KR : ×, KA : ○, KN : ●, PR : +, PA : △, PN : ▲

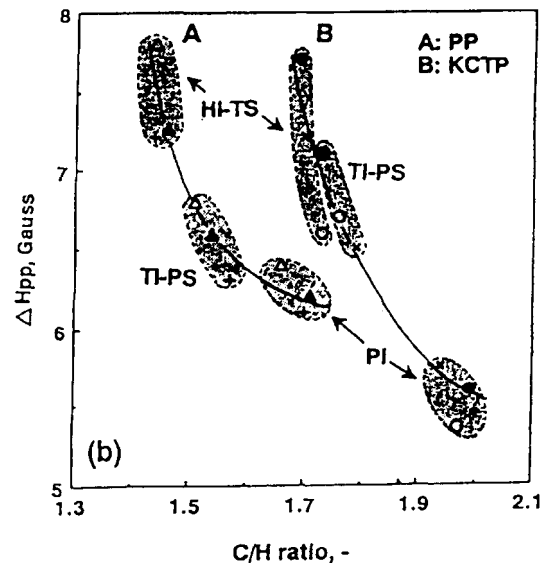
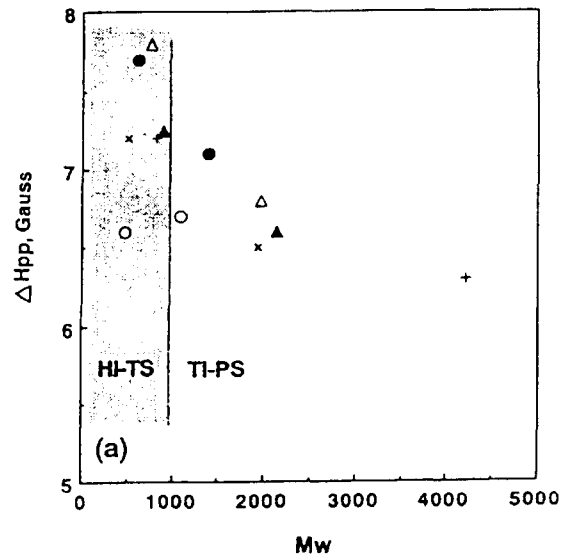


Fig.4 Relationships between peak-to-peak linewidth ( $\Delta H_{pp}$ ) and average molecular weight (Mw : a), and C/H atomic ratio (b) for the solvent-fractionated coal tar (KCTP) and petroleum (PP) pitches; KR : ×, KA : ○, KN : ●, PR : +, PA : △, PN : ▲

各々一本の特性曲線で整理できる。HI-TS, TI-PS, PIとC/H比が増加し高分子化、重合が進行するにつれて $\Delta H_{pp}$ は単調に小さくなっていくことが図から明らかである。各ピッチのC/H比の増加、すなわち水素の割合の減少に伴う $\Delta H_{pp}$ 値の減少は、スピンと水素との相互作用(hyperfine interaction)が $\Delta H_{pp}$ の変化に強い影響を及ぼしていることを示唆している。コールタールピッチは石油ピッチより高いC/H比を表しているにもかかわらず石油ピッチの $\Delta H_{pp}$ 値の減少曲線の延長上に乗っていない。この理由はピッチの構造が明確でないので深い考察はできない。

また、石油ピッチの各々のフラクションについての $\Delta H_{pp}$ 値はエアープロンピッチが窒素プロンピッチに比べやや増大している。エアープロンコールタールピッチは窒素プロンピッチに比べ $\Delta H_{pp}$ 値が若干小さくなっており、両者は対照的である。このことはエアープロンピッチの化学結合の特徴に差があることを示唆している。スピンの水素との相互作用が少ない状態で存在している可能性、スピン同士の相互作用、高分子化による分子の運動性の低下などの影響を併せて考慮する必要がある。

Fig.5にスピン濃度(Ns/g)の変化に対する $\Delta H_{pp}$ の変化を示した。一般にスピン同士の相互作用はお互いの距離の3乗に逆比例しており、スピン同士の距離が少しでも短くなればスピン間の相互作用はより強くなりスピンスピン緩和時間( $T_2$ )の減少すなわち $\Delta H_{pp}$ は大きくなる<sup>18)</sup>。他

方スピン濃度の増大につれてスピン同士の交換が起こり $\Delta H_{pp}$ を小さくする効果もあろう。Table. 3で示したようにエアールおよび窒素プロンピッチのHI-TSからTI-PSフラクションでの分子量増加率が2~3倍にすぎないのに比べそのスピン濃度(Ns/g)の増加率は1桁の上昇を伴う。モルスピン濃度(Ns/mol)でみると増加率は更に高くなる。つまり、スピン濃度が大きくなればスピン同士の相互作用も強くなり、特に、スピン濃度が大きく水素割合が少ないコールタールピッチ試料ではスピン間の相互作用の影響も無視できないかも知れない。いずれにしてもFig.5に示したように、コールタールピッチと石油ピッチともにスピン濃度が高くなるにつれ $\Delta H_{pp}$ は狭くなっている、スピン同士の交換による効果がより優先すると言えよう。 $\Delta H_{pp}$ 値の増大させる因子も考慮した詳細な議論は今後の課題である。既述したように、コールタールピッチはエアープロンピッチの方が、石油ピッチには窒素プロンピッチの $\Delta H_{pp}$ 値が大きくなっている。このことからエアープロイングに対する両ピッチの高分子化の反応機構に何らかの相違があると推測される。

原料ピッチのプロイングによって脱水素および脱アルキル化、さらに多環芳香族環構造も発達させピッチは次第に高分子化していく特徴がある。この過程はとりもなおさずC/H値の増大を伴う。多環芳香族環構造が発達しその中のスピンの非局在化がより顕著になってくると考えられる。

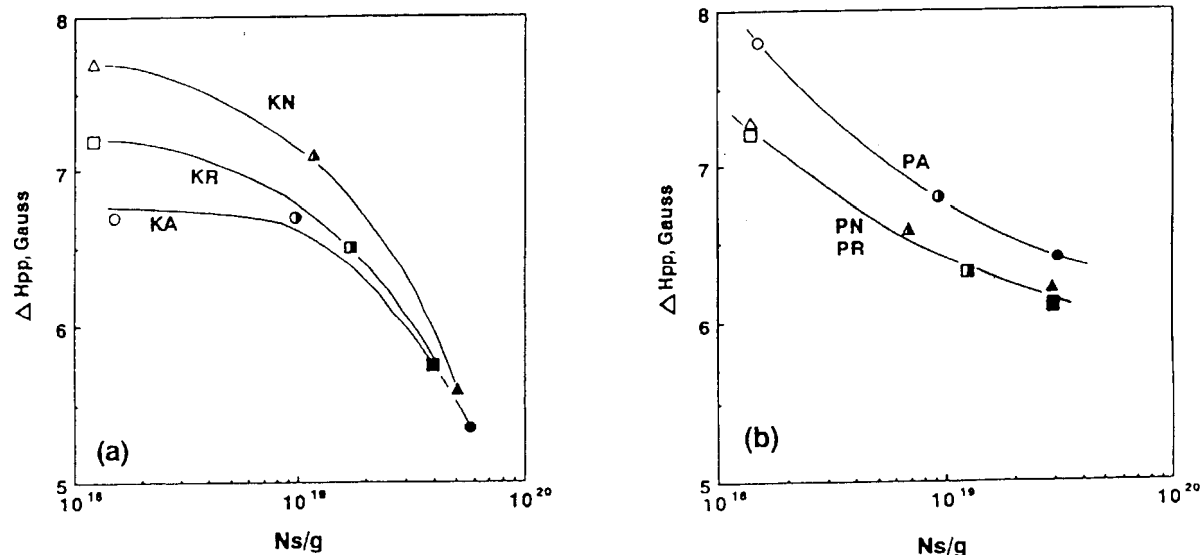


Fig.5 Relationships between spin concentration (Ns/g) and peak-to-peak linewidth ( $\Delta H_{pp}$ ) for the coal tar (a) and petroleum (b) pitches;

KR, PR :  $\square$ , KA, PA :  $\circ$ , KN, PN :  $\triangle$

HI-TS : open, TI-PS : half-closed, PI : closed points

すなわちスピンはより動き回り易くなる可能性が高くなる。この場合はスピンと格子間のエネルギー交換作用による exchange narrowing 効果による  $\Delta H_{pp}$  値の減少も考慮していく必要がある(18), 19)。換言すれば、ピッチの高分子化に伴いスピン濃度が急増するにもかかわらず  $\Delta H_{pp}$  値が小さくなるのは、ピッチ中に水素含有割合の減少によるスピンと水素との相互作用の減少と、ピッチの芳香族環構造の発達によるスピンと格子間の交換作用の増加の影響がスピン同士の相互作用よりもっと大きいためと考えられる。

### 3.4.3 スペクトルの形

一般に、 $\Delta H_{pp}$  はスピンとその周囲との相互作用の強さおよび緩和時間に依存するが、スペクトルの形は相互作用のタイプによって決まる。緩和がスピン-格子相互作用によって規制され、さらに均一系ではローレンツ型のスペクトルを表す。不均一なスピン系ではすべてのスピンが同時に共鳴を起こすのではなく、スピンスピン相互作用がスピン-格子緩和に比べ十分ゆっくりしているなら、スペクトルはガウス型になる(19), 20)。

Fig.6 はローレンツとガウス微分形を同定する規格化作図法(18), 20) により、各フラクションのスペクトル形の変化を示したものである。コールタールピッチと石油ピッチともに、各フラクションのスペクトルの形は理想のガウス型とローレンツ型の間位置しているが、HI-TS より TI-PS が、TI-PS より PI フラクションの方がローレンツ型に近

づいて行く特徴を表している。この現象は、ピッチの多環芳香族環が発達する程、スピンの非局在化およびスピンと格子間の相互作用が大きくなる現象として解釈される。

コールタールピッチの方は石油ピッチよりスペクトルの形の変化が大きく、同じフラクションにおいてはエアブロンの方が窒素ブロンの方よりガウス型に近づいている。エアブロンしたピッチでは比較的不均一なスピン分布または多環芳香族環の発達度が小さいことと推測される。つまり、コールタールピッチの場合、エアブロンピッチ中のスピンの存在できる領域が小さく、スピン同士の相互作用が弱くなり、窒素ブロンピッチより  $\Delta H_{pp}$  が狭くなる。

石油ピッチはより小さい多環芳香族環に多くのアルキル側鎖が付いている構造的特徴から各フラクション間、またはエア-と窒素ブロンピッチ間のスペクトル形の変化がコールタールピッチのように著しくない。両ピッチの PI フラクションはスペクトルの形の差が認められない。さらに、石油ピッチのエアブローイング反応では側鎖のアルキル基が攻撃されやすく(6)、前述した IR スペクトルの結果からもエアブロン石油ピッチにはかなりの脂肪族 CH 基が存在していることを考慮すれば、石油ピッチは芳香族環構造の大きさに著しい変化を伴わずにスピン濃度が増加する特徴を持っていると考えられる。

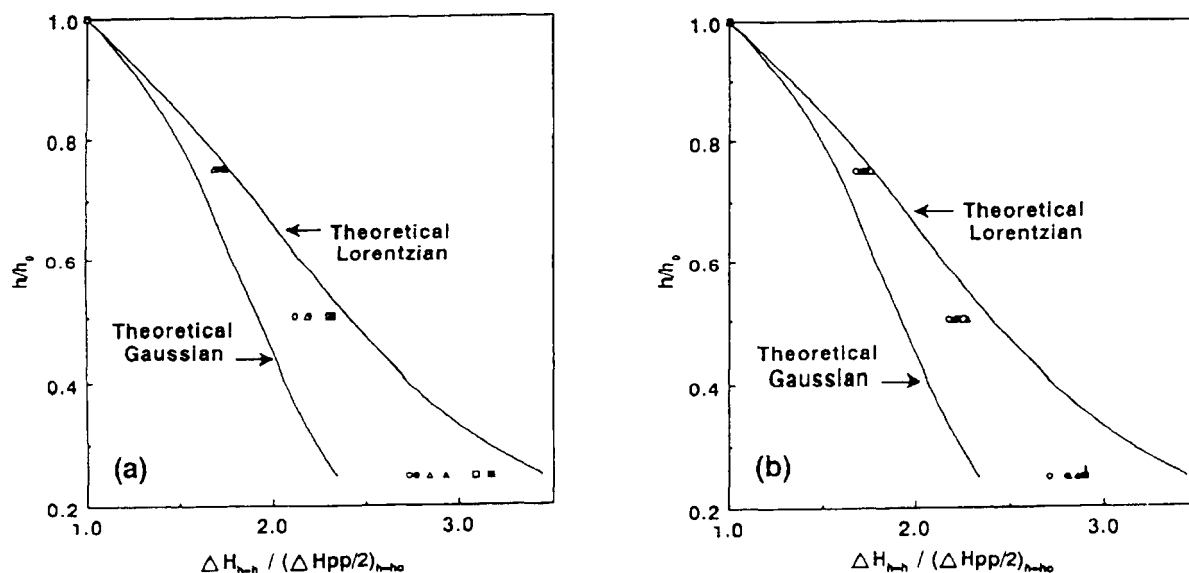


Fig.6 Shape-characterization of the 1st-derivative ESR spectra for the solvent-fractionated coal tar (a) and petroleum (b) pitches; HI-TS (○, ●), TI-PS (△, ▲), PI (□, ■), KA, PA : open points, KN, PN : closed points,  $h_0$  : maximum peak height,  $h$  : height in ordinate of arbitrary point on the spectrum,  $\Delta H$  : width in abscissa of arbitrary point on the spectrum.



## 4. 結 論

コールタールピッチおよび石油ピッチからピッチ類のエアープロンピッチおよび窒素プロンピッチを調製し、それらの溶剤分別物の化学構造の特徴をESRを用い比較評価した結果、次のことが明らかになった。

- 1) コールタールピッチの場合、スピンの安定な存在に必要な多環芳香族構造が原料ピッチから発達しているのでエアーまたは窒素プロンピッチ間のスピン濃度の変化は認められなかった。両ピッチ間の平均分子量の変化、 $\Delta H_{pp}$  値とスペクトルの形の変化挙動からエアープロンコールタールピッチの方が窒素プロンピッチの方より環の小さい状態で高分子化されていた。
- 2) 石油ピッチの場合、コールタールピッチより小さい多環芳香族環に多くのアルキル側鎖が付いている構造的特徴から、プロイング過程で芳香族環の大きさには著しい変化を伴わず高分子化していると予測される。

ESRパラメータとしてスピン濃度、ピーク間幅、スペクトル形の変化を用い、ピッチ類の化学構造を評価するのは有効である。さらに、ESRスペクトルの飽和、高温でスピンの *in-situ* 分析などを加えればもっとピッチ類の特徴に関する多くの情報が得られると思われる。

## 文 献

- 1) T. Maeda, S. M. Zeng, K. Tokumitsu, J. Mondori and I. Mochida, *Carbon* **31** (1993) 407-412.
- 2) 山口千春, 松好弘明, 水取重司, 馬場澄子, 熊谷治夫, 真田雄三, 炭素 **1994** [No.162] 78-83.
- 3) J. B. Barr and I. C. Lewis, *Carbon* **16** (1978) 439-444.
- 4) J. H. Choi, H. Kumagai, T. Chiba and Y. Sanada, *Carbon*, in press.
- 5) I. C. Lewis and L. S. Singer, *J. Phys. Chem.* **85** (1981) 354-359.
- 6) S. M. Zeng, T. Maeda, K. Tokumitsu, J. Mondori and I. Mochida, *Carbon* **31** (1993) 413-419.
- 7) 崔 在薫, 熊谷治夫, 横山 晋, 真田雄三, 第19回炭素材料学会年会, 京都, 1992.12.2-4, 1B01.
- 8) L.S. Singer and I.C.Lewis, *Carbon* **16** (1978) 417-423.
- 9) L. R. Rudnick and D. R. Tuetting, *Fuel Sci. & Tech. Int'l* **7** (1989) 57-68.
- 10) S. B. Tilden, The 17th Biennial Conf. on Carbon, Kentucky, 1985.6.16-21, 422-423.
- 11) K. Azami, T. Yokono, Y. Sanada and S. Uemura, *Carbon* **27** (1989) 177-183.
- 12) T. Yokono, T. Obara, Y. Sanada, S. Shimomura, and T. Imamura, *Carbon* **24** (1986) 29-32.
- 13) 金子友彦, 横野哲朗, 真田雄三, 炭素 **1991** [No. 149] 225-230.
- 14) T. Kaneko, L. E. Henao, T. Yokono, T. Ehara and Y. Sanada, *J. Mat. Sci. Letters* **9** (1990) 351-352.
- 15) O. Ito, T. Kakuta and M. Iino, *Carbon* **27** (1989) 869-875.
- 16) J. H. Choi, H. Kumagai, M. Satou, S. Yokoyama and Y. Sanada, The 21st Biennial Conf. on Carbon, Buffalo, 1993.6.13-18, 282-283.
- 17) 持田 勲, 炭素材の化学と工学, (1990) p.78-79, 朝倉書店.
- 18) 磯部太郎ら訳, アルガー電子スピン共鳴—実験技術とその応用—(現代科学), (1973) p.44-51, 吉岡書店.
- 19) 相馬純吉, 実験化学講座続13 - 電子スピン共鳴吸収 (日本化学会編), (1967) p.100-107, 丸善.
- 20) 木下 実, 実験化学講座続13 - 電子スピン共鳴吸収 (日本化学会編), (1967) p.240-242, 丸善.

# 11

## Formation of Protonic Acid Sites from Hydrogen Molecules and Their Roles in Acid-Catalyzed Reactions

Hideshi Hattori,<sup>1,2</sup> Tetsuya Shishido<sup>2</sup>, Junpei Tsuji<sup>2</sup>, Takahiro Nagase<sup>2</sup>, and Hideaki Kita<sup>2</sup>

<sup>1</sup>Center for Advanced Research of Energy Technology (CARET), Hokkaido University, Sapporo 060, Japan

<sup>2</sup>Graduate School of Environmental Earth Science, Hokkaido University, Sapporo 060, Japan

The formation of protonic acid sites from molecular hydrogen was studied by IR of adsorbed pyridine and TPD of adsorbed hydrogen for solid acid catalysts with or without metallic components such as Pt/SO<sub>4</sub><sup>2-</sup>-ZrO<sub>2</sub>, Co-Mo/SiO<sub>2</sub>-Al<sub>2</sub>O<sub>3</sub>, Pt-ZSM5, a mixture of Pt/SiO<sub>2</sub> and H-ZSM5, H-ZSM5, and SiO<sub>2</sub>-Al<sub>2</sub>O<sub>3</sub>. The hydrogen adsorption facilitated at a high temperature for all catalysts. On heating in the presence of hydrogen, protonic acid sites were generated in compensation of Lewis acid sites. The reversal change proceeded on outgassing gaseous hydrogen. Promoting effects of hydrogen on the catalytic activity were observed for cumene cracking and pentane isomerization over the solid acid catalysts with metallic components. For cumene cracking over the metal-free catalysts such as H-ZSM5 and SiO<sub>2</sub>-Al<sub>2</sub>O<sub>3</sub>, the promoting effects of hydrogen were not appreciable. The importance of the concept of molecular hydrogen-originated protonic acid sites is stressed.

### INTRODUCTION

For zirconium oxide modified with platinum and sulfate ion (Pt/SO<sub>4</sub><sup>2-</sup>-ZrO<sub>2</sub>), the catalytic activity for skeletal isomerization of alkanes are markedly enhanced in the presence of hydrogen[1]. The promotion effects of hydrogen on the acid-catalyzed reactions are rationalized by the generation of protonic acid sites from molecular hydrogen[2,3]. The formation of the protonic acid sites is suggested to occur as follows. Hydrogen molecule is dissociatively adsorbed on the platinum surface to form hydrogen atoms which undergo spillover onto the support. The hydrogen atoms migrate on the support to reach Lewis acid site at which hydrogen atom loses an electron to form a proton. A second hydrogen atom reacts with the electron trapped on the Lewis acid site to form hydride ion.

In the present paper, we wish to report that the formation of protonic acid sites from hydrogen molecules is not a phenomenon restrictly observed for Pt/SO<sub>4</sub><sup>2-</sup>-ZrO<sub>2</sub>, but observable for other catalysts, and that the promoting effects of hydrogen are actually realized in the acid-catalyzed reactions.

### EXPERIMENTAL METHODS

#### Catalysts

Pt/SO<sub>4</sub><sup>2-</sup>-ZrO<sub>2</sub> was prepared by impregnation of SO<sub>4</sub><sup>2-</sup>-ZrO<sub>2</sub> with H<sub>2</sub>PtCl<sub>6</sub> aq. followed by calcination at 873K in air. Detailed procedures are described elsewhere[2,3]. The catalyst was treated with hydrogen at 623K prior to use for reaction and measurement of IR and TPD. H-ZSM5 was prepared by ion-exchange of Na-ZSM5 supplied by TOSOH with NH<sub>4</sub>Cl aq. followed by calcination at 803K in air. Pt-ZSM5 was prepared by ion-exchange of Na-ZSM5 with Pt(NH<sub>3</sub>)<sub>4</sub>Cl<sub>2</sub>. SiO<sub>2</sub>-Al<sub>2</sub>O<sub>3</sub> was supplied by Catalyst Society, Japan as a reference catalyst JRC SAL-2. Co-Mo/SiO<sub>2</sub>-Al<sub>2</sub>O<sub>3</sub> was prepared by successive impregnation of SiO<sub>2</sub>-Al<sub>2</sub>O<sub>3</sub> with Co(NO<sub>3</sub>)<sub>2</sub> aq. and (NH<sub>4</sub>)<sub>6</sub>Mo<sub>7</sub>O<sub>24</sub> aq. followed by calcination at 773K in air.

#### IR of adsorbed pyridine

IR of adsorbed pyridine was measured to see the change in the type of acid sites. Following the pretreatment, the catalyst was exposed to pyridine at 423K followed by outgassing at 673K. Hydrogen was introduced to the IR cell at room temperature, and the catalyst was heated up to 673K by 50K increment. After cooling to room temperature, the catalyst was outgassed while heated up to 673K by 50K increment. IR spectrum was measured at room temperature after each increment of the temperature.

#### TPD of adsorbed hydrogen

TPD of adsorbed hydrogen was measured for the catalyst adsorbing hydrogen or deuterium at different temperatures. TPD for the successive adsorption of D<sub>2</sub> and H<sub>2</sub> was also measured for Pt/SO<sub>4</sub><sup>2-</sup>-ZrO<sub>2</sub>. At first H<sub>2</sub> was adsorbed at 423K for 15min and outgassed at the same temperature. Then, D<sub>2</sub> was adsorbed at 423K for 15min and the catalyst was cooled to room temperature followed by outgassing for 15min. TPD was run at the heating rate 10K/min; the desorbed gas was analyzed by mass spectrometry.

#### Activity measurements

Cumene cracking and pentane isomerization were carried out to see the effects of hydrogen on the catalytic activities. A high pressure flow reactor and a pulse reactor were employed for cumene cracking, and a pulse reactor was employed for pentane isomerization.

## RESULTS AND DISCUSSION

#### TPD of hydrogen

TPD plots for D<sub>2</sub> adsorbed on H-ZSM5 at different temperatures are shown in Fig. 1. Desorbed gases were composed mainly of D<sub>2</sub>, only small quantities of HD and H<sub>2</sub> being detected though they are not shown in Fig. 1. The peak area increased with an increase in the adsorption temperature. It appears that a step requiring a high energy exists in the adsorption of D<sub>2</sub> on H-ZSM5. Essentially the same phenomena were

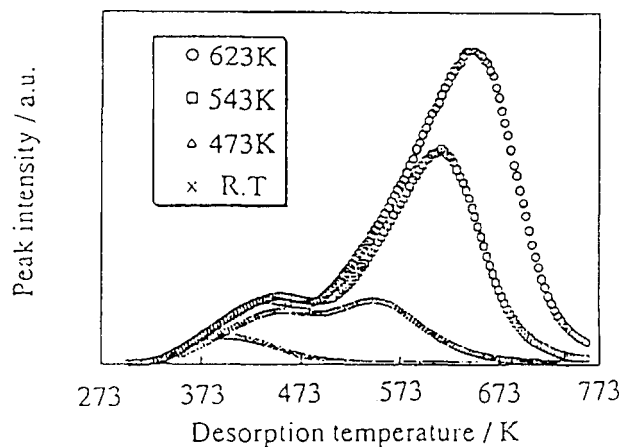


Fig.1 TPD for D<sub>2</sub> adsorbed on H-ZSM5 at different temperatures

observed for other catalysts such as  $\text{Pt}/\text{SO}_4^{2-}\text{-ZrO}_2$ ,  $\text{Co-Mo}/\text{Al}_2\text{O}_3$ , and a mixture of  $\text{Pt}/\text{SiO}_2$  and H-ZSM5 in the sense that the desorption peaks become larger as the adsorption temperatures were raised.

TPD plots for the sequential adsorption of  $\text{H}_2$  and  $\text{D}_2$  on  $\text{Pt}/\text{SO}_4^{2-}\text{-ZrO}_2$  are shown in Fig. 2. The desorption peaks for  $\text{D}_2$ , HD, and  $\text{H}_2$  appeared at different temperatures, 410, 440, and 465 K, in the ratio 1.5; 1; 1.3, respectively. If D and H were completely mixed on the surface, binomial distribution of  $\text{D}_2$ , HD, and  $\text{H}_2$  would have been expected, and  $[\text{HD}]^2/[\text{H}_2]\text{x}[\text{D}_2]$  should have been close to 4.

The observed value was 0.52. The mixing of H and D was incomplete on the surface. The result indicates hydrogen spillover and importance of the migration of hydrogen atoms away from active centers into the surrounding regions of the surface of  $\text{SO}_4^{2-}\text{-ZrO}_2$ . Since  $\text{H}_2$  was not adsorbed on  $\text{SO}_4^{2-}\text{-ZrO}_2$ , it is suggested that dissociative adsorption of hydrogen occurs only at the Pt centers.

#### IR of adsorbed pyridine

Variations of the number of protonic acid and Lewis acid sites with heating in the presence of hydrogen and successive outgassing are shown in Fig. 3 for H-ZSM5. Heating in the presence of hydrogen resulted in the formation of protonic acid sites in compensation of Lewis acid sites. Outgassing the gas phase hydrogen resulted in the restoration of Lewis acid sites and the decrease in protonic acid sites. The same results were observed for all catalysts examined, though easiness of the interconversion between protonic acid sites and Lewis acid sites was dependent on the type of catalyst. These results are the same as those observed for  $\text{Pt}/\text{SO}_4^{2-}\text{-ZrO}_2$ [2,3].

#### Effects of hydrogen on the catalytic activities

For  $\text{Pt}/\text{SO}_4^{2-}\text{-ZrO}_2$ , the promoting effects of hydrogen on the catalytic activities were prominently observable under the hydrogen pressure of 1 atm. The effect of hydrogen on the cumene cracking over  $\text{Pt}/\text{SO}_4^{2-}\text{-ZrO}_2$  is shown in Fig. 4. The formation of benzene was about 30% in the hydrogen carrier, but markedly decreased as the carrier was switched into helium. The activity gradually recovered as the carrier was switched again into hydrogen. The promoting effect of hydrogen was reversible.

Although the generation of protonic acid sites by heating in the presence of hydrogen was observed for H-ZSM5 by IR of adsorbed pyridine, the promotion effect of hydrogen on the cumene cracking was not appreciable even under the hydrogen pressure of 30 atm. The mechanisms for the formation of protonic acid sites on the metal-free catalysts are different from the catalysts with metallic components. For metal-free catalysts, hydrogen molecule should dissociate directly into  $\text{H}^+$

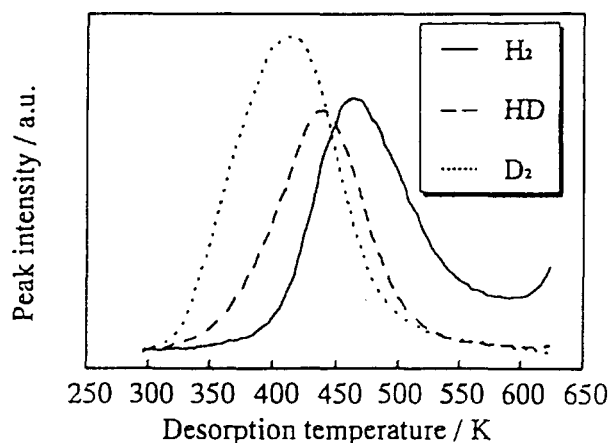


Fig.2 TPD for sequential adsorption of  $\text{H}_2$  and  $\text{D}_2$  on  $\text{Pt}/\text{SO}_4^{2-}\text{-ZrO}_2$

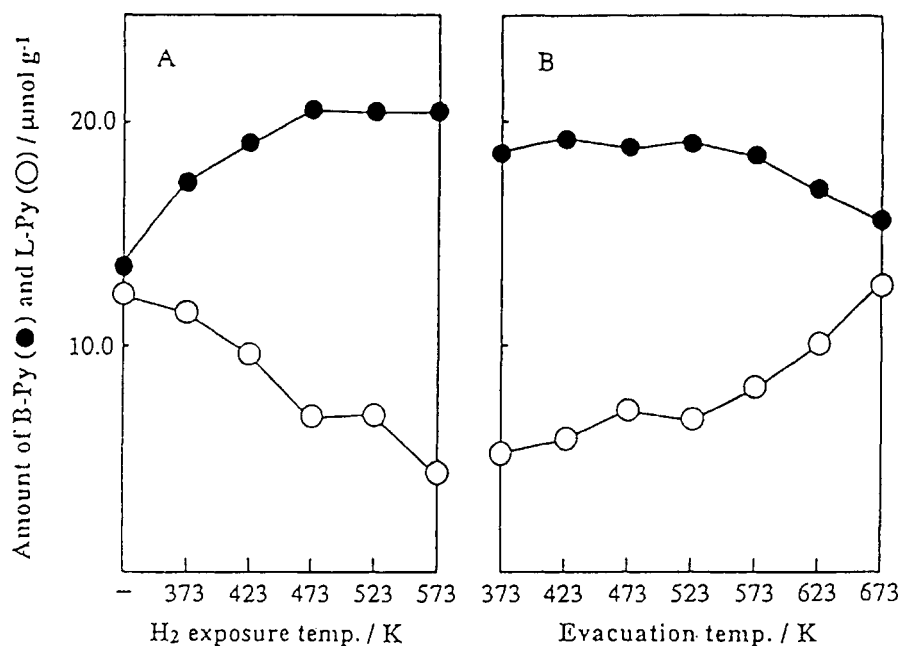


Fig.3 Variation of protonic and Lewis acid sites as functions of the heating temperature in the presence of hydrogen (A) and outgassing temperature (B)

and H<sup>+</sup> on Lewis acid site. The adsorption of molecular hydrogen is retarded in the presence of cumene which is adsorbed more strongly than hydrogen.

For Co-Mo/SiO<sub>2</sub>-Al<sub>2</sub>O<sub>3</sub>, the effect of hydrogen became appreciable under the hydrogen pressure of 30 atm. The formation of benzene in the cumene cracking under hydrogen carrier at 30 atm is compared with that obtained under helium carrier in Fig. 5. The catalytic activity is much higher in the presence of hydrogen than in the absence of hydrogen. Since the active sites for cumene cracking are protonic acid sites, it is strongly suggested that the protonic acid sites formed in the

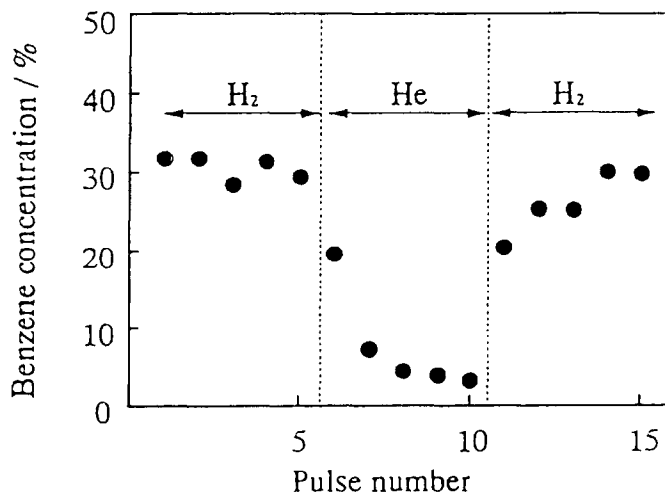


Fig.4 Cumene cracking over Pt/SO<sub>4</sub><sup>2-</sup>-ZrO<sub>2</sub> in the presence and absence of hydrogen (pulse reactor, 1 atm, reaction at 423K)

presence of hydrogen act as catalytically active sites. It is to be noted that the activity did not decrease with time in the presence of hydrogen while the activity decreases considerably in the absence of hydrogen.

The promoting effects of hydrogen were observed for the reactions other than cumene cracking. An example is skeletal isomerization of pentane over Pt-ZSM5. In the presence of hydrogen, the formation of isopentane is prominent, and the formation of smaller molecules is suppressed. In the absence of hydrogen, the formation of isopentane becomes suppressed, but the formation of smaller molecules resulting from cracking is enhanced. It is suggested that the protonic acid sites originating from molecular hydrogen are effective for skeletal isomerization of pentane, and

that the sites causing formation of smaller molecules are eliminated in the presence of hydrogen. Although the sites responsible for the formation of the smaller molecules are not definite, Lewis acid sites may be such sites, because in the presence of hydrogen, Lewis acid sites lose its function on accepting an  $H^+$  ion.

#### Model for active site formation

All the results for the effects of hydrogen observed for different types of catalyst indicate that protonic acid sites are formed from molecular hydrogen and act as catalytically active sites for acid-catalyzed reactions. The schematic model for the formation of protonic acid sites is illustrated in Fig. 6. Hydrogen molecule is dissociatively adsorbed on the centers such as platinum species and Co-Mo species to form atomic hydrogens. The hydrogen atoms spillover onto the support and migrate to Lewis acid sites where the hydrogen atom releases an electron to become a proton which is stabilized on the O atom nearby. The electron trapped on the Lewis acid site may react with a second hydrogen atom to form hydride which is stabilized on the Lewis acid site. As a whole, protonic acid site is formed and the Lewis acid site loses its function.

The concept of molecular hydrogen originated protonic acid sites is important in understanding catalysis by solid acid catalysts. The concept is rather versatile and applicable not only to  $Pt/SO_4^{2-}-ZrO_2$  but also to other solid acid catalysts. The contribution of the protonic acid

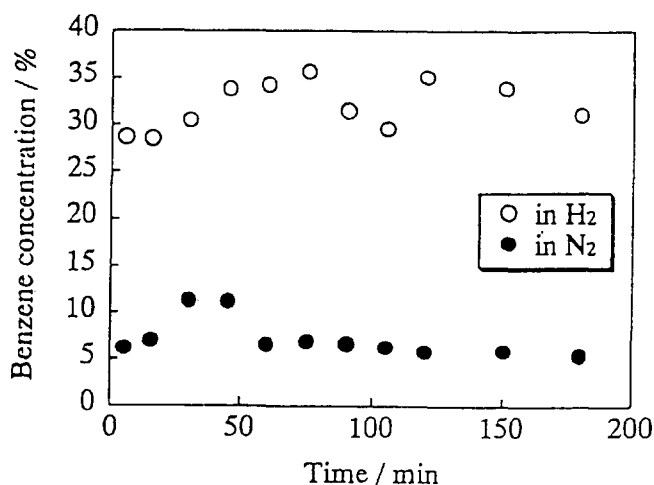


Fig.5 Cumene cracking over Co-Mo/SiO<sub>2</sub>-Al<sub>2</sub>O<sub>3</sub> in the presence and absence of hydrogen (flow reactor, 30 atm, reaction at 523K)

sites should be taken into account in the processes carried out in the presence of hydrogen such as hydrocracking and hydrotreating processes. The concept also suggests the possibility that acidic properties can be controlled by adjusting the hydrogen pressure and temperature.

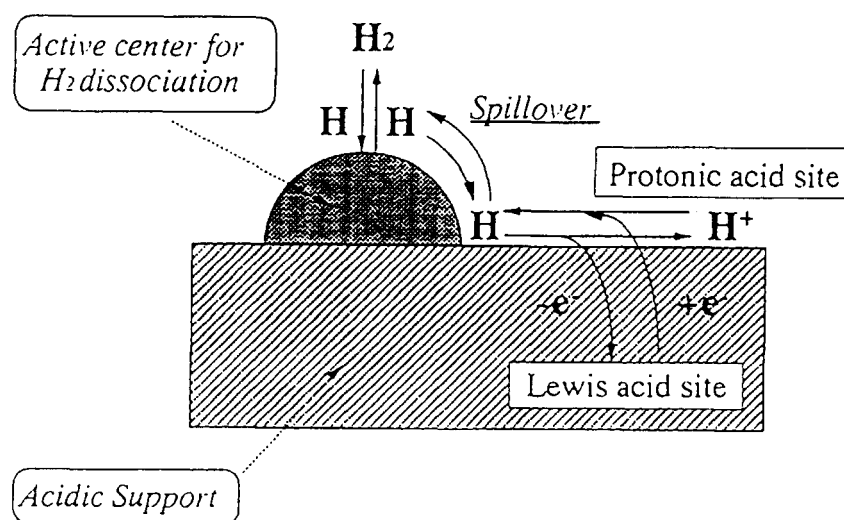


Fig.6 Model for molecular hydrogen-originated protonic acid site

#### REFERENCES

- 1 T. Hosoi, T. Shimadzu, S. Ito, S. Baba, H. Takaoka, T. Imai, and N. Yokoyama, Prepr. Symp. Div. Petr. Chem. Am. Chem. Soc., 1988, p. 562.
- 2 K. Ebitani, J. Konishi, and H. Hattori, J. Catal., 130(1991)257.
- 3 K. Ebitani, J. Tsuji, H. Hattori, and H. Kita, J. Catal. 135 (1992)609.

## Highly Active Absorbent for SO<sub>2</sub> Removal Prepared from Coal Fly Ash

Hiroaki Tsuchiai,<sup>†,‡</sup> Tomohiro Ishizuka,<sup>‡</sup> Tsutomu Ueno,<sup>‡</sup> Hideshi Hattori,<sup>\*,†</sup> and Hideaki Kita<sup>†</sup>

*Division of Materials Science, Graduate School of Environmental Earth Science, Hokkaido University, Sapporo 060, Japan, and Department of Research and Development, Hokkaido Electric Power Co., Inc., 4-9-2-1 Utsukushigaoka, Toyohira-ku, Sapporo 004, Japan*

The absorbent for SO<sub>2</sub> from the flue gas of a coal-fired electric power station was prepared from calcium oxide, calcium sulfate, and coal fly ash and examined for the relation between the desulfurization activity and the structure. The activity is closely related to the progress of the hydration reaction taking place during preparation procedures. The activity increased with the hydration time and reached a maximum activity in 12 h. The hydration resulted in the formations of ettringite and calcium silicate. By elevation of the temperature for drying the hydration products, the activity markedly increased up to 400 °C, which was caused by the removal of water covering the calcium component in the ettringite. For the efficient removal of SO<sub>2</sub>, the existence of NO in the flue gas is required. NO<sub>x</sub> plays a catalytic role for oxidation of SO<sub>2</sub> to SO<sub>3</sub> which reacts with CaO to form CaSO<sub>4</sub> as a final product.

### Introduction

Reduction of emissions of air pollutants is required for industrial operations. In particular, SO<sub>2</sub> and NO<sub>x</sub> are the main targets to be reduced (Livengood, 1991). Among the stationary sources of emissions of air pollutants are coal-fired electric power plants which discharge large amounts of SO<sub>2</sub> and NO<sub>x</sub>. For example, a coal-fired power plant of 600 MW capacity burning coals containing 1.2% sulfur releases 1785 m<sup>3</sup> h<sup>-1</sup> (NTP) SO<sub>2</sub> and 318 m<sup>3</sup> h<sup>-1</sup> (NTP) NO<sub>x</sub>. A typical composition of the flue gas is SO<sub>2</sub> 350 ppm, NO<sub>x</sub> 125 ppm, O<sub>2</sub> 5.2%, CO<sub>2</sub> 13%, H<sub>2</sub>O 7.8%.

For the removal of SO<sub>2</sub> from flue gas, a wet process using calcium carbonate as an absorbent is most commonly adopted in commercial plants (Dalton, 1990). The wet process shows a high efficiency but needs a large amount of water. The desulfurization is believed to be initiated by dissolution of SO<sub>2</sub> into water followed by reaction with calcium carbonate to form calcium sulfite as a precipitate. The calcium sulfite is oxidized by air to form calcium sulfate dihydrate as a final product (Dalton, 1990).

A dry process using calcium hydroxide as an absorbent is used commercially but is not as common as the wet process (Tischer, 1991). In the dry process, a powdery calcium hydroxide is injected into the duct. The efficiency of this duct injection dry process, however, is not high. A large fraction of calcium hydroxide remains unreacted. The low utilization efficiency of calcium in the dry process is considered to be due to the formation of calcium sulfate which covers the outer surface of the calcium hydroxide particles (Brown et al., 1991).

Jozewicz and Rochelle (1986) reported that calcium hydroxide becomes active for semidry desulfurization by the addition of coal fly ash and claimed that calcium silicate formed by the reaction of calcium hydroxide with a silicone compound eluted from coal fly ash in the preparative procedures is an active material to absorb SO<sub>2</sub> (Jozewicz and Rochelle, 1986). The calcium silicate

formed has a large surface area capable of adsorbing a large amount of water. SO<sub>2</sub> dissolves into the water to react with calcium ion. The final products are calcium sulfite and calcium sulfate, calcium sulfite being formed predominantly. This ADVACATE (ADVANCED SILICATE) absorbent has been tested in a 10 MW-scale pilot plant, and 89% of SO<sub>2</sub> removal and 61% of lime utilization were achieved (Lepovitz et al., 1993).

Ueno found that the absorbent prepared from calcium oxide, calcium sulfate, and coal fly ash shows a high calcium utilization efficiency in the dry desulfurization process (Ueno, 1986). He reported that the aging of the slurry containing calcium oxide, calcium sulfate, and coal fly ash at about 100 °C and the successive drying are essential for an active absorbent. The high activity is considered to be due to the formation of microporous structures in the absorbent. This absorbent has actually been used in the dry-type flue gas desulfurization system installed at the Tomato-Atsuma Power Station, Hokkaido Electric Power Co., for the treatment of the flue gas 644 000 m<sup>3</sup> h<sup>-1</sup> (NTP) since 1991.

Other than calcium hydroxide based absorbents, alkali alumina is emerging as one of the candidates for highly efficient SO<sub>2</sub> and NO<sub>x</sub> removal. A proof-of-concept test was conducted, and SO<sub>2</sub> removal of 99% or more and NO<sub>x</sub> removal of 95% or more were simultaneously achieved during 6500 h of operation in a 5 MW-scale pilot plant (Haslbeck et al., 1993). In this process,  $\gamma$ -alumina was used as a regenerative adsorbent in a fluidized bed reactor. SO<sub>2</sub> is captured in the form of Na<sub>2</sub>SO<sub>4</sub>.

The present paper aims to elucidate the nature of the absorbent practically used at the Tomato-Atsuma Power Station. We wish to report the structural changes of the absorbent during aging and drying periods in conjunction with the activity changes with preparative conditions.

### Experimental Section

**Preparation of the Absorbent.** Absorbents were prepared from calcium oxide, calcium sulfate, and coal fly ash. The calcium oxide used was of industrial grade

\* Author to whom correspondence should be addressed.

<sup>†</sup> Hokkaido University.

<sup>‡</sup> Hokkaido Electric Power Co.



(Wako Pure Chemical Industries). The calcium sulfate was reagent grade calcium sulfate hemihydrate (Wako Pure Chemical Industries). In the practical desulfurization system, a spent absorbent was used as the source of calcium sulfate, because the spent absorbent contains calcium sulfate formed by the reaction of  $\text{SO}_2$  removal. Coal fly ash was supplied by Hokkaido Electric Power Company, Tomato-Atsuma Power Station, and had the following composition:  $\text{SiO}_2$  59%,  $\text{Al}_2\text{O}_3$  24%,  $\text{CaO}$  1.4%, and the mean particle size was  $21\text{ }\mu\text{m}$  determined by a laser diffraction method with dry-type dispersion.

For the preparation of 200 g of absorbent, calcium oxide (45.4 g) was added to 1 L of water at a temperature of  $65\text{ }^\circ\text{C}$ . The temperature of the slurry increased to about  $90\text{ }^\circ\text{C}$  upon addition of calcium oxide. To the slurry, hemihydrate calcium sulfate (64.0 g) and coal fly ash (80.0 g) were added with stirring. The resulting slurry was heated at  $95\text{ }^\circ\text{C}$  normally for 15 h with stirring. In some experiments, the hydration period was varied from 3 to 30 h. After hydration, the absorbent slurry was filtered and dried normally at  $200\text{ }^\circ\text{C}$  for 2 h. In some experiments, the absorbent slurry was dried in a vacuum or dried in air in the temperature range  $70\text{--}600\text{ }^\circ\text{C}$ . The resulting absorbent had the following composition: calcium hydroxide 30%, calcium sulfate 30%, coal fly ash 40%, neglecting  $\text{H}_2\text{O}$  and  $\text{CO}_2$ .

The calcium hydroxide used as a reference absorbent was prepared similarly by slurrying the calcium oxide and drying at  $200\text{ }^\circ\text{C}$ . The resulting calcium hydroxide had a surface area of  $18\text{ m}^2/\text{g}$  and a pore volume of  $1.4\text{ cm}^3/\text{g}$ .

**Activity Test.** A flow reactor was employed for the measurement of the activity of the absorbent for desulfurization. The absorbent (50 mL, 23–26 g) was dispersed on cotton (5 g) and placed in the reactor made of quartz, 40 mm in diameter. The absorbent bed packed with the absorbent dispersed on the cotton was 150 mm long. The model flue gas was composed of  $\text{SO}_2$  2250 ppm,  $\text{NO}$  700 ppm,  $\text{O}_2$  6%,  $\text{CO}_2$  13%,  $\text{H}_2\text{O}$  10%, and  $\text{N}_2$  as a balance. The composition was selected for simulating the composition of the flue gas of a coal-fired boiler. The flow rate of the model gas was 1 L/min, and the reaction temperature was  $130\text{ }^\circ\text{C}$  at the center of the absorbent bed.

At the outlet of the reactor, water was removed with a cold trap and the flue gas was analyzed by the following methods: nondispersive IR spectroscopy for  $\text{SO}_2$  and  $\text{CO}_2$ , atmospheric chemical luminescence for  $\text{NO}_x$ , and paramagnetic susceptibility for  $\text{O}_2$ . The activity was expressed as the time to keep the removal of  $\text{SO}_2$  above 80% divided by the weight of calcium hydroxide contained in the adsorbent. The activity means the capacity of the absorbent rather than the kinetics.

**Chemical and Physical Analyses.** The amount of calcium oxide contained in the absorbent was determined by X-ray fluorescence (XRF). The amount of carbonate ion was measured by neutralization titration and was calculated for the amount of calcium carbonate. The sulfur and carbon contents were measured by nondispersive IR spectroscopy. The sample (50 mg) was placed in a ceramic crucible and covered with small spoonful amounts of tin metal, iron metal, and tungsten metal in turn. The crucible was then heated by a high-frequency induction coil to convert sulfur compounds to  $\text{SO}_2$  for detection by IR spectroscopy.

The specific surface area was measured by nitrogen adsorption based on the Brunauer–Emmett–Teller

(BET) method for the sample dried and degassed at  $200\text{ }^\circ\text{C}$ . The pore volume was measured by the mercury intrusion method based on the Washburn equation for the sample dried and degassed at  $200\text{ }^\circ\text{C}$ . The weight loss by drying the absorbent was measured by thermal gravimetric analysis. The absorbent (10 mg) dried in a vacuum was placed in a platinum cup and heated by an IR lamp from ambient temperature to  $130\text{ }^\circ\text{C}$  at the speed of  $10\text{ }^\circ\text{C}/\text{min}$ . Then, the temperature was held for 20 min to measure the weight loss at  $130\text{ }^\circ\text{C}$ . The temperature was then increased similarly by  $100\text{ }^\circ\text{C}$  increments to  $600\text{ }^\circ\text{C}$ .

XRD patterns were recorded on a Rigaku RAD-C system for the powdered samples less than  $44\text{ }\mu\text{m}$  with  $\text{Cu-K}\alpha$  radiation in the range of diffraction angle ( $2\theta$ )  $5\text{--}90^\circ$  at a sweep rate of  $3\text{ deg}/\text{min}$ .

SEM photographs were taken on a JEOL JSM-35CF system with an accelerating voltage of 25 kV for the samples coated with gold metal by ion sputtering.

## Results

**Activity.** The absorbent prepared from coal fly ash, lime, and gypsum shows a higher calcium utilization compared with calcium hydroxide. The calcium utilization is defined as the percentage of the amount of calcium reacted with  $\text{SO}_2$  to the amount of calcium contained in the absorbent. The present absorbent prepared under the normal conditions achieved 84% of the calcium utilization, while calcium hydroxide achieved only 36%. These data were measured on each sample when the  $\text{SO}_2$  removal percent decreased to 0%. The time with the model gas was 41 h for the present absorbent and 186 h for calcium hydroxide.

As shown in Figure 1, the present absorbent maintained 100% removal of  $\text{SO}_2$  for 52 min per unit weight of calcium hydroxide and the activity decayed slowly beyond the duration of 100% removal. On the other hand, calcium hydroxide maintained 100% removal for a shorter time and showed a drastic decrease in activity afterward.

It should be noted that the present absorbent shows a higher activity not only for  $\text{SO}_2$  removal but also for  $\text{NO}_x$  removal, although the duration of the 100% removal for  $\text{NO}_x$  was shorter as compared with that for  $\text{SO}_2$ . However, the percent removal decayed more rapidly for  $\text{NO}_x$  than for  $\text{SO}_2$ . During the reaction time of 123–205 min, the outlet concentration of  $\text{NO}_x$  exceeded the inlet concentration. This was not seen in the case of calcium hydroxide. The amount of  $\text{NO}_x$  released from the absorbent was 7.7% of the amount of  $\text{NO}_x$  once adsorbed or absorbed. It appears that  $\text{NO}_x$  compounds in the absorbent were replaced by  $\text{SO}_2$  compounds probably because calcium compounds interact more strongly with  $\text{SO}_2$  than with  $\text{NO}_x$ .

**Effect of Hydration Period.** The activity of the absorbent for  $\text{SO}_2$  removal depended on the hydration period in the preparation procedures. The variation of the activity as a function of hydration period is shown in Figure 2. The absorbent showed an activity of 55 min/g Ca without hydration, while calcium hydroxide showed an activity of 31 min/g Ca. Even for the sample with the hydration time of 0 min, the sample was dried at  $200\text{ }^\circ\text{C}$  before use in the reaction. During the drying period, the hydration reaction may proceed to some extent, which may cause a high activity as compared to calcium hydroxide. The activity rapidly increased with hydration period and reached a maximum around 15

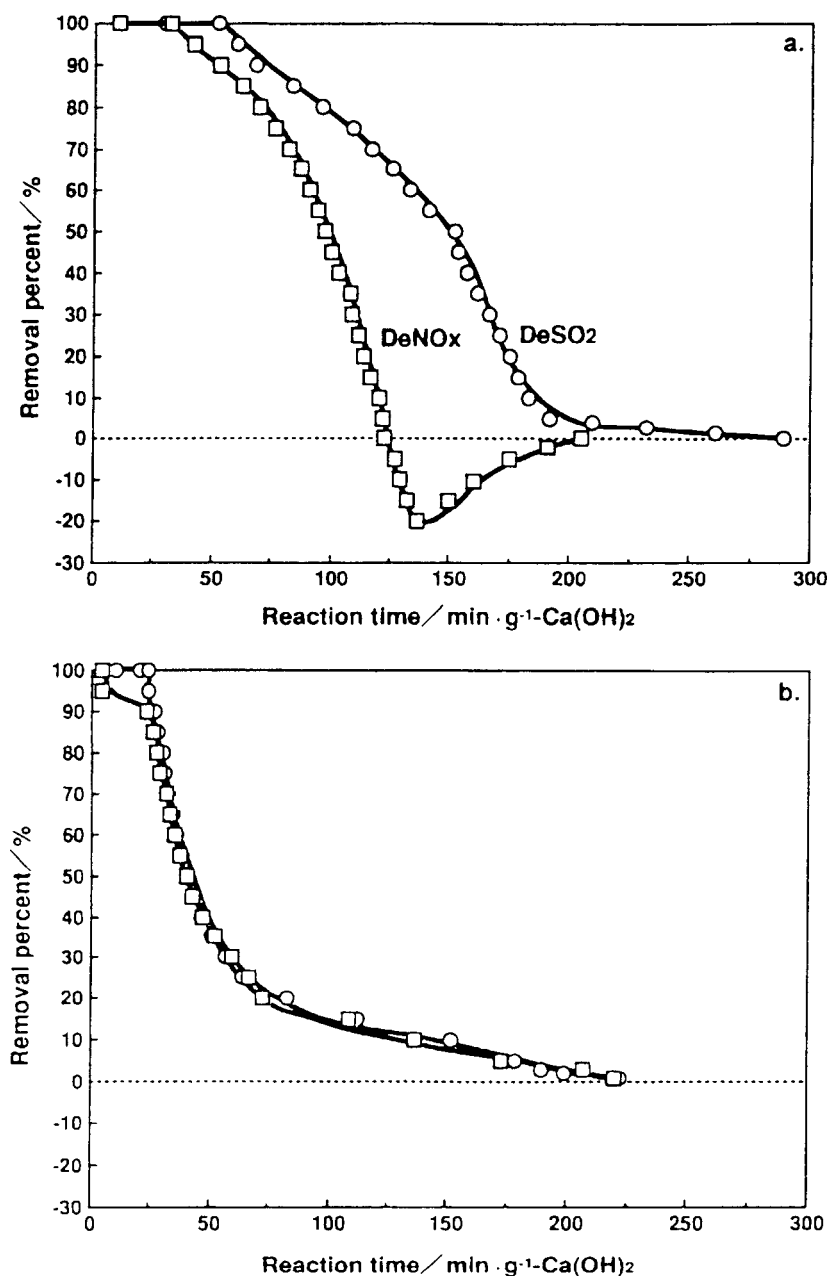


Figure 1. Time courses of the SO<sub>2</sub> and NO<sub>x</sub> removal percent for the absorbent and Ca(OH)<sub>2</sub>. Reaction time is expressed as the time divided by weight of calcium hydroxide. (a) Present absorbent prepared under the normal conditions. (b) Calcium hydroxide. ○: Removal percent for SO<sub>2</sub>. □: Removal percent for NO<sub>x</sub>.

h. Beyond 15 h of hydration, the activity gradually decreased.

**Drying Temperature.** Figure 3 shows weight loss during drying the sample initially dried at 130 °C for 2 h. The weight loss is mainly due to the removal of water, which was prominent in the temperature range 130–300 °C.

The drying temperature greatly affects the activity of the absorbent. The variation of the activity as a function of the drying temperature is shown in Figure 4 together with the variation of the surface area. The activity of the present absorbent markedly increased with an increase in the drying temperature and reached

a maximum when the absorbent was dried at 400 °C. Above a drying temperature of 400 °C, the activity decreased.

The surface area of the absorbent gradually increased and reached a maximum when the absorbent was dried at 250 °C. In contrast to the activity, the surface area decreased when dried at 400 °C and higher temperatures. Similar results were observed for a related material and explained by a sintering process (Borgwardt and Rochelle, 1990).

The calcium carbonate content notably increased with an increase in the drying temperature. The calcium carbonate content in the absorbent dried at 200 °C was

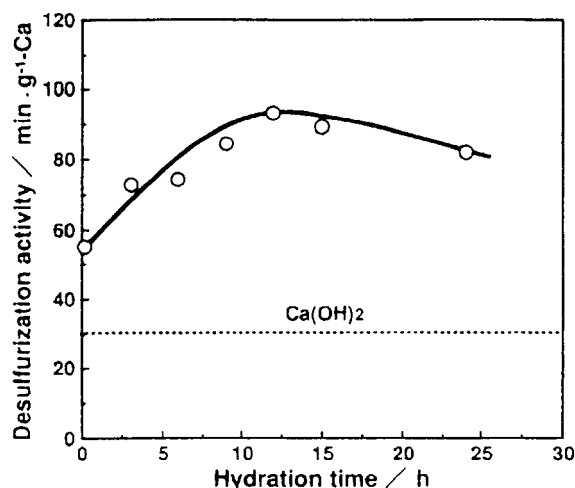


Figure 2. Effect of hydration period on the desulfurization activity of the absorbent. Starting materials:  $\text{Ca(OH)}_2$  30%,  $\text{CaSO}_4$  30%, coal fly ash 40%.

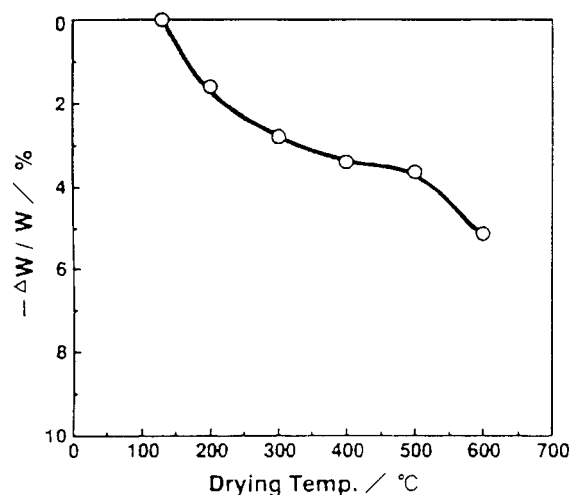


Figure 3. Effect of drying temperature on the weight loss of the absorbent.  $W$ : Initial weight of the absorbent dried in air at 130 °C for 2 h.  $\Delta W$ : Weight change by heating at the target temperature.

14%, while the amount increased to 19% when the absorbent was dried at 600 °C. The formation of calcium carbonate may result from dehydration of calcium hydroxide to calcium oxide followed by reaction with  $\text{CO}_2$  in air.

Figure 5 shows the variation of the amount of calcium sulfate as a function of drying temperature. The amount of calcium sulfate is represented by the sum of the XRD peak intensities at  $2\theta = 25.4^\circ$  and  $2\theta = 14.7^\circ$ . The peak at  $2\theta = 25.4^\circ$  is ascribed to anhydrous calcium sulfate and the peak at  $2\theta = 25.4^\circ$  to hemihydrate calcium sulfate. Above 400 °C, the intensity markedly increased, indicating that calcium sulfate crystallites developed when dried above 400 °C.

**Structure.** XRD patterns of the present absorbent were measured to examine the structural change during drying and desulfurization and are shown in Figure 6. The XRD pattern was measured for the absorbent dried in a vacuum at ambient temperature to study the hydration products, because it was reported that the hydration products are difficult to measure by XRD

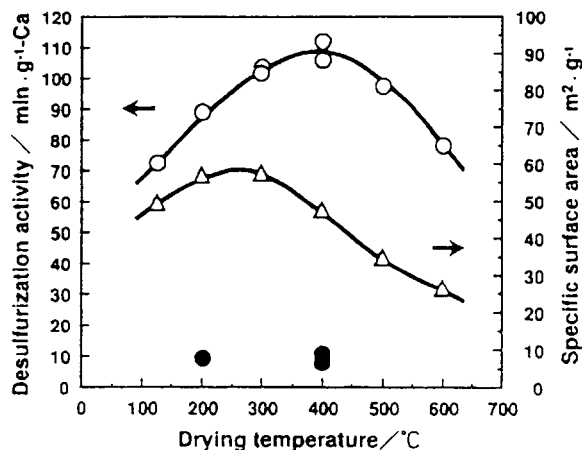


Figure 4. Effect of drying temperature on the desulfurization activity. Starting materials:  $\text{Ca(OH)}_2$  30%,  $\text{CaSO}_4$  30%, coal fly ash 40%. Hydration time: 15 h. O: Activity in the presence of NO. ●: Activity in the absence of NO.

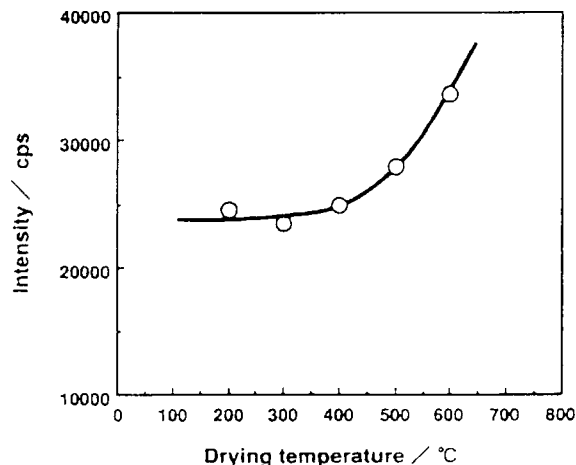


Figure 5. XRD peak intensity of  $\text{CaSO}_4$  under various drying temperatures. The intensity is the sum of the XRD peak intensities at  $2\theta = 25.4^\circ$  and  $2\theta = 14.7^\circ$ .

analysis after drying at a high temperature (Skoblinkskaya et al., 1975).

In Figure 6, parts a–c are the XRD patterns of the vacuum-dried absorbent, the absorbent prepared under the normal conditions dried at 200 °C, and the absorbent after being used for the activity test for 18 h, respectively. For the vacuum-dried absorbent, the peaks characteristic of ettringite ( $\text{Ca}_6\text{Al}_2(\text{SO}_4)_3(\text{SiO}_4)_3(\text{OH})_{12} \cdot 26\text{H}_2\text{O}$ ) appeared at  $2\theta = 9.14^\circ$ ,  $15.8^\circ$ ,  $22.9^\circ$ , and the peaks characteristic of the monosulfate ( $\text{Ca}_4\text{Al}_2\text{SO}_{10} \cdot 12\text{H}_2\text{O}$ ) appeared at  $9.93^\circ$  and  $19.9^\circ$ . The peaks for unreacted calcium hydroxide and calcium sulfate were also appreciable. For the absorbent prepared under the normal conditions, the peaks for the ettringite and the monosulfate disappeared, while the peaks for unreacted calcium hydroxide and calcium sulfate remained. For the absorbent used for the activity test, the peaks for anhydrous calcium sulfate markedly increased. The peaks for calcium sulfite, which is one of the possible products in desulfurization, were not found. The intensity of the peaks for calcium hydroxide apparently decreased after use in the activity test. It is suggested that  $\text{SO}_2$  in the model gas is removed and fixed as anhydrous calcium sulfate.

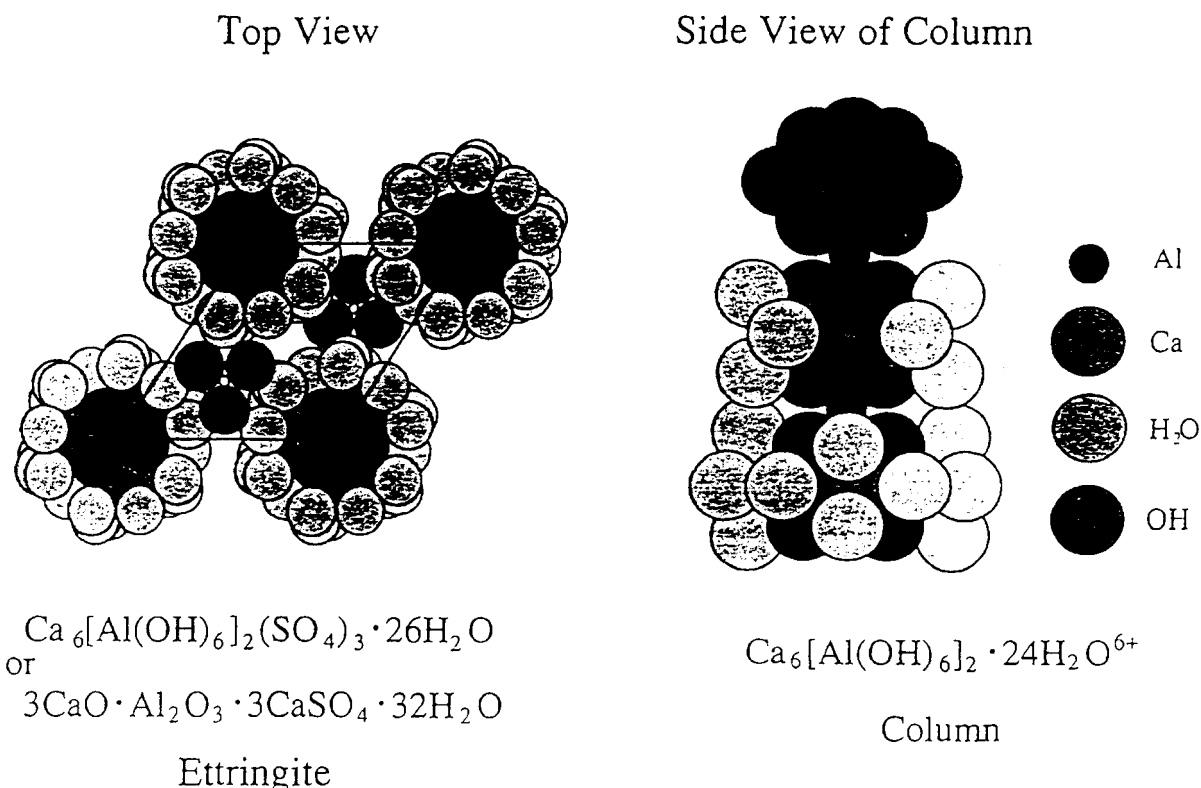


Figure 9. Crystal structure of ettringite.

### Discussion

The absorbent prepared from calcium hydroxide, calcium sulfate, and coal fly ash is highly active for removal of  $\text{SO}_2$ .  $\text{SO}_2$  is absorbed in the absorbent to form anhydrous calcium sulfate as a final product. Absorption of  $\text{SO}_2$  into calcium hydroxide also produces anhydrous calcium sulfate. The present absorbent is characterized by a high calcium utilization as compared to calcium hydroxide. More than 80% of calcium in the absorbent is utilized for  $\text{SO}_2$  absorption to form calcium sulfate.

A low calcium utilization for calcium hydroxide may be caused primarily by a low surface area.  $\text{SO}_2$  reacts with calcium hydroxide at the surface layer. The outer surface of the calcium hydroxide particles converts to calcium sulfate, but the inner part of the calcium hydroxide particle is left unchanged. Only the surface layers of calcium hydroxide are utilized for  $\text{SO}_2$  absorption. For the present absorbent, however, most of the calcium in the absorbent is located in such a position that  $\text{SO}_2$  molecules are accessible. This location of calcium may occur during preparative procedures and/or the  $\text{SO}_2$  absorption period.

As shown in Figure 2, the activity for  $\text{SO}_2$  absorption increased with the aging time of preparative procedures in the initial 12 h. During this period, the surface area and pore volume also increased. During the 12 h aging time, ettringite and monosulfate are formed as evidenced by the XRD pattern. In addition, the formation of ettringite was observed by SEM as a needle-like formula. It is apparent that calcium hydroxide, calcium sulfate, and components eluted from coal fly ash undergo a hydration reaction during the aging period. One of the hydration products is ettringite.

Ettringite has the formula  $\text{Ca}_6[\text{Al}(\text{OH})_6]_2(\text{SO}_4)_3 \cdot 26\text{H}_2\text{O}$ , and its crystal looks like a hexagonal prism consisting of columns and channels parallel with the main axis (Skoblinskaya et al., 1975; Moore and Taylor, 1968). The schematic structures are illustrated in Figure 9. The composition of the column is  $[\text{Ca}_6[\text{Al}(\text{OH})_6]_2 \cdot 24\text{H}_2\text{O}]^{6+}$ , and the channels are filled with  $[(\text{SO}_4)_3 \cdot 2\text{H}_2\text{O}]^{6-}$ . Each aluminum atom is linked to six hydroxyl groups, and each calcium atom is linked to two hydroxyl groups and four  $\text{H}_2\text{O}$  molecules. Each  $\text{H}_2\text{O}$  molecule interacts with only one calcium atom, so that the bonding between  $\text{H}_2\text{O}$  molecules and calcium atoms does not participate in the column strength in the longitudinal direction. Nevertheless, these  $\text{H}_2\text{O}$  molecules form the surface of the column where the positive charge is distributed (Moore and Taylor, 1970). The negative charge is distributed among sulfate ions in the channel (Moore and Taylor, 1970). Thus, columns and channels are united. Therefore, even though the crystal is dried to lose combined water, the column structure could be maintained, while the pore structure of high surface area is created.

It is reported that ettringite crystallites gradually decompose as the hydration period is prolonged (Mosalamy et al., 1984; Daimon et al., 1982). Although the decomposition of the ettringite structure was not clearly observed by XRD following an aging period of more than 12 h, it is plausible that the fraction of ettringite reached a maximum at the aging time of 12 h. This explains the activity maximum appearing at the aging time of 12 h.

By drying the hydration product at  $200^\circ\text{C}$ , the XRD pattern for ettringite disappeared. The disappearance of the XRD pattern does not necessarily indicate the decomposition of the ettringite structure. It was reported that the ettringite structure that once disap-

peared from the XRD pattern by heating at a high temperature restores its structure when exposed to water vapor to facilitate rehydration (Skoblinskaya et al., 1975; Skoblinskaya and Krasilnikov, 1975). Even though the peaks characteristic to ettringite disappear from the XRD pattern, the ettringite structure is intrinsically retained when dried at 200 °C. It is to be noted that removal of water by drying at 200 °C should result in the formation of pores.

By drying the hydration product above 400 °C, the intensity of the XRD peak ascribed to calcium sulfate increased as shown in Figure 4. Ettringite to form calcium sulfate decomposed irreversibly (Fukuda, 1984). At the same time, the CO<sub>2</sub> content increased. The decrease in the activity on drying above 400 °C is considered to be due to the decomposition of the ettringite structure and the adsorption of CO<sub>2</sub> to convert calcium hydroxide into calcium carbonate.

It is, therefore, plausible that the calcium utilization efficiency becomes high when calcium is included in the ettringite structure, though it cannot be excluded that calcium components other than ettringite are also utilized for absorption of SO<sub>2</sub>.

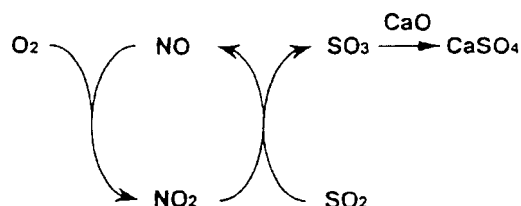
An alternative explanation for the role of ettringite in the absorption of SO<sub>2</sub> may be as follows. Ettringite itself is not capable of absorbing SO<sub>2</sub>, but it makes the absorbent porous to facilitate the access of SO<sub>2</sub> to the calcium components present in different forms such as calcium silicate and calcium oxide.

Jozewicz and Rochelle (1986) reported that an amorphous compound prepared by slurring calcium hydroxide with coal fly ash and recycled absorbents in water at elevated temperature showed a high activity for SO<sub>2</sub> removal (Rochelle and Jozewicz, 1989). They observed the formation of calcium silicate hydrate in the amorphous compound by XRD analysis and showed the correlations of the activity with both BET surface area and moisture content. Because the calcium silicate hydrate has a high surface area, it can retain much water. Therefore, it was concluded that a calcium silicate hydrate is an active material for SO<sub>2</sub> removal (Jozewicz and Rochelle, 1986).

Apparently, the recycled absorbent contains an appreciable amount of calcium sulfate. Therefore, it is most likely that ettringite was formed in the hydration period, though Rochelle et al. did not report the formation of ettringite. Besides the calcium silicate hydrate, it seems probable that ettringite is also active for SO<sub>2</sub> removal in their absorption system.

One of the characteristic features of the present absorbent is that the absorbent exhibits a high activity in the presence of NO. Concerning the enhancement of SO<sub>2</sub> absorption by the presence of NO, it was reported previously (Medellin et al., 1978; Chu and Rochelle, 1989). Medellin et al. (1978) mentioned that the reaction proceeds through a gas phase reaction. In the absence of NO, the absorbent showed only a small activity for SO<sub>2</sub> absorption as shown in Figure 4. NO should play an important role in the absorption of SO<sub>2</sub>. Since SO<sub>2</sub> is absorbed in the form of calcium sulfate as the final product, SO<sub>2</sub> should be oxidized to SO<sub>3</sub> before reaction with the component of calcium oxide to form calcium sulfate. The requirement of the presence of NO suggests that NO plays a role in the oxidation of SO<sub>2</sub>. Considering that NO<sub>2</sub> is a strong oxidant, it is plausible that the oxidation of SO<sub>2</sub> to SO<sub>3</sub> proceeds by the action of NO<sub>2</sub> that is formed by oxidation of NO. The oxidation

**Scheme 1. Desulfurization Reaction Enhanced by the Presence of NO**



reaction of NO to NO<sub>2</sub> was reported to be thermodynamically feasible (Xue et al., 1993).

The proposed scheme for the role of NO and NO<sub>2</sub> is illustrated in Scheme 1. In this scheme, NO and NO<sub>2</sub> act as catalysts to oxidize SO<sub>2</sub> to SO<sub>3</sub>. The catalytic role of NO and NO<sub>2</sub> is similar to that observed in the lead chamber method to produce sulfuric acid from SO<sub>2</sub>. The NO and NO<sub>2</sub> do not seem to react with SO<sub>2</sub> in the gas phase but do on the surface of the absorbent. On this point, more information will be reported shortly.

### Literature Cited

- Abo-El-Enein, S. A.; Al-Nuaimi, K. Kh.; Marusin, S. L.; El-Hemaly, S. A. S. Hydration Kinetics and Microstructure of Ettringite. *TIZ* 1985, 109, 116–118.
- Borgwardt, R. H.; Rochelle, G. T. Sintering and Sulfation of Calcium Silicate–Calcium Aluminate. *Ind. Eng. Chem. Res.* 1990, 29, 2118–2123.
- Brown, C. A.; Maibodi, M.; McGuire, L. M. 1.7MW Pilot Results for the Duct Injection FGD Process Using Hydrated Lime Upstream of an ESP. Proceeding. The 1991 SO<sub>2</sub> Control Symposium, Washington, DC, December 1991.
- Chu, P.; Rochelle, G. T. Removal of SO<sub>2</sub> and NO<sub>x</sub> from Stack Gas by Reaction with Calcium Hydroxide Solids. *JAPCA* 1989, 39, 175–179.
- Daimon, M.; Yamaguchi, O.; Oosawa, H.; Goto, S. Hydration Reaction of Fly Ash in the Presence of Gypsum (Japanese). *Semento Gijutsu Nenpo* 1982, 36, 65–68.
- Dalton, S. M. State-of-the-Art of Flue Gas Desulfurization Technologies. Proceeding. Power Gen '90, Orlando, FL, December 1990.
- Fukuda, M. Ettringite (Japanese). *Tsuchi-to-Kiso*. 1984, 32, 49–50.
- Haslbeck, J. L.; Woods, M. C.; Ma, W. T.; Harkins, S. M.; Black, J. B. NOXSO SO<sub>2</sub>/NO<sub>x</sub> Flue Gas Treatment Process: Proof-of-Concept Test. Proceeding. The 1993 SO<sub>2</sub> Control Symposium. Boston, MA, Augst 1993.
- Jozewicz, W.; Rochelle, G. T. Fly Ash Recycle in Dry Scrubbing. *Environ. Prog.* 1986, 5, 219–223.
- Khalil, A. A.; El-Didamony, H. Study of the Hydration Products of the System CaO–Al<sub>2</sub>O<sub>3</sub>–SO<sub>3</sub>–SiO<sub>2</sub> with Varying CaO Mole Ratio. *Thermochim. Acta* 1980, 40, 337–347.
- Kind, K. K.; Rochelle, G. T. Preparation of Calcium Silicate Reagent from Fly Ash and Lime in a Flow Reactor. *J. Air Waste Manage. Assoc.* 1994, 44, 869–876.
- Lepovitz, L. R.; Brown, C. A.; Pearson, T. E.; Boyer, J. F.; Burnett, T. A.; Norwood, V. M.; Puschaver, E. J.; Sedman, C. B.; Toole-O'Neil, B. 10MW Demonstration of the ADVACATE Flue Gas Desulfurization Process. Proceeding. The 1993 SO<sub>2</sub> Control Symposium. Boston, MA, August 1993.
- Livengood, C. D. Combined NO<sub>x</sub>/SO<sub>2</sub> Removal in Spray Dryer FGD Systems. Proceeding. Acid Rain Retrofit Seminar: The Effective Use of Lime, Philadelphia, PA; National Lime Association, January 1991.
- Medellin, P. M.; Weger, E.; Dudukovic, M. P. Removal of SO<sub>2</sub> and NO<sub>x</sub> from Simulated Flue Gases by Alkalized Alumina in a Radial Flow Fixed Bed. *Ind. Eng. Chem. Process Des. Dev.* 1978, 17, 528–536.
- Moore, A. E.; Taylor, H. F. W. Crystal Structure of Ettringite. *Nature (London)* 1968, 218, 1048–1049.
- Moore, A. E.; Taylor, H. F. W. Crystal Structure of Ettringite. *Acta Crystallogr.* 1970, B26, 386–393.
- Mosalamy, F. H.; Shater, M. A.; El-Didamony, H. Hydration Mechanism of Tricalcium Aluminate with Gypsum at 1:1 Mole

- Ratio at Low Water/Solid Ratio and in Suspension. *Thermochim. Acta* 1984, 74, 113-121.
- Rochelle, G. T.; Jozewicz, W. Process for Removing Sulfur from Sulfur-Containing Gases. U.S. Patent No. 4804521, February 14, 1989.
- Skoblinskaya, N. N.; Krasilnikov, K. G. Changes in Crystal Structure of Ettringite on Dehydration 1. *Cem. Concr. Res.* 1975, 5, 381-393.
- Skoblinskaya, N. N.; Krasilnikov, K. G.; Nikitina, L. V.; Varlamov, V. P. Changes in Crystal Structure of Ettringite on Dehydration 2. *Cem. Concr. Res.* 1975, 5, 419-431.
- Tischer, R. E. Furnace and In-duct Sorbent Injection. Proceeding. Acid Rain Retrofit Seminar: The Effective Use of Lime, Philadelphia, PA; National Lime Association, 1991.
- Ueno, T. Process for Preparing Desulfurizing and Denitrating Agents. U.S. Patent No. 4629721, December 16, 1986.
- Xue, E.; Seshan, K.; van Ommen, J. G.; Ross, J. R. H. Catalytic Role of Diesel Engine Particulate Emission: Studies on Model Reactions over a EuroPt (Pt/SiO<sub>2</sub>). *Appl. Catal. B: Environ.* 1993, 2, 183-197.
- Yuan, H. S. Hydration of Lime-Fly Ash Paste at High Temperature. *CBI Res.* 1979, No. 10, 1-13.

Received for review July 5, 1994

Revised manuscript received December 29, 1994

Accepted January 9, 1995\*

IE9404137

\* Abstract published in *Advance ACS Abstracts*, March 1, 1995.

## $^{29}\text{Si}$ -NMR study of the absorbent for flue gas desulfurization

Hideshi Hattori, Nariyasu Kanuka, and Ryu-ichi Kanai

Center for Advanced Research of Energy Technology, Hokkaido University, Sapporo 060, Japan

### 1. INTRODUCTION

The flue gas from a coal fired boiler contains a high concentration of  $\text{SO}_2$  which should be removed before emitted from a chimney for protection of environment from pollution. A wet desulfurization system is commonly adopted for flue gas desulfurization (FGD), and exhibits a high utilization efficiency of Ca component in the absorbent, but needs a large amount of water. As dry FGD systems, a duct injection and a slurry spraying are adopted. The efficiency, however, is not so high as compared to a wet FGD system.

Recently, the  $\text{SO}_2$  absorbent which exhibits a high utilization efficiency of Ca component in a dry FGD process was prepared from a coal fly-ash,  $\text{Ca}(\text{OH})_2$ , and  $\text{CaSO}_4$  by hydrothermal reaction. The dry FGD process using this absorbent has been commercially operated since 1991. The process is schematically illustrated in Fig.1.

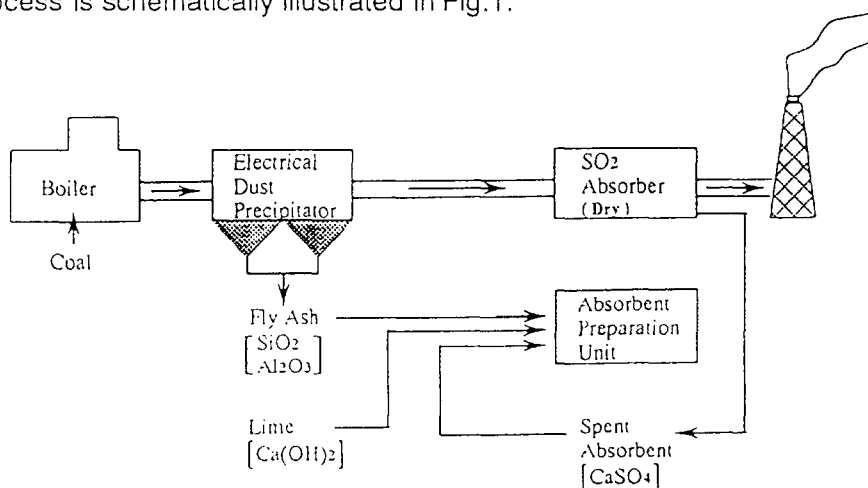


Fig. 1 Process flow of FGD for coal fired boiler

A coal fly-ash collected at the electrostatic precipitator is mixed with  $\text{Ca}(\text{OH})_2$  (lime) and  $\text{CaSO}_4$  (gypsum), and transferred to the absorbent preparation unit where hydrothermal reaction is taken to produce active absorbent. The absorbent is extruded into granules, dried, and placed in the  $\text{SO}_2$  absorber where  $\text{SO}_2$  is removed from dirty flue gas to emit a clean flue gas.  $\text{SO}_2$  is fixed in the form of  $\text{CaSO}_4$ . The utilization efficiency of Ca component converting into  $\text{CaSO}_4$  exceeds 90%.

In the present paper, we study the structural changes of the absorbent during the hydrothermal reaction and  $\text{SO}_2$  absorption by  $^{29}\text{Si}$ -MASNMR using a model absorbent of

calcium silicate hydrate to elucidate the mechanisms for a high utilization efficiency of Ca component. It is revealed that the structural changes during the absorption of SO<sub>2</sub> enable Ca component present in a bulk to be exposed to the flue gas.

## 2. EXPERIMENTAL METHODS

### 2.1. Preparation of the absorbent

For preparation of a model absorbent of calcium silicate hydrate, a mixture of Ca(OH)<sub>2</sub> and SiO<sub>2</sub>·xH<sub>2</sub>O was heated at 363K for 20h in a water with stirring. The resulting slurry was filtered, washed with water and dried at 373K and then 473K for 3h. The ratio CaO/SiO<sub>2</sub> was adjusted to 1.4 (mol/mol). The absorbent prepared using fly-ash was prepared as follows. To a hot water at about 343K, CaO, fly-ash and spent absorbent (CaSO<sub>4</sub> source) were added and stirred with a mill. The slurry was hydrated for 12 h at 363K and then dried at 473K for 1 h. A physical mixture of Ca(OH)<sub>2</sub> and SiO<sub>2</sub>·xH<sub>2</sub>O was prepared by grinding the compounds in a mortar.

### 2.2. Reaction procedures

The desulfurization was carried out at 303 K in a flow reactor with a model flue gas composed of SO<sub>2</sub> 1000ppm, NO<sub>x</sub> 1000ppm, O<sub>2</sub> 10%, H<sub>2</sub>O 10%, and He balance. The flow rate was 200 ml/min using 0.5 g of the absorbent. The concentrations of SO<sub>2</sub> and NO<sub>x</sub> were measured by infrared spectroscopy and chemiluminescence, respectively.

### 2.3. NMR measurement

<sup>29</sup>Si-MASNMR spectrum was measured for the powdery sample on a Bruker MSL-200 in the mode of high power decoupling. The main conditions for measurement were as follows; observed frequency 39.8Mhz, observed spectral width 10kHz, pulse width (90° pulse) 4.0 ms, pulse interval 7 s(10 ms delay), data points 8192, line broadening factor 30Hz, accumulation 5000, reference of <sup>29</sup>Si chemical shift Q8M8(11.72ppm).

## 3. RESULTS AND DISCUSSION

The percentages SO<sub>2</sub> removal are plotted against the time on stream in Fig. 2 for the calcium silicate hydrate, the absorbent prepared from fly-ash, and the physical mixture. For both the calcium silicate and the absorbent prepared from fly-ash, SO<sub>2</sub> removal kept 100% for the initial 1 h, and then decreased gradually to about 30 %, and kept this level for a long time on stream. The physical mixture scarcely absorbed SO<sub>2</sub> except for the initial few min. The Ca(OH)<sub>2</sub> became active by combination with SiO<sub>2</sub>. There seem to be two different mechanisms for absorption of SO<sub>2</sub>, one occurring in the initial stage of the time on stream which results in 100% SO<sub>2</sub> removal, and the other in the later stage of the time on stream which results in about 30% SO<sub>2</sub> removal.

The presence of NO<sub>x</sub> and H<sub>2</sub>O is required for SO<sub>2</sub> absorption. Without NO<sub>x</sub> or H<sub>2</sub>O, SO<sub>2</sub> absorption was not appreciable.

<sup>29</sup>Si-MASNMR spectra for the calcium silicates prepared with different hydration period are shown in Fig. 3 together with that for the raw material silicic acid. The peak at -112 ppm observed for the silicic acid is assigned to the cross-linked framework(Q<sup>4</sup>). After hydration of 20min, Q<sup>4</sup> peak disappeared, and two peaks appeared at -83 ppm and -79 ppm which are assigned to middle group in chain (Q<sup>2</sup>) and chain end group (Q<sup>1</sup>), respectively. On prolonging the hydration time to 12h, the peaks did not change much in both intensity and chemical shift, only a slight broadening of the peaks was observed. It is indicated that Si-O-Si



bonds of  $Q^4$  structure rapidly cleave and convert into straight chain Si-O-Si as hydration with  $Ca(OH)_2$  starts.

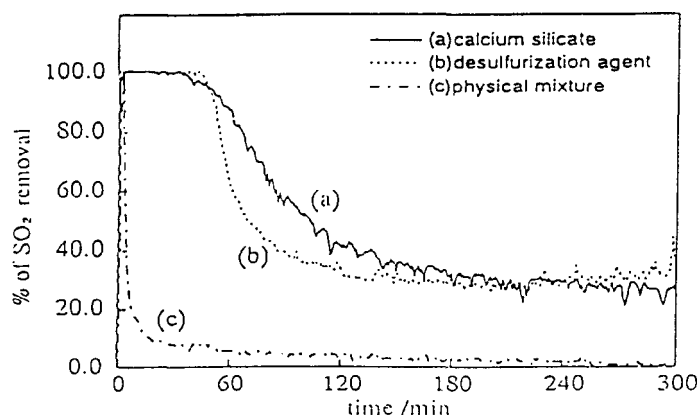


Fig. 2 The percentage  $SO_2$  removal vs. time on stream

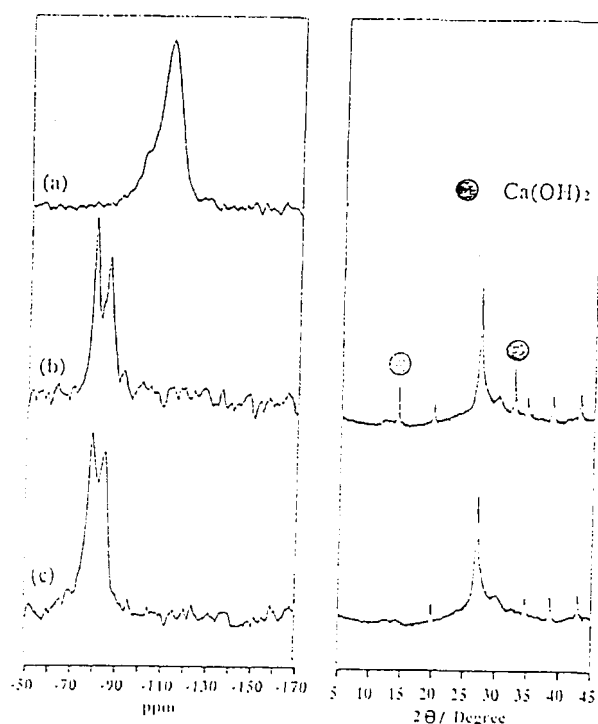


Fig. 3  $^{29}Si$ -MASNMR spectra and XRD patterns of the sample hydrated for different period. (a) silicic acid, (b) hydrated for 20 min, (c) hydrated for 12 h

From the intensity ratio of  $Q^2/Q^1$ , the averaged chain length of the silicate can be calculated. One silicate chain was calculated to consist of about 4  $SiO_4$  tetrahedra regardless the hydration time.

To examine the structural change during desulfurization,  $^{29}Si$ -MASNMR spectra were measured for the samples being allowed to react for different time on stream and, shown in Fig. 4. The percentages of  $SO_2$  removal in 1h, 1.5h, 5h, and 20 h were 100%, 100%, 58%, 27%, and 10%, respectively. The samples reacted for 1h and 1.5h, which still kept high  $SO_2$  removal, showed the peaks for  $Q^1$  and  $Q^2$ . As the reaction proceeded, the peak intensity for  $Q^1$  slightly decreased. In this period, the Ca ions interacting with non-cross linked O of  $Q^1$  participate in the  $SO_2$  removal. For the samples reacted for 5h and 20 h, which showed low  $SO_2$  removal, the appearance of the peaks for  $Q^3$  and  $Q^4$  with concomitant decrease in the peak intensity for  $Q^1$  and  $Q^2$  was observed. In the period where the  $SO_2$  removal level is low, the Ca ions interacting with non-cross linked O of  $Q^2$  participate in the  $SO_2$  removal.

The surface area of the sample did not change much with the time on stream, though  $CaSO_4$  was accumulated on the sample. It is suggested that the original surface present on the sample before  $SO_2$  absorption decreases with the formation of  $CaSO_4$ , and a new surface appears with the formation of silica framework as the  $SO_2$  absorption proceeds.

The structural change of the absorbent during  $SO_2$  absorption is illustrated in Fig. 5. In the initial stage of the reaction,  $SO_2$  is absorbed by the CaO component located on the

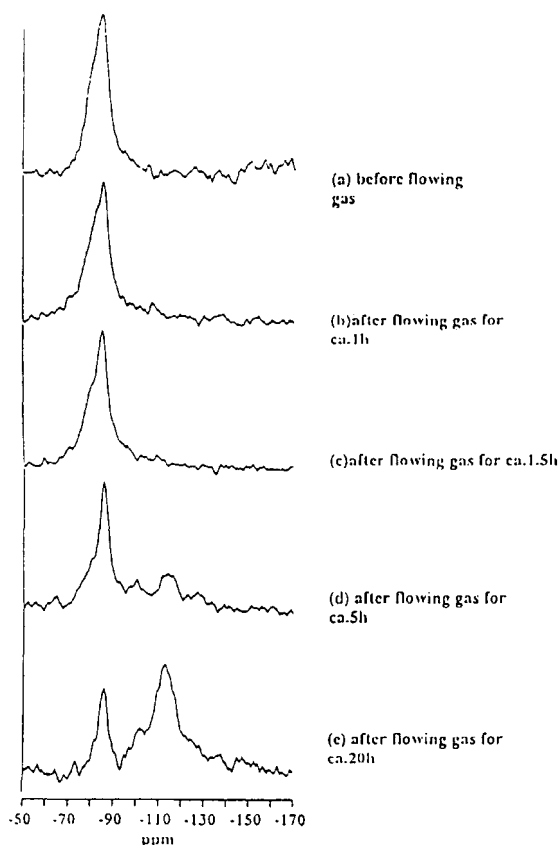


Fig. 4  $^{29}\text{Si}$ -MASNMR spectra of calcium silicate used for different time on stream

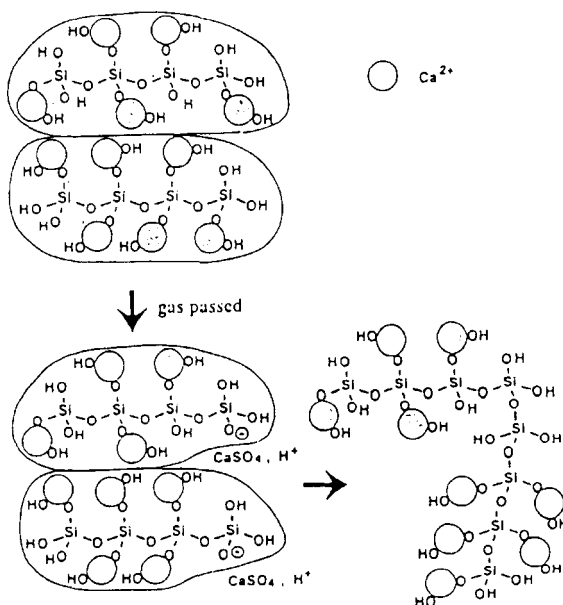


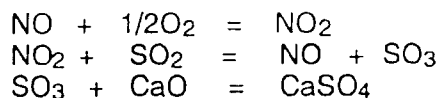
Fig. 5 Model for structural change during desulfurization

outer surface of the particles consisting of several silicate chains. The high SO<sub>2</sub> removal observed in the initial stage of the reaction proceeds by this mechanism.

As CaO component converts to CaSO<sub>4</sub> and expelled from the particle, Si-O-Si bonds begin to form. The formation of new Si-O-Si bonds results in exposure of Ca component located in a bulk to the surface. In this way the Ca component located in the bulk of the absorbent becomes utilized for SO<sub>2</sub> absorption, and therefore, the utilization efficiency of Ca is able to exceed 90%. The low SO<sub>2</sub> removal observed in the later stage of reaction which persists for a long period proceeds by this mechanism.

When simple Ca(OH)<sub>2</sub> is used, CaSO<sub>4</sub> is formed on the outer surface of the particles, and the CaSO<sub>4</sub> layers cover the unreacted Ca(OH)<sub>2</sub> to be inactive. In the case of the absorbent of calcium silicate, SO<sub>2</sub> absorption is accompanied by the structural change in Si-O-Si framework, which enable Ca component in the bulk to expose to the gaseous SO<sub>2</sub>. As a result, a high Ca utilization efficiency is attained.

Finally, the role of NO which is required for SO<sub>2</sub> absorption is suggested to be a catalyst. The SO<sub>2</sub> proceeds through the following reactions.



The NO and NO<sub>2</sub> act as catalyst for the SO<sub>2</sub> absorption to form CaSO<sub>4</sub>.

Reduction of NO on Au single-crystal electrodes in alkaline solution<sup>1</sup>

Shuichi Suzuki, Teruyuki Nakato, Hideshi Hattori, Hideaki Kita \*

*Division of Material Science, Graduate School of Environmental Earth Science, Hokkaido University, Sapporo 060, Japan*

Received 21 November 1994; in revised form 6 February 1995

## Abstract

The electrochemical behavior of nitrogen compounds on Au(111), Au(100) and Au(110) was investigated in alkaline solution. Each crystal plane was identified by Pb underpotential deposition (UPD) waves in perchloric acid solution. The UPD waves were unchanged after oxidation and reduction of a surface monolayer of Au atoms on the respective electrodes. NO underwent a "disproportionation" to  $\text{NO}_2^-$  and reduced species in the alkaline solution. However, only NO was electrochemically active.

Cyclic voltammograms obtained in an alkaline solution containing dissolved NO showed a main reduction peak at ca. 0 V RHE and an oxidation peak at ca. 0.6 V, almost independent of the crystal plane in contrast with the case of Pt electrodes. We concluded from the voltammetric study that the former peak is due to the production of  $\text{NH}_2\text{OH}$ , and that oxidation of  $\text{NH}_2\text{OH}$  remaining near the surface gives the latter peak. The products in the two peaks were identified using in-situ "one-point touch" differential electrochemical mass spectroscopy:  $\text{NH}_2\text{OH}$  was mainly oxidized to NO;  $\text{N}_2\text{H}_4$ , which apparently gave the same oxidation peak at ca. 0.6 V, yielded  $\text{N}_2$  exclusively.

**Keywords:** Electroreduction; Nitrous oxide; Pollution control; Gold electrodes; Surface structure effects

## 1. Introduction

Nitrogen compounds have been the subject of much concern with respect to environmental problems. Many studies have been performed with the aim of removing nitrogenous pollutants from exhaust gases and air. For example, the decomposition of nitrogen compounds in a gas solid system has been widely studied by various methods using polycrystalline and single-crystal metals. Similarly, studies in the liquid phase have been performed under various conditions [1]. Most investigations using platinum have been performed with polycrystalline electrodes in acidic solution [2–6]. For example Dutta and Landolt [2] studied the electrochemical behavior of NO on a rotating Pt electrode in 4 M  $\text{H}_2\text{SO}_4$ . They reported that NO oxidation proceeds via two steps: the first step is the oxidation of NO to  $\text{HNO}_2$ , which is kinetically fast and diffusion controlled, and the second step is the oxidation of  $\text{HNO}_2$  to  $\text{HNO}_3$ . NO reduction also proceeds via two steps, of which the first is a one-electron diffusion-con-

trolled reduction process. Janssen et al. [3] have shown that  $\text{N}_2\text{O}$  is formed in the first step, followed by  $\text{NH}_2\text{OH}$ ,  $\text{N}_2\text{H}_4$  and  $\text{NH}_3$  in the second step. They reported the presence of the nitrosyl group ( $-\text{NOH}$ ) as a reaction intermediate, in agreement with other authors [4–6]. When  $\text{NOH}$ - and  $\text{NHOH}$ -like species are formed as the reaction intermediates,  $\text{N}_2\text{O}$  and  $\text{N}_2$  will be produced by dimerization and dehydration. Vielstich and coworkers [7] investigated the oxidative and reductive electrolyses of  $\text{NH}_3$ ,  $\text{NH}_2\text{OH}$ ,  $\text{NO}_2^-$ , and  $\text{NO}_3^-$  on a Pt polycrystalline electrode in alkaline solution by means of differential electrochemical mass spectroscopy (DEMS). They concluded that these species form a common reaction intermediate which is either oxidized to  $\text{N}_2$  or reduced to  $\text{NH}_3$ .

Recently, the Pt single-crystal electrode has become widely available in the laboratory and work on well-defined surfaces has been reported by several groups [8–10]. We have found that the electrochemical behavior of a series of nitrogen compounds on Pt single-crystal electrodes is remarkably structure sensitive. For example  $\text{NO}_2^-$  is reduced to  $\text{NH}_3$  easily on Pt(100) (current efficiency above 80%) but with difficulty on Pt(111) and Pt(110) [8]. More interestingly, this reduction is suppressed in the hydrogen adsorption region, even though the reduction requires a hydrogen atom. The hydrogen adsorption appar-

<sup>1</sup> Dedicated to Professor Kenichi Honda, Professor Hiroaki Matsuda and Professor Reita Tamamushi on the occasion of their 70th birthdays.

\* Corresponding author.

ently inhibits the  $\text{NO}_2^-$  reduction, and consequently we transferred our interest to Au electrodes which do not adsorb hydrogen. A few electrochemical studies of nitrogen compounds have been performed on polycrystalline Au [11,12], but to our knowledge there have been none on single-crystal Au. In addition, the work reported was carried out in acidic solutions. Single-crystal Au has recently attracted interest in the field of surface science and has been used in electrochemistry in studies of the surface reconstruction and underpotential deposition (UPD) of other metals which were performed using scanning tunneling microscopy [13,14], second harmonic generation (SHG) [15], electroreflectance [16] and capacitance measurements [17].

The aim of the present work was to investigate not only the electrochemical activity of the gold electrode toward nitrogen compounds but also the effect of the crystallographic structure of the surface. We report results obtained on Au(111), Au(100) and Au(110) using both conventional cyclic voltammetry and one-point touch differential electrochemical mass spectroscopy (DEMS) which we have recently developed [18].

## 2. Experimental

Au(111), Au(100) and Au(110) single-crystal electrodes were prepared by Clavilier's method [19,20]. These electrodes (about 3 mm in diameter) were flame-annealed and quenched in Ar-saturated Milli-Q water just before each measurement, and were used in the dipping mode. Cyclic voltammograms (CVs) of the electrode surface were recorded in a blank solution of 0.1 M  $\text{HClO}_4$  and in 10 mM  $\text{Pb}^{2+}$  + 0.1 M  $\text{HClO}_4$ .

We chose alkaline phosphate buffer solution (ionic strength 0.2 M, pH 11.9) as the electrolyte solution since nitrogen compound reactions are pH sensitive and NO undergoes reduction on a Pt electrode in alkaline solution [1,8]. The electrolyte solution was prepared from  $\text{Na}_3\text{PO}_4$  (guaranteed grade, Wako Pure Chemical Industries Co.) and Milli-Q water. All nitrogen compounds were of guaranteed grade (Kanto Chemical Co.). Nitric oxide (99.7%, Sumitomo Seika Chemicals Co.) was passed through a wash bottle containing 2 M NaOH before use to remove possible  $\text{NO}_2$  and other impurities [8]. After the introduction of NO, the solution composition was examined by UV–visible absorbance (JASCO Ubest-30 UV–visible spectrometer).

Electrochemical measurements were performed with a constant Ar flow over the solution to avoid any effect of the three-phase zone. Mass spectroscopy cyclic voltammograms (MSCVs) were measured using the one-point touch DEMS developed in our laboratory [18] simultaneously with cyclic voltammetry. In MSCV measurements, the electrodes were kept in the dipping mode. The mass spectrometer (Anelva AQA-200 quadrupole mass spec-

trometer) was used with an emission current of 2 mA and its microchannel plate was polarized at 800 V. All potentials are reported on the RHE scale.

## 3. Results and discussion

### 3.1. Identification of each crystal plane

The oxidation–reduction wave of the electrode surface (O-wave) was used to identify the surface structure. Figs. 1(a)–1(c) show the characteristic CVs obtained on the three low index planes at  $50 \text{ mV s}^{-1}$  in 0.1 M  $\text{HClO}_4$ . These O waves are different from each other as reported in literature [16]. However, the oxidation of electrode surface causes islands and pits [21,22], and therefore it is possible that the surface is perturbed to some extent. To check this possibility, we investigated the UPD-Pb wave which appears in the potential region negative of the O-wave. The UPD-Pb waves on Au(111), Au(100) and Au(110) at  $50 \text{ mV s}^{-1}$  are shown as the solid curves in Figs. 2(a)–2(c). The potential was limited to the region negative of 1.0 V.

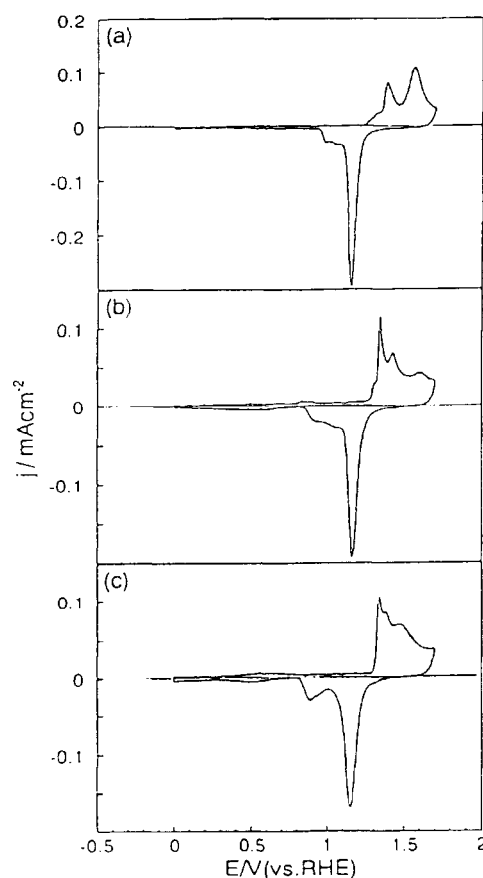


Fig. 1. CVs on (a) Au(111), (b) Au(100) and (c) Au(110) in 0.1 M  $\text{HClO}_4$  (scan rate,  $50 \text{ mV s}^{-1}$ ).

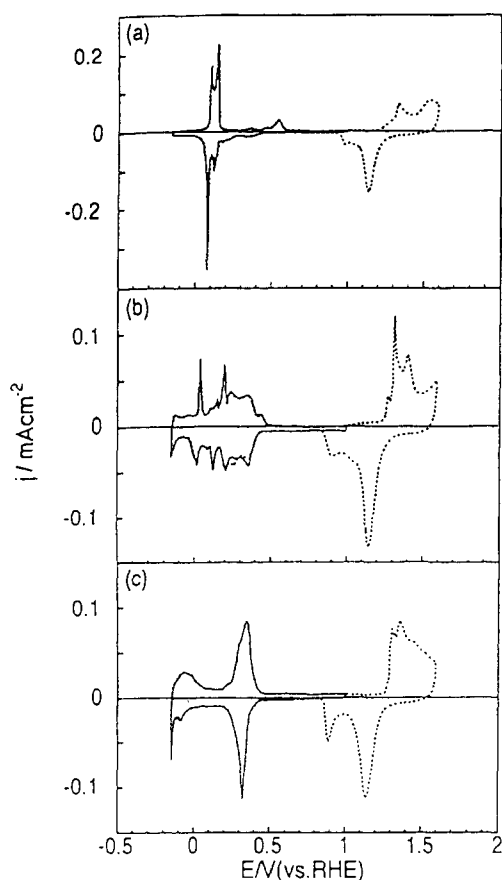


Fig. 2. UPD-Pb waves for (a) Au(111), (b) Au(100) and (c) Au(110) in 0.1 M  $\text{HClO}_4$  (—) and 0.1 M  $\text{HClO}_4$  + 10 mM  $\text{Pb}^{2+}$  (·····) (scan rate,  $50 \text{ mV s}^{-1}$ ). The scan was initiated from 0.9 V in the positive direction.

These curves are clearly structure sensitive, in agreement with other work [23,24], and can safely be used to identify each plane. We estimated the electric charge for Pb deposition on Au(111), Au(100) and Au(110) to be  $267 \mu\text{C cm}^{-2}$ ,  $234 \mu\text{C cm}^{-2}$  and  $223 \mu\text{C cm}^{-2}$  respectively. Except for Au(110), these values are close to that expected for monolayer coverage, provided that one Pb atom occupies two UPD-H sites [25]. The charge for Au(110) is ca. 50% greater than the monolayer value. A similar phenomenon has been observed for hydrogen adsorption on Pt(110). For UPD-Pb on Au(111), it has been reported that the right-hand peak in the negative-going scan (Fig. 2(a)) is due to a random cluster formation and the main left-hand peak is due to cluster growth and coalescence [26]. The possibility of surface rearrangement by the oxidation–reduction treatment was checked by recording the UPD-Pb wave after treatment. It can be seen from the results (the upper limit potential was 1.6 V), shown by the dotted curves in Figs. 2(a)–2(c), that there was no change in the

UPD-Pb waves. This shows that either the surface oxidation–reduction treatment does not cause rearrangement of the surface (at least at a sweep rate of  $50 \text{ mV s}^{-1}$ ) or, if it does, the surface is rapidly recovered within the time span of the potential sweep used. It is not yet clear which mechanism is operating. Since the measurements in this study were performed in phosphate buffer solution, the effect of the phosphate ion was examined by adding 5 mM  $\text{PO}_4^{3-}$  to the 0.1 M  $\text{HClO}_4$  solution. No change was observed in the CVs. Since the oxidation–reduction treatment does not affect the surface structure, the O-wave in the blank solution is confirmed as being suitable for identification of the crystal plane.

### 3.2. "Disproportionation" reaction of NO

Several oxidation states are allowed for nitrogen. NO is less thermodynamically stable than  $\text{N}_2$ ,  $\text{N}_2\text{O}$ ,  $\text{NH}_2\text{OH}$ ,  $\text{N}_2\text{H}_4$  and  $\text{NH}_3$ . Thus it is possible that NO may "disproportionate" in combination with an appropriately oxidized species. This possibility was investigated by examining UV–visible absorption spectra after introducing NO into the solution. The spectrum showed three strong absorption bands at exactly the wavelengths as those of  $\text{NO}_2^-$ :  $\lambda = 355 \text{ nm}$  ( $\epsilon = 2.40$ ),  $\lambda = 287 \text{ nm}$  ( $\epsilon = 1.51$ ) and  $\lambda = 210 \text{ nm}$  ( $\epsilon = 5.75 \times 10^3$ ) [27]. This shows that the dissolved NO undergoes "disproportionation" and produces  $\text{NO}_2^-$ . The concentration of  $\text{NO}_2^-$  formed in the solution was estimated by using the calibration curve obtained separately from the absorbance of the solutions containing  $\text{NO}_2^-$  at different concentrations. The absorption band at 355 nm was used in the calibration because the absorbance at 210 nm is too large to be used for quantitative analysis. Fig. 3 shows the time dependence of the  $\text{NO}_2^-$  concentration after a sample of  $\text{Na}_3\text{PO}_4$  solution through which NO had been bubbled for 5 min was placed in a spectrometer cell. The initial  $\text{NO}_2^-$  concentration (after bubbling NO for 5 min) was 3.6 mM and it gradually increased to 4.5 mM at 130

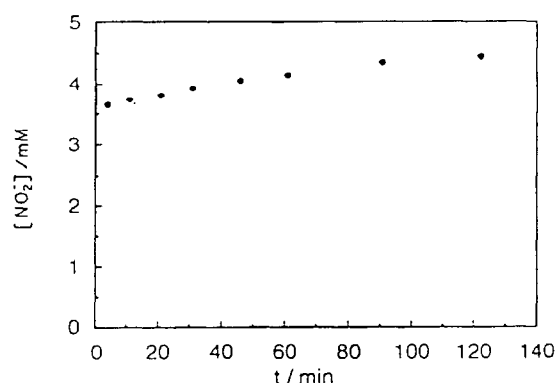
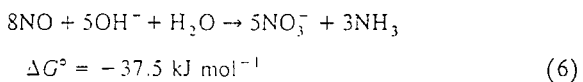
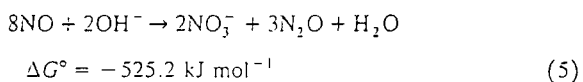
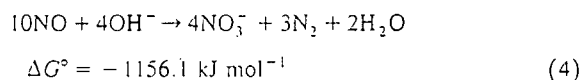
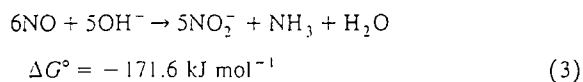
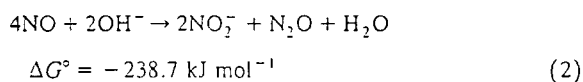
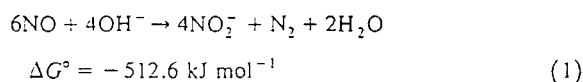


Fig. 3. Change in the concentration of  $\text{NO}_2^-$  in  $\text{Na}_3\text{PO}_4$  solution (pH 12) after NO bubbling for 5 min.

min. This increase was caused by the “disproportionation” of the NO remaining in the solution in the spectrometer cell. Hence, the concentration of NO immediately after bubbling for 5 min must be more than double the increase in  $\text{NO}_2^-$  due to a counter-species, i.e. more than ca. 2 mM. Since the counter-species was not detected by the UV-visible examination, we assumed the existence of possible “disproportionation” reactions, including the production of  $\text{NO}_2^-$  or  $\text{NO}_3^-$ , and calculated the corresponding standard Gibbs energy changes. Reactions producing  $\text{NH}_2\text{OH}$  and  $\text{N}_2\text{H}_4$  were excluded because these species were not found in the solution, as described later. The possible reactions were as follows:



Although  $\text{NO}_2^-$  has already been detected by UV-visible spectroscopy,  $\text{NO}_3^-$  could also be generated thermodynamically by Eqs. (4)–(6). Since all the nitrogen species involved in the above reactions, i.e.  $\text{NO}_3^-$ ,  $\text{NO}_2^-$ ,  $\text{N}_2$ ,  $\text{N}_2\text{O}$  and  $\text{NH}_3$ , were inactive on the Au electrodes, we could not identify the predominant process among Eqs. (1)–(6). However, it should be noted that the coexistence of these products will not affect the results given below because they are electroinactive.

### 3.3. Effect of the three-phase zone

First we examined the effect of the three-phase zone formed at the edge of the electrode in the dipping mode.

The CVs obtained on Au(111) in contact with the solution containing dissolved NO and with NO and Ar gas phases are compared in Fig. 4. It can be seen that the current under the NO flow in gas phase is more than 10 times greater than that under Ar flow, suggesting a large contribution of NO from the gas phase. Such a large contribution would make it difficult to examine the effect of the surface structure on the electrode reaction. Therefore the results reported in the remainder of this paper were obtained under Ar flow.

### 3.4. Electroreduction of NO

Figure 4(b) shows the CV obtained at  $50 \text{ mV s}^{-1}$  on Au(111) in NO-saturated  $\text{Na}_3\text{PO}_4$  (pH 12) under Ar flow. The electrode potential was first scanned in the positive direction from 0.9 V and then in the negative direction. The cathodic current started at ca. 0.25 V and formed a peak at ca. 0.03 V. This peak was enhanced at a higher scan rate, but not as much as expected from a proportional relation. This peak is attributed to a transient change in the NO concentration near the electrode surface. A similar phenomenon (called overshoot) has been observed in  $\text{O}_2$  reduction [28]. At more negative potentials the hydrogen evolution reaction became predominant. The broken curve in Fig. 4(b) represents the hydrogen evolution current in the blank solution. When the electrode potential was reversed to a negative limit of  $-0.6 \text{ V}$ , a constant cathodic current of ca.  $0.1 \text{ mA cm}^{-2}$  flowed in the potential region

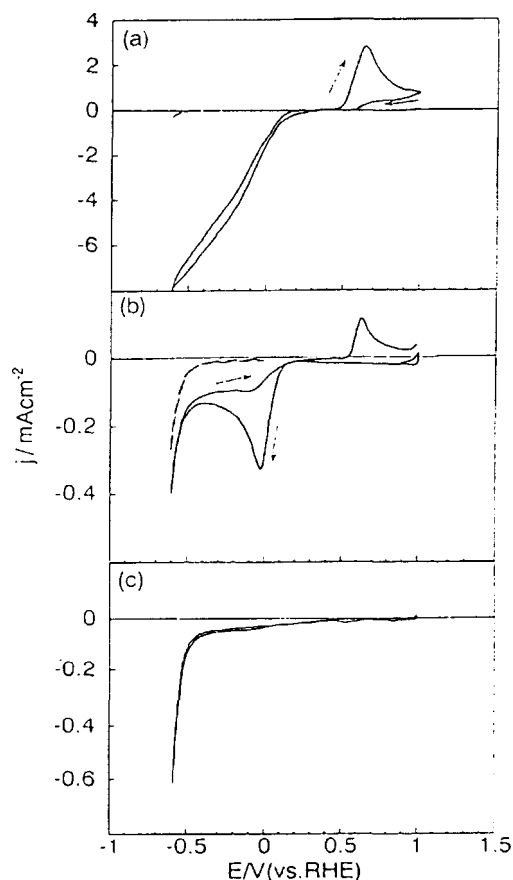


Fig. 4. CVs obtained on Au(111) in solutions containing dissolved NO (pH = 11.9) with (a) NO flow and (b) Ar flow in the gas phase, and (c) after purging by bubbling with Ar for 15 min (scan rate,  $50 \text{ mV s}^{-1}$ ). The scan was initiated from 0.9 V in the positive direction.

up to  $-0.05$  V. In contrast with a Pt electrode [8], the current obtained on Au does not decrease in the above potential region. This is because Au does not adsorb the hydrogen. This constant current represents the limiting diffusion current of the dissolved NO, and is several times smaller than the limiting current observed for  $H_2$  ionization. If we take into account multielectron transfer in NO reduction, the NO concentration will be a tenth of the  $H_2$  concentration, i.e. ca.  $0.1$  mM. Such a low NO concentration can be attributed to NO consumption due to the continuous "disproportionation" and escape from the solution surface to the gas phase. In the positive-going scan, the anodic peak appeared clearly at ca.  $0.6$  V and increased with increasing scan rate. This behavior will be discussed later.

Figs. 5(a) and 5(b) show CVs obtained on Au(100) and Au(110). The results were the same as that for Au(111). The cathodic wave at  $< 0.25$  V and the anodic peak at  $0.6$  V were seen on all the surfaces. Therefore we can conclude that the reactions which cause the cathodic wave and the anodic peak are almost surface-structure insensitive, in contrast with the case of Pt single-crystal electrode. The only difference noticed was the broad cathodic hump centered at ca.  $0.6$  V in the negative-going scan on Au(100) and Au(110) but not on Au(111). The electric charge for this hump was about  $1$  mC  $cm^{-2}$ . This value is too large to be explained by reconstruction of the electrode surface and its subsequent lifting or by specific adsorption of phosphate anions. Thus a reduction involving nitrogen compounds should occur. The DEMS experiment showed that NO is reduced to  $N_2O$  in this potential region, as described later.

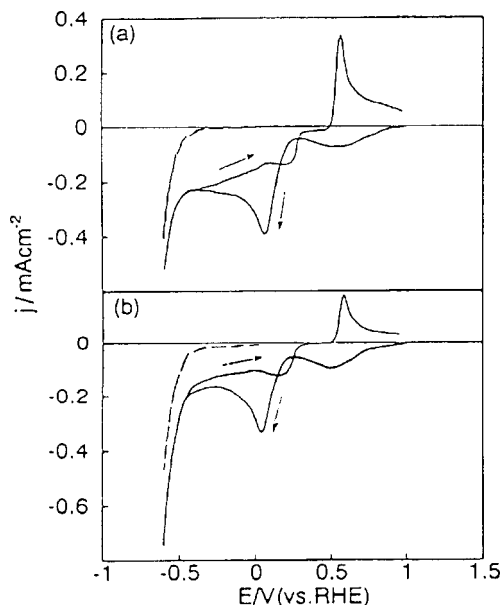


Fig. 5. CVs obtained on (a) Au(100) and (b) Au(110) in  $Na_3PO_4$  solution containing dissolved NO (pH 11.9) (scan rate,  $50$  mV  $s^{-1}$ ). The scan was initiated from  $0.9$  V in the positive direction.

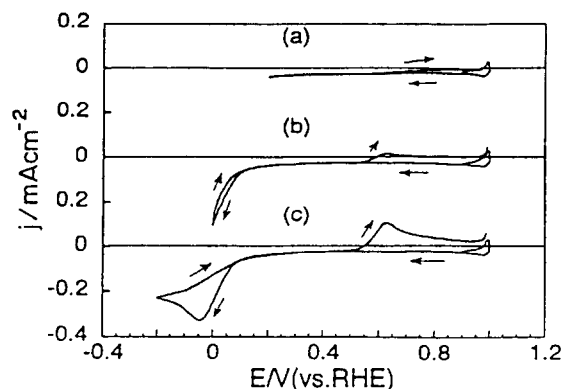


Fig. 6. CVs with a negative limiting potential of (a)  $0.2$  V, (b)  $0$  V and (c)  $-0.2$  V on Au(111) in solution containing dissolved NO (scan rate,  $50$  mV  $s^{-1}$ ). The scan was initiated from  $0.9$  V in the positive direction.

We recorded CVs after bubbling Ar for  $15$  min in order to purge the dissolved NO (Fig. 4(c)). All peaks except the hydrogen evolution current disappeared, though  $NO_2^-$  remained in the solution as a result of the "disproportionation". The same CV was observed in the solution containing only  $NO_2^-$ . Thus all peaks in Figs. 4(b), 5(a) and 5(b) are attributed to dissolved NO.

In order to determine whether there was a relation between the cathodic wave and the anodic peak at  $0.6$  V, we changed the negative limiting potential from  $0.2$  V to  $0$  V and  $-0.2$  V. The results are shown in Fig. 6. At  $0.2$  V no anodic peak appeared, suggesting that this peak is not due to the direct oxidation of NO. The anodic peak began to appear when the limiting potential became negative of  $0.2$  V. The more negative it became, the larger was the peak. Thus, we conclude that this anodic peak is due to the re-oxidation of products formed from NO at potentials below  $0.2$  V in the preceding negative-going scan. We estimated the ratio of the charge of the anodic peak to that of the cathodic waves in a potential range from  $-0.4$  to  $0.25$  V (both in the negative- and positive-going scans). The results were  $24\%$ ,  $23\%$  and  $18\%$  on Au(111), Au(100) and Au(110) at  $50$  mV  $s^{-1}$ . These values show that a large amount of the product in the cathodic waves diffuses out into the solution before re-oxidation in the following anodic peak, provided that the same number of electrons is involved in both processes. The ratio was dependent on sweep rate. For example on Au(111) it was  $1.9\%$  at  $5$  mV  $s^{-1}$  and  $30\%$  at  $100$  mV  $s^{-1}$ . At a slower sweep rate, more product can diffuse out and hence a smaller anodic peak is obtained. This result supports the conclusion that the anodic peak is due to the re-oxidation of the reduced products.

Possible reduction products of NO with a lower oxidation number are  $N_2$ ,  $N_2O$ ,  $NH_2OH$ ,  $N_2H_4$  and  $NH_3$ . However,  $N_2$ ,  $N_2O$  and  $NH_3$  were electroinactive on Au electrodes in alkaline solution, and  $N_2$  and  $N_2O$  were excluded from the DEMS experiments (as described later).

$\text{NH}_2\text{OH}$  and  $\text{N}_2\text{H}_4$  were electroactive and oxidized on the Au electrode as shown in Figs. 7(a)–7(d) recorded at 5 and 100  $\text{mV s}^{-1}$  on Au(110). These reactions were also structure insensitive. In both CVs of  $\text{NH}_2\text{OH}$  and  $\text{N}_2\text{H}_4$ , the same anodic peak appeared at about 0.6 V and almost constant anodic currents flowed after the peak. These constant currents are assumed to be due to the limiting diffusion of  $\text{NH}_2\text{OH}$  and  $\text{N}_2\text{H}_4$  as discussed later. Bubbling Ar through the solution for 15 min had no effect on the CVs. This suggests that the concentrations of  $\text{NH}_2\text{OH}$  (0.1–2 mM) and  $\text{N}_2\text{H}_4$  (2 mM) do not change, and that these substances are non-volatile even in alkaline solution. Hence, if  $\text{NH}_2\text{OH}$  and/or  $\text{N}_2\text{H}_4$  are formed in the "disproportionation", the anodic peak at 0.6 V should appear after purging NO by Ar bubbling, which was not the case (Fig. 5(c)).

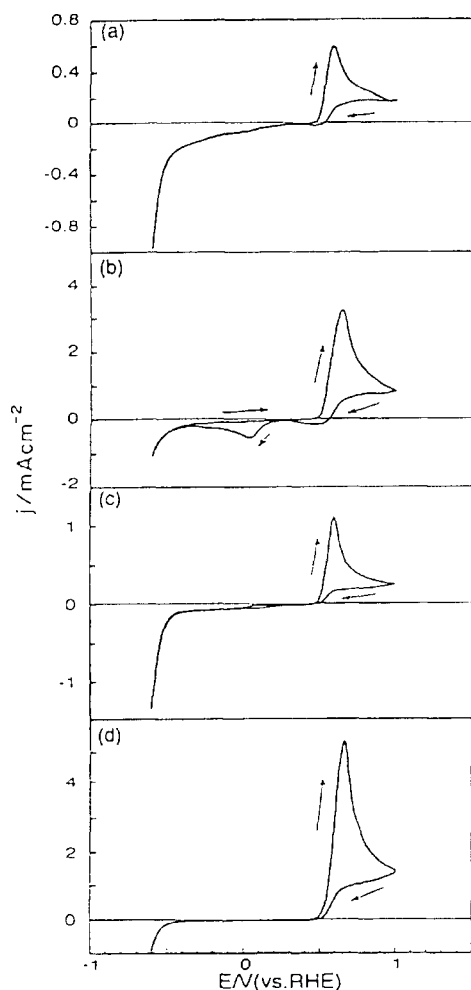
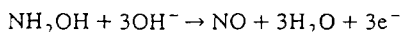
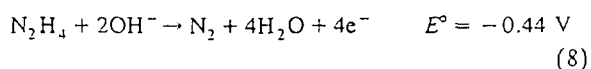


Fig. 7. CVs on Au(110) in  $\text{Na}_3\text{PO}_4$  (pH 11.9) + 1 mM  $(\text{NH}_2\text{OH})_2\text{SO}_4$  at (a) 5  $\text{mV s}^{-1}$  and (b) 100  $\text{mV s}^{-1}$ , and in  $\text{Na}_3\text{PO}_4$  (pH 11.9) + 2 mM  $\text{N}_2\text{H}_4\text{SO}_4$  at (c) 5  $\text{mV s}^{-1}$  and (d) 100  $\text{mV s}^{-1}$ .

Although the same anodic peak was observed in the CVs of  $\text{NH}_2\text{OH}$  and  $\text{N}_2\text{H}_4$ , the oxidation products will be different since, at the high scan rate of 100  $\text{mV s}^{-1}$ , the negative-going scan in the CV gave the cathodic peak at ca. 0.03 V, which has already been attributed to NO, for  $\text{NH}_2\text{OH}$  but not for  $\text{N}_2\text{H}_4$ . This suggests that  $\text{NH}_2\text{OH}$  is oxidized to NO at the anodic peak. Some of the NO produced in this way remains near the electrode surface and is reduced in the negative-going scan. In the case of  $\text{N}_2\text{H}_4$ ,  $\text{N}_2$  is generated at the anodic peak as described in the next section. Thus the oxidation processes can be expressed as follows:

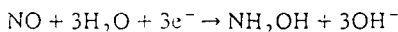


$$E^\circ = 0.264 \text{ V} \quad (7)$$



These reactions are thermodynamically possible (pH 12). In addition, the ratio of the limiting current of the oxidation of  $\text{NH}_2\text{OH}$  (2 mM) to that of  $\text{N}_2\text{H}_4$  (2 mM) in Fig. 7 is 0.8 at 5  $\text{mV s}^{-1}$  and 0.7 at 100  $\text{mV s}^{-1}$ . These values are close to the value of 0.75 expected from Eqs. (7) and (8).

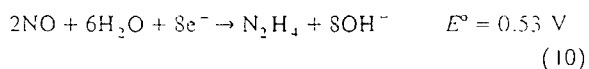
In view of the above results, we finally interpret the CV of NO (Fig. 5(b)) as follows. The NO dissolved in alkaline solution is reduced to  $\text{NH}_2\text{OH}$  at potentials below 0.25 V in the negative-going scan, giving the cathodic wave:



$$E^\circ = 0.264 \text{ V} \quad (9)$$

Then the product  $\text{NH}_2\text{OH}$  is re-oxidized to NO at ca. 0.6 V in the following positive-going scan, giving the anodic peak.

The formation of  $\text{N}_2\text{H}_4$  may be possible in the reduction of NO:



However, it was excluded as explained below.

### 3.5. DEMS experiments

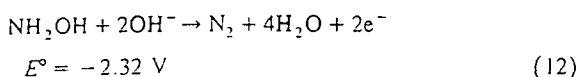
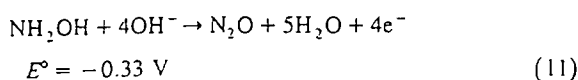
We performed in-situ one-point touch DEMS measurements in order to obtain direct evidence for the interpretation suggested above.

First, in order to confirm the products of the  $\text{N}_2\text{H}_4$  oxidation, i.e. Eq. (8), the MSCV (5  $\text{mV s}^{-1}$ ) of  $\text{N}_2\text{H}_4$  was recorded on the three planes. As for the CV, no dependence of the product distribution on surface structure was found. Fig. 8 shows the result for Au(111). The signal intensity at  $m/e = 28$  ( $\text{N}_2$ ) increased from ca. 0.5 V in accord with the anodic peak in the CV (Fig. 7(c)), although a time lag was noticed. This time lag is due to diffusion of products in the solution and the Teflon mem-



brane. No other volatile products, such as NO ( $m/e = 30$ ),  $N_2O$  ( $m/e = 44$ ) and  $NO_2$  ( $m/e = 46$ ), were detected. Thus, Eq. (8) is confirmed.

Fig. 9 shows the MSCV ( $2 \text{ mV s}^{-1}$ ) of  $NH_2OH$  on Au(111). The signal intensities of  $N_2$  ( $m/e = 28$ ),  $N_2O$  and NO changed in the potential region around the anodic peak in the CV of  $NH_2OH$ . The maximum increase in the MS current is in the ratio  $\Delta J(NO) : \Delta J(N_2) : \Delta J(N_2O) = 1 : 0.17 : 0.063$ , and hence NO can be assumed to be the main product, supporting the above interpretation (Eq. (7)). Small quantities  $N_2$  and  $N_2O$ , which were not detected on the CV, are formed as by-products by the following reactions:



Again, the product distribution was insensitive to surface structure.

Thus in the negative-going scan the NO produced at the anodic peak by Eq. (7) is reduced to  $NH_2OH$  by Eq. (9), but the corresponding peak at ca. 0.03 V was not observed on the CV at a slow scan rate such as  $5 \text{ mV s}^{-1}$  (Fig. 7(a)) because of the loss of products by diffusion into the bulk of the solution.  $NO_2$  ( $m/e = 46$ ) was not detected by DEMS.  $NO_2$  dissolves easily in alkaline media, and hence we cannot establish the formation of  $NO_2$  conclusively.

Finally, we examined the MSCV of NO. In this case,

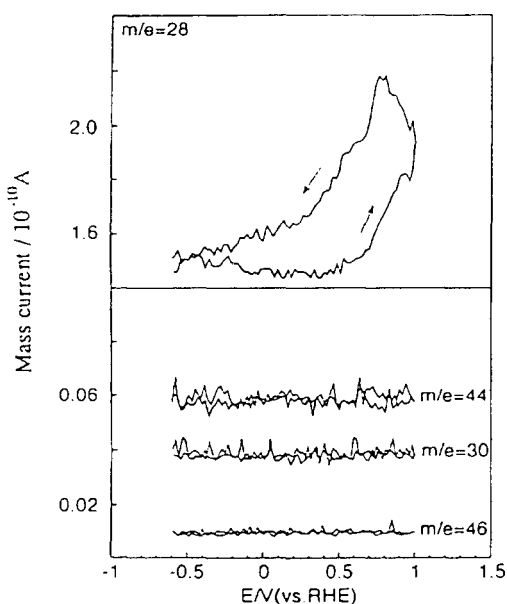


Fig. 8. MSCV for Au(111) in  $Na_3PO_4$  (pH 11.9) +  $5 \text{ mM } N_2H_4SO_4$  (scan rate,  $5 \text{ mV s}^{-1}$ ).

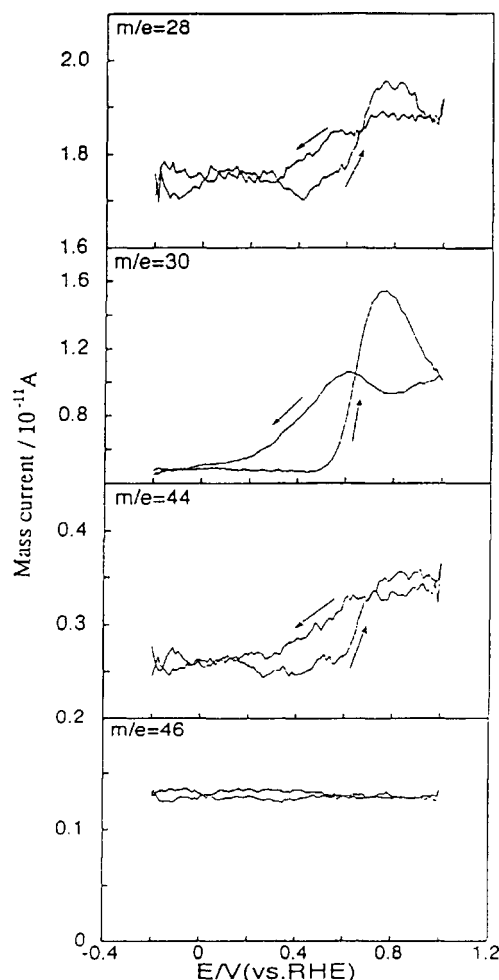


Fig. 9. MSCV for Au(111) in  $Na_3PO_4$  (pH 11.9) +  $5 \text{ mM } NH_2OH$  (scan rate,  $2 \text{ mV s}^{-1}$ ).

measurements were performed with NO flowing over the solution in order to avoid a baseline shift. Fig. 10 shows the MSCV observed on Au(110) at  $5 \text{ mV s}^{-1}$ . The MS signals of NO,  $N_2$  and  $N_2O$  clearly increased from ca. 0.5 V in the positive-going scan, in accordance with the CV, demonstrating that oxidation of  $NH_2OH$  takes place. The ratio  $\Delta J(NO) : \Delta J(N_2) : \Delta J(N_2O)$  was  $1 : 0.17 : 0.065$ , exactly as in Fig. 9. This confirms that the dissolved NO is reduced to  $NH_2OH$  in the negative-going scan. In fact, the MSCV did not show any signals for the gaseous products of  $N_2$  and  $N_2O$  in the corresponding potential range. The formation of  $N_2H_4$  is also excluded since, if it is formed, the proportion of  $\Delta J(N_2)$  should be enhanced by Eq. (8), which was not the case. In our previous work on Pt(100) [8], NO was reduced to  $NH_3$  with a current efficiency in excess of 80%. The difference is attributed to the stability of the reaction intermediate of nitrosyl group on Pt(100).

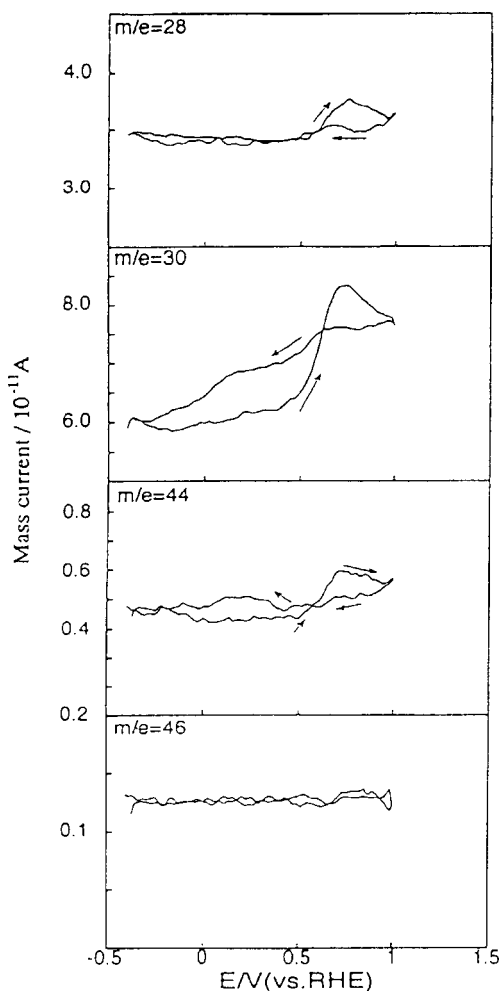


Fig. 10. MSCV for Au(110) in  $\text{Na}_3\text{PO}_4$  (pH 11.9) containing dissolved NO (scan rate:  $5 \text{ mV s}^{-1}$ ).

The process from  $\text{NH}_2\text{OH}$  to  $\text{NH}_3$  can be taken as structure sensitive.

There is a slight increase in the  $\text{N}_2\text{O}$  signal intensity ( $m/e = 44$ ) in the negative-going scan before the potential reaches the region of the main reduction. This corresponds to the broad hump observed on the CV at ca. 0.6 V on Au(110) (Fig. 5(b)). A similar increase is expected on Au(100) as its CV has the same shape as that on Au(110) (Fig. 5(a)).

### Acknowledgement

This work was supported by Grant-in-Aid 05453116 from the Ministry of Education, Science and Culture, Japan.

### References

- [1] W.J. Plieth in A.J. Bard (Ed.), *Encyclopedia of Electrochemistry of the Elements*, Vol. 8, Dekker, New York, 1978, Ch. 5.
- [2] D. Dutta and D. Landolt, *J. Electrochem. Soc.*, 119 (1972) 1320.
- [3] L.J. Janssen, M.M. Pieterse and E. Barendrecht, *Electrochim. Acta*, 22 (1977) 27.
- [4] G.R. Gao and L. Meites, *J. Phys. Chem.*, 70 (1966) 3260.
- [5] H.N. Heckner, *J. Electroanal. Chem.*, 83 (1977) 51.
- [6] D. Moeller and K.H. Heckner, *J. Electroanal. Chem.*, 36 (1972) 277.
- [7] S. Wasmus, E.J. Vasini, M. Krausa, H.T. Mishima and W. Vielstich, *Electrochim. Acta*, 39 (1994) 23.
- [8] S. Ye, H. Hattori and H. Kita, *Ber. Bunsenges. Phys. Chem.*, 96 (1992) 1884.
- [9] A. Rodes, R. Gomez, J.M. Orts, J.M. Feliu and A. Aldaz, *J. Electroanal. Chem.*, 359 (1993) 315.
- [10] A. Ahmadi, E. Bracey, R.W. Evans and G. Attard, *J. Electroanal. Chem.*, 350 (1993) 297.
- [11] C.T. Garcia, A.J. Calandra and A.J. Arvia, *Electrochim. Acta*, 17 (1972) 2181.
- [12] H.W. Salzberg, *J. Electrochem. Soc.*, 121 (1974) 1451.
- [13] T. Hachiya, H. Honbo and K. Itaya, *J. Electroanal. Chem.*, 315 (1991) 275.
- [14] X.P. Gao, A. Hamelin and M.J. Weaver, *Phys. Rev. Lett.*, 67 (1991) 618.
- [15] A. Friedrich, B. Pettinger, D.M. Kolb, G. Lupke, R. Steinhoff and G. Marowsky, *Chem. Phys. Lett.*, 163 (1989) 123.
- [16] D.M. Kolb and J. Schneider, *Electrochim. Acta*, 31 (1986) 929.
- [17] S. Strbac, A. Hamelin and R.R. Adzic, *J. Electroanal. Chem.*, 362 (1993) 47.
- [18] Y. Gao, H. Tsuji, H. Hattori and H. Kita, *J. Electroanal. Chem.*, 372 (1994) 195.
- [19] J. Clavilier, R. Faure, G. Guinet and R. Durand, *J. Electroanal. Chem.*, 107 (1980) 205.
- [20] H. Kita, S. Ye, A. Aramata and N. Furuya, *J. Electroanal. Chem.*, 295 (1990) 317.
- [21] X.P. Gao and M.J. Weaver, *J. Electroanal. Chem.*, 367 (1994) 259.
- [22] H. Honbo, S. Sugawara and K. Itaya, *Anal. Chem.*, 62 (1990) 2424.
- [23] A. Hamelin, *J. Electroanal. Chem.*, 165 (1984) 167.
- [24] K. Engelsmann, W.J. Lorenz and E. Schmidt, *J. Electroanal. Chem.*, 114 (1980) 1.
- [25] N. Furuya and S. Motoo, *J. Electroanal. Chem.*, 98 (1979) 189.
- [26] N.J. Tao, J. Pan, Y. Li, P.I. Oden, J.A. Deroose and S.M. Lindsay, *Surf. Sci. Lett.*, 271 (1992) 338.
- [27] Chemical Society of Japan (Ed.), *Kagakubinran* (4th edn.), Maruzen, Tokyo, 1993.
- [28] H. Kita, H.W. Lei and Y. Gao, *J. Electroanal. Chem.*, 379 (1994) 407.

Jointly published by  
Elsevier Science B.V., Amsterdam  
and Akadémiai Kiadó, Budapest

React.Kinet.Catal.Lett.,  
Vol. 56, No. 2, 363-369  
(1995).

RKCL2734

THERMAL ACTIVATION OF KF/ALUMINA CATALYST FOR DOUBLE BOND  
ISOMERIZATION AND MICHAEL ADDITION

Hideto Tsuji, Hajime Kabashima, Hideaki Kita and  
Hideshi Hattori\*

Center for Advanced Research of Energy Technology (CARET),  
Hokkaido University, Sapporo 060, Japan

*Received May 4, 1995*  
*Accepted June 20, 1995*

KF/alumina catalyst exhibits activity for double bond isomerization of 1-pentene at 273 K when pretreated in vacuo in the temperature range 573-673 K, while the activity for Michael addition of nitromethane to butene-2-one does not change much with the pretreatment temperature.

INTRODUCTION

Since KF/alumina was introduced by Clark and Ando et al. [1] as an effective solid catalyst to promote many base-catalyzed reactions [2], the catalyst has been widely applied to many organic syntheses [3]. Because the basic sites on KF/alumina are possibly related to the very hard anion F<sup>-</sup>, the catalyst may show characteristic performances which

0133-1736/95/US\$ 9.50.  
© Akadémiai Kiadó, Budapest.  
All rights reserved.

differentiate KF/alumina from the oxide type solid base catalysts such as alkaline earth oxides [4].

In organic syntheses, KF/alumina has been used in most cases with a drying pretreatment below 473 K. Such a pretreatment, however, will leave the possibility that considerable amounts of H<sub>2</sub>O and CO<sub>2</sub> still remain on the surface and block the active sites. In the present work, we attempted to activate KF/alumina by thermal treatment at various higher temperatures, and found that KF/alumina revealed the active sites for double bond isomerization of 1-pentene on the thermal treatment above 573 K. We also examined the dependence of the catalytic activity of KF/alumina for Michael addition of nitromethane to butene-2-one on the pretreatment temperature.

#### EXPERIMENTAL

KF/alumina was purchased from Fluka. Calcium oxide used as a reference catalyst was prepared by *in situ* decomposition of Ca(OH)<sub>2</sub> (Kanto Chemicals) at 873 K. The BET surface area was measured by nitrogen adsorption at liquid nitrogen temperature. All reactants were purified by passage through 3A molecular sieves to be free from water and carbon dioxide.

Isomerization of 1-pentene was carried out in an H-shaped glass batch reactor. The two branches of the reactor were separated by a breakable seal. A sample of the catalyst was placed in one branch, outgassed at an elevated temperature for 2 h, and sealed. Purified 1-pentene was stored in the other branch until it was introduced through the breakable seal by distillation into the branch containing the catalyst thermostated at liquid nitrogen temperature. Reaction was initiated by melting the reactant rapidly at a reaction temperature of 273 K followed by stirring. After certain reaction time, the products were filtered out from the catalyst and then analyzed by GC with an OV-101 capillary column.

Michael addition of nitromethane to butene-2-one was carried out by the same procedures. The products were analyzed by GC with DEGS column.

## RESULTS AND DISCUSSION

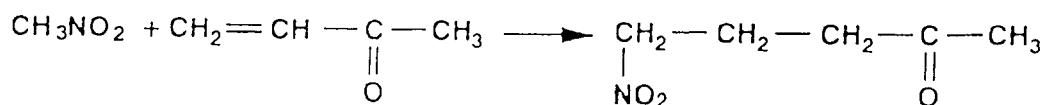
The catalytic activity of KF/alumina for the 1-pentene isomerization at 273 K is shown in Fig.1 as a function of the pretreatment temperature. With the increase of the pretreatment temperature, the activity appeared at 573 K and reached a maximum at 623 K. The products were composed exclusively of *cis*- and *trans*-2-pentenenes. The activity rapidly decreased with a further increase of the pretreatment temperature above 623 K, and disappeared at 723 K. The fact that the catalyst needs to be outgassed at the temperatures above 573 K to reveal the active sites for the 1-pentene isomerization indicates that the active sites are covered with water and/or carbon dioxide when pretreated below 573 K. We also observed that the activity disappeared when the thermally activated catalyst was exposed to air.

The activities and selectivities of  $\gamma$ -alumina (reference catalyst JRC-ALO4 supplied from Catalysis Society of Japan), non-supported KF (spray dried type supplied by Fluka), and CaO for the 1-pentene isomerization were also examined, respectively. The CaO catalyst pretreated at 873 K exhibited much higher activity than the KF/alumina pretreated at 623 K, but  $\gamma$ -alumina pretreated at 623 K and non-supported KF pretreated at 623 K did not show any appreciable activity. The activity of non-supported KF is taken to be much lower than that of KF/alumina even a small surface area of non-supported KF ( $0.5\text{m}^2\text{g}^{-1}$ ) was taken into account. This suggests that the active sites of the KF/alumina preheated above 573 K are generated by the interaction of KF with the surface of alumina.

We found a high *cis/trans* ratio in the products of 2-pentene at a conversion of 90 % on the KF/alumina. It is well known that solid base catalysts exhibit a high selectivity for *cis*-2-olefin in the 1-olefin isomerization since the intermediates are stabilized in the *cis*-form  $\pi$ -allylic anion [4]. However, in the case of many oxide type solid base catalysts such as alkaline earth oxides, the product distribution appears close to the equilibrium one at a high conversion since rotational isomerization between *cis*- and *trans*-2-olefin occurs. A high *cis/trans* ratio observed for KF/alumina at a high conversion suggests that the rotational isomerization is slow on the KF/alumina. This will be one of the characteristic features for the solid base catalyst in which  $F^-$  anions act as basic sites.

The surface areas of KF/aluminas pretreated at 573, 673 and 773 K were 39, 38 and 31 m<sup>2</sup>g<sup>-1</sup>, respectively. The surface area did not change much in the pretreatment temperature range of 573 K to 773 K. It is concluded that the rapid decrease in the activity of KF/alumina above a pretreatment temperature of 673 K is not caused by the decrease in the surface area. The surface chemical state of the KF/alumina seems to change with thermal treatment above 673 K.

Michael addition of nitromethane to butene-2-one proceeds on KF/alumina to produce 5-nitropentane-2-one.



The catalytic activities of KF/alumina pretreated at different temperatures for Michael addition of nitromethane to butene-2-one are also shown in Fig.1. The activities of  $\gamma$ -alumina and CaO were negligibly small, but non-supported KF exhibited an activity of about 1% to that of KF/alumina. The

activity was also obtained by the pretreatment of KF/alumina at 623 K.

The pretreatment temperature dependence for Michael addition was different from that for the 1-pentene isomerization. Ando et al. reported [5] that the catalytic activity for Michael addition of nitroethane to butene-2-one was lower on the KF/alumina dried at 873 K (760 Torr) than that

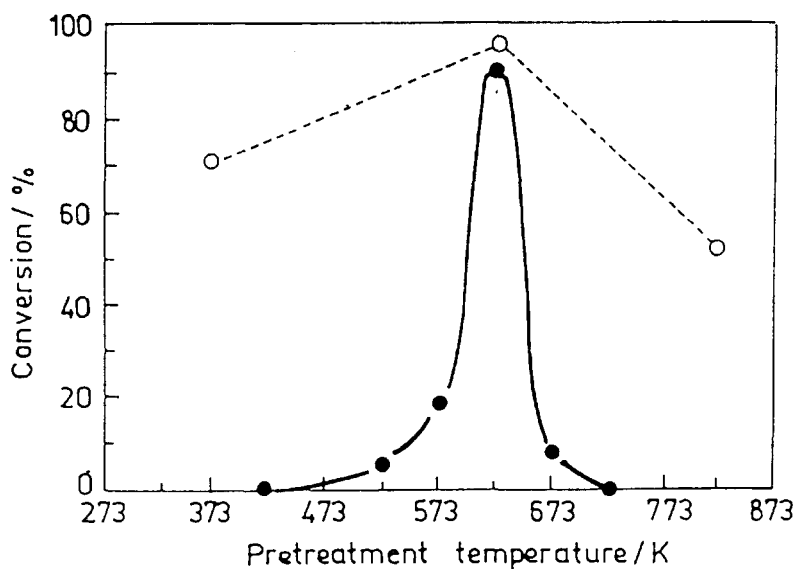


Fig. 1. Variation of the activities of Fluka KF/alumina for 1-pentene isomerization and Michael addition of nitromethane to butene-2-one at 273 K as a function of pretreatment temperature.

- (●) 1-pentene isomerization; KF/alumina, 200 mg; 1-pentene, 4 mmol; Reaction time, 0.5 h
- (○) Michael addition of nitromethane to butene-2-one; nitromethane, 12 mmol; butene-2-one, 4 mmol; Reaction time, 0.5 h; Conversion was calculated by the decrease in butene-2-one percentage

dried at 473 K (0.1 Torr). They also asserted that the decrease in the activity on the highly dried catalyst resulted from blocking pore structure which has the ability to entrap the reactant. Nevertheless, the highly dried catalyst exhibits the activity for Michael addition to some extent in the results. We also observed the activity of KF/alumina pretreated at 823 K in vacuo for Michael addition of nitromethane to butene-2-one. The conversion was 56 % relative to that of the catalyst pretreated at 623 K under the same reaction conditions. The fact that the activity for Michael addition did not change much with the pretreatment temperature in contrast to a large change in the activity for the 1-pentene isomerization indicates that the active sites for these reactions are different. The considerable activity for Michael addition and the negligible activity for the 1-pentene isomerization over non-supported KF also suggest that the active sites for these reactions are different. Consequently, at least two types of basic sites are taken to be generated on KF/alumina. Their generation depends strongly upon the pretreatment conditions.

As for basic sites on KF/alumina, several active species on the surface were proposed [5-7]. Weinstock et al. proposed that the enhanced reactivity of KF/alumina was a consequence of potassium hydroxide and/or aluminate formation by the reaction of KF with alumina surface [6]. On the other hand, Ando et al. carried out a titration analysis of the basic sites on KF/alumina [7]. They reported that all the reactivity cannot be explained by the presence of potassium hydroxide and/or aluminate, and the active fluoride also contributes to the strong basicity. However, none of these active species has been confirmed as yet. Although elucidation of the definite active sites for the reactions is not possible at present, the possibility to control the generation of different active sites on KF/alumina by the thermal treatment is demonstrated in the present study.



been confirmed as yet. Although elucidation of the definite active sites for the reactions is not possible at present, the possibility to control the generation of different active sites on KF/alumina by the thermal treatment is demonstrated in the present study.

## REFERENCES

1. J.H.Clark: *Chem.Rev.*, **80**, 429 (1980); T.Ando, J.Yamawaki: *Synth.Org.Chem.Jpn.*, **39**, 14 (1981).
2. J.H.Clark, D.G.Cork, M.S.Robertson: *Chem.Lett.*, 1145(1983); J.Yamawaki, T.Kawate, T.Ando, T.Hanafusa: *Bull.Chem.Soc.Jpn.*, **56**, 1885 (1983); D.Villemin: *J.Chem. Soc.Chem.Comm.*, 1092 (1983); D.Villemin: *Chem.Ind. (London)*, 166(1985); J.M.Campelo, M.S.Climent, J.M.Marinas: *React.Kinet.Catal.Lett.*, **47**, 7 (1992).
3. D.Villemin, M.Ricard: *Tetrahedron Lett.*, **25**, 1059 (1984); D.Villemin, R.Racha: *Tetrahedron Lett.*, **27**, 1789 (1986); A.B.Alloun, D.Villemin: *Synth. Commun.*, **19**, 2567 (1989); D.Villemin, A.B.Alloun: *ibid.*, **20**, 3325 (1990); D.Villemin, A.B.Alloun: *ibid.*, **22**, 1351 (1992).
4. K.Tanabe, M.Misono, Y.Ono, H.Hattori: *New Solid Acids and Bases*, Kodansha, Tokyo, 1989.
5. T.Ando, S.J.Brown, J.H.Clark, D.G.Cork, T.Hanafusa, J.Ichihara, J.M.Miller, M.S.Robertson: *J.Chem.Soc., Perkin Trans., 2*, 1133 (1986).
6. L.M.Weinstock, J.M.Stevenson, S.A.Tomellini, S.H.Pan, T.Utne, R.B.Jobson, F.Reinhold: *Tetrahedron Lett.*, **27**, 3845 (1986).
7. T.Ando, J.H.Clark, D.G.Cork, T.Hanafusa, J.Ichihara, T.Kimura: *Tetrahedron Lett.*, **28**, 1421 (1987).



ELSEVIER

Physica B 208 &amp; 209 (1995) 649–650

PHYSICA B

# The state of platinum in a $\text{Pt}/\text{SO}_4^{2-}/\text{ZrO}_2$ super acid catalyst

T. Tanaka<sup>a,\*</sup>, T. Shishido<sup>b</sup>, H. Hattori<sup>b</sup>, K. Ebitani<sup>c</sup>, S. Yoshida<sup>a</sup><sup>a</sup>*Division of Molecular Engineering, School of Engineering, Kyoto University, Kyoto 606-01, Japan*<sup>b</sup>*Graduate School of Environmental Earth Science, Hokkaido University, Sapporo 060, Japan*<sup>c</sup>*Department of Chemical Engineering, Tokyo Institute of Technology, Meguro-ku 103, Japan*

## Abstract

The state of platinum in a  $\text{Pt}/\text{SO}_4^{2-}/\text{ZrO}_2$  super acid catalyst has been investigated by means of Pt L-edge XAFS. The XANES showed that Pt is electron deficient after the activation by hydrogen treatment, while EXAFS results indicated the presence of Pt–O and Pt–Pt pairs as in  $\text{PtO}_2$  and Pt metal, respectively. The reported contradictory results that Pt is metallic by XRD analysis and Pt is in an oxidized state by XPS are explained by the present work; an oxidized platinum particle with a metallic core is present in the activated catalyst.

## 1. Introduction

It has been reported by several groups that the addition of platinum to  $\text{SO}_4^{2-}/\text{ZrO}_2$  enhances catalytic performance in the skeletal isomerization of alkanes in the presence of hydrogen [1]. However, the role and the state of platinum have been left unclear and the several hypotheses are now in conflict. There are three kinds of different interpretation of X-ray photoelectron spectra of Pt on  $\text{SO}_4^{2-}/\text{ZrO}_2$ : (1) Pt is mainly in an oxidized state with some metallic phase inside [2]; (2) Pt is sulfided in the activated catalyst [3], and (3) Pt is metallic even after calcination in air [4]. To elucidate the state of platinum, we carried out XAFS experiment for Pt L-edge absorption. We will report the state of Pt on  $\text{SO}_4^{2-}/\text{ZrO}_2$  elucidated from XANES/EXAFS analyses.

## 2. Experimental

A  $\text{Pt}/\text{SO}_4^{2-}/\text{ZrO}_2$  sample (Pt loading: 0.5 wt%) was prepared as reported previously [2]. X-ray absorption

(XA) experiments were carried out at BL7C station at Photon Factory in National Laboratory for High Energy Physics (proposal no. 90-154). The sample was dealt under an inert condition during the XA experiment to avoid the oxidation.

## 3. Results and Discussion

Fig. 1 shows Pt  $L_3$ -edge XANES of the sample after calcination, as well as after subsequent treatment with  $\text{H}_2$  together with that of Pt foil and  $\text{PtO}_2$ . Large white line absorption in the case of  $\text{PtO}_2$  is due to the vacancy in 5-d orbitals of Pt atoms. In the case of the calcined sample, white line is more intense than that for Pt foil, showing that Pt is electron-deficient. The white line height decreased by  $\text{H}_2$  treatment of the sample, suggesting that platinum is reduced. However, still the absorption is more intense than that of Pt foil. The absorption at high energy side, the oscillation by EXAFS is seen for both the samples. The oscillation is similar to that of Pt foil but intensity is much weaker although the presence of platinum metal particle was found by XRD. This may be due to the coexistence of another Pt compound or

\* Corresponding author.

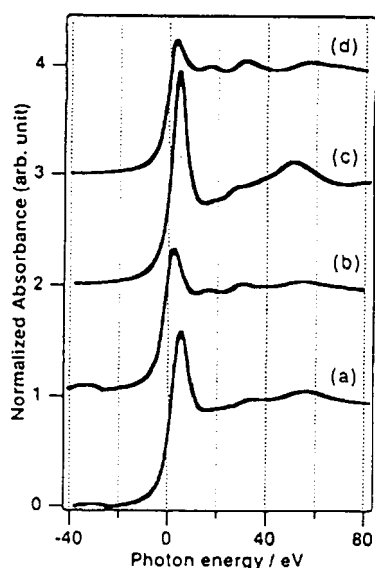


Fig. 1. Normalized Pt  $L_{3}$ -edge XANES of (a) calcined  $\text{Pt}/\text{SO}_4^{2-}/\text{ZrO}_2$ , (b)  $\text{H}_2$ -treated  $\text{SO}_4^{2-}/\text{ZrO}_2$ , (c)  $\text{PtO}_2$  and (d) Pt foil.

amorphous phase. The information from XANES, the presence of electron-deficient Pt, is not enough to identify the state of Pt because we can not assert whether Pt is present as electron-deficient metal particles or Pt is a mixture of cations or metal.

Fig. 2 shows the Fourier transforms of Pt  $L_{3}$ -edge  $k^3$ -weighted EXAFS of the samples, Pt foil and  $\text{PtO}_2$ . Both the samples exhibit the peak due to the scattering by neighboring Pt atoms at the same position for Pt–Pt scattering in Pt foil although the height is less than half of that for Pt foil. This indicates that small Pt particles are formed on  $\text{SO}_4^{2-}/\text{ZrO}_2$ . However, an evident peak, which is absent in Pt foil EXAFS, is found in the range of 1–2 Å for both the samples. The position is the same as that found in the case of  $\text{PtO}_2$ , showing that the peak is due to the presence of Pt–O pairs. However, Pt–Pt scattering peak corresponding to that in the case of  $\text{PtO}_2$  is not seen. This implies that Pt–O–Pt configuration is

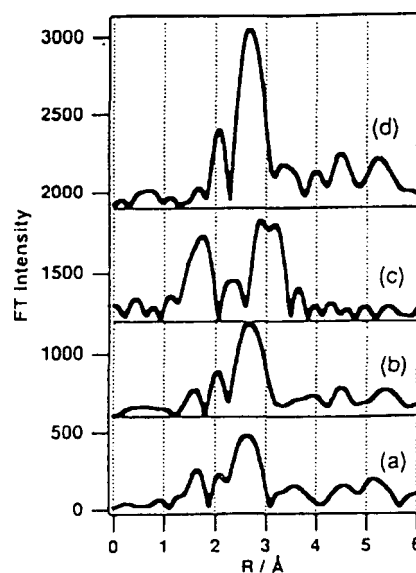


Fig. 2. Fourier transforms of  $k^3$ -weighted EXAFS of (a) calcined  $\text{Pt}/\text{SO}_4^{2-}/\text{ZrO}_2$ , (b)  $\text{H}_2$  treated  $\text{Pt}/\text{SO}_4^{2-}/\text{ZrO}_2$ , (c)  $\text{PtO}_2$  and (d) Pt foil.

absent or disordering if any. This is the direct evidence that Pt oxide phase is present in the sample together with a small Pt metal particles. Taking into account that CO molecules are not adsorbed on the sample [2], we conclude that Pt is present as a particle covered with platinum oxide and containing Pt metal as a core. Therefore, it can be explained that Pt cation was dominantly detected by XPS [2] and the presence of Pt metal particle was shown by XRD [4].

## References

- [1] T. Hosoi et al., *Prep. Symp. Div. Pet. Chem. Am. Chem. Soc.* (1988) 562.
- [2] K. Ebitani et al., *J. Catal.* 135 (1992) 60.
- [3] Z. Páál, M. Muhler and R. Schrögl, *J. Catal.* 143 (1993) 318.
- [4] A. Sayari and A. Dicko, *J. Catal.* 145 (1994) 561.

# Cationic Mobility in MgX Zeolite: An FTIR Study

Gianmarlo Martra, Nadia Damilano and Salvatore Coluccia\*

*Dipartimento di Chimica Inorganica, Chimica Fisica e Chimica dei Materiali, Università di Torino, via P. Giuria 7, 10125 Torino, Italy*

Hidetoshi Tsuji and Hideshi Hattori

*Center for Advanced Research of Energy Technology, Hokkaido University, Sapporo 060, Japan*

The effects of hydration on NaX and MgX zeolites are compared by studying their infrared spectra in the region of the frame vibrational modes. Evidence is found that water promotes the transfer of  $Mg^{2+}$  cations from sites I, inside the prismatic units, to sites I', in the sodalites. These conclusions are supported by the spectra in the far-IR region, where  $Mg^{2+}$ -frame stretching vibrations can be observed.

Zeolites with faujasite framework (X and Y) belong to a class of structurally well defined microporous adsorbents, which are effective catalysts for many chemical reactions. Cations, which are necessary to compensate the extra charge associated with the presence of  $Al^{3+}$ , greatly affect the catalytic properties of the material and, consequently, determination of their nature and location are of great interest both for theoretical and technical purposes. Monovalent and divalent ions have been widely investigated and reviewed, though among alkaline-earth oxides structural characteristics of  $Ca^{2+}$  have been studied in much more detail<sup>1–4</sup> than  $Mg^{2+}$  ions, which have the same charge but considerably smaller size.

Related to this topic, and as a part of a broader analysis of zeolites in which the introduction of basic functions is attempted,<sup>5</sup> an IR study of an MgX sample has been carried out, correlating the observed spectral features to the hydration state of the zeolite, strongly influencing the distribution of the  $Mg^{2+}$  ions in the extraframework sites.

## Experimental

### Materials

The starting material was the sodium form of zeolite X (Linde Molecular Sieves 13X, Si/Al = 1.2). A magnesium-exchanged sample was prepared by exchange of NaX with 1 mol l<sup>-1</sup> aqueous magnesium nitrate solution (0.05 g-zeolite/ml-soln.) at room temperature, followed by washing, drying and calcination (5 h at 823 K in air). Details on preparation and composition have been given previously.<sup>5</sup>

### Measurements

The samples were pressed in the form of self-supported pellets and then placed into IR cells permanently attached to conventional vacuum systems (residual pressure =  $1 \times 10^{-6}$  Torr; 1 Torr = 133 Pa) allowing all thermal treatments and adsorption-desorption experiments to be carried out *in situ*. Pellets for far-IR spectra had to be extremely thin and, consequently, were very fragile.

IR spectra (resolution 4 cm<sup>-1</sup>) were obtained with a Bruker IFS 113v spectrometer. For the far-IR measurements the cell was equipped with silicon windows, and a 6.25 Mylar beam splitter and DTGS detector were employed. All spectra are reported in Absorbance.

Before the adsorption experiments, H<sub>2</sub>O was purified by several freeze-pump-thaw cycles.

Computer graphics modelling was carried out by means of the software program Insight II, distributed by Biosym Technology, running on an SGI 4D/35 workstation.

## Results and Discussion

The medium-IR spectra of the NaX and MgX sample dehydrated at increasing temperature up to 473 K are shown in Fig. 1 and 2, respectively. Two spectral ranges are reported in both cases: range A (1750–1550 cm<sup>-1</sup>), where the absorption due to the deformation mode of the water molecules inside the zeolitic cavities<sup>4</sup> is observed, and range B (800–400 cm<sup>-1</sup>), where bands due to lattice vibrations show up.<sup>1,4</sup>

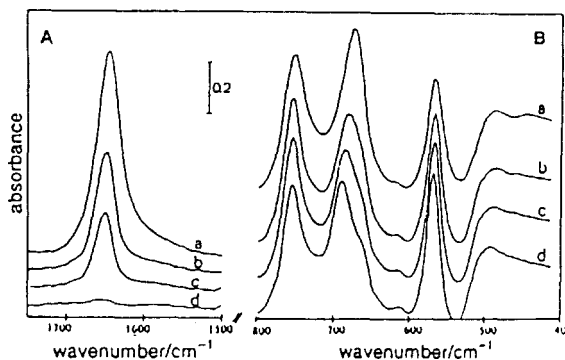


Fig. 1 IR spectra of the NaX sample outgassed at: (a) 300; (b) 323; (c) 373 and (d) 473 K for 40 min at each stage

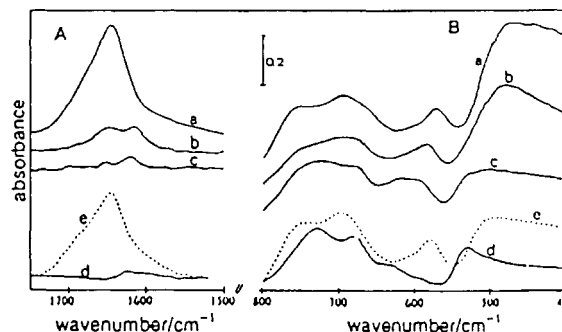


Fig. 2 IR spectra of the MgX sample outgassed at: (a) 300; (b) 323; (c) 373 and (d) 473 K for 40 min at each stage. Curve (e): readorption of water vapour (18 Torr; 15 min of contact) and subsequent outgassing at 300 K for 40 min.

In the case of the NaX zeolite (Fig. 1), an intense and symmetric band with a maximum at  $1645\text{ cm}^{-1}$  is present in range A after outgassing at RT (curve a), assignable to the deformation mode of water molecules physisorbed in the cavities and adsorbed on sodium ions.<sup>1,4</sup> As the outgassing temperature increases, this band progressively decreases in intensity and shifts slightly to higher frequency (curves b, c). It is hardly observable after heating at 473 K (curve d) indicating that after this treatment most molecular water has been desorbed.

In the low frequency region (Fig. 1B) the sample outgassed at RT (curve a) exhibits well resolved bands at 755, 680, 570 and  $490\text{ cm}^{-1}$ . Their nature has been discussed by Flanigen<sup>1</sup> and Jacobs *et al.*<sup>4</sup> and a schematic assignment of such absorptions is reported in Table 1. In particular, it has been noticed that the signal due to the T—O—T deformation mode is quite sensitive to the structural features of the prismatic units.<sup>1</sup> The progressive dehydration up to 473 K does not produce significant changes in the spectrum in region B (curves b–d), indicating that the spectral features of the frame of the NaX zeolite are not affected by the hydration state of the material. Only a component on the low-frequency side of the broad and complex absorption at  $680\text{ cm}^{-1}$  disappears upon dehydration (curve a), leaving a dominant peak at  $690\text{ cm}^{-1}$  and a shoulder at ca.  $670\text{ cm}^{-1}$  (curve d). It is fully restored when water is allowed onto the sample and is assignable to the rocking mode of  $\text{H}_2\text{O}$  adsorbed on  $\text{Na}^+$  ions. Noticeably, further modifications were not observed by outgassing at higher temperature up to 973 K (spectra not reported for brevity) and this indicates that the zeolitic structure is preserved under the adopted experimental conditions.

The spectra of the MgX zeolite, shown in Fig. 2, are quite different from those of the parent NaX sample. After outgassing at RT (Fig. 2A, curve a), the absorption due to the  $\delta_{\text{H}_2\text{O}}$  mode appears much broader and asymmetric, with a major peak at  $1645\text{ cm}^{-1}$  and shoulders at ca. 1695 and, extremely weak, at  $1615\text{ cm}^{-1}$ . By dehydration at 323 K, the intensity of such signals strongly decreases, and two weak bands with ill defined maxima at 1645 and  $1615\text{ cm}^{-1}$  can be observed in the spectrum (curve b). The component at higher frequency further decreases in intensity by increasing the outgassing temperature (curve c), and completely disappears after the treatment at 473 K (curve d). The band at  $1615\text{ cm}^{-1}$  appears to be less affected by the dehydration process, slightly decreasing in intensity after outgassing at 373 K (curve c) and practically disappearing after the treatment at 473 K (curve d).

The spectral behaviour just described agrees well with the data reported in the literature on zeolites containing divalent cations,<sup>4</sup> which owing to their larger charge interact stronger with the water molecules. The bending is expected to shift further to lower frequencies<sup>6</sup> and, on such a basis, the absorption at  $1615\text{ cm}^{-1}$  can be assigned to molecular water adsorbed on  $\text{Mg}^{2+}$  cations.

The rest of the signal at higher frequency is attributable to water molecules physisorbed in the cavities and adsorbed on residual monovalent  $\text{Na}^+$  ions. The broadness of this component as compared with the peak observed in the case of the

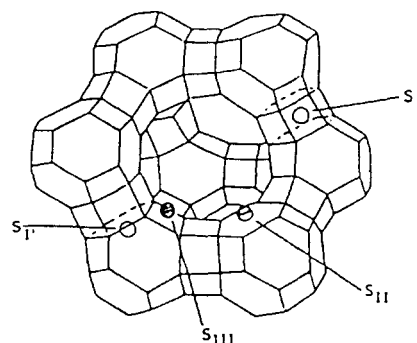
NaX zeolite suggests a somewhat larger heterogeneity of  $\text{Na}^+$  ions, still present in MgX, towards coordination of molecular water.

However, the most significant spectroscopic differences between NaX and MgX samples were observed in the low frequency range (Fig. 2B). In the spectrum of the MgX sample outgassed at RT (Fig. 2B, curve a) all components previously described for the sodium form are present, but they appear weaker, broader and strongly overlapped. As the exchange procedures do not affect the crystallinity of the zeolite,<sup>5</sup> these differences between the lattice vibrational spectrum of NaX and MgX samples can be ascribed to changes in the vibrational properties of the zeolitic frame due to the presence of  $\text{Mg}^{2+}$  ions. In particular, as the nature of the counter-cations influences the electronic<sup>7</sup> and vibrational<sup>8</sup> features of the lattice, it can be considered that the simultaneous presence of monovalent and divalent counter-cations could produce some distortions in the zeolitic binding structure. It can then be supposed that, for the NaX sample, the presence of identical cations homogeneously distributed at the various sites produces ordered and extended ensembles of similar O—T—O and T—O—T oscillators, generating the well shaped bands observed in Fig. 1B, while in the case of the sample containing  $\text{Mg}^{2+}$  cations and also some residual  $\text{Na}^+$ , ensembles with slightly different frequencies are generated, with consequent broadening of the bands. Such heterogeneity will be discussed in a future report.<sup>9</sup>

However, the most significant peculiarity of the MgX system is the dependence of the lattice modes behaviour on hydration conditions; in this case progressive dehydration of the sample produces significant modifications in the spectrum (Fig. 2B, curves b–d). All components are involved in this process (curves a–d), but the band initially centered at  $570\text{ cm}^{-1}$  (curve a) seems particularly affected by water removal. It progressively shifts to higher frequency and decreases in intensity (curves b, c) and finally disappears after outgassing at 473 K (curve d). Subsequent water adsorption (curve e) fully restores the initial spectrum, indicating that the observed modifications are due to reversible changes in the zeolitic structure, associated with the dehydration process.

The effects observed in the IR spectra in Fig. 2 might well be generated by the displacement of cations as already suggested by other studies, which showed that the removal of molecular water induces the displacement of divalent cations to different extraframework sites, producing a general readjustment of the structure.<sup>1,10</sup> The different extraframework sites which may allocate cations in a faujasite-type structure are indicated in Scheme 1 by different symbols and by conventional lettering.

Specifically, Anderson *et al.*<sup>10</sup> showed by X-ray diffraction (XRD) that in the hydrated form  $\text{Mg}^{2+}$  ions occupy prefer-



Scheme 1

Table 1 Vibrations of faujasites

| IR mode                    | $\nu/\text{cm}^{-1}$ |
|----------------------------|----------------------|
| T—O—T symmetric stretching | 820–720              |
| O—T—O symmetric stretching | 720–650              |
| T—O—T deformation          | 650–500              |
| O—T—O deformation          | 500–420              |

T = Si or Al atom in tetrahedral coordination; ref. 1, 4.

entially sites I' facing sodalites and sites II and III facing the supercages, whereas after dehydration they are located in sites I and in sites II, this redistribution being accompanied by some deformation of the framework. The displacement of  $Mg^{2+}$  ions can be rationalized on the basis of the high charge to radius ratio, which justifies the large hydration energy value ( $-1900 \text{ kJ mol}^{-1}$ ) and leads them to positions where the coordination sphere can approach its maximum of six ligands.<sup>11</sup>

The spectral behaviour observed during the dehydration of the MgX sample can then be interpreted as follows: (a) in the hydrated form, the ligand sphere of the  $Mg^{2+}$  ions located in the sodalites and in the supercages consists of both water molecules and oxygen atoms of the framework;<sup>10</sup> (b) removal of molecular water produces the loss of  $H_2O$  ligands and the divalent cations move to sites where their positive charge can be more efficiently shielded, strongly interacting with the frame oxygen atoms. In particular,  $Mg^{2+}$  ions located in the I' sites move to the I sites, at the centre of the prismatic units, where they are surrounded octahedrally by six oxygen lattice atoms.<sup>10</sup> This produces a deformation of the oxygen rings which constitute the windows connecting the prisms with the sodalites. Significantly, the spectral component more heavily affected by the dehydration process is the band at  $570 \text{ cm}^{-1}$ , which, as commented on previously, is very sensitive to the structural features of the prismatic units.<sup>1</sup>

A plausible scheme of this process is reported in Plate 1, where the space available for the motion of an  $Mg^{2+}$  ion from a site I' to a related site I was evaluated by the Connolly algorithm,<sup>12</sup> using as probe a sphere with the dimensions of the  $Mg^{2+}$  ion. Schematically, when in site I', the coordination sphere of the  $Mg^{2+}$  cation is assumed to include three oxygen atoms of the hexagonal window and three  $H_2O$  molecules.

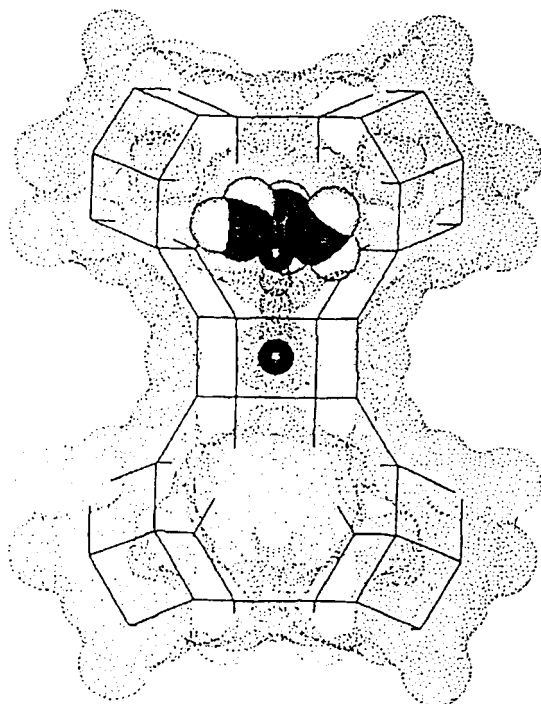


Plate 1 Computer-generated schemes of the motion of a  $Mg^{2+}$  ion from site I' to site I. When in site I', the cation is assumed to be stabilized by three  $H_2O$  molecules and three oxygen atoms of a hexagonal ring.

Table 2 Stretching modes/ $\text{cm}^{-1}$  of  $Na^+$  and  $Mg^{2+}$  in the various sites of X-zeolites

| vibrations                                 | site II        | site I         | site I' | site III |
|--------------------------------------------|----------------|----------------|---------|----------|
| Na-X <sub>exp., hydr.</sub> <sup>a</sup>   | 184            | 151            | 108     | 65       |
| Na-X <sub>exp., dehydr.</sub> <sup>a</sup> | 187            | 155            | 108     | 65       |
| Na-X <sub>exp., dehydr.</sub> <sup>b</sup> | 189            | 156            | 110     | 67       |
| Mg-X <sub>calc.</sub>                      | 310            | 260            | 170     | 110      |
| Mg-X <sub>exp., hydr.</sub>                | — <sup>c</sup> | — <sup>c</sup> | 180     | 120      |
| Mg-X <sub>exp., dehydr.</sub>              | 400–250        | —              | —       | 110      |

<sup>a</sup> This work; <sup>b</sup> from ref. 14; <sup>c</sup> covered by lattice modes.

The absence of similar effects for the NaX sample is attributable to the lower value of the charge to radius ratio of the  $Na^+$  ions. In this case, the loss of some of the ligands by water desorption does not involve the motion of the cations, which are stabilized by the reduced coordination sphere of the oxygen lattice of the site where they are located. Evidence for such a process was provided by the spectra recorded in the far-IR region, where vibrational modes of the cations against the lattice can be observed.<sup>2,13,14</sup>

Spectra of NaX in this region have already been presented<sup>14</sup> showing four bands clearly assignable to the stretching modes of  $Na^+$  cations in different sites, as reported in Table 2, and also bands at  $300$  and  $250 \text{ cm}^{-1}$  due to lattice modes. Our NaX sample outgassed at RT showed similar bands which do not deserve further discussion. The spectrum does not change after outgassing at  $473 \text{ K}$ , when all molecular water is desorbed (Table 2).

Results obtained in the case of MgX are sharply different. Curve a in Fig. 3 reproduces the far-IR spectrum of the MgX sample outgassed at RT which, to our knowledge, has not been published and commented on. Major bands are observed at  $360$ ,  $280$ ,  $180$ ,  $150$  and  $120 \text{ cm}^{-1}$ .

Ozin *et al.*<sup>2</sup> showed that the Brodskii equation  $\nu_i \propto M_i^{-1/2} R_i^{-3/2}$ , relating the vibrational frequency  $\nu_i$  of the motion against the lattice of a cation located in a site  $i$ , the mass  $M$  and the ionic radius  $R$  of such a cation, can be successfully applied to the assignment of experimentally observed cation–lattice modes. Using the proportional factor obtained from the analysis of the spectra of the NaX zeolite, interpreted on the basis of the literature data available for this system,<sup>2,14</sup> the absorption frequencies of  $Mg^{2+}$  cation–lattice vibrational modes have been calculated (Table 2). Accordingly, the bands observed at  $180$  and  $120 \text{ cm}^{-1}$  can be assigned to  $Mg^{2+}$  ions located in sites I' and III, respectively.

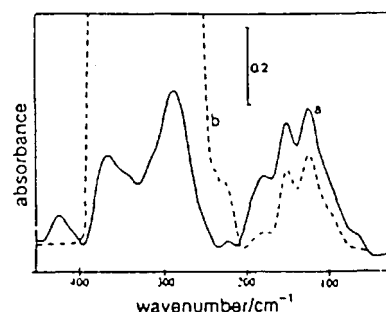


Fig. 3 Far-IR spectra of the MgX sample outgassed at (a)  $300$  and (b)  $473 \text{ K}$  for  $40 \text{ min}$  at each stage. Subsequent admission of water restores spectrum (a).

while the peak at  $150\text{ cm}^{-1}$  is assignable to residual<sup>10</sup>  $\text{Na}^+$  ions in sites I.<sup>2,14</sup>

The bands due to  $\text{Mg}^{2+}$  cations in sites I and II are expected at  $260$  and at  $310\text{ cm}^{-1}$ , respectively, but the presence in this range of absorptions due to lattice modes<sup>1-4,14</sup> renders a punctual recognition quite difficult. However, it should be considered that the results by Anderson *et al.*<sup>10</sup> indicate that in the hydrated form,  $\text{Mg}^{2+}$  ions should not occupy sites I.

The removal of molecular water by dehydration at  $473\text{ K}$  produces drastic changes in the spectrum (Fig. 3, curve b) with a very intense band growing up in the  $400\text{--}250\text{ cm}^{-1}$  range. Among the components at lower frequencies, those at  $120\text{ cm}^{-1}$ , due to  $\text{Mg}^{2+}$  in sites III and at  $150\text{ cm}^{-1}$ , due to residual  $\text{Na}^+$  ions, are only slightly affected, whereas the intensity of the band at  $180\text{ cm}^{-1}$  is drastically reduced. A subsequent admission of water fully restores the initial spectrum a and the cycle may be repeated indefinitely. The observed modifications in the absorptions due to the cations against lattice vibrations confirm that displacements of the counter-cations and changes in their interaction with the framework occur by water desorption. Significantly, the signal at  $180\text{ cm}^{-1}$  due to  $\text{Mg}^{2+}$  ions located in site I' vanishes, indicating that cations tend to move away from this position. Moreover, the increase of the absorption intensity at  $250\text{--}400\text{ cm}^{-1}$ , where also the band due to  $\text{Mg}^{2+}$  in site I is expected, suggests that such sites become populated after dehydration. Also,  $\text{Mg}^{2+}$  ions in sites II absorb in this region. Such sites were populated already in the presence of water,<sup>10</sup> but after dehydration the cations interact more strongly with the oxygen atoms of the hexagonal windows connecting supercages and sodalites. The intensity of the signal in such a region is really outstanding and unfortunately no data have been found in the literature to be compared with these results. It might well be ascribed to a very high value of the transition dipole moment of the vibrations involving dehydrated  $\text{Mg}^{2+}$  ions in close contact with the surrounding oxygen atoms,<sup>10</sup> increasing the covalent character of the bond between the counter-cations and the lattice. Molecular dynamics calculations, not yet available on model systems, might help in interpreting this observation.

Unfortunately, the difficulty in preparing very thin pellets for far-IR spectra and their fragility limited the possibility of performing systematic experiments where the hydration of the sample is gradually changed.

The authors are grateful to MURST and ASP (Associazione per lo Sviluppo Scientifico e Tecnologico del Piemonte) for financial support. Dr. Siliva Bordiga is acknowledged for assistance in computer modelling, and Professor C. R. A. Catlow and Professor A. Zecchina for helpful discussions.

## References

- 1 E. M. Flanigen, in *Zeolite Chemistry and Catalysis*, ed. J. A. Rabo, ACS Monograph 171, American Chemical Society, Washington DC, 1976, ch. 2, p. 80.
- 2 G. A. Ozin, M. D. Baker, J. Godber and W. Shihua, *J. Am. Chem. Soc.*, 1985, 107, 1995, and references therein.
- 3 C. Brémard and M. Le Maire, *J. Phys. Chem.*, 1993, 97, 9695.
- 4 W. P. J. H. Jacobs, J. H. M. C. van Wolput and R. A. van Santen, *Zeolites*, 1993, 13, 170, and references therein.
- 5 H. Tsuji, F. Yagi, H. Hattori and H. Kita, in *New Frontiers in Catalysis, Proceedings of the 10th International Congress on Catalysis*, ed. L. Guzzi, F. Solymosi and P. Tétényi, Akadémiai Kiadó, Budapest 1993, vol. B, p. 1171.
- 6 K. Nakamoto, *Infrared Spectra of Inorganic and Coordination Compounds*, Wiley Interscience, New York, 1970, p. 167, and references therein.
- 7 H. Huang and S. Kaliaguine, *J. Chem. Soc., Faraday Trans.*, 1992, 88, 751.
- 8 R. A. van Santen and D. L. Vogel, in *Advances in Solid-State Chemistry*, The Royal Institution, London, 1989, vol. 1, p. 151.
- 9 S. Coluccia, N. Daminiano and G. Martra, in preparation.
- 10 A. A. Anderson, Y. F. Shepelev and Y. I. Smolin, *Zeolites*, 1990, 10, 32.
- 11 David E. Fenton, in *Comprehensive Coordination Chemistry*, ed. G. Wilkinson, R. D. Gillard and J. A. McCleverty, Pergamon Press, Oxford, 1987, vol. 3, ch. 23, p. 3.
- 12 M. L. Connolly, *J. Appl. Crystallogr.*, 1983, 16, 548.
- 13 I. A. Brodskii and S. P. Zhadanov and A. E. Stanevic, *Opt. Spectrosc. (Eng. Transl.)*, 1971, 30, 58.
- 14 K. Peuker and D. Kunath, *J. Chem. Soc., Faraday Trans. 1*, 1981, 77, 2079.

Paper S/01634G; Received 14th March, 1995

[Regular Paper]

## Chemical Structure of Organic Sulfur Compounds in Extracted Oils and Hydrogenated Oils Derived from Coals Examined by Means of GC-FPD and GC-LVEI MS

Susumu YOKOYAMA<sup>†1)\*</sup>, Akikazu OHTANI<sup>†1)</sup>, Mitsuyosi MURAJI<sup>†1)</sup>, Hiroshi SUGIBUCHI<sup>†1)</sup>,  
Mohamed M. Y. BAKR<sup>†2)</sup>, Masaaki SATOU<sup>†1)</sup>, and Yuzo SANADA<sup>†1)</sup>

<sup>†1)</sup> Center for Advanced Research of Energy Technology, Hokkaido University,  
Kita 13 Nishi 8, Kita-ku, Sapporo 060

<sup>†2)</sup> Geology Dept., Faculty of Science, Alexandria University, Alexandria, Egypt

(Received June 1, 1994)

The purpose of this study is to elucidate the bonding types of organic sulfur compounds in macromolecular coal structure. High sulfur containing coals, Illinois No. 6 (C: 77.7, S: 2.4 wt%) and Miike coal (C: 84.5, S: 1.1 wt%, Japan) were examined. It consisted of study on the chemical structure of sulfur containing compounds in extracted oils which are *n*-hexane soluble, and hydrogenated oil derived from pyridine insoluble residue by hydrogenation. Capillary column GC equipped with FPD detector, which enables to determine specifically the sulfur element, and for this purpose, GC-LVEI MS analyses were provided. Species of organic sulfur compounds in extracted oil and hydrogenated oils were determined, to compare between those of lower rank Illinois No. 6 coal and bituminous Miike coal. The 2-4 ring aromatic thiophenes consisting of C<sub>1</sub>-C<sub>5</sub> benzothiophenes, C<sub>6</sub>-C<sub>4</sub> dibenzothiophenes and benzonaphthothiophene were found in the higher ranking Miike coal, whereas the lower ranking Illinois No. 6 coal contained 2-3 ring aromatic thiophenes with C<sub>1</sub>-C<sub>6</sub> benzothiophene and C<sub>6</sub>-C<sub>6</sub> dibenzothiophene. Species and alkyl carbon distribution of organic sulfur compounds for both extracted oil and hydrogenated oil were found to be approximately similar with each other.

### 1. Introduction

Some coals contain considerably high amounts of sulfur. Unrestricted use of such coals cause serious global atmospheric pollution problems, such as acid rain, as well as corrosion of processing apparatuses, poisoning of catalytic activities, etc. Resolution of these problems requires close examination of various properties concerning sulfur compounds, emphasis being placed on particular types of bonding of sulfur containing structures<sup>1)-7)</sup>.

In our previous paper, low molecular compounds extracted from coal by solvent, and coal liquefaction oil derived from a matrix of coal macromolecules by hydrogenolysis, were investigated. The purpose was to clarify the correlation of chemical structures for hydrocarbons derived from different constituents of coal: low molecular weight compounds and macromolecular components<sup>8)</sup>. Similar interest has been directed to observe organic sulfur compounds in coal. In this study, the chemical structures of organic sulfur compounds in coal were inves-

tigated. It concerned with *n*-hexane soluble parts of coal, which consisted of low molecular weight component mixed solely or bonded with noncovalent bonds, such as hydrogen bound to a coal macromolecule matrix. On the other hand, sulfur component incorporated into coal macromolecule were also investigated by converting pyridine insoluble residue to *n*-hexane soluble oil by hydrogenation.

These organic sulfur compounds were examined by means of capillary column-gas chromatography equipped with a FPD detector (GC-FPD) and by GC-LVEI MS spectroscopic method. GC-FPD analysis is an effective procedure for selective differentiation of organic sulfur compounds mixed with hydrocarbons in each compound class fractions.

### 2. Experiment

Elemental analyses of coals are shown in Table 1. Miike (Japanese) coal is characterized by relatively high sulfur content of 1.1 wt%, which is one of higher rank of bituminous coal. Illinois No. 6 coal, also, is relatively high sulfur content,

\* To whom correspondence should be addressed.



Table 1 Analyses of Coal Samples and Respective Oil Yields

| Coal samples   | Elementary analyses [wt%, d.a.f.] |     |     |     | $O_{(diff.)}$      | Yields [wt%, coal basis] |                  |                     |
|----------------|-----------------------------------|-----|-----|-----|--------------------|--------------------------|------------------|---------------------|
|                | C                                 | H   | N   | S   |                    | PI <sup>a)</sup>         | HS <sup>b)</sup> | PI-HS <sup>c)</sup> |
| Illinois No. 6 | 77.7                              | 5.0 | 1.4 | 2.4 | 13.5 <sup>d)</sup> | 79.8                     | 1.8              | 8.2                 |
| Miike          | 84.5                              | 6.1 | 1.2 | 1.1 | 7.1                | 80.5                     | 4.0              | 13.2                |

a) PI: Pyridine insolubles. b) HS: Extracted oil. c) PI-HS: Hydrogenated oil. d) Data on m.a.f. basis, proposed by Argonne premium coal sample program.

| Oil samples      | Compound classes [wt%, oil basis] |      |      |      |       | Recovery |
|------------------|-----------------------------------|------|------|------|-------|----------|
|                  | Fr-P                              | Fr-M | Fr-D | Fr-T | Fr-PP |          |
| Illinois No. 6   |                                   |      |      |      |       |          |
| Extracted oil    | 7.6                               | 6.4  | 8.9  | 12.6 | 25.8  | 61.3     |
| Hydrogenated oil | 3.9                               | 4.4  | 6.6  | 12.9 | 55.1  | 82.9     |
| Miike            |                                   |      |      |      |       |          |
| Extracted oil    | 11.1                              | 7.1  | 11.5 | 9.7  | 42.6  | 82.0     |
| Hydrogenated oil | 7.6                               | 5.1  | 8.6  | 18.0 | 43.2  | 82.5     |

about 2.4 wt%, belonging to a high volatile bituminous coal.

The procedure of sample preparation is shown in Fig. 1. These two coals were extracted with pyridine, benzene and *n*-hexane, in this order, to obtain extracts soluble in respective solvents. The *n*-hexane soluble portions, oils (HS), were used for this study. On the other hand, hydrogenation of pyridine insoluble residue (PI) of Illinois No. 6 coal and Miike coal were performed under milder reaction conditions: initial hydrogen pressure of 100 kg/cm<sup>2</sup> at 400°C for 60 min. Products of reaction were separated by solvent extraction, using benzene and *n*-hexane, into benzene soluble, *n*-hexane insoluble asphaltene and benzene, *n*-hexane soluble oil (PI-HS). Oil derived from hydrogenation were designated "hydrogenated oil." Otherwise, oils derived from solvent extraction of coals were designated "extraction oils." Both oils, thus prepared, were further separated into compound class fractions by NH<sub>2</sub> column HPLC, namely, saturated hydrocarbons (Fr-P), aromatic hydrocarbons with different aromatic ring numbers (Fr-M, D and T) and polar compounds (Fr-PP)<sup>9)</sup>. Each compound class fractions, except for Fr-PP, were analysed by GC equipped with FID, and sulfur selective detector FPD, and GC-low voltage electron impact ionization (LVEI) MS. GC-MS instrument used was Hitachi model M-52 with Hitachi data processing on model 002B and M-003 electric computer. Capillary columns of 50 m, coated with SE-52 for GC and GC-MS, were used.

### 3. Results and Discussion

The product yields of extracted oil and hydrogenated oil and respective compound class fractions are shown in Table 1. Each compound class fraction was determined by GC-FPD to specifical-

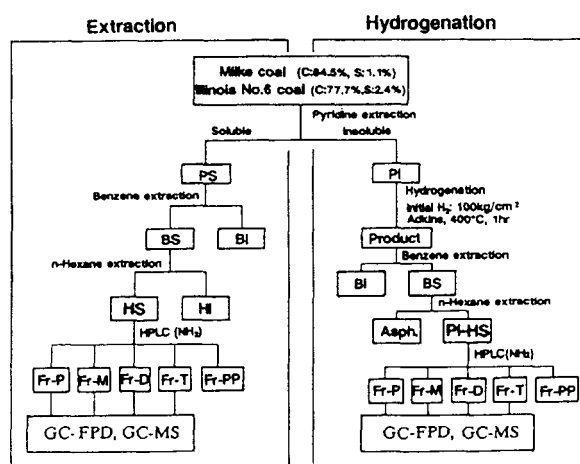



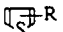

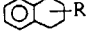
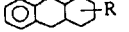

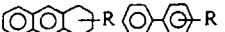
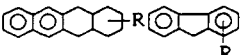
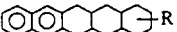
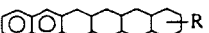
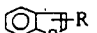

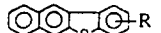
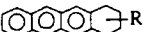







Fig. 1 Scheme of Sample Preparation

ly detect organic sulfur compounds. The GC chromatograms of Fr-D and T of extracted oil and hydrogenated oil from Miike coal indicated response to organic sulfur compounds. Regarding Illinois No. 6 coal, Fr-D and T responded similarly to the GC-FPD detection, for extracted oil and hydrogenated oil. Conversely, sulfur compounds were not detected in another fraction of Fr-P and M for both oils derived from Miike coal and Illinois No. 6 coal, respectively, by means of GC-FPD analyses.

Shown in Table 2 are the classification of organic sulfur compounds and accompanying hydrocarbon compounds for explanation of analytical procedure of their structural analyses. Thiophene type compounds, differing in aromatic ring numbers, can be classified into respective compound class fractions corresponding to the number of aromatic rings, similar to that of hydrocarbon compound classes, by means of NH<sub>2</sub> column HPLC<sup>4)</sup>. Each of the compound class

Table 2 Classification of Organic Sulfur Compounds by Compound Class Showing the Determinants

| Compound classes | Z numbers | Compound types                                                                       |                                                                                                                                                                             |
|------------------|-----------|--------------------------------------------------------------------------------------|-----------------------------------------------------------------------------------------------------------------------------------------------------------------------------|
|                  |           | Hydrocarbons                                                                         | Sulfur compounds                                                                                                                                                            |
|                  |           | GC-FID                                                                               | GC-FPD                                                                                                                                                                      |
| HPLC             |           |                                                                                      | GC-MS                                                                                                                                                                       |
| Fr-P             | Z=+2S     |                                                                                      |                                                                                          |
|                  | +2        |     |                                                                                                                                                                             |
|                  | 0         |     |                                                                                                                                                                             |
| Fr-M             | -4S       |                                                                                      |                                                                                          |
|                  | -6        |     |                                                                                                                                                                             |
|                  | -8        |     |                                                                                                                                                                             |
|                  | -10       |    |                                                                                                                                                                             |
| Fr-D             | -12       |     |                                                                                                                                                                             |
|                  | -14       |    |                                                                                                                                                                             |
|                  | -16       |    |                                                                                                                                                                             |
|                  | -18       |    |                                                                                                                                                                             |
|                  | -20, -10S |    |                                                                                          |
| Fr-T             | -18, -22S |    |                                                                                          |
|                  | -20       |  |                                                                                                                                                                             |
|                  | -22       |  |                                                                                                                                                                             |
|                  | -24       |  |                                                                                                                                                                             |
|                  | -26, -16S |  |   |
| Fr-PP            |           | Polar compounds                                                                      |                                                                                                                                                                             |

fractions is subjected to GC-LVEI MS analyses and classified into individual compound types by Z numbers which represent numbers of naphthenic and aromatic rings of saturates and hydroaromatics<sup>10)</sup> and those of sulfur incorporated compounds.

### 3. 1. Extracted Oils

Fr-T of Miike extracted oil clearly contains sulfur compounds, in reference to GC-FPD chromatogram, shown in Fig. 3 (top). GC-LVEI MS analysis and an estimation of Z number thereof were made to elucidate compound types for Fr-T of Miike extracted oil. Total ion chromatogram (TIC) and ion chromatograms of respective homologous series of compound types estimated by Z number, are shown in Fig. 2. These chromatograms are designated as Z number mass chromatograms. Tentative ring structures corresponding to Z numbers are shown in this figure. Generally, decreasing Z numbers indicate increasing ring numbers, especially concerning Fr-T, aromatic ring numbers increase. Shown in the

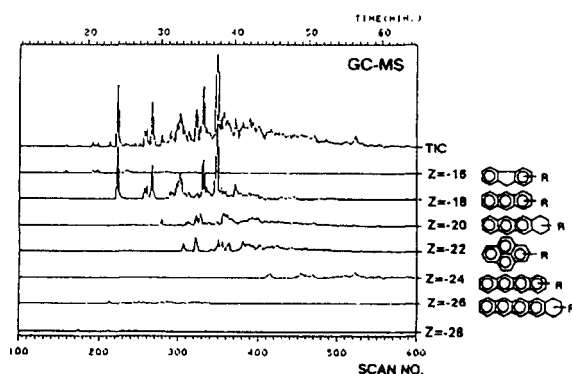


Fig. 2 Total Ion Chromatogram (TIC) and Z Number Mass Chromatograms of Fr-T for Miike Extracted Oil

figure is an interesting tendency: the range of Z number mass chromatograms shift gradually to a higher scan number, that means, a longer retention time of GC, with decreasing Z number. Since

decreasing  $Z$  numbers correspond to larger aromatic ring systems, this is an understandable phenomenon involving the relationship between chemical structures of aromatic rings and respective retention times of GC. For compound type  $Z=-26$ , though chromatogram peaks are small, there is a different trend between chemical structure predicted by  $Z$  number and scan number. It is assumed that the assignment of this homologous series is incorrect as to the apparent  $Z$  number of  $Z=-26$ , because larger aromatic ring compounds like this one are expected to have larger retention times, probably.

This  $Z$  number mass chromatogram of the apparent  $Z=-26$  is shown again in Fig. 3 (bottom) recorded at high sensitivity. The GC-FPD chromatogram of Fr-T, shown in Fig. 3 (top), is compared with this  $Z$  number mass chromatogram of apparent  $Z$  number of  $-26$ . Both chromatographic patterns of the early eluted part of GC-FPD chromatogram and  $Z$  number mass chromatograms of  $Z=-26$ , tentatively assigned, are quite similar with each other. From these results, it can be assumed that components of these peaks belong to sulfur containing compounds, such as  $Z=-16S$  instead of apparent  $Z$  number of  $Z=-26$ .  $Z=-16S$  is the actual  $Z$  number because of the following reason. Mass chromatograms related to molecular weight of alkyl homologue of dibenzothiophenes ( $M/z=184, 198, 212, 226, 240$ ), which belong to  $Z=-16S$ , were drawn and are shown in Fig. 3 (bottom). Mass chromatograms of these mass numbers, belonging to dibenzothiophene homologue, agree quite well with  $Z$  number mass chromatograms of  $Z=-16S$ . Therefore, we can conclude, undoubtedly, that organic sulfur compounds in Fr-T for Miike extracted oil can be determined as dibenzothiophene homologues from alkyl carbon 0 to 4. The latter eluted section of the FPD chromatogram was also predominant and suggested the occurrence of another type of organic sulfur compounds. These GC-FPD peaks were not assigned, at this time, to respective sulfur containing compounds, except for peak No. 6.

Apparent  $Z$  number, of phenanthrene series ( $Cal>4$ ) and benzonaphthothiophene series, cannot be distinguished only by compound type analysis using GC-LVEI MS.  $Z$  number mass chromatograms of  $Z=-18$ , phenanthrene series and/or  $Z=-22S$ , benzonaphthothiophene series, and mass chromatograms of these alkyl homologue, (i.e.  $M/z=178, 192, 206, 220, 234$ , and  $248$ ) are also shown in Fig. 4 (bottom), which are compared to the GC-FID chromatogram of Fr-T, shown in Fig. 4 (top). The  $Z$  number mass

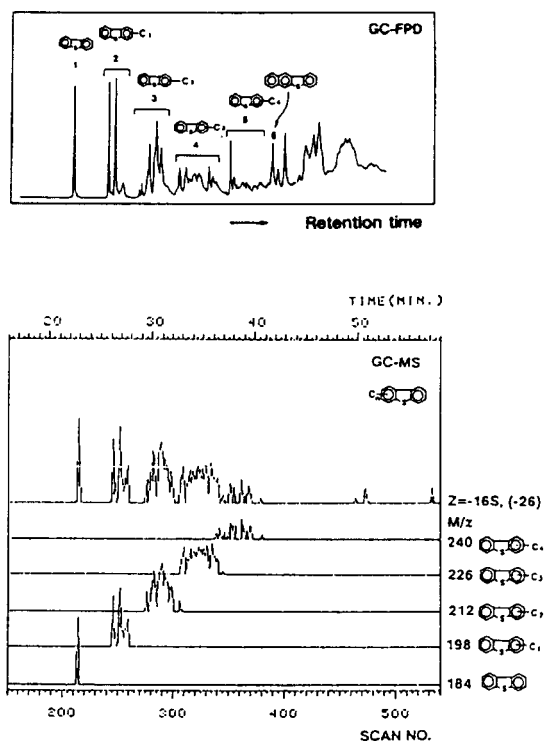


Fig. 3 GC-FPD Chromatogram and  $Z$  Number Mass Chromatogram of  $Z=-16S$  and Its Mass Chromatograms of Fr-T for Miike Extracted Oil

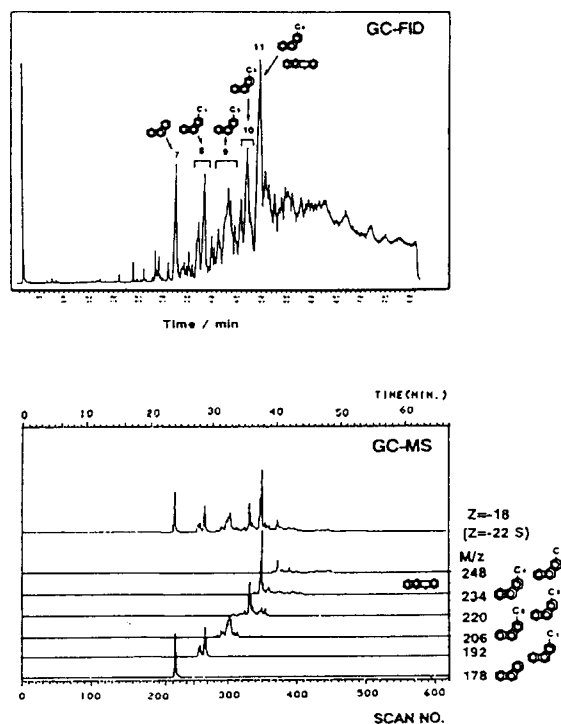


Fig. 4 GC-FID Chromatogram and  $Z$  Number Mass Chromatogram of  $Z=-18$  and Its Mass Chromatograms of Fr-T for Miike Extracted Oil

chromatogram of  $Z=-18S$  consists of these mass chromatograms of phenanthrene homologue, and also agrees fairly well with the FID gas chromatogram. The first compound belonging to the  $Z=-22S$  homologous series is benzonaphthothiophene having a molecular weight of 234. The mass chromatogram of  $M/z$  234, therefore, can be assumed to also contain this sulfur compound, except for  $C_4$ -phenanthrene. The predominant peak of  $M/z$  234 mass chromatogram coincided not only with peak No. 11 in FID chromatogram (Fig. 4, top) but also with the No. 6 in FPD chromatogram (Fig. 3, top). This revealed co-elution of organic sulfur compound with  $C_4$ -phenanthrene. Co-injection of reference compound, benzonaphthothiophene, to Fr-T indicated the co-elution with  $C_4$ -phenanthrene. These peaks of FPD (No. 6) and FID chromatogram (No. 11), therefore, can be assigned to benzonaphthothiophene with some amount of  $C_4$ -phenanthrene overlapping.

GC-FPD chromatogram of Fr-D of Miike extracted oil is shown in Fig. 8(1). Fr-D was expected to contain 2-ring aromatic thiophene series, benzothiophenes, which can be separated by  $NH_2$  column HPLC (shown in Table 2). Discussions on the results of analyses of Illinois No. 6 coal follows: this extracted oil exhibited GC-FPD chromatogram on Fr-D, as shown in Fig. 5 (top), indicating the occurrence of organic sulfur compounds. For confirmation of presence of these organic sulfur compounds, similar procedure by means of GC-FPD and GC-LVEI MS analysis described above, was applied for these assignments.

$Z$  number mass chromatogram of  $Z=-10S$ , which corresponds to benzothiophene derivatives, are shown in Fig. 5 (bottom), and mass chromatograms of alkyl benzothiophenes, representing mass numbers of 134, 148, 162, 176, 190, and 204, are also indicated. Mass chromatograms belonging to benzothiophenes coincide with the  $Z$  number mass chromatogram of  $Z=-10S$ , respectively. This  $Z$  number mass chromatogram also corresponds to the GC-FPD chromatogram (shown in Fig. 5, top), as well. From these results, we can confirm the occurrence of benzothiophene homologue in Fr-D for Illinois No. 6 coal extracted oil. In the case of Fr-T for Illinois No. 6 coal, dibenzothiophene homologue was assigned similarly following the procedure for Miike extracted oil Fr-T.

Shown in Table 3 are summarized results of analyses on organic sulfur compounds for extracted oils of Illinois No. 6 coal and Miike coal. It is noteworthy that two high-sulfur coals contain

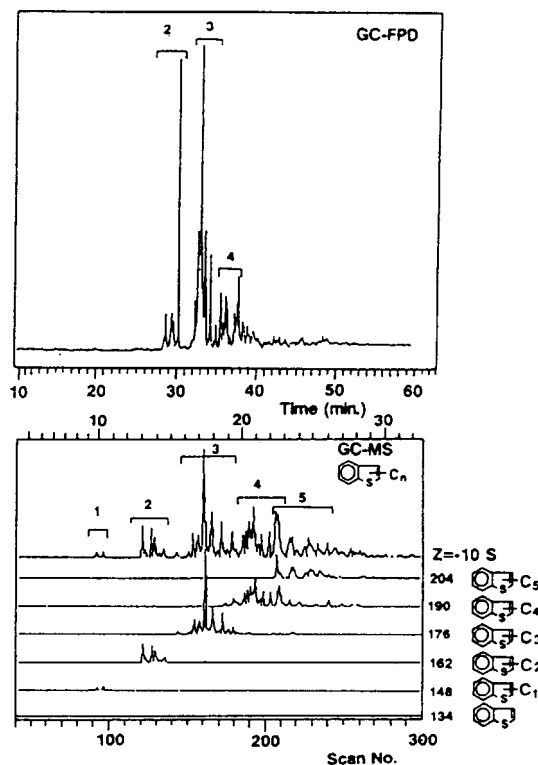


Fig. 5 GC-FPD Chromatogram and  $Z$  Number Mass Chromatogram of  $Z=-10S$  and Its Mass Chromatograms of Fr-D for Illinois No. 6 Extracted Oil

the same species of organic sulfur compounds, except for benzonaphthothiophene included in Miike coal. Higher ranking Miike coal contained a greater-ring of sulfur compound, benzonaphthothiophene.

### 3. 2. Hydrogenated Oil

Pyridine insoluble residues consist of macromolecular coal structure with three dimensional cross-linking of various aromatic unit structures. If hydrogenation exclusively causes molecular cleavage at methylenes and ether bridges bonding aromatic-unit-cluster with less occurrence of breakdown and hydrogenation of aromatic ring structure, low molecular components reflected on aromatic unit structure may be produced. Reaction products which are  $n$ -hexane soluble portion, hydrogenated oil, are extremely interesting for the elucidation of coal macromolecular structure, including sulfur containing moiety.

Pyridine insoluble residues from Illinois No. 6 coal and Miike coal were depolymerized by hydrogenation under comparatively milder condition to avoid severe reaction, such as degradation and hydrogenation of aromatic ring. Hydrogenated oils thus prepared are assumed to

posses aromatic unit structure without extreme alteration, and accepted for measurement of mass spectrometry to acquire accurate structural analysis to grasp information pertaining to chemical structure of sulfur containing moiety included in the macromolecular coal structure. Compound class fractions, Fr-D and T, containing organic sulfur compounds were investigated by the same analytical method used for GC-FPD and GC-LVEI MS, which was adopted for extraction oils.

The result of GC-LVEI MS on organic sulfur compounds contained in hydrogenated oil Fr-D of Illinois No. 6 coal is shown in Fig. 6. Here, Z number mass chromatogram of  $Z=-10S$ , benzothiophenes, and its corresponding mass chromatogram (134, 148, 162, 176, ...) are exhibited. Comparing these with the results of its extracted oil (Fig. 5, bottom), both Z number mass chromatograms and these mass chromatograms between liquefied oil and extracted oil indicate the occurrence of similar sulfur components, but with different relative amounts among different carbon numbers of alkyl groups substituted for benzothiophene ring.

Molecular weight distribution of benzo- and dibenzothiophenes of extracted oil and liquefied oil of Illinois No. 6 coal, respectively, are compared and shown in Fig. 7. Contents of benzo- and dibenzothiophenes were estimated by measurements of peak intensities of respective mass chromatograms for GC-LVEI MS analyses. The numbers indicated in these figures represent the carbon numbers in alkyl substitution to benzo- and dibenzothiophene rings. The range of alkyl carbon number distribution for extracted oil and liquefied oil are approximately the same from 1 or 2 to 6 for benzothiophene, and from 0 to 6 for dibenzothiophene. For both thiophene compounds, contents were greater for extracted oil than for liquefied oil. GC-FPD chromatogram of Fr-D for Miike hydrogenated oil is shown in Fig. 8 (bottom) with that of extracted oil (top). Later elution chromatogram for extracted oil are greater than that of hydrogenated oil, which revealed, for extracted oil, that larger alkyl group was substituted for benzothiophene ring.

In Table 3, the species of thiophene compound type for hydrogenated oil are shown compared for two kinds of coal, lower rank Illinois No. 6 coal and higher rank Miike coal. Species of thiophene compounds in respective compound classes resemble the results of extracted oil derived from their parent coals. Similarity of organic sulfur components between those of extracted oil and those of hydrogenated oil may be predicted

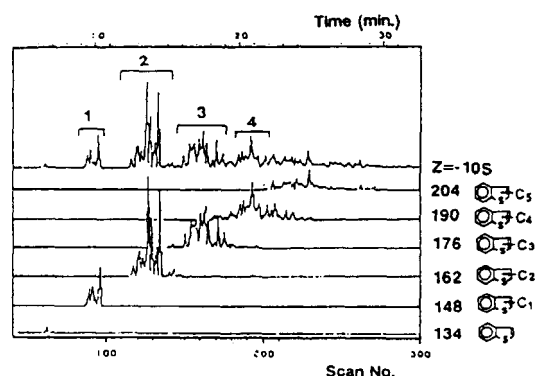


Fig. 6 Z Number Mass Chromatogram of  $Z=-10S$  and Its Mass Chromatograms of Fr-D for Illinois No. 6 Hydrogenated Oil

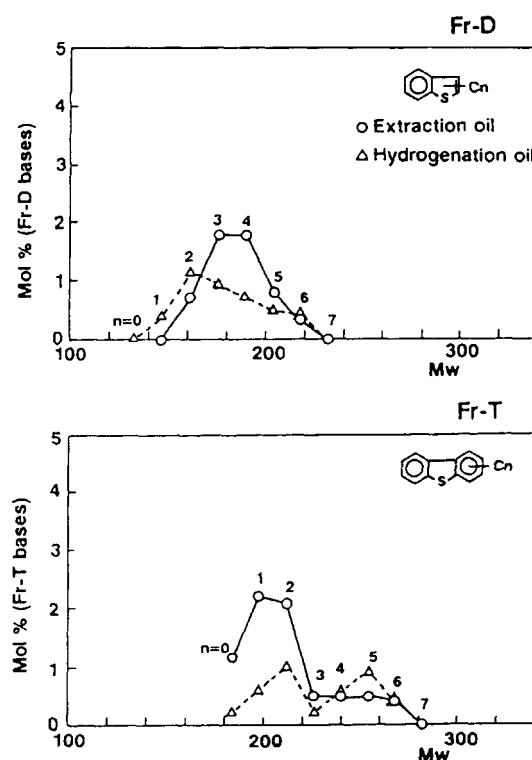
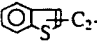
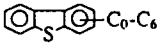
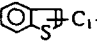

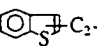
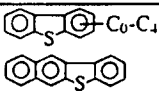
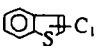
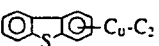


Fig. 7 Distribution of Molecular Weight for Organic Sulfur Compound Types between Extracted Oil and Hydrogenated Oil for Illinois No. 6 Coal

precisely from similar results for hydrocarbon compound types between both oils<sup>8)</sup>. A lower content of organic sulfur compounds of the hydrogenated oil, Illinois No. 6 coal, results from the occurrence of desulfurization of thiophene rings accompanied with hydrocracking of methylenic and ether linkage connecting aromatics and aromatic thiophene unit structures.

Table 3 Organic Sulfur Compound Types in Extracted Oil and Hydrogenated Oil between Two Different Rank of Coals

|                     | Extracted oil                                                                                                 |                                                                                                 | Hydrogenated oil                                                                                 |                                                                                                   |
|---------------------|---------------------------------------------------------------------------------------------------------------|-------------------------------------------------------------------------------------------------|--------------------------------------------------------------------------------------------------|---------------------------------------------------------------------------------------------------|
|                     | Fr-D                                                                                                          | Fr-T                                                                                            | Fr-D                                                                                             | Fr-T                                                                                              |
| Illinois No. 6 coal | <br>(5.5 mol%) <sup>a)</sup> | <br>(7.7 mol%) | <br>(3.9 mol%) | <br>(3.8 mol%) |
| Miike coal          | <br>(5.5 mol%) <sup>a)</sup> | <br>(7.7 mol%) | <br>(3.9 mol%) | <br>(3.8 mol%) |

a) Compound class bases.

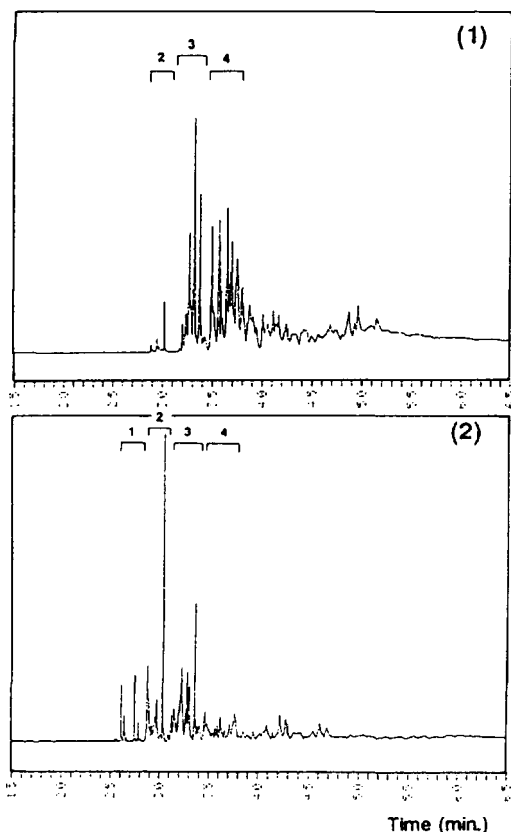


Fig. 8 GC-FPD Chromatograms of Fr-D for Extracted Oil (1) and Hydrogenated Oil (2) Obtained from Miike Coal

#### 4. Conclusion

For the lower ranking Illinois No. 6 coal,

extracted oil and hydrogenated oils contain 2-ring benzothiophenes and 3-ring dibenzothiophenes having approximately the same distribution range of alkyl carbon numbers, substituted to respective aromatic thiophene rings. On the other hand, higher ranking bituminous Miike (Japanese) coal also contains similar aromatic thiophene type of benzo- and dibenzothiophene, added benzonaphthothiophene. It was observed that alkyl carbon substitution to aromatic thiophene rings for Miike coal tended to be shorter than that in case of lower ranking Illinois No. 6 coal. This tendency reflected the deeper maturation for higher ranking Miike coal.

#### References

- 1) Stock, L. M., Wolny, R., Bal, B., *Energy & Fuels*, 3, 651 (1989).
- 2) Sinninghe Damste, J.S., Leeuw, J. W., *Fuel Processing Technology*, 30, 109 (1992).
- 3) Kong, C., Lee, M. L., Iwao, M., Tominaga, Y., Pratap, R., Thompson, R. D., Castle, R. N., *Fuel*, 63, 702 (1984).
- 4) Nishioka, M., Lee, M. L., Castle, R. N., *Fuel*, 65, 390 (1986).
- 5) Boudou, J. P., Boulegue, J., Malechaux, L., Nip, M., Leeuw, J. W. de, Boon, J. J., *Fuel*, 66, 1558 (1987).
- 6) Philp, R. P., Bakel, A., *Energy & Fuels*, 2, 59 (1988).
- 7) Eglinton, T. I., Sinninghe Damste, J. S., Kohnen, M. E. L., Leeuw, J. W. de, *Fuel*, 69, 1395 (1990).
- 8) Yokoyama, S., Ohtani, K., Satoh, M., Sanada, Y., Preprint of 27th Coal Science Congress, Tokyo, 1990, p. 297.
- 9) Yokoyama, S., Tuzuki, N., Uchino, H., Katou, T., Sanada, Y., *Nippon Kagaku Kaishi*, 1983, 405.
- 10) Uchino, H., Yokoyama, S., Satoh, M., Sanada, Y., *Fuel*, 64, 842 (1988).

## 要 旨

石炭抽出オイルおよび水素化分解オイルの GC-FPD, GC-LVEI MS による  
有機硫黄化合物の化学構造に関する研究横山 晋<sup>†1)</sup>, 大谷明数<sup>†1)</sup>, 村路光義<sup>†1)</sup>, 杉淵宏志<sup>†1)</sup>, M. BAKR<sup>†2)</sup>, 佐藤正昭<sup>†1)</sup>, 真田雄三<sup>†1)</sup><sup>†1)</sup> 北海道大学エネルギー先端工学研究センター, 060 札幌市北区北 13 条西 8 丁目<sup>†2)</sup> Geology Dept., Faculty of Science, Alexandria University, Alexandria, Egypt

石炭中の有機硫黄の結合形態を究明するために、イリノイ No. 6 炭 (C: 77.7, S: 2.4 wt%) および三池炭 (C: 84.5, S: 1.1 wt% d. a. f.) をピリジン溶剤で抽出し、この *n*-ヘキサン可溶分 (抽出オイル) と、ピリジン抽出残さ炭については水素化分解反応を行い、生成したオイル分 (水素化分解オイル) を本研究の試料として用いた。両オイルを NH<sub>2</sub> カラム HPLC によって化合物クラスフラクションに分別し、各フラクションの GC-FID/FPD 分析から Fr-D (ナフタレン類), T (3,4 環芳香族類) に有機硫黄化合物を検出した。

イリノイ No. 6 炭, 三池炭の抽出オイル Fr-D, T について、GC-LVEI (低電圧イオン化電子衝撃法) MS 分析によって Z

数を求め、この Z 数マスキロマトグラムと GC-FPD クロマトグラムの比較によって有機硫黄化合物の解析を行った。Fr-D には C<sub>2</sub>-C<sub>5</sub>/C<sub>6</sub>-ベンゾチオフェン類, Fr-T には C<sub>0</sub>-C<sub>4</sub>/C<sub>6</sub>-ジベンゾチオフェン類の各同族体に帰属できた。

イリノイ No. 6 炭, 三池炭の各水素化分解オイルについても、Fr-D, T に有機硫黄化合物の存在が確認された。同様な解析法によって硫黄化合物タイプを解析し、それぞれベンゾチオフェン同族体, ジベンゾチオフェン同族体に帰属することができ、抽出オイルと類似した有機硫黄化合物が存在することを認めた。

## Keywords

Coal, Extraction, Hydrogenation, Organic sulfur compound, GCMS, Chemical structure

## 論文

## 石炭水素化分解生成オイルのGC-MS/MS 分析

(キーワード 石炭液化油, GC-MS, GC-MS/MS, 化学構造)

— 1994.12. 8 受理 —

北海道大学\*<sup>1</sup> 横山 晋, 中村 久志, 伊藤 好江  
 佐藤 正昭, 真田 雄三  
 石油公団\*<sup>2</sup> 鈴木 優, 町原 勉

## 1. 緒 言

石炭液化油は多種に亘る化合物タイプとこの同族体の極めて複雑な構成成分からなり, このため異性体をも含めた個々の成分の同定には著しい困難を伴う。GC-MS 分析はこの研究分野に顕著な進展をもたらし, 化石燃料油の化学構造に関して, (1)化合物タイプ同族体の分布 (SIM 法<sup>1)</sup>, マスクロマトグラム法<sup>2)</sup>), (2) 個々の化合物の同定<sup>3)4)</sup>に対して大きな成果を挙げた。

著者<sup>5)</sup>らもこれまで, HPLC により石炭液化油を化合物クラス (飽和炭化水素, 芳香族環数毎の各フラクション) に分離し, このフラクションに対して GC-MS 分析を適用した。これには低電圧イオン化法 (LV) の電子衝撃法 (EI) MS 分析によって Z 数マスキロマトグラムとしてデータ処理して, 化合物タイプ同族体に分類, 整理し, この高電圧イオン化法 (HV) EI MS 分析によって各成分の同定を試みた<sup>5)</sup>。しかし, これらのオイル成分は HPLC などで予備分離を行ったフラクションではあるが, 高分解能キャピラリーカラム GC によってでも個々の成分に分離するのが難しい。このため, (2)の研究目的に対して, GC からの複数成分の共溶出のために MS スペクトルに重複を生じ, 個々の化学種の同定を困難にしている。

MS/MS 分析計は, MS 分析計を 2 台連結した (タンデム MS) 装置である。これに GC を組み合わせた GC-MS/MS 分析計は, 混合物を最初に GC によって保持時間の差で分離を行い, 分離されない共溶出成分

分については第 1 段 MS において質量による分離を行う。これによって, ほぼ単一成分のイオン (ペアレントイオン) に分離することができ, 第 2 段 MS によって, この MS スペクトル (ドータースペクトル) を測定する。これより重複のない, 単一成分に由来する MS スペクトルが得られる。Fig. 1 は三連四重極型 (Q1, Q2, Q3) の GC-MS/MS 分析計の分離, 分析の概要である。

石炭液化油に対して GC-MS/MS 分析の適用は, これまで主に (1)化合物タイプ同族体の分布 についての報告であり<sup>6)7)</sup>, また(2)の「個々の成分の同定、に

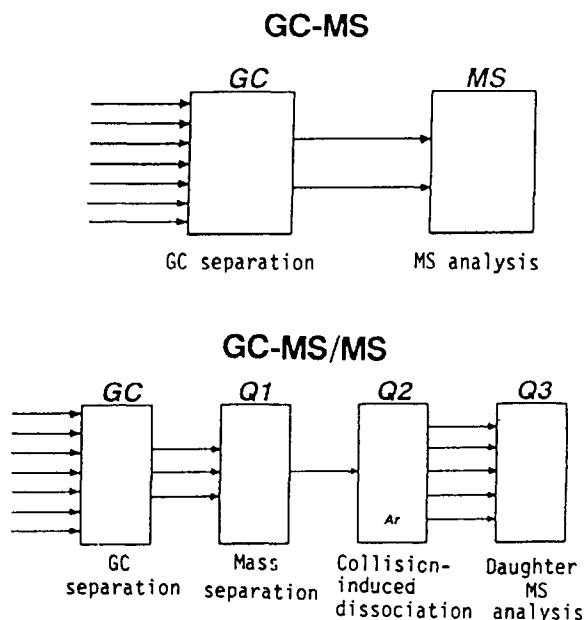


Fig. 1 Schematic representation of GC-MS and GC-MS/MS

\*1 エネルギー先端工学研究センター

札幌市北区北13条西8丁目

\*2 石油開発技術センター

千葉市美浜区浜田1丁目2番2



関する研究は系統的には行われていない。GC-MS/MS 法は GC-MS 法の限界を、画期的に解決できることが期待される。本研究では、既報<sup>5)</sup>の GC-MS 法で用いた赤平炭液化油オイル分に対して GC-MS/MS 法を適用し、両法の結果を比較して GC-MS/MS 法の有効性を明らかにした。これより液化油オイルを化合物タイプ同族体系列に従って MS スペクトルの収集、データベースの構築を目指しており、本報では 1 環芳香族化合物に対する結果について述べた。

## 2. 実験

赤平炭の高圧水素化分解反応 (400℃, 1 hr, 水素初圧 100 kg/cm<sup>2</sup>, アドキンス触媒) によって生成したオイル分を、酸、アルカリ洗浄して中性オイルを得た。このオイルをアミンカラムの HPLC によって化合物クラスフラクションに分離し、このうち 1 環芳香族類 (Fr-M) を本研究の試料とした。GC-MS 分析については既に発表してある<sup>5)</sup>。

GC-MS/MS 分析は、ドゥータモードで測定した。イオン化法は LV (10 eV) EI 法である。Table 1 に示した化合物タイプ同族体 ( $Z=-6, -8, -10, -12$ ) に属する化合物の分子量 ( $M$ ) を選んで、それぞれのペアレントイオンを Q1 で分離し、Q2 の衝突解離室へ導入した。Q2 での衝突解離条件はイオンの衝突加速電圧 -20 eV, 衝突アルゴン圧力 0.9 mm Torr である。Q3 でのドゥータスキャンは  $M/z 20 \sim (M+20)$  の範囲を 0.5 秒毎に掃引し、ドゥータスペクトルを測定した。装置は Finnigan Mat 社製 TSQ700 である。GC は固定相液体 DB-5 の 30 m シリカキャピラリーカラムを用い、初温 50 または 100℃, 3℃/min. で 300℃ 迄昇温させた。

## 3. 結果および考察

多数成分の複雑な混合物からなる石炭液化油は、類似の構造特性を持ったフラクションへの分離と、この詳細な構造解析によって進められてきた。NH<sub>2</sub> カラムの HPLC によって化合物クラス (飽和炭化水素, 芳香族環数毎, 更に極性化合物の各フラクション) に分離することによって、引き続きスペクトル分析による構造解析が極めて容易になり、精度良く行う事ができる。著者らはこれ迄液化油の化合物クラスフラクションに対して、LVEI MS 分析による構造解析を行い、各化合物クラスに対してナフテン環を形成するヒドロ芳香族類 (化合物タイプ) の帰属、およびこの同族体の分布について解析を行ってきた<sup>12)</sup>。更に、液化油の個々の成分を同定するのに、上述の化合物タイ

プ同族体に基づいて分類、整理を進める方法をとった<sup>5)</sup>。この MS データの分類、整理法は液化油の多数成分を構造の特徴によつて的確に把握出来るので、データ収集に対して利点が多い。以下にこの分類、整理の概念を述べる。



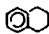
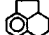
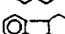

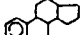
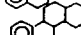
炭化水素の一般式は  $C_nH_{2n+2}$  で示され、ナフテン環、芳香環の形成によって水素の不足数  $Z$  が  $Z=2-(C_A+2R)$  によって決まる。この  $Z$  数によって液化オイルを化合物タイプに分類、表示する事ができる。 $C_A$  は分子中の芳香族炭素個数、 $R$  は芳香環、ナフテン環の全環数である。化合物タイプの環構造に置換したアルキル基炭素数 ( $Cal$ ) の異なる一連の化合物群は、同じ  $Z$  数を持った同族体である。この分子量  $M$  は母核環の分子量 ( $MM$ ) に  $CH_2$  基の質量数 14 ずつ増加する。1 環芳香族類の化合物タイプ同族体を、一覧にして Table 1 に示した。NH<sub>2</sub> カラム HPLC によって化合物クラスに分離できるが、更に、鎖状飽和炭化水素、芳香族環構造にナフテン環の挿入した各化合物タイプは、引き続き GC-MS による構造解析において  $Z$  数を帰属して解析される。これは、同じ  $Z$  数を持つ化合物タイプ同族体の分子イオンを、コンピュータ処理によって選び出し、時間関数によってイオンの強度を検知し、これを  $Z$  数マスキロマトグラムとして記録、分類できる<sup>5)</sup>。1 環芳香族化合物クラスの内、化合物タイプのモノナフテノベンゼン類 ( $Z=-8$ ) について、GC-MS による  $Z$  数マスキロマトグラム並びにこの同族体のマスキロマトグラムを Fig. 2 に示した。

この各化合物タイプ同族体に分類した  $Z$  数マスキロマトグラム、更にこの各マスキロマトグラムは電算機処理によって特定のイオンを分離したものであり、実際に GC によって分離されているものでない。従って、各マスキロマトグラムの間で GC 保持時間が接近する場合には、お互いの成分が重複して共溶出することになる。このため MS スペクトルはこれら成分の重複したスペクトルとなって観測され、個々の成分の同定が難しくなる。GC-MS/MS 分析では、この共溶出成分は更に MS 分離されるので、ほぼ単一成分の MS スペクトルとして測定される。

### 3.1 GC-MS/MS 分析

三連四重極型の GC-MS/MS 分析計は GC-Q1-Q2-Q3 の各ユニットの配列システムで構成されており、Q1 または Q3 MS を質量領域でスキャン、或いは特定質量に設定する事によって、1) ペアレント MS モード、2) ドゥータ MS モード、3) ニュートラル MS モードでそれぞれ異なる構造情報に基づく MS スペク

Table 1 Compound types and their molecular weight for monoaromatics (Fr-M)

| Compound class | Compound types |                                   |                       |                                                                                   | Molecular weight |                 |     |     |              |
|----------------|----------------|-----------------------------------|-----------------------|-----------------------------------------------------------------------------------|------------------|-----------------|-----|-----|--------------|
|                | Z numbers      | Molecular formulas                | Names                 | Ring structure                                                                    | MM <sup>*1</sup> | M <sup>*2</sup> |     |     |              |
|                |                |                                   |                       |                                                                                   |                  | Cal             |     |     |              |
|                |                |                                   |                       |                                                                                   |                  | 1               | 2   | 3   | 4 5          |
| Mono-aromatics | -6             | C <sub>n</sub> H <sub>2n-6</sub>  | Alkylbenzenes         |  | 78               | 92              | 106 | 120 | 134 148..... |
|                | -8             | C <sub>n</sub> H <sub>2n-8</sub>  | Mononaphthenobenzenes |  | 118              | 132             | 146 | 160 | 174 188..... |
|                |                |                                   |                       |  | 132              | 146             | 160 | 174 | 188 202..... |
|                | -10            | C <sub>n</sub> H <sub>2n-10</sub> | Dinaphthenobenzenes   |  | 158              | 172             | 186 | 200 | 214 228..... |
|                |                |                                   |                       |  | 172              | 186             | 200 | 214 | 228 242..... |
|                |                |                                   |                       |  | 186              | 200             | 214 | 228 | 242 256..... |
|                | -12            | C <sub>n</sub> H <sub>2n-12</sub> | Trinaphthenobenzenes  |  | 226              | 240             | 254 | 268 | 282 296..... |
|                |                |                                   |                       |  | 240              | 254             | 268 | 282 | 296 310..... |

\*1 Molecular weight of parent ring structure

\*2 M=MM+14·Cal

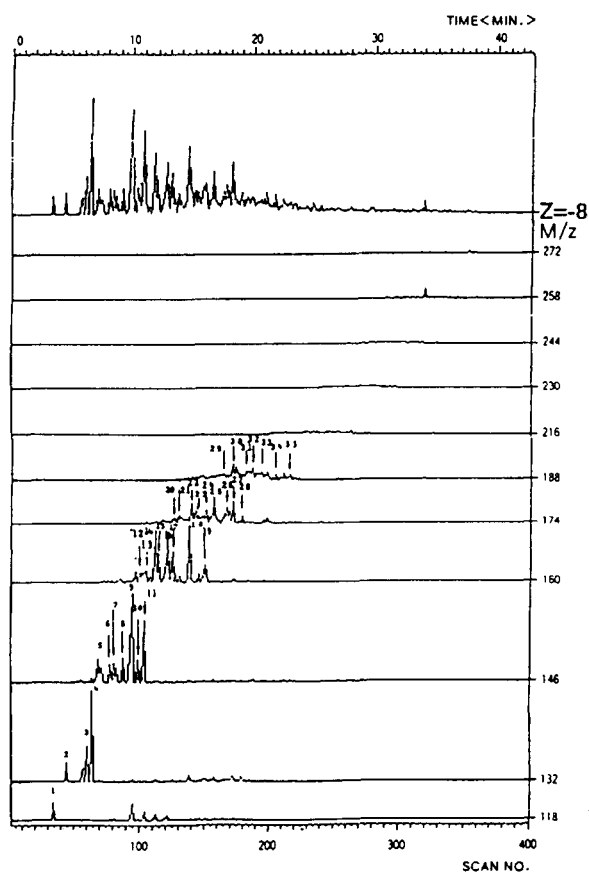

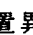
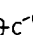

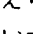
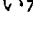


Fig. 2 Z mass chromatogram of Z=-8 and its mass chromatograms

トルデータが得られる。個々の化合物の同定を目的とした本研究では、ドゥータモードによってMSスペクトルを得る。

### 3.1.1 GC分離

HPLCによって分離した1環芳香族類には、Table 1に示す化合物タイプが含まれている。これらの異なる化合物タイプの間では分子量が同じ異性体はない。GC-MS/MS分析によって、化合物クラスフラクションは最初にGCの保持時間(Rt)の差違によって分離される。無極性に近い固定相液体カラムでは、各化合物タイプ同族系列はほぼ分子量の大きさ(沸点)によって、log Rt-Mの関係が一定で、それぞれ異なる相関線によって分離される<sup>8)</sup>。このため、同じRtにおいて、異なる分子量を持つ他の化合物タイプの成分が、GCの共溶出となって分離できない。これは次(3.1.2)に説明する、第1段のQ1 MSでの質量分離によって解決できる。

一方、同じ化合物タイプの環異性体( )、およびこれに置換するアルキル基の位置異性体( )、構造異性体( )の間では、Rtは可なり接近していることが考えられるが、これらの異性体同士で僅かでもRtに違いがあればGC-MS/MS分析で問題とならない。

### 3.1.2 MS分離

化合物クラスフラクションにおける上述のGC分離挙動から、GCの共溶出成分はそれぞれ分子量の異なる

る成分が大部分である。これがイオン化室に導入され、電子衝撃法によってベアレントイオンを生成する。ここで Q1MS 分析計は特定の  $M/z$  を持つベアレントイオンのみを選択、通過させる (ベアレント MS 分析計)。選択するベアレントイオンは1環芳香族類については、Table 1 の各化合物タイプ同族系列に属する成分の分子量のものである。Q1で単一の分子イオンにマスフィルターされたベアレントイオンは、Q2の衝突解離室に導かれ、ここでアルゴンガスとの衝突によって分解、フラグメントイオン (ドゥータイオン, Collision-induced dissociation (CID) イオン) を生成する。これを Q3MS 分析計でドゥータスキャンして、ドゥータ (または CID) MS スペクトルを測定する (ドゥータ MS 分析計)。これによって、複雑な液化油混合物から、単一分子成分の CID MS スペクトルが取得できる。

Fig. 3 は Q1MS を  $Z=-8$  (テトラリン, インダン

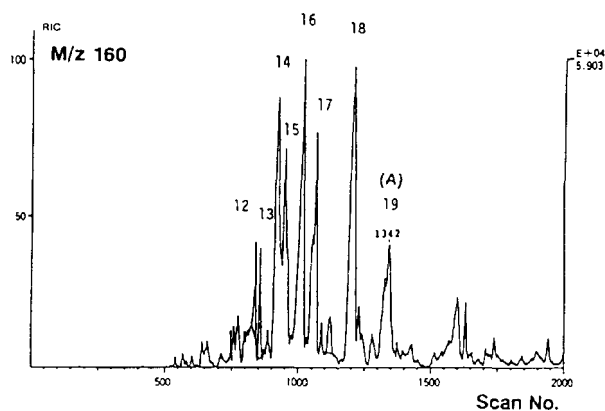


Fig. 3 RIC of  $M/z=160$  for compound type of  $Z=-8$  measured by GC-MS/MS

類) の  $M/z=160$  に設定して、ドゥータモードで測定した TIC (RIC) (Total (Reconstructed) ion chromatogram) である。GC-MS/MS によって  $M=160$  の異性体成分のみが分離されている事を示す。各 Scan No. (Rt に相当する) におけるドゥータ MS スペクトルは直結の電子計算機から呼出し、出力、記録される。TIC の主要ピークにおける Scan No. でのドゥータスペクトルを Fig. 4 (次頁) に示した。M + 1, M + 2 の同位体イオンを含めて、 $M/z=160$  以外の質量数のベアレントイオンは MS 分離されている。従って、このドゥータスペクトルは  $M/z=160$  の分子イオンとこのフラグメントイオンの限られたピーク数であり、フラグメントの同位体イオンも存在しないので、スペクトルは比較的単純である。

異性体成分の間でスペクトルが異なっており、化学構造の相違を反映した結果である。スペクトルはそれぞれ類似して、異なる特徴的パターンの一群からなり、異なる構造異性体によるものと考えられる。同定のために標準 EI MS スペクトルとの照合を試みたが、データバンク<sup>9)</sup> のデータ不足と各群の異性体同士の間でスペクトルが類似している場合があり (例えば、Fig. 4 ピーク No.12, 13, 18, 19), 特定の化学種に帰属できなかった。この結果を Table 2 に示した。

### 3.2 GC-MS/MS の分離能

前報<sup>5)</sup> では同じ赤平炭液化油 Fr-M の個々の成分を GC-MS 分析によって検討した。GC-LV (10eV) EI MS の  $M/z=160$  についてのマスクロマトグラムを、GC-MS/MS の結果 (Fig. 3) と比較するために Fig. 5 に示した。両法は共に極めて複雑な混合物から、特定のマスナンバーを持つ分子イオン ( $M/z=160$ ) を検出したもので、GC-MS/MS の RIC (Fig. 3) と

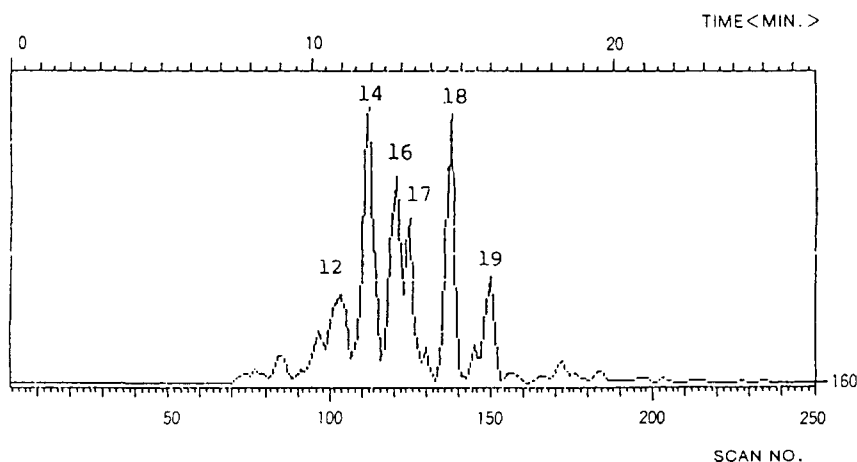
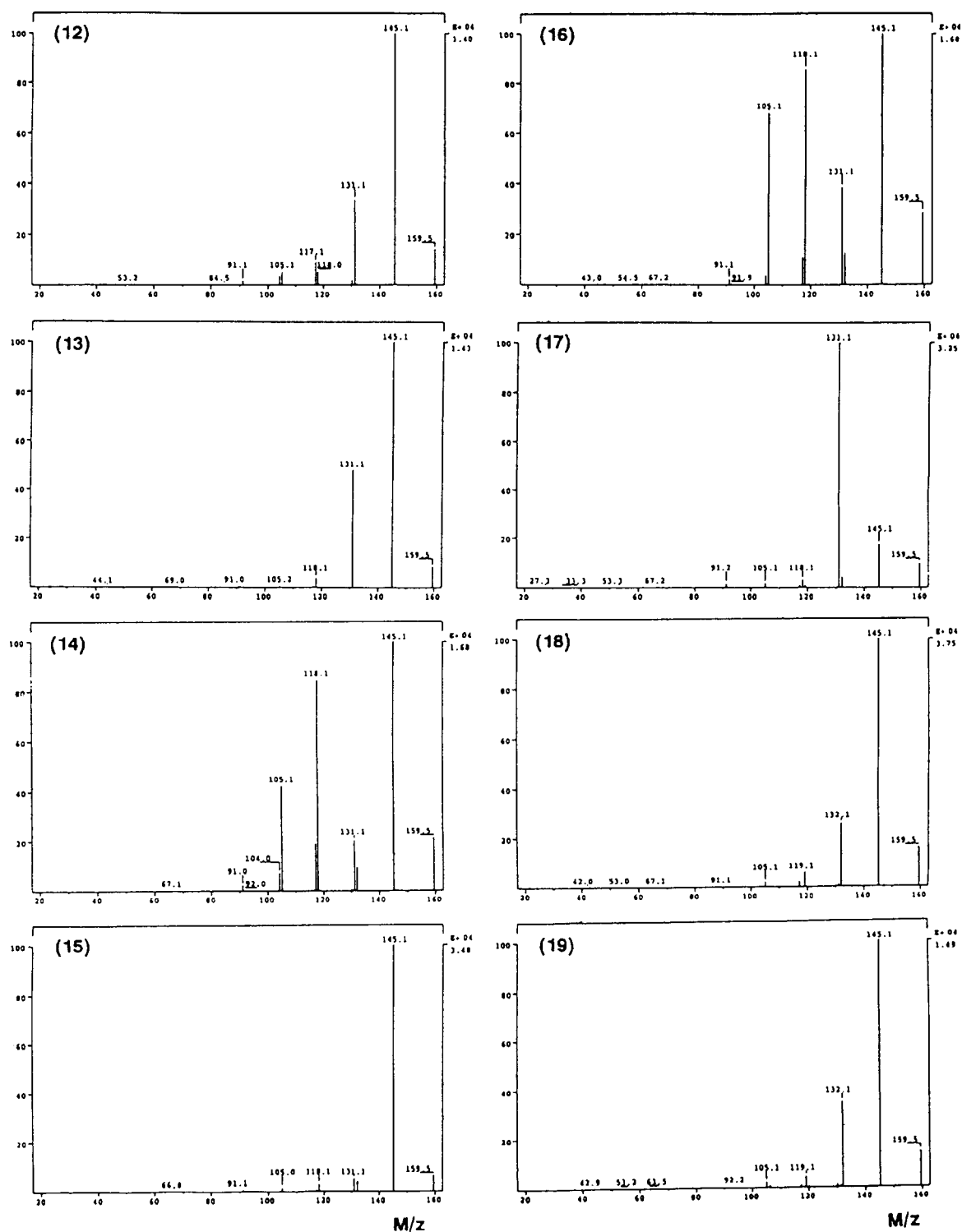


Fig. 5 Mass chromatogram of  $M/z=160$  for compound type of  $Z=-8$  measured by GC-MS

Fig. 4 CID MS spectra for isomers of  $M=160$  ( $Z=-8$ )The numbers correspond to Peak No. in RIC ( $M/z=160$ ) shown in Fig.3

GC-LVEI MS のマスクロマトグラム (Fig. 5) が酷似するのは当然である。しかし GC-MS 分析は既述した通り重複した分子イオンの内から、 $M/z=160$  の分子イオンのみをコンピュータ処理によって、選択、記録したものであり、実際に GC 分離されたものではない。両者のクロマトグラムの分解能の違いは、GC-MS/MS では掃引の繰り返し時間が 0.5 秒に対して、GC-MS では約 7 秒によるためである。

GC-MS 分析における  $M/z=160$  のマスクロマトグラム (Fig. 5) で、Scan No.150 (ピーク No.19) の LVEI MS スペクトルを Fig. 6-1 に示した。MS スペクトルは主として分子イオンが観測されているので、偶数マスナンバーの  $M/z=160$  (化合物 A : 100%, 相対強度), 174 (B : 40), 188 (C : 8) 190 (D : 10) の各成分が重複している事が明かである (奇数マスナンバーはこれらの同位体及びフラグメントイオンである)。GC-MS 分析における化合物の同定には、HVEI MS マススペクトルからフラグメントピークの解析によって行う。Fig. 6-2 はピーク No.19 (Fig. 5) の HV (20eV) EI MS スペクトルである。A, B, C, D の 4 成分の各 MS スペクトルが重複しているために、スペクトルは複雑になり、これから成分の帰属は難しい。

GC-MS 分析で  $M/z=160$  のマスクロマトグラム (Fig. 5) におけるピーク No.19 の重複した A, B, C, D の各成分は、GC-MS/MS 分析によってそれぞれ単一成分のスペクトルとして観測する事ができる。GC-MS/MS 分析によって、 $M/z=160$  の分子イオンのみを Q1MS で分離し、この RIC (Fig. 3) における Scan No.1342 (ピーク No.19) の CID MS スペクト

ルを呼び出せば、これが A 成分のスペクトルである。Fig. 4-(19)にこの CID スペクトルを示してある。一方、(B)成分については、GC-MS/MS 分析において  $M/z=174$  のペアレント MS 分離を行う。この RIC を Fig. 7 に示した。GC-MS 分析における  $M/z=174$  のマスクロマトグラム (Fig. 2 参照) と良く対応しており、GC-MS/MS のペアレントイオンの選択的分離に注目できる。Scan No.1378 のピーク No.24 が B 成分であり、このドータスペクトルを Fig. 8 に示した。GC-MS 分析では A, B, C, D の 4 成分の重複したスペクトル (Fig. 6-2) として得られたのに対して、GC-MS/MS 分析によって A 及び B 成分の単一成分から由来の MS スペクトルを収得する事ができた。なお、C, D 成分は微量成分であるので、CID MS スペクトルの出力をしていない。

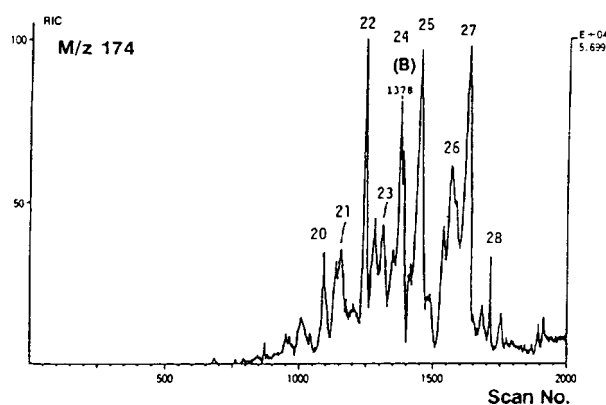


Fig. 7 RIC of  $M/z=174$  for compound type of  $Z=-8$  measured by GC-MS/MS

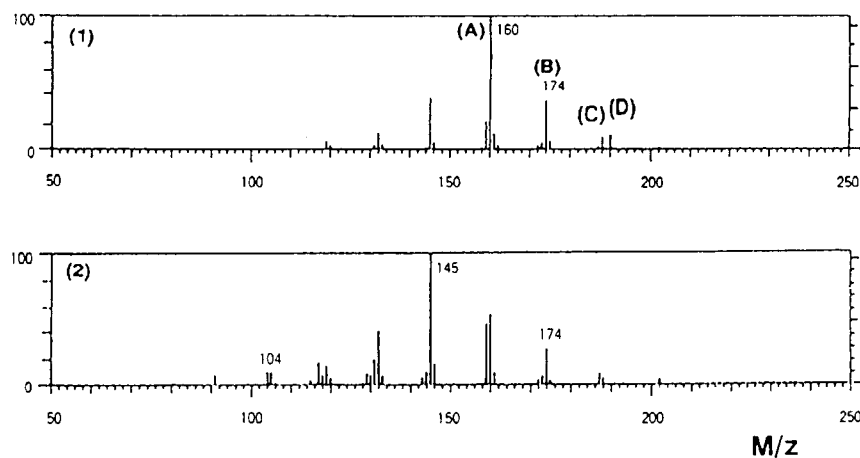


Fig. 6 LVEI MS spectrum (1) and HVEI MS spectrum (2) on Peak No. 19 in mass chromatogram of  $M/z=160$  shown in Fig.5

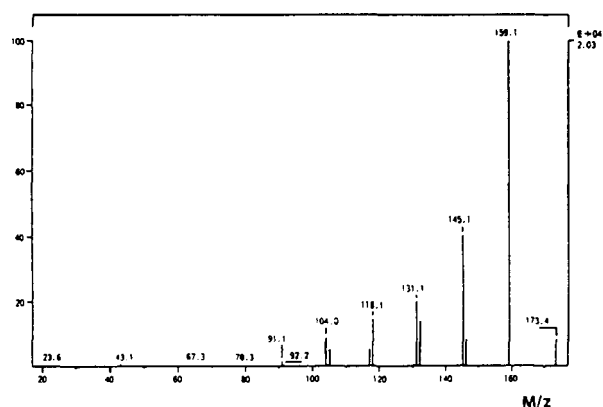


Fig. 8 CID MS spectrum on Peak No. 24 in RIC of  $M/z=174$  shown in Fig. 7

### 3.3 CID と EI MS スペクトルの比較

MS/MS 分析におけるドゥータイオンの生成は、Q1 MS によって分離された特定のペアレントイオンを衝突解離室に導入させ、これを中性分子のガス（通常アルゴン）によって衝突、解離させて行う。ドゥータ MS スペクトル（CID MS スペクトル）はこの衝突エネルギーによって影響され、ペアレントイオンへの衝突解離電圧およびアルゴン圧力によって決まる。アルゴン圧力（ $\sim 2$  mm Torr）および衝突解離電圧（Collision offset voltage :  $\sim 40$  eV）が高い程、ベースピーク（最強ピーク：100%）は低質量側のフラグメントイオンに移り、高質量側イオンの強度は低くなる傾向が認められている<sup>10)</sup>。高エネルギーによる衝突によって、高質量フラグメントが解裂して低質量フラグメントイオンを生成し易いためであり、この結果、スペクトルの定性能は減ずる。

MS スペクトルによる同定は、1) 標準スペクトルとの照合、2) スペクトルの解析によってなされる。CID MS スペクトルにおいて、(1)のための CID MS スペクトルの収集は殆どなされていないのが現状である。これに代わる、CID MS スペクトルを EI MS スペクトルの標準データと照合させる検索法も成功していない<sup>10)</sup>。(2)による同定法については、衝突解離の機構が分子構造を反映した部分構造へのフラグメントイオンである事が重要である。そこで CID MS スペクトルを EI MS スペクトルと比較して、CID スペクトルの特徴を明らかにする必要がある。

GC-HV (20 eV) EI MS 分析における  $M/z=160$  のマス chromatogram (図は掲示していない) は、GC-LVEI MS のそれ (Fig. 5) と、および GC-MS/MS の RIC (Fig. 3) と共に良い対応である。

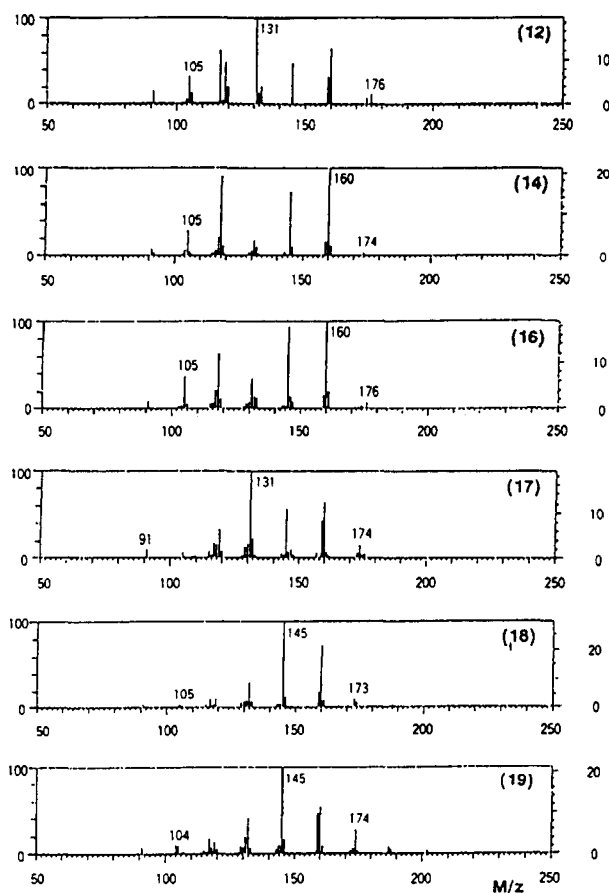


Fig. 9 EI MS spectra for isomers of  $M=160$  ( $Z=-8$ )  
The numbers correspond to Peak No. in mass chromatogram ( $M/z=160$ ) shown in Fig. 5

GC-MS/MS におけるこの RIC の各ピーク No. に対応する、EI MS スペクトルを Fig. 9 に示した。GC-MS では、分子イオン  $M/z=160$  の外に、GC における共溶出のために  $M/z=174, 176$  の成分に由来するスペクトルが重複して現れているが、ピーク No. 19 を除いて著しいものではない。これより EI および CID MS スペクトル (Fig. 4) の比較から、ピークは共に同じ  $M/z$  の値であり、両法による解裂イオンはほぼ同じであると言える。即ち、CID 法による解裂機構は EI 法と類似であり、分子の部分構造を特徴的に反映した分解のされ方である事が分かる。しかし、CID MS スペクトルのピーク強度は EI スペクトルと大きく異なる場合があり、両者のイオン化方法の差異として注目される。このことは、標準スペクトルとして CID MS スペクトルの収集が、EI スペクトルと共に重要であることを示唆する。

### 3.4 石炭液化油の MS/MS スペクトル

多種類の化合物クラス、タイプ同族系からなる複雑

Table 2 CID MS spectra of Z=-8 compound type for Akabira coal hydrogenation oil

| Molecular weight<br>Formula            | Peak No. *1 | Scan No. *2 | Compounds                                                             | Mass numbers (M/z)<br>(Intensities %)                                   |
|----------------------------------------|-------------|-------------|-----------------------------------------------------------------------|-------------------------------------------------------------------------|
| 118<br>C <sub>9</sub> H <sub>10</sub>  | 1           | 34          | Indan                                                                 |                                                                         |
| 132<br>C <sub>10</sub> H <sub>12</sub> | 2           | 44          |                                                                       |                                                                         |
|                                        | 3           | 60          | C <sub>1</sub> -Indan                                                 | 132(10), 117(100)                                                       |
|                                        | 4           | 64          | 1,2,3,4-Tetrahydro-naphthalene                                        | 132(19), 104(100), 91(18)                                               |
| 146<br>C <sub>11</sub> H <sub>14</sub> | 5           | 69          | 1,2,3,4-Tetrahydro-2-methylnaphthalene                                | 146(18), 131(29), 118(11), 91(37)                                       |
|                                        | 6           | 78          | 1,2,3,4-Tetrahydro-1-methylnaphthalene                                | 146(11), 131(100), 118(18)                                              |
|                                        | 7           | 82          | C <sub>2</sub> -Indan                                                 | 146(16), 131(53), 117(100)                                              |
|                                        | 8           | 88          | 2,3-Dihydro-4,6-dimethylindene                                        | 146(15), 131(100)                                                       |
|                                        | 9           | 94          | 1,2,3,4-Tetrahydro-5/6-methylnaphthalene                              | 146(31), 131(96), 118(100), 105(20)                                     |
|                                        | 10          | 99          | 1,2,3,4-Tetrahydro-1-methylnaphthalene                                | 146(18), 131(100)                                                       |
|                                        | 11          | 104         | C <sub>1</sub> -Tetralin                                              | 146(31), 131(100), 118(90), 105(24)                                     |
| 160<br>C <sub>12</sub> H <sub>16</sub> | 12          | 103         | 2,3-Dihydro-1,1,3/1,1,4/1,1,5/1,1,6/1,4,7/1,5,7/4,5,7-trimethylindene | 160(17), 145(100), 131(33)                                              |
|                                        | 13          | 105         |                                                                       | 160(4), 145(100), 131(49)                                               |
|                                        | 14          | 112         | 1,2,3,4-Tetrahydro-2,6/2,7-dimethylnaphthalene                        | 160(22), 145(100), 132(10), 131(20), 118(85), 117(19), 105(43)          |
|                                        | 15          | 114         | Trimethyl-indan                                                       | 160(7), 145(100)                                                        |
|                                        | 16          | 121         | 1,2,3,4-Tetrahydro-2,6/2,7-dimethylnaphthalene                        | 160(28), 145(100), 132(12), 131(38), 118(86), 117(11), 105(69)          |
|                                        | 17          | 125         | C <sub>2</sub> -Tetralin                                              | 160(10), 145(18), 131(100)                                              |
|                                        | 18          | 138         | 1,2,3,4-Tetrahydro-5,6/5,7/6,7-dimethylnaphthalene                    | 160(16), 145(100), 132(26)                                              |
|                                        | 19          | 150         | naphthalene                                                           | 160(14), 145(100), 132(38)                                              |
| 174<br>C <sub>13</sub> H <sub>18</sub> | 20          | 126         | C <sub>3</sub> -Tetralin                                              | 174(9), 159(100), 145(86), 131(22), 118(96)                             |
|                                        | 21          | 130         | C <sub>3</sub> -Tetralin                                              | 174(6), 159(100), 145(39), 132(13), 131(17)                             |
|                                        | 22          | 140         | 1,2,3,4-Tetrahydro-1,5,7-trimethylnaphthalene                         | 174(5), 159(100), 132(14), 132(14), 131(16)                             |
|                                        | 23          | 143         | C <sub>3</sub> -Tetralin                                              | 174(7), 159(32), 145(100), 132(19), 131(10), 118(15), 105(12)           |
|                                        | 24          | 151         | C <sub>3</sub> -Tetralin                                              | 174(9), 159(100), 145(40), 132(14), 131(20), 118(15)                    |
|                                        | 25          | 157         | C <sub>3</sub> -Tetralin                                              | 174(10), 159(100), 145(47), 132(35), 131(16), 119(19)                   |
|                                        | 26          | 168         | C <sub>3</sub> -Tetralin                                              | 174(10), 159(100), 145(40), 132(42), 119(16)                            |
|                                        | 27          | 172         | C <sub>3</sub> -Tetralin                                              | 174(5), 159(100), 146(11), 132(6)                                       |
|                                        | 28          | 179         | C <sub>3</sub> -Tetralin                                              | 174(8), 159(74), 145(100)                                               |
| 188<br>C <sub>14</sub> H <sub>20</sub> | 29          | 163         |                                                                       |                                                                         |
|                                        | 30          | 172         |                                                                       |                                                                         |
|                                        | 31          | 183         | C <sub>4</sub> -Tetralin                                              | 188(3), 173(100), 159(16)                                               |
|                                        | 32          | 186         | C <sub>4</sub> -Tetralin                                              | 188(8), 173(100), 159(70), 146(16), 145(60), 131(24), 118(14)           |
|                                        | 33          | 192         | C <sub>4</sub> -Tetralin                                              | 188(11), 173(100), 159(72), 145(99), 133(10), 132(21), 131(12), 119(12) |
|                                        | 34          | 205         | C <sub>4</sub> -Tetralin                                              | 188(4), 173(20), 159(100), 145(18), 132(16)                             |
|                                        | 35          | 216         |                                                                       |                                                                         |

\*1 Correspond to the peak numbers in Fig.2(GC-LVEI MS)

\*2 Correspond to Scan No. in Fig.2 and Fig.5

な石炭液化油成分の同定に、GC-MS/MS 分析の適用は GC-MS 法の難点を大幅に解決できる画期的な手段である。石炭液化油の MS スペクトルを収集するのに、前報<sup>5)</sup>では各化合物タイプ同族系列によって成分を分類し、スペクトルを整理する事について提案した。GC-MS/MS 分析によって、ほぼ単一成分に由来する個々の液化油成分の MS スペクトルが得られるので、ここでも“化合物タイプ”同族系列毎に MS スペクトルの収集を試みた。

1 環芳香族類のモノナフテノベンゼン類 (Z=-8) の Z 数マスキングクロマトグラム (Fig. 2) の主要ピークについて、CID MS スペクトルをパターン係数表で Table 2 に示した。各分子量における異性体の間で、スペクトルが類似している場合があり、これから成分を限定するのは難しい。更に GC の保持指標による同定法<sup>11)</sup>を併用する必要がある。現時点では、GC-MS/MS 分析から化合物の帰属に迄至らないが、この CID MS スペクトルは同定の過程における有力な知見として、更に同定後の CID MS スペクトルのデータベースとして貴重な資料となる。

#### 4. 結 論

高分解能キャピラリーカラムを備えた GC-MS 分析法によってでも、複雑な混合物からなる石炭液化油成分を個々の成分に分離、同定するのに、装置の分離能の面で難点があった。この解決方策として、GC-MS/MS 分析法は質量に基づく分離を GC 分離と組み合わせる事により、この問題点を解決する事ができた。

石炭液化油を化合物タイプ (Z 数) 同族系列毎に分類、整理した Z 数マスキングクロマトグラムは、液化油の構成成分を普遍性のある指標として用いる事ができる。そしてこの表示法による石炭液化油成分の CID MS スペクトルの収集、および蓄積は、個々の成分の同定、更に CID MS スペクトルのデータベースとして意義が大きい。

(後 記)

本論文は文部省科学研究費補助金 (課題番号 05650847) により行われたものである。付記してここに感謝の意を表す。

なお、Fr-M、Z=-8 化合物タイプ同族体の CID MS スペクトルは、該研究成果報告書 (平成 6 年度) に掲載されている。また、Fr-M (1 環芳香族類)、Fr-D (2 環芳香族類)、Fr-T (3,4 環芳香族類) 化合物タイプ同族体については、著書「横山 晋, 鈴木 俊, 石炭液化油の質量分析-液化オイル成分のデータ

MS スペクトル, 北大生協印刷, 平成7年9月」に収録してある。

# 文 献

- 1) Youtcheff, J. S., Given, P. H., Baset, Z. and Sundaram, M. S., *Org. Geochem.*, 5, (3), 157 (1983)
- 2) Wang, T. -G. and Simoneit, B. R. T., *Fuel*, 69, 12 (1990), 70, 819 (1991)
- 3) Lee, M. L., Novotny, M. V. and Bartle, K. D., *Analytical Chemistry of Polycyclic Aromatic Compounds* (Academic Press)
- 4) Hazai, I., Alexander, G. and Szekely, T., *J. Chromatography*, 367, 117 (1986)
- 5) 横山 晋, 伊藤好江, 佐藤正昭, 真田雄三, 第30回石炭科学会議発表論文集, p.256 (1993)
- 6) Wang, T. -G., Simoneit, B. R. T., Philp, R. P. and Yu, C. -P., *Energy & Fuels*, 4, 1770 (1990)
- 7) Ciuppek, J. D., Cooks, R. G., Wood, K. V. and Ferguson, C. R., *Fuel*, 62, 829 (1983)
- 8) 三宅 担, 実験化学講座, 続9 ガスクロマトグラフィ (丸善) p. 252 (昭40年)
- 9) MS スペクトル検索システム (株デービーエス)
- 10) Bente, P. F. and Mc Lafferty, F. W., *Mass Spectrometry part B*, Editor, Merritt, C., Mc Ewen, Jr. C. N., Chapter 3, Marcell Dekker, Inc.
- 11) Lee, M. L., Vassilaros, D. L., White, C. M., and Novotny, M., *Anal. Chem.*, 51, 768 (1979)
- 12) 佐藤正昭, 谷本昌隆, 横山 晋, 真田雄三, 日化, 1987, No.1, 67

## GC-MS/MS Analyses of Coal Hydrogenation Oil

Susumu YOKOYAMA<sup>\*1</sup>, Hisashi NAKAMURA<sup>\*1</sup>, Yoshie ITOH<sup>\*1</sup>, Masaaki SATOU<sup>\*1</sup>, Yuzo SANADA<sup>\*1</sup>  
Masaru SUZUKI<sup>\*2</sup> and Tsutomu MACHIHARA<sup>\*2</sup>

( \*1 Center for Advanced Research of Energy Technology,  
Hokkaido University  
\*2 Technology Reserch Center, Japan National Oil Corporation )

**SYNOPSIS** : — In a previous paper, coal hydrogenation oil was subjected to GC-MS analysis for the elucidation of the chemical structure for its individual components. However, the mass spectra often had an overlap of some components and the interpretation of the spectra became very difficult.

In this study, GC-MS/MS analyses, which has a superior efficiency by the combination of GC and mass separations, were applied to resolve the problems mentioned above of the GC-MS method. After the first separation of the monoaromatic fraction by a high resolution capillary column GC, specific mass numbers of the components belonging to the homologous series of the compound type were selected for the second separation into unimolecular parent ion. Daughter mass spectra derived from the unimolecular parent ion were obtained by scanning the daughter mass range at the second mass analyser.

Main peaks of Z number mass chromatogram of Z=-8, mononaphthenobenzenes, were measured for their daughter mass spectra. Acquisition of mass spectra with arrangement of Z number mass chromatograms are an effective procedure for the identification of individual compounds of coal liquid and a database of mass spectra.

### Key Words

Coal hydrogenation, Oil, GC MS, GC MS MS, Chemical structure



## Vapor Pressure Estimation for Hydrocarbons in a Coal Derived Liquid

Shin-ya HARIKAE, Masaaki SATOU, Tadatoshi CHIBA,  
Susumu YOKOYAMA and Yuzo SANADA

Center for Advanced Research of Energy Technology,  
Hokkaido University, Sapporo 060, Japan

### 1. INTRODUCTION

The vapor pressure as well as the boiling point is one of the most fundamental properties for process design and control. In spite of numerous studies on vapor pressure estimation for pure organic compounds, their applicability to coal derived liquids has never been confirmed yet[1,2]. In our previous studies[3-5], simple equations for estimation of boiling point, molar volume and refractive index were derived on the basis of a new group contribution method, i.e., relationships between the chemical structure of hydrocarbons in coal derived liquid and their physical properties. This study aims at extension of our conception to vapor pressure estimation.

### 2. EXPERIMENT

Hydrocarbons in a recycle solvent derived from Wyoming coal liquefaction were characterized following a program of analytical methods using high performance liquid chromatography(HPLC) with an amine column and mass spectrometry(GC/MS)[6]. The recycle solvent was first separated by a spinning band distillation apparatus into 24 fractions having a boiling point temperature range from 464K to 630K, each fraction with a temperature interval of 2K to 28K. Some representative fractions were further separated into chemically homologous compounds called "compound classes" according to the number of aromatic rings by a HPLC. There were six hydrocarbon compound classes; alkanes(Fr-P), monoaromatics(Fr-M), naphthalene type diaromatics(Fr-D1), biphenyl type diaromatics(Fr-D2), tri- and tetra-aromatics (Fr-T1 and T2) and poly-, polar compounds (Fr-PP). GC/MS measurement was carried out to find the average numbers of total carbons, aromatic rings and naphthenic rings of each compound class.

The same narrow cut distillates were also separated into hydrocarbon portion(Fr-HC) and Fr-PP by the same HPLC. The vapor pressure of Fr-HC was determined from isothermal gas chromatographic measurement of relative retentions[7] on a non-polar OV-1 column. Measurements were made at every 10K from 373 to 573K. The experimental scheme is shown in Fig. 1.

### 3. RESULTS AND DISCUSSIONS

In our previous studies[3-5], the influences of component groups such as aromatic

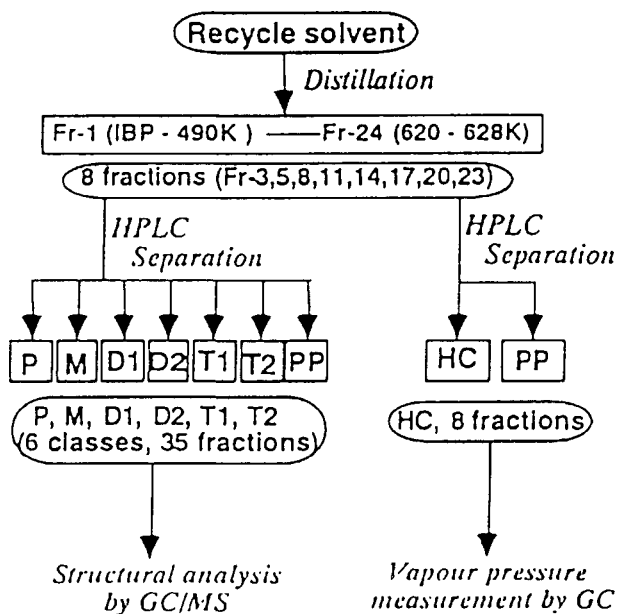


Fig.1 Experimental scheme

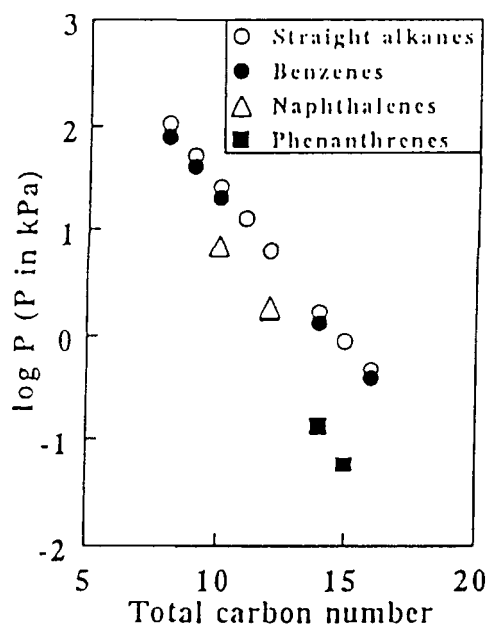


Fig.2 Change in vapour pressure of straight alkanes and aromatic hydrocarbons at 400K with total carbon number

ring and naphthenic ring to the values of boiling point, molar volume and refractive index have been systematically examined. In brief, the difference between the value of a property of a given compound and that of a reference is attributed to the contribution of a certain structural feature. For example, straight alkanes are selected for hydrocarbons as the reference and the structural contributions are evaluated on the basis of aromatic rings, naphthenic rings and so on. The property of a given non-paraffinic molecule is the sum of all the non-paraffinic structures being incremental to that of reference.

### 3.1. Vapor pressure of pure hydrocarbons

Figure 2 shows change of logarithmic values of the vapor pressure at 400K with the total carbon number for straight alkanes, benzenes, naphthalenes and phenanthrenes with one straight alkyl side chain, where values of vapor pressure are available as Antoine constants[8]. The relationships between the logarithmic values of the vapor pressure and total carbon number are linear for the homologous series, so far tested. Furthermore, each linear relationship is parallel with each other. In other words, the difference of logarithmic values of the vapor pressure of hydrocarbon homologue with those of straight alkanes ( $\delta \log P$ ) having the same total carbons is invariable with the total carbon number. The difference gradually increases with the aromatic ring number.

In Figure 3, the values of  $\delta \log P$  for these hydrocarbon homologous series are plotted against the reciprocal of temperature. The values are seen to be inversely proportional to the reciprocal of temperature with the slope becoming gradually steep with the number

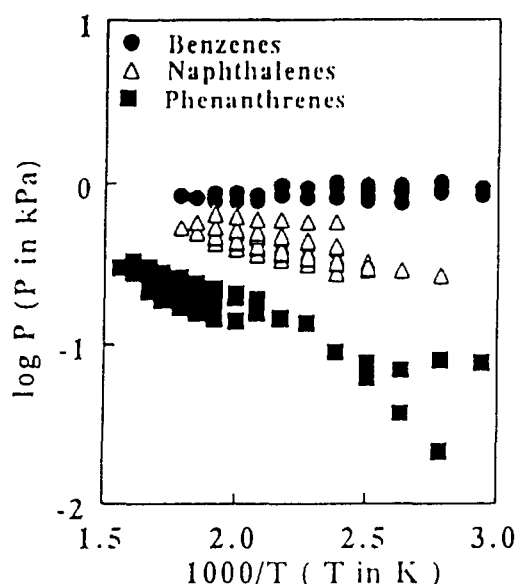


Fig. 3 Difference of logarithmic value of vapor pressure of aromatic hydrocarbons with those of straight alkanes

the particular component groups and the absolute temperature, respectively. Here, aromatic rings, naphthenic rings and aromatic conjunction carbons are considered as the component groups. The above equation means that the vapor pressure of hydrocarbons are calculated by adding the total increments of vapor pressure to those of the straight alkanes with the same total carbon number.

The  $P_{\text{paraff.}}$  is expressed as a function of the total carbon number ( $N_t$ ) of a given hydrocarbon as

$$\log P_{\text{paraff.}} = (2.439 - 347.9 / T - 7.105 \times 10^{-1} \times \log T) \times N_t + 4.153 \quad (2)$$

which was obtained by a regression analysis based on the vapor pressure of straight alkanes with total carbon numbers from 6 to 30 in the temperature range 300 to 720 K in the literature [8]. The correlation coefficient and average absolute error between the literature values of temperature and values calculated using Equation (2) at a given vapor pressure are 0.998 and 1 K, respectively. This equation is a generalized version of Antoine equation using the total carbon number as a parameter.

The values of group contributions ( $P_i$ ) in Equation (1) were also determined by the regression analysis. The results are listed in Table 1. The values of 0.865 and 9 K were obtained for the correlation coefficient and average absolute error, respectively. The influence of aromatic conjunction carbons to the value of vapor pressure can not be systematically considered because few data are available in literatures.

### 3.2. Vapor pressure of hydrocarbons in a recycle solvent

The major purpose of this study lies in the estimation of the vapor pressure for

of aromatic rings.

In the same manner, influence of naphthenic ring to the vapor pressure was examined. As a result, the values of  $\delta \log P$  were found to be less than those of aromatic rings, and to be inversely proportional to the reciprocal of temperature with the slope gradually becoming steep with the numbers of naphthenic rings.

Based on the above findings, the following equation is derived for vapor pressure calculation.

$$\begin{aligned} \log P &= \log P_{\text{paraff.}} + \delta \log P \\ &= \log P_{\text{paraff.}} + \sum (P_i \times N_i) / T \end{aligned} \quad (1)$$

where,  $P$ ,  $P_{\text{paraff.}}$ ,  $P_i$ ,  $N_i$  and  $T$  represent the vapor pressure of a given hydrocarbon, the vapor pressure of straight alkanes having the same total carbon number, the incremental vapor pressure contributed by  $i$ -th component groups, the number of

Table 1 Component contribution to vapor pressure

| Component group                | Contribution (Pi) |
|--------------------------------|-------------------|
| Aromatic ring                  | -91.63            |
| Naphthenic ring                | -42.56            |
| Aromatic<br>conjunction carbon | -29.57            |

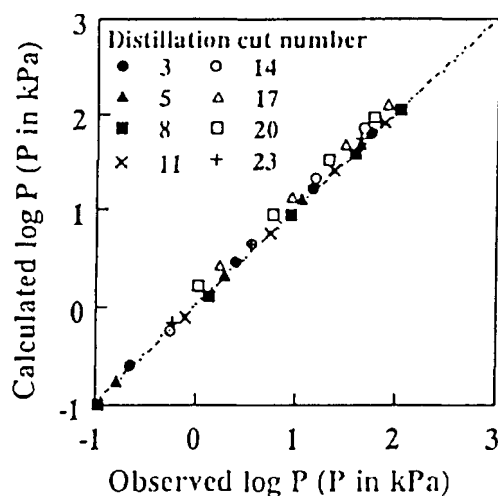


Fig.4 Comparison between observed and calculated log P

hydrocarbon mixture in a recycle solvent as well as of pure hydrocarbons. Application of the present method to a recycle solvent gives a good agreement between calculated and observed vapor pressures, as summarized in Figure 4. The average absolute error between the literature values of temperature and values calculated using Equation (2) at a given vapor pressure is as small as 8K.

Hence, it is now possible to estimate the vapor pressure of various hydrocarbons such as alkanes, aromatics, hydroaromatics and their alkyl derivatives in both forms of pure substance and mixture over a range of total carbon number from 6 to 20.

#### 4. CONCLUSION

It was clarified that the difference ( $\delta \log P$ ) of logarithmic values of the vapor pressure of hydrocarbon homologue with those of straight alkanes having the same total carbons is invariable at a given temperature with the total carbon number.

The value of  $\delta \log P$  was found to be inversely proportional to the reciprocal of temperature with the slope gradually becoming steep with the numbers of aromatic and naphthenic rings. A simple equation is proposed based on these findings.

#### REFERENCES

1. H. Hartounian and D.T. Allen, *Fuel*, 68(1989) 480
2. L.E. Vajdi and D.T. Allen, *Fuel*, 68(1989) 1388
3. M. Satou, S. Yokoyama and Y. Sanada, *Fuel*, 71(1992) 565
4. M. Satou, H. Nemoto, S. Yokoyama and Y. Sanada, *Energy&Fuels*, 5(1991) 638
5. M. Satou, H. Yamaguchi, T. Murai, S. Yokoyama and Y. Sanada, *Sekiyu Gakkaishi*, 35(1992) 466
6. H. Uchino, S. Yokoyama, M. Satou and Y. Sanada, *Fuel*, 64(1985) 842
7. D.J. Hamilton, *J. Chromatogr.*, 195(1980) 75
8. R.M. Stephenson and S. Malanowski, *Handbook of the Thermodynamics of Organic Compounds*, Elsevier, New York, 1987

[Regular Paper]

## Refining of Coal Liquid —Structural Analysis of Hydrogenated SRC-II Distillates with HPLC-GC/MS—

Katsumori TANABE\*†<sup>1)</sup>, Masaaki SATOU, Susumu YOKOYAMA, and Yuzo SANADAMetals Research Institute, Faculty of Engineering, Hokkaido University,  
N-13 W-8, Kita-ku, Sapporo, 060

(Received December 8, 1994)

An SRC-II heavy distillate and twelve hydrogenated coal liquids derived thereof were separated into compound class fractions by an HPLC equipped with an amine column. Compound type analysis of each aromatic compound class was performed by MS to investigate changes in the composition of the coal liquefaction solvent as a function of the severity of hydrogenation reactions. The hydroaromatics yields of the solvent increased with increasing severity of hydrogenation at the expense of aromatic and polar compounds. The reaction conditions of 400°C, 30 min are suitable for hydrogenation of SRC-II heavy distillate from the viewpoint of a coal liquefaction solvent. It appears that production of organic gasses is consistent with the reduction of yields of alkyl side carbon and naphthenic rings, and production of light oil is in agreement with the decrease of a yield of aromatic rings.

### 1. Introduction

It is generally accepted that the most important role of the coal liquefaction solvent is to donate hydrogen enough to stabilize free radicals derived from coal pyrolysis. The reaction rate depends on the temperature, pressure, catalyst and quality of the solvent. A hydrogenated anthracene oil and/or tetralin, which have high hydrogen-donor properties, increase the reaction rate and also reduce the effect of pressure and catalyst on the reaction rate. The solvent is recovered from liquefied products by distillation in commercial scale processes. There are some commercial scale processes, which increase the hydrogen donor quality of recycle solvents. To improve the hydrogen-donor property of the solvent, a recycle solvent is often hydrogenated with a Co-Mo or a Ni-Mo catalyst. There must be suitable conditions for the hydrogenation of the solvent. For instance, tetralin is a hydrogen-donor, but decalin is not. Hydrogen-donor property of the solvent was deteriorated by isomerization and ring opening under highly severe conditions. It may, therefore, be thought that there is an optimum condition for hydrogenation of each solvent. It is highly important to understand the hydrogenation

reaction of the coal liquefaction solvent, for continuous operation of a commercial plant.

On the other hand, it is necessary to conduct a detailed and rapid analysis of the chemical composition of the hydrogenated solvent, for the purpose to understand the hydrogen-donor property of the solvent. Several methods were reported for the evaluation of average structural parameters of the solvent with NMR and IR<sup>1)-8)</sup>. In the meanwhile, some studies on the complex organic structures of the solvent by MS analysis were performed by Swansiger *et al.*<sup>9)</sup>, Boduszynski *et al.*<sup>10)</sup> and Niwa *et al.*<sup>11)</sup>. In the authors' preceding papers<sup>12)-15)</sup>, detailed 'compound type' analysis for coal hydrogenation liquids according to aromatic rings (*Ra*), naphthenic rings (*Rn*) and alkyl carbon (*Cal*) diagram parameters were reported, with the HPLC-MS procedure. Aromatic/hydroaromatic compound type and alkyl side chain carbon distribution of complex mixture oils were clarified, based on the separating behavior of HPLC and the type analyses according to *Z* value by MS.

Numerous studies have been reported on hydrogenation of model compounds; phenanthrene and pyrene. On the other hand, a few studies on changes in composition of the coal liquefaction solvent as a function of severity of hydrogenation have been performed. Green *et al.*<sup>16)</sup> have reported on changes in chemical class-type fractions resulting from hydrotreatment of SRC-II distillates at different levels of severity. Boduszynski *et al.*<sup>17)</sup>

\* To whom correspondence should be addressed.

†<sup>1)</sup> (Present) Mizushima Refinery, Japan Energy Corp., 2-1  
Ushio-dori, Kurashiki, Okayama 712

have studied changes of fifty homologous series of aromatic and hydroaromatic hydrocarbons at mild and severe hydrogenation of SRC distillates. Rosal *et al.*<sup>18)</sup> have studied the changes in composition during hydrogenation of an anthracene oil. Detailed information on how the structure of solvents changes with variations in severity of hydrogenation has been extremely limited.

This work was pursued to obtain detailed information on hydrogenation reactions affecting coal liquefaction solvent. Two kinds of hydrogenation experiments using SRC-II heavy distillate were performed, using a conventional petroleum hydrotreating catalyst. Hydrogenation products were analyzed by the HPLC-MS method to observe aromatic and hydroaromatic structural changes with severity of the reaction.

## 2. Experimental

### 2.1. Materials

A heavy fraction of SRC-II distillate, obtained

Table 1 General Properties of Feed

| Sample kind                 |               | SRC-II heavy distillate |             |
|-----------------------------|---------------|-------------------------|-------------|
| Density                     | [g/ml]        | 1.077                   |             |
| Viscosity                   | [cSt, 98.9°C] | 3.83                    |             |
| Flash point                 | [°C]          | 163                     |             |
| Distillation                |               | ASTM D-86               | ASTM D-2887 |
|                             | IBP           | 286                     | 236         |
|                             | 5%            | 303                     | 280         |
|                             | 10%           | 309                     | 291         |
|                             | 20%           | 317                     | 308         |
|                             | 30%           | 326                     | 318         |
|                             | 40%           | 334                     | 330         |
|                             | 50%           | 342                     | 343         |
|                             | 60%           | 353                     | 357         |
|                             | 70%           | 370                     | 373         |
|                             | 80%           |                         | 395         |
|                             | 90%           |                         | 434         |
|                             | 95%           |                         | 469         |
|                             | EP            | 371                     | 545         |
|                             | Recovery, %   | 73                      |             |
| Ash                         | [wt%]         | 0.08                    |             |
| Carbon                      | [wt%]         | 89.1                    |             |
| Hydrogen                    | [wt%]         | 7.7                     |             |
| Nitrogen                    | [wt%]         | 1.1                     |             |
| Sulfur                      | [wt%]         | 0.5                     |             |
| Oxygen <sup>a)</sup>        | [wt%]         | 1.6                     |             |
| Pyridine insolubles         | [wt%]         | trace                   |             |
| Benzene insolubles          | [wt%]         | trace                   |             |
| <i>n</i> -Hexane insolubles | [wt%]         | 3.90                    |             |

a) by difference.

from the pilot plant of The Pittsburgh & Midway Coal Mining Company, was used here as a feed oil, and general properties are shown in Table 1. The boiling temperature range was from 236 to 545°C, at atmospheric and reduced pressures. A commercially available petroleum hydrotreating catalyst, consisting of cobalt, molybdenum and nickel supported on alumina, was used. Prior to use, the catalyst was pulverized by an agate mortar.

### 2.2. Hydrogenation

A 500 ml capacity conventional autoclave was used in the experimental hydrogenation. The feed oil (30 g) was placed in the autoclave with 3 g of the catalyst. A feed pressure of hydrogen was initially 10.1 MPa at room temperature. Experimental hydrogenation was conducted, subjected to the conditions shown in Table 2. There were two series of experimental hydrogenation in this study. In Experiment 1, the duration was 30 min and the reaction temperature was varied from 360 to 460°C. In Experiment 2, the temperature was fixed at 400°C and the duration was increased to 120 min. The reactor was heated at a rate of 3°C/min to the reaction temperature, and maintained for the duration. After the reaction, the autoclave was rapidly cooled to room temperature by blowing air. The gas in the autoclave was partially collected in a sampling bottle during purging, and the liquid product was recovered with benzene.

### 2.3. Separations

The scheme of the experiment is shown in Fig. 1. The SRC-II heavy distillate and products of hydrogenation were separated into solvent fractions and 'compound class' fractions. First, the liquid product was separated into oil (*n*-hexane soluble) and asphaltene (*n*-hexane insoluble-benzene soluble) by solvent extraction with a sequence of benzene and *n*-hexane. An oil fraction was distilled at atmospheric pressure, and a solvent fraction (>200°C) was obtained.

The solvent fractions were separated into six hydrocarbon fractions, called 'compound classes,' according to the number of aromatic rings confirmed by HPLC<sup>12,13)</sup>. The liquid chromatograph used was a Jasco model Tri-Rotor equipped with a Zorbax NH<sub>2</sub> column (7.9 mm×250 mm, Du Pont Ltd.). These compound classes were paraf-

Table 2 Conditions of Hydrogenation

|                        |       | Experiment-1                           | Experiment-2    |
|------------------------|-------|----------------------------------------|-----------------|
| Reaction temperature   | [°C]  | 360, 380, 400, 410, 420, 430, 440, 460 | 400             |
| Reaction time          | [min] | 30                                     | 15, 30, 60, 120 |
| Oil feed               | [g]   | 30                                     | 30              |
| Catalyst               | [g]   | 3                                      | 3               |
| Hydrogen feed pressure | [MPa] | 10.1                                   | 10.1            |

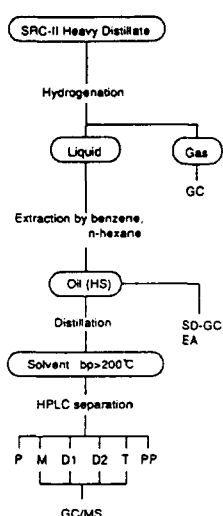


Fig. 1 Scheme of Experiments

fin (P), monoaromatics (M), naphthalene type diaromatics (D1), biphenyl type diaromatics (D2), tri- and/or tetra-aromatics (T), poly-aromatics and/or polar compounds (PP). A 50 mg sample was passed through the column, and the compound classes were separated according to the retention volume. Fractions were developed by sequential elution with a series of *n*-hexane and chloroform. The samples were injected repeatedly, and a total of 400 mg of the samples were recovered. After recovery of the elute by evaporation, the content of each compound class was determined by gravimetric method.

## 2. 4. Analyses

The analysis of the sampled gas, which included both hydrocarbon and inorganic gas, was performed with Shimadzu models GC-6A (FID, TCD), respectively. The volume of hydrogen consumed by the hydrogenation reaction was calculated from the pressure drop during the reaction, based on the ideal gas equation.

The distillation curves of the oil fractions were obtained by SD-GC method<sup>13</sup> with a Shimadzu model GC-D1. The calibration of the boiling point of the simulated distillation was based on *n*-paraffins (*n*-C10, C13, C15, C17, C21, C26, C30, C36, C40) as reagents. Also, elemental analysis was performed on the oil fractions. Determination of the carbon, hydrogen and nitrogen content was performed by the Analytical Center of Hokkaido University.

The low voltage ionization (10 eV) EI-MS technique was used to analyze the aromatic hydrocarbon compound classes (M, D1, D2 and T). The spectra were obtained at scanning intervals of 3 sec with a Hitachi model M-52 GC-MS system and were processed by a Hitachi model 002B computer system. The details of the EI-MS procedure were described previously<sup>13)-15)</sup>.

## 3. Results and Discussion

### 3. 1. Material Balance

The results of the experimental hydrogenation are shown in Table 3. In this table, the percentages of recovery are summarized as a function of severity of hydrogenation. It is clear that a major

Table 3 Overall Material Balances of Hydrogenation

| Sample                      | Feed  | Experiment-1 |      |      |      |      |      |      |      | Experiment-2 |      |      |      |      |
|-----------------------------|-------|--------------|------|------|------|------|------|------|------|--------------|------|------|------|------|
|                             |       | H-1          | H-2  | H-3  | H-4  | H-5  | H-6  | H-7  | H-8  | H-9          | H-10 | H-11 | H-12 |      |
| Temperature                 | [°C]  | 360          | 380  | 400  | 410  | 420  | 430  | 440  | 460  | 400          | 400  | 400  | 400  |      |
| Time                        | [min] | 30           | 30   | 30   | 30   | 30   | 30   | 30   | 30   | 15           | 30   | 60   | 120  |      |
| Feed                        | [wt%] | 100          | 100  | 100  | 100  | 100  | 100  | 100  | 100  | 100          | 100  | 100  | 100  |      |
| Hydrogen consumption        | [wt%] | 0.9          | 1.3  | 2.2  | 2.2  | 2.5  | 3.3  | 4.3  | 5.6  | 1.6          | 2.1  | 3.1  | 6.2  |      |
| Organic gas                 | [wt%] | 0.8          | 0.9  | 2.1  | 3.6  | 2.8  | 7.2  | 9.8  | 19.7 | 1.2          | 1.9  | 4.7  | 5.0  |      |
| Oil fraction                |       |              |      |      |      |      |      |      |      |              |      |      |      |      |
| Light oil (<200°C)          | [wt%] |              | 1.0  | 1.4  | 2.4  | 3.6  | 2.7  | 3.5  | 4.6  | 3.4          | 2.0  | 3.2  | 4.5  | 3.7  |
| Solvent (200°C<)            | [wt%] | 96.1         | 93.5 | 89.4 | 86.5 | 80.2 | 81.3 | 74.7 | 62.7 | 47.8         | 89.2 | 89.3 | 79.3 | 74.4 |
| Hexane insoluble            | [wt%] | 3.9          | 0.4  | 0.5  | 0.1  | 0.0  | 0.2  | 0.3  | 0.3  | 0.5          | 0.3  | 0.1  | 0.0  | 0.1  |
| Benzene insoluble           | [wt%] | trace        | 2.4  | 3.2  | 2.2  | 0.5  | 2.5  | 3.1  | 1.0  | 2.7          | 0.0  | 1.4  | 7.1  | 1.6  |
| Recovery                    | [wt%] |              | 98.1 | 95.4 | 93.3 | 87.9 | 89.5 | 88.8 | 78.4 | 74.1         | 92.7 | 95.9 | 95.6 | 84.8 |
| Loss                        | [wt%] |              | 1.9  | 4.6  | 6.7  | 12.1 | 10.5 | 11.2 | 21.6 | 25.9         | 7.3  | 4.1  | 4.4  | 15.2 |
| H/C of oil fractions        |       | 1.03         | 1.03 | 1.06 | 1.06 | 1.06 | 1.07 | 1.04 | 0.98 | 0.88         | 1.07 | 1.08 | 1.07 | 1.09 |
| Elementals of oil fractions | [wt%] |              |      |      |      |      |      |      |      |              |      |      |      |      |
| C                           |       | 89.1         | 89.8 | 90.5 | 90.6 | 91.2 | 90.7 | 91.4 | 91.8 | 92.6         | 90.7 | 90.9 | 91.4 | 91.2 |
| H                           |       | 7.7          | 7.8  | 8.0  | 8.0  | 8.2  | 8.2  | 8.0  | 7.6  | 6.8          | 8.1  | 8.3  | 8.2  | 8.4  |
| N                           |       | 1.1          | 0.8  | 0.3  | 0.6  | 0.4  | 0.4  | 0.4  | 0.0  | 0.4          | 0.6  | 0.3  | 0.0  | 0.0  |
| O <sup>d)</sup>             |       | 2.1          | 1.6  | 1.2  | 0.8  | 0.2  | 0.7  | 0.2  | 0.6  | 0.2          | 0.6  | 0.5  | 0.4  | 0.4  |

a) by difference.

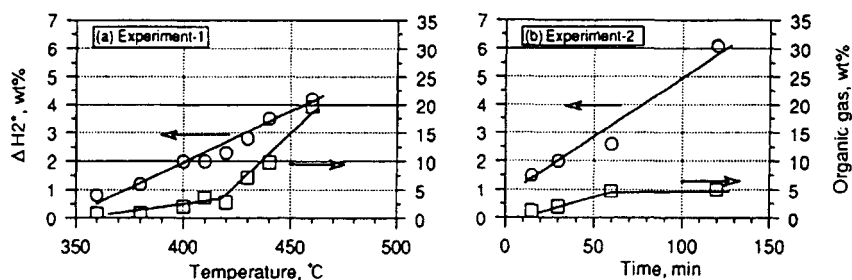


Fig. 2 Hydrogen Consumption and Organic Gas

part of SRC-II distillate was oil and that there was a small amount of asphaltene. Obviously, no coking reaction occurred, because there was a small amount of asphaltene and benzene insoluble in the recovered material. The yield of solvent decreased with raise of the reaction temperature, and this tendency became pronounced over 430°C. The solvent obtained by the reaction at 460°C was close to 50% of the product's yield. Further, at this temperature, the amount of light oil having a boiling point below 200°C, organic gasses and loss increased. The loss was a part of the light oil fraction that escaped during distillation and recovery of the extraction solvent. It could be supposed that at over 430°C this gas and light oil were produced by a dealkylation reaction and a hydrocracking reaction.

The results of reactions at 400°C are also shown in Table 3. The yield of solvent fraction shows a slight decline as duration was increased. The yield of the solvent fraction obtained by the reaction after 120 min was about 74%. For recovery of the recycle solvent, it was proposed that a duration of reaction less than 30 min is suitable because it produces a small amount of gas and light oil.

### 3. 2. Hydrogen Consumption

The amounts of hydrogen and organic gasses (C<sub>1</sub>-C<sub>4</sub>) produced through the reaction were measured by GC analysis. The volume of gasses was calculated from the pressure and the volume of the autoclave based on the ideal gas equation. The hydrogen consumption and the organic gasses produced are shown in Fig. 2. In these figures,  $\Delta H_2^*$  is the amount of hydrogen consumed mainly by the hydrogenation of aromatic rings.  $\Delta H_2^*$  was calculated by subtracting the hydrogen consumed by the production of organic gasses from the total hydrogen consumed in the reaction. For these calculations, it is assumed that one mole of hydrogen gas is consumed to produce one mole of organic gas. Accordingly,  $\Delta H_2^*$  was only consumed by hydrogenating aromatic rings, breaking naphthenic rings, denitrogenizing and deoxygen-

izing.

As shown in Fig. 2, the plots of  $\Delta H_2^*$  corresponding to respective reaction temperatures formed a near straight line and it may be assumed that the hydrogenation reaction had occurred. On the other hand, the organic gasses produced increased slightly with rise of the reaction temperature under 420°C. Substantial production of organic gas, however, occurred at over 430°C. The yield of the organic gasses obtained at 460°C amounted to about 20%. It is also assumed that dealkylation and decomposition of naphthenic rings occurred at over 430°C. Shown also in Fig. 2,  $\Delta H_2^*$  and organic gasses were produced in reactions after 15 to 120 min, at 400°C.  $\Delta H_2^*$  increased linearly with extended duration of reaction, which is the same as in Experiment 1. On the other hand, the organic gasses varied from 4.7 wt% after 60 min, to 5.0 wt% after 120 min. Accordingly, it is assumed that the temperature limits dealkylation and decomposition. Obviously, olefin and carbon oxide were not produced in these experiments. It was seen that the amounts of propane and butane increased with a rise in the reaction temperature (the data is not included in this paper). But, it is noted that for the duration of reaction, the amount of organic gasses remains constant.

### 3. 3. Oil Fraction

The results of elemental analysis of the oil fraction (hexane soluble) are also shown in Table 3. It is noted that both nitrogen and oxygen were removed by hydrogenation and, therefore, a deheteroatom reaction occurred. It is thought that under 400°C, nitrogen compounds decomposed more easily than oxygen compounds. H/C atomic ratio of the oil fractions was slightly increased by a raising the reaction temperature to 430°C. On the other hand, it was reduced to below that of SRC-II distillate at over 430°C. The H/C atomic ratio was increased by hydrogenation in the low range of severity of reactions, and at greater range of severity, ring-opening reactions



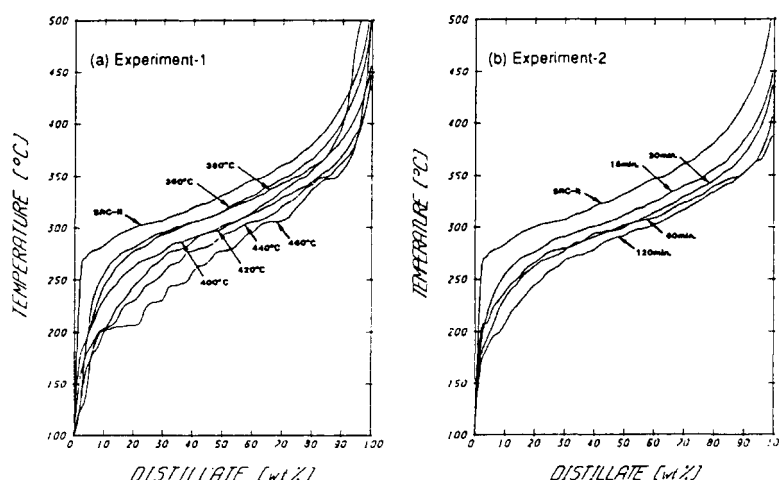


Fig. 3 Distillation Curves of the Oil Fractions

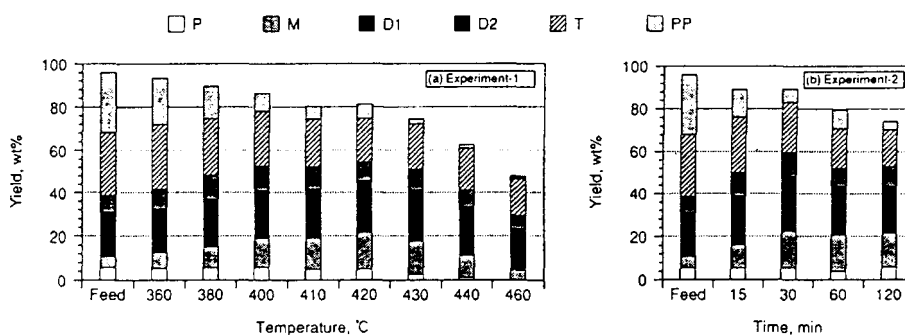


Fig. 4 HPLC Separations of Solvent Fractions

and dealkylation occurred. A change in the amounts of alkyl side chains will be discussed later.

Distillation curves derived by SD-GC for feed and oil fractions are shown in Fig. 3. 90 wt% of SRC-II distillate is limited to a boiling range from 250 to 450°C. The distillation curves shifted to lower temperatures with increase of severity of reaction. The boiling point of 50% oil fraction distillation was at 420°C, which was 40°C lower than that of SRC-II distillate. It has been found that the shapes of these distillation curves, of the oil fraction derived at higher reaction temperature, vary incrementally. Hence, the removal of alkyl groups occurred at higher temperatures.

#### 3. 4. HPLC Fractions

Solvent fractions (>200°C) of SRC-II distillate and its hydrogenated products are separated into six compound class fractions by an HPLC equipped with an amine column. The compound class contents of solvent fractions determined by gravimetry are shown in Fig. 4. P, M, D1, D2, T

and PP stand for paraffin, monoaromatics, naphthalene type diaromatics, biphenyl type diaromatics, tri/tetra aromatics, and poly/polar compounds, respectively. The compound classes are indicated along with the feed. The yield of PP definitely decreased with raise of temperature and extended duration of reaction. It is obvious that a decrease of T and an increase of M, D1 and D2 are brought about by hydrogenation of aromatic rings of tri/tetra-aromatics. All compound class fractions, however, decreased at over 430°C, owing to reduced solvent fractions. The reason for this decrease has been explained by a naphthenic ring opening reaction and dealkylation. It should be noted, however, that P did not increase, significantly. Judging from this fact, it is apparent that a high degree of hydrogenation of aromatic rings did not occur. In contrast with the Experiment 1, PP decreased slightly from 30 to 120 min in Experiment 2. We believe that a higher temperature will be necessary to reduce

heteroatom compounds completely.

### 3. 5. Compound Type

Compound type analyses of the aromatic compound classes (M, D1, D2, T) separated by HPLC were carried out by EI-MS. Molecular ions without fragmentation were detected by the LV (10 eV)-EI method<sup>13</sup>. Consequently, the  $m/z$  peaks are the molecular weights. The molecular weight distribution measured included odd mass numbers because of the presence of isotopes. In this study, the odd mass numbers were intentionally neglected to simplify the mass spectrum. The identification of compound type was performed to assign the  $Z$  value by selecting the molecular ion peaks belonging to the same compound type. In the cited condition of hydrogenation, it was thought that there were no olefins. The structural assignment of components in the solvents was carried out on the basis of a combination of HPLC separation characteristics and compound type analyses by MS<sup>13</sup>. The respective  $m/z$  peaks correspond to the mass number of the molecules and the  $m/z$  distribution represents the profile of molecular weight distribution. The identification of compound types by mass was performed to assign the  $Z$  value by selecting the molecular ion peaks belonging to the same compound type. These peaks appear at 14 mass number intervals, and a homologous series of alkylated aromatic compounds differing by 14 mass units (equivalent to a  $\text{CH}_2$  group) show an increase of the carbon number of alkyl side chains ( $Cal$ ).

The  $Z$  value of a component, which indicates hydrogen deficiency compared with the  $n$ -paraffin with the same carbon number, is related to the aromatic carbon number ( $Ca$ ) and total ring number ( $Rt$ ), representing the sum of aromatic ( $Ra$ ) and naphthenic rings ( $Rn$ ), in the Eq. (1):

$$Z = 2 - (Ca + 2Rt) \quad (1)$$

Compound class separation by HPLC specifies a limited range of  $Z$  values (e.g. Fr-P,  $Z \leq +2$ ; Fr-M,  $Z \leq -6$ ; Fr-D1,  $Z \leq -12$ ; Fr-D2,  $Z \leq -14$ ; Fr-T,  $Z \leq -18$ ), because fractions at a given elution volume contain specific aromatic ring classes (aromatic carbon number  $Ca$ ). Then the real  $Z$  value can easily be chosen from the apparent  $Z$  values, differing by intervals of 14. Real  $Z$  values are further confirmed by the following evidence. The molecular weights of bare aromatic/hydroaromatic ring systems ( $MM$ ) are compared with the lightest compound belonging to the homologous series. When the value of  $MM$  for a specific ring system agree with the molecular

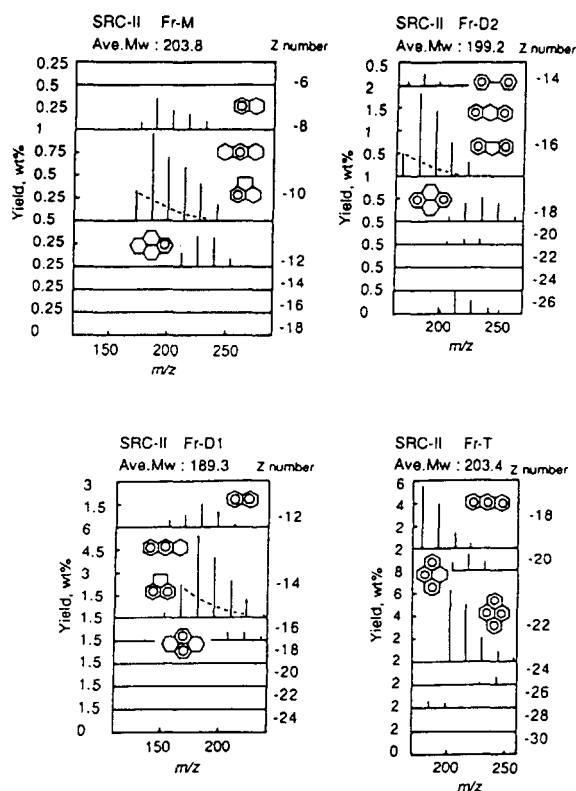


Fig. 5  $Ra-Rn-Cal$  Diagram of SRC-II Distillate

weight at the lowest end of the  $m/z$  distribution for the corresponding  $Z$  series, the aromatic/hydroaromatic ring system can be assigned this  $Z$  value.

The  $Ra-Rn-Cal$  diagram<sup>14</sup> of the SRC-II distillate is shown in Fig. 5. SRC-II distillate was mainly composed of D1 and T, especially acenaphthenes ( $Z = -14$ ), anthracenes ( $Z = -18$ ) and pyrenes ( $Z = -22$ ). These three components made up over 40 wt% of the SRC-II distillate. It has been found that the average molecular weights of all compound class were almost 200 regardless of the bare aromatic/hydroaromatic ring structure, and whether the naphthenic ring numbers were 1 or 2. For the fraction D1,  $Z = -12$  only includes naphthalenes but  $Z = -14$  includes acenaphthenes (minimum molecular weight; 154) and/or tetrahydro-anthracenes (minimum molecular weight; 182). As can be seen in this figure, the distribution of  $Z = -14$  has a discontinuity at  $m/z = 182$ , representing the presence of tetrahydro-anthracenes. It is difficult to separate  $C_2$ -acenaphthene from tetrahydro-anthracene in the peak of  $m/z = 184$  only by the HPLC-MS method. Ishikawa *et al.*<sup>19</sup> reported that it is possible to distinguish  $C_2$ -phenanthrene from tetrahydro-

pyrene assuming that a distribution of alkyl carbons of one aromatic/hydroaromatic ring system compound is smooth. In this study, acenaphthenes and tetrahydro-anthracenes were distinguished by a distribution of alkyl side chains. It was assumed that the *Cal* distribution of the acenaphthenes decreases from the maximum of C<sub>1</sub>-acenaphthene in a constant rate. Contents of acenaphthenes and tetrahydro-anthracenes were calculated as follows;

$$m = 1.1 \quad (2)$$

$$I_{n+1,ac} = I_{n,ac}/m \quad (n = 1, 2, 3, \dots) \quad (3)$$

$$I_{n-1,4H-an} = I_{n+1} - I_{n+1,ac} \quad (4)$$

where:  $I_{n,ac}$  = wt% of C<sub>n</sub>-acenaphthene;  $I_{n-1,4H-an}$  = wt% of C<sub>n-1</sub> tetrahydro-anthracene;  $I_{n+1}$  = wt% of a molecule with  $m/z = 154 + 14 \times (n+1)$ .

Then a correlation coefficient of a linear regression analysis of the *Cal* distribution of tetrahydro-anthracene was calculated. The same calculations were performed from  $m=1.2$  to  $m=5.0$  by 0.1 step. The *Cal* distributions of acenaphthene and tetrahydro-anthracene were finally determined so as to give the best correlation coefficient. Shown in Fig. 5 are break lines exhibiting different ring structures which have the same Z number.

Detailed compound type distributions could be understood from those compound type analyses, and then changes of compound contents with severity of reaction were recognized from several view points. A discussion was conducted on changes of major chemical components, total ring numbers and hydrogen numbers added to

aromatic/hydroaromatic ring system.

Shown in Fig. 6 are the major components of SRC-II heavy distillate and hydrogenated coal liquids derived thereof in terms of reaction temperatures. SRC-II heavy distillate contained mainly pyrene, anthracene, tetrahydro-anthracene, acenaphthene and naphthalene. For the naphthalenes, naphthalene decreased and tetralin increased significantly up to 420°C, but at 460°C, naphthalene increased and tetralin decreased. The total amount of naphthalenes increased gradually at 420 and 460°C. The anthracenes included dihydro-, tetrahydro-, octahydro- and anthracene, and the pyrenes included dihydro-, tetrahydro-, hexahydro- and pyrene. It was found that raise of reaction temperature caused anthracene and pyrene to decrease, and on the other hand, dihydro-, hexahydro-anthracene and all the hydro-pyrenes increased, and later on decreased. The total amount of anthracenes and pyrenes increased at 380°C, and later on decreased.

Many studies were reported on hydrogenation reactions of poly fused aromatics. Shabtai *et al.*<sup>20)</sup> have reported that 9,10-dihydro-phenanthrene and 1,2,3,4-tetrahydro-phenanthrene were primary products. Perhydro-phenanthrene was formed, only slowly, presumably because of the sterically hindered central ring of its precursor, sym-octahydro-phenanthrene. Wu *et al.*<sup>21)</sup> have also reported that the saturated outer ring cracked at temperatures exceeding 427°C, forming mostly *n*-butyltetralins. In this study, the same tendency was observed with the complicated aromatic and hydroaromatic mixtures by detailed compound type analyses using HPLC-MS method. A scheme of the hydrotreating reaction is shown in Fig. 7. It was clear, that at 380°C hydroaromatic

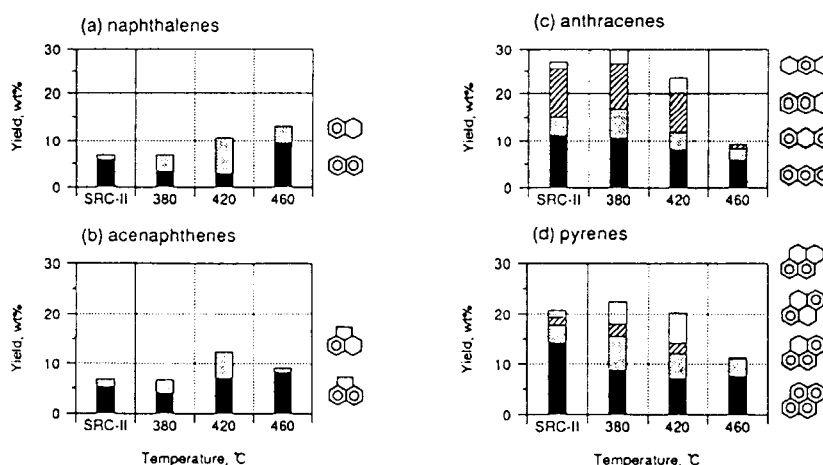


Fig. 6 Distributions of Compound Type

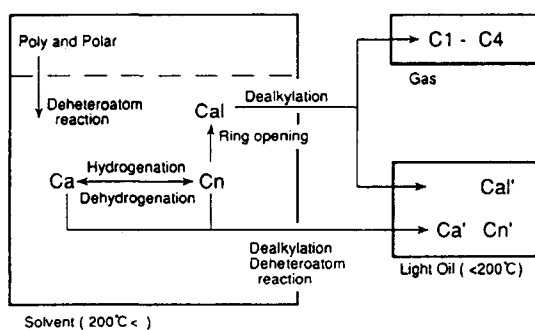


Fig. 7 Possible Reaction Paths

compounds greatly increase with hydrogenation of aromatic rings, and that total aromatic and hydroaromatic compounds increase with deheteroatom reaction of polar components. At 420 and 460°C, hydroaromatics almost always decreased and naphthalenes rapidly increased, because of naphthenic ring opening and dealkylation.

By continuing hydrogenation, pyrene becomes dihydro, tetrahydro, hexahydro, decahydro, hexadecahydro-pyrene, but the total ring number (aromatic and naphthenic rings) is constant at 4 rings through the entire reaction. Stephens *et al.*<sup>22</sup> have found that for hydrogenation of pyrene at 348°C and 1250 psig the hydrogenated species with the largest concentration is dihydro-pyrene followed by hexahydro-pyrene and tetrahydro-pyrene. For these experiments, the concentration of decahydro- and perhydro-pyrene was less than 1% of the product mixture. Shown in Fig. 8 are the changes in the hydropyrene contents for more detailed reaction temperatures. Dihydro-pyrene, tetrahydro-pyrene, hexahydro-pyrene were most abundant at 380, 410, 420°C, respectively. It is clear that the preferable hydrogenation temperature of pyrenes as coal liquefaction solvent is thought to be from 410 to 420°C, because of its more abundant hydroaromatic content. At over 430°C, hexahydro-pyrene decreased remarkably and the total amount of pyrenes also decreased. Dehydrogenation of hydroaromatics did not cause changes in the total amount of pyrenes. This is, therefore, one evidence of ring opening and dealkylation. This is consistent in the production of large amounts of organic gasses.

A study of the changes of aromatics, hydroaromatics, poly aromatics and polar compound, paraffin and light oil (>200°C) is shown in Fig. 9. Up to 380°C, the increase of hydroaromatics is greater with consumption of aromatics. On the other hand, at over 440°C, hydroaromatics markedly decrease, while light oil and aromatics

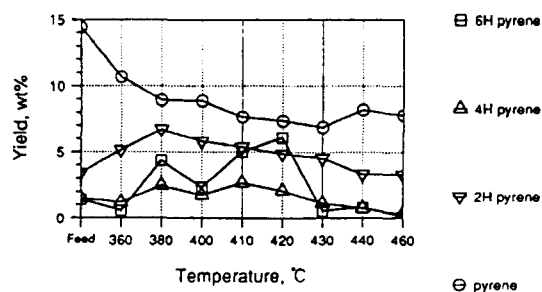


Fig. 8 Contents of Pyrene and Hydro-pyrenes

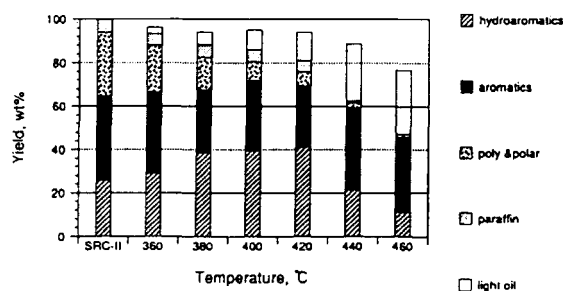


Fig. 9 Contents of Hydroaromatics, Aromatics, Poly/polar Compound, Paraffin and Light Oil, according to Reaction Temperature

increase. The same changes of chemical components such as pyrenes were observed in the whole solvent. Since the main purpose of hydrogenation of the solvent is to optimize conversion of aromatics to hydroaromatics that are potential hydrogen donor, the optimum reaction temperature is thought to be 420°C. A light oil yield is about 13 wt% at 420°C, however, and then an excess yield of light oil is undesirable for recycle solvents. It is clear, therefore, that the optimum reaction temperature will be at 400°C.

To determine the optimum duration of a reaction, reaction temperature was held constant at 400°C in Experiment-2. Shown in Fig. 10 are the changes in the yield of hydroaromatics, aromatics, PP, P and light oil in terms of reaction duration. Over 60 min hydroaromatics decreases and light oil and gas increase. In other words, extended reaction decreases the solvent yield. It is recognized in this experiment that the optimum hydrogenation conditions for SRC-II heavy distillate are at 400°C for 30 min from the viewpoint of the economy of coal liquefaction solvent.

### 3.6. Distribution of Ca, Cn and Cal in the Solvent Fraction

The distribution of compound classes separated by HPLC and the distribution of compound types

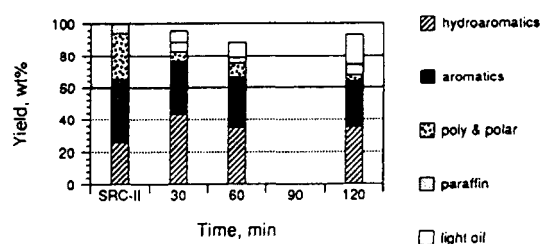


Fig. 10. Contents of Hydroaromatics, Aromatics, Poly/polar Compound, Paraffin and Light Oil, according to Reaction Time

assigned by MS were described above. From the analysis of the chemical structures, the distribution of the alkyl carbon number was discussed. Average carbon number of alkyl side chains was calculated by the equation below;

$$Cal(av.) = \frac{\sum_i Cal_i \times Mol_i}{\sum_i Mol_i} \quad (5)$$

where:  $Cal(av.)$ =average alkyl carbon number per molecule;  $i=i$  molecule,  $Cal$ =alkyl carbon number of each molecule;  $Mol$ =mol percent of each molecule based on the solvent fraction.

The average alkyl carbon number is plotted as a function of the reaction temperature and duration (Fig. 11). For feed, naphthalenes and acenaphthenes have an alkyl carbon number of 3.5. Biphenyls and fluorenes, anthracenes and pyrenes have an alkyl carbon number close to 1.0. With a rise of reaction temperature the  $Cal(av.)$  of the naphthalenes and acenaphthenes decreased by a value of 2.0 while that of the anthracenes and pyrenes decreased by a value of 0.5. The  $Cal(av.)$  of biphenyls and fluorenes firstly increased and decreased to become in the same as the SRC-II. This was caused by a mistake in the assignment of mass spectra or by ring opening reactions. The  $Cal(av.)$  of most of the compounds decreased with

a rise in temperature. In this figure the relationship between  $Cal(av.)$  and the duration of reaction is also shown. At 120 min the  $Cal(av.)$  of naphthalenes and acenaphthenes decreased by a value of 2.0 while that of the anthracenes and pyrenes decreased by a value of 0.3.

The greater the reaction severity (temperature or duration), the less the  $Cal(av.)$ . This represents dealkylation. It can be assumed that organic gasses were thought to be derived from the alkyl side chains. The calculations of the weight ratios of the alkyl chains were, therefore, performed. For this purpose it was necessary to calculate the weight percentage of  $Ca$ ,  $Cn$  and  $Cal$ . Bare aromatic/hydroaromatic ring systems ( $Ra$  and  $Rn$ ) can be decided as shown in Fig. 5 by the compound type analyses. The weight percentages of  $Ca$ ,  $Cn$  and  $Cal$  of aromatic compound classes based on the solvent fractions were, therefore, calculated using the equation;

$$Wal = \sum_i \frac{Cal_i \times 14}{MW_i} \times wt\%i \quad (6)$$

$$Wn = \sum_i \frac{Cn_i \times 14}{MW_i} \times wt\%i \quad (7)$$

$$Wa = 100 - (P + PP) - (Wal + Wn) \quad (8)$$

where:  $Wal$ ,  $Wn$ ,  $Wa$ =weight percent of alkyl side chains, naphthenic rings, aromatic rings;  $i=i$  molecule;  $Cal$ =alkyl carbon number;  $Cn$ =naphthenic carbon number;  $MW$ =molecular weight of each molecule;  $P$ =wt% of paraffin;  $PP$ =wt% of poly/polar compound.

It is difficult to determine  $Wa$ ,  $Wn$  and  $Wal$  of  $PP$  fractions directly, therefore it is assumed that those of the  $PP$  fractions are equal to those of the hydroaromatic fractions. Total yields of  $Cal$ ,  $Cn$  and  $Ca$  ( $Wal^*$ ,  $Wn^*$  and  $Wa^*$ ) were calculated as below;

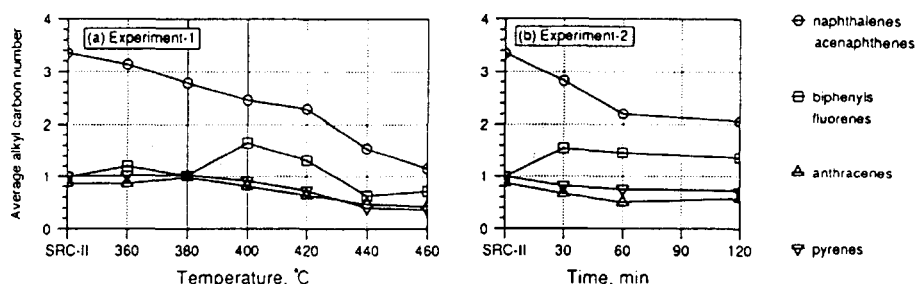


Fig. 11 The Average Alkyl Carbon Number

$$Wal^* = Wal + \frac{Wal}{100 - (P + PP)} \times (PP - Het) \times wt\% \quad (9)$$

$$Wn^* = Wn + \frac{Wn}{100 - (P + PP)} \times (PP - Het) \times wt\% \quad (10)$$

$$Wa^* = Wa + \frac{Wa}{100 - (P + PP)} \times (PP - Het) \times wt\% \quad (11)$$

where:  $P$ ,  $PP$ =wt% of paraffin, poly/polar compound;  $Het$ =wt% of oxygen and nitrogen calculated by elemental analysis;  $wt\%$ =yield of solvent fraction.

Weight percent of  $Ca$ ,  $Cn$  and  $Cal$  of each solvent fraction is shown in Fig. 12. The yields of  $Ca$ ,  $Cn$  and  $Cal$  in SRC-II heavy distillate are 67.5, 11.0 and 9.0 wt% and those in the solvent fraction derived from it at 460°C are 39.6, 4.6, 3.7 wt%, respectively. It is clear that each yield of  $Ca$ ,  $Cn$  and  $Cal$  decrease significantly. As shown in Fig. 7, the decreases of

$Ca$ ,  $Cn$  and  $Cal$  should be converted to the organic gasses and the light oil. When naphthenic ring openings only occur, it has been observed that  $Cal$  increases in proportion to the decrease of  $Cn$ .  $Cal$  of all hydrogenated solvent fractions, however, are less than that of SRC-II distillate in this study. It is thought, therefore, that naphthenic ring openings are always followed by dealkylation. It is reasonable to believe that most parts of the decreases of  $Cn$  and  $Cal$  is converted into organic gasses. The decrease of  $Ca$ ,  $Cn$  and  $Cal$  was supposed to have shifted to the organic gasses and the light oil fraction.

Shown in Fig. 13 are the decrease of  $Ca$ ,  $Cn$  and  $Cal$  ( $\Delta Ca$ ,  $\Delta Cn$  and  $\Delta Cal$ ) vs. the production of light oil and organic gasses. In Experiment-1, at temperature below 420°C,  $Ca$  and  $Cal$  only decrease, and at over 440°C,  $Cn$  also decreases. On the other hand, in Experiment-2, when duration is over 60 min,  $Cn$  decreases. It is generally accepted that there are several pathways of  $Ca$ ,  $Cn$  and  $Cal$ , shifted to the light oil and organic gasses, as shown in Fig. 7. It is also considered that  $Ca$ ,  $Cn$  and  $Cal$  decrease by

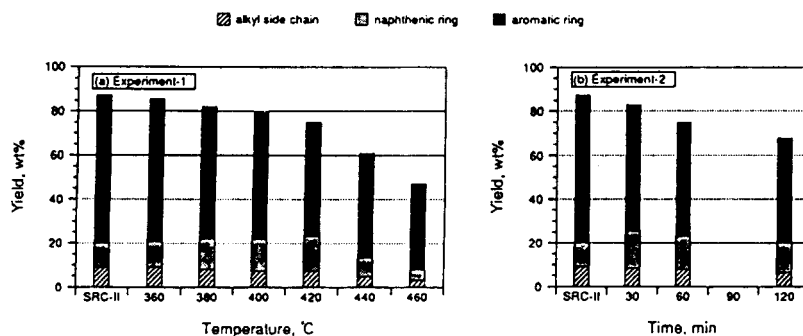


Fig. 12 The Yields of  $Ra$ ,  $Rn$  and  $Cal$  for Solvent Fractions

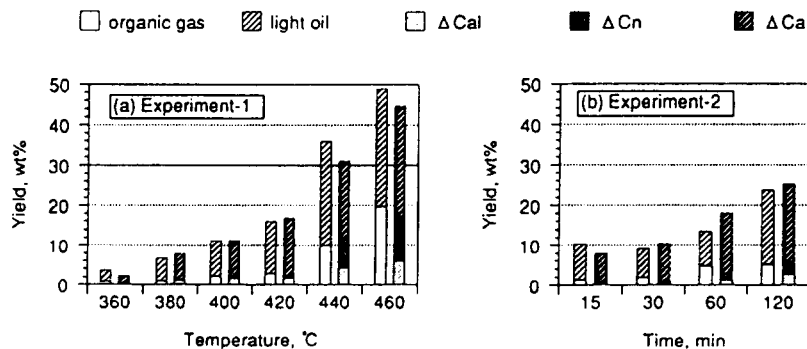


Fig. 13 Organic Gas and Light Oil vs.  $\Delta Cal$ ,  $\Delta Cn$  and  $\Delta Ca$

hydrogenation, naphthenic ring opening reaction and dealkylation, respectively. As shown in Fig. 13, the decrease of *Cn* and *Cal* are in good agreement with the production of organic gasses. On the other hand, the decrease of *Ca* is in agreement with the production of light oil. We have come to the conclusion, therefore, that the organic gasses are produced from alkyl carbons and naphthenic rings, and the light oil is shifted from aromatics that have lower boiling points by dealkylation and breaking of naphthenic rings.

#### 4. Conclusions

This study of hydrogenation of SRC-II heavy distillate over conventional Co-Mo-Ni/Al<sub>2</sub>O<sub>3</sub> catalyst at varying severity of reactions led us to the following conclusions:

- (1) The detailed chemical structures of hydrogenated products were revealed by the HPLC-MS analytical method. Using this method, distributions of aromatics, hydroaromatics and alkyl carbon in complicated aromatic and hydroaromatic compounds mixtures could be evaluated.
- (2) The reaction condition of 400°C, 30 min is suitable for the hydrogenation of SRC-II heavy distillate, from the viewpoint of the coal liquefaction solvent. At these conditions, the content of hydroaromatics as hydrogen donor components and recovery of the solvent fraction were maximized.
- (3) It appears, that production of organic gasses is consistent with the reduction of alkyl side carbon and naphthenic rings, and production of light oil is in agreement with the decrease of aromatic rings.

#### References

- 1) Seshadri, K.S., Ruberto, R.G., Jewell, D.M., Maione, H.P., *Fuel*, **57**, 549 (1978).
- 2) Clarke, J.W., Rantell, T.D., Snape, C.E., *Fuel*, **61**, 707 (1982).
- 3) Farnum, S.A., Farnum, B.W., Bitzan, E.F., Willson, W.G., Baker, G.G., *Fuel*, **62**, 799 (1983).
- 4) Haw, J.F., Glass, T.E., Dorn, H.C., *Anal. Chem.*, **53**, 2332 (1981).
- 5) Petrakis, L., Ruberto, R.G., Young, D.C., Gates, B.C., *Ind. Eng. Chem., Process Des. Dev.*, **22**, 292 (1983).
- 6) Petrakis, L., Young, D.C., Ruberto, R.G., Gates, B.C., *Ind. Eng. Chem., Process Des. Dev.*, **22**, 298 (1983).
- 7) Curtis, C.W., Guin, J.A., Jeng, J.F., Tarrer, A.R., *Fuel*, **60**, 677 (1981).
- 8) Ruberto, R.G., Cronauer, D.C., Jewell, D.M., Seshadri, K.S., *Fuel*, **56**, 17 (1977).
- 9) Swansiger, J.T., Best, H.T., Danner, D.A., Youngless, T.L., *Anal. Chem.*, **54**, 2576 (1982).
- 10) Boduszynski, M.M., Hurtubise, R.J., Allen, T.W., Silver, H.F., *Fuel*, **64**, 242 (1985).
- 11) Niwa, Y., Ishikawa, K., Morita, Y., Sugimoto, Y., *J. Fuel Soc. Jpn.*, **64**, 174 (1985).
- 12) Yokoyama, S., Tsuzuki, N., Uchino, H., Katou, T., Sanada, Y., *J. Chem. Soc. Jpn.*, 405 (1983).
- 13) Uchino, H., Yokoyama, S., Satou, M., Sanada, Y., *Fuel*, **64**, 842 (1985).
- 14) Satou, M., Tanimoto, M., Yokoyama, S., Sanada, Y., *J. Chem. Soc. Jpn.*, 67 (1987).
- 15) Yokoyama, S., Tanabe, K., Satou, M., Sanada, Y., *J. Fuel Soc. Jpn.*, **65**, 721 (1986).
- 16) Green, J.B., Grizzle, P.L., Thomson, J.S., Hoff, R.J., Green, J.A., *Fuel*, **64**, 1581 (1985).
- 17) Boduszynski, M.M., Hurtubise, R.J., Allen, T.W., Silver, H.F., *Fuel*, **65**, 223 (1986).
- 18) Rosal, R., Diez, F.V., Sastre, H., *Fuel*, **71**, 761 (1992).
- 19) Ishikawa, K., Niwa, Y., Morita, Y., *J. Fuel Soc. Jpn.*, **64**, 329 (1985).
- 20) Shabtai, J., Veluswamy, L., Oblad, A.G., *Am. Chem. Soc., Prep. Div. Fuel Chem.*, **23**, 107 (1978).
- 21) Wu, W., Haaynes Jr., H.W., *Am. Chem. Soc., Symp. Ser.*, **20**, 65 (1975).
- 22) Stephens, H.P., Chapman, R.N., *Am. Chem. Soc., Prep. Div. Fuel Chem.*, **28**, 161 (1983).

## 要 旨

石炭液化油の改質  
—HPLC-GC/MS による水素化 SRC-II 重質留分の構造解析—

田辺 克守<sup>†1)</sup>, 佐藤 正昭, 横山 晋, 真田 雄三

北海道大学工学部金属化学研究施設, 060 札幌市北区北 13 条西 8 丁目

<sup>†1)</sup>(現在) (株) ジャパンエナジー 水島製油所, 712 岡山県倉敷市潮通 2-1

SRC-II 重質留分および水素化反応の過酷度の異なる 12 種の水素化生成油を, アミン系カラムを装着した高速液体クロマトグラフィーにより芳香環数毎の化合物クラスに分離した。ついで, 水素化反応の過酷度と生成油の石炭液化用溶剤留分の化学組成変化の関係を調べるため, 各々の芳香族化合物クラスについて質量分析計による Z 数別化合物タイプ分析を実施した。水素化反応の過酷度が増すに従い溶剤留分中の部分水素化芳

香族収率が増加し, 芳香族収率および極性化合物収率は減少した。SRC-II の水素化は部分水素化芳香族を最大にすること, および溶剤留分の確保という観点から, 400°C, 30 分が最適であった。

また見かけ上, 生成有機ガス量はナフテン環およびアルキル側鎖減少量と, 軽質油生成量は芳香環減少量とよく一致した。

.....

**Keywords**

Coal liquid, Hydrogenation, Composition, HPLC-GC/MS method



アルカリ添加燃焼ガスのふく射吸収  
計測法における新しい関係式\*粥川 尚之<sup>\*1</sup>, 山崎 康男<sup>\*2</sup>New Relationships for Emission-Absorption Measurements  
of Alkali-Seeded Combustion Gases

Naoyuki KAYUKAWA and Yasuo YAMAZAKI

Numerical studies on emission-absorption measurements of potassium-seeded kerosene-oxygen combustion gases were carried out. It was found that the ratio of the optical thicknesses at two arbitrary wing wavelengths of the potassium 766.5 nm resonance line was nearly equal to the ratio of the respective atomic absorption coefficients which were calculated based on the temperature measured by the emission-absorption method at the far-wing wavelength. Using the formula, the optical collision cross section as well as the pressure and Doppler broadenings of the potassium doublet could be predicted theoretically with an error of less than one percent. The optimal difference between the far-and near-wing wavelengths is 1.0-2.0 nm. The error in the above optical quantities and also the seed atom number density are insensitive to the near-wing wave-length.

**Key Words:** Spectroscopic Measurement, Flame, Chemical Equilibrium, Numerical Analysis, Potassium Resonance Line, Absorption Coefficient, Pressure Broadening

## 1. 緒 言

燃焼ガスやアルカリ添加燃焼プラズマの温度計測にしばしば用いられる2光路ふく射吸収法<sup>(1)</sup>は、発光原子の共鳴線のウィング波長で、ガスのふく射と参照ランプの透過光強度を別々に計測し、ランプフィラメントとガスのふく射関数の性質を利用してガス温度を測る方法である。この場合、光学厚さが1より十分小さくなる遠ウィング波長を用いると計測値はガスコア温度に十分近くなるとされている<sup>(2)</sup>。

また、光学厚さが発光原子数密度に比例することを用いて発光原子数密度の測定実験も行われている<sup>(3)</sup>。しかし、原子数密度の測定値はスペクトル形状に強く依存し、さらに多成分の燃焼ガスでは圧力広がり幅の計算に必要な光学衝突断面積のデータがほとんどないためふく射吸収法による密度計測法は確立していない。そのため、Baumanら<sup>(4)</sup>は、温度計測と同時に多チャンネル高速スペクトロメータを併用し、関数フィッティングでスペクトルを特定し石炭燃焼プラズマのカ

リウム原子数密度を測定している。

本報告では、化学平衡にあるカリウムシード灯油燃焼ガスを想定してふく射吸収法の数値シミュレーションを行う。まず空間的に非一様な温度と密度分布をもつガスの共鳴線回りの自己吸収効果が温度と密度の計測値に与える影響と、圧力広がり幅と吸収係数の見積もり法を検討する。さらに共鳴線中心より短波長のウィング波長帯に設定した2波長におけるそれぞれの光学厚さの比と、遠ウィングの温度計測値で評価したそれら2波長の原子吸収係数の比の間に有用な新しい関係が成り立つことを示す。これにより、多成分の燃焼ガスにおけるシード原子の実効光学衝突断面積、およびスペクトル形状の決定に重要な圧力広がり幅とドップラー広がり幅の比を簡単な2波長ふく射吸収光学系で計測することができる。さらに対象ガスごとに光学特性値を決定できるため、これまで特定のガスで測定された光学衝突断面積で算定されていた発光原子数密度の計測精度を大幅に改善できる可能性がある。

## 2. ふく射吸収法の原理

燃焼ガスは化学平衡組成、局所熱平衡であり考察する波長帯にはシードカリウム原子以外の共鳴線はないものとする。図1に2光路ふく射吸収光学系の基本構

\* 原稿受付 平成6年4月19日。

<sup>\*1</sup> 正員、北海道大学エネルギー先端工学研究センタ (〒060 札幌市北区北13条西8丁目)。<sup>\*2</sup> (株)JDR (〒163 東京都新宿区西新宿2-1-1)。

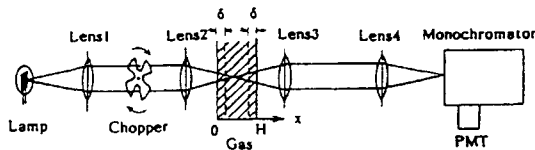


図1 チョッパを用いた2光路ふく射吸収光学系の基本構成

成を示す。

参照ランプから波長  $\lambda$ , 強度  $I(0)$  の光が入射する場合, 厚さ  $H$  のガスを透過した光強度は, 近似的に一次元ふく射輸送方程式の解として以下で与えられる<sup>(5)</sup>。

$$I(H) = I(0) \cdot e^{-\tau} + e^{-\tau} \cdot \int_0^H dx \cdot k \cdot B \cdot e^{\tau x} \quad \dots (1)$$

ただし,  $B$  はプランクのふく射関数,  $k$  は吸収係数であり, 座標  $x$  でのガスの光学厚さを次式で定義する。

$$\tau_x = \int_0^x k[T(x')] dx' \quad \dots (2)$$

式(1)右辺第1項はランプ光の透過光強度, 第2項はシード原子のふく射強度  $I_0$  を表す。ここで考察する温度範囲は 1000~3000 K であり, カリウムの二重共鳴線近傍では, ウィーン近似  $h\nu/k_B T \gg 1$  が成り立つので,

$$B(\lambda, T) = \frac{2hc}{\lambda^5} \cdot \exp\left(-\frac{hc}{\lambda k_B T}\right) \quad \dots (3)$$

と置ける。  $c$ ,  $k_B$ ,  $h$  は光速, ボルツマン定数, プランク定数である。したがって, 入射光学系の透過率を1と仮定しフィラメントの輝度温度を  $T_L$  とすると,  $I(0) = B(\lambda, T_L)$  である。また式(1)の左辺を全強度  $I_{0+L}$  と置くと光学厚さ  $\tau(\lambda)$  の実験式として,

$$\tau = \ln \left[ \frac{I(0)}{I_{0+L} - I_0} \right] \quad \dots (4)$$

を得る。また式(1)を満たすある一定温度を  $T_m$  とすれば  $B(\lambda, T_m) = I_0 / (1 - e^{-\tau})$  である。したがって  $B(\lambda, T_L)$  との比を取り式(4)を用いると,

$$\frac{T_m}{T_L} = \left[ 1 - \frac{\lambda k_B T_L}{hc} \ln \frac{I_0}{I(0) + I_0 - I_{0+L}} \right]^{-1} \quad \dots (5)$$

すなわち,  $I(0)$ ,  $T_L$  を既知として, 強度  $I_0$  と  $I_{0+L}$  を識別して計測できれば, 光学厚さとガス温度がわかる。 $I_0$  と  $I_{0+L}$  の分離には図1のようにチョッパによる時分割法が用いられることが多いが, 同一時刻で分離するには  $I(0)$ ,  $I_{0+L}$  と  $I_0$  を互いに直交する直線偏光で区別する偏光ふく射吸収法が有効である<sup>(6)</sup>。

ガス温度が光路上で一様  $T_0$  であれば, 式(5)により  $\lambda$  と  $T_L$  によらず  $T_m = T_0$  が示される。また,  $T_L$  を変化させ, 共鳴線  $\lambda_r$  回りで,  $I_{0+L} = B(\lambda_r, T_0) = B(\lambda_r, T_L)$ , すなわち  $T_L = T_0$  となる状態を利用してガス温度が得られる(古典的反転法)。

一方, 光路上で温度分布があると計測値  $T_m$  は設定波長ごとに異なる値となる。共鳴線まわりでは  $\tau \gg 1$ , したがって  $I_{0+L} \sim I_0$  となり, 計測値は非常に低くなる。しかし吸収係数は共鳴線から離れると急速に減少しウィング波長帯では波長にあまり依存しなくなる。したがってその空間積分としての光学厚さは,  $\tau \sim$  一定  $\ll 1$  となり,  $T_m$  とコア温度  $T_c$  との差は一定値に漸近する。ガスの非一様性と計測値と設定波長の関係は原子数密度に関しても温度とほぼ同じ傾向である。以上のように温度  $T_m$  は発光原子数密度やスペクトル形状を直接知ることなく測定される。しかし  $\tau$  を計測し,  $\tau/H$  から原子数密度  $N_K$  を計算するには吸収係数の温度と波長依存性を正確に知る必要がある。

### 3. スペクトル関数, 吸収係数 および半幅幅

気体原子のスペクトルは, 発光原子の熱運動によるドップラー広がり  $\Delta\nu_D$  が主体である場合ガウス関数となり, 粒子間の衝突による圧力広がり  $\Delta\nu_P$  が主体的であればローレンツ関数となる。燃焼ガスではそれらを統計的独立事象と考え共鳴線  $i$  の理論原子スペクトルを次のフォークト (Voigt) 関数で与える<sup>(7)</sup>。

$$P_{Vi} = \gamma_i \frac{a_i}{\pi} \int_{-\infty}^{+\infty} \frac{\exp(-y^2)}{a_i^2 + (\omega_i - y)^2} dy \quad \dots (6)$$

ここで  $\gamma_i = 2\sqrt{\ln 2/\pi} / \Delta\nu_{Di}$ ,  $\Delta\nu_{Di} = \sqrt{8R_K T \ln 2} / \lambda_i$ ,  $R_K$  はカリウムのガス定数,  $a_i = \Delta\nu_P \sqrt{\ln 2} / \Delta\nu_{Di}$ ,  $\omega_i = 2(\nu - \nu_i) \sqrt{\ln 2} / \Delta\nu_{Di}$  である。定数  $a_i$  は実質的にドップラー広がりに対する圧力広がりの比を表し通常1のオーダーである。一般にフォークト関数を採用すべき波長帯は共鳴線のごく近傍であり, それ以外の波長では, 式(6)で  $\omega_i \gg y$  と置いて積分を実行し以下のローレンツスペクトルを得る。

$$P_{Li} = \frac{\gamma_i}{\sqrt{\pi}} \cdot \frac{a_i}{a_i^2 + \omega_i^2} = \frac{2\Delta\nu_P/\pi}{\Delta\nu_P^2 + 4(\nu - \nu_i)^2} \quad \dots (7)$$

ただし  $\nu = c/\lambda$  は周波数である。これからウィングスペクトルはドップラー広がりに関係であり圧力幅の見積もりの重要性がわかる。原子スペクトル関数  $P_i(\lambda)$  が与えられると数密度  $N_K$  のガスの吸収係数  $k$  は,

$$k = \sum_i G_i \cdot N_K \cdot P_i = \sum_i N_K \cdot \kappa_i \quad \dots (8)$$

となる。ただし,  $G_i = \lambda_i^2 (g_2/g_1) A_{21} / 8\pi$ ,  $A_{21}$  は自然放射係数,  $g_1, g_2$  は準位1, 2の統計的重み,  $\kappa_i$  は共鳴線  $i$  の原子吸収係数である。カリウムでは  $\lambda_1 = 766.5 \text{ nm} (4^2S_{1/2} - 4^2P_{3/2})$  と  $\lambda_2 = 769.9 \text{ nm} (4^2S_{1/2} - 4P_{1/2})$  の二重共鳴線はその他の共鳴線と比較して非常に強いため, 近似的に  $i=1, 2$  の和を全吸収係数と考え得る。これらの共鳴線の  $A_{21}$  と  $g_2/g_1$  は文献(8)により,  $\lambda_1$  で

$$A_{21}=0.40 \cdot 10^8 \text{ s}^{-1}, \quad g_2/g_1=4/2, \quad \lambda_2 \text{ で } A_{21}=0.39 \cdot 10^8 \text{ s}^{-1}, \\ g_2/g_1=2/2 \text{ である.}$$

圧力広がり  $\Delta\nu_p$  は, 一般に同種粒子との衝突によるホルツマルク広がり, 荷電粒子との相互作用によるシュタルク広がり, および異種中性粒子との衝突によるローレンツ広がりとの和であるが, ここで対象とするカリウムシード率は1%程度で電離度は0.1%以下であるためローレンツ広がりのみを考える。したがって,

$$\Delta\nu_p = \sum_{j \neq k} N_j \langle \nu_{jk} \rangle Q_{jk} \dots\dots\dots (9)$$

ここで  $Q_{jk}$  はカリウム原子と  $j$  種粒子との光学衝突断面積,  $N_j$  はカリウム以外の  $j$  種粒子の数密度,  $\langle \nu_{jk} \rangle$  はワクスワエル平均相対速さである。

実際のカリウムシード燃焼ガスのウイング強度は式(6), あるいは式(7)より1けた程度強いとされている。そのおもな原因として, 各燃焼ガス成分のよく射の重なりやすさなど固体粒子の連続スペクトルの影響が考えられるが, いずれも理論的な見積りには困難である。このため文献(9)では指数則を実測スペクトルにフィットする方法が提唱されている。すなわち, 式(7)に遠ウイング近似  $a_i^2 \ll \omega_i^2$  を施し, フォークト強度と一致する波長を  $\lambda_v$  として,

$$P_i = \gamma_i \frac{1}{\pi} \frac{a_i}{\omega_i(\lambda_v)^2} \cdot \frac{\lambda_v^n}{\lambda^n} \cdot \frac{(\lambda_i - \lambda)^n}{(\lambda_i + \lambda)^n} \dots\dots\dots (10)$$

でスペクトル形状を与える。石炭燃焼プラズマの実測スペクトルにフィットする指数  $n$  と  $\lambda_v$  は,  $\lambda_i$  のウイングで,  $n=-1.07$ ,  $\lambda_v=\lambda_i \pm 2.3 \text{ nm}$ ,  $\lambda_2$  のウイングで  $n=-1.25$ ,  $\lambda_v=\lambda_2 \pm 1.5 \text{ nm}$  が推奨されている。しかしこのようなスペクトル関数は規格化の条件,

$$\int_0^\infty P(\nu) d\nu = 1 \dots\dots\dots (11)$$

を満たさず物理的意味合いに乏しい。そこで本稿では全波長域で原子当たり一定強さのバツクグラウンド  $x_n$

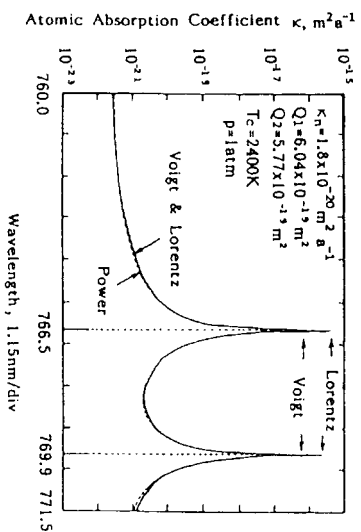


図 2 バツクグラウンドを考慮した原子吸収係数  $x_i + x_n$ ,  $x_L + x_n$  と指数則  $x_p$  の比較

があるものとする。この場合  $x_n$  を差引いたスペクトルが規格化条件(11)を満たす。図 2 に  $x_n=1.8 \times 10^{-20} \text{ m}^2 \cdot \text{a}$  (a: atom) の場合の各原子吸収係数  $x_v + x_n$ ,  $x_L + x_n$ ,  $x_p$  を比較する。ただしカリウムの光学衝突断面積は比較のために便宜上文献(9)と同じ値, すなわちアセチレン空気燃焼炎にに対する Hofmann<sup>(10)</sup> の測定値  $Q_1=6.04 \times 10^{-19} \text{ m}^2$ ,  $Q_2=5.77 \times 10^{-19} \text{ m}^2$  を用いた。またバツクグラウンドとしては, この場合, 実測スペクトル  $x_p$  にできるだけ近い  $x_v + x_n$  あるいは  $x_L + x_n$  を与える値を採用している。図から広い波長帯にわたる指数則とフォークトあるいはローレンツスペクトルに実質的な差はなく実際の燃焼ガス中のカリウムのウイングスペクトルは理論値に一定の  $x_n$  を加算することと記述できることがわかる。以下では共鳴線を中心とする  $\pm 0.1 \text{ nm}$  でフォークト関数を用いそれ以外ではローレンツ関数を用いる。なお実験的に  $x_n$  は, 例えばウイングの点数における実測値と式(7)の理論値との差の平均値として, あるいは本稿で提案する関係式(15)を異なる3波長に適用して得られる二つの代数式を圧力広がり定数  $\alpha$  と  $x_n$  について解くことにより与えられるが, 本稿では式(15)の成立を示すことを主題とするために以下では  $x_n$  を既知として扱う。

これまで光学衝突断面積は測定対象によらず上記の文献(8)の値が使われていることが多い。しかし断面積は衝突の相手により異なり, 実質的な光学衝突断面積はガスの組成に依存している。したがって,  $Q_{jk}$  は未知量と考えなければならない。ここでは文献(10)により  $Q_{jk}$  の温度依存性のみを次式で与える。

$$Q_{jk} = C \langle \nu_{jk} \rangle^{-2/5} \dots\dots\dots (12)$$

$C$  は未知定数である。  $\langle \nu_{jk} \rangle = \sqrt{8 k_B T / \pi m_{jk}}$ ,  $m_{jk} = m_j m_k / (m_j + m_k)$  であり, 共鳴線ごとの  $Q_{jk}$  の差を無視すると, 式(9)から,

$$\Delta\nu_p = \alpha p \cdot T^{-0.7} \sum_{j \neq k} X_j (1/M_j + 1/M_k)^{0.3} \\ = \alpha \cdot f(T, p) \dots\dots\dots (13)$$

となる。  $M_j$ ,  $M_k$  は分子量,  $X_j$  は  $j$  成分のモル分率で以下の数値計算では温度と圧力の既知の量とする。ローレンツ広がりのみを考えているので荷電粒子は  $j$  に含まない。  $\alpha$  は実験で決めるべき未知定数である。

式(8)から,  $k=k_1+k_2+N_k \cdot x_n=N_k \cdot x(\lambda, \alpha, T)$  と置ける。ここで遠ウイングと近ウイングの適当な2波長  $\lambda_i$  と  $\lambda_n$  の光学厚さの比を取れば,  $\nu_i/\nu_n$  は定義からバツクグラウンドを考慮した全吸収係数の空間平均値の比に等しい。したがって,

$$\frac{\tau_i}{\tau_n} = \frac{N_{kmin} \cdot x(\lambda_n, \alpha, T_{min})}{N_{kmin} \cdot x(\lambda_i, \alpha, T_{min})}$$

$$\begin{aligned}
&= \frac{N_{kmn} \cdot x(\lambda_n, \alpha, T_{mn})}{N_{kmf} \cdot x(\lambda_n, \alpha, T_{mf})} \cdot \frac{x(\lambda_n, \alpha, T_{mf})}{x(\lambda_f, \alpha, T_{mf})} \\
&= \phi(\lambda_n, \alpha, N_{kmn}, N_{kmf}, T_{mn}, T_{mf}) \\
&\quad \times \Psi(\lambda_n, \lambda_f, \alpha, T_{mf}) \dots \dots \dots (14)
\end{aligned}$$

添字  $mn, mf$  はそれぞれ近ウィング、遠ウィングの計測値を表す。ここで関数  $\Psi$  の温度依存は遠ウィングの計測値  $T_{mf}$  で見積もられている。関数  $\Psi$  は  $\alpha$  のみを未知量として含む。したがって  $\Psi$  を実験で決定できれば  $\alpha, \Delta\nu_p$ , 光学衝突断面積の実効値, スペクトル形状の計算に必要な  $\alpha$  値を決定でき、カリウムの原子吸収係数を求めることができる。

#### 4. 数 値 解 析

灯油酸素燃焼火炎に水酸化カリウム 48% 水溶液を K シード率で 1 wt% 添加した燃焼ガスにより数値解析を行う。灯油の組成を, C: 84.79%, H: 15.0%, O: 0.2%, N: 0.001%, S: 0.006% とした場合, 圧力広がりに関連する断熱平衡火炎の化学種は, CO, CO<sub>2</sub>, H, HO, HS, H<sub>2</sub>, H<sub>2</sub>O, H<sub>3</sub>N, KO, HNO, NO<sub>2</sub>, N<sub>2</sub>, N<sub>2</sub>O, O, O<sub>2</sub>, SO<sub>2</sub>, SO<sub>3</sub>, S, K, K<sub>2</sub>O, H<sub>2</sub>S, K<sub>2</sub>CO<sub>3</sub>, KOH, H<sub>2</sub>N, COS の 25 種である。一例として当量比 1, シード率 1%,  $p=1$  atm の場合のこれらのモル分率 ( $10^{-10}$  以上) と温度の関係を図 3 に示す。ガスの厚さを  $H=0.1$  m, 厚さ  $\delta$  の境界層内の温度分布  $T(x)$  を  $1/7$  乗則で与える。局所カリウム密度は  $N_K(x)=X_K(T) \cdot p/k_B T$  で計算する。

計算は以下の手順によった。フォークト関数のパラメータ  $\alpha$  は文献(10)から 1 のオーダー, したがって  $\alpha$  は  $10^7$  のオーダーであることを考慮してまず  $\alpha$  を仮定しこれを真の値  $\alpha_0$  とする。次に波長  $\lambda$  を固定して式

(2) より光学厚さ, 式(1) より  $I_0, I_{a+L}$  を見積もり, 式(5) から  $T_m$ , さらに  $\tau/\kappa(\lambda, \alpha_a, T_m)/H$  より  $N_{Km}$  を求め, 温度の計測誤差と真の圧力広がりがかかっている場合の密度の計測誤差を評価する。また適当な 2 波長を選び式(14)で定義した関数  $\Psi$  の性質を調べる。検討するパラメータ範囲は,  $T_c=2200 \sim 2600$  K,  $T_w=1000$  K  $\sim T_c$ ,  $p=0.5 \sim 3.0$  atm ( $x$  によらず一定),  $x_n=0.0 \sim 5.0 \cdot 10^{-21}$  m<sup>2</sup>a<sup>-1</sup>,  $\alpha_0=1.0 \cdot 10^7 \sim 5.0 \cdot 10^7$  とする。

#### 5. 計 算 結 果

図 4 に圧力を変えたときの 766.5 nm 共鳴線とウィングのふく射と吸収スペクトルを示す。低温境界層ではふく射関数の温度特性によりふく射が強く吸収が相対的に強いいため共鳴線回りで強い自己吸収が起こっている様子がわかる。このため  $I_0 \sim I_{a+L}$  でありガスは不透明になる。圧力とともに圧力広がりが増え自己吸収の範囲が拡大し同時に中心波長の強度が低下する。係数  $\alpha_a$  を増加した場合も同様の傾向を示す。壁温度が自己吸収波長帯の広がりを与える影響は少ないが,  $T_w$  が低い場合強度全体が著しく低下する。図 5 に圧力をパラメータとした光学厚さを示す。光学厚さは圧力とともに増加し,  $\tau=1$  となるウィング波長は短波長側へ移動する。

図 6 に  $\tau=1$  における温度と密度の計測値とそれぞれの主流の値との誤差が壁温度と圧力に対してどのように変わるかを示す。 $\tau < 1$  の波長での誤差はこれらの値より少ない一定値に漸近する。以上から, 適切な遠ウィング波長(例えば,  $\tau \leq 0.5$ )を選べば低温境界層をもつガスの主流温度を 1% 前後, 密度を 10% 以下の不確かさで計り得ることがわかる。ただし密度については圧力広がり of 正確な見積もりが前提となる。また図 6

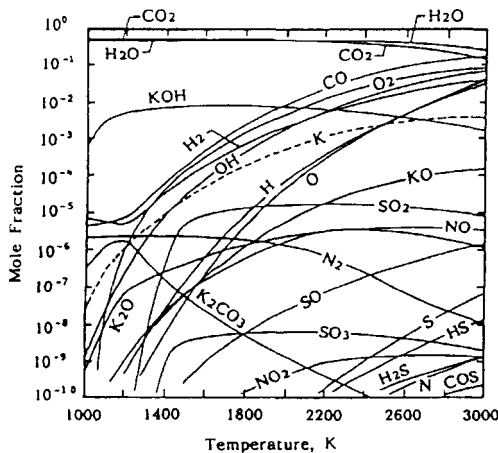


図 3 カリウムシード灯油酸素燃焼ガスの組成 (荷電粒子を除く,  $p=1$  atm,  $\phi=1$ , K シード率 1 wt%)

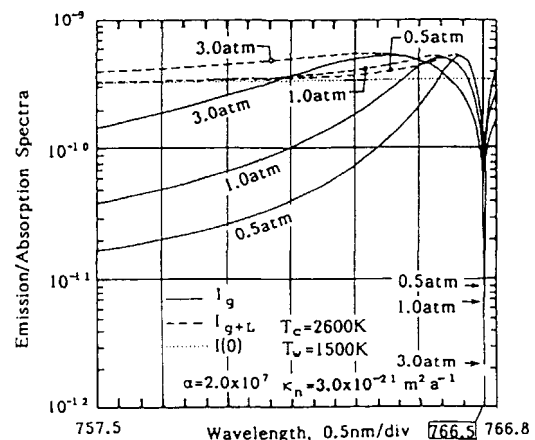


図 4 非一様ガスにおけるカリウム 766.5 nm 共鳴線回りのふく射・吸収スペクトル

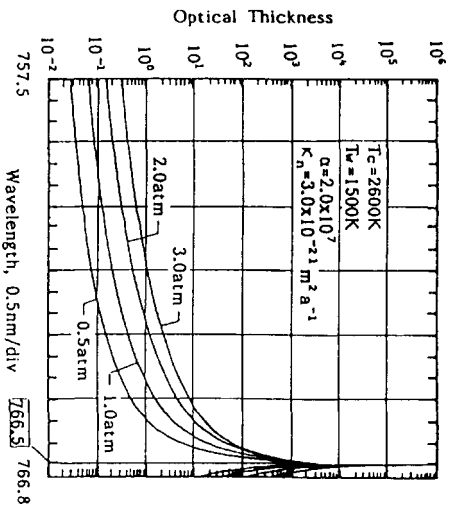


図 5 種々の圧力における 766.5 nm 共鳴線回りの光学厚さ

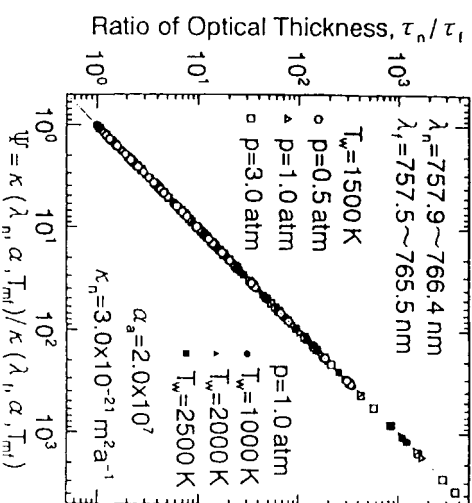


図 7  $\tau_n/\tau$  と  $\kappa(\lambda_n, \alpha, T_{mn})/\kappa(\lambda_l, \alpha, T_{ml}) \equiv \Psi$  との関係

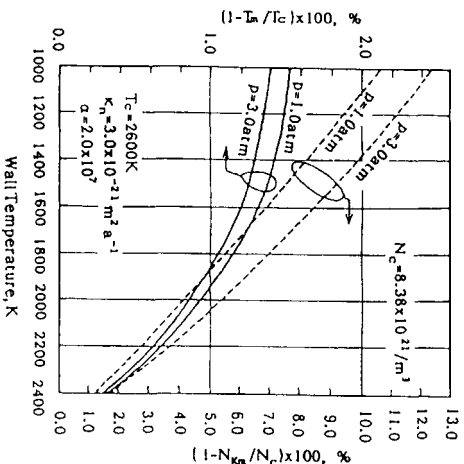


図 6 ウィング波長 ( $\tau=1$ ) における計測値  $T_m, N_{km}$  とコフの値  $T_c, N_c$  との誤差

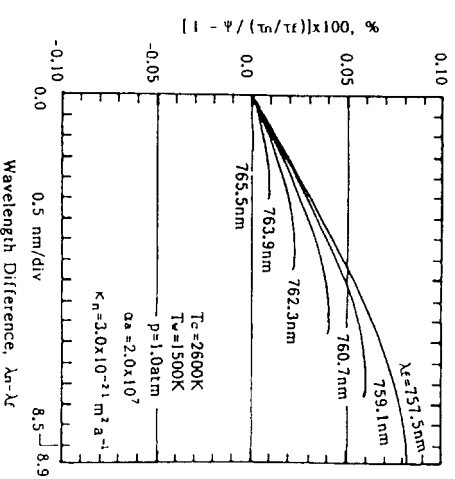


図 8  $\lambda_l$  および  $\lambda_n - \lambda_l$  と  $\tau_n/\tau$  と  $\Psi$  の誤差との関係

から 1~3 atm の圧力変化に対する計測誤差は、温度で 0.2% 以下、密度で 2% 以下であり通常の燃焼ガス流の圧力温度範囲では壁温度が計測誤差に及ぼす影響が大きいいといえる。しかし  $T_m$  と  $N_{km}$  の誤差に及ぼす圧力の影響は逆になる。

次に、適当に選んだウィング波長  $\lambda_l$  と近ウィング波長  $\lambda_n (> \lambda_l)$  の光学厚さの比  $\tau_n/\tau$  と関数  $\Psi$  の関係を図 7 に示す。各○印等は種々の、圧力、壁温度に対応し、ここでは  $\lambda_l$  を 757.5 nm から 765.5 nm まで 1.65 nm ごとに変化させ、 $\lambda_n$  を  $\lambda_l + 0.4$  nm から 766.4 nm まで変化させた結果である。この結果から  $\lambda_n$  あるいは  $\lambda_l$  によらず  $\tau_n/\tau$  と関数  $\Psi$  はほぼ等しいことがわかる。したがって、式 (14) から、

$$\frac{\tau_n}{\tau} \approx \Psi(\lambda_n, \lambda_l, \alpha, T_{ml}) \dots \dots \dots (15)$$

$$\Phi(\alpha, \lambda_n, N_{kmn}, N_{kml}, T_{mn}, T_{ml}) \equiv 1 \dots \dots \dots (16)$$

となる。関係式 (15) の左辺と右辺の値は、圧力、壁温度、バツングラウンド、係数  $\alpha$ 、および  $\lambda_l, \lambda_n$  でわずかに異なるが、本稿で検討したパラメータ範囲で、いずれも 99.9% 以上の確かさで成立している。このことを図 8 に示す。ただし  $\lambda_l$  が高く  $T_w$  が低い場合、 $\Delta\lambda = \lambda_n - \lambda_l \geq 5.0$  nm 以上では  $\tau_n/\tau$  と  $\Psi$  の一致度は 99.9% をわずかに下回る。しかし  $\lambda_n - \lambda_l$  を小さくすれば上記の関係を十分な精度で成立する。

2 章で述べたように、 $\tau$  と  $T_{ml}$  は原子数密度や光学諸量を知ることなく与えられる。したがって式 (15) を未定数  $\alpha$  の代数式とみなすことができる。数値シミュレーションではよく射・吸収強度を計算するために与える  $\alpha$  を真値  $\alpha_0$  と考えるが、実験ではその必要はない。図 9 に式 (15) より計算した値  $\alpha_0$  と真値  $\alpha_0$  の誤

差を波長差  $\Delta\lambda$  に対して示す。ただし、 $\lambda_n$  は 766.0 nm に固定し  $\lambda_f$  を 0.4 nm ごとに変えて計算している。図 10 は  $\alpha_c$  の見積もり誤差に対する壁温度と圧力の影響を計算した結果である。両者の誤差は  $T_w$  が低い場合でも 0.5% 以内であり、 $\lambda_f$  が  $\lambda_n$  に近づくにつれ減少し、 $\alpha_a$  が大きな場合  $\Delta\lambda \leq 2$  nm で急激に増加する。その理由は、 $\lambda_f$  が共鳴線に近い場合、直値  $\alpha_a$  で与えられる  $\tau_n/\tau_f$  と  $\psi$  に含まれる  $T_{m_f}$  の波長依存性は前者が大きく、 $\Delta\lambda$  に対して  $\alpha_c$  が大きく変わる性質による。図の場合、誤差零を与える  $\lambda_f$  は、 $r=1$  の波長よりわずかに共鳴線寄りである。すなわち最適波長差は、対象によるが、おおよその値として  $\Delta\lambda=1.0\sim 2.0$  nm である。

定数  $\alpha$  が測定できることはその他の光学パラメータを決定できることを意味する。以下、 $\alpha_a$  と主流温度  $T_c$  で計算される値を真値とし、 $\alpha_c$  と  $T_{m_f}$  で見積もられる値の誤差を検討する。図 11 は光学断面積であり誤差は 1% 以内であることがわかる。次に圧力広がり幅

の見積もり誤差に及ぼす壁温度の影響を図 12 に示す。誤差は  $\lambda_n - \lambda_f$  によらず、 $T_w=1000\sim 2600$  K の範囲でおよそ 1% 以内となる。さらに、図 13 に示すようにフォークト関数の計算で重要な  $a$  値は、 $T_w=1000\sim 2600$  K の範囲で 2.5% 以内の誤差で決定し得る。計

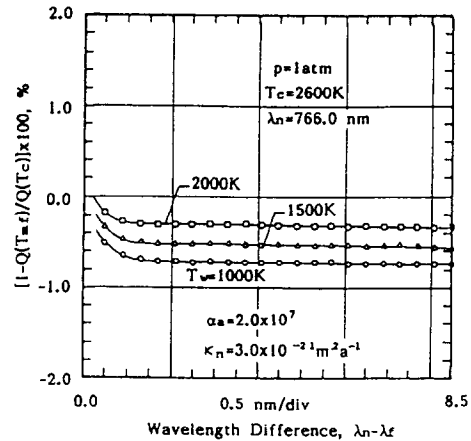


図 11 式(15)による光学断面積の見積もり誤差

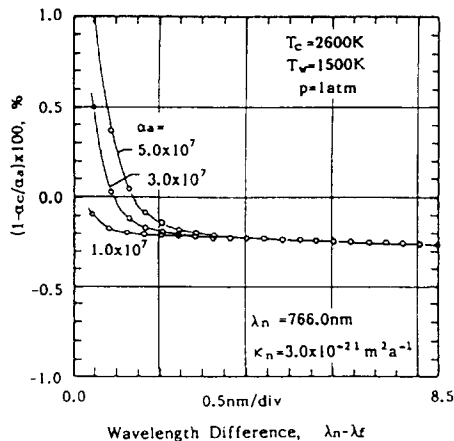


図 9 関係式(15)から計算される  $\alpha_c$  と真値  $\alpha_a$  の誤差

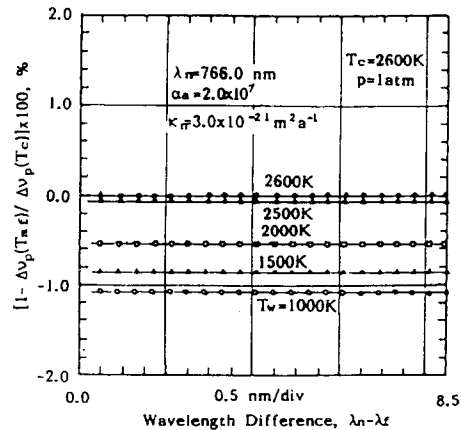


図 12 式(15)による圧力広がりを見積もり誤差

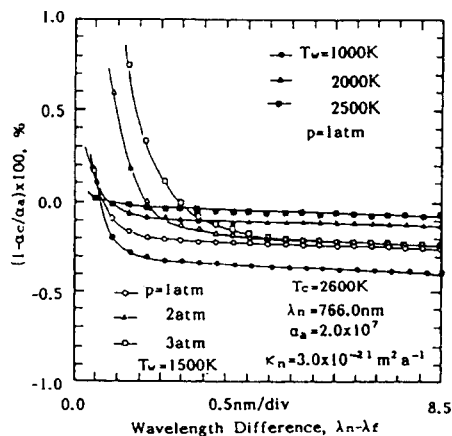


図 10  $\alpha_c$  の誤差に及ぼす圧力と壁温度の影響

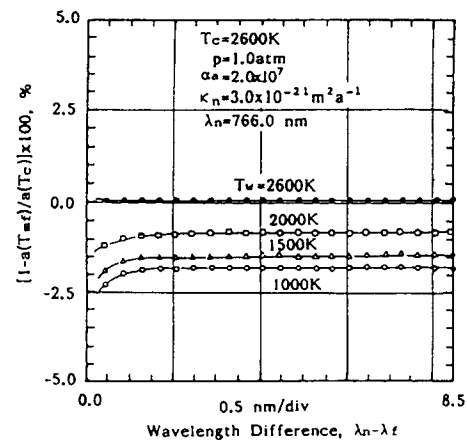


図 13 式(15)による  $a$  値の見積もり誤差

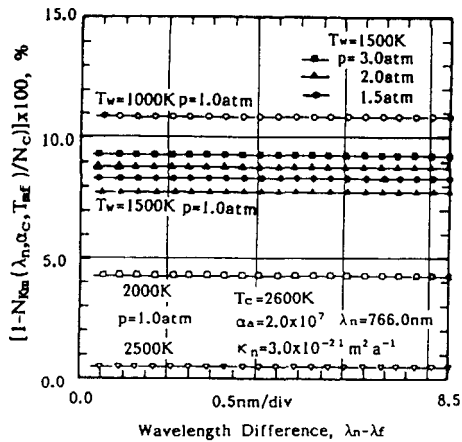


図 14 関係式(17)を用いたカリウム原子数密度の評価誤差

算値  $a(\alpha_c, T_{mf})$  は定義から共鳴線  $\lambda_1, \lambda_2$  でわずかに異なるが、真値  $a(\alpha_a, T_c)$  との誤差には共鳴線ごとの差は見られない。

以上で求めた  $\alpha_c$  と  $N_{Kmn} = \tau_n / H\kappa(\lambda_n, \alpha_c, T_{mn})$  の関係を用いると、新しい密度の評価式として、式(16)より、

$$N_{Km} = \frac{\tau_m}{H\kappa(\lambda_n, \alpha_c, T_{mf})} \quad \dots\dots\dots (17)$$

を得る。これより  $N_{Km}$  を求めた結果を図 14 に示す。主流の値  $N_c$  との誤差は、直接  $N_{Km} = \tau / H\kappa(\lambda, \alpha_a, T_m)$  から求めた図 6 の結果よりわずかに大きい。新しい評価式によれば誤差は波長に依存しないことは注目すべきである。

## 6. 結 論

光路上で不均一温度分布をもつ化学平衡のカリウムシード灯油酸素燃焼断熱火炎のシード原子数密度と光学定数を、カリウムの共鳴線 766.5 nm のウィングを利用した 2 光路ふく射吸収法で計測する数値実験により以下の結論を得た。

(1) アルカリシード燃焼ガスのスペクトルは理論値に一定強さのバックグラウンドを加算すれば指数則と同程度の近似で実際の強度を記述できる。

(2) 2 波長、 $\lambda_n > \lambda_f$  における原子吸収係数の比を  $\lambda_f$  の計測温度で評価した関数  $\Psi = \kappa(\lambda_n, \alpha, T_{mf}) / \kappa(\lambda_f, \alpha, T_{mf})$  は、それぞれの波長における光学厚さの比  $\tau_n / \tau_f$  ときわめてよい精度で等しい。この結論はガス圧力、温度の非一様性、バックグラウンド、共鳴線の半値幅、および波長の選び方にほとんど依存しない。

(3) ガスの化学組成が既知の場合、関係式  $\tau_n / \tau_f = \Psi$  を用いて、コア温度と密度に対応するシード原子の光学定数を高い精度で計測できる可能性がある。近ウィング  $\lambda_n$  を共鳴線近くに選んだ場合、圧力広がり幅を最も正確に与える理論最適遠ウィング波長の目安は光学厚さが 1 よりわずかに大きい波長である。

(4) 本解析で得られた密度評価式によればコアのシード原子数密度を 10% 以下の誤差で計測することができる。この場合の計測誤差は 2 波長の選び方によらず一定であり、これまでのように、測定対象によらず同じ光学断面積を用いる 1 波長法<sup>(3)(4)(9)</sup> と比べて大幅に精度が改善される可能性がある。

本解析で得られた計測法の具体的な光学系は種々の構成が考えられる。例えば、チョッパを用いる図 1 の場合、レンズ 3 の後でビームスプリッタにより等強度に光を 2 分割し、それぞれ適当なフィルタで 2 波長を設定すればよい。また、時間分解能に制限がない偏光ふく射吸収法<sup>(6)</sup> を 2 波長に拡張すればきわめて時間分解能の高い光学系を構成することも可能である。これらについては別に報告する予定である。

本研究で使用した燃焼ガス組成解析プログラムをご提供いただいた電子技術総合研究所高野清南博士に謝意を表す。また本学工学部附属先端電磁流体実験施設の諸氏からいただいた有益な討論に感謝する。なお本研究の一部は「財団法人マツダ財団研究助成金」により実施した。

## 文 献

- (1) Riedmuller W., ほか 2 名, *Z. Naturforsch.*, 23a(1968), 731.
- (2) Daily, J. W. and Kruger, C. H., *AIAA Paper*, 76-134 (1975).
- (3) Onda, K., ほか 2 名, *J. Quant. Spectrosc. Radiat. Transf.*, 26(1981), 147.
- (4) Bauman, L. E. and Wolverton, M. K., *Proc. 9th Int. Conf. MHD*, II(1986).
- (5) Self, S. A. and Kruger, C. H., *J. Energy*, 1-1(1977), 31.
- (6) Kayukawa, N., *Rev. Sci. Instrum.*, 53-11(1982), 1653.
- (7) Michel, A. C. G. and Zemansky, M. W., *Resonance Radiation and Excited Atoms*, 3rd ed., (1971), 162, Camb. Univ Press.
- (8) Radzig, A. A. and Smirnov, B. M., *Reference Data on Atoms, Molecules and Ions*, (1985), 226, Springer-Verlag.
- (9) Bauman, L. E., *J. Thermophys. Heat Transf.*, 7-1(1993), 26.
- (10) Hofmann, F. W. and Kohn, H., *J. Opt. Soc. Am.*, 51-5 (1961), 512.

# The Effects of Plasma Fluctuation in MHD Generators\*

(Studies with a Numerical Turbulence Model)

Naoyuki KAYUKAWA\*\*

The effects of the spatiotemporal inhomogeneity of a plasma in thermal equilibrium on the local and output characteristics of a Faraday-type MHD generator were investigated using numerically modeled turbulent velocity and temperature data. The conditions of Saha equilibrium in the range of the mean temperature level and the maximum turbulent frequency were given. The mean conductivity formula was also given as a function of the rms fluctuation. The average correlations between the electric field fluctuations and those of the conductivity in the mean Ohm's law were evaluated in terms of the mean electrical parameters. Rosa's  $G$ -factor was modified to include the spatiotemporal conductivity variance. It was shown that the one-dimensional anisotropic model somewhat underestimates the effective resistance of the turbulent MHD plasma with a two-dimensional anisotropy.

**Key Words:** MHD Power Generation, Combustion Plasma, Turbulence, Correlation, Effective Conductivity

## 1. Introduction

In many magnetohydrodynamic plasmas, the electrical fields fluctuate in time and space due to fluid-dynamical turbulence and/or combustion. In such circumstances, statistically averaged phenomena must be dealt with. However, the effect of the plasma fluctuation on the mean behavior of the electrical parameters has not yet been considered. We investigate the following subjects in this paper for a plasma in thermal equilibrium using simulated velocity and temperature turbulence data:

(1) The temperature of the electrons and that of the gas atoms are almost always equal in combustion plasmas. However, the ionization and the recombination reactions may not balance instantaneously when temperature is low and the fluctuation is rapid. From this viewpoint, the condition is examined in Sec. 2 under which the Saha equilibrium is established. We also evaluate the error in the average electron density when the density is calculated from Saha's relationship.

(2) The electrical conductivity of the Saha plasma is a strong nonlinear function of the temperature. Therefore, the conductivity calculated from the average temperature may be different from the average of the conductivity itself. To date this effect has been ignored. In Sec. 4, we derive a formula for the average conductivity that will take the temperature fluctuation into account.

(3) The mean behavior of the turbulent plasma should be described by the mean conservation equations for the mass, momentum and energy, the mean generalized Ohm's law and the Maxwell's equations simplified by the MHD approximations.

In most papers published so far<sup>(1)</sup> the turbulence model appropriate to ordinary fluids has been used approximately in the MHD conservation equations, but no model has been considered for the electrical equations, and instantaneous formulae have been used elsewhere. Clearly, the mean generalized Ohm's law includes the correlation between the conductivity fluctuation and the electrical counterpart. Therefore, it is meaningful to examine the effect of gaseous turbulence on the mean electrical parameter. In Secs. 6 and 7, using a one-dimensional nonuniform plasma, where the exact solutions can be obtained in space and time, we examine the influence of the fluctuation on the local mean electrical phenomena and on the power output characteristics of an MHD generator. The

\* Received 3rd February, 1994. Japanese original: Trans. Jpn. Soc. Mech. Eng., Vol. 59, No. 562, B (1993) pp. 1863-1869. (Received 8th October, 1992)

\*\* Center for Advanced Research of Energy Technology, Hokkaido University, Kita-ku, Kita 13, Nishi 8, Sapporo 060, Japan



mean correlations will also be given explicitly as functions of the mean electric field and the current. In Sec. 8, in order to discuss the applicability of the one-dimensional model to a two-dimensional plasma, we analyze the instantaneous electrical phenomena under 2D turbulent velocity and temperature in the cross section of the MHD channel.

## 2. Relationship between Electron Number Density and Temperature Turbulence

Here, employing the ionization recombination rate equation for a combustion plasma, we investigate the response of the electron density to the fluctuation of the gaseous temperature and evaluate the influence of the mean temperature level and the fluctuation frequency on the mean electron number density. Denoting the electron density by  $n_e$  and the seed atom number density by  $n_K$ , the rate equation can be written as follows:

$$\frac{dn_e}{dt} = (\alpha_e + \alpha_g)(n_K K - n_e^2) \quad (1)$$

Here, the ionization equilibrium constant  $K$  is a unique function of the temperature and is given by

$$K = \left( \frac{2\pi m_e k T}{h^2} \right)^{3/2} \exp\left(-\frac{\epsilon}{kT}\right) \quad (2)$$

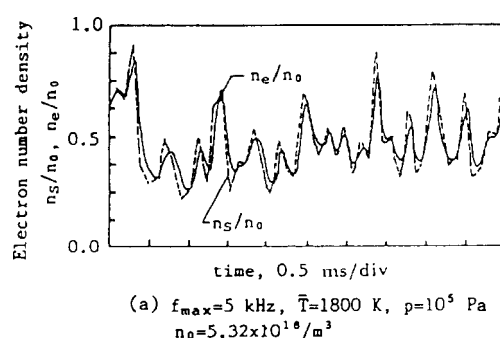


Fig. 1(a) Nonequilibrium effect in the electron number density in a plasma with low-frequency temperature turbulence

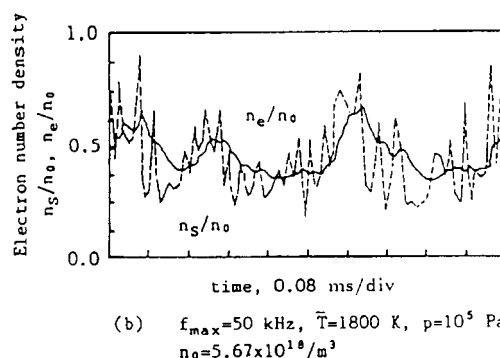


Fig. 1(b) Nonequilibrium effect in the electron number density in a plasma with high-frequency temperature turbulence

where  $\epsilon$  is the ionization potential, and  $m_e$ ,  $k$  and  $h$  are the electron mass, Boltzmann's constant and Planck's constant, respectively. The Saha equilibrium value  $n_s(t)$  can be calculated from the equation  $n_K K - n_s^2 = 0$ . The recombination coefficients  $\alpha_e$  and  $\alpha_g$  are those of the reaction processes, where the third body is the electron and the gaseous particle, respectively. These are given by<sup>(2)</sup>  $\alpha_e = 1.09 \times 10^{-20} n_e T^{-4.5}$  and by<sup>(3)</sup>  $\alpha_g = 1.7 \times 10^{-28} n_g T^{-3.5}$ . Equation (1) can be solved if we know the time-dependent temperature  $T(t)$  which is specified by an inverse Fourier transform method as described in Sec. 3. The gas particle density was evaluated by assuming the ideal gas law and the adiabatic condition. The calculated results are shown in Fig. 1(a) for a case with low maximum frequency and in Fig. 1(b) for one with high maximum frequency. The dotted lines are the Saha equilibrium values, which have the same time dependence as the given temperature. The normalization base density  $n_0$  is the maximum  $n_s$  value obtained in the time range analysed. Figure 1 shows a part of the whole period analysed.

From Fig. 1(b) we see that, if the temperature fluctuation is rapid, then the phase of the electron density fluctuation becomes different from that of the given temperature and the turbulence level decreases. Figures 2 and 3 show how the error in  $n_s$  changes with  $T$  and  $f_{\max}$  when the mean density is evaluated as the Saha equilibrium value. The error bars denote the finite number of samples. The error in  $n_s$  has maxima with respect to the maximum frequency because the turbulence data have been generated from the spectrum of first-order Markov type, which has a maximum spectrum at zero frequency and has spectrum decreasing to zero at higher frequencies. The results shown above mean that the electron number density can be estimated from Saha's equation if the mean

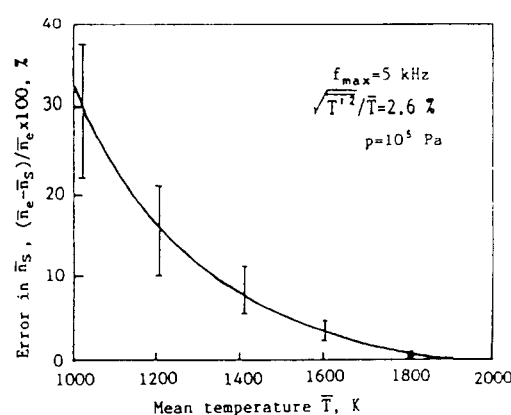


Fig. 2 Relation between the error in the mean electron density calculated by Saha equilibrium and the mean temperature

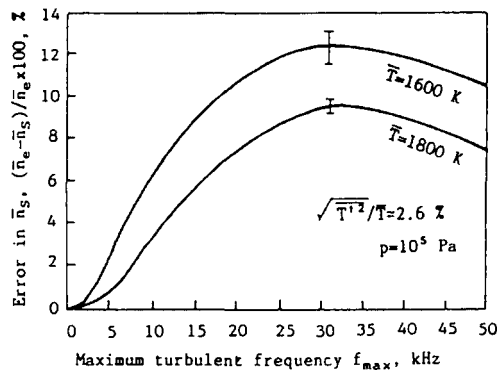


Fig. 3 Relation between the error in the mean electron density calculated by Saha equilibrium and the maximum turbulence frequency

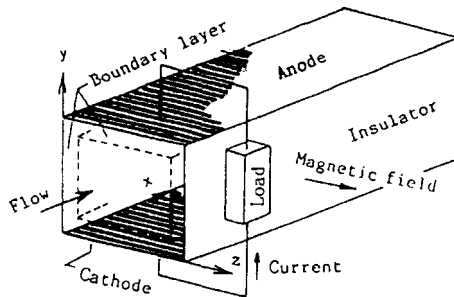


Fig. 4 MHD generator channel and the coordinate system

temperature is higher than about 1800 K and the frequency  $f_{\max}$  is lower than several kHz. When the temperature is lower than this and the frequency is higher than a few kHz, the Saha equilibrium equation cannot be adopted. In what follows, for simplicity we consider plasmas in the range of the Saha equilibrium conditions.

### 3. Numerical Data of the Velocity and the Temperature Fluctuation

The MHD generator channel and the coordinate system are shown in Fig. 4. We assume that the magnetic field  $B$  is in the  $z$  direction and uniform, that the electrodes are positioned at  $y=0$  and  $H$  and that the insulator walls are at  $z=0$  and  $W$ . The mean velocity and the temperature are given by the  $1/7$ th law within the boundary layers with a thickness  $\delta$ . In the  $y$  direction, only the fluctuation part of the velocity is considered and we assume no velocity component in the  $z$  direction, since the latter has primarily no influence on the electrical behavior. The fluctuation of the velocity components in the axial and in the electrode direction is denoted by  $u'$  and  $v'$ , respectively and that of the temperature by  $T'$ . The inverse Fourier transform method may be used for the turbu-

lent power spectrum to calculate approximately the time series data of the fluctuation  $g'=(u', v', T')$ . Here, we employ the following spectrum of the first-order Markov type, because the spectrum of the MHD plasma is undetermined.

$$S_g(f) = \frac{\overline{g'^2} \xi}{\xi^2 + 4\pi^2 f^2} \quad (3)$$

In the above,  $\overline{g'^2}$  is the variance of the fluctuation and  $\xi$  is a constant. Introducing the random phase angle  $\theta_j$ , the fluctuation data can be calculated from<sup>(4)</sup>

$$g'(t) = C_g \sum_{j=1}^n \sqrt{4\pi S_g \Delta f_j} \cdot \cos(2\pi f_j t + \theta_j). \quad (4)$$

In the following analyses, the coefficient  $C_g$  was chosen to be  $C_u=7$ ,  $C_T=5$  and  $C_v=4$  so that the average intensity would equal the empirical turbulence level, and the maximum frequency was assumed to be 1.7 kHz and the minimum to be 35 Hz. In order to make the variance zero on the walls and to obtain a maximum within the boundary layer<sup>(5)</sup>, we assumed the following weighting function for  $\overline{g'^2}$ .

$$\sqrt{\overline{g'^2}} = \left( \frac{A_g}{B_g} \right) \left( \frac{2y}{H} \right)^{1/C_g} \exp \left( -B_g \frac{y}{H} \right) \quad (5)$$

Here,  $H$  is the electrode height. The constants  $A_g$  and  $B_g$  can be determined by specifying the maximum and the minimum variance respectively at the point  $y_{\max}$  where Eq.(5) reaches the extremum, and at the center  $y=H/2$ . The signs of the fluctuations were determined statistically so that the signs of the mean correlations  $\overline{u'v'}$  or  $\overline{v'T'}$  are opposite to that of the gradient of the mean velocity  $\overline{u}$  or mean temperature  $\overline{T}$ .

Examples of the axial velocity and the temperature at a vicinity close to the wall and in the core are shown in Figs. 5 and 6, where  $Y$  is the nondimensional distance  $y/H$ , and  $\delta/H$  was assumed to be 0.1818. The mean velocity and the temperature are given by  $\overline{u} = \overline{u_c}(y/\delta)^{1/7}$  and  $\overline{T} = T_w + (\overline{T_c} - T_w)(y/\delta)^{1/7}$ , respectively. The mean correlations  $\overline{u'v'}$ ,  $\overline{v'T'}$ ,  $\overline{\sigma'u'}$  and  $\overline{\sigma'v'}$  are distributed as shown in Fig. 7. The turbulent conductivity has the same sign as the turbulent temperature, and the correlations  $\overline{u'v'}$  and  $\overline{v'T'}$  take statistically the opposite sign to those of  $d\overline{u}/dy$  and  $d\overline{T}/dy$ . Therefore,  $\overline{\sigma'u'}$  is positive in the whole space, while  $\overline{\sigma'v'}$  is negative on the cathode side and positive on the anode side. In the above, the electrical conductivity was approximated by the following formula that fits the chemical equilibrium composition analysis<sup>(6)</sup> of a KOH-seeded kerosene-oxygen combustion plasma with 1 wt % of potassium seed.

$$\sigma(T, p) = 89.9 \frac{T^{1.005}}{p^{0.511}} \exp \left( -\frac{e\epsilon}{2kT} \right) \quad (6)$$

It should be noted that the maxima and minima of the variance calculated as above are smaller than those assumed in Eq.(5) to specify the coefficients  $A_g$  and

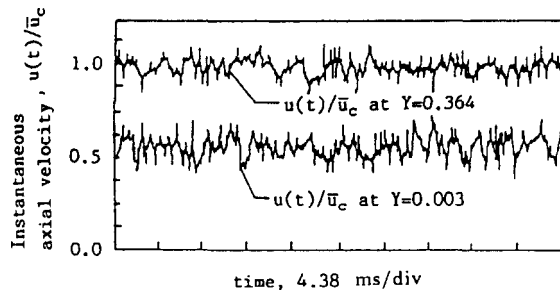


Fig. 5 Examples of the axial velocity turbulence data of 1D nonuniform model

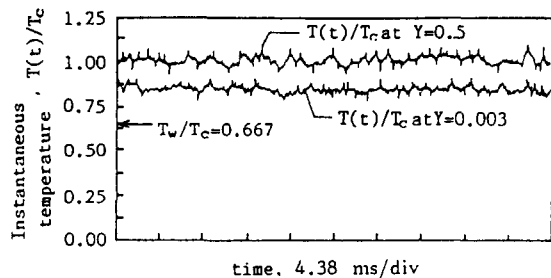
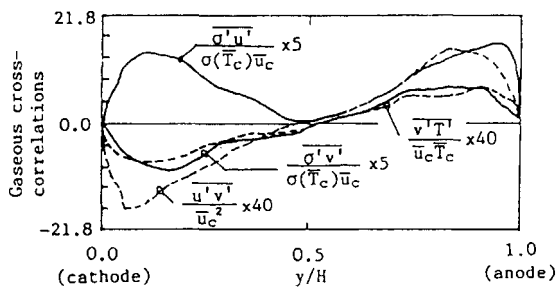


Fig. 6 Examples of the temperature turbulence data of 1D nonuniform model



$B_p$ , because of a finite number of samples and finite number of discrete frequencies considered.

#### 4. Effects of Turbulence on Mean Conductivity

The spatial distribution of the conductivity calculated from the data shown in Fig. 6 is given in Fig. 8. Compared with the temperature, the conductivity fluctuation is more noticeable. We note the mean conductivity increase in comparison with  $\sigma(\bar{T})$ ; this increment due to the temperature fluctuation was calculated approximately from Eq.(7). Results are shown in Fig. 9.

$$\bar{\sigma} = \sigma(\bar{T}) + \frac{1}{2} \cdot \frac{d^2 \sigma(\bar{T})}{d\bar{T}^2} \cdot \overline{T'^2} \quad (7)$$

Equation (7) well describes the mean conductivity of an equilibrium turbulent plasma. The conductivity increment depends markedly on the mean temperature, that is, from 10 to 20% in the temperature range

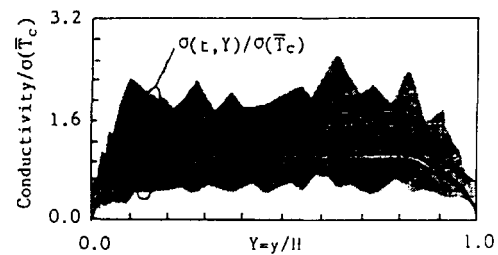


Fig. 8 Distribution of the conductivity in space and time

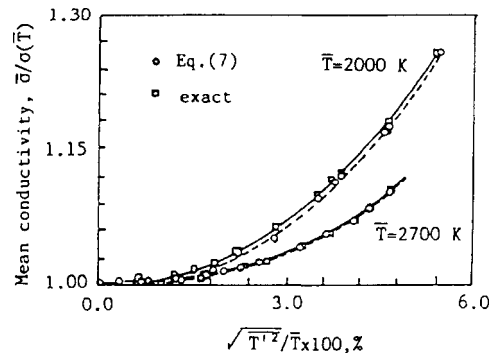


Fig. 9 Relation between the mean conductivity and the mean temperature

occurring in boundary layers and a few percent in the core temperature range. The mean intensity of the turbulence  $\sqrt{T'^2}$  is approximately proportional to the gradient of the mean temperature, so that if the fluctuation is not taken into account, a significant error may result when performing calculations for regions near the walls.

#### 5. Average Electrical Parameters and Electrical Correlations

In this paper, we deal with the influence of velocity and temperature on the electrical parameters. Therefore, the basic equations are the generalized Ohm's law and Maxwell's equations. Neglecting the ion slip and the induced magnetic field, we can write the instantaneous forms as

$$\mathbf{J} = \sigma(\mathbf{E} + \mathbf{V} \times \mathbf{B}) - \mu \mathbf{J} \times \mathbf{B} \quad (8)$$

$$\nabla \times \mathbf{E} = 0 \quad \mathbf{E} = -\nabla \phi \quad (9)$$

$$\nabla \cdot \mathbf{J} = 0 \quad \mathbf{J} = \nabla \times \psi, \quad (10)$$

where  $\mathbf{E}$  and  $\mathbf{J}$  are the electric field and the current density, and  $\phi$  and  $\psi$  are the electric potential and the current stream function. The time average of the first-order fluctuation is zero and the fluctuation in mobility can be neglected because of its weak dependence on the temperature. Thus, we can write

$$\bar{\mathbf{J}} = \bar{\sigma}(\bar{\mathbf{E}} + \bar{\mathbf{V}} \times \mathbf{B}) - \mu \bar{\mathbf{J}} \times \mathbf{B} + \bar{\sigma}' \bar{\mathbf{E}}' + \bar{\sigma}' \bar{\mathbf{V}}' \times \mathbf{B}. \quad (11)$$

The averages of Eqs.(9) and (10) take the same form. As shown above, the mean current density  $\bar{\mathbf{J}}$

and the mean electric field  $\bar{E}$  can be determined if the correlations  $\overline{\sigma' E'}$  and  $\overline{\sigma' v'}$  can be specified. The latter is related only to the plasma properties, while the former is affected generally not only by the plasma states but also by the external electrical load. Thus, we assume here a Faraday channel with infinitely segmented electrodes and perfectly insulated walls.

Once the mean current is given, the source term in the equation of motion can be written as  $\bar{J} \times B$ . On the other hand, the energy equation has the mean source term of the form  $\bar{J} \cdot \bar{E}$  or  $\bar{J}^2 / \bar{\sigma}$ , which may be written as follows:

$$\bar{J} \cdot \bar{E} = \bar{J} \cdot \bar{E} + \bar{J}' \cdot \bar{E}' \quad (12)$$

$$\bar{J}^2 / \bar{\sigma} = \bar{J} \cdot \bar{E} + \bar{J}' \cdot \bar{E}' + \bar{J} \cdot (\bar{V} \times B) + \bar{J}' \cdot (\bar{V}' \times B) \quad (13)$$

Therefore, in order to close the turbulent MHD equations, the evaluation of both  $\bar{J}' \cdot \bar{E}'$  and  $\bar{J}' \cdot (\bar{V}' \times B)$  is also necessary.

## 6. Solutions for 1D Nonuniform Plasmas

As seen in Eqs.(8) and (9), the electrical parameters of Saha equilibrium plasmas depend explicitly upon only the spatial coordinates. In this respect, the spatially averaged formulae for the effective current, the electric field and the conductivity have been studied in several papers. Rosa<sup>(7)</sup> has proposed an effective conductivity formula of  $\sigma_{eff} = \langle \sigma \rangle / G_*$  based on a one-dimensional plasma nonuniformity in the electrode direction only. Here, the bracket  $\langle \rangle$  means the spatial average. With Hall's parameter  $\beta = \mu B$ ,  $G_*$  is defined as

$$G_* = \langle \sigma \rangle \left\langle \frac{1 + \beta^2}{\sigma} \right\rangle - \langle \beta \rangle^2. \quad (14)$$

This factor accounts for the increment of the plasma resistance due to the spatial nonuniformity and is always larger than unity except in the case of uniform plasma. In this paper, we employ Rosa's model for the spatial nonuniformity. According to this and to the infinite segmentation of electrodes,  $E_x$  and  $J_y$  are constant with respect to  $y$ , and from the assumption of a Faraday channel,  $\langle J_x \rangle = 0$ . Then the solutions of the potential and the current stream function can be obtained as follows:

$$\phi = -E_x(t)x - \int_0^y E_y(t, y') dy' + V_c \quad (15)$$

$$\psi = -J_y(t) + \int_0^y J_x(t, y') dy' \quad (16)$$

The output voltage is given by  $V_c - V_A = \phi(t, x, H)$ , and  $I/W = \phi(t, P, H)$  gives the output current per unit width in the  $z$  direction, where  $P$  is the electrode pitch. The electric field  $E_y$  and the current density  $J_x$  can be calculated from

$$E_y = \mu B + \left( \frac{1 + \beta^2}{\sigma} - \frac{\beta \langle \beta \rangle}{\langle \sigma \rangle} \right)$$

$$- \beta \left( v' - \frac{\langle \sigma v' \rangle}{\langle \sigma \rangle} \right) B \quad (17)$$

$$J_x = \left( \sigma \frac{\langle \beta \rangle}{\langle \sigma \rangle} - \beta \right) J_y + \sigma \left( v' - \frac{\langle \sigma v' \rangle}{\langle \sigma \rangle} \right) B. \quad (18)$$

Hall's electric field  $E_x$  is determined by the condition  $\langle J_x \rangle = 0$ , and the output current density by  $J_y = I/PW$ . We calculate the time mean values by adding the number of instantaneous solutions for the velocity and the temperature data given in Sec. 3, the fluctuations by subtracting the time mean from the instant value, and the mean correlations by taking the product of any two fluctuations.

Figure 10 shows the solution  $\phi(t, 0, y)$ , where,  $\delta/H = 0.1818$ ,  $\beta = 3.15$ , and the load  $R_L PW \sigma_c / H = 4.0$ . The solution for the case without fluctuation is indicated by  $\phi_*$ . The plot of a constant stream function  $\psi = \text{const}(=0)$  under the same plasma and load conditions is shown by  $x/H$  as a function of  $y/H$  in Fig. 11. Also, the power output per electrode is shown in Fig. 12. The power is supplied to the external load, when the electric field and the current density have opposite sign, so that a lower negative value means a higher power output.

From the results given above, we see that at first the local electric field fluctuates significantly. The open voltage  $V_0$  shows less fluctuation because it is affected by the velocity fluctuation only. However, the behavior of the electrode potential under loaded conditions is greatly affected by the conductivity turbulence. This tendency coincides with the experimental observations. Furthermore, the mean cathode potential decreases in comparison with that of a plasma without fluctuation and the power output decreases considerably. The mean path of the current becomes asymmetrical due to the spatial characteristics of the correlation  $\overline{\sigma' v'}$ .

## 7. Correlations and the Effective $G$ -Factor

In this section, we evaluate the mean correlation  $\overline{\sigma' E'} = \overline{\sigma E} - \bar{\sigma} \bar{E}$  in terms of  $\bar{J}$ ,  $\bar{E}$  and  $\bar{u}$ . We took the conductivity fluctuation up to  $\sigma'^3$  into account in

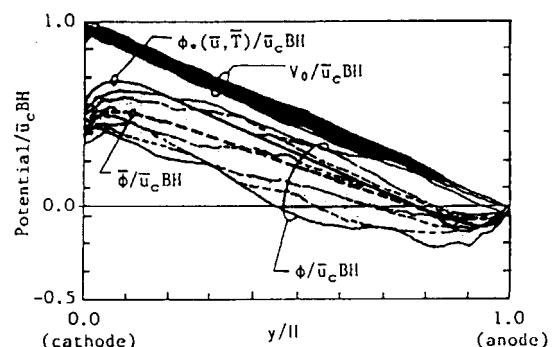


Fig. 10 Potential distribution in space and time

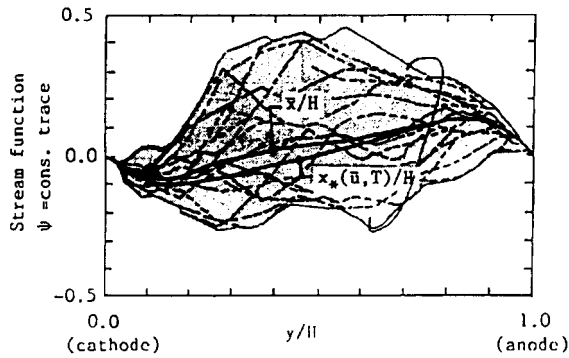


Fig. 11 Distribution of the current stream function in space and time

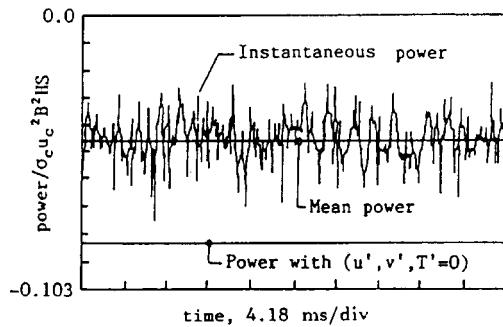


Fig. 12 Electrical power output

substitution of the solutions  $E_x$  and  $E_y$  given in Sec. 6 into  $\bar{\sigma}\bar{E}$ . Considering the results shown in Fig. 7, we can neglect the spatial average  $\bar{\sigma}'v' \sim 0$ ; then we obtain the solutions as Eqs. (19) and (20):

$$\bar{\sigma}'E_x' \approx -\frac{\bar{\sigma}\langle\sigma'\rangle}{\langle\bar{\sigma}\rangle^2}\beta\bar{J}_y + O(\bar{\sigma}^4) \quad (19)$$

$$\begin{aligned} \bar{\sigma}'E_y' \approx & -\frac{\bar{\sigma}^2}{\bar{\sigma}}E_y + \beta\left(\frac{\bar{\sigma}\langle\sigma'\rangle}{\langle\bar{\sigma}\rangle} - \frac{\bar{\sigma}^2}{\bar{\sigma}}\right)E_x \\ & + \bar{\sigma}'u'B + \bar{u}B\frac{\bar{\sigma}^2}{\bar{\sigma}} - \beta\bar{\sigma}'v'B + O(\bar{\sigma}^3) \end{aligned} \quad (20)$$

As regards the other correlations, it can be shown numerically that  $\bar{J}' \cdot \bar{E}' \sim \bar{J}_y E_y' \sim 0.03 \bar{J}_y E_y$ ,  $\bar{v}'J_x' \sim 0$ , and  $\bar{u}'J_y' \sim 0$ . The correlation  $\bar{\sigma}'E_y'$  is positive between the electrodes and has a similar distribution in  $y$  as  $\bar{\sigma}'u'$ . The correlation  $\bar{\sigma}'E_x'$  is negative near the electrodes and positive in the outer region. Its magnitude is about  $\bar{\sigma}'E_y'/20$ . It is also shown numerically that  $\bar{\sigma}'\langle\sigma'\rangle \sim \bar{\sigma}^2/10$ .

Defining the effective conductivity as

$$\sigma_{\text{eff}} = \frac{\langle\bar{\sigma}\rangle}{\bar{G}} = -\frac{J_y H}{V_0 - V_c} \quad (21)$$

we obtain  $\bar{G}$  by the substitution of Eqs. (19) and (20) into Eq. (10) as follows:

$$\begin{aligned} \bar{G} = & \langle\bar{\sigma}\rangle \left\langle \frac{1+\beta^2}{\bar{\sigma}} \right\rangle - \langle\beta\rangle^2 \\ & + \langle\bar{\sigma}\rangle \left\langle \frac{1+\beta^2}{\bar{\sigma}} \cdot \frac{\bar{\sigma}^2}{\bar{\sigma}^2} \right\rangle - \langle\beta\rangle^2 \frac{\langle\bar{\sigma}'\rangle^2}{\langle\bar{\sigma}\rangle^2} \end{aligned}$$

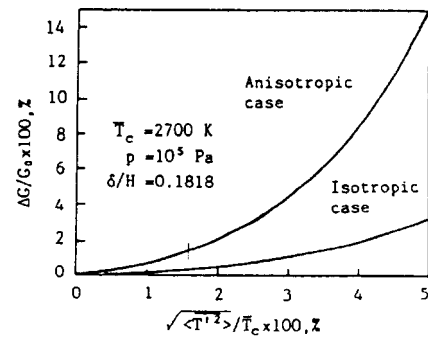


Fig. 13 Effects of the temperature fluctuation on the mean G-factor

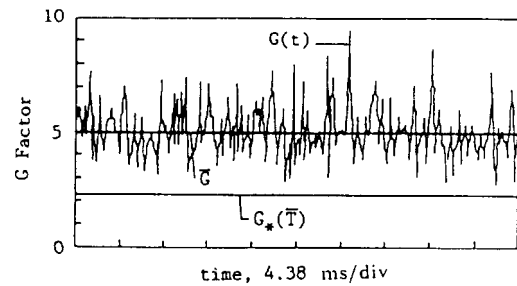


Fig. 14  $G(t)$ ,  $\bar{G}$  and  $G_*$  (Numerical conditions are the same as for Fig. 13)

$$+ O\left(\beta^2 \frac{\langle\bar{\sigma}'^2\rangle}{\langle\bar{\sigma}\rangle^4}\right) = G_0 + \Delta G \quad (22)$$

The first and second terms on the right-hand side are replaced by  $G_0$ , which describes the decrease in the conductivity due to the conductivity nonuniformity in the space. The influence of the spatiotemporal variance is accounted for by  $\Delta G$ . In the case of a plasma without fluctuation, we can set  $\bar{G} = G_0 = G_*$ .

In Fig. 13, the relation of  $\bar{G}/G_0$  to the temperature turbulence is shown for the case of  $T_w = 1800$  K,  $\delta/H = 0.1818$  and  $p = 105$  kPa. It is seen that in a spatially nonuniform plasma  $\Delta G/G_0$  is about 10%, and in a plasma that fluctuates in time but is uniform in space,  $\Delta G/G_0$  is about 3%. It should be noted that  $\bar{\sigma}$  in  $G_0$  includes the effect of the temperature fluctuation. When  $G_0$  is calculated from the mean temperature only, as is generally the case, then for the present plasma model  $G_*/\bar{G} \sim 50\%$  as seen in Fig. 14. In this case, the plasma resistance may be underestimated and the power output overestimated to a considerable extent.

## 8. Effects of Two-Dimensional Turbulence

Although an exact solution can be obtained for a one-dimensional nonuniform plasma, that model cannot describe the real situation accurately. Here, we examine the validity of the 1D model using 2D nonuniformity and fluctuations within the channel

cross-sectional plane. Since axial convection is much larger than the transverse flow in an MHD channel, to a good approximation we can neglect the variation in the  $x$  direction. Accordingly,  $E_x$  is constant over the cross section. Rearranging Eqs. (8) and (9) in terms of the electric potential, we obtain

$$\phi_{yy} + (1 + \beta^2)\phi_{zz} + \frac{\sigma_y}{\sigma}\phi_y + (1 + \beta^2)\frac{\sigma_z}{\sigma}\phi_z + u_y B - v_y B - \frac{\sigma_y}{\sigma}(\beta E_x - uB + \beta vB) = 0, \quad (23)$$

where the subscripts, except in  $E_x$ , denote partial differentiation with respect to  $y$  and  $z$ . The time series data of the velocity and the temperature were given at the FDM mesh points by adding the fluctuation component to the mean 1/7 th profile, where the method explained in Sec. 3, (i.e. the weighting function  $\sqrt{g^{(2)}}$ ) was extended to two dimensions. The boundary layer thickness of  $\delta/H = \delta/W = 0.15$  and a wall temperature of  $T_w = 1800$  K were assumed. Examples of the instantaneous distribution of the velocity and the temperature are given in Figs. 15 and 16, respectively. In these cases, the velocity variance is from 3.4 to 9.7% of  $\bar{u}_c$  and that of the temperature is from 2.7 to 3.8% of the mean core value 2800 K.

Using these data and the boundary conditions  $\partial\phi/\partial z = 0$  on the electrodes and  $J_z = 0$  on the insulator walls, the distribution of the potential was calculated as shown in Fig. 17, where  $V_c/\bar{u}_c B H = 0.54$  and  $\beta = 1.93$ . The potential fluctuation in the electrode boundary layers is significant, and this means that the 1D model which neglects the variation in the  $z$  direction is not appropriate. Although no figures are presented here, it should be mentioned that with decreasing wall temperatures, an eddy current appears in the insulator

boundary layers and results in decreases in  $J_y$ , the output current and the open voltage.

A number of the analyses mentioned above were performed and the results were added to obtain the mean plasma resistance. Final results are compared in Fig. 18 with those of the 1D model. It is shown that if we assume the 2D model to be correct, the 1D model overestimates the plasma resistance when the wall temperature is high, while it underestimates the resistance when the wall temperature is low. The actual wall temperature may be less than about 2000 K. Therefore, we conclude that the influence of the plasma turbulence in time and space upon the effective mean values is more critical than is estimated by the 1D turbulent model.

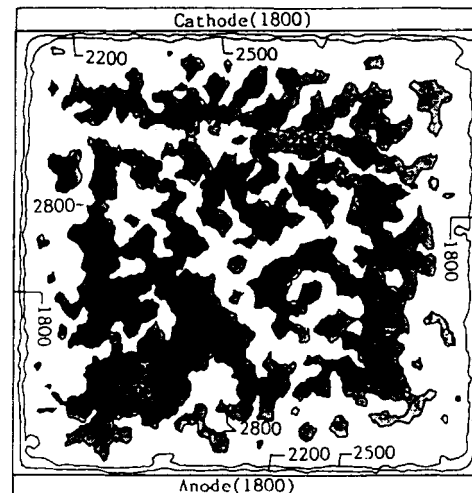


Fig. 16 An example of the two-dimensional turbulence of the temperature [isotherm plot, dark area:  $2800 \text{ K} \leq T \leq 3090 \text{ K}$  (= + M point)]

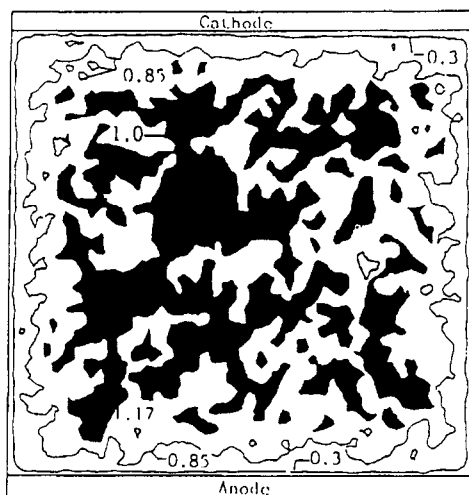


Fig. 15 An example of the two-dimensional turbulence of the axial velocity data [constant  $u/\bar{u}_c$  plots, dark area:  $1 \leq u/\bar{u}_c \leq 1.17$  (= + M point)]

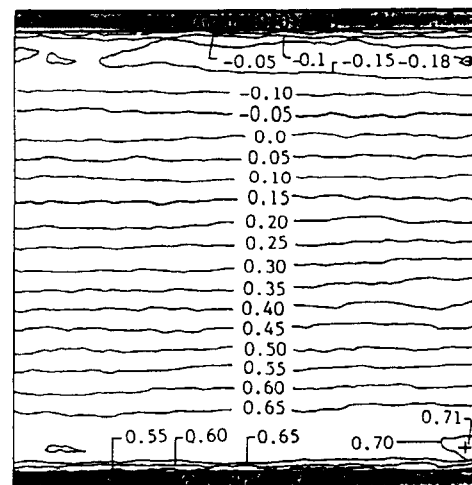


Fig. 17 Distribution of the equipotential lines in the cross plane

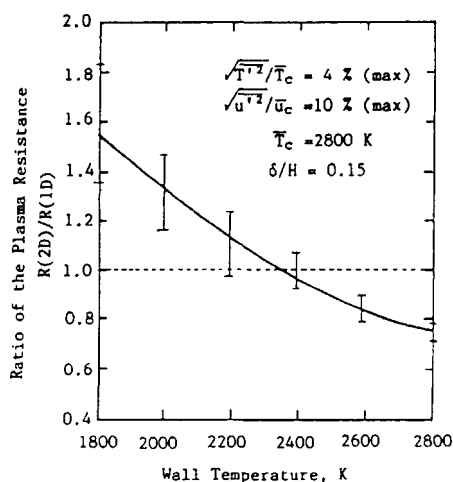


Fig. 18 Errors in the effective resistance in the evaluation with the one-dimensional model

### 9. Conclusions and Discussions

In order to pursue the influence of the statistical fluctuation of Saha equilibrium plasmas upon the mean performance of a combustion plasma MHD power generator, we first clarified the range of the turbulent maximum frequency and the lowest temperature level for which Saha's equilibrium can be assumed. It was confirmed that it is sufficient to take into account the temperature fluctuation up to the second order in the evaluation of mean scalar conductivity. Next, the electrical behavior was analyzed with the use of statistical numerical data of velocity and temperature, from which it was shown that the deterioration of the output characteristics of an MHD generator due to turbulence is crucial. In order to evaluate this effect in terms of effective conductivity, the mean correlations between the conductivity fluctuation and the electric field counterparts in the mean generalized Ohm's law were explicitly given, and then the conventional  $G$ -factor was modified to take the temporal fluctuation into account. Finally, the mean plasma resistance obtained by the potential analysis for two-dimensional turbulent plasmas was compared with the result of the one-dimensional model. It was concluded that the 1D turbulence model somewhat overestimates the power output of an MHD generator.

The influence of the electrical parameter fluctuation upon the plasma behavior was not examined in this paper. In Saha equilibrium plasma with low magnetic Reynolds numbers, the electrical equations have no characteristic time. Therefore, the electrical behavior affects the thermal and fluid-dynamical plasma performance only through the Lorentz force

and Joule heat terms. The former may suppress turbulence  $u'$  and  $v'$  perpendicular to the magnetic field in the core region and in the electrode boundary layers, where the current density is large. Hence, the turbulence effect is certainly less than those presented in this paper. For quantitative evaluation, we must solve the entire set of time-dependent MHD equations. The effect of Joule heat term may differ depending upon the amount of the local Joule heating and the heat conduction to the walls. When the thermal diffusion is sufficient, the plasma fluctuation induced by the electric field may be ignored. In the opposite case, an electrothermal instability<sup>(8)</sup> may be induced. In thermal equilibrium plasmas, this phenomenon occurs dominantly in low-temperature boundary layers near electrodes with high frequencies in general, so that the assumption of Saha equilibrium may not be adopted. Discussion of such turbulent plasmas is beyond the scope of the present paper.

### Acknowledgements

The author would like to express his deep appreciation to Dr. S. Oikawa, Instructor of the Department of Nuclear Engineering, Hokkaido University, Japan, for his valuable discussions and help in performing numerical calculations.

### References

- (1) For example, Maxwell, C.D., Markham, D.M., Demetriades, S.T. and Oliver, D.A., Coupled Electrical and Fluid Calculations in the Cross Plane in Linear MHD Generators, Proc. 16th SEAM, Pittsburgh(1977), Paper VII. 3.
- (2) Kruger, C.H. and Mitchner, M., Partially Ionized Gases, (1973), p. 36, John Wiley.
- (3) Cony, M.W.E., Electron-Ion Recombination in Seeded Combustion Products, J. Phys. D, Appl. Phys., Vol. 3(1970), p. 1703.
- (4) Hino, M., Supekutoru Kaiseki (Spectrum Analysis), (in Japanese), (1986), p. 42, Asakura Shoten.
- (5) For example, Kamemoto, K and Toyokura, T., Ryutai Rikigaku (Fluid-dynamics), (in Japanese), (1976), p. 87, Jikkyo Shyuppan.
- (6) Takano, S., Composition of Kerosene+O<sub>2</sub>+KOH Combustion Plasmas, (1988), (Private Communication).
- (7) Rosa, R.J., Hall and Ion-Slip Effects in a Nonuniform Gas, Phys. Fluids, Vol. 5, No. 9 (1962), p. 1081.
- (8) Kayukawa, N., Electrothermal Stability of Magnetohydrodynamic Plasma under Two-Component Magnetic Field, J. Propuls. Power, Vol. 2, No. 1(1986), p. 31.

## 流体変動を伴う弱電離プラズマの相関電流の評価

正員 及川 俊一 (北海道大学)  
 非会員 三井 恒明 (北海道大学)  
 正員 粥川 尚之 (北海道大学)  
 正員 青木 義明 (北海道大学)  
 正員 榎戸 武揚 (北海道大学)

## An Estimation of Correlation Currents in Partially Ionized Plasma with Fluid Fluctuations

Shun-ichi Oikawa, Member, Tsuneaki Mitsui, Non-member, Naoyuki Kayukawa, Member,  
 Yoshiaki Aoki, Member, Takeaki Enoto, Member (Hokkaido University)

The correlations between fluctuations of the flow and those of the electromagnetic fields in a partially ionized plasma were numerically investigated. The currents due to prescribed flow field fluctuations were calculated by the generalized Ohm's law. The time-averaged flow fields were assumed to obey the 1/7-th power law. Intensities of the velocity and temperature fluctuations were given as functions of the distance from the solid wall of the duct. The Reynolds' stresses and the turbulent heat fluxes were also taken into account in evaluating fluctuations of velocity and temperature. Conventional methods ignore these factors in calculating the correlation of electromagnetic fluctuations with those of flow fields. This paper has shown that such a conventional method is valid only for the time-averaged electrical quantities of the plasma. It has also been shown that the externally-applied nonuniform magnetic field, known as the shaped B-field configuration (SFC), is effective in suppressing the Joule dissipation in the presence of these fluctuations.

キーワード: magnetohydrodynamics(MHD), 弱電離プラズマ, 一般化オームの式, shaped B field configuration(SFC), 熱流体変動, 相関電流

## 1. まえがき

燃焼ガスプラズマを作動流体とする MHD 発電機において、発電チャネル内の熱流体場は一般的に乱流状態にあり、それにより電気場も乱れを伴う状態にある。この乱れた弱電離プラズマ中の電磁界を数値解析する場合、従来は適当な乱流モデルに基づく熱流体場の時間平均解としての流体諸量を電気場の基礎方程式の一つである一般化オームの式に直接代入して電気諸量の算出<sup>(1,2)</sup>を行ってきた。この場合、熱流体場の変動と電磁界の変動との相関が全く無視されている。

著者らは、これまでに導電率変動を含む流体乱れと電流及び電界との相関を考慮して、一般化オーム則の乱れモデルを構成し、導電率勾配の存在する電極境界層内では、非等方性乱流減衰の結果、電極近くから主流方向への定常流が発生する<sup>(3)</sup>ことを示した。さらに、速度変動よりも温度変動に伴う導電率変動が、乱れたプラズマ中での電流輸送に重要な影響を持つ<sup>(4)</sup>ことを示した。

本報では、電磁流体変動による相関を考慮した場合の一般化オームの式を検討し、従来より用いられてきた流体変

動を考慮しない式との比較を電磁界の数値解析により行う。これより電磁流体変動による相関を無視することの問題点について検討する。

また MHD 流れでは、電磁力による境界層剥離、電流集中による熱電気不安定性、電磁力の断面内不均衡によって駆動される MHD 二次流れ<sup>(5,6)</sup>による熱電磁空力的不安定性<sup>(7)</sup>等の現象が現れる。これまでに著者らは、このような現象を抑制する方法として、SFC 型磁界配位 (Shaped B-field configuration) を採用することを提案<sup>(8-11)</sup>してきた。

そこで、磁界分布として通常の一様磁界である UFC 型磁界配位 (Uniform B-field configuration)、さらに SFC 型磁界配位を採用した場合における一般化オームの式の相関項に対する磁界分布の影響についても数値解析により検討する。

## 2. 一般化オーム則の時間平均形式

燃焼ガスプラズマ中の電流密度と電界の関係を表す式に一般化オームの式がある。イオンスリップ、さらに電子の圧力勾配を無視した一般化オーム則の瞬時形式は、以下の



ように表される。

$$J = \{\sigma\} \cdot (E + V \times B) - \mu_e J \times B \quad (1)$$

あるいは  $\{M\}$  をケルブロックテンソル<sup>(12)</sup>とし、磁界成分を  $B = (0, B_y, B_z)$  とした場合次式となる。

$$J = \sigma \{M\} \cdot (E + V \times B) \quad (2)$$

$$\{M\} = \frac{1}{1 + \beta_y^2 + \beta_z^2} \begin{bmatrix} 1 & -\beta_z & \beta_y \\ \beta_z & 1 + \beta_y^2 & \beta_y \beta_z \\ -\beta_y & \beta_z \beta_y & 1 + \beta_z^2 \end{bmatrix} \quad (3)$$

$J$ 、 $E$ 、 $V$ 、 $\mu_e$  は電流密度、電界、流速ベクトル及び電子の移動度であり、 $\beta_y$ 、 $\beta_z$  は  $\beta_y = \mu_e B_y$ 、 $\beta_z = \mu_e B_z$  で定義されるホールパラメタである。さらに、 $F = \{M\} \cdot (E + V \times B)$  となるベクトル  $F$  を導入すると式 (2) は以下となる。

$$J = \sigma(T) F(T, V) \quad (4)$$

この一般化オームの式を用いた MHD 発電チャネル内の弱電離プラズマに対する解析において、電流密度等の電気諸量は、瞬時値よりも時間平均値が重要となる。従来の解析手法では、時間平均の電流密度を評価する際に、乱流モデルを用いてナビエーストックスの方程式より得られた熱流体諸量の時間平均値  $\bar{T}$ 、 $\bar{V}$  を式 (4) に直接代入し、次式として電気諸量を算出してきた。

$$\bar{J} = \sigma(\bar{T}) F(\bar{T}, \bar{V}) \quad (5)$$

しかし電磁流体変動を考慮した一般化オームの式の時間平均形式は、式 (4) の  $J$ 、 $\sigma$ 、 $F$  にレイノルズ分解を施し次式となる。

$$\bar{J} = \bar{\sigma} \bar{F} + \overline{\sigma' F'} \quad (6)$$

$\bar{\phantom{x}}$  は時間平均、 $'$  は乱流変動を表す。さらに式 (6) 右辺第 2 項を分解し次式を得る。

$$\bar{J} = \bar{\sigma} \bar{F} - \frac{\overline{\sigma' \sigma'} \bar{F}}{\bar{\sigma}} + \frac{\overline{\sigma' J'}}{\bar{\sigma}} - \frac{\overline{\sigma' \sigma' F'}}{\bar{\sigma}} \quad (7)$$

①
②
③

式 (7) の①、②、③項は、熱流体変動とそれに伴う電磁界の変動を考慮することにより、時間平均形式の一般化オーム則に新たに付加されるべき MHD 相關量である。本形式では、時間平均電流  $\bar{J}$  に対する寄与を表す。以下に一樣磁界分布 UFC 型と SFC 型磁界分布のもとで、分割電極ファラデー型 MHD チャネル断面における電気場の二次元解析を行い、これらの相關量の時間平均電流に対する影響、さらに磁界分布の違いが時間平均電流及び各相關項に及ぼす影響を明らかにする。

### 3. 解析モデル

(3.1) 磁界配位 オープンサイクル MHD 発電機における作動流体の作動温度が、2500(K)~3000(K) 程度であるのに対し、電極面では電極材料として金属を用いる場

合、材料の耐久性の問題から電極面温度を 1000(K) 程度に冷却する必要がある。このため電極付近の境界層では、プラズマ温度とともに導電率は低下する。この高抵抗領域での、ホール効果による電極面に平行なホール電流成分に起因する電流パスの増加は、電力損失<sup>(13)</sup>となる。いま、プラズマが電極壁の垂直方向にのみ不均一であり、電極高さに比べ絶縁壁間隔が十分に狭いとすれば、 $B_y \ll B_z$  と仮定できる。この時、式 (1) からホール電流は次式で与えられる。

$$J_z = \left( \frac{(\mu_e B_z)}{(\sigma)} \sigma - \mu_e B_z \right) J_y \quad (8)$$

但し、 $\langle \phantom{x} \rangle$  は空間平均を表し、 $J_y$  はファラデー結線の MHD 発電機においては、発電に寄与する電流成分でありファラデー電流と呼ばれる。冷電極の近傍では導電率  $\sigma$  が低いいためホール電流は右辺第 2 項に支配されるが、ファラデー結線の条件 ( $J_x = 0$ ) よりコア (主流部) では第 1 項が第 2 に較べ若干大きくなる。結果的に電極近傍の磁界が強ければ高抵抗の境界層における電流パスが長くなる。これより低導電率層の電圧降下に加え、ホール効果で電圧降下が増加することになる。しかし導電率と移動度の間には、電子密度  $n_e$  を介し、

$$\sigma = en_e \mu \quad (9)$$

なる関係が成立するため、もし磁界が、

$$\frac{B_z}{n_e} = \text{const.} \quad (10)$$

を満たす空間分布を持つ場合、式 (8) からファラデー電流に拘らず局所ホール電流は零になることが判る。このような磁界分布は理想 SFC 磁界分布と言えるものであるが、電子数密度は、プラズマ温度に対応し電極境界層内で急峻な分布となり、そのような電子数密度分布と相似な磁界分布を実現することは現実問題として不可能である。そこで、ここでは主流部で強く、電極境界層部で弱い磁界分布を SFC 磁界分布として採用した。このような磁界は、MHD チャネルの四隅に平行に超伝導コイルを配置することによって得られる。一樣な UFC 磁界は、クレセントコイル<sup>(9)</sup>により発生する。解析体系、SFC 磁界分布を図 1、2 に示す。

(3.2) 流体場 熱流体の平均場は、乱流 1/7 乗則分布を仮定する。即ち、電極壁と絶縁壁の境界層厚さを  $\delta$ 、主流速度を  $\bar{U}_c$ 、主流温度を  $\bar{T}_c$ 、壁面温度を  $T_w$  とし、 $0 \leq y/\delta \leq 1$ 、 $0 \leq z/\delta \leq 1$  における分布を次式で与える。

$$\frac{\bar{U}}{\bar{U}_c} = \frac{\bar{T} - T_w}{\bar{T}_c - T_w} = \left( \frac{y}{\delta} \right)^{1/7} \left( \frac{z}{\delta} \right)^{1/7} = \xi^{1/7} \zeta^{1/7} \quad (11)$$

電極境界層では  $\zeta = 1$ 、絶縁壁境界層では  $\xi = 1$ 、コアでは  $\xi = \zeta = 1$  である。速度変動、温度変動の標準偏差については、混合距離理論<sup>(14)</sup>に基づき次のようにモデル化する。即ち混合距離を  $\ell$ 、乱流動粘性係数を  $\nu_t$  とし、

$$U' \sim V' \sim W' \sim \frac{\nu_t}{\ell} \quad (12)$$

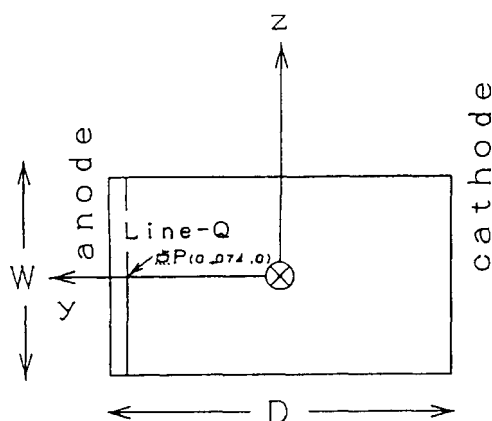


図1 解析体系  
Fig. 1. Analysis system.

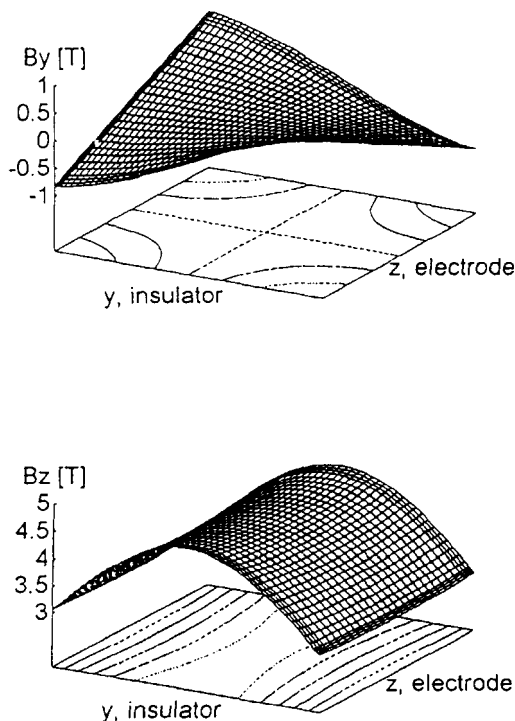


図2 SFC 磁界分布  
Fig. 2. SFC-type magnetic field distribution.

$$t \sim -(\gamma - 1)M^2 \frac{\bar{T}_c}{\bar{U}_c} v \quad (13)$$

$$t = \sqrt{T'^2}, \quad v = \sqrt{V'^2} \quad (14)$$

$$\ell = \kappa y \quad (15)$$

$$\nu_t = \ell^2 |\nabla \bar{U}| \quad (16)$$

とする。但し、 $\kappa$ はカルマン定数、 $\gamma$ は比熱比、 $M$ はマッハ数であり、主流部に近い境界層部 ( $\lambda \leq \xi \leq 1, \lambda \leq \zeta \leq 1$ ) 及び主流部 ( $1 \leq \xi, 1 \leq \zeta$ ) では動粘性係数を一定とした。 $U'$ は主流速度乱れ、 $V'$ は電極壁に垂直な速度乱れ、 $W'$ は平行な速度乱れを、 $t, v$ は温度及び速度の標準偏差<sup>(15)</sup>を表す。乱れ速度の各成分の分散の大きさの関係は、MHDプラズマに関して資料が無い場合通常流体の経験値<sup>(16)</sup>を参考に次のように与える。

$$\bar{U'^2} : \bar{V'^2} : \bar{W'^2} = 4.9 : 1.0 : 2.4 \quad (17)$$

さらに実験機での測定データ<sup>(17)</sup>を参考にそれぞれの分散に空間的に分布を持たせてある。また、燃焼ガスプラズマの不安定性、シード物質の不良混合等が発生した場合に起こる導電率変動を想定し、仮想的に温度変動の標準偏差を2倍 (Case-2)~3倍 (Case-3) に設定した場合の解析も行っている。

速度と温度の相互相関については、以下に示すような勾配拡散型のモデルを用いMHDダクト断面内の場所により相関量の符号を考慮<sup>(20)</sup>した。

$$\overline{V'U'} = -\nu_t \frac{\partial \bar{U}}{\partial y} \quad (18)$$

$$\overline{V'T'} = -\frac{\nu_t}{P_t} \frac{\partial \bar{T}}{\partial y} \quad (19)$$

ここで  $P_t$  はプラントル数である。また式(17~19)において絶縁壁境界層では  $V'$  を  $W'$  に、 $y$  を  $z$  で置き換える。以上を考慮し、乱数を基に発生した熱流体場の変動量を平均分布である  $1/7$  乗則分布に重畳して、変動速度三成分と温度変動を与え瞬時値とした。

(3.3) 電気場 3.2節から得られるプラズマの乱れモデルについて、 $y$ - $z$ 断面内を三角形一次要素を用いた有限要素法により電磁界の解析を行う。磁界の変動は、磁気レイノルズ数  $R_m$  が非常に小さい ( $R_m \ll 1$ ) ので無視する。支配方程式は、式(1)の一般化オームの式と中性プラズマに対する電流連続の式 ( $\nabla \cdot \mathbf{J} = 0$ )、及び定常電界の式<sup>(18)</sup> ( $\nabla \cdot \mathbf{E} = 0$ ) である。無限分割電極近似を採用することによって、これらの式で、電位  $\phi$  を除いて  $x$  方向の変化は、 $y$ - $z$ 断面内の変化に比べて十分に小さいとし  $\partial/\partial x = 0$  と置くことができる。したがってホール電界  $E_x$  は  $y, z$  によらず、ダクト断面内で一定となる。磁界の2成分  $B_y, B_z$  を考慮し、電気場の支配方程式をまとめると以下になる。

$$\frac{\partial}{\partial y} \left\{ \sigma_{yx} (E_x + v B_z - w B_y) + \sigma_{yy} \left( -\frac{\partial \phi}{\partial y} - u B_z \right) + \sigma_{yz} \left( -\frac{\partial \phi}{\partial z} + u B_y \right) \right\}$$

表 1 数値条件

Table 1. Numerical conditions.

| 燃焼ガス         | カリウムシード石炭燃焼ガス                  |
|--------------|--------------------------------|
| 熱入力          | : 6.25(MWth)                   |
| ダクト幅 (電極間距離) | : D=0.15(m)                    |
| (絶縁壁間距離)     | : W=0.05(m)                    |
| チャネルアスペクト比   | : D/W=3.00                     |
| 主流速度         | : $U_c=800$ (m/sec)            |
| 主流温度         | : $T_c=2900$ (K)               |
| 壁面温度         | : $T_w=1400$ (K)               |
| 境界層厚さ        | : $\delta=0.01$ (m)            |
| 負荷率          | : 0.5                          |
| 境界層の内層厚      | : $\lambda=0.185\delta$        |
| カルマン定数       | : $\kappa=0.41$                |
| マッハ数         | : $M=0.9$                      |
| 乱流プラントル数     | : $Pr=0.9$                     |
| 磁界分布 (UFC)   | : $(B_x, B_y, B_z)=(0,0;3.97)$ |
| (SFC)        | : $(B_x)=(3.00\sim4.59)$ [T]   |
|              | : $(B_y)=(-0.83\sim0.83)$ [T]  |

$$+ \frac{\partial}{\partial z} \left\{ \sigma_{zx} (E_x + vB_z - wB_y) \right. \\ \left. + \sigma_{zy} \left( -\frac{\partial \phi}{\partial y} - uB_z \right) + \sigma_{zz} \left( -\frac{\partial \phi}{\partial z} + uB_y \right) \right\} = 0 \quad (20)$$

ここで $\sigma$ の添え字は偏微分を表す。境界条件は次式で与えられる。

$$\phi(-D/2, z) = \phi_c(\text{const.}) \quad (21)$$

$$\phi(D/2, z) = \phi_a = 0 \quad (22)$$

$$J_z(y, W/2) = J_z(y, -W/2) = 0 \quad (23)$$

また電極結線としてファラデー型を想定し、軸方向に流れる正味のホール電流は無い。

$$I_{Hall} = \int \int_{y-z} J_x dy dz = 0 \quad (24)$$

この条件から一定値  $E_x$  が求められる。電気場の時間平均値に対しその時定数は熱流体場に比べ十分短く、変動は流体場に時間遅れなく追従すると考えられる。従って与えた熱流体場に対する解のアンサンブル平均をもって電気場の時間平均値を求めることができる。平均と分散及び相関量を十分精度よく評価するため、本論文では5000組の熱流体場に対する解析を行っている。但し、本解析では熱流体変動に伴う変動電流に働くローレンツ制動力の効果あるいは乱流減衰の影響を無視した。弱電離プラズマ中の乱流減衰効果については文献<sup>(19)</sup>を参照されたい。その他の数値条件は、表1に示す。

#### 4. 解析結果及び考察

(4.1) 時間平均電流 :  $\bar{J}$  磁界分布を UFC 型、SFC 型としたそれぞれについて、従来よりの乱れを持たない乱流1/7乗則に従う流体温度、速度分布を与えた場合 (Case-0) と、流体変動を考慮した場合 (Case-1)、また温度変動のみを2倍 (Case-2)、3倍 (Case-3) とした場合の時間

表 2 UFC、SFC 型磁界配位での電極面付近 Line-

Q 上の時間平均最大電流値

Table 2. Time-averaged maximum current densities on Line-Q for UFC and SFC magnetic field distributions near electrodes.

|     |                     | Case-0 | Case-1 | Case-2 | Case-3 |
|-----|---------------------|--------|--------|--------|--------|
| UFC | $\bar{J}_x(A/cm^2)$ | 1.30   | 1.33   | 1.39   | 1.45   |
|     | $\bar{J}_y(A/cm^2)$ | -1.48  | -1.50  | -1.54  | -1.61  |
|     | $\bar{J}_z(A/cm^2)$ | -0.13  | -0.13  | -0.14  | -0.18  |
| SFC | $\bar{J}_x(A/cm^2)$ | 1.02   | 1.04   | 1.07   | 1.07   |
|     | $\bar{J}_y(A/cm^2)$ | -1.58  | -1.60  | -1.64  | -1.69  |
|     | $\bar{J}_z(A/cm^2)$ | -0.14  | -0.14  | -0.16  | -0.20  |

平均電流の (空間的な) 最大値を表2に記載する。いずれの電流成分も電極近傍において最大となっている。ここで Case-1 の温度変動は最大で、 $t_{max}/T = 0.0246$  としている。ここで扱う最大値は、MHD ダクト内 y-z 断面上最も重要な解析対象領域である図1中の電極面付近 Line-Q 上の計算値である。

表2より、磁界分布 SFC 型の場合 UFC 型に較べ時間平均電流において各々の温度変動に対して  $J_y$  成分では若干の増加があり、 $J_z$  成分では20%程度減少している。

これまでに、流体分布として時間平均値のみを与えた場合の数値解析より、SFC 型磁界配位を採用することにより、有効電流であるファラデー電流は減少させることなくホール電流を抑制する効果が確認されてきたが、流体変動を考慮した本解析の場合でも同様の結果が得られた。また  $J_z$  成分については、電流値自体が非常に小さな値であり磁界配位変化の影響はさほど表れない。また電流三成分いずれについても、乱れを考慮しない Case-0 に比べ、乱れを考慮した Case-1~Case-3 では電流値は増加している。しかし、その大きさは数%程度である。

(4.2) ポテンシャル分布 :  $\bar{\phi}$  図3に Case-1 の場合における電極中心線上の平均ポテンシャル分布を示す。UFC 型と比較して SFC 型の場合は、電極電位からみたプラズマ中の電位の極値との差である電圧ドロップ  $\Delta\bar{\phi}$  が減少している。これによって  $\bar{J} \cdot \bar{E} > 0$  となる領域でのジュール熱としての電力損失を低減することが可能となる。

(4.3) 流体乱れと電流及び電界の相関 ここでは、式(7)の流体乱れに起因する電磁界の変動と熱流体場の変動との相関電流①、②、③項が時間平均電流に対する寄与について考察する。これらの Line-Q 上における x 成分の電流の最大値を UFC、SFC のそれぞれについて表3に示す。また断面内コア領域の時間平均電流の空間平均値、即ち  $\langle \bar{J}_{core} \rangle$  に対する百分率を併せて示す。ここで百分率を計算する際の平均電流は UFC で、 $\sim 1.6(A/cm^2)$ 、SFC では  $\sim 1.7(A/cm^2)$  である。

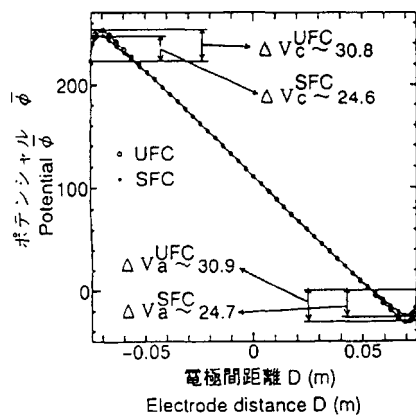


図3 電極中心線上(z=0)の平均ポテンシャル分布  
Fig. 3. Average potential distribution between electrodes on the line of z=0.

表3 UFC、SFC型磁界配位での電極面付近の一般化オームの式における各相関項電流換算値  
Table 3. Current density of correlation in generalized Ohm's law near electrodes in the UFC and SFC.

|                      | (A/cm <sup>2</sup> )                   | Case-1        | Case-2         | Case-3         |
|----------------------|----------------------------------------|---------------|----------------|----------------|
| UFC<br>x成分<br>百分率(%) | ① $-\frac{\sigma' \sigma' F}{\sigma}$  | -0.234<br>15% | -1.617<br>100% | -8.080<br>500% |
|                      | ② $\frac{\sigma' J'}{\sigma}$          | 0.060<br>4%   | 0.251<br>16%   | 0.539<br>34%   |
|                      | ③ $-\frac{\sigma' \sigma' F'}{\sigma}$ | 0.030<br>1.8% | 0.632<br>40%   | 5.261<br>329%  |
| SFC<br>x成分<br>百分率(%) | ① $-\frac{\sigma' \sigma' F}{\sigma}$  | -0.176<br>10% | -1.209<br>70%  | -5.717<br>336% |
|                      | ② $\frac{\sigma' J'}{\sigma}$          | 0.040<br>2%   | 0.176<br>10%   | 0.341<br>32%   |
|                      | ③ $-\frac{\sigma' \sigma' F'}{\sigma}$ | 0.024<br>1%   | 0.480<br>28%   | 3.783<br>222%  |

これらの結果から、先ず磁界分布の影響に関しては次の事が言える。表2でSFC磁界配位では、流体乱れの程度に関わらず、時間平均電流のホール電流成分が減少することを示したが、導電率と電流あるいは実効的に働く電界との乱れの相関もたらす各相関電流①、②、③項それぞれについてもSFC磁界配位では大きく減少する。

次にCase-1→Case-3と温度乱れの強度を増した場合の、①、②、③項の変化を考察する。表3に示した各相関量x成分について、温度乱れが大きくなるにつれ大きく変化した電流値を増している。表3に示していないy成分及びz成分についても同様の傾向を示す。これは相関量各項とも導電率の変動 $\sigma'$ を含んでおり、導電率が温度に対して非常に強い非線形的な依存性を持つためであると解釈できる。しかし表2で調べたように結果的に時間平均電流は大きくは変化しない。このことは、相関電流の符号に関連している。例えば、平均電流の大部分を駆動する $\sigma F$ と、①項の

$-\sigma' \sigma' F / \sigma$ では、 $\sigma' \sigma'$ が常に正であるので両者は逆方向の電流となり相殺される。以上の理由により、各相関電流は温度変動の影響を大きく受けるが、正味の時間平均電流に及ぼす影響は結果的に余り大きくない。従って本解析で与えた乱れの程度では、時間平均電流密度に着目する限りにおいて、電磁界の変動量である相関電流の影響はほとんど無いと言える。しかし、著者らが既に指摘したように<sup>(21)</sup>電極アークなど、乱れの強い領域での局所現象を解析する場合はこれら相関項は重要な影響を持つ。そこで、図4に各磁界配位で電極面中心付近の点(図1上の点P)を代表して抽出し、一般化オームの式の各相関量のx、y成分値を、乱れの強さに対してまとめたものを示し、また流体乱れとして温度乱れのみを与えた場合を図5に示す。

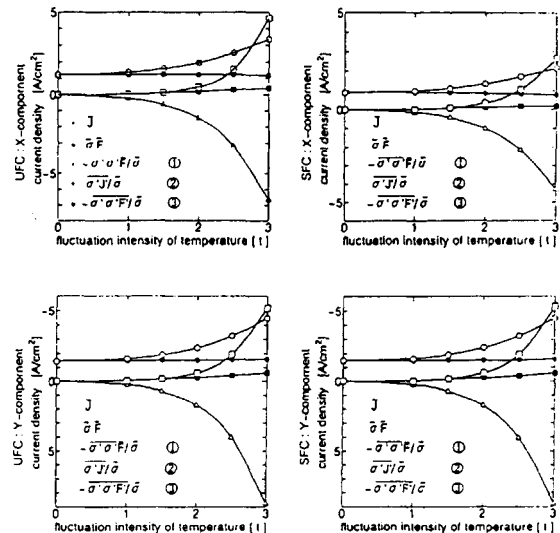


図4 一般化オーム則の各相関項の流体乱れの強さに対する依存性  
Fig. 4. Correlation currents vs fluctuation intensity.

これまで一般に、ホール電流、ファラデー電流の評価を行う場合、定常のN-S方程式より得られた時間平均の温度、速度を、直接一般化オームの式(1)に代入してきた。つまり、 $\bar{J} = \sigma(\bar{T})F(\bar{T}, \bar{V}) = \sigma F$ とし、(6)式の右辺第2項、即ち(7)式の右辺第2項以下を全く無視して扱ってきた。しかし、図4より、本解析に用いた電磁流体変動を考慮した一般化オームの式での評価では、①、②、③項の各相関量は、温度変動が強くなるにつれその電流値を増し、さらには時間平均電流と同程度以上の電流値を持つこととなる。つまり $\bar{J}$ を $\sigma(\bar{T})F(\bar{T}, \bar{V})$ として解析した従来の方法でも大きな誤差は生じないが、これを $\sigma(\bar{T})F(\bar{T}, \bar{V})$ だと考えるのは間違いであり、相関項 $\sigma' F'$ の存在を忘れてはならない。従って、電磁流体変動における各相関を評価する場合、下式で表される関係に注意しなくてはならない。

$$\bar{J} = \sigma F + \sigma' F'$$

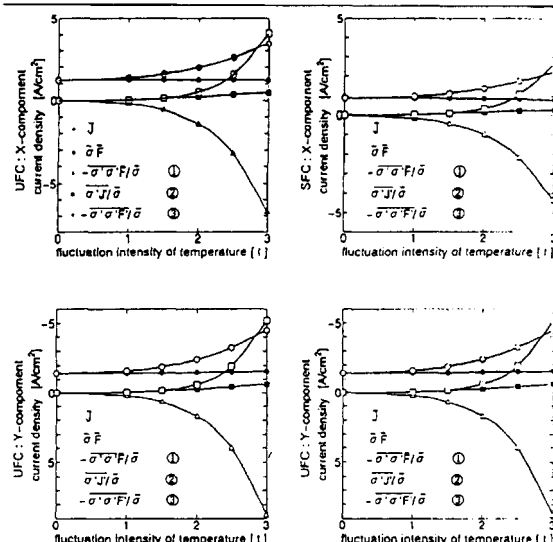


図5 一般化オーム則の各相関項の流体乱れの強さに対する依存性 (温度乱れの場合)

Fig. 5. Correlation currents vs fluctuation intensity (temperature fluctuation only.)

$$\begin{aligned}
 &= \overline{\sigma F} - \frac{\overline{\sigma' \sigma' F}}{\overline{\sigma}} + \frac{\overline{\sigma' J'}}{\overline{\sigma}} - \frac{\overline{\sigma' \sigma' F'}}{\overline{\sigma}} \\
 &\quad \text{①} \quad \text{②} \quad \text{③} \\
 &\approx \sigma(\overline{T}) F(\overline{T}, \overline{V}) \\
 &\neq \overline{\sigma(T) F(T, V)} \quad (25)
 \end{aligned}$$

また速度乱れを考慮した図4と考慮しない図5を比較した場合、大きな違いが無いことから流体乱れは、乱れたプラズマ中の電流輸送に関し温度乱れが支配的であることが確認できる。

(4.4) ホール電界及び電氣的積分諸量 次に、UFC型およびSFC型磁界配位について、ホール電界、電極電流、出力密度の結果を表4に示す。

表4より、どの設定条件下においても各積分量とも、ホール電流( $J_x$ )の抑制効果によって、UFC型よりSFC型の磁界分布の場合、2~3%程度大きくなっている。また電磁流体変動を考慮した場合は、考慮しない場合より多少の増加傾向を示す。この電気出力の増加の原因としては、時間平均導電率 $\sigma$ が温度変動と共に増加するためではなく(電流輸送を支配する実効的な導電率は減少する)<sup>(3)</sup>、乱流熱流束 $\overline{T'V'}$ が関係している。この式 $\overline{T'V'}$ は(19)のモデルにより、陽極側では正、陰極側では負となる。ここで相関 $\overline{\sigma'V'}$ を考える。導電率 $\sigma$ の温度依存性により $\overline{\sigma'V'}$ と $\overline{T'V'}$ は同符号となる。電極面近傍のホール電流は、導電率の低下に伴い式(8)より、 $J_x \sim -\beta_x J_y > 0$ となり陽極と陰極で共に正である。従ってこの相関によって駆動される電流 $\overline{\sigma'V'} \times B_z$ は陽極側ではホール電流 $J_x$ を増加させる方向、陰極側では減少させる方向となる。これより陽極と陰極とでは、陰極の方が電極付近の電圧降下の減少により、電流が流れやす

表4 熱流体変動に対する電気諸量の変化

Table 4. Electrical quantities for various fluid fluctuation intensities.

|             |        | ホール電界<br>(V/cm)    | 電極電流<br>(A/cm <sup>2</sup> ) | 出力密度<br>(MW/m <sup>3</sup> ) |
|-------------|--------|--------------------|------------------------------|------------------------------|
| UFC<br>(分散) | Case-0 | -14.48             | -1.26                        | 18.74                        |
|             | Case-1 | -14.64<br>(0.0277) | -1.28<br>(0.0003)            | 19.00<br>(0.0559)            |
|             | Case-2 | -15.03<br>(0.106)  | -1.33<br>(0.0010)            | 19.71<br>(0.225)             |
|             | Case-3 | -15.50<br>(0.214)  | -1.39<br>(0.0021)            | 20.69<br>(0.489)             |
| SFC<br>(分散) | Case-0 | -15.29             | -1.34                        | 19.85                        |
|             | Case-1 | -15.42<br>(0.0218) | -1.36<br>(0.0002)            | 20.09<br>(0.0008)            |
|             | Case-2 | -15.73<br>(0.0810) | -1.40<br>(0.0008)            | 20.71<br>(0.1836)            |
|             | Case-3 | -16.08<br>(0.1534) | 1.45<br>(0.0017)             | 21.55<br>(0.3795)            |

くなっている。トムソンの定理より、電流パスはジュール熱損失を最小となるよう選ばれるが、この効果は陰極で実現しやすく、よって陰極の影響が支配的に現れていると言える。

## 5. まとめ

現実的な相関及び強さを持った温度変動、速度変動を乱数を用いて与えた場合の、時間平均電磁界の解析を、UFC及びSFC磁界配位のもとで行った。結果を以下のようにまとめる。

1. 電磁流体変動を考慮した一般化オームの式においても、SFC型磁界配位を採用することにより、局所ホール電流を抑制する効果が確認された。
2. 電流密度及び総電気出力に着目する限りにおいて、熱流体乱れを考慮する本解析と、考慮しない従来の解析法では、ほぼ同じ結果を与えることが解った。
3. しかし、2のことは、導電率変動を含む流体乱れと電流及び電界の相関である式(7)の①、②、③項が無視できるほど小さいのではなく、各相関電流の打ち消し合いの効果からもたらされる。
4. 乱れを伴う電磁流体場の平均現象を局所現象を含めて精度よく解析するためには、電磁力の作用を考慮した熱流体場のモデル化が第一義的に重要である。

なお、本研究の数値計算は文部省核融合科学研究所汎用計算機利用共同研究により行った。

(平成6年12月26日受付、平成7年4月14日再受付)

# On the applicability of optical depth-atomic absorption relationship to measurements of alkali seeded combustion flames<sup>1</sup>

N. Kayukawa

*Center for Advanced Research of Energy Technology, Hokkaido University, Kita-ku, Kita 13,  
Nishi 8, Sapporo 060, Japan*

Received 1 November 1994; accepted 4 May 1995

---

## Abstract

The applicability of the new depth-atomic absorption relationship to measurements of optical properties of an alkali metal in a non-uniform multi-component combustion flame was numerically studied. The relationship describes the equality between the ratio of the optical depths at far to near wing wavelengths and that of the atomic absorption coefficients at the respective wavelengths. An introduction of biases into theoretical wing intensities and the evaluation of the ratio of the atomic absorption coefficients with far wing temperatures are essential features in the formalism. It is shown that the relationship has sufficient sensitivities to the change of optical quantities to be measured under realistic flame pressures, temperatures and wing spectral levels when the two wavelengths are adequately separated.

*Keywords:* Spectroscopy; Flame; Alkali metal; Optical depth; AAC

---

## 1. Introduction

The knowledge of the flame temperature, the ground state atom density and the spectral properties of a specific radiating atom is of basic importance in combustion chemistry, radiation heat transfer and in the field of combustion plasma technology. The monochromatic emission absorption method developed by Strong and Bundy [1] has been widely used to measure flame temperature employing an isolated spectrum emitted from alkali atoms added to the flame as the emission source or the seed to enhance the flame's

---

<sup>1</sup> Presented at the 30th Anniversary Conference of the Japan Society of Calorimetry and Thermal Analysis, Osaka, Japan, 31 October–2 November 1994.

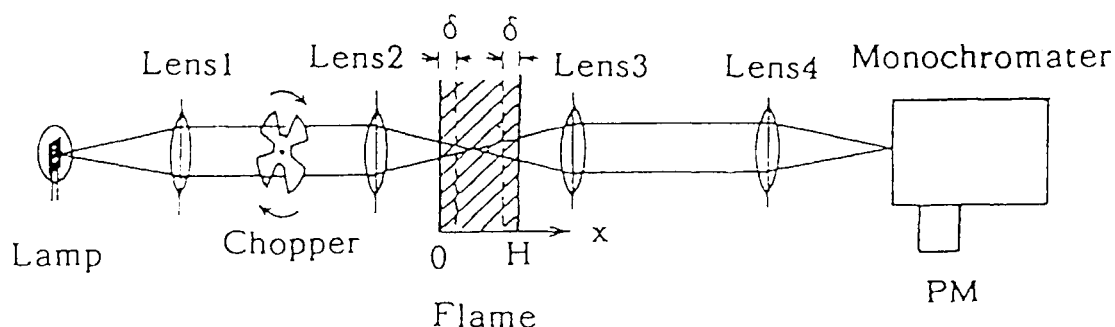


Fig. 1. A basic optical scheme of monochromatic emission-absorption measurement and the optical path coordinate.

electrical conductivity. In the optical scheme shown in Fig. 1, the flame temperature and the optical depth can be calculated by discriminatively measured monochromatic signals of each the lamp plus flame emission, flame emission only, and pre-flame lamp. Even when the flame temperature is non-uniform on the line of sight as in the case of channel flows with a hot core region bounded by cold boundary layers, it is known [2] that the temperature measured at an appropriately far wing wavelength is close to the hottest temperature in the core with definite errors of less than a few percent.

In principle, the ground state number density of the emitting species can be calculated by the optical depth per unit length divided by the atomic absorption coefficient (AAC). However, reliable measurement of the AAC requires correct identification of the collision dominated half width of the resonance line (Lorentz breadth), which further requires a correct optical cross section (OCS) of the emitting atom. The correct Lorentz breadth may be obtainable by taking the effect of flame constituents and the adequate modelling of the OCS dependence on the flame temperature. In the past, emission absorption density measurements of fossil fuel fired magnetohydrodynamic channel flows [3,4], constant OCS data of Hofmann and Kohn [5] or Hinnov and Kohn [6] obtained in a uniform acetylene–air flame based on Hinnov's intensity density method [7] have been employed. The contribution of flame constituents on the collision process has also been neglected. A part of the relatively large error of from several tens to a hundred percent may have resulted from the uncertainty in the OCS and the Lorentz breadth.

Recently, we have shown [8] in the two wavelength emission absorption method that the ratio of the far wing optical depth to the near wing counterpart was closely equal to the ratio of the AAC at the same wavelengths, provided that the latter ratio was evaluated by the temperature measured at the far wing wavelength. This depth–AAC relationship can be used to calculate the OCS and the Lorentz breadth with the measurements of two wing optical depths and the far wing temperature. However, the experimental applicability is crucially dependent on the sensitivity of the relationship to the variation of the quantity to be measured. This paper is devoted mainly to examine the appropriate range of the wavelength separation, the gas pressure, the temperature non-uniformity and the bias level. The use of biases has been proposed to describe actual wing spectra, which, as observed by Bauman [9], are higher than the theoretical values by an order of magnitude.

The flame is a kerosene oxygen combustion gas in chemical equilibrium seeded with 48% KOH aq. by 1 wt.% of potassium. An example of the calculated mole fractions of

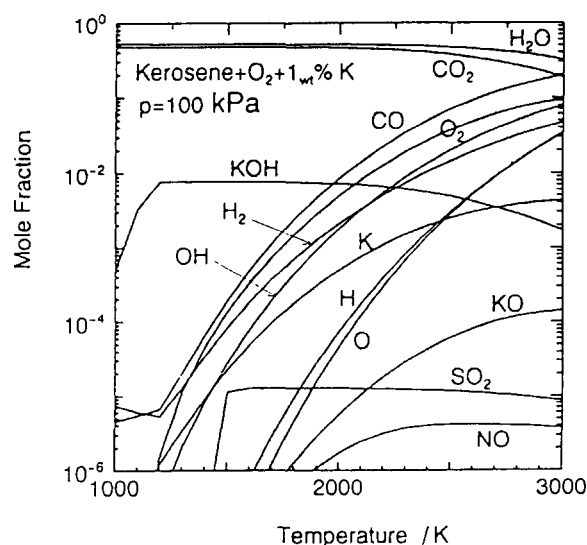


Fig. 2. Major chemical constituents of kerosene-oxygen combustion flame with 1 wt.% potassium under atmospheric pressure and an  $O_2$  equivalence ratio of 1.0.

the major constituents is given in Fig. 2. In the following calculations, we considered 27 neutral species in thermodynamic equilibrium. It is assumed that the flame has non-uniform temperature distribution on the optical path with boundary layers of the 1/7th temperature profile and a constant temperature core layer (see Fig. 1).

## 2. Emission absorption theory and the depth-AAC relationship

The optical depth  $\tau(\lambda)$  at the wavelength  $\lambda$  is defined as the integration of the absorption coefficient  $\kappa(\lambda, x) = N(x)\kappa(\lambda, x)$  along the optical path  $x$ :

$$\tau(\lambda) \equiv \int_0^H k(\lambda, x) dx = \int_0^H N(x)\kappa(\lambda, x) dx \quad (1)$$

where  $\kappa(\lambda, x)$  and  $N(x)$  are the AAC and the potassium number density, respectively. The AAC  $\kappa(\lambda, x)$  is a function of  $x$  due to temperature non-uniformity. For potassium D-lines the total absorption coefficient may be the sum of each contribution from the resonance line  $\lambda_1$  (766.5 nm) and  $\lambda_2$  (769.9 nm). Introducing a constant bias  $\kappa_n$  per emitting atom, the AAC is given by

$$\kappa(\lambda, x) = \sum_{i=1}^2 G_i P_i + \kappa_n \quad (2)$$

Here,  $G_i \equiv \lambda_i^2 \cdot (g_h / g_l) \cdot A_{hl} / 8\pi$ ,  $g_h$  and  $g_l$  are the statistical weight of the excited and ground levels, and  $A_{hl}$  is Einstein's coefficient of spontaneous emission. According to Radzig and Smirnov [10],  $G_1 = 1.87 \times 10^{-5} \text{ m}^2 \text{ s}^{-1}$  and  $G_2 = 0.92 \times 10^{-5} \text{ m}^2 \text{ s}^{-1}$ . The probability function  $P_i$  is generally given by the following Voigt function [11]:



$$P_i^v 2 \frac{\sqrt{\ln 2 / \pi}}{\Delta \nu_{Di}} \frac{a_i}{\pi} \int_{-\infty}^{\infty} \frac{\exp(-y^2)}{a_i^2 + (\omega_i - y)^2} dy \quad (3)$$

For wing spectra, Eq. (3) can be simplified by the approximation  $\omega_i \gg y$  to result in the following Lorentz function:

$$P_i^L = \frac{2}{\pi} \frac{\Delta \nu_p}{\Delta \nu_p^2 + 4(\nu - \nu_i)^2} \quad (4)$$

Here,  $a_i \equiv \Delta \nu_{Di} \sqrt{(\ln 2) / \Delta \nu_p}$ ,  $\Delta \nu_{Di} = \sqrt{(8\pi RT \ln 2) / \lambda_i}$  is the Doppler breadth,  $\Delta \nu_p$  is the Lorentz breadth,  $R$  is the potassium gas constant,  $T$  is the temperature  $\omega_i = (\nu - \nu_i) \sqrt{(\ln 2) / \Delta \nu_{Di}}$ ,  $\nu_i = c / \lambda_i$  is the frequency of the  $i$ th resonance center,  $\nu = c / \lambda$ , and  $c$  is the speed of light. The Lorentz breadth  $\Delta \nu_p$  is defined by

$$\Delta \nu_p = \sum_{s \neq K} N_s \langle v_{sK} \rangle Q_{sK} \quad (5)$$

where  $N_s$  is the number density of neutral species except potassium, and  $\langle v_{sK} \rangle = \sqrt{(8k_B T / \pi m_{sK})}$  is the relative speed, where  $k_B$  and  $m_{sK} = m_s m_K / (m_s + m_K)$  are the Boltzmann constant and the reduced mass, respectively.

In many past emission absorption studies on the potassium seeded combustion plasmas, a constant optical cross section  $Q_{sK}$  has been assumed, i.e.  $Q_{sK} = 6.0 \times 10^{-19} \text{ m}^2$  for  $\lambda_1$  or  $Q_{sK} = 5.77 \times 10^{-19} \text{ m}^2$  for  $\lambda_2$  [5]. Also, the effect of each component on the Lorentz breadth has been neglected. However, as mentioned above, the OCS of potassium may be different in each flame with different temperature and collision partners. Therefore, according to Margnau and Watson [12], we assume here the temperature dependence of the OCS as  $Q_{sK} = C \langle v_{sK} \rangle^{-2/5}$ , where  $C$  is a constant of the order of  $10^{-37} \text{ m}^6 \text{ s}^{-1}$ , that relates to Van der Waals' force and the model of the interaction potential. However, no rigorous expression of  $C$  has yet been given for alkali metals in combustion gases. Neglecting the difference in  $Q_{sK}$  for  $\lambda_1$  and  $\lambda_2$ , we can write Eq. (5) as

$$\Delta \nu_p = \alpha p T^{-0.7} \sum_{s \neq K} X_s \left( \frac{1}{M_s} + \frac{1}{M_K} \right)^{0.3} \quad (6)$$

Here, the new constant coefficient is defined as  $\alpha \equiv C(8R_0/\pi)^{0.3}/k_B$ ,  $R_0$  is the universal gas constant,  $p$  is the pressure,  $M_s$  and  $M_K$  are the molecular weight of  $s$  and  $K$ , respectively.  $X_s$  is the mole fraction of  $s$ , which is calculated by the equilibrium combustion analysis as function of the temperature and pressure. The flame temperature can be evaluated by the following formula [13]:

$$T_m(\lambda) = T_L \left( 1 - \frac{\lambda k_B T_L}{hc} \ln \left( \frac{K_1 \phi_g(\lambda)}{\phi_g(\lambda) + \phi_L(\lambda) - \phi_{g+L}(\lambda)} \right) \right)^{-1} \quad (7)$$

where the suffix m stands for the measured value,  $h$  is Planck's constant,  $K_1$  is the transmissivity of the incident system (lenses 1 and 2 in Fig. 1) and  $T_L$  is the brightness temperature of the lamp filament.  $\phi_L(\lambda)$  is the lamp light intensity defined under the condition of no absorption (no potassium). The intensities  $\phi_{g+L}(\lambda)$  and  $\phi_g(\lambda)$  are the emissions with and without the incidence of the lamp light, respectively. Assuming no optical loss in the detection system after lens 3,  $\phi_{g+L}(\lambda)$  and  $\phi_g(\lambda)$  are given approximately by the solution of the one-dimensional radiation transfer equation [2] as follows:

$$\phi_g(\lambda) = \exp(-\tau(\lambda)) \int_0^H (k(\lambda, x) B(\lambda, x) \exp(\int_0^x k(\lambda, x') dx')) dx \quad (8)$$

$$\phi_{g+L}(\lambda) = \phi_L(\lambda) \exp(-\tau(\lambda)) + \phi_g(\lambda) \quad (9)$$

where  $B(\lambda, x)$  is Planck's blackbody function, which is given under Wien's approximation  $hc/k_B T \lambda \gg 1$  as

$$B(\lambda, x) = \frac{2hc}{\lambda^3} \exp\left(-\frac{hc}{\lambda k_B T(x)}\right) \quad (10)$$

The lamp emission is given by  $\phi_L(\lambda) = B(\lambda, T_L)$ . The experimental formula of the optical depth  $\tau(\lambda)$  can be obtained from Eq. (9) as

$$\tau(\lambda) = \ln\left(\frac{\phi_L(\lambda)}{\phi_{g+L}(\lambda) - \phi_g(\lambda)}\right) \quad (11)$$

The temperature given by Eq. (7) is derived from the ratio  $B(\lambda, T_m)/B(\lambda, T_L)$  by assuming constant properties at  $T_m$  in Eq. (8). For wavelengths outside the center region, typically at optical depths of less than unity,  $T_m$  and absorption coefficients evaluated with  $T_m$  well describe the values corresponding to the core region [2]. Therefore, if the coefficient  $\alpha$ , namely the Lorentz breadth is known, the core potassium density can be approximately evaluated by

$$N_m(\lambda) = \frac{\tau(\lambda)}{H\kappa(\lambda, \alpha, T_m(\lambda))} \quad (12)$$

where the absorption coefficient per atom is defined by Eq. (2). In cases where an exact AAC is known, the error in  $N_m(\lambda)$  relative to the core value is about 10% at wing wavelengths, where  $\tau(\lambda) \leq 1.0$ .

A method so far known to determine the Lorentz breadth is the intensity density method developed by Hinnov [7], which, unfortunately, cannot be applied to non-uniform gases and fixed potassium density.

On the other hand, we have shown numerically that there exists the following approximate equality in two wavelength emission absorption spectroscopy [8]:

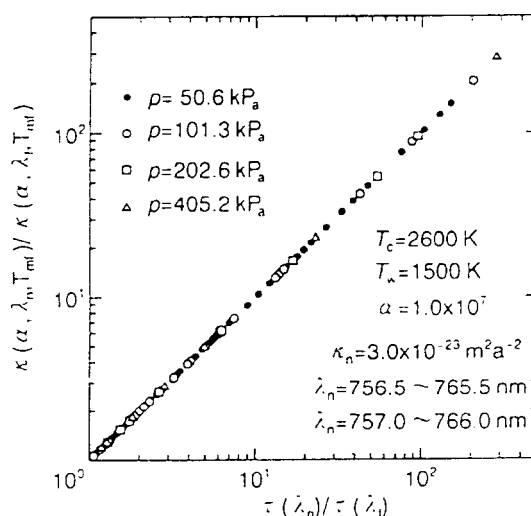


Fig. 3. Relationship between the ratio of optical depths  $T(\lambda_n)/T(\lambda_f)$  and the ratio of atomic absorption coefficients  $\kappa(\lambda_n, \alpha, T_m)/\kappa(\lambda_f, \alpha, T_m)$  for various wavelength separations  $\lambda_n - \lambda_f$  and pressures.

$$\frac{\tau(\lambda_n)}{\tau(\lambda_f)} \equiv \frac{\kappa(\lambda_n, \alpha, T_m(\lambda_f))}{\kappa(\lambda_f, \alpha, T_m(\lambda_f))} \quad (13)$$

where  $\lambda_n$  and  $\lambda_f$  are the near and far wing wavelengths, respectively. It is to be noted that the temperature dependence of the AAC at  $\lambda_n$  is described by  $T_m(\lambda_f)$ . Together with an appropriate modelling of the temperature dependence of the Lorentz breadth as in Eq. (6), the accuracy of Eq. (13) is assured by the use of  $T_m(\lambda_f)$  in  $\kappa(\lambda, \alpha, T)$  at  $\lambda_n$ . Assuming the non-uniform temperatures in boundary layers as  $T_g(x) = T_w + (T_c - T_w)(x/\delta)^{1/2}$ , we can calculate emission absorption spectra from Eqs. (8) and (9), the optical depth from Eq. (11) and the AAC from Eq. (2). The coefficient  $\alpha$ , the bias  $\kappa_n$ , the pressure  $p$ , the boundary and core temperatures  $T_w$  and  $T_c$  are considered as given parameters with fixed  $\delta$  and  $H$  in the following calculation. The ratios  $\tau(\lambda_n)/T(\lambda_f)$  and  $\kappa(\lambda_n, \alpha, T_m(\lambda_f))/\kappa(\lambda_f, \alpha, T_m(\lambda_f))$  thus calculated for  $\delta = 0.02$  m and  $H = 0.1$  m are plotted in Fig. 3 under various wavelength separation  $\Delta\lambda = \lambda_n - \lambda_f$  and pressures. This result clearly demonstrates the equality (13). The equality has been confirmed also for a wide range of temperatures  $T_w = 900$ – $2000$  K,  $T_c = 2000$ – $3000$  K and biases  $\kappa_n = 1.0 \times 10^{-25}$ – $1.56 \times 10^{-21} \text{ m}^2 \text{ atom}^{-1}$ .

### 3. Sensitivity of the depth–AAC relationship

The depth–AAC relationship (Eq. 13) can be regarded as an algebraic equation with respect to the coefficient  $\alpha$ . However, experimental determination of  $\alpha$  with measured optical depths and temperatures requires a high sensitivity of the relationship to the variation of  $\alpha$ . We define the sensitivity  $S$  as

$$S(\alpha) \equiv \frac{\tau(\lambda_n)}{\tau(\lambda_f)} - \frac{\kappa(\lambda_n, \alpha, T_m(\lambda_f))}{\kappa(\lambda_f, \alpha, T_m(\lambda_f))} \quad (14)$$

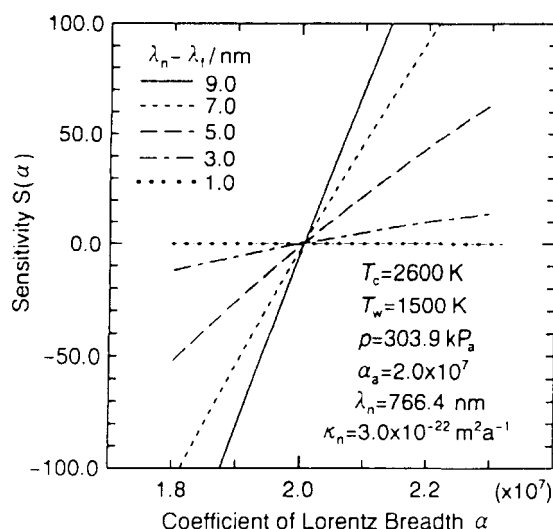


Fig. 4. Sensitivity of the depth–AAC relationship to  $\alpha$  at different separations of far and near wavelengths.

Fig. 4 shows the sensitivity to the coefficient  $\alpha$  under various wavelength separations. Here,  $\alpha_a$  is the prescribed “true” coefficient and the horizontal axis are arbitrarily assumed values. The ratio  $\tau(\lambda_n)/\tau(\lambda_f)$  and  $T_m(\lambda_f)$  are calculated with  $\alpha_a$ . The point where the curve intersects the line  $S(\alpha) = 0$  gives experimental values of  $\alpha$ . We see that the sensitivity decreases when  $\lambda_n$  and  $\lambda_f$  are close to each other. However, it is sufficiently high when  $\lambda_n - \lambda_f \geq 5.0$  nm with  $\lambda_n$  fixed at 766.4 nm in the present case. That the  $\alpha$  value of the intersection is close to the prescribed value irrespective of  $\Delta\lambda$  may indicate that quite accurate measurements of the Lorentz breadth can be expected by this formalism.

In Figs. 5–7 the sensitivity is calculated with varying the pressure, the boundary temperature and the bias level, respectively, under fixed  $\lambda_n$  and  $\lambda_f$ . Figs. 5 and 6 indicate that the sensitivity is high enough, and it is insensitive to the gas pressure and especially to

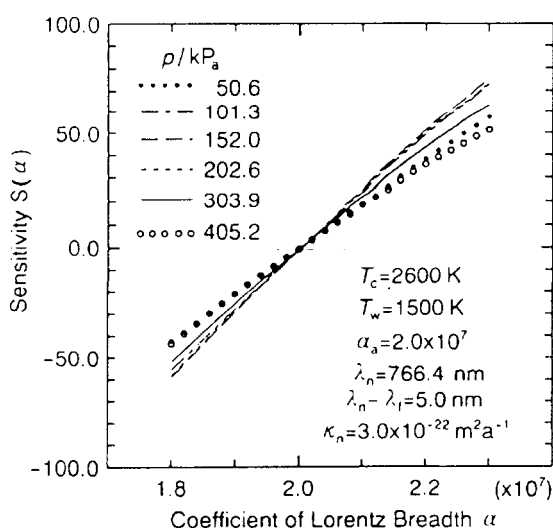


Fig. 5. Sensitivity of the depth–AAC relationship to  $\alpha$  at different gas pressures.

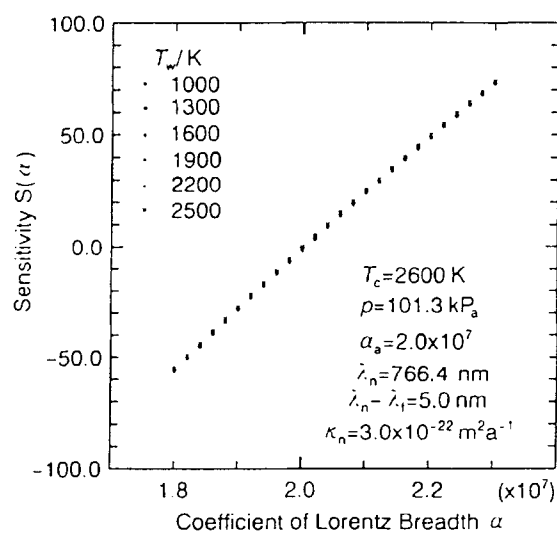


Fig. 6. Sensitivity of the depth–AAC relationship to  $\alpha$  at different boundary edge temperatures.

the temperature non-uniformity. However, it is sensitive to the bias. Fig. 7 shows that in cases of extremely low or extremely high bias levels the applicability of the depths–AAC relationship becomes doubtful. The highest sensitivity can be expected for the bias of order  $10^{-23}$ – $10^{-22}$   $\text{m}^2 \text{atom}^{-1}$ . Referring to Ref. [4], this order of  $\kappa_n$  well describes the wing intensity of the potassium seeded coal combustion plasmas.

The sensitivity has a common tendency to increase with the increase in the wave length difference. However, it is also affected by  $\lambda_n$  as well as  $\lambda_f$  itself. If  $\lambda_n$  is set extremely close to the center, the separation of the flame emission from the flame plus lamp emission becomes difficult due to self-absorption effects [2]. Also, when  $\lambda_f$  is extremely far away from the center a large error may be introduced due to low signal to noise ratio

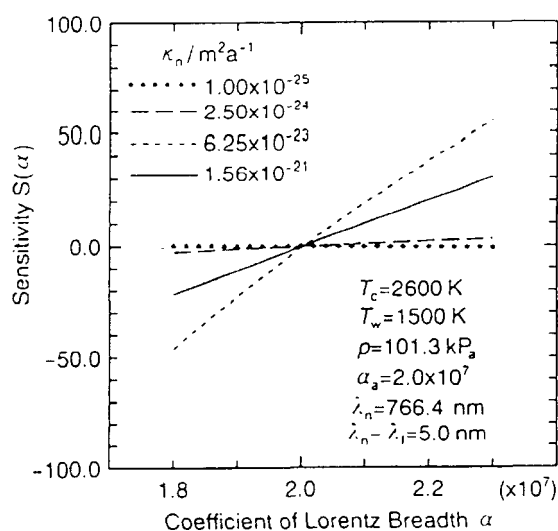


Fig. 7. Sensitivity of the depth–AAC relationship to  $\alpha$  at different wing bias levels.

in the flame emission. The determination of optimum sets of  $\lambda_n$  and  $\lambda_f$  is an important subject of further experimental work.

#### 4. Concluding remarks

The depth–atomic absorption relationship, the equality of the ratio of the near wing to the far wing optical depths to the ratio of the respective atomic absorption coefficients, has been outlined. It is emphasized that the formalism is based on the appropriate modeling of both the Lorentz breadth and the optical cross section.

The evaluation both of the atomic absorption coefficient with the far wing temperature and the wing spectra with the bias are essential in the proposed measurement scheme. The appropriate bias can be calculated by comparing the measured spectra with the theoretical values.

Numerical studies on the applicability of the new formula to the measurement of the Lorentz breadth and the optical cross section of alkali atoms in a non-uniform combustion flame have shown that, when the separation of two wing wavelengths is adequate, the relationship has sufficient sensitivity against the coefficient of the Lorentz breadth which is to be determined experimentally under realistic pressures, the temperature non-uniformities and the level of wing spectral intensities.

#### Acknowledgements

The author thanks his colleagues in The Center for Advanced Research of Energy Technology, Hokkaido University, for their useful comments. A part of this work was supported by The Matsuda Foundation's Research Grant.

#### References

- [1] H.M. Strong and F.P. Bundy, *J. Appl. Phys.*, 25 (1954) 1521.
- [2] J.W. Daily and C.H. Kruger, *J. Quant. Spectrosc. Radiat. Transfer*, 17 (1977) 327.
- [3] K. Onda, Y. Kaga and K. Kato, *J. Quant. Spectrosc. Radiat. Transfer*, 26 (1981) 147.
- [4] L.E. Bauman, *J. Thermophys. Heat Transfer*, 6 (1992) 746.
- [5] F.W. Hofmann and H. Kohn, *J. Opt. Soc. Am.*, 51 (1961) 512.
- [6] E. Hinnov and H. Kohn, *J. Opt. Soc. Am.*, 47 (1957) 156.
- [7] E. Hinnov, *J. Opt. Soc. Am.*, 47 (1957) 151.
- [8] N. Kayukawa and Y. Yamazaki, *Trans. Jpn. Soc. Mech. Eng.*, 61 (1995) 333.
- [9] L.E. Bauman, *J. Thermophys. Heat Transfer*, 7 (1993) 25.
- [10] A.A. Radzig and B.M. Smirnov, *Reference Data on Atoms, Molecules, and Ions*, Springer-Verlag, Berlin, 1985, p. 226.
- [11] A.C.G. Mitchell and M.W. Zemansky, *Resonance Radiation and Excited Atoms*, 3rd edn., Cambridge University Press, New York, 1971, p. 101.
- [12] H. Margenau and W.W. Watson, *Rev. Modern Phys.*, 8 (1936) 22.
- [13] J.W. Daily and C.H. Kruger, *AIAA 14th Aerospace Sciences Meeting*, (1976) AIAA Paper No. 76–134.

# Plasma diagnostics of magnetohydrodynamic generators

N. Okinaka, S. Oikawa\*, S. Yatsu, Y. Aoki and N. Kayukawa

*Center for Advanced Research of Energy Technology, Hokkaido University, N-13 W-8, Sapporo 060, Japan*

*\*Department of Nuclear Engineering, Hokkaido University, N-13 W-8, Sapporo 060, Japan*

Received 20 April 1992

---

## Abstract

Average measurements of conductivities and Hall parameters in a Faraday-type Magnetohydrodynamic (MHD) generator are presented. The measurement scheme is simple and requires no optical observations other than probes that provide two-dimensional voltage field measurements in the generator. No corrections are made for the conductivity profiles at the generator walls. The use of this scheme for the estimation of average flow velocities is described, and may provide a valuable tool to diagnose the generator performance in real time.

---

## 1. Introduction

To date, efforts to measure electrical conductivities of Magnetohydrodynamic (MHD) plasma have mainly been directed toward spectroscopic, microwave, or induction coil measurements, as reported in the literature [1–4]. Although such methods attempt to provide local measurements and conductivity profiles, they require special access ports, such as mirrors, moving mechanisms, etc., which are difficult to provide inside the warm bore of an MHD magnet.

Bulk conductivity measurements, however crude, provide useful information that can be utilized for the analysis or performance diagnosis of MHD generators. To the knowledge of the author few measurements of electrical conductivity distributions in an operating generator with MHD interaction have been reported [5].

In contrast, the technique presented here can provide simultaneous measurements of the bulk electrical conductivity and Hall parameter distributions in a Faraday-type MHD generator. It needs no special access ports, is rugged, and relies totally on electrical signal processing that can be obtained by simple electrical conductors out of the magnet bore.

The experimental observation of channel conductivities can be important in evaluating the performance of interaction-dominated generators. Measurable changes in the electrical conductivity can occur owing to the transition to subsonic conditions in such generators.

## 2. Theoretical background

The two-dimensional Ohm laws relate the interaction of the hydroelectromagnetic force fields in an MHD generator as follows:

$$J_x = \sigma E_x - \beta J_y, \quad (1)$$

$$J_y = \sigma(UB - E_y) + \beta J_x, \quad (2)$$

where the positive directions of the quantities  $J_x, J_y, E_x$  and  $E_y$  are shown in Fig. 1, and the symbols refer to physical parameters as described in Nomenclature<sup>1</sup>. The perturbed form of these equations reads

$$J'_x = \sigma E'_x - \beta J'_y, \quad (3)$$

$$J'_y = -\sigma E'_y + \beta J'_x, \quad (4)$$

subject to the assumption that all hydrodynamic parameters have zero perturbation, hence  $\sigma' = \beta' = U' = 0$ . Electrical perturbations of the quantities  $J'_x, J'_y, E'_x$  and  $E'_y$  can be easily induced in the generator by providing an excitational axial current  $I'_x$  from one end of the generator to the other. Presuming that there are no wall defects, one can assume that  $I_x$  flows in the core of the generator causing a  $J'_x = I'_x/A$  distribution which, via the interaction with the  $B$  field, gives rise to  $E'_x, J'_y$  and  $E'_y$  fields. Should the excitational frequencies be on the order of the resonant duct frequencies of the generator  $f \sim U/L$ , one may expect that the assumption of  $U' = 0$  is not justified. The inertia of fluid particles, however, does not allow them to respond to higher frequencies where electrical perturbation quantities may be described by Eqs (3) and (4), from which one concludes

$$\sigma = \frac{(J'_y)^2 + (J'_x)^2}{E'_x J'_x + E'_y J'_y}, \quad (5)$$

$$\beta = \frac{E'_x J'_y + E'_y J'_x}{E'_x J'_x + E'_y J'_y}, \quad (6)$$

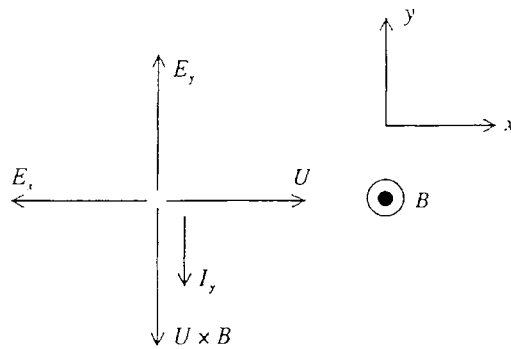


Fig. 1. Channel flow and directions.

<sup>1</sup> See nomenclature on page 219.



indicating that the measurements of  $E'_x$ ,  $E'_y$  and  $J'_y$  allow the quantitative evaluation of the electrical conductivity  $\sigma$  and the Hall parameter  $\beta$  simultaneously. Oikawa et al. showed [6] that with increasing temperature fluctuations, the effective conductivity decreases in the model of the Generalized Ohm's law in partially ionized plasmas with the spatial gradient of electrical conductivity, although the time-averaged conductivity increases because of the nonlinear dependence of the conductivity on temperature. It has also been shown that effects of plasma non-uniformity on evaluation of  $\sigma$  and  $\beta$  can be ignored when one can set the excitational frequencies be on the order of the resonant duct frequencies of the generator.

Having acquired  $\sigma$  and  $\beta$ , one can evaluate from Eq. (2) that the plasma velocity in the core of the generator is

$$U = \frac{\frac{J_y - \beta J_x}{\sigma} - E_y}{B}, \quad (7)$$

where the nonperturbed quantities  $J_x$ ,  $J_y$  and  $E_y$  can be measured simultaneously with the perturbation quantities. For a Faraday-type generator with fine segmentation,  $J_x = 0$ ; hence, from Eq. (7)

$$U = \frac{\frac{J_y}{\sigma} - E_y}{B}. \quad (8)$$

### 3. MEM spectral analysis

The mathematical properties of the maximum entropy method (MEM) proposed by Burg [7] have been discussed in detail by Lacoss [8], Burg [9], Ulrych [10], and others, and the algorithm and program for computing the MEM power spectral densities and autocorrelational functions have been reported in detail by Andersen [11], and Hino [12]. A brief summary of the MEM spectral estimation of time-series data with equal sampling period  $\Delta t$  is given in the Appendix. The MEM power spectrum  $P(f)$  can be calculated from Eq. (A.1) using the values of  $P_m$  (Eqs (A.3) and (A.8)),  $\gamma_{mk}$  (Eqs (A.4) and (A.5)), and the autocorrelation function  $R(m)$  (Eqs (A.6) and (A.7)).

In order to precisely determine the frequency spectrum by MEM, suitable criteria are required for determining the optimum value of the prediction-error filter order  $M$ : the MEM spectrum is considered to be established as long as this criterion is satisfactory (see Sections 4 and 6). The choice of  $M$  is a critical problem. Many workers have discussed this and have proposed several kinds of criteria for choosing  $M$ . Taking into account the statistical properties of the time-series data under analysis. Haykin and Kesler reported that  $M$  lies in the range from  $0.05N$  to  $0.2N$  [13], where  $N$  is the data length. From a similar point of view, Akaike and Nakagawa also reported that  $2\sqrt{N} < M < 3\sqrt{N}$  [14]. As  $N = 1024$ , the values of  $M$  range from 51 to 205 for the former and from 64 to 96 for the latter. These are too rough to determine the value of  $M$ . Here, it should be recalled that the spectral density estimate by autoregression (AR) takes on a form equivalent to the MEM estimate [15]. Thus, in the present study, we can adopt the following three criteria: the Final Prediction-Error (FPE) [16], Akaike's Information Criterion (AIC) [17], and the Autoregressive Transfer Function Criterion (CAT) [18]. The optimum value of  $M$  is determined by the minimization of FPE, AIC, and CAT. The expressions for the criteria are given in the Appendix and some discussions of them are given in Section 6.

#### 4. Experimental verification of measurements

##### 4.1. MHD channel and electrical excitation system

The experimental demonstration of this measurement technique was performed in the shock-tube MHD generator at Hokkaido University. The operating parameters of the generator are shown in Table 1. The channel was of the segmented Faraday type with 25 electrode pairs. The cross section of the MHD channel is shown schematically in Fig. 2. The channel was finely segmented by electrodes of 12 mm pitch, providing ideal Faraday load configuration, with no axial current flow in the core of the generator.

The signal from a laboratory sine wave generator, shown in Fig. 3, amplified by a 1.2 kW

Table 1  
Typical channel operating conditions

|                                               |                                     |
|-----------------------------------------------|-------------------------------------|
| Working gas                                   | argon                               |
| Seed                                          | 1% potassium<br>(powder $K_2CO_3$ ) |
| Inlet Mach number                             | 0.8                                 |
| Peak current density $J_y$ , A/m <sup>2</sup> | 8000                                |
| Peak Hall field $E_x$ , V/m                   | ~ 1200                              |

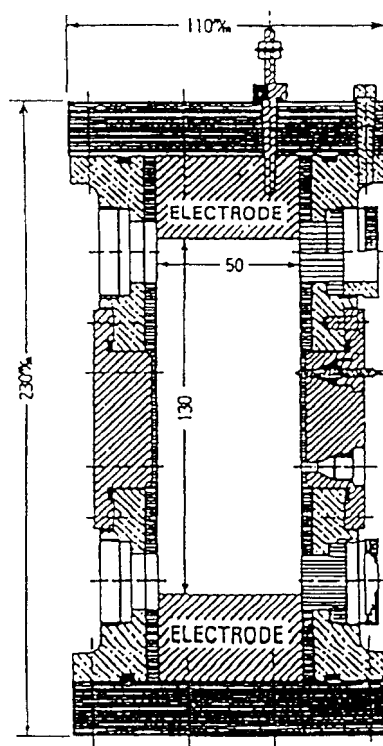


Fig. 2. Cross sectional view of experimental generator.

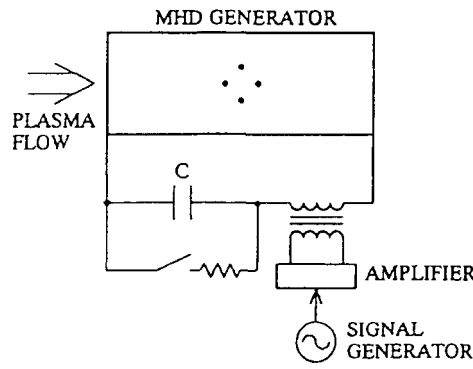


Fig. 3. Channel excitation system.

audio amplifier was connected in series with capacitor C which sustained the channel Hall voltage. The amplifier output provided a sinusoidal axial current excitation  $I_x$  from the inlet to the outlet of the channel, resulting in  $J'_x = I'_x/A$  distribution.  $E'_y$  and  $E'_x$  responses were detected by the sidewall probes with the use of high frequency voltage transducers and  $J'_y$  was acquired from the load current measurement with high-frequency current transducers. NF Design Block wave memories were used for the voltage and current data acquisition and, in addition to the perturbation measurements, provided average (dc) measurements of the above electrical quantities.

#### 4.2. Data analysis

The perturbation quantities were analyzed by a maximum entropy spectral analysis after subtracting their dc bias by recording the signals in the ac mode of wave memories. Prior to data acquisition, the channel responses to various excitational frequencies were observed. As shown in Fig. 4, appreciable noise was generated in the channel with its excitation. The signal was totally immersed in the noise when the excitational frequency was 40 kHz, which coincided with the characteristic flow time in the channel at its operating conditions. At 10 kHz, however, an appreciable signal-to-noise ratio was obtained which enabled the evaluation of the desired perturbation quantities and the calculation of the electrical conductivity  $\sigma$  and the Hall parameter  $\beta$  at the measurement stations. The results of the calculations are presented in Table 2, which shows simultaneously measured static pressures, current densities, and electrical fields.

Table 2  
Results of measurements

|                                          |      |      |      |
|------------------------------------------|------|------|------|
| Magnetic field density $B$ , T           | 1.0  | 1.5  | 2.0  |
| Electrical conductivity $\sigma$ , S/m   | 9.0  | 9.1  | 8.8  |
| Hall parameter $\beta$                   | 0.90 | 1.14 | 1.35 |
| Statistic pressure, kPa                  | 120  | 118  | 121  |
| Cross flow electric field $E_y$ , V/m    | 466  | 688  | 925  |
| Current density $J_y$ , A/m <sup>2</sup> | 3040 | 4660 | 5950 |
| Axial field $E_x$ , V/m                  | 305  | 584  | 912  |
| Velocity $U$ , m/s                       | 804  | 800  | 801  |

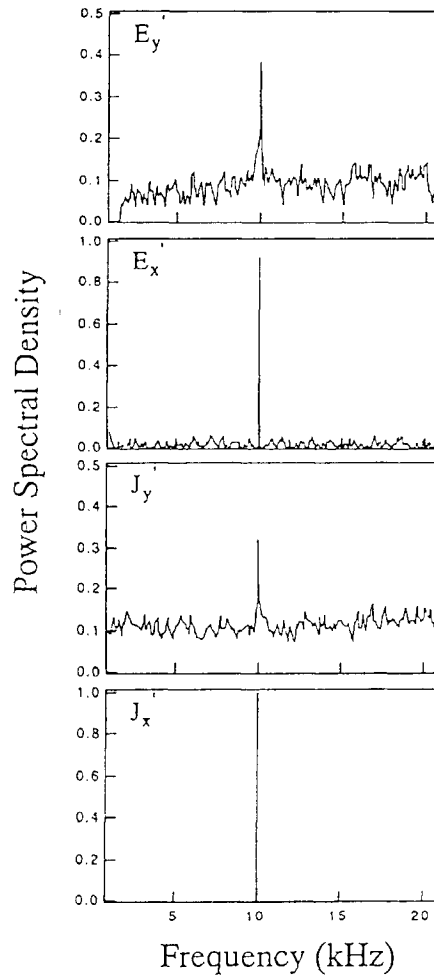


Fig. 4. MEM spectra of data ( $E_y'$ ,  $E_x'$ ,  $J_y'$  and  $J_x'$  from upper to lower figure).

It is important to mention here that the analysis was performed without the consideration of the influence of electrical conductivity profiles at the channel walls on the measurements. The current densities estimated from the electrode or axial current measurements are usually lower than the actual values in the generator owing to the blockage of current flow by the cold boundary layers. Hence, the above estimates of  $\sigma$  and  $\beta$  are average ones between two measuring points and reflect the core values less reliably as boundary layers develop and fill the entire generator.

##### 5. Measurement of fluid dynamic quantities

As mentioned earlier, measurement of the plasma velocity can be performed by the measurement of  $J_y$  and  $E_y$ . These may be substituted together with the already found  $\sigma$  and  $\beta$  values in Eq. (8).  $E_y$ , estimated from the cross-flow plasma voltage, traverses by the sidewall probes as depicted

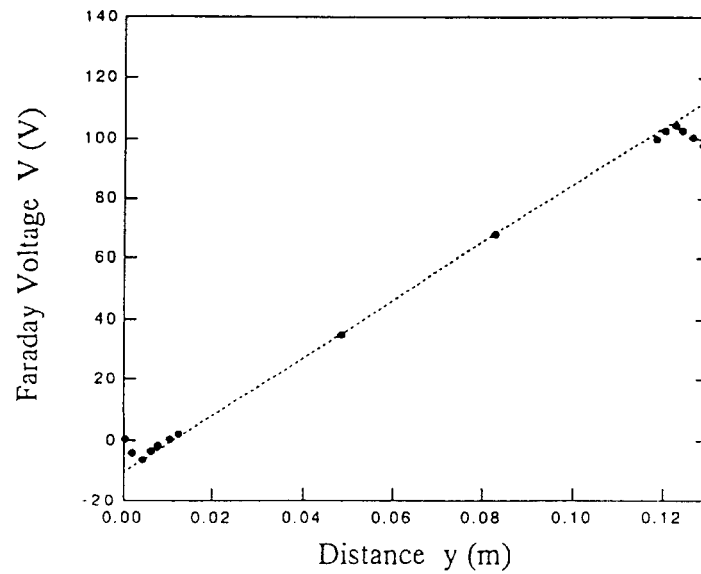


Fig. 5. Faraday voltage distribution.

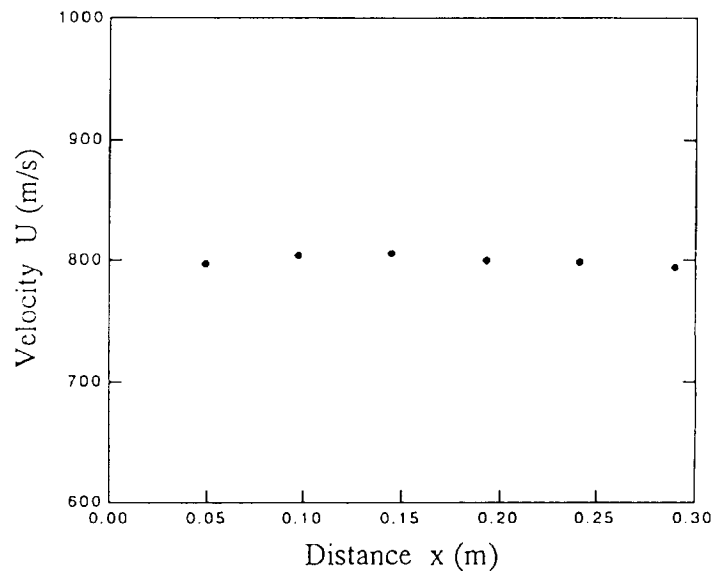


Fig. 6. Velocity distribution.

in Fig. 5,  $J_y$  and  $E_x$  deduced from the electrode currents and the interelectrode voltages at the measurement station, respectively, are shown in Table 2. The plasma velocities calculated from Eq. (8) above are also presented in the same table. The measured velocities are average quantities and no corrections for boundary layers were attempted. Small variations in  $B$  were not effective to change the velocity measurements appreciably, as shown in Fig. 6.

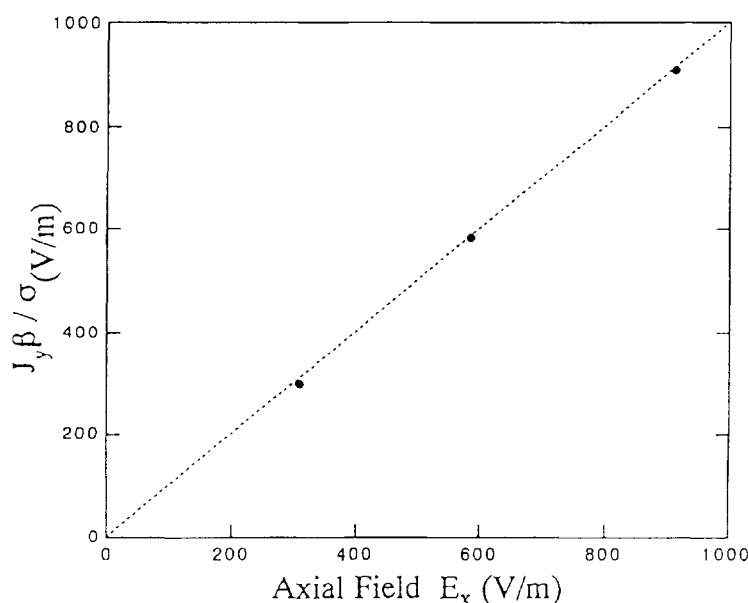


Fig. 7. Comparison of  $E_x$  measurement with  $J_y \beta / \sigma$ .

A comparison between the measured axial field  $E_x$  with that calculated from  $E_x = J_y \beta / \sigma$  for  $J_x = 0$  is shown in Fig. 7, providing verification of the validity of the measurements and the theory behind them. It is also shown that MHD interaction in the channel is weak.

The experimental measurements can easily be performed automatically by the use of proper filters that can detect the amplitudes and phases of the electrical perturbation quantities in response to the  $I_x$  excitation. The algebraic calculations for the evaluations of the quantities  $\sigma$ ,  $\beta$  and  $U$  in real time can be done by a microcomputer and the results may be displayed on an  $x - y$  plotter. The development of the necessary electronic circuitry is presently in progress and results will be reported in due time.

## 6. Determination of optimum filter order $M$

Although the superiority of MEM over other conventional spectral estimation methods, particularly for short data length, is recognized, the usefulness of this approach is limited by the lack of a criterion for choosing the optimum prediction error filter order  $M$ . In Figs 8 and 9, MEM autocorrelation functions and power spectral densities for  $E_y$  are shown with the variations of the prediction error filter order  $m$ . As seen in the figures, for too small an  $m$ , a highly smoothed spectrum is obtained, and, for an excessively large an  $m$ , spurious detail is introduced into the spectrum. Accordingly, the correct choice of  $M$  is required for obtaining a meaningful estimate of the power spectrum as well as of the autocorrelation function.

The estimation procedure proposed by Akaike [16], called the final prediction error (FPE, Eq. (A.9)), was the first successful method, and its application to MEM spectral analysis can remove

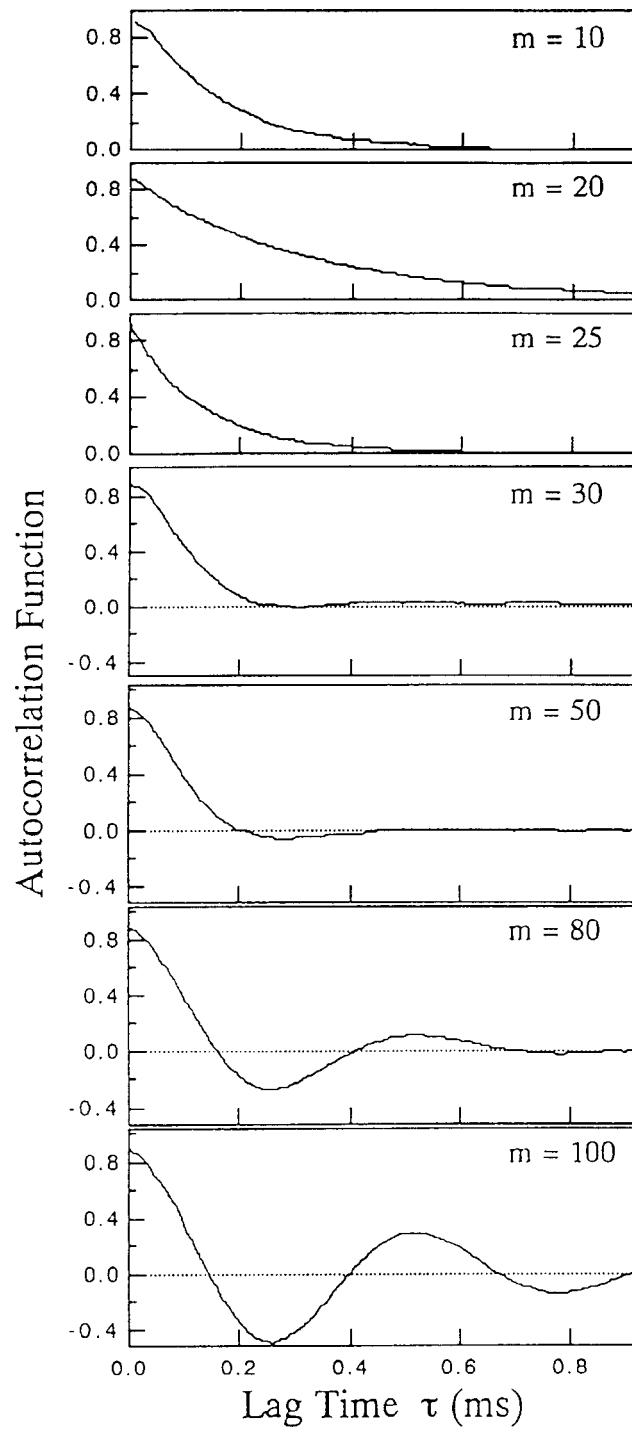


Fig. 8. MEM autocorrelation function for  $E_y$  with variation of  $m$  (10, 20, 25, 30, 50, 80 and 100 from upper to lower figure).

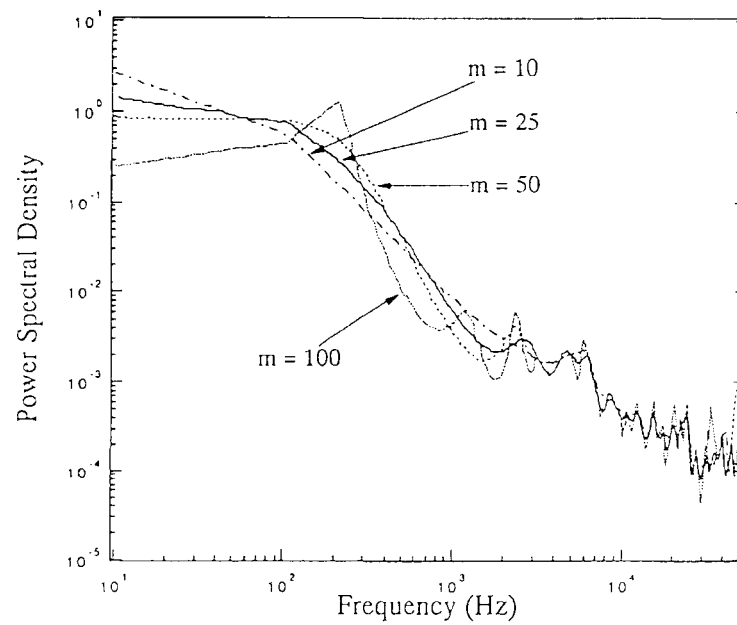


Fig. 9. MEM power spectral densities for  $E_y$  with variation of  $m$ . - - - :  $m = 10$ , — :  $m = 25$ , - · - :  $m = 50$ , · · · :  $m = 100$ .

the main shortcoming of this technique in some cases. However, the minimum often disappears in the calculated FPE curve. In the present study, a rather small minimum was observed, though it clearly appeared (Fig. 10(a)). The second criterion, also proposed by Akaike [17], called the information theoretical criterion (AIC, Eq. (A.10)), is an important technique known as a versatile statistical identification criterion. AIC and FPE are expected to give identical results for  $M$ . Unfortunately, the application of AIC to the present data was unsatisfactory (Fig. 10(b)). Thus, a third criterion is required for more distinct determination of  $M$ . The third criterion, proposed by Parzen [18], is known as the autoregressive transfer function criterion (CAT, Eq. (A.11)). This scheme is considered to behave in a way similar to AIC. The results of the CAT indicated an extremely sharp minimum at the same position of  $m$  as that of FPE (Fig. 10(c)). Thus, the optimum value of  $M$  is 25, and it can be safely said that with  $M = 25$  the true spectral density as well as the corresponding autocorrelation function was obtained by a combination of FPE, AIC and CAT, though the comparative properties of these three criteria require much further study.

## 7. Conclusions

A measurement technique for monitoring the average plasma electrical conductivity and Hall parameter distributions in MHD generators is described. As the measurements involved are only electrical in nature, they are characterized as rugged and well suited for MHD channels, where no special access ports inside the warm bore of the magnet are needed. With suitable data acquisition and the processing equipment that is being developed, core velocity distributions measurements in the channel may be possible in real time, without any optical observation.



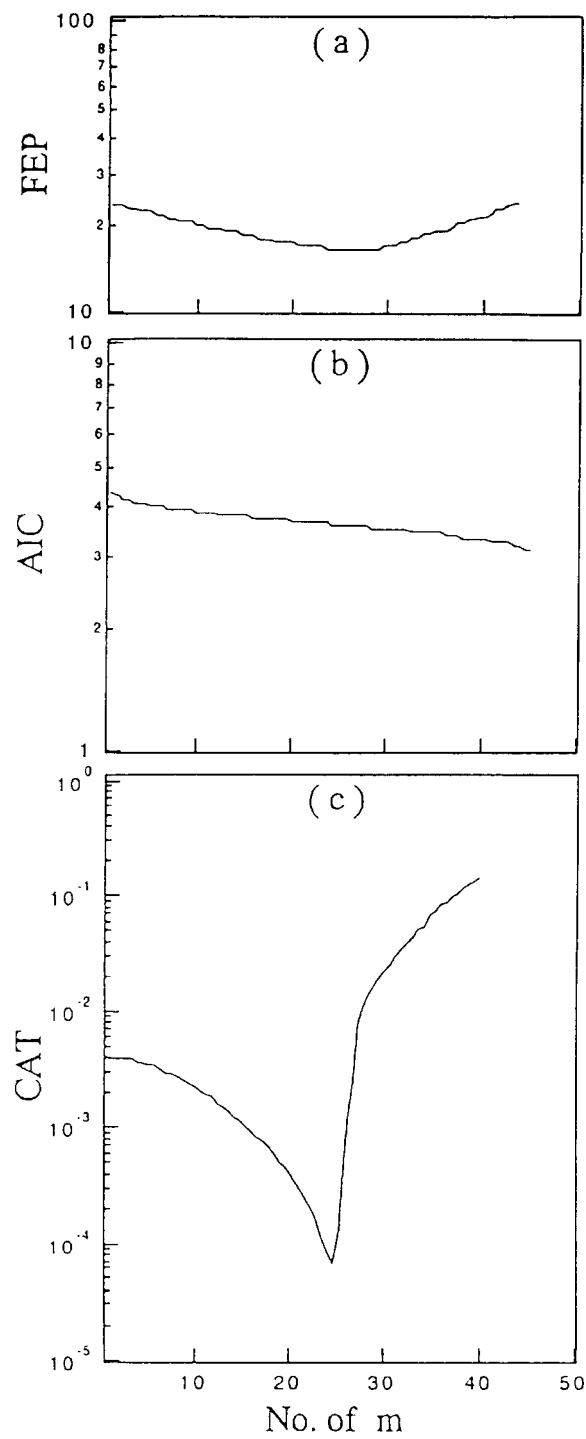


Fig. 10. Three kinds of MEM criteria calculated for time-series data of  $E_y$  with variation of  $m$  (a) FEP, (b) AIC, (c) CAT.

### Appendix. Maximum Entropy Method (MEM)

The MEM power spectrum  $P(f)$  is estimated from the relationship [11, 12]

$$P(f) = \frac{P_m \Delta t}{\left| 1 + \sum_{k=1}^m \gamma_{mk} \exp(-i2\pi f k \Delta t) \right|^2}, \quad (\text{A1})$$

where  $P_m$  is the output power of a prediction-error filter of order  $m$  and  $\gamma_{mk}$  ( $m = 0, 1, 2, \dots, M$ ;  $k = 0, 1, 2, \dots, m$ ;  $M$  is the optimum filter order) is the corresponding filter coefficient.  $P_m$  and  $\gamma_{mk}$  are determined by the equation

$$\begin{bmatrix} R(0) & R(-1) & \cdots & R(-m) \\ R(1) & R(0) & \cdots & R(1-m) \\ \vdots & \vdots & \ddots & \vdots \\ R(m-1) & R(m-2) & \cdots & R(-1) \\ R(m) & R(m-1) & \cdots & R(0) \end{bmatrix} \begin{bmatrix} 1 \\ \gamma_{m1} \\ \vdots \\ \gamma_{mm} \end{bmatrix} = \begin{bmatrix} P_m \\ 0 \\ \vdots \\ 0 \\ 0 \end{bmatrix}. \quad (\text{A2})$$

This matrix equation is the set of  $m+1$  equations pertaining to a prediction-error filter of order  $m$ .  $R(m)$  is the autocorrelation function with  $m$ ,  $\gamma_{mk}$  and  $P_m$ .

Equation (A2) can be solved using Burg's procedure [9-12], giving

$$P_m = \frac{1}{2(N-m)} \sum_{k=1}^{N-m} \left[ \left( X_i + \sum_{k=1}^m \gamma_{mk} X_{i+k} \right)^2 + \left( X_{i+m} + \sum_{k=1}^m \gamma_{mk} X_{i+m-k} \right)^2 \right] \quad (\text{A3})$$

and

$$\gamma_{mk} = \frac{-2 \sum_{i=1}^{N-m} b_{mi} b_{mi}^*}{\sum_{i=1}^{N-m} (b_{mi}^2 b_{mi}^{*2})}, \quad (\text{A4})$$

where

$$\begin{aligned} b_{mi} &= b_{m-1\ i} + \gamma_{m-1\ m-1} b_{m-1\ i}^*, \\ b_{mi}^* &= b_{m-1\ i}^* + \gamma_{m-1\ m-1} b_{m-1\ i+1}, \\ b_{0i} &= b_{0i}^* = X_i, \\ b_{1i} &= X_i \text{ and } b_{1i}^* = X_{i+1}. \end{aligned}$$

The coefficients  $\gamma_{mk}$  for  $k < m$  are determined by the recursion formula derived from the  $m$  in the lower matrix of Eq. (A2) as follows:

$$\gamma_{mk} = \gamma_{m-1\ k} \gamma_{mm} \cdots \gamma_{m-1\ m-k} \quad (k = 1, 2, \dots, m-1). \quad (\text{A5})$$

In the  $m$ th line of Eq. (A2),  $R(m)$  is obtained by

$$R(m) = - \sum_{k=1}^m \gamma_{mk} R(m-k) \quad (\text{A6})$$

and by using an extended form of  $R(m)$ :

$$R(m + \ell) = - \sum_{k=1}^m \gamma_{mk} R(m - k + \ell) \quad (\ell \geq 1). \quad (\text{A7})$$

The recursion formula for  $P_m$  is derived by inserting Eq. (A7) into Eq. (A2), that is,

$$P_m = P_{m-1}(1 - \gamma_{mm}^2). \quad (\text{A8})$$

The expressions for the three criteria required for the MEM estimate are as follows [16–18]:

$$\text{FPE}(m) = \frac{N + m + 1}{N - m - 1} P_m, \quad (\text{A9})$$

$$\text{AIC}(m) = \ell n P_m + \frac{2m}{N}, \quad (\text{A10})$$

and

$$\text{CAT}(m) = \frac{1}{N} \sum_{k=1}^m \frac{N - k}{N P_k} - \frac{N - m}{N P_m}, \quad (\text{A11})$$

where

$$\text{CAT}(0) = - \left( 1 + \frac{1}{N} \right).$$

#### Nomenclature

|          |                                                  |
|----------|--------------------------------------------------|
| $B$      | magnetic field density, T                        |
| $E_x$    | axial (Hall) field, V/m                          |
| $E_y$    | cross flow (Faraday) field, V/m                  |
| $f$      | frequency, Hz                                    |
| $J_x$    | axial (Hall) current density, A/m <sup>2</sup>   |
| $J_y$    | load (Faraday) current density, A/m <sup>2</sup> |
| $M$      | optimum filter order                             |
| $m$      | prediction error filter order                    |
| $P(f)$   | MEM power spectral density                       |
| $R(m)$   | Autocorrelation function with $m$                |
| $T$      | plasma static temperature, K                     |
| $U$      | flow velocity, m/s                               |
| $\beta$  | Hall parameter                                   |
| $\sigma$ | electrical conductivity, S/m                     |
| $(\ )'$  | perturbation quantities                          |

## References

- [1] J.W. Daily and C.H. Kruger, Effect of cold boundary layers on spectroscopic temperature measurements in combustion gas flows, in: 14th Aerospace Sciences Meeting (AIAA, New York, 1976) p. 76.
- [2] R.K. James and C.H. Kruger, Boundary layers on measurements in the electrode wall of a combustion driven MHD channel, in: Proc. 18th Symp. on Engineering Aspect of Magnetohydrodynamics (MHD Energy and MHD Research and Development Institute, inc., Montana, 1979) p. 1.
- [3] G.P. Gupta, V.K. Rohagi and M.I. James, Effect of interelectrode current leakage on the electrical characteristics of a Faraday MHD generator, in: Proc. 10th Int. Conf. on MHD Electrical Power Generation, Vol. 2(X) (Society for MHD Electrical Power Generation of India, India, 1989) p. 95.
- [4] L.C. Farrar, R.J. Pollina and R.J. Rosa, Effect of coal slag on MHD generator electrical behavior, in: Proc. 27th Symp. on Engineering Aspect of Magnetohydrodynamics Vol. 6(2) (TRW Inc., Nevada, 1989) p. 1.
- [5] W. Unkel, J. Schwoerer, J.D. Teare and J.F. Louis, Investigative data analysis technique for MHD generators, in: 19th Aerospace Sciences Meeting (AIAA, New York, 1981) p. 81.
- [6] S. Oikawa and N. Kayukawa, *Jpn. J. Appl. Phys.* 10 (1993) 4768.
- [7] J.P. Burg, Maximum entropy spectral analysis, in: 37th Ann. Int. Meeting Soc. of Explor. Geophys. (Oklahoma City, 1967); *Modern Spectrum Analysis* (IEEE Press, New York, 1978) p. 34.
- [8] R.T. Lacoss, *Geophysics* 36 (1971) 661.
- [9] J.P. Burg, A new analysis technique for time series data (Advanced Study Institute on Signal Processing, NATO, Enschede, The Netherlands, 1968); *Modern Spectrum Analysis* (IEEE Press, New York, 1978) p. 42.
- [10] T.J. Ulrych, *J. Geophys. Res.* 77 (1972) 1396.
- [11] M. Andersen, *Geophysics* 39 (1974) 69.
- [12] M. Hino, *Supekutoru Kaiseki (Spectrum Analysis)* (Asakura Shoten, Tokyo, 1974) (in Japanese).
- [13] S. Haykin and S. Kesler, in: *Nonlinear Method of Spectral Analysis*, ed. S. Haykin (Springer-Verlag, Berlin, 1979) p. 9.
- [14] H. Akaike and T. Nakagawa, *Dainamikku Sisutemu no Toukeiteki Kaiseki to Seigyo (Statistical Analysis and Control in Dynamic System)* (Saiensu-sha, Tokyo, 1972) (in Japanese).
- [15] E. Parzen, in: *Multivariate Analysis*, ed. P.R. Krishnaiah (Academic Press, New York, 1967).
- [16] H. Akaike, *Ann. Inst. Statist. Math.* 21 (1969) 243.
- [17] H. Akaike, *IEEE Trans. Autom. Contr. AC-19* (1974) 716; *Modern Spectrum Analysis* (IEEE Press, New York, 1978) p. 234.
- [18] E. Parzen, *IEEE Trans. Autom. Contr. AC-19* (1974) 723; *Modern Spectrum Analysis* (IEEE Press, New York, 1978) p. 226.

## Consideration of Optimal Magnet Coil Design Using Nb-Ti Superconductor for 200 MWe Magnetohydrodynamic Generator

Ryo NISHIMURA\*, Yoshiaki AOKI and Naoyuki KAYUKAWA

*Advanced MHD Research Institute, Faculty of Engineering, Hokkaido University, North 19 West 8, Sapporo 060, Japan*

(Received March 10, 1994; accepted for publication March 18, 1995)

We report on the effect of the cross-sectional shape of a magnet coil upon the reduction of the magnetohydrodynamic (MHD) channel length. We have optimized a cross-sectional shape of a magnet coil, including an MHD channel, for a 200 MWe coal-fired Faraday-type MHD generator. It is shown that the channel length can be shortened by more than 30% and the stored energy of the magnet coil can be reduced in comparison with the case of the crescent-shaped coil producing a uniform magnetic field without the decrease of enthalpy extraction. Also, for a stand-alone commercial MHD/steam combined plant, it is estimated by this coil shape optimization that the capital cost can be decreased by more than 8% and the cost of electricity can be reduced by about 3%.

**KEYWORDS:** MHD, MHD power generation, Faraday-type MHD generator, magnet coil, optimization

### 1. Introduction

A magnetohydrodynamic (MHD) generator is based on the same induction principle as a conventional electric generator except that the electric conductor is an ionized fluid instead of the solid windings of an armature. The essential elements of a simplified MHD generator are shown in Fig. 1. A magnetic flux density  $B$  is applied transversely to the motion of an electric conductive gas flow with a velocity  $u$  in a duct. Charged particles moving with the gas will experience an induced electric field  $u \times B$  which tends to drive an electric current in the direction perpendicular to both  $u$  and  $B$ . The current is collected by pairs of electrodes.<sup>1,2)</sup>

Performance of an MHD generator is crucially dependent upon the electromagnetic parameter distribution among the cross section of the channel. Particularly, an optimal design of the applied magnetic field distribution across the plasma flow is needed to achieve the improved generator characteristics. However, almost all analyses and experiments have so far been carried out with a uniform magnetic field.

For commercial applications, the reduction of both the plant cost and the cost of electricity is an important subject. For example, a superconducting magnet and an MHD channel are expensive subsystems. It is estimated that the magnet and the channel represent about 10% and 8% of the total plant cost, respectively. It is also estimated that a 20% increase in magnet cost results in a 1% increase in the cost of electricity. These estimations are based on a stand-alone 500 MWe commercial plant. For a retrofit configuration or a small-scale plant, the percentage of plant cost attributable to the magnet and the channel becomes larger.<sup>1)</sup>

In this paper, we propose a method to decrease both the capital cost and the cost of electricity of power generation for relatively large scale open-cycle MHD generators by increasing the enthalpy extraction per unit length and by reducing the stored energy of the magnet coil. We have examined the effects of the mag-

net coil shape as well as nonuniformity of the applied magnetic field along the length of the channel under specified gaseous conditions at the inlet and a given stagnation pressure at the outlet.

### 2. Basic Equations

For the calculation of the electrical power output, the enthalpy extraction and the channel length, the stationary turbulent one-dimensional equations have been solved. The coordinate system used in the calculation is shown in Fig. 2. The equations are solved under the following assumptions.

- The channel is a Faraday-type with infinitely segmented electrode walls and perfectly insulating sidewalls.
- The constant velocity condition is adopted.
- The gas velocity has only an  $x$ -component.
- The  $z$ -components of the electrical field and cur-

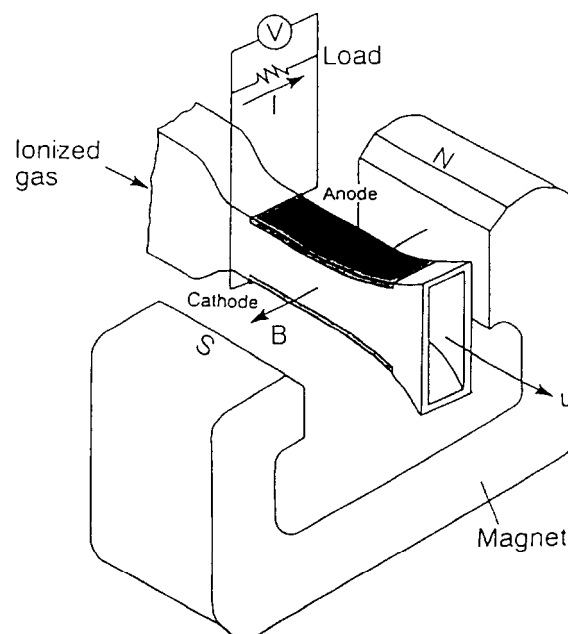


Fig. 1. Simplified MHD generator.

\*Present Address: Department of Electrical and Information Engineering, Yamagata University, 4-3-16 Jonan, Yonezawa 992, Japan.

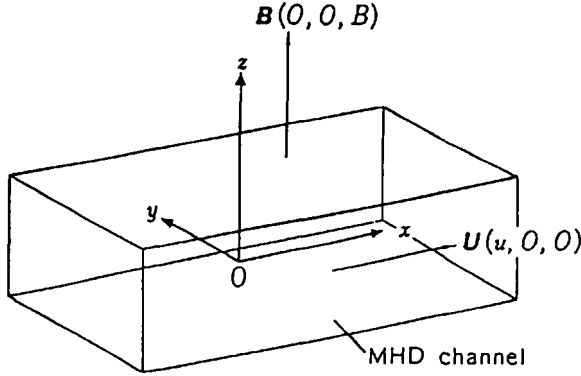


Fig. 2. Coordinate system used for analysis, and an MHD channel.

rent density and the effects of the  $x$ - and  $y$ -components of the magnetic field are neglected.

(e) The gas pressure is constant over the channel cross section.

The 1-D equations with the MHD source terms averaged over the cross section are written as follows for the constant velocity condition.<sup>3)</sup>

Continuity:

$$\frac{1}{A} \frac{dA}{dx} = -\frac{1}{\rho} \left[ \left( \frac{\partial \rho}{\partial T} \right)_P \frac{dT}{dx} + \left( \frac{\partial \rho}{\partial P} \right)_T \frac{dP}{dx} \right] \quad (1)$$

Momentum:

$$\frac{dP}{dx} = \langle J \times B \rangle_{av} - f \quad (2)$$

Energy:

$$\rho u \left[ \left( \frac{\partial h}{\partial T} \right)_P \frac{dT}{dx} + \left( \frac{\partial h}{\partial P} \right)_T \frac{dP}{dx} \right] = \langle J \cdot E \rangle_{av} - q \quad (3)$$

Here,  $A$  is the cross-sectional area,  $\rho$  the density,  $u$  the velocity,  $T$  the temperature,  $P$  the pressure,  $h$  the enthalpy,  $J = (j_x, j_y, 0)$  the electrical current density,  $B = (0, 0, B_z)$  the magnetic flux density, and  $E = (E_x, E_y, 0)$  the electrical field, respectively. The brackets  $\langle \rangle_{av}$  indicate the average over the channel cross section. Equations (1), (2) and (3) are solved by using the Runge-Kutta-Fehlberg method with the initial conditions specified at the inlet. The channel length is determined at the axial point where the stagnation pressure reaches a specified level.

The frictional force  $f$  and the heat-transfer loss  $q$  per unit volume are given by the following formulae:<sup>3)</sup>

$$f = 2C_f \rho u^2 / D_h \quad (4)$$

$$q = 4S_i \rho u C_p (T_{sl} - T_*) / D_h \quad (5)$$

where  $C_f$  is the frictional coefficient,  $S_i$  the Stanton number,  $D_h$  the mean hydraulic diameter,  $T_{sl}$  the slag surface temperature, and  $C_p$  the specific heat at constant pressure, respectively.

The electric field and the current density inside the MHD channel cross section are calculated by using Maxwell's equations and the generalized Ohm's law, neglecting the effect of the ion slip:<sup>3)</sup>

$$\nabla \times E = 0, \quad (6)$$

$$\nabla \cdot J = 0, \quad (7)$$

$$J = \sigma(E + u \times B) - \mu_e J \times B, \quad (8)$$

where  $\sigma$  is the electrical conductivity,  $u = (u, 0, 0)$  the velocity of the working fluid, and  $\mu_e$  the electron mobility, respectively. The magnetic field is calculated by the usual Biot-Savart's law.

Under the assumptions (a) and (d), eqs. (6) and (7) imply that

$$E_x = E_{x0} = \text{const in } y \text{ and } z, \quad (9)$$

$$E_y = E_y(y) \text{ (const in } z), \quad (10)$$

$$j_y = j_y(z) \text{ (const in } y). \quad (11)$$

In order to consider the effects of the plasma nonuniformity in both  $y$ - and  $z$ -directions, we define the parameters  $S_1$ – $S_5$  as follows:<sup>4)</sup>

$$S_1 = \left[ \left\langle \frac{1 + \beta_z^2}{\sigma} \right\rangle_y \langle u B_z \rangle_y \right]_z, \quad (12.a)$$

$$S_2 = \left[ \left\langle \frac{1 + \beta_z^2}{\sigma} \right\rangle_y \langle \beta_z \rangle_y \right]_z, \quad (12.b)$$

$$S_3 = \left[ \left\langle \frac{1 + \beta_z^2}{\sigma} \right\rangle_y \right]_z, \quad (12.c)$$

$$S_4 = \left[ \left\langle \frac{1 + \beta_z^2}{\sigma} \right\rangle_y \langle u B_z \rangle_y \langle \beta_z \rangle_y \right]_z, \quad (12.d)$$

$$S_5 = [\langle \sigma \rangle_y]_z - \left[ \left\langle \frac{1 + \beta_z^2}{\sigma} \right\rangle_y \langle \beta_z \rangle_y^2 \right]_z, \quad (12.e)$$

where  $\langle \rangle_y$  denotes the  $y$ -average,  $[\ ]_z$  denotes the  $z$ -average and  $\beta_z$  is the Hall parameter defined as  $\beta_z = \mu_e B_z$ . The  $y$ - and  $z$ -averages are calculated for the  $yz$ -cross section of the channel. The  $y$ -averages are calculated by integrating the quantities with respect to  $y$  between the electrodes facing each other for a fixed value for  $z$ . Then, the  $z$ -averages are calculated by integrating the  $y$ -averages with respect to  $z$  between the insulating walls facing each other.

By using these parameters, we can write the average values of the electrodynamic quantities inside the channel as follows:<sup>4)</sup>

$$\langle E_y \rangle_y = \frac{S_1 S_3 + S_2 S_4}{S_3 S_5 + S_2^2} K \quad (13)$$

$$E_{x0} = \frac{S_2 \langle E_y \rangle_y - S_4}{S_5} \quad (14)$$

$$[j_y]_z = \frac{S_1 S_3 + S_2 S_4}{S_5} (K - 1) \quad (15)$$

$$[\langle j_z \rangle_y]_z = 0 \quad (16)$$

where  $K$  is the load factor defined as the ratio of the load resistance to the sum of the load and internal resistance. And  $(S_1 S_3 + S_2 S_4) / (S_3 S_5 + S_2^2)$  in eq. (13) corresponds to emf.

We introduce the parameter  $G$  as follows to describe the plasma nonuniformity:<sup>4)</sup>

$$G = \frac{[\langle \sigma \rangle_y]_z S_3}{S_3 S_3 + S_3^2} \quad (17)$$

If plasma nonuniformity exists only in the  $y$ -direction, the above parameter  $G$  becomes Rosa's  $G$ -Factor.<sup>3)</sup> Using this parameter, we rewrite eq. (15) as

$$[j_y]_z = \frac{[\langle \sigma \rangle_y]_z S_1 S_3 + S_2 S_4}{G S_3 S_3 + S_3^2} (K-1). \quad (18)$$

Then the generator power output density is calculated as  $[j_y]_z \langle E_y \rangle_y$ .<sup>4)</sup>

### 3. Procedure of Analysis

In order to minimize the length of an MHD channel, the coil shape is optimized with the following procedures:

(i) A crescent coil was determined to produce the maximum uniform magnetic field under the given limitations (reference crescent coil).

(ii) For this crescent coil, a constant velocity channel is determined. This channel was used as the reference channel.

(iii) The crescent coil obtained in (i) is segmented by rectangular elements.

(iv) Again applying the constant velocity condition, the 1-D analysis is carried out in order to find the element which makes the least contribution to the power generation.

(v) This element is moved in order to minimize the channel length.

(vi) The above relocation procedure (iv)-(v) was repeated until all elements are placed at the appropriate positions where the shortest channel length is obtained without the decrease of the enthalpy extraction.

We define a channel aspect ratio  $D/W$  as the ratio of the channel width  $D$  to the height  $W$ . For each inlet channel aspect ratio, the coil shape is optimized in order to find the optimal inlet channel aspect ratio which gives the maximum power output and the shortest channel length.

The above procedure can be applied to any coupled system of an MHD channel and a magnet coil with arbitrary sizes because it is the steepest-gradient method.

### 4. Numerical Results

The adopted conditions for the working gas, the MHD channel and the magnet coil are as follows:

(a) The electrode distance  $D$  is varied, while the insulator distance  $W$  is fixed.

(b) The magnet coil is parallel to the channel axis.

(c) The effect of the end turn of the coil is neglected.

(d) The velocity and the temperature have the same boundary layer thickness with the 1/7th turbulent profile.

(e) The plasma is  $K_2CO_3$ -seeded coal-fired gas obeying the semiperfect gas law.

The thermodynamic and transport properties of the working gas are approximately given by the following formulae.<sup>5)</sup>

$$\sigma = 7.8272 \left( \frac{T}{2565} \right)^{13.367} \left( \frac{P}{1.1752} \right)^{-0.5930} \times \exp \left( 8.9547 \times 10^{-3} \times \frac{T}{2565} \right) \quad (19)$$

$$\mu_e = 0.48 \left( \frac{T}{2565} \right)^{0.9161} P^{-1.190} \quad (20)$$

$$h = 1.4145 \times 10^6 P^{-0.0045923} (T \times 10^{-3})^{1.3423} \quad (21)$$

$$\rho = 0.39501 P^{1.0016} (T \times 10^{-3})^{-1.1152} \quad (22)$$

The above formulae are the least square approximations of the thermodynamic properties of a coal (Illinois #6) combustion gas. The properties are the solutions of the NASA SP-273 chemical equilibrium computer code modified to include the electron collision frequency, mobility and electrical conductivity.<sup>6)</sup>

The other parameters for numerical evaluation are listed in Table I. The stagnation pressure, the stagnation temperature and the Mach number at the inlet are 5.4 atm, 3200 K, and 1.53, respectively, for these parameters.

Also, we assume that Nb-Ti superconducting wire stabilized in a copper matrix is used for the magnet coil material.

#### 4.1 Crescent coil case (Uniform magnetic field)

It is well known that a crescent coil with a cross section that consists of two ellipses, as shown in Fig. 3, can produce a uniform magnetic field in direction  $z$  within the intersection region. The field strength is given by the following equation:<sup>3)</sup>

$$B_z = \frac{\mu_0 J_c C}{1 + R_1/R_2} \quad (23)$$

where  $R_1$  and  $R_2$  are the radii of the ellipses,  $C$  is the distance between the centers of the two ellipses, and  $J_c$  is the overall coil current density.

Table II shows the design parameters  $R_1$ ,  $R_2$  and  $C$  and the magnetic flux density of the reference crescent coil for each inlet channel aspect ratio. Table III shows the channel sizes, electrical parameters and power output.

Table I. Basic parameters of MHD channel for numerical evaluation.

|                                              |                         |
|----------------------------------------------|-------------------------|
| Channel cross-sectional area                 | 4800 cm <sup>2</sup>    |
| Maximum coil cross-sectional area (Total)    | 4600 cm <sup>2</sup>    |
| Static pressure at the inlet                 | 2.3 atm                 |
| Stagnation pressure at the outlet            | 1 atm                   |
| Core flow velocity at the inlet              | 1500 m/s                |
| Core flow temperature at the inlet           | 2800 K                  |
| Boundary layer thickness at the inlet        | 5 cm                    |
| Minimum distance between the coil and plasma |                         |
| in direction $y$ ( $\Delta_y$ )              | 10 cm (see Fig. 3)      |
| in direction $z$ ( $\Delta_z$ )              | 10 cm (see Fig. 3)      |
| Maximum coil current density                 | $10^8$ A/m <sup>2</sup> |
| Slag layer thickness                         | 1.5 mm                  |
| Slag surface temperature                     | 1870 K                  |
| Wall temperature                             | 1000 K                  |
| Load factor                                  | 0.8                     |

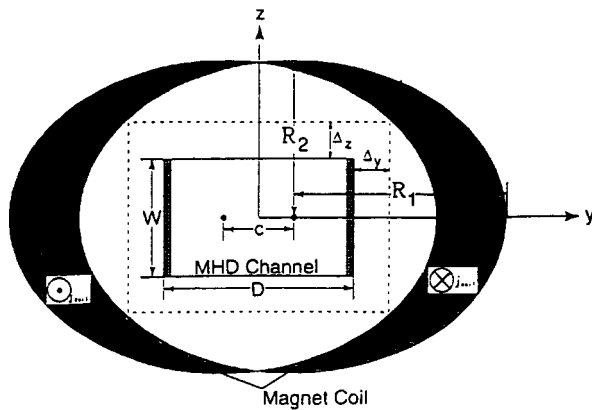


Fig. 3. Cross section of a crescent coil and an MHD channel and the coordinate system.

#### 4.2 Optimal coil case

In order to further improve the generator performance, we optimized the coil cross-sectional shape. Using the procedure described in §3, the coil shape was optimized to minimize the channel length without the decrease of the power output. The crescent coil was segmented by 92 rectangular elements with the size of

Table II. The design parameters and the magnetic flux density of the reference crescent coil.

| Inlet channel aspect ratio $D/W$ | $R_1$ (cm) | $R_2$ (cm) | $C$ (cm) | Magnetic flux density $B_{\max}$ (T) |
|----------------------------------|------------|------------|----------|--------------------------------------|
| 0.33                             | 137        | 120        | 10       | 5.6                                  |
| 0.5                              | 170        | 97         | 12       | 5.4                                  |
| 1                                | 214        | 90         | 13       | 4.7                                  |
| 2                                | 288        | 76         | 15       | 4.0                                  |

Table III. The sizes, the electrical parameters and the power output for the reference crescent coil (uniform magnetic field).

| Inlet channel aspect ratio | Channel length (m) | $D_{\text{inlet}}$ (cm) | $D_{\text{outlet}}$ (cm) | $W$ (cm) | Power output (MW) | Enthalpy extraction (%) | $J_{y,\max}$ (A/cm <sup>2</sup> ) | $E_{z,\max}$ (V/cm) |
|----------------------------|--------------------|-------------------------|--------------------------|----------|-------------------|-------------------------|-----------------------------------|---------------------|
| 0.33                       | 4.4                | 40                      | 196                      | 120      | 196               | 15                      | -1.0                              | -50                 |
| 0.5                        | 4.1                | 49                      | 240                      | 98       | 199               | 15                      | -1.0                              | -55                 |
| 1                          | 4.6                | 69                      | 340                      | 69       | 199               | 15                      | -1.0                              | -54                 |
| 2                          | 5.7                | 98                      | 479                      | 49       | 193               | 15                      | -1.0                              | -46                 |

Table IV. The sizes, the electrical parameters and the power output for the optimal coil.

| Inlet channel aspect ratio | Channel length (m) | $D_{\text{inlet}}$ (cm) | $D_{\text{outlet}}$ (cm) | $W$ (cm) | Power output (MW) | Enthalpy extraction (%) | $J_{y,\max}$ (A/cm <sup>2</sup> ) | $E_{z,\max}$ (V/cm) | $B_{\max}$ (T) |
|----------------------------|--------------------|-------------------------|--------------------------|----------|-------------------|-------------------------|-----------------------------------|---------------------|----------------|
| 0.33                       | 3.2                | 40                      | 196                      | 120      | 199               | 15                      | -1.1                              | -73                 | 11.0           |
| 0.5                        | 3.1                | 49                      | 240                      | 98       | 201               | 15                      | -1.2                              | -71                 | 11.6           |
| 1                          | 3.1                | 69                      | 340                      | 69       | 204               | 15                      | -1.3                              | -59                 | 8.8            |
| 2                          | 4.3                | 98                      | 479                      | 49       | 193               | 15                      | -1.2                              | -37                 | 11.9           |

a) inside the coil.

5 cm × 10 cm and relocated element by element.

Table IV shows the channel sizes, electrical parameters, power output, and the maximum magnetic flux density for the optimal coil. We can see that the optimal inlet channel aspect ratio exists between 0.5 and 1. Figure 4 shows the arrangement of the optimal coil and MHD channel for the case where  $D/W=1$  at the inlet. As shown in Fig. 5, this optimal coil can be constructed by the combination of saddle coils.<sup>7)</sup> By this optimization, the channel length is shortened by more than 30% in comparison with the uniform-magnetic-field design. This also means that the enthalpy extraction per unit channel length is improved by more than 23% on the average.

This optimal coils shape will be changed if the basic specifications, *e.g.*, the cross-sectional area of the coil and channel, are changed.

#### 5. Discussion

The following is the discussion for the case where  $D/W=1$  at the inlet.

##### 5.1 Generator characteristics

Figure 6 shows the value of the  $G$ -parameter at each axial point, and Fig. 7 shows the distribution of electrical power output density. For the optimal coil case, the power output density near the inlet is much higher than that in the uniform-magnetic-field case and most of the power is generated in the upstream region. However, it is shown that the power is not generated so much near the outlet because the effective plasma resistance increases rapidly due to the rapid increase of the  $G$ -parameter. Because the power generated near the inlet is large enough, the channel length is shortened without decreasing the power output.

Figure 8 shows the distribution of the magnetic field produced by the optimal coil. We can see that the optimized magnetic field is almost uniform at the inlet.



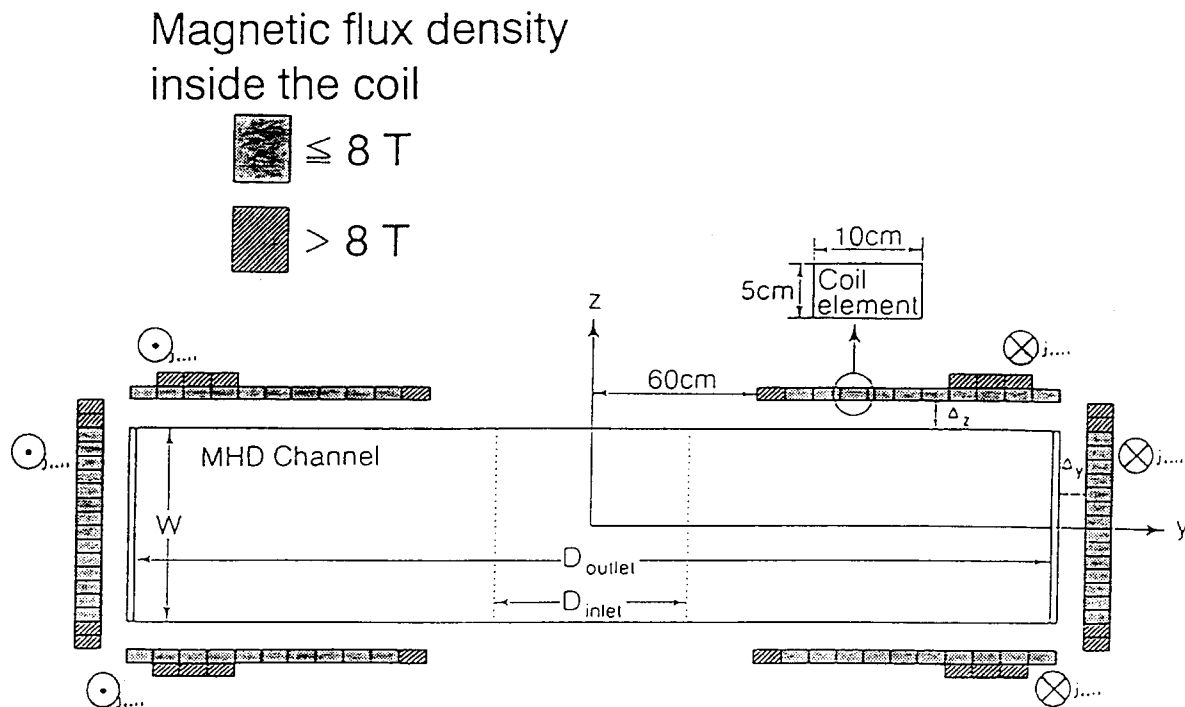


Fig. 4. Cross section of the optimal coil and the MHD channel for the case where  $D/W=1$  at the inlet.

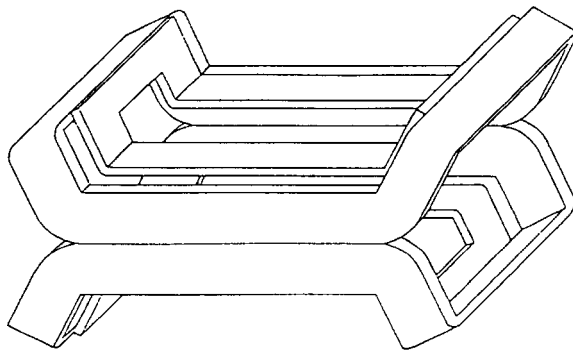


Fig. 5. Schematic design of the optimal coil.

However, it becomes nonuniform near the outlet. It is strengthened at the central region of the channel cross section and weakened near the electrodes. This also means that the magnetic field should be strengthened and should be uniform near the inlet in order to reduce the plasma nonuniformity, to obtain high power output density and to shorten the channel length without a decrease of power output.

The Faraday current density ( $J_y$ ) and the Hall electric field ( $E_x$ ) have a great influence on channel life. Although the maximum values of these parameters obtained in this analysis are higher than the present level of a prototype channel ( $J_y=1 \text{ A/cm}^2$ ,  $E_x=25 \text{ V/cm}$ ), this problem will be solved by:

- Adjustment of the conditions, such as the distribution of the load factor along the channel length and the gas

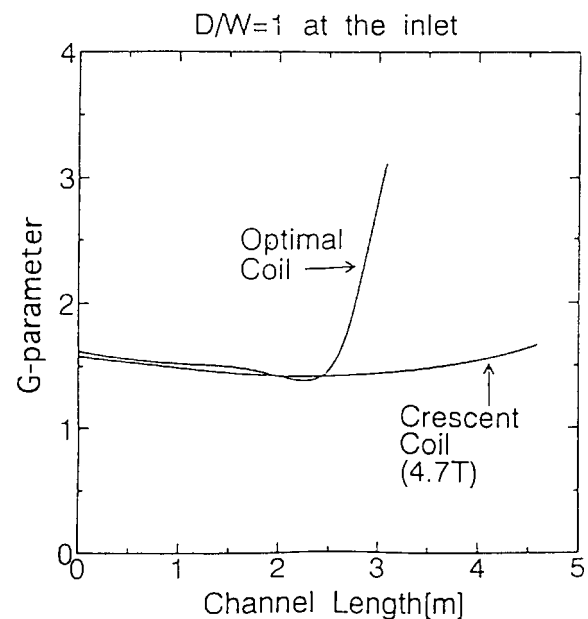


Fig. 6. G-parameter distribution along the channel length.

pressure.

- Improvement of channel structure.

## 5.2 Coil current density

We have assumed the coil current density to be  $10^5 \text{ A/m}^2$ . Though this value is higher than values used in other research, it can be realized by the adjustment of

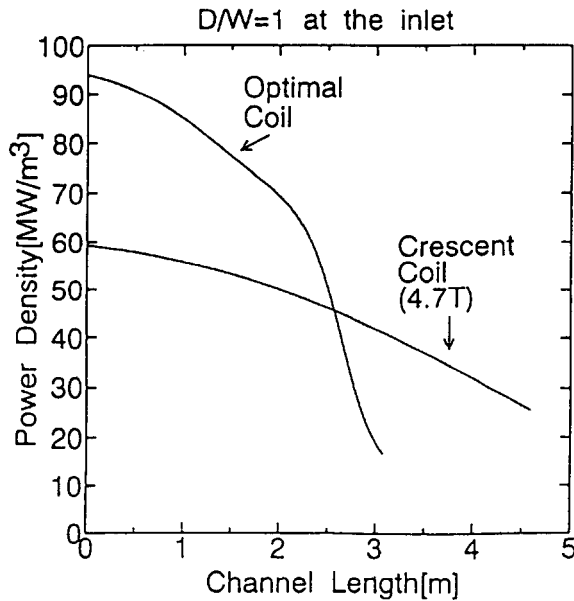


Fig. 7. Power output density distribution along the channel length.

the Nb/Ti-ratio of superconductor and the improvement of the coil-cooling method.<sup>3)</sup>

### 5.3 Effects of $B_y$ on the generator characteristics

The  $y$ -component of the magnetic flux density  $B_y$  has been neglected in the above 1-D analysis. In order to estimate its effects, we perform two-dimensional analyses by using the finite element method (FEM) for the channel cross section with the optimal coil.

Table V shows the electrical quantities of the channel at each channel axial point, comparing the case

Table V. The effect of  $B_y$  on the generator characteristics ( $D/W=1$  at the inlet).

(a) Neglecting  $B_y$  ( $B_y=0$ )

| Distance from the inlet (m) | Power output density (MW/m <sup>3</sup> ) | Faraday voltage (kV) | Averaged $J_z$ (A/cm <sup>2</sup> ) | $E_z$ (V/cm) |
|-----------------------------|-------------------------------------------|----------------------|-------------------------------------|--------------|
| 0                           | 104                                       | 4.8                  | 1.5                                 | 13.7         |
| 1                           | 86                                        | 7.2                  | 1.2                                 | 22           |
| 2                           | 66                                        | 12.3                 | 0.9                                 | 42           |
| 3                           | 20                                        | 20.0                 | 0.3                                 | 37           |

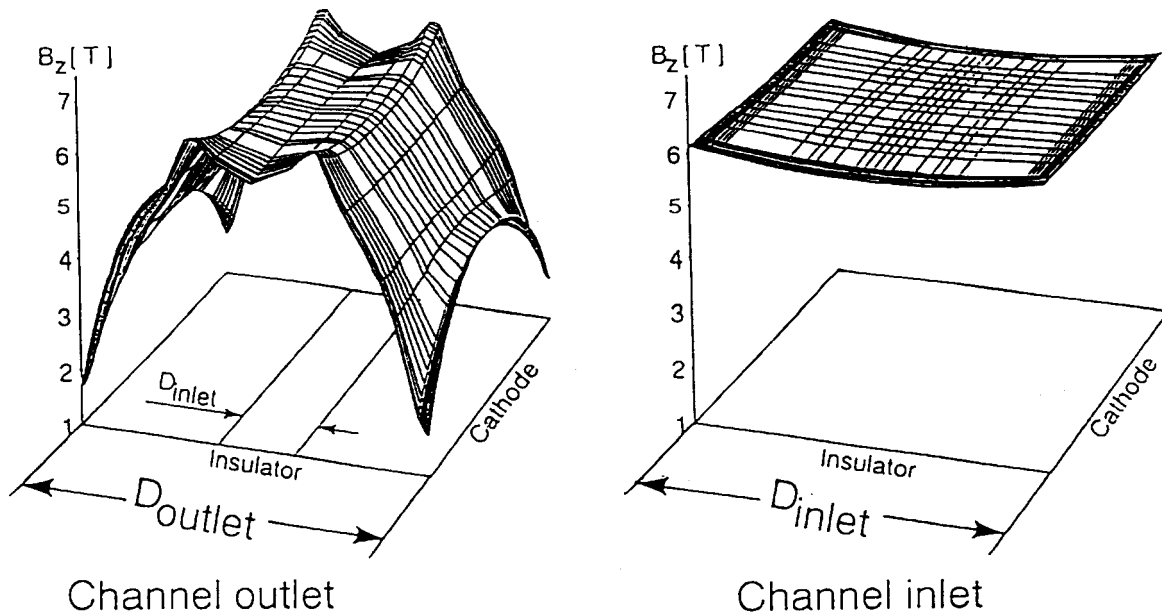
(b) Considering  $B_y$

| Distance from the inlet (m) | Power output density (MW/m <sup>3</sup> ) | Faraday voltage (kV) | Averaged $J_z$ (A/cm <sup>2</sup> ) | $E_z$ (V/cm) |
|-----------------------------|-------------------------------------------|----------------------|-------------------------------------|--------------|
| 0                           | 104                                       | 4.8                  | 1.5                                 | 13.7         |
| 1                           | 86                                        | 7.2                  | 1.2                                 | 22           |
| 2                           | 66                                        | 12.3                 | 1.0                                 | 43           |
| 3                           | 20                                        | 20.0                 | 0.4                                 | 39           |

neglecting  $B_y$  and the case considering it. As shown in this table,  $B_y$  hardly contributes to the generator performance.

### 5.4 Validity of the analytical model adopted in 1-D analysis

In this 1-D analysis, not only  $B_y$  but also the effects of  $J_z$  and  $E_z$  are neglected. In order to estimate the effects of these  $z$ -components of electrodynamic quantities, we perform 2-D analyses for the optimal-magnetic-field case neglecting the effects of  $B_y$ . Figures 9 show the differences in the average Faraday current density (a), the Hall field (b) and the Faraday voltage (c) between the case considering  $J_z$  and  $E_z$  (2-D analysis) and the case neglecting them (1-D analysis) for each channel

Fig. 8. Optimal magnetic flux density distribution over the channel cross section for the case where  $D/W=1$  at the inlet.

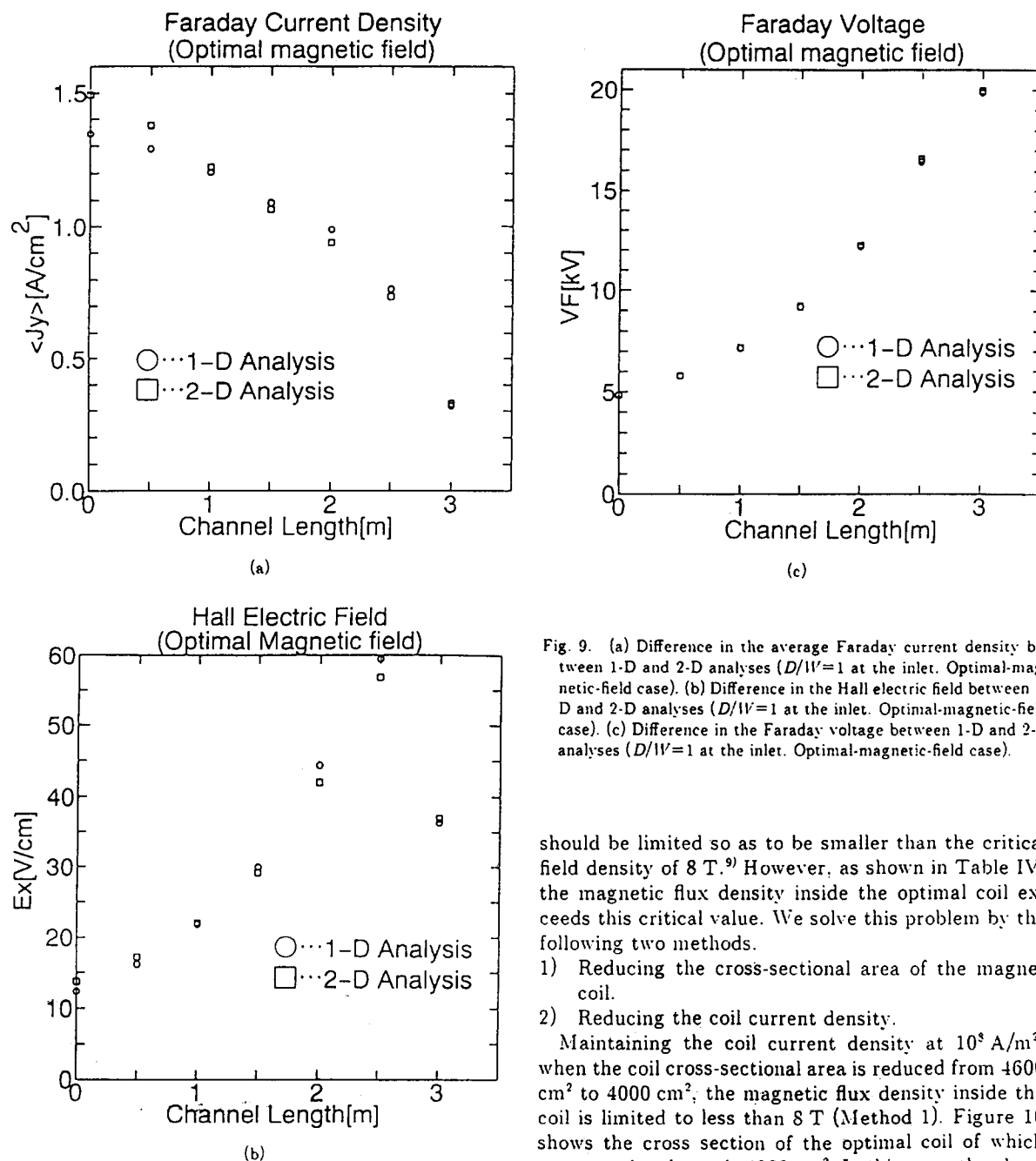


Fig. 9. (a) Difference in the average Faraday current density between 1-D and 2-D analyses ( $D/1V=1$  at the inlet. Optimal-magnetic-field case). (b) Difference in the Hall electric field between 1-D and 2-D analyses ( $D/1V=1$  at the inlet. Optimal-magnetic-field case). (c) Difference in the Faraday voltage between 1-D and 2-D analyses ( $D/1V=1$  at the inlet. Optimal-magnetic-field case).

axial point. As shown in these figures, there is little difference in these electrical quantities between 1-D and 2-D analyses.

From these considerations of the effects of  $B_y$ ,  $J_z$  and  $E_z$ , the analytical model adopted in this 1-D analysis, which neglects them, is suitable for estimating the electrical characteristics of the large-scale MHD generator.

#### 5.5 Methods of limiting the magnetic field inside the coil

In order to use the Nb-Ti superconductor for the magnet coil, the magnetic flux density inside the coil

should be limited so as to be smaller than the critical field density of 8 T.<sup>9)</sup> However, as shown in Table IV, the magnetic flux density inside the optimal coil exceeds this critical value. We solve this problem by the following two methods.

- 1) Reducing the cross-sectional area of the magnet coil.
- 2) Reducing the coil current density.

Maintaining the coil current density at  $10^8$  A/m<sup>2</sup>, when the coil cross-sectional area is reduced from 4600 cm<sup>2</sup> to 4000 cm<sup>2</sup>, the magnetic flux density inside the coil is limited to less than 8 T (Method 1). Figure 10 shows the cross section of the optimal coil of which cross-sectional area is 4000 cm<sup>2</sup>. In this case, the channel length is shortened by 20%.

Also, when the coil current density is reduced from  $10^8$  A/m<sup>2</sup> to  $0.9 \times 10^8$  A/m<sup>2</sup> without changing the shape of the optimal coil illustrated in Fig. 4, the magnetic flux density inside the coil is limited below the critical value (Method 2). In this case, the channel length is shortened by about 24%.

Table VI shows the sizes, electrical parameters and power output for the optimal coils obtained by the above two methods.

#### 5.6 Cost reduction by coil-shape optimization

As described in ref. 1, the MHD channel represents about 8% and the superconducting magnet represents

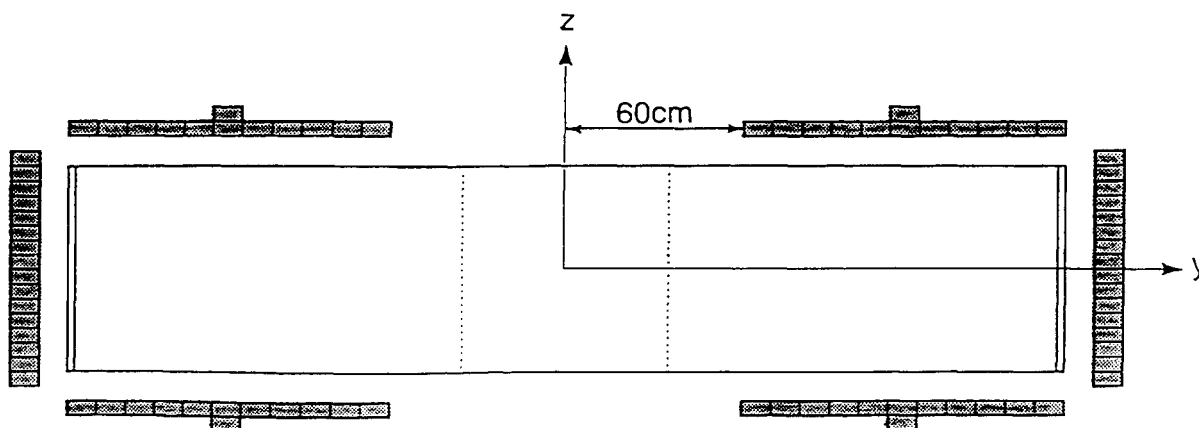


Fig. 10. Cross section of the optimal coil of which cross-sectional area is 4000 cm<sup>2</sup> and the MHD channel for the case where  $D/W=1$  at the inlet (Coil current density is  $10^5$  A/m<sup>2</sup>).

Table VI. The sizes, the electrical parameters and the power output for the optimal coil.

|          | Coil cross sectional area (cm <sup>2</sup> ) | Coil current density (A/m <sup>2</sup> ) | Channel length (m) | $D_{inlet}$ (cm) | $D_{outlet}$ (cm) | $W$ (cm) | Power output (MW) | Enthalpy extraction (%) | $J_{y=0.5}$ (A/cm <sup>2</sup> ) | $E_{z=0.5}$ (V/cm) |
|----------|----------------------------------------------|------------------------------------------|--------------------|------------------|-------------------|----------|-------------------|-------------------------|----------------------------------|--------------------|
| Method 1 | 4000                                         | $10^5$                                   | 3.9                | 69               | 340               | 69       | 200               | 15                      | 1.2                              | -46                |
| Method 2 | 4600                                         | $0.9 \times 10^5$                        | 3.7                | 69               | 340               | 69       | 201               | 15                      | -1.2                             | -51                |

a) inside the coil.

Table VII. The coil-energy parameter of optimal coils and the reference crescent coil.

|                         | Warm bore volume $V$ (m <sup>3</sup> ) | Square of the magnetic field $B^2$ (T <sup>2</sup> ) | Coil-energy parameter $VB^2$ (m <sup>3</sup> T <sup>2</sup> ) |
|-------------------------|----------------------------------------|------------------------------------------------------|---------------------------------------------------------------|
| Optimal coil (Method 1) | 12.64                                  | 22.1 <sup>a)</sup>                                   | 280                                                           |
| Optimal coil (Method 2) | 11.99                                  | 23.4 <sup>a)</sup>                                   | 280                                                           |
| Reference crescent coil | 30.77                                  | 22.1                                                 | 680                                                           |

<sup>a)</sup>the mean square volume inside the warm bore.

about 10% of the total plant cost.

When Method 2 (combination of coil-shape optimization and reduction of coil current density) is adopted, the channel length is shortened by about 24%. This means that the channel cost can be decreased by about 24%, assuming that the channel cost is roughly proportional to the length.

For the large-scale magnet, the magnet cost is roughly proportional to the stored energy that can be represented as  $VB^2$  (product of the warm bore volume  $V$  and the square of the magnetic field  $B^2$ ).<sup>1)</sup> Also, the 20% decrease in magnet cost results in a decrease of the electricity cost by 1%.<sup>1)</sup> Table VII shows the coil energy parameter  $VB^2$  of the optimal coils obtained by Method 1 and Method 2, compared with that of the reference crescent coil. When Method 2 is adopted, the stored energy is decreased by about 60%.

From the above considerations, the capital cost and the cost of electricity can be reduced by 8% and 3%, re-

spectively, when Method 2 is adopted.

## 6. Conclusions

In order to shorten the length of the Faraday-type MHD channel, we optimized the coil cross-sectional shape assuming a supersonic constant-velocity channel. We obtained the following results:

(1) With the coil shape optimization, the length of the MHD channel and the magnet coil system can be shortened by more than 30% without decrease of the enthalpy extraction in comparison with the case of the crescent coil producing the uniform magnetic field.

(2) The optimal inlet channel aspect ratio that gives the maximum power output and the shortest length is between 0.5 and 1.

(3) For the channel where  $D/W=1$  at the inlet, the stored energy of the magnet coil can be decreased by about 60% by the coil shape optimization, in comparison with the crescent-coil case.

(4) It is also estimated that the total capital cost of the commercial MHD/steam combined-cycle plant adopting this channel and coil system can be decreased by more than 8% and that the cost of electricity can be reduced by about 3% by the combination of this type of coil-shape optimization and the coil-current-density reduction.

- 1) W. R. Owens: Proc. Int. Workshop on MHD Superconducting Magnets, 1991, Bologna, p. 103.
- 2) M. Mitchner and C. H. Kruger, Jr.: *Partially Ionized Gases* (Wiley-Interscience Publication, New York, 1973) Chap. IV, p. 214.

- 3) R. J. Rosa: *Magnetohydrodynamic Energy Conversion* (Hemisphere, New York, 1987).
- 4) R. Nishimura, Y. Aoki and N. Kayukawa: Jpn. J. Appl. Phys. **32** (1993) 3270.
- 5) M. Ishikawa and J. Umoto: Proc. 6th Symp. Efficient Use of Energy and Direct Electrical Power Generation, 1983, Sapporo, p. 226.
- 6) J. T. Lineberry, F. L. Galanga, R. W. Clemons and Y. C. L. Wu: Proc. Specialists Meet. Coal Fired MHD Power Generation 1981, Sydney, p. 6.5.1.
- 7) F. Negrini, S. Ceresara, G. Martinelli, R. Penco, F. Vivaldi, P. Molino, C. Luzzatto, I. Montanari and G. M. Veca: Proc. 30th Symp. Engineering Aspects of Magnetohydrodynamics, 1992, Baltimore, p. I.1.1.
- 8) H. Ogiwara *et al.*: *Oyo Chodendo* (Applied Superconduction) (Nikkan Kogyo Shimbunsha, Tokyo, 1984) Chap. 3 [in Japanese].
- 9) T. Okamura, N. Harada, R. Yoshikawa, H. Yamasaki, S. Kabashima, S. Shioda, H. Hasegawa, M. Ishimura, Y. Douzono, H. Mukaida and S. Ikeda: Proc. 29th Symp. Engineering Aspects of Magnetohydrodynamics, 1991, New Orleans, p. IV.5.1.

## Facilities for in situ ion beam studies in transmission electron microscopes

Charles W. Allen<sup>a</sup>, Somei Ohnuki<sup>b</sup> and Heishichiro Takahashi<sup>b</sup>

<sup>a</sup>HVEM-Tandem Facility, Materials Science Division, Argonne National Laboratory, Argonne, IL 60439 USA

<sup>b</sup>Faculty of Engineering, Hokkaido University, Sapporo, 060 JAPAN.

Interfacing an ion accelerator to a transmission electron microscope (TEM) allows the analytical functions of TEM imaging and electron diffraction from very small regions to be employed during ion-irradiation effects studies. At present there are ten such installations in Japan, one in France and one in the USA. General specifications of facilities which are operational in 1993 are summarized, and additional facilities which are planned or being proposed are briefly described.

### 1. INTRODUCTION

Irradiation effects studies employing transmission electron microscopes (TEM) as analytical tools have been conducted for almost as many years as the materials community has employed TEM, motivated at least initially by materials needs for nuclear reactor development. Such studies have focussed on irradiation-induced and irradiation-enhanced microstructural and chemical changes, including phase transformations such as precipitation and dissolution, crystallization and amorphization, and order-disorder reactions. From the introduction of high voltage electron microscopes (HVEM) in the mid-1960s, studies of electron irradiation effects have constituted an important part of HVEM application in metallurgy and materials science. While electron accelerators had existed for several decades earlier, it was the introduction of HVEMs in the 1960s which made large electron flux and thus high dose studies possible in a known area of specimen with simultaneous observation and characterization of that area. For irradiation effects studies two additional developments are of especial importance, (1) the availability of specimen holders in which specimen temperature can be controlled in the range 10–2200 K during an experiment and (2) the interfacing of ion accelerators which allows in situ TEM studies of irradiation effects and the ion beam modification of materials by ion implantation.

The importance of in situ experiments in general is threefold; (1) such experiments can be performed rather quickly, often with a stream of simultaneously generated analytical information; (2) particularly for experiments at elevated or cryogenic temperatures, analysis at temperature may be essential in order to avoid mitigating effects during warmup or cooldown; (3) realtime observation of one region may be essential in correctly concluding what is the physical mechanism of a phenomenon. The purpose of this presentation is to survey briefly the present and near-term state of in situ ion beam capability internationally in the context of transmission electron microscopy.

### 2. FACILITIES—OPERATIONAL

At this writing there are twelve installations in the world utilizing transmission electron microscopes (TEM) with in situ ion beam capability. Table 1 summarizes several relevant specifications for each of the facilities which was operational during 1993. Also included as footnotes to Table 1 are installations which are planned to be brought into service in 1994. An excellent historical perspective of ion beam studies performed in TEM has been presented by Ishino [1].

With regard to Table 1, it is clear that the spectrum of specifications, both for TEMs and for ion accelerators is very broad. At present, three of the installations utilize high voltage

Table 1. Transmission electron microscopes with in situ ion-beam capability. Operational in 1993.

| LOCATION (DATE*)               | NATION | REF  | ACCELERATOR VOLTAGE                                  | TEM VOLTAGE    |
|--------------------------------|--------|------|------------------------------------------------------|----------------|
| Argonne (1981)                 | USA    | [2]  | 0.2–2 MV<br>20–650 kV<br>(Not simultaneous dual ion) | 0.1–1.2 MV**   |
| CSNSM-CNRS (1980)              | France | [3]  | 5–200 kV                                             | 100–120 kV     |
| ERIEPI(1983)                   | Japan  | [4]  | 20 kV                                                | 100–200 kV     |
| Hitachi, Ltd. (1984)           | Japan  | [5]  | 10–400 kV                                            | 100–200 kV     |
| Hokkaido U. (1984)             | Japan  | [6]  | 20–300 kV                                            | 0.4–1.3 MV     |
| Inst. Phys. Chem. (1987)       | Japan  | -    | 0.4–1.0 MV                                           | 100–200 kV     |
| JAERI—Tokai(1990)              | Japan  | [7]  | Two 2–40 kV<br>(Simultaneous dual ion)               | 100–400 kV***  |
| JAERI—Tokai (1986)             | Japan  | [8]  | 10 kV                                                | 100 kV         |
| Kyushu U. (1991)<br>(Kasuga)   | Japan  | [9]  | 0.1–10 kV                                            | 40–200 kV      |
| Kyushu U. (1988)<br>(Hakozaki) |        | [10] | 1–30 kV                                              | 0.25–1.25 MV   |
| NRIM—Tsukuba (1989)            | Japan  | -    | 10–100 kV<br>10–30 kV<br>(Simultaneous dual ion)     | 100–200 kV**** |
| U. Tokyo—Tokai (1978)          | Japan  | [11] | 10–400 kV                                            | 100–200 kV     |

\* Year in which the first in situ ion beam experiment was performed.

\*\* In 1994, 100–300 or 400 kV TEM is planned at Argonne, interfaced to existing ion accelerators. Not simultaneous dual ion.

\*\*\* Transferred from JAERI—Tokai to JAERI—Takasaki late in 1993 where IVEM is now interfaced to 40 kV and 300 kV accelerators for in situ dual ion irradiations.

\*\*\*\* In 1994, 0.4–1.25 MV HVEM is planned at NRIM, interfaced to 30–200 and 10–100 kV ion implanters. Simultaneous dual ion.

electron microscopes (HVEM: >400 kV) and only one involves an intermediate voltage electron microscope (IVEM: 300–400 kV). All but two of the sites (Argonne and CSNSM—Orsay) are located in Japan.

As indicated in the footnotes of Table 1, during 1994, an HVEM is planned for the National Research Institute for Metals (NRIM—Tsukuba) with dual ion capability, and an IVEM, for the HVEM-Tandem Facility at Argonne

Table 2. Transmission electron microscopes (TEM) with in situ ion-beam capability. Proposed.

| LOCATION (DATE*)   | NATION | ION ACCELERATION VOLTAGE                                                                                     | TEM VOLTAGE                            |
|--------------------|--------|--------------------------------------------------------------------------------------------------------------|----------------------------------------|
| Argonne (1996)**   | USA    | 20–400 kV<br>0.3–3.0 MV<br>(Simultaneous dual ion)<br>and<br>1–20 kV<br>20–400 kV<br>(Simultaneous dual ion) | 0.1–2.0 MV<br><br>100–300 or 400 kV*** |
| Hokkaido U. (1995) | Japan  | 20–300 kV                                                                                                    | 0.4–1.3 MV                             |
| Kyushu U. (1995)   | Japan  | 1–50 kV<br>20–400 kV<br>(Simultaneous dual ion)                                                              | 0.25–1.5 MV                            |

\* Proposed starting date for project.

\*\* Project known as HVEM-Tandem II; HVEM known as MICROLAB.

\*\*\* Intermediate voltage electron microscope indicated in second footnote of Table 1.

National Laboratory, the latter utilizing existing accelerators individually, i.e., not for in situ dual ion irradiation studies.

Most of the facilities listed in Table 1 have been developed for the research programs of specific groups within the individual institutions. The possibility for collaboration of other scientists and engineers with these groups always exists, however. In addition, the Argonne facility is funded for the materials research community specifically as a user facility, free of charge for non-proprietary studies.

### 3. FACILITIES—PROPOSED

Table 2 summarizes installations which have been proposed prior to the end of 1993. Each of these is an upgrade of an existing facility, which includes a new HVEM to replace aging existing equipment. Several other new installations or significant modifications of existing facilities were still in the preproposal stage in this period, and inclusion in this report was deemed to be premature therefore.

With significant improvements in microscope design and the adaptation of techniques for elemental microanalysis during in situ experiments, important scientific and technological contributions by users of these new facilities and of those already planned can be expected, which heretofore have not been possible due to experimental limitations.

Argonne National Laboratory is proposing to replace most of the equipment of the present HVEM-Tandem Facility with state-of-the-art equipment. The proposed HVEM is a 2 MV version of the 3 MV instrument constructed by Hitachi during 1992/93 for the Research Center for Ultra High Voltage Electron Microscopy at Osaka University. The specimen regions of these instruments are unusually large and accessible, designed specifically for in situ studies involving a spectrum of analytical techniques.

Hokkaido University is planning to replace the present HVEM-ion accelerator system. The new system will be employed for surface modification studies involving the implantation of various ions, including metals. In



approximately the same time frame, the HVEM Laboratory at Kyushu University is proposing to replace the present HVEM-ion accelerator system with a similar, state-of-the-art HVEM interfaced to two accelerators for dual ion studies. The new HVEM is expected to provide various functions for observation of structural, chemical and electronic changes in materials.

#### 4. ACKNOWLEDGMENTS

The authors are grateful to the many persons who have contributed information regarding their facilities for this brief report and to their own research facility sponsors. The HVEM-Tandem Facility at Argonne is funded by the U. S. Department of Energy, BES-Materials Sciences, under Contract W-31-109-Eng-38. The HVEM at Hokkaido University was funded by the Japanese Ministry of Education and the ongoing operation of the facility, by Hokkaido University.

#### REFERENCES

1. S. Ishino, J. Nucl. Mater. 206 (1993) in press.
2. A. Taylor, J. R. Wallace, E. A. Ryan, A. Phillippides and J. R. Wroebel, Nucl. Instr. and Meth. 189 (1981) 211.
3. M. O. Ruault, M. Lerne, B. Jouffrey and J. Chaumont, J. Phys. E (Sci. Instrum.) 11 (1978) 1125.
4. H. Kusanagi, H. Kimura, M. Tokiwai and T. Suzuki, J. Nucl. Mater. 133 & 134 (1985) 473.
5. Nucl. Instrum. and Methods in Phys. Res. A269 (1986) 491.
6. T. Takeyama, S. Ohnuki and H. Takahashi, J. Nucl. Mater., 133&134 (1985) 571.
7. S. Furuno, K. Hojou, H. Otsu, K. Izui, T. A. Sasaki, T. Tsukamoto and T. Hata, J. Electron Microsc., 41 (1992) 273.
8. K. Hojou, S. Furuno, H. Otsu, K. Izui and T. Tsukamoto, J. Nucl. Mater. 155-157 (1988) 298.
9. T. Muroga, R. Sakamoto, M. Fukui, N. Yoshida and T. Tsukamoto, J. Nucl. Mater. 196-198 (1992) 1013.
10. C. Kinoshita, H. Abe, K. Fukumoto, K. Nakai and K. Shinohara, Ultramic. 39 (1991) 205.
11. S. Ishino, H. Kawanishi and K. Fukuy, Proc. 4th Topical Meeting on The Technology of Controlled Nuclear Fusion, 1980 CONF-801011 (1981) 1683.

#### FACILITY FAX [OFFICE] NUMBERS

- Argonne National Laboratory (Charles W. Allen) 708-252-4798; [708-252-4157 or 708-252-5222].
- Central Research Institute of Electric Power Industry (Hideo Kusanagi) 3-3480-1668; [3-3480-2111].
- Energy Research Laboratory—Hitachi Ltd. (Shigeki Oono) 294-53-2830; [294-53-3111].
- Centre de Spectrometrie Nucleaire et de Spectrometrie de Masse-CNRS (Marie-Odile Ruault) 1 69 41 52 68; [1 69 41 67 50].
- Hokkaido University (Heishichiro Takahashi) 11-757-3537; [11-716-2111 Ext. 6767].
- Institute of Physical and Chemical Research (Wako) (Eiichi Yagi) 48-462-4648; [48-462-1111 Ext. 3333 or 4671].
- Japan Atomic Energy Research Institute—Takasaki (Hiroshi Naramoto) 273-46-9687; [273-46-9420].
- Japan Atomic Energy Research Institute—Tokai (Shigemi Furuno, Kiichi Hojou) 292-82-5927; [292-82-6474 or 6360].
- Kyushu University (Hakozaki Campus) (Chiken Kinoshita, Yoshitsugo Tomokiyo) 92-641-7098, 92-632-0434; [92-641-1101 Ext. 5813 or 5970].
- Kyushu University (Kasuga Campus) (Naoaki Yoshida, Takeo Muroga) 92-582-4201; [92-573-9611 Ext. 510 or 516].
- National Research Institute for Metals (Tsukuba) (Kazuo Furuya) 298-51-4556; [298-51-6311].
- University of Tokyo (Tokai Campus) (Shiori Ishino) 33-812-1794 or 3-3818-3455; [3-3812-2111 Ext.6986].

## Microchemical Change and Grain Boundary Migration due to Excess Defects Flow under Irradiation

H. Takahashi, N. Hashimoto and S. Watanabe  
Faculty of Engineering, Hokkaido University,  
Kita-ku, Kita-13, Nishi-8, Sapporo 060, Japan

A Fe-Cr-Ni model alloy was electron-irradiated using a high voltage electron microscopy (1000kV), and in situ observation on structural evolution and microchemical analyses were carried out. When the Fe-Cr-Ni alloy was irradiated, the nucleation of dislocation loops followed by voids was observed and at the same time a grain boundary migration occurred. The compositional analysis after irradiation of an area including a grain boundary indicated nickel enrichment and chromium depletion near the grain boundary. It is suggested that when the radiation-induced point defects flow into the grain boundary, boundary migration and solute redistribution are induced and the magnitudes depend on net point defects flow, especially that of interstitial atoms. The microchemical changes were also simulated by model calculation.

### 1. Introduction

Austenitic stainless steels, such as type 316, have been considered as the primary candidate structural materials for fusion reactors, and are used as light-water reactor core components [1,2,3]. In these steels radiation-induced solute redistribution (segregation) at grain boundaries and grain boundary migration cause deleterious effects on their physical, chemical and mechanical properties [4]. Therefore it is of great importance to investigate the mechanisms for retardation of radiation-induced solute redistribution (RISR) [5,6], namely, segregation, and then the behaviors of grain boundary migration with the segregation under irradiation [7,8].

This paper is focused on RISR and the grain boundary migration behavior during electron irradiation of Fe-Cr-Ni alloy systems. The grain boundary migration behavior is also discussed based on solute segregation and point defect flow by comparing it with computer simulation.

### 2. Radiation-induced phenomena

It is well-known that many kinds of phenomena are induced during irradiation of materials by high energy

particles such as neutrons, electrons and ions. The main radiation-induced phenomena (RIP) are, radiation-induced segregation (RIS), radiation-enhanced diffusion, precipitation dissolution, radiation-induced grain boundary migration and/or radiation-induced amorphization etc. These RIPs are closely related to point defects behavior introduced due to collision with high energy particles.

In present paper the RIP occurred near a grain boundary associated with segregation and boundary migration will be discussed.

The segregation of solute under irradiation is induced inverse Kirkendall effect which is attributed to excess point defects migration, and it has been clarified that the point defects interact with solute in the alloys and under sized solute flow toward the same direction of interstitial atom diffusion, while over sized one migrates to inverse direction of vacancy due to exchange mechanism of diffusion. As the result the under-sized solute is enriched and over sized one tends to deplete from defect sink.

A typical example of RIS at grain boundary for various alloys is given in Table 1.

From this table it can be seen that the results obtained after ir-

radiation by electrons,  $C^+$  ions and neutrons for different kinds of crystalline systems indicate enrichment and depletion of solute concentration for the under sized solutes and over sized solutes comparing to solvent atom in each alloy systems, respectively. However, for the case of  $C^+$  ions irradiation the segregation

Table 1 Segregation and size factor

| Electron Irradiation |                |                  |
|----------------------|----------------|------------------|
| Alloy systems        | Redistribution | Size factors (%) |
| Cu-Ni                | Enrichment     | - 2.504          |
| Cu-Ag                | Depletion      | + 13.067         |
| Cu-Fe                | Precipitation  | - 0.313          |
|                      | Enrichment     |                  |
| Cu-Si                | Precipitation  | 3.443            |
|                      | Depletion      |                  |
| Ni-Cu                | Depletion      | + 2.564          |
| Ni-Al                | Depletion      | + 14.928         |
| Ag-Cu                | Enrichment     | - 11.557         |
| Ni-Si                | ( Enrichment ) | + 6.100          |
| Fe-Mn                | Depletion      | + 2.590          |
| Fe-Cr                | Depletion      | + 0.628          |
| Fe-Mo                | Depletion      | + 9.890          |
| Fe-Ti                | Depletion      | + 14.397         |
| Fe-Si                | -              | + 3.768          |

| $C^+$ ion-Irradiation |            |  |
|-----------------------|------------|--|
| Fe-13 Cr              | Enrichment |  |
| Cr                    |            |  |
| Fe-13Cr-1 Si          | Enrichment |  |
| Cr                    |            |  |
| Si                    | Enrichment |  |
| Fe-13Cr-1 Ti          | Depletion  |  |
| Cr                    |            |  |
| Ti                    | Enrichment |  |

| Neutron-Irradiation |                |                  |
|---------------------|----------------|------------------|
| Alloy systems       | Redistribution | Size factors (%) |
| V-3 Fe              | Enrichment     | - 18.86          |
| V-3 Mo              | Depletion      | + 9.83           |
| V-3 Nb              | Depletion      | + 27.93          |

behavior is different from that of other irradiation, namely in Fe-Cr and Fe-Cr-Si alloys, Cr and Si under  $C^+$  ion irradiation are identified as enrichment even though the solutes are over sized ones. On the other hand, in Fe-Cr-Ti alloy Cr depletes according to size effect and Ti is enriched. This fact depends on the interaction between the implanted C atom and solute. The alloying elements of Cr, Si and Ti are carbide former elements, therefore the segregation behavior is influenced by the affinity among them. Especially, Ti atom is stronger carbide former than others so that Ti carbide is preferentially formed rather than Cr carbide. As a result of

consumption of implanted C atoms to form carbide with Ti, the Cr behaves to cause the depletion according to size effect.

### 3. Effect of solute on point defect migration

It is indicated above that point defects interact with solutes according to size effect. Therefore it is important to estimate the interaction energy between defect and solute to understand segregation process. The migration energies of vacancy and interstitials during irradiation can be estimated by measuring the growth rate of interstitial loop and the nucleated loop density as a function of temperature, respectively.

Figs.1 and 2 show the examples of them for 316 stainless steel and modified steels by adding over sized

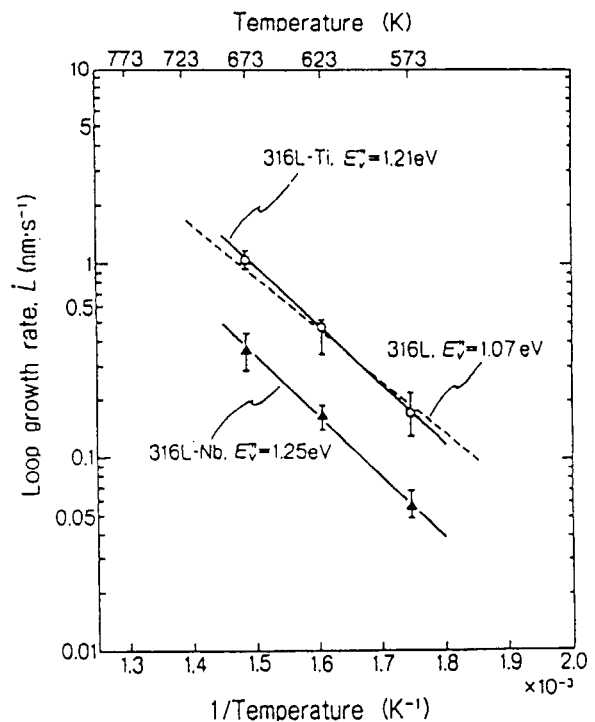


Fig.1 Temperature dependence of dislocation loop growth rate in 316 steels.

Ti, Zr, Hf and Nb elements. It can be found that the values of defect migration energy in the modified ones were greater than that of the standard 316 stainless steel without modification. The differences among the values might be corresponded that of binding

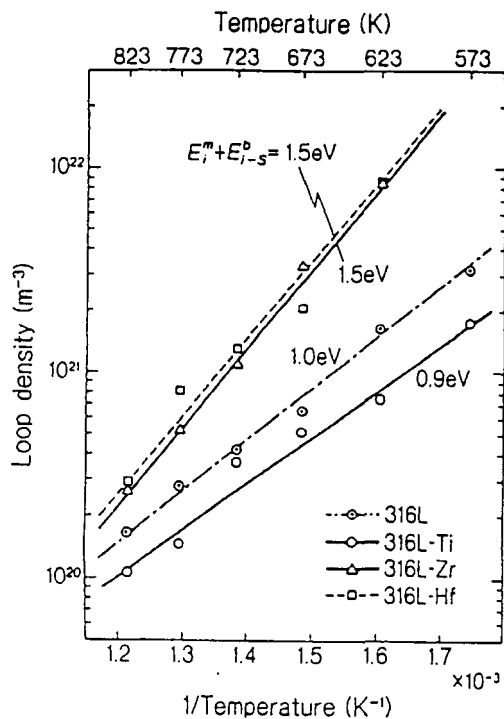


Fig.2 Temperature dependence of dislocation loop density.

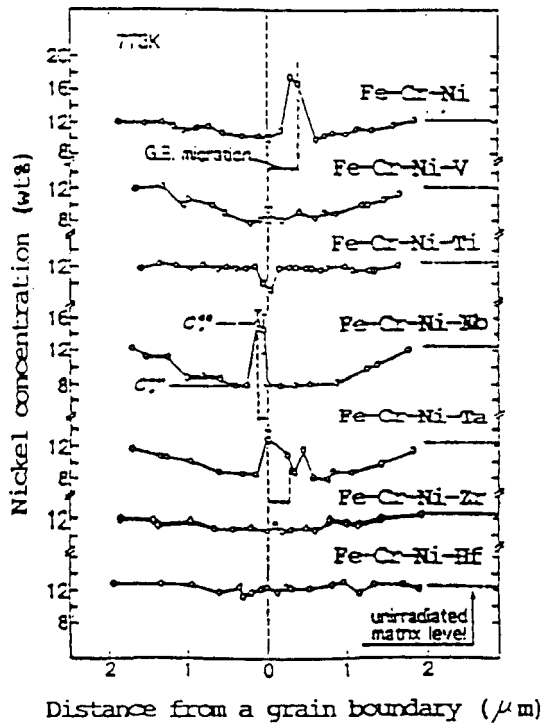


Fig.3 Ni concentration profile near a grain boundary in modified 316 stainless steel after electron irradiation.

energy between point defect and solute. This increment of the migration energy also influences defect mobility and/or net defect flow, therefore the amount of segregation at defect sink.

Fig.3 shows the concentration profile of nickel solute after electron irradiation of the same modified 316 stainless steels described above (each 3 at% addition). The amount of concentration change due to segregation is different depending on additional element and larger additive such as Zr and Hf shows strong retardation effect against the segregation. From the results on interaction energy and this segregation tendency it is obvious that the addition of element with strong binding energy with point defect is very effective for segregation retardation.

Fig.4 shows an example of comparison of concentration profile near a grain boundary between experimental and simulation calculation using the -

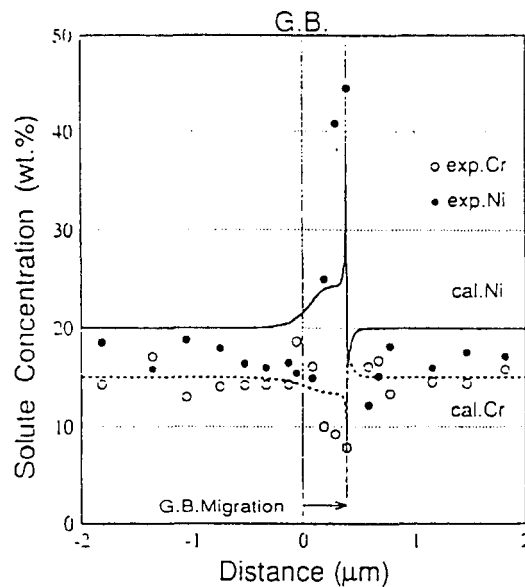


Fig.4 Concentration profiles near a grain boundary obtained from experimental result and computer calculation.

coupled rate equation with defect flux[9,10]. This profile was calculated considering the values of migration energy obtained from the experiment for the same alloy systems.

It can be seen that both

concentration profiles is qualitatively coincident. However, for the more precise quantitative analysis not only the theoretical treatment but also the more detailed experimental analysis are required.

#### 4. Segregation and grain boundary migration

The grain boundary migrations were observed during electron irradiation of Fe-Cr-Ni alloy at 763 to 783 K and the occurrence of boundary migration seems to be dependent on orientation relationship between the boundary interfaces, because the migration did not occur when crystalline orientations of the interface between two grains are close and the grain boundary consisting of two grains with large orientation difference migrated remarkably as being given in Table 2.

Table 2 Orientation relationship of irradiated grain and boundary interface.

| Irradiated Plane | G.B.Plane     |
|------------------|---------------|
| (110) / (110)    | (200) → (311) |
|                  | (200) → (331) |
|                  | (111) → (200) |
|                  | (111) → (311) |
| (110) / (013)    | (200) → (311) |
| (110) / (122)    | (220) → (420) |
| (110) / (123)    | (111) → (331) |

→ Direction of Migration

The boundary migration began before formation of voids and continued to migrate even after the void nucleation. When the migrating boundary front reached some voids, they shrank quickly and the boundary migration velocity was accelerated.

Fig. 5 shows the relation between the boundary migration and irradiation dose in the temperature range of 763 and 783 K. There is not

remarkable difference in the migration distance up to 1 dpa. However, above 1 dpa, the distance strongly depended on irradiation temperature. At lower temperature of 763 K, the migration distance is not largely decreased even at higher irradiation dose, but

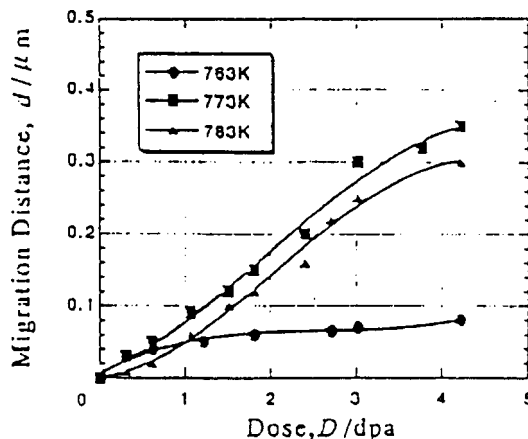


Fig.5 Grain boundary migration in Fe-Cr-Ni alloy as a function of irradiation dose.

at higher temperatures of 773 K and 783 K the distance increased with increasing irradiation dose. The distance of boundary migration at given doses of 1.8 and 4.2 dpa were shown in Fig. 6 as a function of irradiation temperatures.

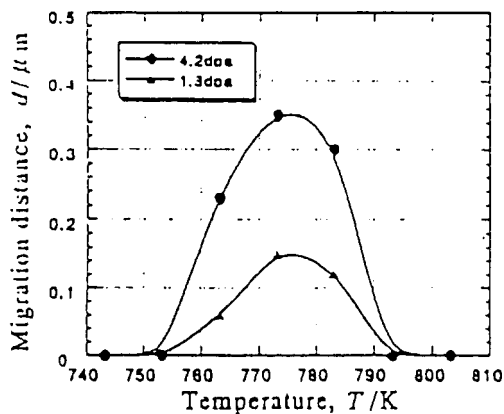


Fig.6 Grain boundary migration distance as a function of irradiation temperature.

A peak value of the migration distance was obtained at 773 K irradiation. The temperature giving maximum grain boundary migration was close to that of minimum void number density.

After irradiation of a region

including a grain boundary, the solutes concentration in this area was analyzed using EDS. As the general characteristics of the segregation behavior, nickel was enriched and chromium was depleted at the grain boundary region.

Fig.7 shows the temperature dependence of the amount of solute segregation which was defined as a difference between the concentration near grain boundary regions irradiated and unirradiated. Nickel enrichment and chromium depletion took place at all temperatures examined. Both concentration changes were prominent at 773 K and 783 K. Thus

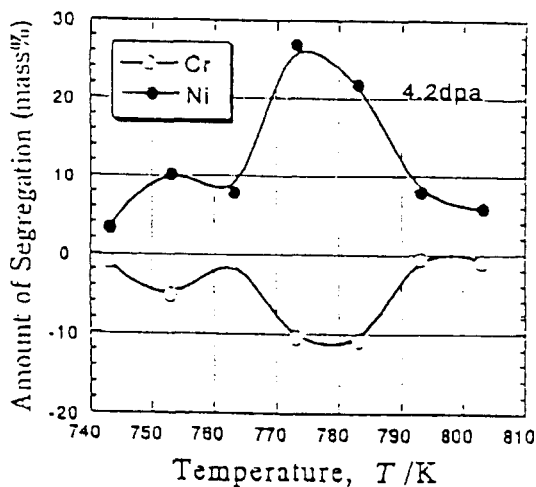


Fig.7 Temperature dependence of segregation after irradiation to 4.2 dpa.

temperature dependence of segregation is similar tendency to that of grain boundary migration rate and the migrated distance. These facts also suggest that the behavior of the boundary migration is related to that of radiation introduced point defect flow. That is, a coincidence of maximum changes of solutes concentration and migration distance at a given dose is indicating that point defect flow induces the grain boundary migration. Namely the excess vacancy and interstitial atom introduced during electron irradiation tend to migrate toward grain boundary and simultaneously the segregation is high according to the size effect [11,12,13].

Fig.8 shows a relation between the amount of solute segregation and

grain boundary migration distance. The amount of segregation increases with the migration distance. This suggests that in the process of boundary migration the solute concentration continues to change at the grain boundary.

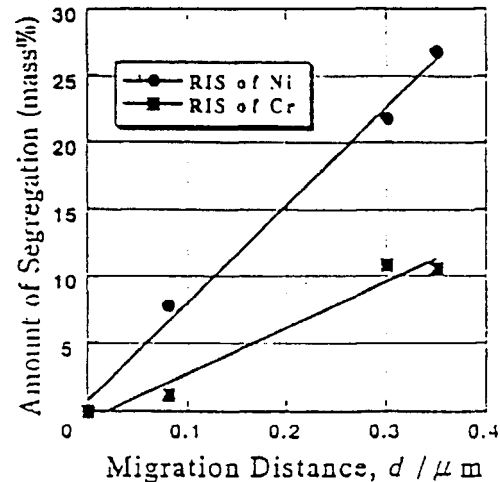


Fig.8 Relationship between amount of segregation and grain boundary migration distance in Fe-Cr-Ni alloy (Cr is amount of depletion)

This tendency is remarkable for nickel rather than chromium, because diffusion of nickel solute as interstitials toward grain boundary is very fast, while oversized chromium diffuses away from the boundary. Furthermore these facts suggest that the role of interstitials is very important for grain boundary migration under irradiation, that is, the interstitials migrated to grain boundary interface contributes to grow the interface, i.e., boundary migration. Therefore, the migrating distance of the grain boundary is reflecting the effective flux of point defects.

The more detailed mechanism of boundary migration related to point defect flow with solute redistribution should be studied as a future investigation, especially by considering the nature of boundary interface.

## 5. Concluding remarks

During electron irradiation of Fe-Cr-Ni alloys, the redistribution of nickel and chromium solutes near grain boundary according to size effect and the grain boundary migration occurred. At the same time the occurrence and

direction of boundary migration depends on the orientation relationship between two grain facing each other. These results are suggesting that grain boundary migration is strongly attributed to point defects flow into grain boundary, mostly interstitial atoms and vacancies may assist the rearrangement of interstitial atoms at the interface through boundary diffusion. However, the detailed migration mechanism should be investigated based on defects flow and atomic rearrangement process at boundary interface.

#### References

- [1] B.M.Gordon and W.G.Gordon, Nucl. Eng.Design, 98(1984), 109.
- [2] H.Gross, H.P.Fuchs, H.J. Lippert and W. Dambietz., Nucl. Eng. Design, 108(1988), 433.
- [3] H.Hanninen and I.Aho-Mantila, Proc. 3rd Int. Symp. on Environmental Degradation of materials in nuclear Power Systems -Water reactors, Eds. by G.J. Theus and J.R.Weeks, The Metallurgical Society, Wandale, PA, (1988), p.77.
- [4] J.F.Bates, R.W.Powell and E.R. Gilbert, Effects of radiation on Materials, 10 th Conf., ASTM STP 725, Eds. by D.Kramer, H.R.Brager and J.S.Perrin, American Society for Testing and Materials, Philadelphia, (1980), p.713.
- [5] P.R.Okamoto and L.E.Rehn, J.Nucl. Mater., 83(1979), 2.
- [6] H.Takahashi, S.Ohnuki and T.Takeyama, J.Nucl.Mater., 103&104 (1981), 1415.
- [7] K.Nakata, Y.Katano, I.Masaoka and K.Shiraishi, J.Nucl., Mater., 133 & 134 (1985), 575.
- [8] W.V.Vaidya, J.Nucl.Mater., 113 (1983) 219.
- [9] H.Wiedersich, P.R.Okamoto and N.Q.Lam, J.Nucl.Mater., 53(1979) 98
- [10] A.D.Marwick, J.Nucl.Mater., 135 (1985) 68.
- [11] P.R.Okamoto and H.Wiedersich, J. Nucl. Mater., 53(1974), 242.
- [12] T.Takeyama, H.Takahashi and S.Ohnuki, J.Nucl.Mater., 108 & 109(1982), 465.
- [13] R.A.Johnson and N.Q.Lam, Phys. Rev., B13 (1976), 4364.

# SOLID TRANSMUTATION EFFECT IN FUSION REACTOR MATERIALS

S. Ohnuki, H. Kinoshita\* and H. Takahashi\*

Materials Science and Technology, Faculty of Engineering Hokkaido University, Sapporo  
060

\*Energy Research Center, Hokkaido University, Sapporo 060

Addition of 1at% Ni to V and V-10Ti, followed by irradiation along with the Ni free metals in HFIR to 17.7 dpa at 400C has been used to study the influence of He on microstructural evolution and embrittlement. Approximately 15.3. % of the V transmuted to Cr in these alloys. The 50 atppm He generated from the  $^{58}\text{Ni}(n,r)$   $^{59}\text{Ni}(n,a)$   $^{56}\text{Fe}$  sequence was found to exert much less influence than either the Ni directly or the Cr formed by transmutation. The V-10Ti and V-10Ti-1Ni alloys developed an extreme fragility and broke into smaller pieces during handling. The embrittlement was found to arise from the strongly synergistic effects of Cr and Ti in elevating the ductile-to-brittle transition temperature.

## 1. Introduction

Transmutation effect has been considered with only the point of gaseous elements, such as He and H. However, recent studies [1,2] have pointed out the obvious effect of solid transmutation on microstructural change in neutron irradiated materials which has considered to be used for fusion reactor materials. In this work the solid transmutation effect in V base alloy will be discussed as a typical example.

## 2. Experimental procedure

V, V-1Ni, V-10Ti and V-10Ti-1Ni (nominal compositions, all in at%) specimens were irradiated in the HFIR target position at 400C to 17.7 dpa. The residual radioactivity after two years decay was 10 mR/h at contact for specimens without Ni and 150 mR/h for Ni-containing specimens. After irradiation density measurement, transmission electron microscopy and scanning electron microscopy were carried out, which were equipped with EDS microanalysis.

## 3. Results

The density change data are shown in Table 1. The density changes are relatively small in V and V-1Ni but significant decreases occurred in both V-10Ti and V-10Ti-1Ni, with Ni additions appearing to decrease the change somewhat. density changes are anticipated to result from both void swelling and transmutation-induced

changes in lattice parameter.

On the broken specimens of both V-10Ti and V-10Ti-1Ni, the fracture surface is dominated primarily by transgranular cleavage facets and secondarily by grain boundary separation. With the exception of a few small precipitates on the grain boundary, there were no reasonable features on the facets or grain boundaries that would indicate the presence of voids or bubbles.

The microstructure observed in V and V-1Ni contained comparable density ( $5 \times 10^{16} \text{ cm}^{-3}$ ) of small ( $< 5 \text{ nm}$ ) cavities. The two specimens developed very different surfaces during electropolishing, however. While the V-1Ni had a very smooth surface the V developed a very irregular surface, indicative of selective electropolishing. The regions protruding above the average surface plane appear to be related to be regions of higher Cr level.

As shown in Table 2, the bulk level of transmutant Cr determined by broad-beam electron scans in the JSM 840 of the surfaces of V, V-10Ti and V-10Ti-1Ni are consistent with  $15.35 \pm 0.35\%$  of the original V having transmuted to Cr. The foil analysis of V and V-1Ni in the JEOL 2000 yielded comparable but somewhat more variable measurements of 16.0 and 14.0% respectively. These results are in excellent agreement with the predictions of Greenwood and Garner [2] who predicted 19.3% at 22 dpa. When interpolated, this yields a predicted value of 15.5% at 17.7 dpa, compared



Table 1. Density change after irradiation.

|            | Unirradiated density<br>g cm <sup>-3</sup> | Irradiated density<br>g cm <sup>-3</sup> | Change (%) <sup>*</sup> |
|------------|--------------------------------------------|------------------------------------------|-------------------------|
| V          | 6.13038                                    | 6.1525                                   | 0.30                    |
| V-1Ni      | 6.19391                                    | 6.1784                                   | -0.25                   |
| V-10Ti     | 5.97293                                    | 5.8336<br>5.8354 <sup>**</sup>           | -2.33<br>-2.30          |
| V-10Ti-1Ni | 5.98426                                    | 5.8955<br>5.8926 <sup>**</sup>           | -1.48<br>-1.53          |

<sup>\*</sup> Change contains contributions from both cavities and transmutation-induced changes in composition. A negative sign implies volumetric swelling.

<sup>\*\*</sup> Second independent measurement.

Table 2. Transmutation measured by EDS

|            | V    | Cr   | Ti  | Ni  | Method <sup>*</sup> | %V→Cr |
|------------|------|------|-----|-----|---------------------|-------|
| Pure V     | 84.3 | 15.7 | -   | -   | SEM/EDS             | 15.7  |
| Pure V     | 84.0 | 16.0 | -   | -   | TEM/EDS             | 16.0  |
| V-1Ni      | 80.0 | 13.9 | -   | 0.9 | TEM/EDS             | 14.0  |
| V-10Ti     | 77.1 | 13.6 | 9.4 | -   | SEM/EDS             | 15.0  |
| V-10Ti-1Ni | 77.0 | 13.7 | 8.7 | 0.7 | SEM/EDS             | 15.3  |

<sup>\*</sup> Scanning electron microscope or transmission electron microscope used to perform x-ray energy dispersive spectroscopy.

to the measured mean of 15.3%.

Typical EDS spectra from the scanning electron microscopy are shown in Figure 1, and clearly show the significant amount of Cr formed. Figure 2 shows that Cr tends to segregate at grain boundaries in the absence of Ni, but not to segregate in Ni's presence. Ni tends to segregate at grain boundaries, however.

#### 4. Discussion

Although Ni was added to enhance He production, a significant role of He on cavity nucleation is not evident. At this point, however, the He build-up was not very large (50 atppm), due to delay required to form <sup>59</sup>Ni from <sup>58</sup>Ni. The small sizes of the cavities are consistent with their invisibility on the fracture surface. Even more important, the extreme fragility seems to be associated with the presence of Ti rather than to the presence of either Ni and He. At this point, it is tempting to also preclude Cr as a cause of the embrittlement, since within 10%, the Cr levels

are all approximately equal in the four alloys. V-Cr binaries (Cr=5.0-14.1%) have been irradiated in FFTF to exposure levels ranging from 42 to 77 dpa at temperatures from 400 to 600 C in earlier studies, and did not exhibit such fragility [3].

The preferential polishing does appear to be associated with segregation of Cr, but the

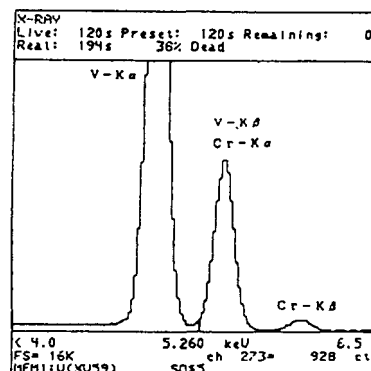


Figure 1. Typical EDS spectrum from V irradiated in HFIR to 17.7 dpa.

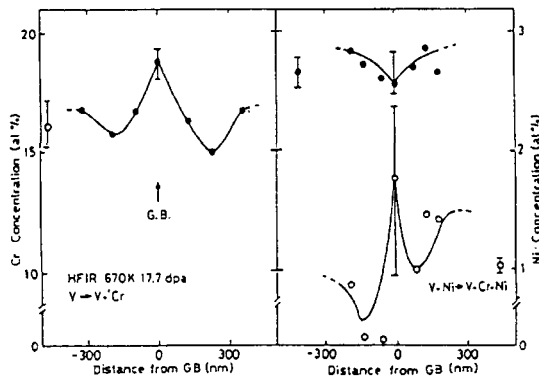


Figure 2. Segregation profile observed on grain boundaries of V and V-1Ni irradiated in HFIR.

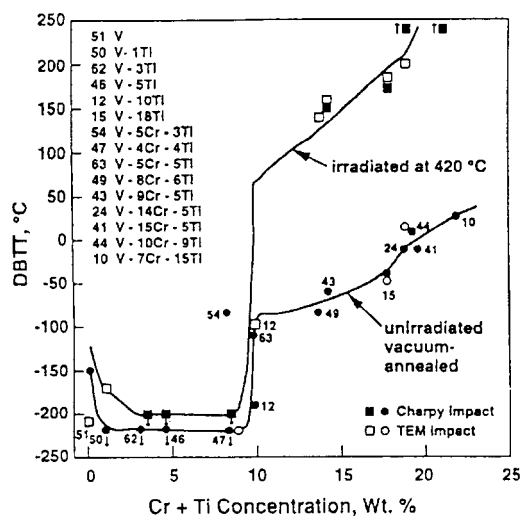


Figure 3. Change of DBTT after irradiation in FFTF [3].

presence of Ni alters Cr segregation at grain boundaries and presumably at other sinks such as dislocations, thereby also influencing the electro-polishing behavior.

While He derived from Ni appears to play no large or direct role on cavity structure or density change in V and V-1Ni, Ni addition appears to depress swelling somewhat in V-10Ti. The density change values should not be interpreted to result from cavity swelling alone, however, since Cr addition tends to increase the density of V alloys [3]. Thus the swelling of V-10Ti and V-10Ti-1Ni may actually be larger than inferred from the data in Table 1.

Ni additions tend to reduce the density of V alloys [3], but they also been shown to exert a strong direct role in alteration of radiation-induced microstructure in electron irradiation [4] and fast reactor irradiation [3], neither of which lead to significant generation of He.

It does appear, however, that the extreme embrittlement does arise from the transmutation of Cr, at least when it occurs in alloys containing significant levels of Ti. Loomis and coworkers [3] have shown that the ductile-to-brittle transition temperature (DBTT) of V-Ti binaries increases strongly for Ti concentrations greater than 5 wt% after fast reactor irradiation. (no significant transmutation) at 420°C to 34-44 dpa, but increases even more strongly V-Ti-Cr alloys for increasing Cr levels above 5% Cr. For (Cr+Ti) levels above 9%, the DBTT after irradiation increases 200°C or more, as shown in Figure 3. Since (Cr+Ti) level of broken specimens after irradiation is on the order of 25%, the DBTT of these specimens may be 250°C or greater. Note that even before irradiation, the DBTT of such high solute alloys is near room temperature.

As shown by Greenwood and Garner [2], however, the transmutation rates experienced by V in HFIR are more than an order of magnitude greater than those expected in fusion neutron spectra or that of liquid metal cooled fission reactors. Mori [5] has calculated that for the International Thermonuclear Experiment Reactor (ITER), transmutation of V to Cr would be less than 1% per year at any position on the first wall when operating at 2 MW/m<sup>2</sup>. Therefore, the extreme fragility exhibited by V-Ti alloys after irradiation in HFIR is completely atypical of the response that will occur in fusion and liquid metal reactors. Therefore, if fusion-relevant tests are to be successfully conducted in mixed spectrum reactors, the thermal component of the neutron flux must be reduced significantly by shielding the specimens with materials that are strong absorbers of low energy neutrons.

This experiment demonstrates once again that the possible influence of solid transmutation must be taken into account when designing and evaluating experiments which will be conducted in neutron spectra which are only surrogates for the spectrum of actual application. A summary of previously-cited situations where transmutation

was found to be an important concern is presented in other papers [1,2]. Also demonstrated in this experiment is the principle that the impact of elemental tailoring of alloys to study the effects of transmutant He is often overshadowed by the direct action of the tailoring agent itself.

## 5. Conclusion

The addition of Ni to V and V-10 Ti appears to influence swelling of these alloys when irradiated at 400°C in HFIR, but its action appears to be related to Ni's direct influence on microstructural evolution, rather than to its role as a source of He. He's role in determination of mechanical properties and embrittlement of V alloys in HFIR is also overshadowed by the influence of large levels of transmutant Cr formed (1%/dpa) during irradiation in HFIR. While increasing Cr levels tend to increase the DBTT, the increase is very strongly synergistic when Ti exists at significant levels in V alloys. The extreme embrittlement observed in this experiment resulting from Cr formation will not be representative of that expected in fusion neutron spectra, where the V-Cr transmutation rate per dpa will be lower than by more than an order of magnitude.

## References

- [1] F.A.Garner and L.R.Greenwood, Mater. Trans. Jap. Inst. Met., 34(1993)985.
- [2] L.R.Greenwood and F.A.Garner, J.Nucl. Mater., 212(1994)635.
- [3] B.A.Loomis et al., J. Nucl. Mater., 212(1994)799.
- [4] D.S.Gelles et al., J. Nucl. Mater., 191(1992)1336.
- [5] M.Mori, ITER/EDA Design Data JA93-JA0132.

## MECHANICAL PROPERTIES OF NEUTRON-IRRADIATED LOWER ACTIVATED Fe-Cr-Mn ALLOYS\*

H. Takahashi, S. Ohnuki and H. Kinoshita

Faculty of Engineering, Hokkaido University, Sapporo 060, Japan

(Received March 3, 1994)

Fe-Cr-Mn steels have been proposed as materials for structural components of the fusion reactor because of their lower radio-activity in comparison with SUS 316 austenitic stainless steels. Therefore, it is required to characterize the material with respect to its mechanical properties and microstructural changes during neutron irradiation for the doses and temperatures relevant for first wall condition. For these objectives, a series of Fe-Cr-Mn-(Al) steels with different compositions have been examined in tensile tests and by electron microscopy after neutron irradiation up to  $8 \times 10^{23}$  n/m<sup>2</sup> at 473 K. The 0.2% proof stress, ultimate tensile stress and total elongation were compared before and after irradiation. The results indicate that both Fe-10%Cr-(20-25)%Mn-3%Al and Fe-10%Cr-30%Mn steels show most radiation-resistant.

**KEYWORDS:** low activation, radiation hardening, defect cluster, alloying element, fusion reactor

### 1. Introduction

Manganese steels are candidate materials for structural components of fusion reactors because of their low induced long-term radioactivity compared to that of typical Fe-Cr-Ni austenitic steels<sup>1,2</sup>. However, recent studies on Fe-Cr-Mn steels have indicated that neutron irradiations at high temperature lead to both degradation of the mechanical properties and phase instabilities caused by manganese loss from the surface<sup>3,4</sup>. Commercial Fe-Cr-Mn steels have been developed for low-temperature non-magnetic structural materials. However, when these steels are used at high temperatures, oxidation resistance, mechanical properties and phase instabilities should be considered<sup>5-8</sup>. There have been some attempts to improve those properties by the addition of alloying elements. For example, the addition of aluminum can improve tensile properties and oxidation resistance of these steels<sup>9,10</sup>.

Recently, fusion devices have been designed to operate at relatively low temperatures and low neutron doses. There are not enough data on mechanical properties of Fe-Cr-Mn steels for these conditions.

The aim of this study is to find the optimum composition of Fe-Cr-Mn steels for irradiations at medium temperatures, and to study the effects of alloying elements and irradiation dose on the mechanical properties.

### 2. Experimental Procedure

Twenty four manganese steels were used in this experiment. Steels composed of (8-11)wt.%Cr, (5-25)wt.%Mn and (0-7)wt.%Al were mainly ferritic structures, and the compositions of (8-11)wt.%Cr, (2.5-10)wt.%Cr and (30-40)wt.%Mn, (0-1.1)wt.%C, (0-0.1)wt.%N were austenitic structures. Detailed chemical compositions have been reported in elsewhere<sup>9,10</sup>. Specimen dimensions are plates of 4 x 16 x 0.2 mm<sup>3</sup> for tensile test and disks of 3mm diameter for microscopic observation. After solution-annealing at 1323 K for 30min in vacuum condition, the specimens were irradiated in aluminum capsule filled with helium. Neutron irradiation was performed in JMTR (Japan Material Testing Reactor) at about 473 K to doses of 5, 11 and 80 x 10<sup>22</sup> n/m<sup>2</sup>. Several specimens of each alloy were assigned for tensile test under the strain rate of  $1.4 \times 10^{-3}$  /s at room temperature. Microstructural examinations were performed by a 200 keV TEM, and compositional analysis (EDS). Electropolishing proceeded using a conventional method employing an electrolyte solution of 5% HClO<sub>4</sub> in CH<sub>3</sub>COOH.

### 3. Results and Discussion

#### 3.1 Solute Concentration Dependence

From tensile test of unirradiated specimens, it has been confirmed that good mechanical properties have been achieved in Fe-10Cr-30Mn and Fe-10Cr-(15-

25)Mn-3Al for austenitic and ferritic steels, respectively. Especially, the addition of Al to manganese steels of Fe-XCr-YMn steels is effective for improving elongation, 0.2% proof stress and ultimate tensile stress (UTS) <sup>9)</sup>.

Figure 1 shows the dependence of manganese content on mechanical properties, 0.2% proof stress, UTS and total elongation, in austenitic Fe-XCr-YMn steels irradiated with different neutron doses. A large amount of elongation was especially shown in Fe-10Cr-30Mn steel even if the irradiation dose increased.

Figure 2 shows the dependence of aluminum content on mechanical properties in Fe-XCr-YMn-Al steels irradiated with different neutron doses. Reasonable elongation and stress were developed by the addition of aluminum until 3%, especially, a large elongation was shown in Fe-10Cr-15Mn-3Al steel even if the irradiation dose increased. Therefore, desirable aluminum content is about 3wt.% even in irradiation condition.

Radiation hardening can be defined as a difference in 0.2% proof stress before and after irradiation <sup>11)</sup>. Figure 3 shows manganese dependence on the radiation hardening in Fe-10Cr-XMn and Fe-10Cr-XMn-3Al steels. In the case of ferritic Fe-10Cr-XMn-3Al steels, radiation hardening increased with increasing of manganese content, which means that relatively lower manganese content could be desirable in the irradiated condition. However, in the case of austenitic Fe-10Cr-XMn steels, radiation hardening was not depend on the manganese content.

To clarify the details in the elongation behavior, the work hardening rate,  $n$ , was determined, as shown in figure 4 for both Fe-10Cr-XMn and Fe-10Cr-XMn-3Al which were unirradiated and irradiated to  $5 \times 10^{22}$  n/m<sup>2</sup>. In the case of Fe-10Cr-XMn, the rate showed a minimum value at middle of manganese content. In the case of Fe-10Cr-XMn-3Al steels, the rate increased a little at the middle of manganese content. In almost all alloys the work hardening rate decreased obviously comparing with that of unirradiated condition. It can be suggested that neutron irradiation to such low doses can reduce the work hardening, which means enhance the homogeneous elongation.

From those results, it is indicated that Fe-10Cr-(15-25)Mn-3Al and Fe-10Cr-30Mn steels, which have good mechanical

properties at unirradiated condition, have desirable properties even if after neutron irradiation.

### 3.2 Dose Dependence

Figure 5 shows neutron dose dependence of mechanical properties in Fe-10Cr-30Mn austenitic steel. With increasing of dose, the proof stress and UTS increased slightly. The elongation decreased, but it showed obviously a saturation at high dose.

Figure 6 shows the dose dependence of mechanical properties in Fe-10Cr-15Mn-3Al ferritic steel. Both proof stress and UTS increased almost linear with the dose, but they showed relatively higher values in comparison with austenitic steels. The elongation decreased with dose until a saturation was reached, though it had relatively lower values in comparison with austenitic steels. Comparing other steels such as 316 steels irradiated to low doses, the yield stress of these Fe-Cr-Mn steels was almost the same or less (12,13).

### 3.3 Radiation Hardening

Radiation hardening can be explained by small sized defect clusters, which act as obstacles for dislocation motion <sup>11)</sup>. In this experiment, small sized cluster formation was confirmed in several steels by means of dark-field images of transmission electron microscopy. The radiation hardening is expressed by the following relation,

$$\Delta\sigma_{0.2} = \alpha\mu b(Nd)^{1/2},$$

where  $\Delta\sigma$  : stress increase,  $\alpha$  : strength factor for the obstacles,  $\mu$  : shear modulus,  $b$  : Burgers vector,  $N$  : number density of defect cluster,  $d$  : mean size of defect cluster.

Figure 7 shows the relation between the increment of proof stress and  $(Nd)^{1/2}$  after irradiation of various steels to two levels of neutron doses of  $5 \times 10^{22}$  (solid symbols) and  $1.1 \times 10^{23}$  n/m<sup>2</sup> (open symbols). The slope of the line from origin lay between 0.11 and 0.24. The highest value is mainly for low manganese steels and high manganese steels with high carbon and nitrogen, and the value tends to decrease with increasing irradiation doses. This means that when the hardening is due to defect clusters which act as obstacles of dislocation motion, the strength of defect clusters could decrease with increasing irradiation doses as a result of

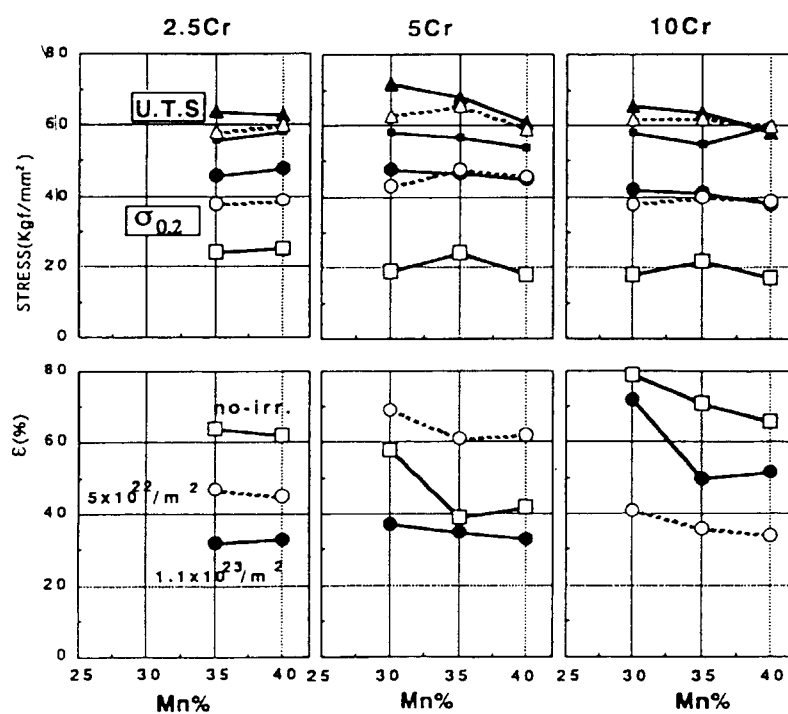


Figure 1. Influence of manganese content on mechanical properties, 0.2% proof stress, UTS and total elongation in austenitic Fe-XCr-YMn steels irradiated with different neutron doses at 473 K.

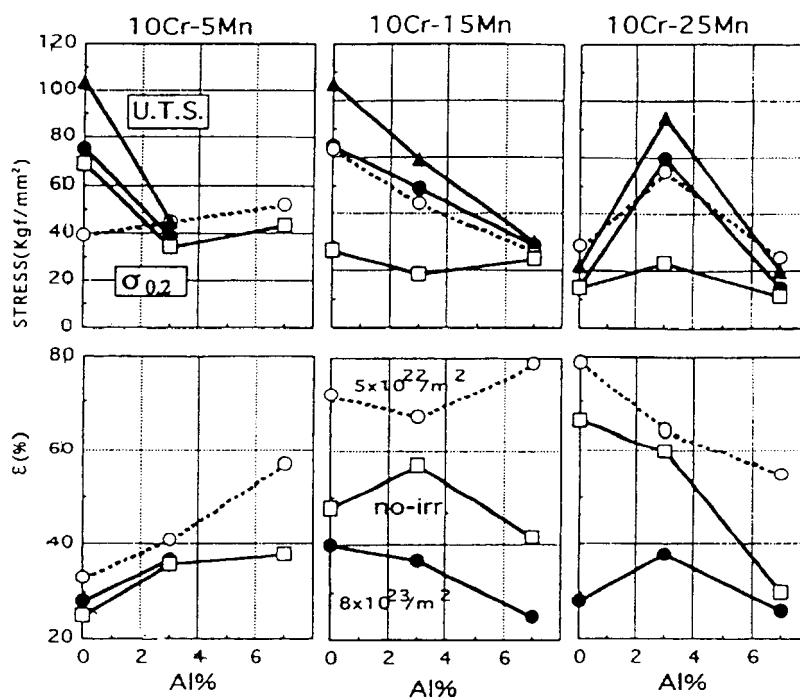


Figure 2. Influence of aluminum content on mechanical properties, 0.2% proof stress, UTS and total elongation in ferritic Fe-XCr-YMn-Al steels irradiated with different neutron doses at 473 K.

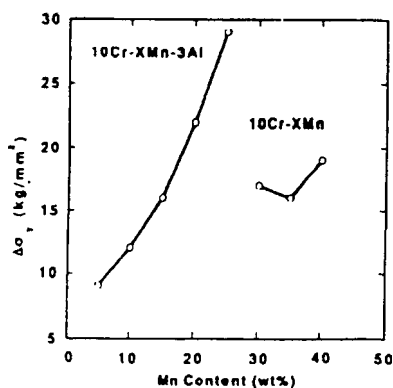


Figure 3. Radiation-hardening as a function of manganese content in Fe-10Cr-xMn and Fe-10Cr-xMn-3Al steels irradiated at 473 K.

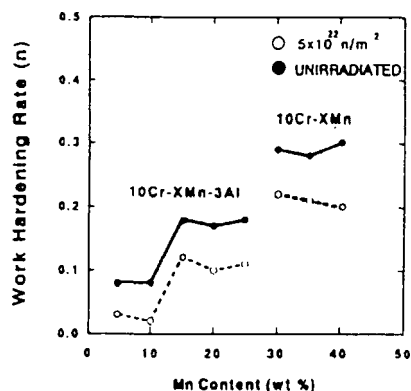


Figure 4. Work hardening rate as a function of manganese content in Fe-10Cr-xMn and Fe-10Cr-xMn-3Al steels irradiated at 473K.

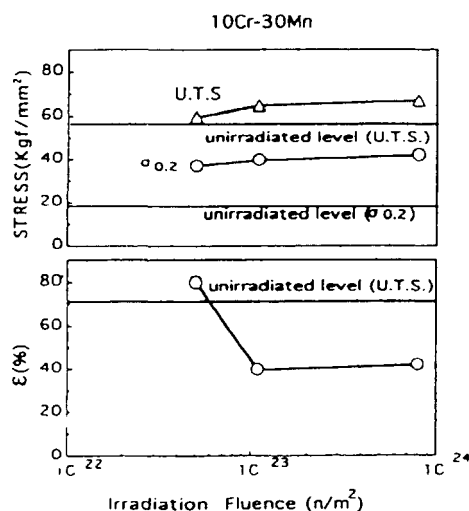


Figure 5. Influence of neutron dose on yield stress, UTS and elongation in Fe-10Cr-30Mn steel.

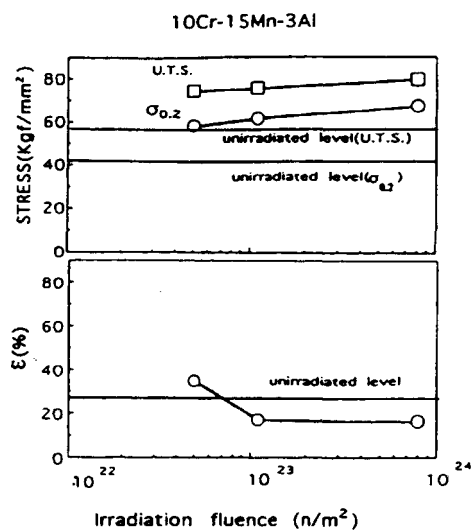


Figure 6. Influence of neutron dose on yield stress, UTS and elongation in Fe-10Cr-15Mn-3Al steel.

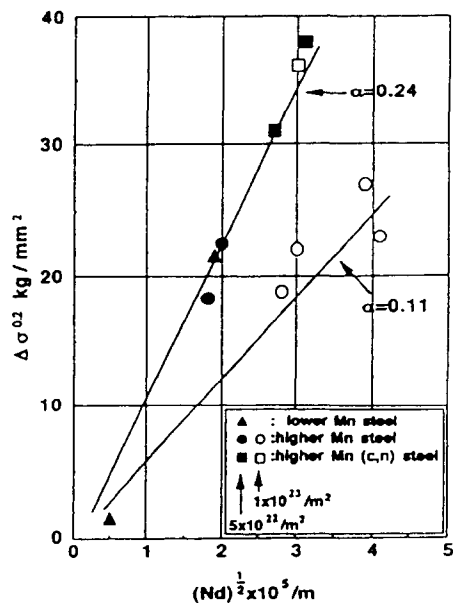


Figure 7. Relation between radiation-hardening and  $(Nd)^{1/2}$  for defect cluster in various steels irradiated at 473 K.

reduction in interstitial impurities such as carbon and nitrogen atoms. Therefore, the fraction of trapped impurities could reduce with increasing of clusters at higher irradiation doses.

In the case of aluminum added steels, the micrographs showed that the size and number density of defect clusters were smaller than in Fe-10Cr-30Mn. This means that aluminum solute could reduce the concentration of free point defects due to defect trapping which enhances the

recombination. Therefore, the defect cluster concentration is reduced.

#### Conclusion

The 0.2% proof stress, ultimate tensile stress and total elongation were measured before and after irradiation to relatively low doses at 473 K. The best results were obtained for compositions of Fe-10%Cr-30%Mn and Fe-10%Cr-(20-25)%Mn-3%Al. The strength of Cr-Mn-(Al) steels was comparable to that of 316 steels even after the irradiation. Radiation hardening can be explained by the increase in strength due to defect cluster formation, which is enhanced by interstitial impurities. The addition of small amount of aluminum to Fe-10Cr-15Mn steels has two effects, a phase instability and a reduction in the defect cluster formation.

#### Acknowledgment

The authors wish to acknowledge Prof. H. Kayano, and Mr. Narui in Oarai branch of Tohoku University for useful discussions, and also thank Mr. A. Yonezawa and S. Watanabe of Hokkaido University for helpful assistance in this experimental work.

#### References

- 1) D.G.Doran, H.L.Heinisch and F.M.Mann: J. Nucl. Mater., 133-134(1985),892.
- 2) F.A.Garner, F.Abe and T.Noda: J. Nucl. Mater., 155-157(1988), 870.
- 3) J.M.McCarthy and F.A.Garner: J. Nucl. Mater., 155-157(1988), 877.
- 4) F.A.Garner and J.M.McCarthy: Reduced Activation Materials for Fusion Reactors, ASTM STP 1047, ed. R.L.Klueh, D.S.Gelles, M.Okada and N.H.Packan, American Society for Testing and Materials, Philadelphia, PA, (1990), p.19.
- 5) Y.Okazaki, M.Mochizuki, K.Miyahara and Y.Hosoi: Reduced Activation Materials for Fusion Reactors, ASTM STP 1047, ed. R.L.Klueh, D.S.Gelles, M.Okada and N.H.Packan, American Society for Testing and Materials, Philadelphia, PA, (1990), p.80.
- 6) N.Yukawa, M.Morinaga, K.Nishiyama, Y.Matsumoto, Y.Murata and H.Ezaki: Reduced Activation Materials for Fusion Reactors, ASTM STP 1047, ed. R.L.Klueh, D.S.Gelles, M.Okada and N.H.Packan, American Society for Testing and Materials, Philadelphia, PA, (1990), p.30.
- 7) W.Schule, E.Lang and A.Panzarasa: Report EUR 11756 EN, (1988).
- 8) J.I.Cole, D.S.Gelles and J.J.Hoyt: J. Nucl. Mater., 191-194 (1992),657.
- 9) H.Takahashi and S.Ohnuki, Proc. High Manganese Austenitic Steels, Chicago, ASM International, (1993), p.161.
- 10) H.Takahashi, K.Shiba, S.Nakahigashigshi, S.Ohnuki, H.Kinoshita and F.A.Garner: Reduced Activation Materials for Fusion Reactors, ASTM STP 1047, ed. R.L.Klueh, D.S.Gelles, M.Okada and N.H.Packan, American Society for Testing and Materials, Philadelphia, PA, (1990),p.93.
- 11) J.Moteff, D.J.Mutual and V.K.Sikka, Defect and Defect Clusters in BCC Metals and Their Alloys, ed. by R.J.Arsennault, ASM (1973) p.198-215.
- 12) H.L.Heinisch, S.D.Atkin and C.Martinez, J. Nucl. Mater., 141-143 (1986) 807-815.
- 13) H.L.Heinisch, M.L.Hamilton, W.F.Sommer and P.D.Ferguson, J. Nucl. Mater., 191-194 (1992) 1177-1182.





Letter to the Editors

Concentration dependence of radiation-induced segregation  
in Fe–Cr–Ni alloy

S. Watanabe, H. Kinoshita, N. Sakaguchi, H. Takahashi

*Ultra-Functional Materials Laboratory, Center for Advanced Research of Energy Technology, Hokkaido University, Kita-ku, Kita-13,  
Nishi-8, Sapporo 060, Japan*

Received 22 April 1994; accepted 7 September 1995

In a previous paper [1], we reported, through theoretical study, that the initial concentration of the alloy component in Fe–Cr–Ni may significantly influence the radiation-induced segregation (RIS). It can also be qualitatively understood in terms of the discriminant which is a function of intrinsic diffusivities and initial concentration of the alloy elements [2]. In this Letter we will show an experimental indication for the concentration dependence on RIS at the grain boundary in Fe–15Cr–(15–40)Ni due to electron irradiation by HVEM. We believe that the present study will reinforce the previous theoretical prediction. The peculiarity in the dependence of elemental concentration of the less diffusivity (Ni diffusion via vacancy mechanism in Fe–Cr–Ni) is thought universal in the RIS in multi-component alloys.

Specimens of Fe–15Cr– $x$ Ni ( $x = 15, 20, 25, 30, 35, 40$ ) alloys with impurity levels of 0.003 C and 0.0011 N (in wt%) were used. After heat treatment at 1273 K for 30 min, the specimens were irradiated up to 7.2 dpa at 723 K with 1 MeV electrons using a high voltage electron microscope. The mean damage rate was  $2.0 \times 10^{-3}$  dpa/s. After irradiation, the chemical composition was determined using a 200 kV transmission electron microscope (JEOL-2000FX) equipped with an energy dispersive X-ray (EDS) analyzer.

Fig. 1 shows the dependence of concentration of alloy elements on segregation amount *at the grain boundary*, fixing the initial Cr concentration to 15 wt% and varying Ni concentration in Fe–15Cr– $x$ Ni alloy. The ordinate,  $\Delta C$ , is the difference between the initial (bulk) concentration and that after irradiation at the grain boundary. The lines indicate theoretical results. We performed the calculation by solving the coupled

rate equations one-dimensionally for concentrations,  $C$ 's, at a time at positions with the appropriate divisions and did so up to the time corresponding to the dose irradiated [1]. In the present calculation we used  $\alpha = 1$ , as the ideal solution condition, and  $\eta = 1.0$ , as the damage efficiency of the electron irradiation at a damage rate of  $2 \times 10^{-3}$  dpa/s and at 723 K. The probe size of 20 nm in diameter for the EDS analysis is, further, assumed [1]. For the other parameters we adopt ones seen in literature [3,4].

A remarkable point is that in Fig. 1 peaks of segregation have been seen in the concentration dependence: Ni lines have maxima and inversely Fe lines have minima at about 30 wt% of the abscissa in the figure. We simulated also (without averaging [1]), in Fig. 2, the dependence of segregation amount at a grain boundary on alloy composition at various doses up to steady state. In Fig. 2 peaks of segregation can also be seen: Ni lines have maxima and inversely Fe lines have minima at an initial Ni concentration of about 20 wt%. Moreover, the peak, in this case, slightly shifts to the lower initial Ni concentration region of the abscissa as the dose is increased. However, the emergence of the peaks could not be seen in Fig. 3, which is the case of varying Cr alloy content and fixing the initial Ni concentration to 20 wt% in the Fe–Cr–Ni alloy at the same irradiation condition.

The above results mean that the fraction of Ni atoms contributing to the segregation decreases as solute Ni concentration increases, while not so for solute Cr. This comes from whether the solute enriches or depletes. Since in the RIS process the fraction of enriched Ni atoms contributing to the segregation at a grain boundary becomes larger when the fraction of

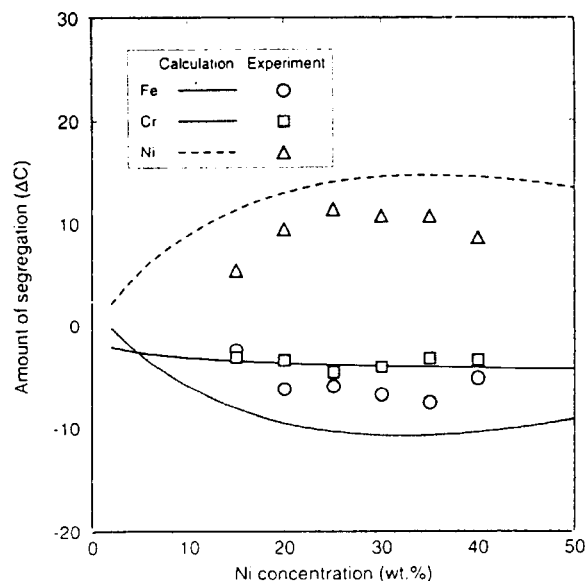


Fig. 1. Concentration dependence of RIS at the grain boundary in Fe-15Cr- $x$ Ni alloy irradiated to 7.2 dpa at 723 K. The initial Cr concentration fixed to 15 wt% and  $\Delta C = C_{G.B.} - C_{Bulk}$ . The theoretical results are indicated by lines, while experimental ones by unfilled characters.

the initial composition is low and, on the contrary, becomes smaller when the initial composition is high, the segregation amount itself thus shows a maximum somewhere in the composition. This is comparative to the fact that a monotonically decreasing function – of

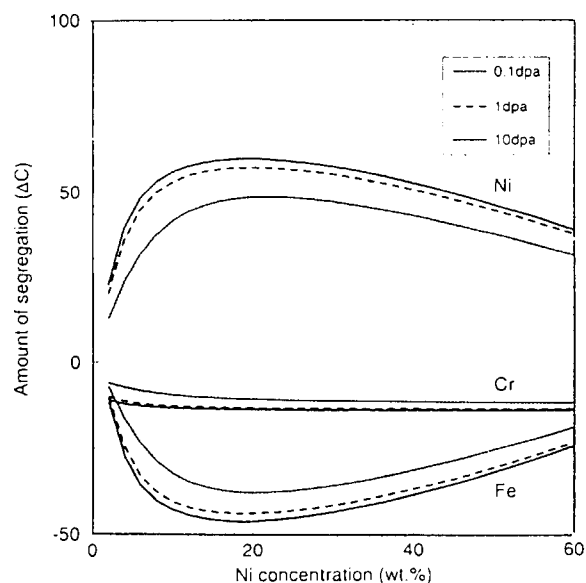


Fig. 2. Concentration dependence of RIS at grain boundary in Fe-15Cr- $x$ Ni alloy after irradiation to various doses at 723 K. The initial Cr concentration was fixed to 15 wt%.

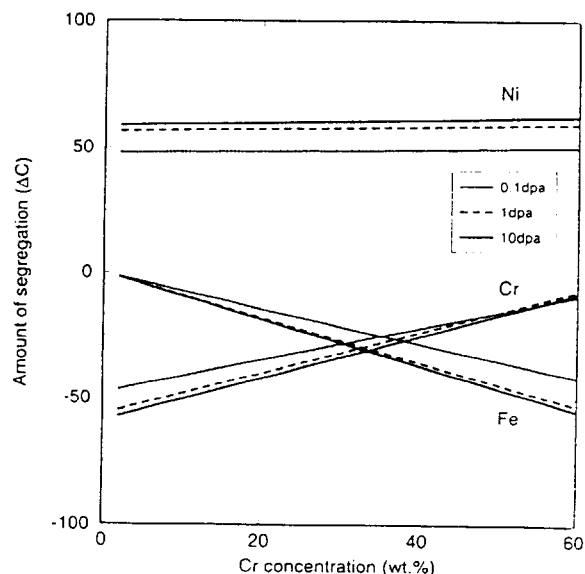


Fig. 3. Concentration dependence of RIS at the grain boundary in Fe- $x$ Cr-20Ni alloy after irradiation to various dose at 723 K. The initial Ni concentration was fixed to 20 wt%.

the fractional segregation amount:  $\Delta C/C_{bulk}$ , multiplied by a linearly increased function – of concentration of the element:  $C_{bulk}$ , gives a salient function. (See Fig. 12 in Ref. [1] for more detail and notice that the temperature is 773 K in that case.) Trivially, for Cr, as in Fig. 3 this does not hold because Cr in the Fe-Cr-Ni alloy is a depletion element in the system. We have reported the similar emergence of a peak in concentration dependence, predicted from a discriminant consideration in Ref. [2] (Table 1).

In concluding remarks, we have studied the concentration dependence of solute elements, Ni and Cr, upon radiation-induced segregation at grain boundaries in the Fe-Cr-Ni alloy system, and evidenced a peculiarity of concentration dependence for the solute Ni. Although further experimental confirmation is necessary, especially, for the Cr variation case, this work might suggest that we should include the initial concentration of the alloy as an important physical factor in the course of the RIS study.

## References

- [1] S. Watanabe, N. Sakaguchi, N. Hashimoto and H. Takahashi, *J. Nucl. Mater.* 224 (1995) 158.
- [2] S. Watanabe and H. Takahashi, *J. Nucl. Mater.* 208 (1994) 191.
- [3] A.D. Marwick, *J. Nucl. Mater.* 135 (1985) 68.
- [4] A.M. Yaout, N.Q. Lam and J.F. Stubbs, *Nucl. Instr. and Meth. B42* (1989) 49.

## Quantitative studies of irradiation-induced segregation and grain boundary migration in Fe–Cr–Ni alloy

S. Watanabe, N. Sakaguchi, N. Hashimoto, H. Takahashi

*Ultra-Functional Materials Laboratory, Center for Advanced Research of Energy Technology, Hokkaido University, Kita-ku, Kita-13, Nishi-8, Sapporo 060, Japan*

Received 6 October 1994; accepted 9 March 1995

### Abstract

An irradiation-induced phenomenon was studied on account of solute segregation and concurrent grain boundary migration in a model Fe–Cr–Ni alloy during electron irradiation with a high voltage electron microscope (1000 kV) and also by computer simulation. The calculation was conducted by solving the coupled rate equations for solute and defect concentrations, which involve the Kirkendall effects at a grain boundary sink, so that the solute redistribution profiles experimentally obtained were quantitatively explained. We also extensively studied the effects of the probe size in the EDS analysis on composition profiles, the Gibbsian segregation in the vicinity of a grain boundary and the discriminant of segregation under irradiation, as well as other important factors that influence the phenomenon.

### 1. Introduction

Irradiation with energetic particles generates solute redistribution in a concentrated alloy because of the preferential interaction between the solute atoms and the induced super-saturated point defects moving toward sinks, such as a surface or a grain boundary. It has been known that radiation-induced segregation (RIS) near grain boundaries and radiation-induced grain boundary migration might cause a significant deleterious effect upon their physical, chemical and/or mechanical properties [1,2] in alloys such as, e.g., a type 316 stainless steel, which have been considered as the primary candidate for structural materials in fusion reactors and which are used as light-water reactor core components [3,4]. It is thus demanded to investigate the mechanism for retardation of radiation-induced solute redistribution [5,6] and behavior of concurrent grain boundary migration [7–10] under irradiation.

It was already known at the end of 1950s that reactor irradiation produced lattice vacancies and interstitial atoms and that radiation-enhanced diffusion could cause instability in reactor materials [11]. Noticeable experimental and theoretical studies on RIS

started in the early '70. Johnson and Lam [12], Okamoto and Wiedersich [13,14], and, independently later, Marwick [15] and Perks et al. [16] extensively studied RIS near alloy surfaces. Recently, RIS in the vicinity of the grain boundary has been of interest [6,17], because of the problem of the irradiation-assisted stress corrosion cracking (IASCC), which promotes the cracking susceptibility in irradiated stainless steels.

In this paper we shall first review recent studies on the irradiation-induced grain boundary migration with segregation in an Fe–Ni–Cr alloy during electron irradiation, which was studied by in-situ observation with a high voltage electron microscope (1MV) [9] and by computer simulation [10,18,19]. Solute segregation and simultaneous grain boundary migration are discussed in a consistent manner based upon the point defect flow. To clarify and confirm the correctness of our physical interpretation of the problem, a model calculation involving coupled rate equations for solute and point defect concentrations has been carried out [6,10]. We shall also extensively discuss, in this paper, the effects of the probe size in the energy-dispersive X-ray spectrometer (EDS) analysis for composition profiles [20], the Gibbsian segregation in the vicinity of grain

boundary [21,22] and the discriminant of segregation under irradiation [6] as well as some other important factors related to the phenomenon.

## 2. Experimental procedure

Specimens of an Fe-Ni-Cr alloy containing 20.1 Ni, 15.2 Cr and, as impurities, 0.003 C and 0.0011 N (in wt%) were used. After heat treatment at 1273 K for 30 min, the specimens were irradiated with 1 MeV electrons in the temperature range from 743 to 803 K using a high voltage electron microscope. The mean damage rate was  $5.0 \times 10^{-4}$  dpa/s. After irradiation, the chemical composition was determined using a 200 kV transmission electron microscope (JEOL-2000FX) equipped with an energy dispersive X-ray analyzer. The directions of irradiation were mainly  $\langle 110 \rangle$ ,  $\langle 122 \rangle$  and  $\langle 123 \rangle$  [9].

## 3. Experimental results

### 3.1. Grain boundary migration during irradiation

The typical microstructures observed during irradiation of regions near a grain boundary were as follows. Under irradiation, the formation of defect clusters such as dislocation loops occurred initially in the matrix and voids were nucleated substantially. The formation of defect clusters near a grain boundary occurred at a lower rate, i.e., dislocation density and number density of voids were lower in a case where grain

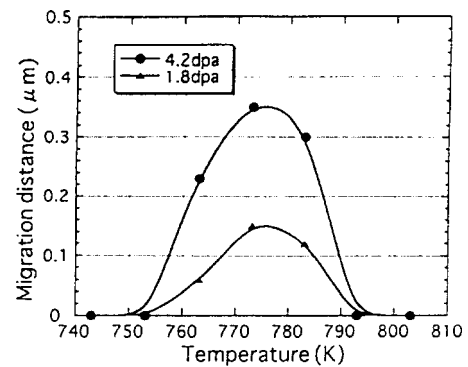


Fig. 1. Temperature dependence of the grain boundary migration distance by electron irradiation [9].

boundary migration took place. Some grain boundaries in the irradiated region migrated but no grain boundary migration occurred in the unirradiated area. Fig. 1 shows the temperature dependence of the migration distance. Similar microstructures were observed at those irradiation temperatures. Grain boundary migration was observed during irradiation at temperatures from 763 to 783 K. The occurrence of a grain boundary migration seems to depend on the orientation of the boundary interfaces. The migration did not occur in the case of symmetrical grain boundaries, while asymmetrical boundaries migrated remarkably, and the migration occurred predominantly in the direction perpendicular to the close packed planes [9]. Boundary migration began before the formation of voids and continued even after the void nucleation.

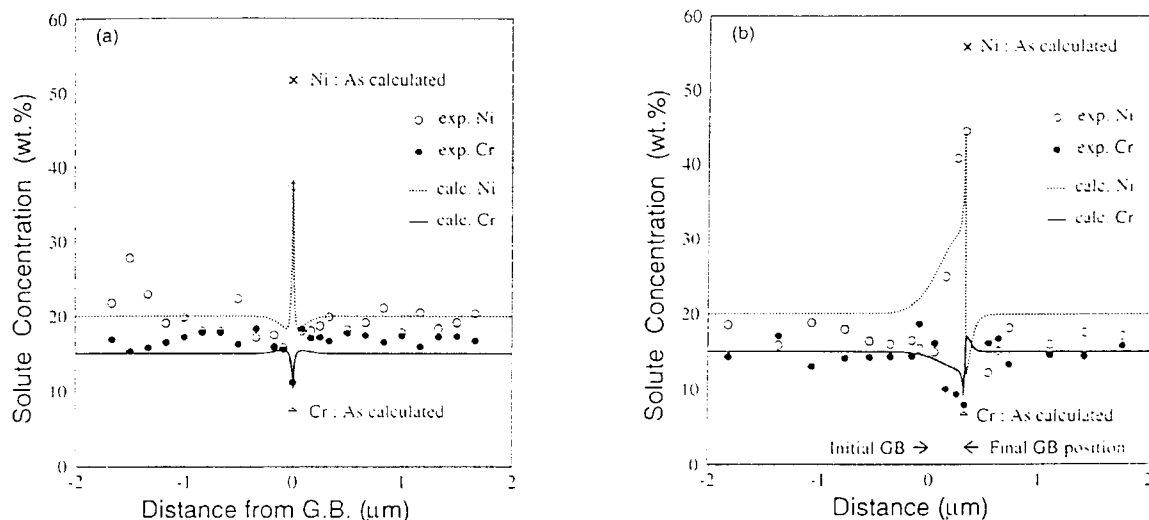


Fig. 2. Solute concentration profiles [9] in Fe-15Cr-20Ni alloy after electron irradiation to 4.2 dpa; (a) at 793 K, (b) at 773 K. Grain boundary migration occurred in (b). Lines are simulation results (averaged by two-dimensional Gaussian formula (S)).

### 3.2. With solute segregation near grain boundary

After irradiation of a region near a grain boundary, the solute concentration near a grain boundary was measured with a 200 kV TEM-EDS instrument. Nickel enrichment and chromium depletion took place at all the temperatures examined. Concentration changes were prominent at 773 and 783 K. The amount of segregation increased almost linearly with the migration distance [9]. Therefore, the solute concentration seemed to change during the migration process. This tendency was more remarkable for nickel than for chromium.

Figs. 2a and 2b show, by dots, typical concentration profiles of nickel and chromium after irradiation to 4.2 dpa. In Fig. 2b the grain boundary migration is accompanied by solute segregation. The boundary positions before and after irradiation are indicated. In general, nickel enrichment and chromium depletion were observed in the grain boundary region. Outside the area of nickel enrichment and chromium depletion, nickel depletion and chromium enrichment were observed. It was also recognized that, at lower temperatures, the solute concentration changes occurred only in the vicinity of the last position of the migrated boundary. This indicates that solute redistribution took place at the migrating boundary. The opposite concentration changes of chromium and nickel outside the region swept by the migrating boundary were large at the lower irradiation temperatures.

The lines in Fig. 2 are results of computer simulation. In the next section we shall theoretically reconsider the observed RIS effect and grain boundary migration. Before discussing the details, we shall first

briefly review the theory and the basic rate equations we used for the simulation.

## 4. Computer simulation and comparison with experimental results

### 4.1 Theory and simulation method

Radiation-induced phenomena have their origin in the coupling between the fluxes of defects and of solute elements. Those defects which are mobile and escape recombination are reincorporated into sinks such as surfaces or grain boundaries. The defect flow in an initially homogeneous alloy then causes enrichment or depletion of the alloying elements in the vicinity of those defect sinks. The concentration gradients induce back diffusion of the segregating elements, and a quasi-steady state may be set up during irradiation whenever the defect-driven solute fluxes are balanced by the back diffusion. On this account, the diffusion process is important because differences in the diffusivities of the components of the alloy drive the solute redistribution. The approach [14,15] is to solve the coupled diffusion equations for vacancies, interstitials and solute atoms to provide the terms which couple the defect and atom fluxes. Solute redistribution near a sink can affect the diffusion of defects to the sink, due to so-called the inverse Kirkendall effect.

The continuity equations we used for the quantities of interest are

$$\frac{dC_{\kappa}}{dt} = -\Omega \nabla \cdot J_{\kappa}, \quad (1)$$

Table 1  
Main parameters used in the present calculation

| Parameter                                  | Notation            | Value                                               | Reference |
|--------------------------------------------|---------------------|-----------------------------------------------------|-----------|
| Vacancy jump rate via Fe atoms             | $\nu_{\text{Fe-v}}$ | $2.5 \times 10^{13}/\text{s}$                       | [15]      |
| Vacancy jump rate via Cr atoms             | $\nu_{\text{Cr-v}}$ | $3.5 \times 10^{13}/\text{s}$                       | [15]      |
| Vacancy jump rate via Ni atoms             | $\nu_{\text{Ni-v}}$ | $1.5 \times 10^{13}/\text{s}$                       | [15]      |
| Interstitial jump rate                     | $\nu_i$             | $5.0 \times 10^{12}/\text{s}$                       | [21]      |
| Vacancy migration energy                   | $E_v^m$             | 1.2 eV                                              | [assumed] |
| Interstitial migration energy via Fe atoms | $E_{\text{Fe-i}}^m$ | 0.3 eV                                              | [21]      |
| Interstitial migration energy via Cr atoms | $E_{\text{Cr-i}}^m$ | 0.3 eV                                              | [21]      |
| Interstitial migration energy via Ni atoms | $E_{\text{Ni-i}}^m$ | 0.9 eV                                              | [21]      |
| Ni-interstitial binding energy             | $E_{\text{Ni}}^b$   | 0.75 eV                                             | [assumed] |
| Formation enthalpy of vacancy              | $E_v^f$             | 1.4 eV                                              | [15]      |
| Formation enthalpy of interstitial         | $E_i^f$             | 4.0 eV                                              | [21]      |
| Formation entropy of vacancy               | $S_v^f$             | 5k                                                  | [21]      |
| Formation entropy of interstitial          | $S_i^f$             | 0                                                   | [21]      |
| Unit cell size                             | $\lambda$           | $3.52 \times 10^{-10}$ m                            | [21]      |
| Internal dislocation density               | $\rho_d$            | $\sim 1.0 \times 10^{14} \text{ m}^{-2}$ (at 773 K) | [assumed] |
| Damage efficiency                          | $\eta$              | 1.0                                                 | [assumed] |

(K denotes elements A, B and C; i.e., Fe, Cr and Ni)

$$\frac{dC_v}{dt} = -\nabla \cdot J_v + \eta K_0 - RC_v C_i - K_{vs} C_s (C_v - C_v^0), \quad (2)$$

$$\frac{dC_i}{dt} = -\nabla \cdot J_i + \eta K_0 - RC_v C_i - K_{is} C_s (C_i - C_i^0), \quad (3)$$

$C_v$  and  $C_i$  are the concentration of vacancies and interstitials, and  $C_v^0$  and  $C_i^0$  are the bulk equilibrium defect concentrations, respectively.

The fluxes,  $J$ , of the three elements (A, B and C) and the two defects (v and i) are of the form

$$\begin{aligned} \Omega J_A &= -D_A \alpha \nabla C_A + d_{Av} C_A \nabla C_v - d_{Ai} C_A \nabla C_i, \\ \Omega J_B &= -D_B \alpha \nabla C_B + d_{Bv} C_B \nabla C_v - d_{Bi} C_B \nabla C_i, \\ \Omega J_C &= -D_C \alpha \nabla C_C + d_{Cv} C_C \nabla C_v - d_{Ci} C_C \nabla C_i, \\ \Omega J_i &= -(d_{Ai} - d_{Ci}) C_i \alpha \nabla C_A - (d_{Bi} - d_{Ci}) C_i \alpha \nabla C_B \\ &\quad - D_i \nabla C_i, \\ \Omega J_v &= (d_{Av} - d_{Cv}) C_v \alpha \nabla C_A + (d_{Bv} - d_{Cv}) C_v \alpha \nabla C_B \\ &\quad - D_v \nabla C_v, \end{aligned} \quad (4)$$

where  $\Omega$ ,  $K_0$ ,  $R$ ,  $\alpha$  and  $K_{vs}$  are the atomic volume, the damage rate, the recombination coefficient, the thermodynamic factor and the internal sink (voids and dislocations) strength coefficient, respectively.

The total diffusivities,  $D$ , and intrinsic diffusivities,  $d$ , are of the form

$$D_A = d_{Av} C_v + d_{Ai} C_i,$$

$$D_v = (d_{Av} + d_{Bv} + d_{Cv}) C_v, \text{ etc.},$$

and

$$d_{\kappa j} = \lambda^2 Z_j \gamma_{j\kappa} / 6$$

with defect ( $j$ ) and solute ( $\kappa$ ) pair jump frequency,  $\nu_{j\kappa} = \nu_{j\kappa}^0 \exp(-E_{j\kappa}^m/kT)$ . Here  $Z$  and  $\lambda$  are the recombination site number and the unit size as a jump distance. The migration energies,  $E_{j\kappa}^m$ , are entered in the partial diffusivity through the Boltzmann factor.

With the appropriate physical parameters in Table 1 for an austenitic Fe–Cr–Ni alloy, and with the boundary conditions:

$$C_v^0 = \exp(S_v^f/k) \exp(-E_v^f/kT),$$

and

$$C_i^0 = \exp(S_i^f/k) \exp(-E_i^f/kT),$$

at the grain boundary, and  $J=0$ , deep in the bulk ( $\sim 10 \mu\text{m}$ ) where  $S_{v,i}^f$  and  $E_{v,i}^f$  are the defect formation entropy and energy, respectively, we solved the one-dimensional Eqs. (1)–(3) for  $C$  numerically as a function of position up to the time corresponding to the dose irradiated. In the actual calculation we used  $\alpha=1$  (ideal solution condition) and  $\eta=1.0$  for the damage

efficiency of the electron irradiation. For the other parameters we adopt ones seen in the literature [15,21]. Since our model alloy is relatively pure, the actual migration energies might be smaller.

The calculations were performed to evaluate concentration profiles one-dimensionally, as a function of time, for various experimental parameters: temperature, production rate, internal sink concentration and solute concentration, etc. The LSODE package of subroutines [24] was used for the numerical integration of the rate equations. In addition, we considered spatial resolution by means of averaging the calculated concentration profile with an appropriate EDS probe size [20]. The latter technique, as we shall discuss in a later section (Section 5.3), is of importance for simulating the actual profile data taken by TEM-EDS analysis.

#### 4.2. Grain boundary migration and segregation

Typical theoretical results on segregation without grain boundary migration are shown by lines in Fig. 2a and with boundary migration, in Fig. 2b. For the calculation of the segregation profile at the migrating boundary we forcibly moved the grain boundary at each time step so that the final grain boundary position coincided to the experimental results ( $\sim 0.36 \mu\text{m}$ ) and that the total sample thickness was kept constant. Fig. 3 shows the grain migration distance versus the time. Obtaining the composition profiles, which are hereafter indicated by “As calculated”, we averaged them by the two dimensional Gaussian average (Eq. (8)) with appropriate choices of parameters of the probe size and the deviation constant. (The probe radius is 10 nm

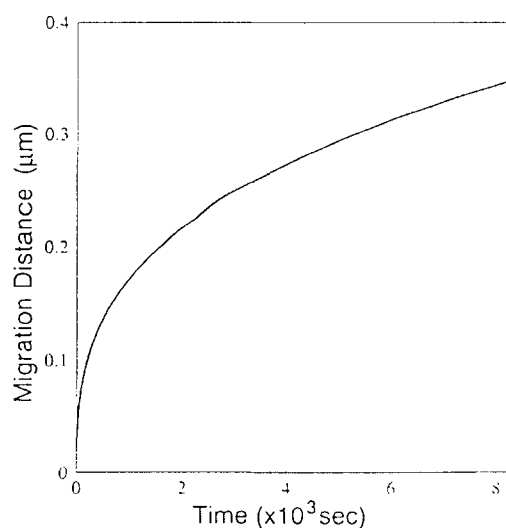


Fig. 3. Time dependence of grain boundary migration used in the simulation.

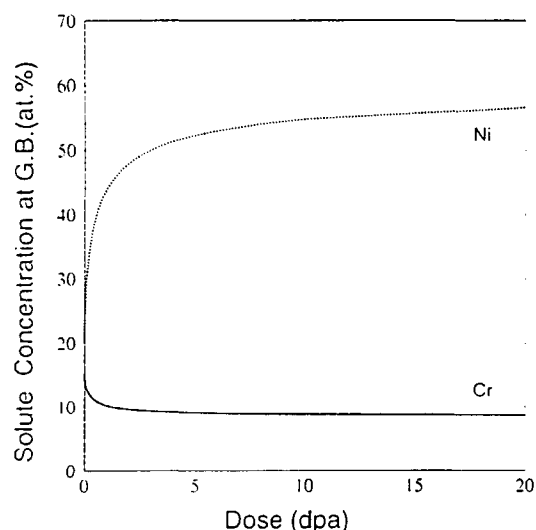


Fig. 4. Calculated dose dependence of solute concentration at a grain boundary in an Fe-15Cr-20Ni (at%) alloy irradiated at  $1 \times 10^{-3}$  dpa s $^{-1}$ , 773 K (without averaging).

and the deviation constant is  $1 \times 10^{-2}$  nm $^{-2}$  in Fig. 2.) From Fig. 2b it is evident that the profile is not symmetric with respect to the grain boundary and that the segregation effect is more pronounced behind the migrating boundary than ahead of it. Disregarding the

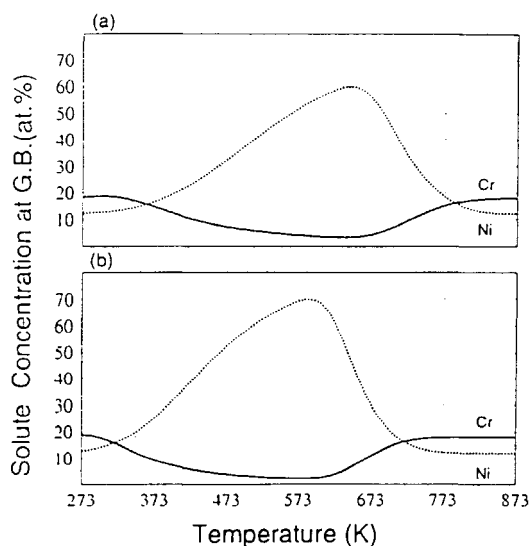


Fig. 5. Calculated temperature dependences of solute concentration at a grain boundary in Fe-18Cr-12Ni alloy irradiated to 3 dpa; (a) at  $1 \times 10^{-3}$  dpa s $^{-1}$ , (b) at  $1 \times 10^{-5}$  dpa s $^{-1}$ .

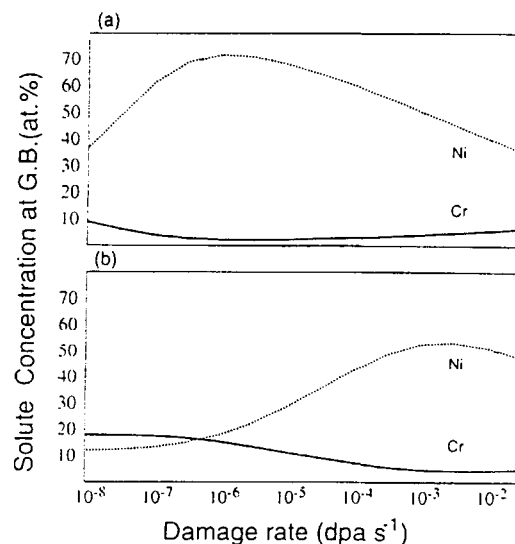


Fig. 6. Calculated damage rate dependences of solute concentration at a grain boundary in Fe-18Cr-12Ni (at%) alloy irradiated to 3 dpa; (a) at 573 K, (b) at 673 K.

details, the overall agreement between the theory and the experiment is remarkably good.

## 5. Discussion

### 5.1. Dose, temperature and damage rate dependences on RIS

In this section we discuss, with simulated results, the effects of main irradiation parameters: dose, temperature and damage rate, on RIS at a grain boundary. Firstly, the dose dependence of RIS is shown in Fig. 4 for an austenitic stainless alloy. The solutes of Ni and Cr at a grain boundary segregate rapidly at a low dose and the segregation increases as dose increases. Segregation of Ni is more pronounced than that of Cr. We show the temperature dependence of RIS at a dose of 3 dpa in Fig. 5 and damage rate dependence in Fig. 6. The cusps or peaks are seen in the both figures and they shift from condition to condition. To clarify the peak shift, we extensively show, in Fig. 7, the RIS at a grain boundary for a constant dose of one dpa as a function of both temperature and damage rate by means of three-dimensional drawings. It is noteworthy that the RIS at a grain boundary is suppressed at higher temperatures and at a lower damage rate because of the back diffusion from the grain boundary after segregation by irradiation; on the other hand, at a lower temperature and at a higher damage rate the suppression of RIS also occurs because, instead of

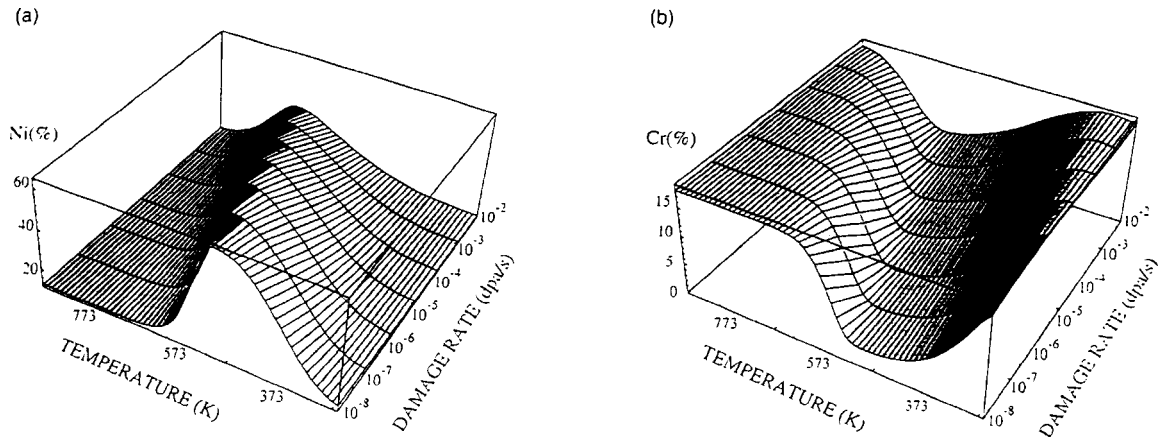


Fig. 7. 3D-plot of damage rate and temperature dependence of RIS at a grain boundary in Fe-18Cr-12Ni alloy irradiated to 1 dpa: (a) for Ni, (b) for Cr.

back-diffusion, recombination becomes dominant. As schematically illustrated in Fig. 8, RIS is considered to be prominent in the intermediate region [25].

### 5.2. The discriminant and concentration dependence in RIS

In Fig. 4 the increase of RIS at a grain boundary seems to saturate at higher doses. There is then a possibility that at a certain dose the increase of the RIS stops, i.e., a quasi-steady state is established. This is the situation that the segregation is balanced with the back-diffusion. We showed, in Fig. 9, dose dependence of the ratio of the solute gradients at a grain boundary in an Fe-20Cr-10Ni (at %) alloy, in order to clarify how the quasi-steady state is accomplished. The inset

of “dynamical calculation” indicates a result from the direct evaluation by solving Eqs. (1)–(3). On the other hand, the inset of “discriminant” shows the ratio of the discriminants,  $M_{Ni}/M_{Cr}$ , where  $M_j$ , a ratio of positional derivatives for vacancy and element concentrations, is given by

$$M_j \equiv \frac{\partial C_j / \partial X}{\partial C_v / \partial X} = \frac{\frac{d_{jv} C_j}{D_j} \sum_{k \neq j} \frac{d_{ki} C_k}{D_k} - \frac{d_{ji} C_j}{D_j} \sum_{k \neq j} \frac{d_{kv} C_k}{D_k}}{\sum_k d_{ki} C_k / D_k} \quad (5)$$

which is obtained considering steady state [6].

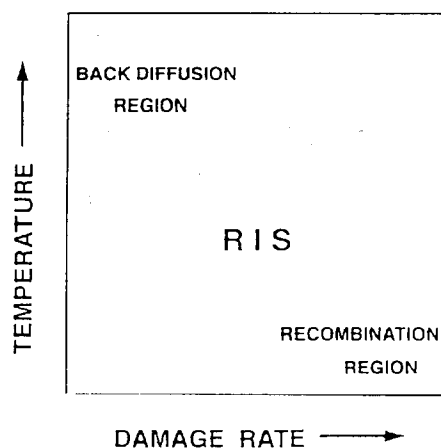


Fig. 8. Schematic diagram to explain dependence of temperature and damage rate on RIS.

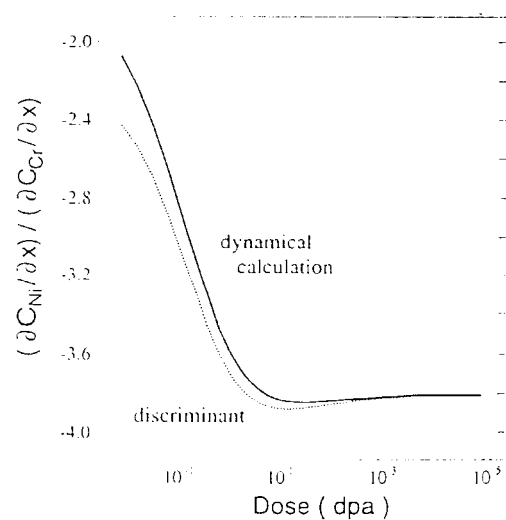


Fig. 9. Calculated dose dependence of  $(\partial C_{Ni}/\partial x)/(\partial C_{Cr}/\partial x)$  at a grain boundary in Fe-20Cr-10Ni (at%) irradiated at  $2 \times 10^{-3}$  dpa s<sup>-1</sup>, 673 K.



Eq. (5) is derived from the condition that the rate change of concentration in Eq. (1)–(3) is zero [6]. Notice that the discriminant is a function of the element concentration at the grain boundary. In the first order approximation,  $M_{Ni}/M_{Cr}$  is proportional to the segregation ratio of the elements at the sink. Therefore we can know from Fig. 9 that the amount of segregation of Ni (enrichment), compared with that of Cr (depletion), increases more as the dose increases and that the two lines of dynamical and discriminant are gradually merging around  $10^5$  dpa; at that time, steady state is established. The criterion may, more practically, be relaxed to approximately 100 dpa in the present case. In another words, we can rely on the discriminant description when dose is more than 100 dpa. As a matter of course, this criterion should be changed at another condition. However, our trial survey suggests that 100 dpa is the most probable criterion under the usual circumstances.

From the discriminant, Eq. (5), we can also infer that the RIS may depend on the initial concentration, viz., a bulk concentration. Watanabe and Takahashi [6] indicated from a discriminant consideration that the dependence of RIS at a grain boundary on the initial concentration might show a peak at a certain concentration of an enriching element, e.g., Ni in an Fe–Cr–Ni alloy, but not so for Cr element. To give an idea for this being probable, we simulated (without averaging), in Fig. 10, the dependence of segregation amount at a grain boundary on alloy composition, fixing the initial Cr concentration to 20 at% in the Fe–Cr–Ni alloy and assuming electron irradiation at 773 K at various doses up to steady state. In Fig. 10 peaks of segregation can

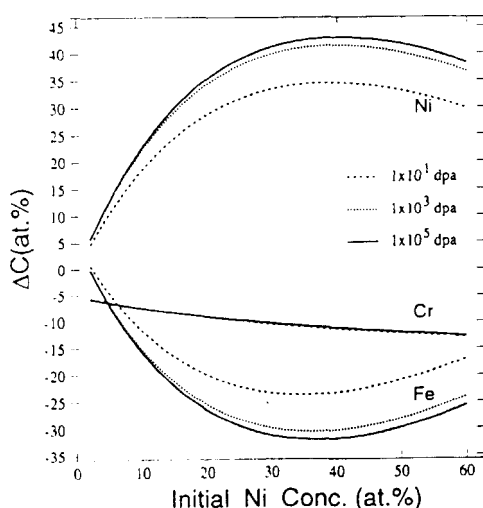


Fig. 10. Simulated concentration dependence on the amount of RIS at a grain boundary for Fe–20Cr– $x$ Ni alloy irradiated at  $2 \times 10^{-3}$  dpa  $s^{-1}$  at 773 K to various doses.

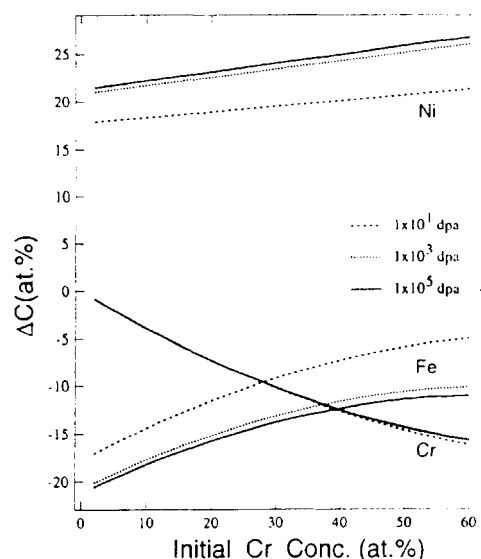
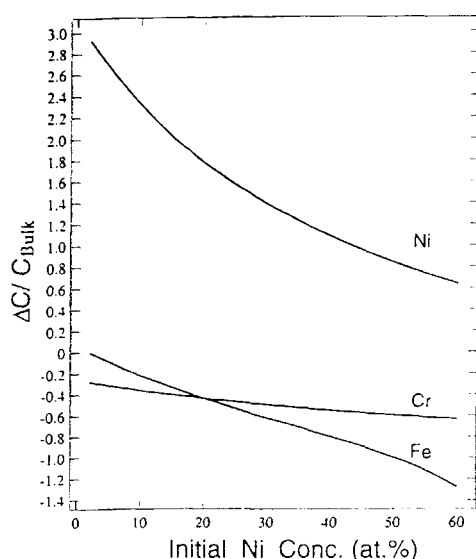


Fig. 11. Same as Fig. 10 in Fe– $x$ Cr–10Ni alloy.

also be seen: Ni lines have maxima and inversely Fe lines have minima at an initial Ni concentration of about 35 at%. Moreover, the peak slightly shifts to the higher initial Ni concentration region of the abscissa as dose is increased. However, this tendency could not be seen in Fig. 11, which is the case of varying Cr alloy content and fixing the initial Ni concentration to 10 at% in the Fe–Cr–Ni alloy at the same irradiation condition. The above things mean that the fraction of Ni atoms contributing to the segregation decreases as solute Ni concentration increases, while not so for solute Cr. This comes from whether the solute enriches or depletes. Since in the RIS process the fraction of enriched Ni atoms contributing to the segregation at a grain boundary becomes larger when the fraction of the initial composition is low and, on the contrary, becomes smaller when the initial composition is high, the segregation amount itself thus shows a maximum at somewhere in the composition. This is comparative to the fact that a monotonically decreasing function – of the fractional segregation amount:  $\Delta C/C_{Bulk}$  in Fig. 12, multiplied by a linearly increasing function – of concentration of the element:  $C_{Bulk}$ , gives a salient function. Trivially, for Cr, as in Fig. 11 this does not hold because Cr in the Fe–Cr–Ni alloy is a depletion element in RIS. We have reported the similar emergence of a peak in concentration dependence, predicted by a discriminant consideration in Ref. [6] (Table 1).

### 5.3. Probe size and spatial resolution in EDS analysis

A TEM-EDS instrument enables one to obtain microchemical information from nano-sized areas in solid

Fig. 12. Concentration dependence of  $\Delta C/C_{\text{Bulk}}$  in Fig. 10.

samples as well as high magnification pictures. In these microscopes the emitted X-rays from the samples are measured with an energy dispersive X-ray spectrometer. Quantitative electron probe microanalysis can then be accomplished when the focused beam is positioned at selected points on a specimen. In addition, elemental identification and X-ray scanning can be performed with these instruments. The recent development of the field emission gun (FEG) makes it possible for TEM analysis to treat regions as small as a nanometer or less, while a conventional TEM, to analyze a ten times larger region, at least.

Even with use of an FEG-TEM at present, however, one is unable to directly detect the atomic scale concentration change in a local region by EDS because, even disregarding the bottom effect, a nanometer electron probe at a sample surface still encircles several atoms or atomic columns. This fact implies that what we acquire as a local profile of the specimen in EDS analysis is spatially averaged information on the true elemental distribution. The bottom effect in a foil of finite thickness, a broadening of probe size due to a scattering of the incident electrons by the atoms comprising the sample, further enhances the averaging effect. On this account, the spatial resolution and its reduction by broadening [26–28] as well as absorption correction [28–30] are important factors in EDS microanalysis.

We shall, in this section, focus on the effect of probe size and the effect of intensity distribution on the evaluation of a composition profile in the EDS analysis. We shall consider averaging with a Gaussian

function, supposing that the probe intensity profile for the EDS is of two dimensional Gaussian form:

$$\rho(R; x, y) = A(R) \exp[-a(x^2 + y^2)], \quad (6)$$

where  $a$  is the deviation constant, and  $A(R)$  is the normalization constant, which is a function of the probe radius,  $R$ . Integration by the normalization condition gives [20]

$$A(R) = \frac{a}{\pi[1 - \exp(-aR^2)]}. \quad (7)$$

Hence, the averaging formula for the two-dimensional Gaussian average for a one-dimensional concentration profile is expressed by [20]

$$\begin{aligned} C(R; X) &= \int_{-R}^R dx \int_{-\sqrt{R^2-x^2}}^{\sqrt{R^2-x^2}} dy A(R) \\ &\quad \times \exp[-a(x^2 + y^2)] C(x + X) \\ &= \int_{-R}^R dx \frac{\sqrt{a/\pi} \exp(-ax^2)}{1 - \exp(-aR^2)} \\ &\quad \times \text{erf}[\sqrt{a(R^2 - x^2)}] C(x + X). \end{aligned} \quad (8)$$

Here we have introduced the error function to account for the  $y$ -component integration. The cross section of the intensity is presumably circular.  $X$  is the component in the  $x$ -coordinate of the probe position.

Fig. 13 shows the effect of the probe size on the average. The average is taken by Eq. (8), changing the probe radius to 1, 10 and 20 nm. The solid line indicated as “As calculated” in Fig. 13 is obtained assum-

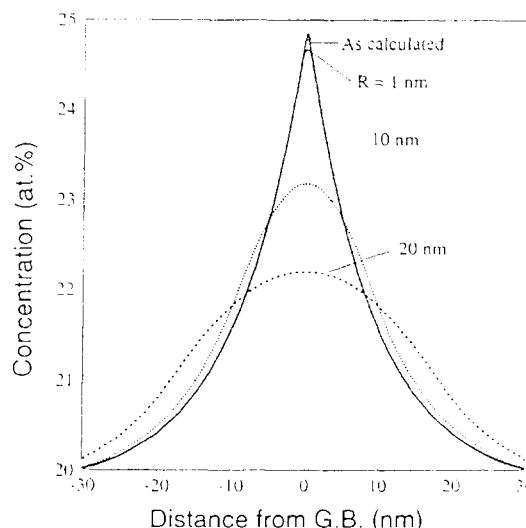


Fig. 13. Simulated concentration profile changes by averaging with two-dimensional Gaussian average at various probe radii.  $R, a = 1 \times 10^{-2} \text{ nm}^{-2}$  [20].

ing 1 dpa electron irradiation near a grain boundary in an Fe–15Cr–20Ni (at%) alloy at 873 K. As can be expected, the averaged profiles are blunted near the grain boundary and the profiles are broadened as the probe size increases. In the Gaussian averages the deviation constant might also be an important factor to be considered. The effect of the deviation constant is not so remarkable for  $a$  less than  $1.0 \times 10^{-2} \text{ nm}^{-2}$ , and that the averaged concentration profile is gradually approaching to the original profile as  $a$  becomes large, corresponding to the probe intensity profile approximating a delta function.

As previously mentioned, the lines in Fig. 2 were obtained by averaging the simulated concentration profile by the two-dimensional Gaussian formula (8), presuming the probe radius 10 nm.

#### 5.4. Gibbsian segregation

In this section we discuss the effect of Gibbsian segregation [22] near a grain boundary. When the alloy system evolves toward equilibrium, a thermodynamic driving force gives rise to either enrichment or depletion of an alloying element at a free surface or a grain boundary, depending on whether the heat of adsorption is negative or positive, respectively. This thermodynamic segregation phenomenon is known as Gibbsian adsorption (GA) for a surface or Gibbsian segregation (GS) for a grain boundary, which tends to minimize the free energy. GS causes a slight modification in alloy compositions, within one or two atomic layers, near a grain boundary. Examples of GS may be found in the literature [31,32], though quantification was poorer because, at that time, relatively primitive instruments were available.

According to Guttman and McLean [22], the expression for the equilibrium concentration of the solute A and B at a grain boundary of a ternary alloy A–B–C is given by (Eq. (15) in Ref. [22] and Eq. (7) in Ref. [21])

$$C_A^{s,eq} = \frac{C_A^b \exp(H_A^a/kT)}{1 + \sum_{j=A,B} [\exp(H_j^a/kT) - 1] C_j^b},$$

$$C_B^{s,eq} = \frac{C_B^b \exp(H_B^a/kT)}{1 + \sum_{j=A,B} [\exp(H_j^a/kT) - 1] C_j^b}, \quad (9)$$

where  $C_A^b$  and  $C_B^b$ , and  $H_A^a$  and  $H_B^a$  are the bulk concentrations and the Gibbsian adsorption enthalpies of A and B atoms, respectively.  $k$  is the Boltzmann constant and  $T$  is the temperature. In 1989, Yacout, Lam and Stubbins [21] have first introduced the fluxes bulk-to-surface and surface-to-bulk by the Gibbsian adsorption and calculated RIS accompanied the GA in Eq. (9) at a surface in an Fe–Cr–Ni alloy. Following their technique we also studied Gibbsian segregation at a grain boundary. The Gibbsian enthalpy used in the calculation is 0.01 eV (–0.01 eV) for the Ni (for Cr) element, respectively. In Fig. 14, we showed the results for Fe–15Cr–20Ni alloys at 793 K before irradiation, in Fig. 14a, and after irradiated to 4.2 dpa, in Fig. 14b. From the figures, we can know that the effect of GS gives rise to very weak segregation; we may need to use an EDS with a fine probe such as an FEG-TEM to observe it, and that the effect is almost unseen after irradiation (c.f. Fig. 2b) because the segregation by RIS becomes dominant. In a low irradiated or in a solution-annealed alloy, however, GS might need to be considered. Using an FEG-TEM-EDS instrument, Kodama et al. [33], seem to have found, recently, an

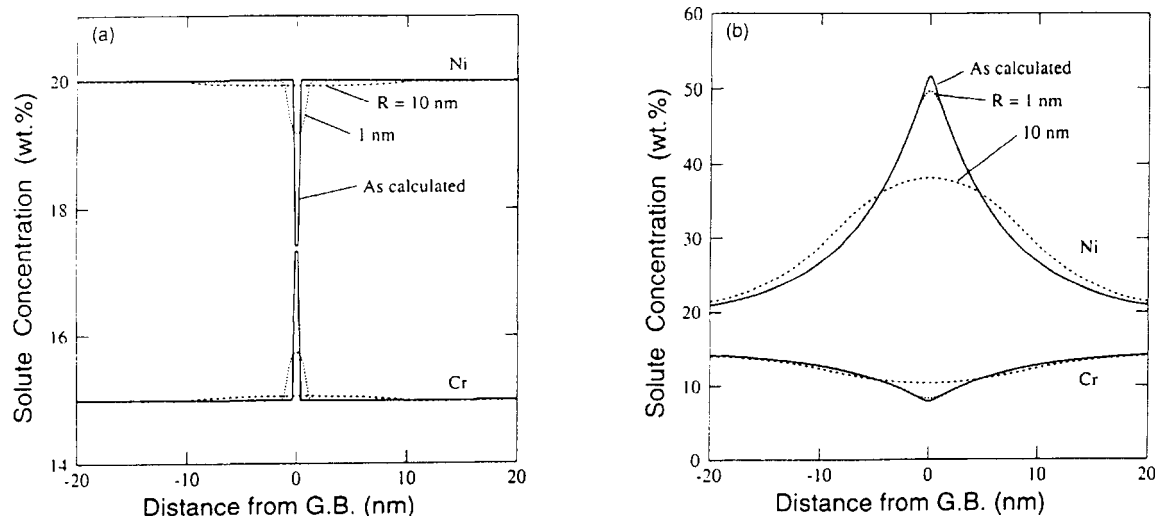


Fig. 14. Gibbsian segregation at a grain boundary at 793 K; (a) before irradiation and (b) after irradiation to 4.2 dpa (cf. Fig. 2b).

evidence that the GS just as in Fig. 14(a) occurred at a grain boundary in a type 304 stainless steel after solution annealing at 1323 K.

#### 5.5. Grain boundary migration with segregation

By irradiation we observed that segregation near grain boundary and simultaneous grain boundary migration occurred such that the concentration profile was asymmetric to both the original and the final grain boundary, and that the segregation effects were more pronounced behind the migrating boundary than ahead of it. The temperature dependencies of the grain boundary migration rate and the amount of segregation are very similar. Therefore, it could be supposed that the boundary migration process is closely connected with the creation of radiation induced point defects. The extrema for the temperature dependencies of the amount of segregation and of the migration occur at the same temperature of 775 K, which indicates the relationship between the point defect flow and the boundary migration process. The point defects (vacancies and interstitial atoms) introduced during irradiation tend to migrate toward the point defect sinks, such as a grain boundary or the specimen surface. Since the grain boundaries are strong defect sinks in a polycrystal, the point defects partly flow into grain boundaries. Consequently, the supersaturated vacancy concentration is decreased in the matrix near a grain boundary so that void nucleation is retarded. It is also suggested that segregation of solute atoms takes place due to the size effect of the solute atoms [13]; namely, that oversized Cr atoms are depleted as a result of their interaction with vacancies and undersized Ni atoms are enriched according to the mixed dumbbell mechanism for the interstitials [12]. Therefore, the occurrence of radiation-induced segregation at grain boundaries means that the point defects flow into the grain boundaries during irradiation. The enrichment of Ni and the depletion of Cr atoms suggest a simultaneous flow of interstitials and vacancies to the grain boundaries.

The diffusivity of the interstitials is higher than that of the vacancies. For example, at 723 K, the diffusivity of the interstitials is about twice as high as that of vacancies. Hence interstitialcy diffusion must be important for grain boundary migration under irradiation. The present results show that the amount of Ni atoms moved toward the grain boundary is larger than that of Cr atoms diffused away from the boundary. At a relatively low temperature, where interstitial can migrate but vacancy can not, we often observe the same tendency. This is probably an indication that the interstitialcy diffusion is predominant in such a RIS process and also in radiation-induced boundary migration, although further confirmative studies might be necessary.

#### 6. Summary and remarks

During irradiation of an Fe–20Ni–15Cr alloy in a HVEM, Ni enrichment and Cr depletion were observed in the vicinity of the grain boundary. Grain boundary migration accompanied with radiation-induced segregation was observed such that: (1) The migration distance showed a linear dependence on the amount of segregation, and (2) The migration occurred predominantly in the perpendicular direction of the close packed planes.

The coupled rate equations for the defect and solute fluxes have been solved numerically and overall agreement with experimental results was obtained. The results of the model calculations for the concentrated alloys which exhibit solute segregation with simultaneous grain boundary migration under irradiation qualitatively reproduce the experimental results. Therefore, the physical model used, which takes into account the coupled point defect flow and the solute atom flow, reflects an important feature of the phenomenon of irradiation-induced segregation accompanied by grain boundary migration.

In concluding remarks, the present study indicates that the radiation-induced point defect flow generates solute redistribution and simultaneous grain boundary migration depending upon the net point defect flow – most probably the interstitial atoms.

We also extensively discussed the effect of the probe size on the composition profiles in the EDS analysis, which turns out to be important when we compare with the experimental data. The dependences of dose, dose rate, temperature and concentration on RIS are extensively studied. It is suggested that RIS show peaks at a certain composition for an enriching solute element such as Ni. The Gibbsian segregation in the vicinity of a grain boundary is also discussed. Experimental confirmation and further investigation on the above are expected in the future.

#### Acknowledgments

It is our pleasure to acknowledge valuable discussions with Mr. H. Kinoshita, and Prof. S. Ohnuki. We are grateful to Dr. N.Q. Lam for his helpful comments concerning the segregation program. S.W. thanks Dr. T. Hashimoto, for giving us his manuscript about the concentration dependence of segregation in a binary alloy and also Mr. M. Kodama, for letting us know the experimental data on Gibbsian segregation. This research was supported in part by the International Scientific Research Program of Ministry of Education, Science and Culture of Japan.

## References

- [1] J.F. Bates, R.W. Powell and E.R. Gilbert, Proc. 10th Conf. on Effects of Radiation on Materials, ASTM-STP 725, eds. D. Kramer, H.R. Brager and J.S. Perrin (American Society for Testing and Materials, Philadelphia, PA 1980) p. 713.
- [2] E.P. Simonen and S.M. Bruemmer, Corrosion '93, No. 93615 (1993).
- [3] H. Gross, H.P. Fuchs, H.J. Lippert and W. Dambeitz, Nucl. Eng. Des. 108 (1988) 433.
- [4] H. Hanien and I. Aho-Mantila, Proc. 3rd Int. Symp. on Environmental Degradation of Materials in Nuclear Power System – Water Reactors, eds. G.J. Theus and J.R. Weeks (The Metallurgical Society of AIME, Warrendale, PA, 1988) p. 77.
- [5] P.R. Okamoto and L.E. Rehn, J. Nucl. Mater. 83 (1979) 2.
- [6] S. Watanabe and H. Takahashi, J. Nucl. Mater. 208 (1994) 191.
- [7] W.V. Vaidya, J. Nucl. Mater. 113 (1983) 219.
- [8] K. Nakata, Y. Katano, I. Masaoka and K. Shiraishi, J. Nucl. Mater. 133&134 (1985) 575.
- [9] H. Takahashi and N. Hashimoto, Mater. Trans. JIM 34 (1993) 1027.
- [10] H. Takahashi, N. Hashimoto and S. Watanabe, Ultramicroscopy 56 (1994) 193.
- [11] F. Seitz, Physics Today (June 1952) 6.
- [12] R.A. Johnson and N.Q. Lam, Phys. Rev. B 13 (1976) 4364.
- [13] P.R. Okamoto and H. Wiedersich, J. Nucl. Mater. 53 (1974) 242.
- [14] H. Wiedersich, P.R. Okamoto and N.Q. Lam, J. Nucl. Mater. 53 (1979) 98.
- [15] A.D. Marwick, J. Nucl. Mater. 135 (1985) 68.
- [16] J.M. Perks, A.D. Marwick and C.A. English, AERE R12121 (1986).
- [17] T. Hashimoto, Y. Isobe and N. Shigenaka, J. Nucl. Mater., to be published.
- [18] H. Takahashi, N. Hashimoto and S. Watanabe, Presented at Symp. on High-Voltage and High-Resolution Electron Microscopy, Max-Planck Institute, Stuttgart, Germany, 1994.
- [19] H. Takahashi, N. Hashimoto, S. Watanabe and N.Q. Lam, Presented at Gordon Research Conf. on Particle–Solid Interactions, Plymouth, 1994.
- [20] S. Watanabe, N. Sakaguchi and H. Takahashi, to be published.
- [21] A.M. Yacout, N.Q. Lam and J.F. Stubbins, Nucl. Instr. and Meth. B42 (1989) 49.
- [22] M. Guttman and D. McLean, in: Interfacial Segregation, eds. W.C. Johnson and J.M. Blakely (American Society for Metals, Metals Park, OH, 1979) p. 261.
- [23] See Table1 in Ref. [10].
- [24] A.C. Hindmarch, in: Scientific Computing, eds. R.S. Steplemann et al. (North-Holland, Amsterdam, 1983) p. 55.
- [25] N. Sakaguchi, Thesis, Hokkaido University, 1993, unpublished, in Japanese.
- [26] G.S. Was and R.M. Kruger, Acta Metall. 33 (1985) 841.
- [27] D.B. Williams and A.D. Romig, Ultramicroscopy 30 (1989) 38.
- [28] J.I. Goldstein, in: Introduction to Analytical Electron Microscopy, eds. J.J. Hren, J.I. Goldstein and D.C. Joy (Plenum, New York, 1979) p. 103.
- [29] G. Cliff and G.W. Lorimer, J. Microsc. 103 (1975), 203.
- [30] Z. Horita, T. Sano and M. Nemoto, Ultramicroscopy 30 (1987), 38.
- [31] P. Doig and P.E.J. Flewitt, J. Microsc. 112 (1977) 16.
- [32] D.R. Clarke, J. Am. Ceram. Soc. 60 (1980) 491.
- [33] M. Kodama, private communication.

## Grain Boundary Segregation Under Irradiation in a HVEM

H. Takahashi, T. Kato\*, S. Watanabe and N. Sakaguchi

*Center for Advanced Research of Energy Technology, Hokkaido University, Kita-ku, kita-13, nishi-8, Sapporo 060, Japan*

*\* Hitachi Research Laboratory, Hitachi, Ltd, Hitachi-Shi, Ibaragiken 317, Japan*

### Abstract

Solute redistribution and microstructural development in the vicinity of grain boundaries in Fe-19Cr-XMn-3Al (X=5,10,15) alloys were studied under electron irradiation to about 10 dpa at 725 K in a high voltage electron microscope in order to simulate the segregation behavior during neutron irradiation. The oversized solute atoms, manganese and aluminum, were depleted at grain boundaries, whereas the concentration of chromium increased even though it is an oversized one. The segregation behavior of aluminum and manganese was related to size effect. However, with increasing manganese concentration the size factor decreased and then the amount of depletion of the solutes decreased with manganese concentration. The enrichment of chromium seemed to be related to chromium-rich precipitate formation at the boundary.

### 1. INTRODUCTION

Austenitic stainless steels and ferritic steels are important candidate materials for fast breeder and fusion reactors. Therefore a lot of irradiation studies have been performed on these candidate materials[1-6]. Furthermore recently the development of lower radio-activation materials has been required in stead of commercial materials containing high radio-activation alloying elements[7]. For instance W and Ta are used instead of Mo and Nb in modified martensitic steels and Ni is replaced with Mn in austenitic stainless steels. The high manganese steels has been also noticed as the low activation steels. However, an important problem of these materials is the phase instability under neutron irradiation at relatively higher temperature. This phase instability is strongly associated with solute segregation caused by point defects flow and it is well known that the grain boundaries are effective sinks for point defects in materials[8]. When the irradiation is carried out for the alloys, a lot of point defects are introduced in the materials. These point defects diffuse towards grain boundaries that it act as the defect sinks. With this process of the defect flow, Segregation of alloying

elements is caused near the grain boundary[9-10]. This radiation-induced segregation(RIS)occurs from the relatively early irradiation stage. Theoretical treatment on the RIS have been done, based on misfit strain energy and predicts the direction of the flow of solute atoms[11-14]. Namely the undersized solutes migrate toward and the oversized ones away from defect sinks during irradiation. This RIS occasionally causes solute enrichment due to the interaction of solutes with impurities[8]

In this paper the segregation behaviors was studied under electron irradiation of Fe-Cr-Mn-Al alloy systems which are lower activation materials using a high voltage electron microscopy(1000kV) in order to clarify the effect of additional aluminum element and manganese content on segregation.

## 2. EXPERIMENTAL PROCEDURE

The materials used for electron-irradiation were Fe-10wt%Cr-Xwt%Mn-3wt%Al(X=5,10 and 15) and for the measurement of lattice parameter by X-ray diffraction were Fe-(8,10,12)wt%Cr-Xwt%Mn-(3wt%Al)(X=5,15,25). These chemical compositions are given in Table 1. The aluminum content is a critical value according to mechanical properties after neutron irradiation and high temperature oxidation resistance data. Disk foils with 3 mm diameter and 0.2 mm thickness were prepared after solution-annealed for 1800 sec. at 1423 K in a vacuum of  $1 \times 10^{-5}$  Pa followed by water quenching, then were electropolished. X-ray diffraction analysis indicated that all of these materials were composed of single ferritic phase structure. The electron irradiation was performed in a H-1300 high voltage electron microscope at Hokkaido University, operated at 1MV. The beam spot size is about 2 microns in diameter and the irradiation flux was measured with a Faraday cup to be  $4.0 \times 10^{23}$  e/m<sup>2</sup>s, corresponding to a mean damage rate of  $1.9 \times 10^{-3}$  dpa/s, assuming a threshold displacement energy of 24 eV. Foils of 400 nm in thickness were irradiated to 10 dpa at 723 K, with the electron beam spot centered across a grain boundary.

After electron irradiation the sample were ion thinned by 4.2 kV argon ions to allow EDS analysis. Radiation-induced solute redistribution in the vicinity of the grain boundary with 100nm nm in thickness was analyzed with a 10 nm electron probe using a 200kV TEM. X-ray diffraction analysis using Cu-K radiation was carried out for a series of nine materials presented in Table 1.

Table 1 Chemical compositions of Fe-Cr-Mn-Al alloys

| Steel            | C     | Si    | Mn    | P     | S     | Ni   | Cr    | Al    | N      | O      |
|------------------|-------|-------|-------|-------|-------|------|-------|-------|--------|--------|
| Fe-10Cr-20Mn-3Al | 0.003 | <0.01 | 19.77 | 0.003 | 0.008 | 0.01 | 10.07 | 3.04  | 0.0020 | 0.0004 |
| Fe-10Cr-25Mn-3Al | 0.004 | <0.01 | 24.73 | 0.003 | 0.009 | 0.01 | 9.85  | 3.07  | 0.0024 | 0.0003 |
| Fe-8Cr-15Mn-3Al  | 0.003 | <0.01 | 15.29 | 0.003 | 0.007 | 0.01 | 8.14  | 2.90  | 0.0070 | 0.0005 |
| Fe-12Cr-15Mn-3Al | 0.002 | <0.01 | 15.13 | 0.003 | 0.006 | 0.01 | 11.70 | 2.88  | 0.0093 | 0.0003 |
| Fe-10Cr-5Mn      | 0.004 | 0.01  | 4.89  | 0.007 | 0.003 | 0.06 | 9.71  | 0.03  | 0.0041 | 0.0113 |
| Fe-10Cr-15Mn     | 0.004 | 0.01  | 13.93 | 0.007 | 0.005 | —    | 9.98  | 0.003 | 0.0038 | 0.0269 |
| Fe-10Cr-5Mn-3Al  | 0.002 | <0.01 | 5.06  | 0.003 | 0.004 | 0.01 | 10.29 | 2.91  | 0.0012 | 0.0004 |
| Fe-10Cr-10Mn-3Al | 0.003 | 0.01  | 9.88  | 0.004 | 0.005 | 0.01 | 10.08 | 2.99  | 0.0024 | 0.0002 |
| Fe-10Cr-15Mn-3Al | 0.005 | <0.01 | 15.03 | 0.003 | 0.007 | 0.01 | 10.02 | 2.93  | 0.0018 | 0.0004 |

Fe: Balance

### 3. RESULTS

#### 3.1 Segregation behaviors of Fe-Cr-Mn-Al alloys

The concentration profiles of chromium, manganese and aluminum in the vicinity of the grain boundary for the Fe-10Cr-XMn-3Al alloys ( $X=5,10,15$ ) after irradiation to 10 dpa at 723 K are shown in Figure 1(a-c). Besides enrichment of chromium, the depletion of manganese and aluminum was recognized at the grain boundary. The concentration changes of manganese, chromium and aluminum depend on the manganese content of the alloy. The ratio of solute concentration at the grain boundary,  $C(g.b.)$  in the Fe-10Cr-XMn-3Al alloy after irradiation to a dose of 10 dpa at 723 K to that in the unirradiated matrix,  $C(unirr)$ , is shown in Figure 2 as a function of manganese content. The ratios,  $C(g.b.irr) / C(unirr)$ , for chromium, manganese and aluminum approached to the value of 1.0 with increasing manganese content. The increment of chromium due to irradiation decreased with manganese content and the relative irradiation induced solute depletion of manganese and aluminum decreased with manganese content.

Furthermore, it is recognized that the amount of the depletion of aluminum after irradiation is greater compared to that of manganese.

On the other hand, in the unirradiated area of the grain boundary, neither enrichment nor depletion of manganese and aluminum was detected after annealing at 723 K without irradiation but the concentration of

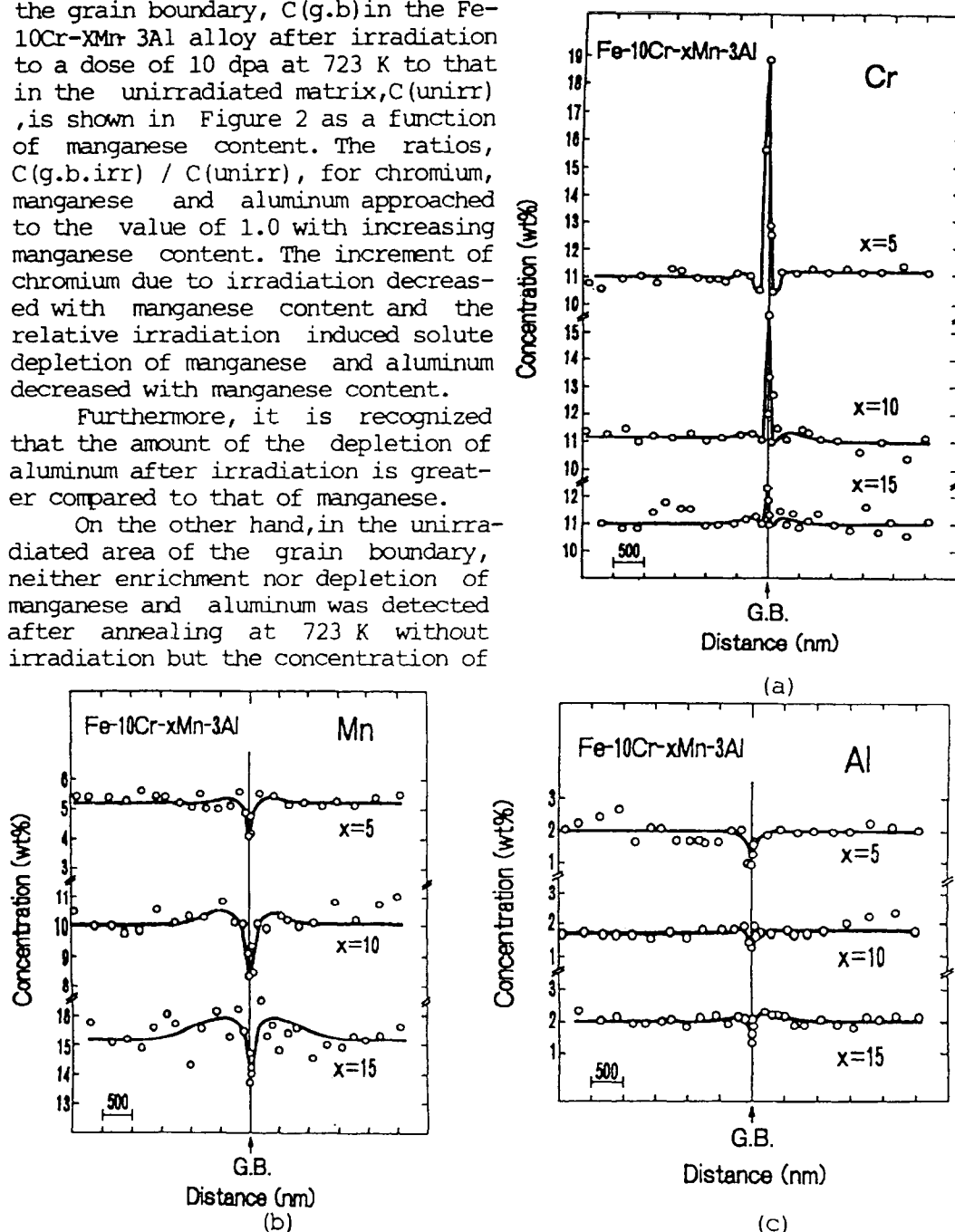


Figure 1(a-c). Concentration profiles of Fe-10Cr-XMn-3Al ( $X=5,10,15$ ) alloys after irradiation at 723 K to a 10 dpa.



chromium still increased at boundary. This chromium enrichment reduced with increasing manganese content in the Fe-10Cr-xMn-3Al alloy as shown in Figure 3. This tendency of segregation was similar to segregation behavior observed in irradiated areas. However, the amount of the chromium enrichment (the difference between the concentration at the grain boundary and that in the matrix in irradiated areas was more than twice the amount of enrichment in unirradiated areas. This suggests that the chromium enrichment is considerably enhanced at grain boundaries, even though manganese and aluminum segregation due to irradiation did not occur.

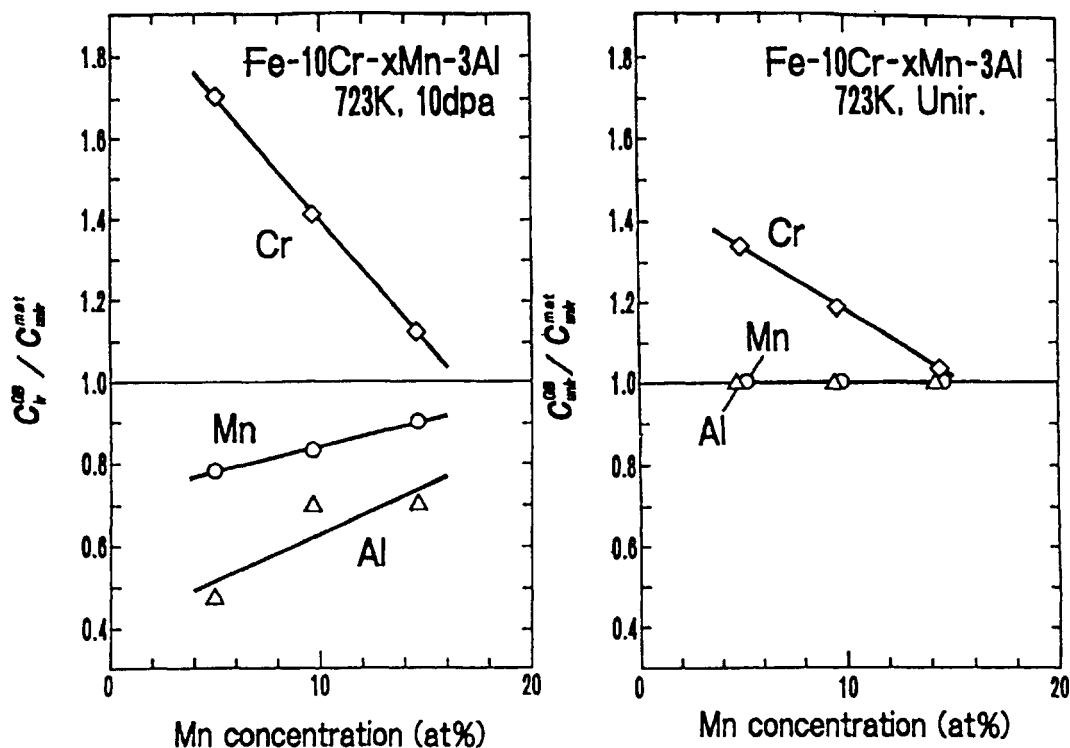


Figure 2. Mn content dependence of solute segregation at grain boundary after irradiation at 723K to 10dpa. Figure 3. Mn content dependence of solute segregation at grain boundary after annealing at 723 K.

### 3.2 Microstructural development during irradiation

A series of typical microstructure of Fe-10Cr-5Cr-3Al alloy during electron irradiation at 723 K is shown in Figure 4. before irradiation, very fine precipitates were often observed in the matrix and furthermore precipitates at grain boundaries were also observed as small dot contrast. These black dot contrasts increased in size during irradiation. The similar behavior was observed for other irradiated Fe-Cr-Mn-Al alloys. Due to further irradiation, interstitial dislocation loops formed and developed to tangle dislocation structures.

Figure 5(a,b) shows the dark field image of microstructure and the electron diffraction pattern from Fe-10Cr-15Mn-3Al alloy after irradiation at 723 K to 10 dpa. On the electron diffractions besides diffraction spots from matrix of ferrite phase, the extra spots were recognized, which corresponded to chi phase as shown in fig.5(b).

and atomic volume was calculated using these parameters.

Figure 8 shows the atomic volume for the Fe-xCr-yMn-Al alloys as a function of manganese and aluminum contents. It is obvious that the atomic volume in each alloy increased with increasing manganese, aluminum and/or chromium concentration. Namely these solute atoms are oversized ones compared to mean atomic size of the solid solution state of the alloy matrix.

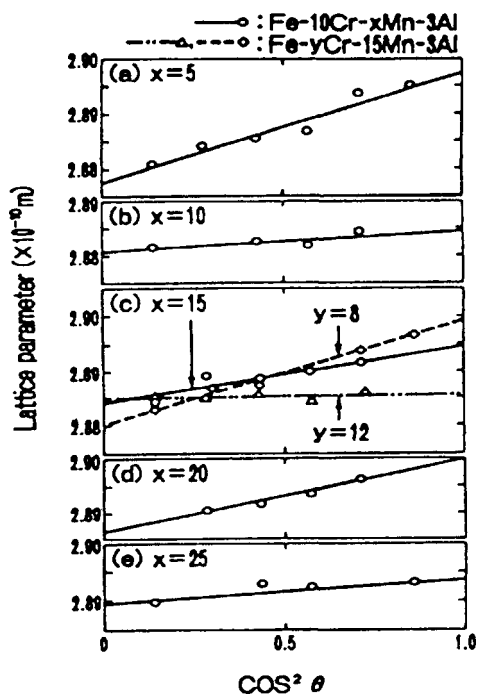


Figure 7. The dependence of lattice parameter on  $\cos^2 \theta$ .

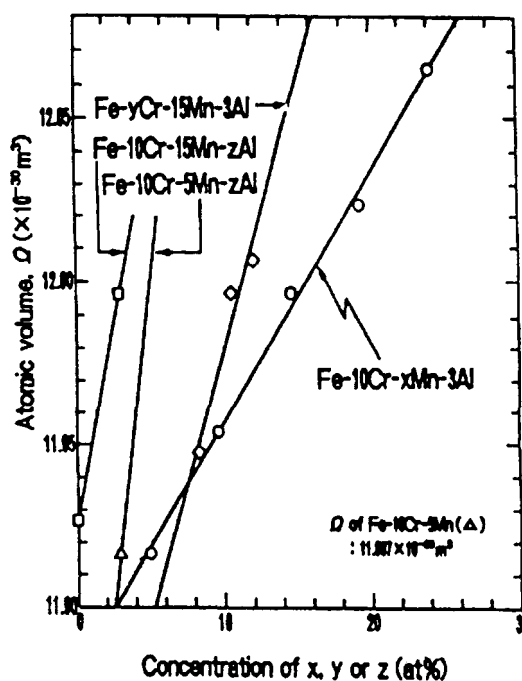


Figure 8. The dependence of atomic volume on solute concentration.

#### 4. DISCUSSION

The volume size factors of manganese, chromium and aluminum in these Fe-Cr-Mn-Al alloys shown in table 2, are the results of volume size factor obtained for each alloy according to a method given by King[18]. This factor is very important to study the influence on radiation-induced solute segregation, as shown in previous studies [9,15-17].

From table 2, all of these solute atoms are found to be oversized, and the magnitude of the size factors are in the order of Al, Cr, Mn. It should be noted that the size factor of aluminum in the Fe-10Cr-5Mn-3Al alloy is greater than that in the Fe-10Cr-15Mn-3Al alloy. This smaller size factor for the alloy with higher manganese content is caused by the enlargement in atomic volume with increasing oversized manganese content, so that results in the reduction of the relative atomic size of aluminum. The amount of the depletion of aluminum at the grain boundary was higher than that of manganese as

Table 2. Volume size factors of Cr, Mn, Al

| Solute atoms | Volume size factor (%) <sup>a)</sup> | Solid solution systems |
|--------------|--------------------------------------|------------------------|
| Mn           | + 6.45                               | Fe-10Cr-xMn-3Al        |
| Cr           | +11.8                                | Fe-yCr-15Mn-3Al        |
| Al           | +47                                  | Fe-10Cr-5Mn-zAl        |
| Al           | +29                                  | Fe-10Cr-15Mn-zAl       |

<sup>a)</sup> The volume size factors are available for the x-, y- and z-range of 5 to 25, 8 to 12 and 0 to 3, respectively.

shown in fig.2. This is attributed to the volume size factor of aluminum being greater than that of manganese as seen in Table 2. The reduction in the amounts of solute depletion at the grain boundary both for manganese and aluminum due to increase in manganese content(fig.2) is attributed to an expansion of the lattice parameter of Fe-10Cr-XMn-3Al alloy and to a concomitant reduction of the relative atomic size of all solutes. For example, the size factor(+47%) reduced to +29% in Fe-10Cr-15Mn-3Al in which manganese concentration increased to 15 wt%. Thus, the tendency and the amount of radiation-induced segregation of manganese and aluminum near grain boundaries can be explained on the basis of the relative magnitude of their volume size factors in Fe-10Cr-XMn-3Al alloys.

However, according to study of neutron irradiated low activation ferritic steel containing Mn by Kimura et al.[21], the grain boundary segregation of Mn solute is not attributed to size effect. This may be come from the impurity effect, namely segregation behavior in pure alloys mainly caused by size effect but in alloy with impurities such as Si, C and others which are strongly interact with segregated solute, the segregation behavior is ruled out from size effect for segregation. Thus, the enrichment of chromium at grain boundary also occurred even under irradiation as a result of formation of Cr rich precipitation even though the chromium of oversized solute should be depleted at the grain boundary. Figure 6 shows the microstructural development near a grain boundary in the Fe-10Cr-5Mn-3Al alloy observed during electron irradiation at 723K. Before irradiation, a few fine plate-like precipitates have already appeared in the matrix and very fine black dot contrasts were also observed on grain boundary. The dark field image of these dot precipitates and the electron diffraction pattern obtained from the area was shown in Figure 7 and 8, respectively. The black dot contrasts increased slightly in size during irradiation up to 10 dpa. Similar precipitate behavior was observed for the Fe-10Cr-10Mn-3Al and Fe-10Cr-15Mn-3Al alloys. However, no void formation and grain boundary migration were observed up to a dose of 10 dpa in any of the specimens. These facts suggest that the grain boundary segregation of chromium in the irradiated area is not related to the void formation [9,15,19] or grain boundary migration[16,20], but is due to the formation of chromium-rich precipitates at grain boundary. From the electron diffraction pattern, these precipitates were identified as chi phases. The formation of these chi phases seems to be enhanced with Al and Mn depletion under irradiation.

Therefore, even if we can suppress the formation of chi phase by heat treatment and /or considering the suitable additional elements, it seems to be difficult to retard the segregation of solute, especially at higher temperature and furthermore the mechanical properties of ferritic steels are very structure sensitive so that low activation high manganese ferritics has still difficult to use for nuclear applications at present time.

## 5. SUMMARY

Compositional changes during electron-irradiation and effects of concentration of alloying elements on size factor and solute segregation were examined. The main results obtained are as follows:

- 1) Over sized manganese and aluminum elements were depleted near grain boundary according to size effects, but chromium concentration increased at grain boundary after annealing without electron-

irradiation and after the irradiation and its amount of enrichment increased due to irradiation.

- 2) Volume size factors decreased with increasing manganese content so that the concentration changes at grain boundary are reduced.
- 3) The amount of segregation depended on the relative sizes among of solute, and thus the depletion of manganese which has a smaller size compared to aluminum was lower than for aluminum.
- 3) The enrichment of chromium at grain boundary was attributed to the formation of irradiation-enhanced chi phase.

#### Acknowledgments

We wish to thank Mr.S.Mochizuki and Mr.K.Sugawara for their operation of electron microscope. This research was supported by the International Scientific Research Program of Monbusho.

#### References

- [1] Wilkes P., Journal of Nuclear Materials, 83(1979)166-175.
- [2] Russell K.C., Journal of Nuclear Materials,83(1979)176-185.
- [3] Muroga T., Garner F.A. and Ohnuki S., Journal of Nuclear Materials,179-181(1991)546-549.
- [4] Ohnuki S.,Takahashi H. and Nagasaki R., Journal of Nuclear Materials,179-181(1988)823-827.
- [5] Watanabe H., Aoki A., Muroga T. and Yoshida N., Journal of Nuclear Materials,179-181(1991)529-533.
- [6] Kato T., Takahashi H. and Izumiya M., Materials Transactions of JIM, 32(1991)921-930.
- [7] Proceedings of the Workshop on Low Activation Materials, Culham, England, April, 1991.
- [8] Gleiter H. and Chalmers B., High Angle Grain Boundaries, Progress in Materials Science, Pergamon,16(1972)p.127.
- [9] Okamoto P.R. and Wiedersich H., Journal of Nuclear Materials, 53(1974)336-345.
- [10] Takeyama T., Ohnuki S. and Takahashi H., Scripta Metallurgica,14 (1980)1105-1110.
- [11] Takeyama T., Ohnuki S. and Takahashi H., Journal of Nuclear Materials,89(1980)253-262.
- [12] Johnson R.A. and Lam N.Q., Physical Review,13(1976)4364-4375.
- [13] Watanabe S. and Takahashi H., Journal of Nuclear Materials,208 (1994)191-194.
- [14] Takahashi H., Hashimoto.N and S.Watanabe, Ultramicroscopy,56 (1994)193-199.
- [15] Takahashi H., Ohnuki S. and Takeyama T., Journal of Nuclear Materials,103 & 104(1981)1415-1419.
- [16] Nakata K. and Masaoka I., Journal of Nuclear Materials,150(1987) 186-193.
- [17] Takahashi H., Takeyama T., Tanikawa K. and Miura R., Journal of Nuclear Materials,133 & 134(1985)566-570.
- [18] King H.W., Journal of Nuclear Materials Science,1(1966)79-90.
- [19] Ohnuki S., Takahashi H. and Takeyama T., Journal of Nuclear Materials, 103 & 104 (1981)1415-1420.
- [20] Takahashi H and Hashimoto N., Materials Transactions of JIM,34(1993)1027-1030.
- [21] Kimura A.,Charlot L.A.,Gelles D.S. and Jones R.H., Journal of Nuclear Materials,212-215(1994)725-729.

## Phase transformation induced by irradiating an $\text{Al}_{62}\text{Cu}_{25.5}\text{Fe}_{12.5}$ icosahedral quasicrystal

Renhui Wang<sup>†</sup>, Xiangxiu Yang<sup>†</sup>, Heishichiro Takahashi<sup>‡</sup> and Somei Ohnuki<sup>‡</sup>

<sup>†</sup> Department of Physics, Wuhan University, 430072 Wuhan, People's Republic of China

<sup>‡</sup> Metal Research Institute, Faculty of Engineering, Hokkaido University, Sapporo 060, Japan

Received 6 October 1994

**Abstract.** The irradiation effect of the  $\text{Al}_{62}\text{Cu}_{25.5}\text{Fe}_{12.5}$  icosahedral quasicrystal (IQC) induced by 120 keV Ar ions and 1 MeV electrons has been studied *in situ* using high-voltage electron microscope–ion accelerator dual-irradiation facilities. The effect is dose and temperature dependent and we can define three critical temperatures  $T_c$ ,  $T_d$  and  $T_p$ . When irradiated at  $T < T_c$ , the IQC is transformed into a crystalline microtwin oriented according to icosahedral symmetry. When  $T > T_c$ , the IQC remains an IQC but with a higher (when  $T > T_d$ ) or lower (when  $T < T_d$ ) degree of perfection. The planar defects originally existing in the  $\text{Al}_{62}\text{Cu}_{25.5}\text{Fe}_{12.5}$  IQC foils are stable when  $T > T_p$  but disappear when  $T < T_p$ . For the  $\text{Al}_{62}\text{Cu}_{25.5}\text{Fe}_{12.5}$  IQC, we found that  $T_c \simeq 400$  K,  $T_d \simeq 450$  K (for 1 MeV electrons) or 550 K (for 120 keV Ar ions) and  $T_p \simeq 600$  K.

### 1. Introduction

Irradiation-induced phase transformation in crystals has been an interesting research field for the past 20 years [1]. Since the discovery of icosahedral quasicrystals (IQCs) in Al-based alloys by Shechtman *et al* [2], there have been some papers studying irradiation-induced phase transformation in IQCs. Urban *et al* [3] and Mayer *et al* [4] irradiated Al–Mn and Al–V IQCs by 1 MeV electrons. They found that IQCs were transformed into an amorphous phase when the irradiation temperature was sufficiently low and observed a reverse transition by post-irradiation heating. Wang *et al* [5] and Wang *et al* [6] studied phase transformations in an  $\text{Al}_{76}\text{Si}_4\text{Mn}_{20}$  IQC induced by 120 keV  $\text{Ar}^+$  ions and/or 1 MeV electrons. They found an amorphization effect when irradiated at lower temperatures (345 K or less for Ar ions; room temperature (RT) or less for electrons) and a disordering effect at medium temperatures. Under special irradiation conditions an  $\text{Al}_{76}\text{Si}_4\text{Mn}_{20}$  simple IQC may be transformed into an ordered face-centred IQC [5]. Recently, Wang *et al* [7] irradiated an  $\text{Al}_{62}\text{Cu}_{25.5}\text{Fe}_{12.5}$  IQC at RT with 120 keV Ar ions and observed an irradiation-induced phase transformation from an IQC to a CsCl(B2)-based structure and a reverse transition during heating.

The high-voltage electron microscope–ion accelerator dual-irradiation facilities installed at Hokkaido University [8] and equipped with a double-tilting heating stage provided a powerful tool for *in situ* observation of the temperature-dependent ion and/or electron irradiation effect. By using this facility we have studied phase transformations in an  $\text{Al}_{62}\text{Cu}_{25.5}\text{Fe}_{12.5}$  IQC induced by irradiation of 1 MeV electrons and 120 keV Ar ions to different doses at different temperatures, and new results are reported.

## 2. Specimen preparation and experimental method

The alloy of composition  $\text{Al}_{62}\text{Cu}_{25.5}\text{Fe}_{12.5}$  was prepared by melting the high-purity elements in an induction furnace under an Ar atmosphere. The ingot was annealed at 1095 K for 47.2 h, cooled for 30 h to RT and then cut into slices of 3 mm in diameter. A synchrotron radiation topography study [9] showed that these slices are perfect IQCs with very large grains ranging from 0.1 to 3 mm in diameter. Foils for transmission electron microscopy (TEM) were prepared by mechanical thinning and  $\text{Ar}^+$  ion milling.

The Hitachi H-1300 high-voltage electron microscope-ion accelerator dual-irradiation facilities equipped with a double-tilting heating stage were used to heat and irradiate the TEM specimens at a given temperature. The high-energy particles utilized in the present work were 1 MeV electrons and/or 120 keV Ar ions. The electron beam current in the small irradiated region of 1  $\mu\text{m}$  diameter was  $9.4 \text{ A cm}^{-2}$  and the argon ion beam current covering the whole TEM specimen was unstable, ranging from 0.3 to  $0.6 \mu\text{A cm}^{-2}$ .

The contrast images and electron diffraction patterns (EDPs) of the specimens were observed *in situ* by the Hitachi H-1300 high-voltage electron microscope operated at 1 MeV. A theoretical calculation shows that the projected range is 74.8 nm with 29.6 nm longitudinal straggling and 30.0 nm lateral straggling when the  $\text{Al}_{62}\text{Cu}_{25.5}\text{Fe}_{12.5}$  alloy is bombarded by 120 keV  $\text{Ar}^+$  ions, which is comparable with the foil thickness of the thin regions. For thicker regions observable by 1 MeV electrons in the high-voltage electron microscope, only the top surface layer of the foil was bombarded by the ions. On the other hand, most of the irradiated 1 MeV electrons were transmitted through the observable regions of the specimen.

## 3. Results

### 3.1. Microstructure and electron diffraction patterns before irradiation

TEM observation showed that the  $\text{Al}_{62}\text{Cu}_{25.5}\text{Fe}_{12.5}$  foils before irradiation are all face-centred IQCs, of which the EDPs along the fivefold (A5), twofold (A2), threefold (A3) and pseudo-twofold (A2P) axes are shown in figures 1(a), 1(b), 1(c) and (d), respectively. The grain is so large that the whole thin region of a foil belongs to a single grain, in accordance with the synchrotron radiation white-beam topography observation [9]. These foils contain high-density planar defects which appear as straight fringes parallel to the intersection lines of these planar defects with the foil surface, as shown in figure 1(e) which was photographed when one A5 axes of this grain is parallel to the incident beam, as studied already by Yang *et al* [10].

### 3.2. Simulated electron diffraction patterns of the CsCl-type microcrystals arranged according to the icosahedral symmetry

Figures 2(a), 2(b), 2(c) and 2(d) are EDPs after the  $\text{Al}_{62}\text{Cu}_{25.5}\text{Fe}_{12.5}$  TEM foils have been irradiated with 120 keV Ar ions, along the original A5, A2, A3 and A2P axes of the IQC, corresponding to figures 1(a), 1(b), 1(c) and 1(d), respectively. These EDPs still show fivefold, twofold, threefold and pseudo-twofold symmetries respectively but are quite different compared with figures 1(a), 1(b), 1(c) and 1(d). Some spots, such as A, B, C and D (in figure 2), are very strong compared with the corresponding spots in figure 1 while others, such as E, F and G (in figure 2), are very broad along the tangential direction and form arc sections. Most of the weak spots in figure 1 disappear in figure 2 and some spots

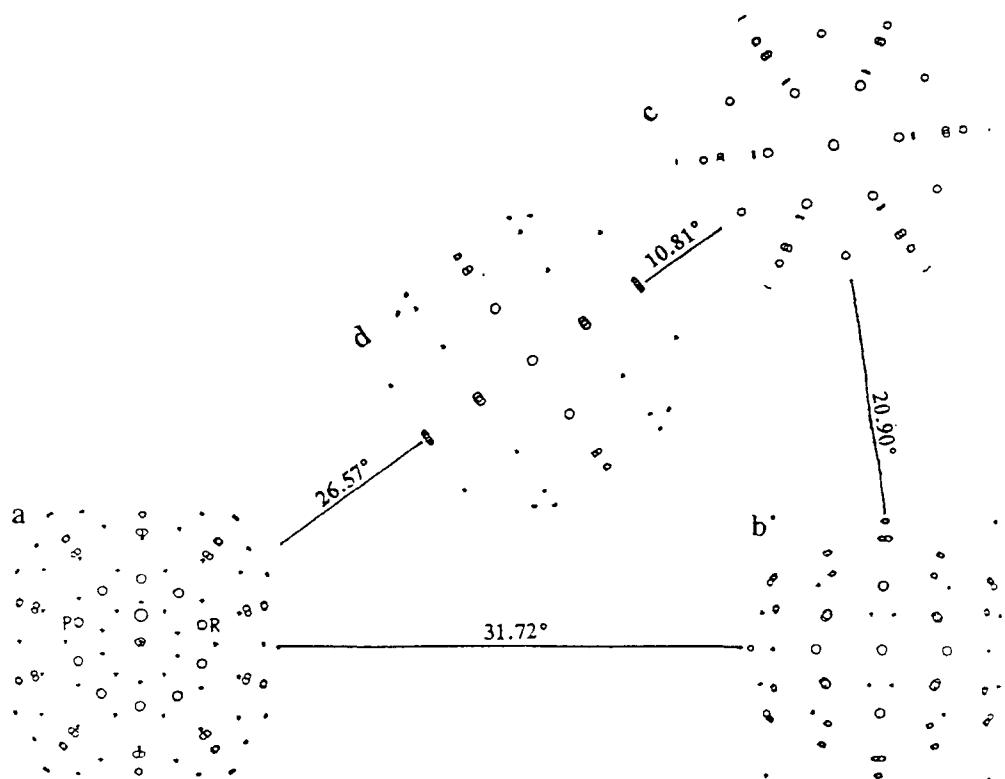


Figure 3. Simulated EDPs along the original icosahedral (a) A5, (b) A2, (c) A3 and (d) A2P zone axes of crystalline microtwins of B2-type phase arranged according to the icosahedral symmetry

still correspond to an IQC (figure 5(f)) but with lower perfection compared with that before irradiation (figure 5(b)).

### 3.4. Heating experiment after electron irradiation

The electron-irradiated TEM foil (at RT) was heated in the high-voltage electron microscope and observed *in situ*. When the temperature was lower than 810 K; no discernible change in the BF images and EDPs of the foil was observed. When the foil was heated to 855 K, some larger grains about  $0.1\ \mu\text{m}$  in size appeared and these eventually grew to yield a polycrystalline aggregate of B2-type grains (about  $0.5\ \mu\text{m}$  in mean diameter) when the heating time was increased to 30 min. These large grains maintained their sizes, shapes and orientations after the foil had been cooled to RT. Figure 6 shows an example of the foil which was irradiated by 1 MeV electrons at RT to a dose of  $3.2 \times 10^{23}\ \text{e}^- \text{cm}^{-2}$ , heated at 855 K for 30 min and then cooled to RT. Figures 6(a) and (c) show dark-field (DF) images by selecting reflections B1 (figure 6(b)) and C1 (figure 6(d)), respectively, where the reflection B1 belongs to the EDP of the  $[113]_B$  (B2) zone axis and the reflection C1 belongs to the EDP of the  $[113]_C$  (B2) zone axis. The fact that grain B in figure 6(a) and grain C in figure 6(c) are bright indicates that the EDPs  $[113]_B$  and  $[113]_C$  are produced by grains B and C, respectively. This indicates that grains B and C are related by a fivefold rotation around the A5(IQC) axis.

For the foil irradiated by 1 MeV electrons at 360 K to a dose of  $1.1 \times 10^{23}\ \text{e}^- \text{cm}^{-2}$ , which was transformed into icosahedral microtwins of B2 phase (figures 5(g) and 5(h)), no change was observed when the heating temperature was lower than 690 K. After the

dependent irradiation effect as follows: at higher temperatures ( $T > T_d$ ), the recovery process dominates, and hence no damage can be found; rather the thermal and irradiation-enhanced diffusion may increase the degree of order of the IQC. When the temperature is lower than the IQC  $\rightarrow$  B2-phase transformation point, irradiation-enhanced diffusion may accelerate this transformation. At medium temperatures ( $T_c < T < T_d$ ), at the beginning of the irradiation, the recovery process is slower than the damage accumulation process which induces a decrease in the degree of order (or of the perfection) of the IQC. On increase in the defect density, defect-enhanced diffusion accelerates the recovery process until a dynamic balance is reached between the recovery and damage processes. Moreover, one can suppose that the planar defects are metastable at temperatures lower than  $T_p$  and hence that irradiation-enhanced diffusion accelerates the disappearance of the planar defects when  $T < T_p$ .

There is a substantial difference between the behaviour of Al-Cu-Fe IQC on the one hand and the Al-Mn [3], Al-V [4] and Al-Si-Mn [6] IQCs on the other hand after low-temperature irradiation. The former is transformed into a stable crystalline phase and the latter are transformed into the amorphous state. This may be explained by the higher degree of imperfection in the rapidly solidified Al-Mn, Al-V and Al-Si-Mn IQCs and the intimate structural relationship between the Al-Cu-Fe face-centred IQC and B2-type phases.

It shall be noted that both the microtwin structure (cf section 3.4 of the present paper) and the large grains (cf [7]) of the B2-type phase transformed from the IQC phase by irradiation can reversibly transform to the IQC phase after heating to 820 K (cf section 3.4) or 880 K [7] under certain conditions. This supports the conclusion that the  $\text{Al}_{62}\text{Cu}_{25.5}\text{Fe}_{12.5}$  IQC phase is stable at higher temperatures and metastable at RT. The transformation temperature may be nearly equal to the temperature  $T_c$  ( $\simeq 400$  K) as revealed by the present study.

### Acknowledgment

This project was supported by the National Natural Science Foundation of China.

### References

- [1] Nolfi F V 1983 *Phase Transformations During Irradiation* (London: Applied Science)
- [2] Shechtman D, Blech I, Gratias D and Cahn J W 1984 *Phys. Rev. Lett.* **53** 1951
- [3] Urban K, Moser N and Kronmüller H 1985 *Phys. Status Solidi a* **91** 411
- [4] Mayer J, Urban K and Fidler J 1987 *Phys. Status Solidi a* **99** 467
- [5] Wang Z G, Deng W F and Wang R 1992 *Phys. Status Solidi a* **133** 299
- [6] Wang R, Takahashi H, Ohnuki S and Wang Z G 1994 *Radiat. Eff. Defects Solids* **129** 173
- [7] Wang Z G, Yang X X and Wang R 1993 *J. Phys.: Condens. Matter* **5** 7569
- [8] Takeyama T, Ohnuki S and Takahashi H 1985 *J. Nucl. Mater.* **133-4** 571
- [9] Zou W H, Wang R, Gui J, Zhao J Y and Jiang J H 1994 *J. Appl. Crystallogr.* **27** 13
- [10] Yang X X, Wang Z G and Wang R 1994 *Phil. Mag. Lett.* **69** 15
- [11] Gratias D, Calvayrac Y, Devaud-Rzepski J, Faudot F, Harmelin M, Quivy A and Bancel P A 1993 *J. Non-Cryst. Solids* **153-4** 482



# Influence of transmutation on microstructure, density change, and embrittlement of vanadium and vanadium alloys irradiated in HFIR

S. Ohnuki <sup>a</sup>, H. Takahashi <sup>a</sup>, K. Shiba <sup>b</sup>, A. Hishinuma <sup>b</sup>, J.E. Pawel <sup>c</sup>, F.A. Garner <sup>d</sup>

<sup>a</sup> Hokkaido University, Sapporo, Japan

<sup>b</sup> Japan Atomic Energy Research Institute, Tokai, Japan

<sup>c</sup> Oak Ridge National Laboratory, Oak Ridge, TN, USA

<sup>d</sup> Pacific Northwest Laboratory, Richland, WA, USA

Received 29 April 1994; accepted 2 September 1994

## Abstract

Addition of 1 at% nickel to vanadium and V–10Ti, followed by irradiation along with the nickel-free metals in HFIR to  $2.3 \times 10^{26} \text{ n m}^{-2}$ ,  $E > 0.1 \text{ MeV}$  (corresponding to 17.7 dpa) at 400°C, has been used to study the influence of helium on microstructural evolution and embrittlement. Approximately 15.3% of the vanadium transmuted to chromium in these alloys. The  $\sim 50 \text{ appm}$  helium generated from the  $^{58}\text{Ni}(n, \gamma)^{59}\text{Ni}(n, \alpha)^{56}\text{Fe}$  sequence was found to exert much less influence than either the nickel directly or the chromium formed by transmutation.

The V–10Ti and V–10Ti–1Ni alloys developed an extreme fragility and broke into smaller pieces in response to minor physical insults during density measurements. A similar behavior was not observed in pure V or V–1Ni. Helium's role in determination of mechanical properties and embrittlement of vanadium alloys in HFIR is overshadowed by the influence of alloying elements such as titanium and chromium. Both elements have been shown to increase the DBTT rather rapidly in the region of 10% (Cr + Ti). Since Cr is produced by transmutation of V, this is a possible mechanism for the embrittlement. Large effects on the DBTT may have also resulted from uncontrolled accumulation of interstitial elements such as C, N, and O during irradiation.

## 1. Introduction

Vanadium-base alloys are currently being investigated for potential applications as structural materials in fusion reactors [1–3]. As with other alloy systems, however, there is concern that the relatively high levels of helium generated in fusion neutron spectra will strongly influence the microstructural evolution, dimensional stability and especially the mechanical properties. In order to study the potential influence of helium/dpa ratio while irradiating vanadium alloys in reactors whose spectra produce much lower levels of helium, a variety of helium enhancement techniques are being employed. Some involve the use of boron additions to produce helium via the  $^{10}\text{B}(n, \alpha)^7\text{Li}$  reac-

tion [4–6], while others involve the preinjection of  $^3\text{He}$  via the “tritium-trick” prior to neutron irradiation [7]. The Dynamic Helium Charging Experiment utilizes pre-doping with tritium as well as continuous generation of tritium via transmutation of the  $^6\text{Li}$ -enriched lithium coolant surrounding the specimens [8].

Another doping technique explored in the current study involves adding natural nickel to vanadium alloys and irradiating them in a mixed spectrum reactor such as the High Flux Isotope Reactor (HFIR) at Oak Ridge National Laboratory. Using this approach, helium is produced via the two-step  $^{58}\text{Ni}(n, \gamma)^{59}\text{Ni}(n, \alpha)^{56}\text{Fe}$  sequence [9]. To explore the feasibility of this approach, both pure vanadium and V–10Ti (at%) were irradiated in HFIR, each as two variants.

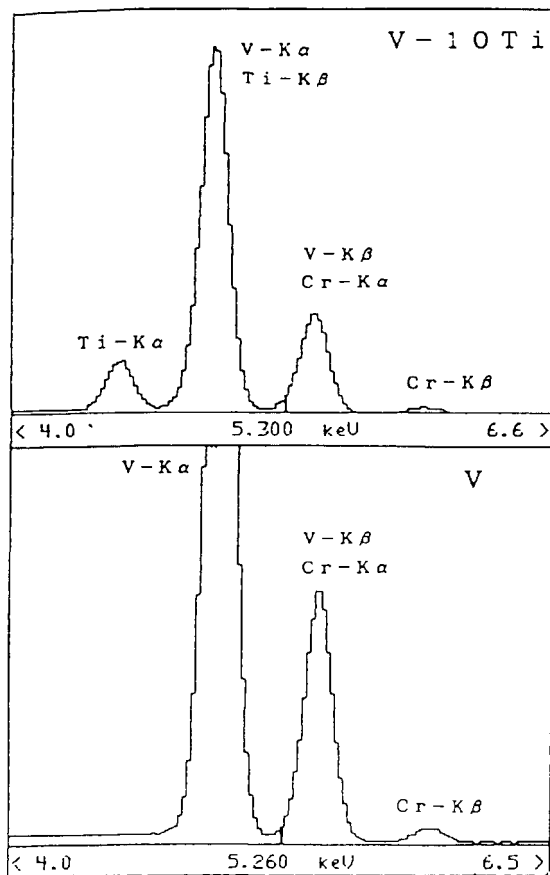


Fig. 5. EDX spectra observed in irradiated V and V-10Ti.

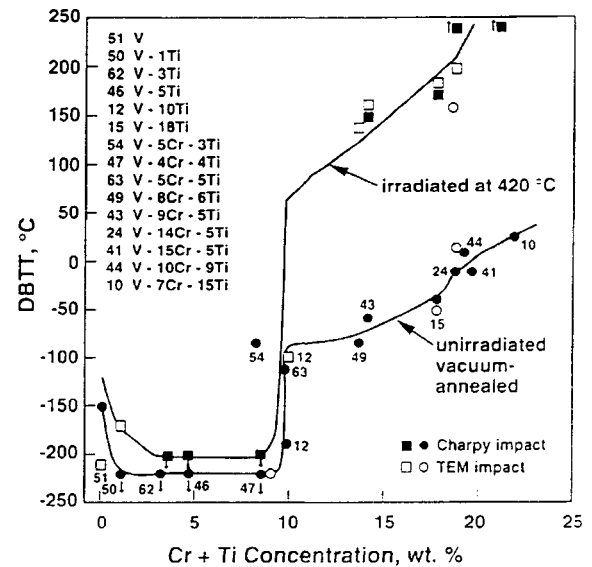


Fig. 7. Dependence of DBTT on solute concentration for V-Cr-Ti alloys irradiated at 420°C in FFTF to 32–44 dpa [18]. Closed symbols denote Charpy impact data. open symbols denote TEM impact data.

presence. Nickel tends to segregate at grain boundaries, however.

#### 4. Discussion

Although nickel was added to enhance the helium production, a significant role of helium on cavity nucle-

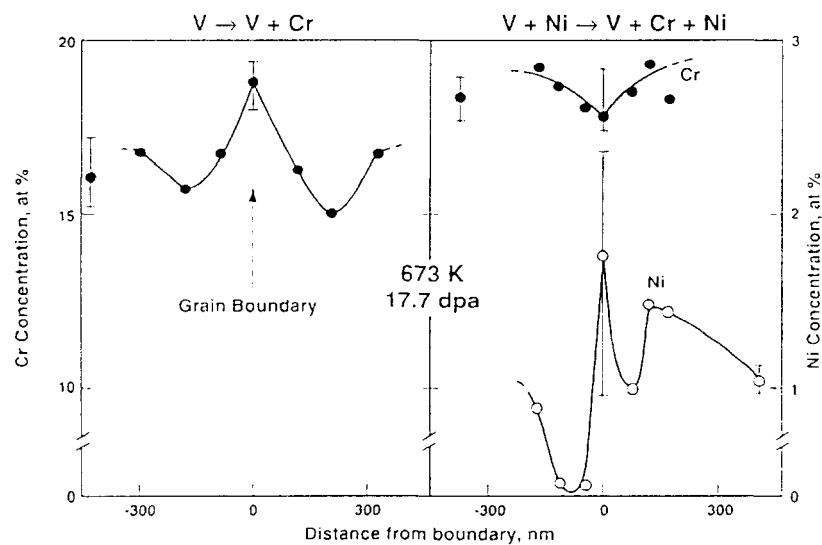


Fig. 6. Segregation profiles observed at grain boundaries in V and V-1Ni.

ation is not evident in Fig. 4. At this point, however, the helium buildup was not very large ( $\sim 50$  appm), due to the delay required to form the  $^{59}\text{Ni}$  from  $^{58}\text{Ni}$ . The small sizes of the cavities are consistent with their invisibility on the fracture surface. Even more important, the extreme fragility seems to be associated with the presence of titanium rather than with the presence of either nickel or helium. At this point, it is tempting also to preclude chromium as a cause of the embrittlement, since within  $\sim 10\%$ , the chromium levels are all approximately equal in the four alloys. V–Cr binaries ( $\text{Cr} = 5.0\text{--}14.1\%$ ) have been irradiated in the Fast Flux Test Facility (FFTF) to exposure levels ranging from 42 to 77 dpa at temperatures from 400 to 600°C in earlier studies, and did not exhibit such fragility [13,14].

The preferential polishing does appear to be associated with segregation of chromium, but the presence of nickel alters chromium segregation at grain boundaries and presumably at other sinks such as dislocations, thereby also influencing the electropolishing behavior.

While helium derived from nickel appears to play no large or direct role in cavity structure or density change in V and V–1Ni, nickel addition appears to depress swelling somewhat in V–10Ti. The density change values should not be interpreted to result from cavity swelling alone, however, since chromium additions tend to increase the density of vanadium alloys [15]. Thus, the swelling of V–10Ti and V–10Ti–1Ni may actually be larger than inferred from the data in Table 2. Swelling appears to have been enhanced in V–10Ti by the transmutation, since only  $\leq 1\%$  swelling was observed after irradiation in FFTF at 420°C to exposures of 36–77 dpa [13].

Nickel additions tend to increase the density of vanadium alloys [15] but they also have been shown to exert a strong direct role in alteration of radiation-induced microstructure in electron irradiations [16] and fast reactor irradiations [17], neither of which lead to significant generation of helium.

Loomis and coworkers [18] have shown that the ductile-to-brittle transition temperature (DBTT) of V–Ti binaries increases strongly for titanium concentrations greater than 5% after fast reactor irradiation (no significant transmutation) at 420°C to 34–44 dpa, but increases even more strongly in V–Ti–Cr alloys for increasing chromium levels above 5% Cr. For (Cr + Ti) levels above 9%, the DBTT after irradiation increases 200°C or more, as shown in Fig. 7. Since the (Cr + Ti) level of the broken specimens after irradiation is on the order of 25%, the DBTT of these specimens may be 250°C or greater. Note that even before irradiation, the DBTT of such high solute alloys is near room temperature. It is interesting to note that vanadium alloys with high chromium and titanium levels irradiated in FFTF also showed significant embrittlement, but that V–3Ti–1Si resisted embrittlement [19,20].

As shown by Greenwood and Garner [12], however, the transmutation rates experienced by vanadium in HFIR are more than an order of magnitude greater than those expected in fusion neutron spectra or that of liquid-metal-cooled fission reactors. Mori [21] has calculated that for the International Thermonuclear Experiment Reactor (ITER), transmutation of vanadium to chromium would be less than 1% per year at any position on the first wall when operating at 2 MW/m<sup>2</sup>. Therefore, the extreme fragility exhibited by V–Ti alloys after irradiation in HFIR may be very atypical of the response that will occur in fusion reactors. Therefore, if fusion-relevant tests are to be successfully conducted in mixed spectrum reactors, the thermal component of the neutron flux must be reduced significantly by shielding the specimens with materials that are strong absorbers of low energy neutrons.

It must also be noted that interstitial impurity elements such as carbon, oxygen, and nitrogen cause embrittlement of vanadium alloys [19]. The environmental pickup of these elements was neither controlled nor measured in this HFIR experiment and may be a significant factor contributing to the embrittlement, although consideration of the diffusion rates for these elements indicates that this possibility is unlikely. It is not so easy to dismiss the possibility of hydrogen embrittlement, however, particularly since the starting materials contained a relatively high concentration of hydrogen, as shown in Table 1.

This experiment demonstrates once again that the possible influence of solid transmutation must be taken into account when designing and evaluating experiments that will be conducted in neutron spectra which are only surrogates for the spectrum of actual application. A summary of previously cited situations where transmutation was found to be an important concern is presented in other papers [22,23]. Also demonstrated in this experiment is the principle that the impact of elemental tailoring of alloys to study the effects of transmutant helium is often overshadowed by the direct action of the tailoring agent itself.

## 5. Conclusions

The addition of nickel to vanadium and to V–10Ti appears to influence swelling of these alloys when irradiated at  $\sim 400^\circ\text{C}$  in HFIR, but its action appears to be related to nickel's direct influence on microstructural evolution, rather than to its role as a source of helium. Helium's role in determination of mechanical properties and embrittlement of vanadium alloys in HFIR is overshadowed by the influence of alloying elements such as titanium and chromium. Both elements have been shown to increase the DBTT rather

rapidly in the region of 10% (Cr + Ti). Since Cr is produced by transmutation of V, this is a possible mechanism for the embrittlement. Large effects on the DBTT may have also resulted from uncontrolled accumulation of interstitial elements, such as C, N, and O during irradiation.

The extreme embrittlement observed in this experiment resulting from chromium formation will not be representative of that expected in fusion neutron spectra, where the  $V \rightarrow Cr$  transmutation rate per dpa will be lower by more than an order of magnitude.

#### Acknowledgements

Work supported by the Japanese Ministry of Education, Science and Culture, under both the US/Japan Collaboration in Fusion Materials using Fission Reactors and the International Scientific Research Program Grant in Aid for Scientific Research. The US participation was supported by the US Department of Energy under Contracts DE-AC06-76RLO 1830 and DE-AC05-84OR21 400. The density measurements were performed at ORNL by L.T. Gibson and at PNL by Gary Whiting. The manuscript was prepared by Loree Swegle and Diane Forsyth.

#### References

- [1] D.L. Smith, J. Nucl. Mater. 122 & 123 (1984) 51.
- [2] D.R. Diercks and B.A. Loomis, J. Nucl. Mater. 141–143 (1986) 1117.
- [3] B.A. Loomis, A.B. Hull and D.L. Smith, J. Nucl. Mater. 179–181 (1991) 148.
- [4] H. Kawanishi, Y. Arai and S. Ishino, J. Nucl. Mater. 191–194 (1992) 933.
- [5] N. Sekimura and F.A. Garner, Fusion Reactor Materials Semiannual Progress Report DOE/ER-03131/13 (1990) pp. 235–237.
- [6] H.M. Chung, Fusion Reactor Materials Semiannual Progress Report DOE/ER-0313/14 (1993) pp. 299–305.
- [7] M. Satou, K. Abe and H. Matsui, J. Nucl. Mater. 191–194 (1992) 938.
- [8] D.L. Smith, H. Matsui, L. Greenwood and B. Loomis, J. Nucl. Mater. 155–157 (1988) 1359.
- [9] C.H. De Raedt, Proc. Conf. on Fast, Thermal and Fusion Reactor Experiments, (American Nuclear Society, La Grange Park, (1982) p. 226.
- [10] J.J. Norgett, J.T. Robinson and I.M. Torrens, Nucl. Eng. Des. 33 (1975) 50.
- [11] H. Kanazawa, T. Sawai and L.J. Turner, Fusion Reactor Materials Semiannual Progress Report DOE/ER-0313/8 (1990) pp. 17–20.
- [12] L.R. Greenwood and F.A. Garner, in J. Nucl. Mater. 212–215 (1994) 635.
- [13] B.A. Loomis, D.L. Smith and F.A. Garner, J. Nucl. Mater. 179–181 (1991) 771.
- [14] F.A. Garner, D.S. Gelles, H. Takahashi, S. Ohnuki, H. Kinoshita and B.A. Loomis, J. Nucl. Mater. 191–194 (1992) 948.
- [15] F.A. Garner and B.A. Loomis, Fusion Reactor Materials Semiannual Progress Report DOE/ER-0313/16 (1994), in press.
- [16] D.S. Gelles, S. Ohnuki, H. Takahashi, H. Matsui and Y. Kohno, J. Nucl. Mater. 191–194 (1992) 1336.
- [17] D.S. Gelles and J.F. Stubbins, J. Nucl. Mater. 212–215 (1994) 778.
- [18] B.A. Loomis, H.M. Chung, L.J. Nowicki and D.L. Smith, J. Nucl. Mater. 212–215 (1994) 799.
- [19] D.N. Braski, Proc. 13th Int. Symp. on Influence of Radiation on Material Properties, Part II, ASTM-STP 956, eds. F.A. Garner, C.H. Henager, Jr. and N. Igata (American Society of Testing and Materials, Philadelphia, 1987) pp. 271–290.
- [20] M.L. Grossbeck and J.A. Horak, Proc. 13th Int. Symp. on Influence of Radiation on Material Properties, Part II, ASTM-STP 956, eds. F.A. Garner, C.H. Henager, Jr. and N. Igata (American Society of Testing and Materials, Philadelphia 1987) pp. 291–309.
- [21] M. Mori, ITER/EDA Design Data, JA93–JA0132.
- [22] F.A. Garner, H.L. Heinisch, R.L. Simons and F.M. Mann, Radiat. Eff. Def. in Solids, 113 (1990) 229.
- [23] F.A. Garner and L.R. Greenwood, Mater. Trans. JIM 34 (1993) 985.

総説，解説，評論等

## 計算機化学の石炭構造研究への応用

(キーワード 石炭化学構造, 計算機支援分子設計, 密度シミュレーション, 非結合性相互作用, 石炭-水相互作用)

— 1995. 5.10 受理 —

大阪大学\*<sup>1</sup> 村田 聡, 三浦 雅博, 野村 正勝  
 東北大学\*<sup>2</sup> 鷹觜 利公, 飯野 雅  
 北海道大学\*<sup>3</sup> 熊谷 治夫, 真田 雄三  
 大阪ガス株式会社\*<sup>4</sup> 中村 和夫

### 1. はじめに

近年計算機の急速な進歩により, 身近に利用できる環境が整ってきた。高速のCPU (central processing unit, 中央演算処理装置) と膨大な記憶空間 (メモリやディスク装置) を必要とする計算化学は, その恩恵をもっとも受けているものの一つであろう。従来の計算化学では分子軌道 (molecular orbital, MO) 法を用いて低分子化合物を取り扱う場合が多かったが, 計算機の性能の向上とともに分子力学 (molecular mechanics, MM) 法および分子動力学 (molecular dynamics, MD) 法といった計算手法を併用することで巨大分子系のシミュレーションが可能となっている。たとえば蛋白質工学および医薬設計の分野では, 計算機支援分子設計 (computer-aided molecular design, CAMD) 技術が実用化されており, パーソナルコンピュータ (パソコン, PC) 上でも MM, MD, MO 計算が可能な HyperChem (KGT) や CAChe (ソニーテクノロジクス) のようなソフトウェアも登場している。これらのソフトウェアを最新の PC 上で動かすことにより, 数年前のエンジニアリングワークステーション (EWS) に匹敵する計算を行うことが可能になっているのである。

著者らは, 1992年からEWSとCAMDソフトを用いて石炭三次元構造に関する共同研究を行ってきた。その経緯をふまえ, 本総説では, 米国のCarlsonらのグ

ループが行った石炭モデルの評価法およびFaulonらが行った石炭構造自動描出法について紹介する。最後に著者らが行った石炭構造モデルの密度シミュレーション, 石炭の会合構造に関するシミュレーションおよび石炭と水との相互作用に関する研究について述べる。なお, これらのシミュレーションの基礎となる MM, MD, MO 計算等については紙数の関係上本説では触れないが, 優れた成書が既に出版されているのでそれを参照されたい<sup>1)~3)</sup>。

### 2. 米国での研究

米国のCarlsonら<sup>4)</sup>は, CAMDを用いて初めて石炭モデルのCAMD計算を行った。彼らは, Given<sup>5)</sup>, Wiser<sup>6)</sup>, Solomon<sup>7)</sup>, Shinn<sup>8)</sup>らによって報告された石炭構造について MM, MD 計算を行い, その最も安定な構造を求めた。最適化構造の例を図1に示す。この構造をもとに, 3次元ネットワークを形成する架橋密度, 水素結合の評価を行うと共に, 真比重や孔隙率を求めている。彼らは, まず求めた安定構造を最小限の大きさの直方体に閉じ込め, その直方体を一辺1 Åの立方体に分割し, これらをstructural volume (空隙容積を除いた分子占有容積), void volume (空隙容積), external volume (外部容積) の3つに分類している。こうして彼らは真比重をモデル分子の分子量とstructural volume から算出した。計算された真比重は, Shinnのモデルで1.23, Wiserのモデルで1.27と, 実際の瀝青炭の測定値1.25-1.30g/cm<sup>3</sup>とよく一致している。また, microporosity [void volume / (structural volume + void volume)] についても言及しており, 計算した直径1.5nm以下の細孔容積の総量はShinnのモ

\*1 工学部 吹田市山田丘2番1号

\*2 反応化学研究所 仙台市青葉区片平2-1-1

\*3 エネルギー先端工学研究センター

札幌市北区北13条西8丁目

\*4 基盤研究所 大阪市此花区西島6丁目19-9

する構造を入力し、MM法およびMD法で最適化する。これを周期的境界条件(periodic boundary conditions, PBC)下でMM, MD計算を行う。すなわち、対象分子を“cell”中に閉じこめcellのサイズを縮める。この状態では分子内、分子間の反発により不安定な状態となっているため、MM, MD計算により再度最適化を行う。この作業を繰り返すことにより、密度-エネルギーの相関図を得る。分子の持つエネルギーは、cellを縮めることにより初めは減少し、ある最小値を経てふたたび増加する。我々は、この最小エネルギーを持つ状態を対象分子の密度と定義した<sup>13)</sup>。この手法は前述のCarlsonの手法と比較すると分子間の相互作用や、分子間に存在するミクロポアを考慮できるという特徴を持っている。

この手法をスチレンオリゴマー(11量体)に適用したところ、得られた値(1.02 g/cm<sup>3</sup>)はアモルファスポリスチレンの密度(1.04-1.065g/cm<sup>3</sup>)と比較的よく一致することが明らかとなった。Polygrafで用いられているDREIDING力場は、(1)式に従って全エネルギーが計算される<sup>16)</sup>。

$$E = (E_s + E_b + E_t + E_i) + (E_{vdw} + E_e + E_h) \quad (1)$$

$E_s$  : 結合伸縮エネルギー

$E_b$  : 変角エネルギー

$E_t$  : ねじれエネルギー

$E_i$  : 結合の反転エネルギー

$E_{vdw}$  : van der Waals 相互作用

$E_e$  : 静電相互作用

$E_h$  : 水素結合

各エネルギー項の内訳から、van der Waals 相互作用( $E_{vdw}$ )の寄与が最も大きいことがわかった。従って、cellを縮めた場合に全エネルギーが徐々に低くなるのは分子内あるいは分子間でvan der Waals 引力が作用しているためと考えられる。

上述の方法を用いて、岩田らが提案した一連の石炭モデル(図4)<sup>17)18)</sup>、天北炭(C%:71.5%, 密度: 1.37 g/cm<sup>3</sup>)、太平洋炭(77.9%, 1.27g/cm<sup>3</sup>)、赤平炭(81.2%, 1.28g/cm<sup>3</sup>)、夕張炭(86.7%, 1.24g/cm<sup>3</sup>)のモデルの密度の算出を試みた<sup>14)</sup>。その結果石炭の密度は次のような値になることがわかった(天北炭:1.29, 太平洋炭: 1.22, 赤平炭: 1.03, 夕張炭: 1.11g/cm<sup>3</sup>)。ここで、赤平炭以外の石炭では、石炭化度が上がるにつれて密度が増加することがわかる。実際の石炭の密度との比較を図5に示した。赤平炭以外の3つのモデルに対

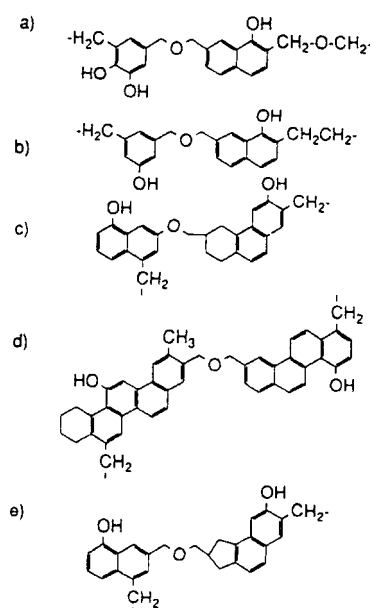


図4 岩田らが提案した石炭の平均構造  
a) 天北炭, b) 太平洋炭, c) 赤平炭,  
d) 夕張炭, e) 赤平炭の修正構造

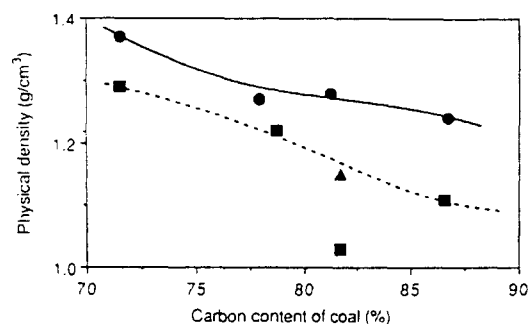


図5 炭素含量と密度の相関  
実測値 (●), 計算値 (■), および赤平炭の修正構造に対する計算値 (▲)

して計算した密度の傾向は、現実のそれとよく対応しているが、赤平炭ではかなり異なる。そこで、赤平炭の構造に着目すると、2つの芳香族ユニットをつなぐ結合は4つのモデルの中で、最も短いことがわかる。我々は、多環芳香族化合物をポリメチレン鎖で架橋した一連のモデル化合物を対象として密度シミュレーションを行っており<sup>13)</sup>、その結果、架橋の長さや密度の計算値との間に相関があることを認めている。そこで、図4eに示すように赤平炭の構造の修正を行い、密度を計算したところ、太平洋炭と夕張炭の間の値が得られた。

最後に、我々が1992年に提出した赤平炭( $C_{390}H_{362}N_6O_{38}$ , 分子量5734)の構造<sup>19)</sup>についての密

表1 石炭化学構造モデルの分子パラメーターおよびエネルギー

| parameter                | Wiser                   | Solomon<br>(modified)    | Shinn                    | Kumagai-Nakamura-Sanada   |                           |                              |
|--------------------------|-------------------------|--------------------------|--------------------------|---------------------------|---------------------------|------------------------------|
| type of coal             | bituminous              | bituminous <sup>1)</sup> | bituminous <sup>2)</sup> | raw lignite               | dried lignite             | re-ad. lignite <sup>3)</sup> |
| no. of atoms             | 393                     | 396                      | 1311                     | 242                       | 242                       | 242                          |
| mol wt                   | 2967                    | 3020                     | 9956                     | 1922                      | 1922                      | 1922                         |
| $C_{ar}/C_{total}$       | 0.70                    | 0.74                     | 0.71                     | 0.57                      | 0.57                      | 0.57                         |
| $H_{ar}/(H_{ar}+H_{al})$ | 0.28                    | 0.40                     | 0.34                     | 0.19                      | 0.19                      | 0.19                         |
| wt fraction              |                         |                          |                          |                           |                           |                              |
| C                        | 0.782                   | 0.823                    | 0.789                    | 0.656                     | 0.656                     | 0.656                        |
| H                        | 0.059                   | 0.056                    | 0.057                    | 0.053                     | 0.053                     | 0.053                        |
| O                        | 0.113                   | 0.090                    | 0.119                    | 0.291                     | 0.291                     | 0.291                        |
| N                        | 0.014                   | 0.009                    | 0.015                    | 0                         | 0                         | 0                            |
| S                        | 0.032                   | 0.021                    | 0.019                    | 0                         | 0                         | 0                            |
| normalized               | $C_{100}H_{90}O_{10.9}$ | $C_{100}H_{81}O_{8.2}$   | $C_{100}H_{87}O_{11.3}$  | $C_{100}H_{97.1}O_{33.3}$ | $C_{100}H_{97.1}O_{33.3}$ | $C_{100}H_{97.1}O_{33.3}$    |
| formula                  | $N_{1.6}S_{1.6}$        | $N_{1.0}S_{1.0}$         | $N_{1.7}S_{0.9}$         |                           |                           |                              |
| energy <sup>4)</sup>     | 1.78                    | 1.75                     | 1.65                     | 1.44                      | 1.11                      | 1.24                         |

1) PSOC 170

2) vitrinite-rich high-volatile bituminous

3) lignite with re-adsorped water

4) normalized energy of minimized structure(kcal/atom)

水素結合の供与・授与基の数は多いが、水素結合の数および個々の水素結合の強さに関しては瀝青炭と大きな相違はないことがわかる。これらの結果はあくまでも提案されたモデルによる計算結果であり、一概に比較することには問題があろう。それぞれのモデルの提出された背景から考慮すると、このようなシミュレーションを行うにはそれなりのモデルを再構築することが今後の課題である。

#### 6. 褐炭/水系の高次構造変化

水分の脱離・吸着に伴う褐炭分子の高次構造変化についてシミュレーションを行った結果について述べる。褐炭の分子モデルは前節と同じモデルを用いた。褐炭分子周辺の水分子数はAllardiceらの文献値<sup>33)</sup>を参考にして設定した。原炭中の199個の水分子を0個まで変化させた場合、褐炭/水系のエネルギーが最小となる褐炭分子の安定構造の立体配座は図12(a)および(b)に示すように伸びた構造から折り畳まれた構造へと変化する。このシミュレーション結果は褐炭を脱水・乾燥すると収縮を起こし見掛けの体積が減少することとよく対応する。水分子数を0個とした褐炭分子に再び水を吸着させたときの褐炭分子の最小エネルギー状態をシミュレーションした。図12(c)に示すように褐炭分子の安定構造の立体配座は水分子数を増加させても大きく変化せず折り畳まれた構造のままである。この結果は脱水・乾燥による褐炭の変化は分子レベルでは不可逆であることを示唆しているものと考えられる。

水分の脱離・吸着に伴う褐炭分子モデルの分子パラメータおよび安定構造中に存在する水素結合の形態を表1および表2に示す。原子1個あたりに基準化した褐炭分子の安定構造のエネルギーは、水分の脱離により原炭(raw lignite)の1.44kcal/molから乾燥褐炭(dried lignite)の1.11kcal/molへと減少する。この結果は乾燥により褐炭分子はエネルギー的により安定な構造へと変化することを示している。乾燥褐炭に水を再吸着させた場合(re-ad. lignite)、安定構造のエネルギーは1.24kcal/molまで増加するが原炭よりは低い値を示す。このことから、乾燥に伴う褐炭の変化はエネルギー的にも不可逆であることが分かる。次に水素結合の変化を見ると、乾燥に伴い褐炭分子中の原子100個当たりのクラスター間水素結合の数は増加し、クラスター間水素結合1個あたりに平均化したエネルギー値は減少している。これらの結果は乾燥により褐炭分子がエネルギー的により安定な構造へと変化する際に水素結合が大きく寄与することを示している。乾燥褐炭に水を再吸着させた場合、原子100個当たりのクラスター間水素結合の数は変化しない。また、クラスター間水素結合1個あたりに平均化したエネルギー値は僅かに増加するのみであることから、乾燥によって形成された水素結合は水を再吸着した場合にも解離しないことが分かる。

上記のような分子レベルの変化は反応性にも大きく関わってくるものと考えられる。最近、Songらは



現在、NEDOL法による石炭液化反応に対して分散系鉄触媒を石炭に担持させる場合の出発原料石炭の水分調整法が検討されているが、これも上記のような観点から突っ込んだ研究が望まれるところである。次世代の石炭転換反応ではエネルギー転換効率が高く選択性の高いプロセスが要求されており、これらの要求に応えるためには石炭の高次構造(凝集構造)および非共有結合を考慮に入れた前処理や転換反応の設計が不可欠となる。シミュレーションより得られる石炭の構造に関する種々の情報は次世代の石炭転換反応プロセスを設計する上で有益な知見をもたらすものと期待される。

#### 7. おわりに

本総説は、主として計算機を用いた石炭化学構造研究を行っている3大学と大阪ガスの研究成果をとりまとめたものである。責任の所在を明らかにする意味で以下に担当の章を記載しておく；第1-3章および第7章：村田、三浦、野村；第4章：鷹薮、飯野；第5-6章：熊谷、真田。

さて、序論につづき、2章では米国での最近の研究成果を、3-6章では著者らの研究成果を紹介した。計算機を用いた石炭構造のシミュレーションは、まだはじまったばかりであるが、徐々にその有用性が明らかにされてきているように思われる。しかしながら、石炭の計算機化学研究にはいくつかの問題点が内包されており、その最大のものは石炭構造を推定する上で芳香族を結ぶ脂肪族部分の構造が未だ充分明らかにされていない点であろう。ここで紹介したシミュレーションでは分子レベルでの石炭構造が要求されており、入力する構造の精度が各種物性評価のシミュレーションに大きな影響を与えることがわかる。しかしこうした問題点にもかかわらず、石炭のゲル構造とその架橋結合の性状や各種相互作用の評価、そして石炭の化学反応性に関し、計算機化学研究が大きな可能性を持っていることを強調しておきたい。

#### 文 献

- 1) 大澤映二編, 実験化学講座, 3巻, “基本操作III コンピュータ利用”, 日本化学会編, 丸善(1991)
- 2) 大澤映二編, 計算化学入門, 講談社(1994)
- 3) 平野恒夫, 田辺和俊編, 分子軌道法MOPACガイドブック, 海文堂(1991)
- 4) Carlson, G. A., *Energy Fuels*, 6, 771 (1992)
- 5) Given, P. H., *Fuel*, 39, 147 (1960)
- 6) Wiser, W. H., *NATO ASI series C*, 124, 325 (1983)
- 7) Solomon, P. R., *New Approaches in Coal Chemistry*, ACS Symposium Series No. 169, ACS, Washington DC, p. 61 (1981)
- 8) Shinn, J. H., *Fuel*, 63, 1187 (1984)
- 9) White, W. E., Bartholomew, C. H., Hecker, W. C. and Smith, D. M., *Adsorpt. Sci. Technol.*, 7, 180 (1990)
- 10) Faulon, J.-L., Hatcher, P. G. and Wenzel, K. A., *Am. Chem. Soc., Div. Fuel Chem., Prepr.*, 37, 900 (1992); Faulon, J.-L., Carlson, G. A. and Hatcher, P. G., *Energy Fuels*, 7, 1062 (1992)
- 11) Hatcher, P. G., Faulon, J.-L., Wenzel, K. A. and Cody, G. D., *Energy Fuels*, 6, 813 (1992)
- 12) Faulon, J.-L., Mathews, J. P., Carlson, G. A. and Hatcher, P. G., *Energy Fuels*, 8, 408 (1994)
- 13) Nakamura, K., Murata, S. and Nomura, M., *Energy Fuels*, 7, 347 (1993)
- 14) Murata, S., Nomura, M., Nakamura, K., Kumagai, H. and Sanada, Y., *Energy Fuels*, 7, 469 (1993)
- 15) Dong, T., Murata, S., Miura, M., Nomura, M. and Nakamura, K., *Energy Fuels*, 7, 1123 (1993)
- 16) Mayo, S. L., Olafson, B. D. and Goddard, III, W. A., *J. Phys. Chem.*, 94, 8897 (1990)
- 17) Iwata, K., Itoh, H. and Ouchi, K., *Fuel, Process. Technol.*, 3, 221 (1980)
- 18) Iwata, K. Dr. thesis, “Studies on average chemical structure of coal”, Hokkaido University (1983)
- 19) Nomura, M., Matsubayashi, K., Ida, T. and Murata, S., *Fuel Process. Technol.*, 31, 169 (1992)
- 20) Takanohashi, T., Iino, M. and Nakamura, K., *Energy Fuels*, 8, 395 (1994)
- 21) Sanokawa, Y., Takanohashi, T. and Iino, M., *Fuel*, 69, 1577 (1990)
- 22) Ishizuka, T., Takanohashi, T., Ito, O. and Iino, M., *Fuel*, 72, 579 (1993)
- 23) Liu, H.-T., Ishizuka, T., Takanohashi, T. and Iino, M., *Energy Fuels*, 7, 1108 (1993)
- 24) 鷹薮利公, 飯野 雅, 中村和夫, 村田 聡, 野村正勝, 第2回日本エネルギー学会大会講演要旨集, p. 7 (1993)
- 25) 鷹薮利公, 飯野 雅, 中村和夫, 化工論文集, 20, 959 (1994)
- 26) Nakamura, K., Takanohashi, T., Iino, M., Kumagai, H., Sanada, Y., Murata, S. and Nomura, M., to

- be submitted. 原子当りに基準化した値。
- 27) Cody, G.D.Jr, Larsen, J.W. and Siskin, M., *Energy Fuels*, 2, 340 (1988) 32) 単純な低分子化合物では安定構造のエネルギーは負の値を取る。
- 28) Fujiwara, M., Ohsuga, H., Takanohashi, T. and Iino, M., *Energy Fuels*, 6, 859 (1992) 33) Allardice, D.J. and Evans, D.G., *Fuel*, 50, 201 (1971)
- 29) 分子パラメータはCarlsonにより提案された *Molecular Parameter*の訳である。 34) Song, C. and Saini, A.K., *Energy Fuels*, 9, 188 (1995)
- 30) Yoshida, T., Nakata, Y., Yosida, R., Ueda, S., Kanda, N. and Maekawa, Y., *Fuel*, 61, 824 (1982) 35) Kumagai, H., Sato, N., Sanada, Y., Nakamura, K., Sasaki, M. and Kotanigawa, T., *Proceedings of 6th Australian Coal Science Conference*, 256-262, Newcastle, Oct. 17-19 (1994)
- 31) 分子の立体配座が最も歪みの少ない、即ち最小エネルギーとなった安定構造のエネルギーを総ての

### Application of Computer Chemistry to the Study of Coal Chemical Structure

Satoru MURATA<sup>\*1</sup>, Masahiro MIURA<sup>\*1</sup>, Masakatsu NOMURA<sup>\*1</sup>,  
Toshimasa TAKANOHASHI<sup>\*2</sup>, Masashi IINO<sup>\*2</sup>, Haruo KUMAGAI<sup>\*3</sup>,  
Yuzo SANADA<sup>\*3</sup> and Kazuo NAKAMURA<sup>\*4</sup>

- ( \*1 Faculty of Engineering, Osaka University  
\*2 Institute for Chemical Reaction Science, Tohoku University  
\*3 Center for Advanced Research of Energy, Hokkaido University  
\*4 Fundamental Research Laboratories, Osaka Gas Co. Ltd. )

**SYNOPSIS** : — Remarkably rapid development of both computer hardware and software has made computer chemistry intimate to chemists. Those who work in coal chemistry often treat macromolecular systems including more than a hundred atoms, the computer-aided molecular design (CAMD) study of which are largely benefited by the development of computer itself. In this review, recent results of CAMD study concerning coal chemical structure are summarized.

After a brief introduction concerning computer utilization in coal chemistry in the first chapter, the results of CAMD study reported by the American group are summarized in chapter 2. In chapters 3 - 6, our results of calculation of physical density of coal model molecules are concisely described based on CAMD studies along with presentation of Zao Zhuang coal by taking into consideration non-bonding interactions in coal molecules and interaction between coal organic materials and water in model structure of brown coal. These studies are conducted at Osaka University, Tohoku University and Hokkaido University, respectively, by the support of Osaka Gas Co. Ltd.

#### Key Words

Coal chemical structure, Computer-aided molecular design, Density simulation, Non-bonding interaction, Interaction between coal and water

炭素の融点はダイヤモンド-黒鉛-炭素液体の3重点が100 Kbar, 4100 Kで、炭素原子クラスターから成る蒸気への昇華熱は710 kJ/molときわめて大きい値である。このような大きな値は共有結合性の大きい高融点金属に属するタングステン、モリブデンもはるかに及ばない。

#### 異性体と構造の特徴

炭素の異性体としてダイヤモンド結晶以外に、常圧下で安定相である黒鉛（グラファイト）結晶が知られている。鉛筆の芯、冷蔵庫の脱臭、水道水の浄化用活性炭、コーヒー焙煎、うなぎを焼くときに用いられる備長炭などわれわれの身のまわりにある炭素は基本的には黒鉛構造を有している。ダイヤモンドは電子の混成軌道が $sp^3$ 、黒鉛のそれは $sp^2$ である。ダイヤモンドは無色透明、電気絶縁体、熱伝導体である。 $sp^3$ ダイヤモンドはSiにつぐ21世紀の半導体素子となるポテンシャルを有している。耐熱性、耐放射線状がSiよりもすぐれており、宇宙空間で機能する素子の主流になるかも知れない。

一方 $sp^2$ 黒鉛結晶は黒色、電気ならびに熱伝導性が大きく、ダイヤモンドと対照的である。黒鉛は黒色物質で何となくきたないイメージを与えるが、この黒いということは可視光線を吸収することにはかならず、伝導キャリアである $\pi$ 電子の準位が連続的に分布しているからである（こんなに簡単に説明しきれものではないだろうが）。黒鉛が $\pi$ 電子を有することから多くの興味ある物性を示し応用が考えられている。強い共有結合を形成している電子対が $\sigma$ 電子であり局在性が

大きいのと対照的に、 $\pi$ 電子は空間的に雲のように拡張し、その移動度はきわめて大きい。自由電子の有効質量を $m_0$ とすると $\pi$ 電子では0.056 $m_0$ 、高速デバイス用として注目されているGaAsのそれは0.076 $m_0$ である。この点に注目して新規の材料を合成する試験、電子の目でみた巨大空間を利用して物理、化学、生体現象を追求し、物質から生命への架け橋にしようとする炭素を中心にした $\pi$ 電子プロジェクトが新技術事業団の支援で平成3年度より発足している。

扱て炭素に $sp^1$ 、 $sp^2$ 型異性体があるならば $sp$ 型の1次元素結晶は存在するだろうか。カルビン（Carbyne）と称される一群の炭素が隕石が衝突してできたクレーターから白色炭素として発見された。実験室において衝撃法により黒鉛から作る試みがなされているが、詳細は不明である。

図1に炭素の異性体の構造を示した。(a)ダイヤモンド、(b)黒鉛、(c)カルビンの仲間に分類されるカルボライト（いわき明星大田沼教授による命名）、(d)フラーレンである。(c)に示す一次元の形はポリアセチレンから骨格を保ったまま水素原子を引き抜けばよいが、実際には黒鉛電極間で放電により生成した炭素クラスターを急冷することにより生成するといわれている。密度は(a)ダイヤモンド3.52 g/cm<sup>3</sup>、(b)黒鉛2.25 g/cm<sup>3</sup>、(c)カルボライト1.46 g/cm<sup>3</sup>（推定）、(d)フラーレン1.65 g/cm<sup>3</sup>である。いずれにしても比重は金属にくらべてはるかに小さく、合成樹脂、天然木材に比べてやや大きいところに位置している。従って比強度、比弾性率は炭素（繊維を例にとれ

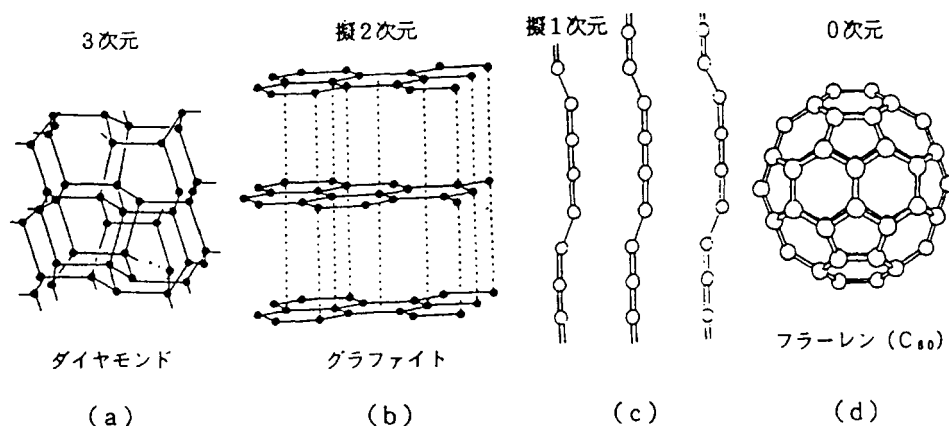


図1 炭素の基本構造  
(炭素素原料科学の進歩 VII (1995)p.14 より引用)

ば)はきわめて大きく、先端材料として注目されることがわかる。

#### 構造と特性の多様性

上述のように炭素の基礎構造には種々の異性体が存在する。さらに忘れてならないのは基本構造に加えて一次構造とそれらの集合構造の多様性である。一般に炭素は有機化学物を前駆体として生成している。C, H, Oに限った有機化合物でもこれらの原子の組み合わせは天文学的な数が可能であり、共有結合からできている炭素も2~3の安定構造にいたる間に非常に多くの形態が存在する可能性がある。すなわち炭素の一次構造、微構造 (microstructure), 組織 (macrostructure, texture) はきわめて多様である。とくに前駆体が固態のまま炭素になる固相炭素化物は、例えば木材から木炭を作るときを考えると、木材の植物組織を保存したまま木炭になっており、従って木炭は元植物の種類に大きく依存している。メソフェーズピッチにみられる液相炭素化では773~923 Kで分解、重縮合などの多数の化学反応が同時に併発するが、系が液相のため炭素に移行する分子 (雑多ではあるが) の再配列が容易に起こるので、固相炭素化ほどではないが生成する炭素はやはり前配体の構造、反応条件に大きく依存す

る。炭素の構造と物性は“生まれ”と“育ち”により決まるといわれる理由はこのようなところにある。

カーボンブラック、フラーレン、ナノチューブ、気相成長ダイヤモンドは、与えられた反応条件下で気相にとびだした炭素原子集団 (クラスター) が安定あるいは準安定な状態で凍結されてとりだされたものである。カーボンブラック、フラーレンは気相成長炭素の超微粒子とみることができる。しかし前者の基本構造は図1の (b), 後者は (d) であるので物性も根本的に異なったものである。ここでも反応条件、共存物質の効果により生成物をコントロールできる。

炭素材料中の細孔、内部表面の特異性を利用した用途、黒鉛結晶の層間 (主として van der Waals 力) にハロゲン、アルカリ金属をそう入した層間化合物の有する物性については紙面の都合で割愛するが、本特集の (3) フラーレン、カーボンナノチューブの合成の最近の進歩, (5) 省エネルギー材料としてのピッチ系炭素繊維, (6) CVD 法によるグラファイト薄膜とヘテログラファイト薄膜の作成, (7) リチウム2次電池における負極用高性能炭素材料に関連している。

# ファインケミカルズと固体塩基触媒

服部 英<sup>\*</sup>, 辻 秀人<sup>\*\*</sup>

## 1. はじめに

近年、固体触媒を用いたファインケミカルズ合成のプロセスは国内においても次々と開発されている。これまで、固体酸は石油精製プロセスに広く用いられてきたのに対し、固体塩基は石油精製や石油化学上流でのプロセスに用いられた例は殆どなかった。しかし、有機合成反応に頼るファインケミカルズ合成においては、炭素-炭素結合を生成する塩基触媒反応は重要であり、固体塩基触媒が適用できるケースは多いと考えられる。新規な固体塩基触媒の調製と触媒作用の研究は報告され続けており、固体塩基触媒の選択の幅は広がりつつあるといえよう。

本稿では、固体塩基触媒を用いた有機合成反応例とファインケミカルズ合成に有用であると思われるモデル反応に対する固体塩基の触媒作用を中心に概説する。また、各種固体塩基触媒の特色についても最後に触れる。

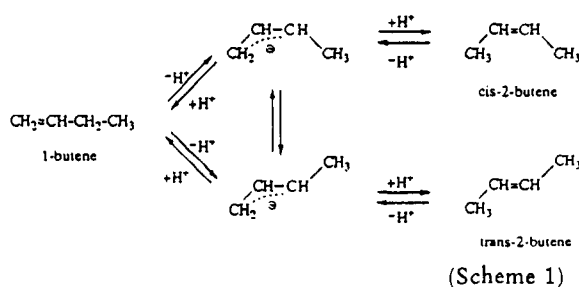
## 2. 固体塩基触媒の触媒作用

この章では、有機合成に固体塩基が用いられた例を紹介する。触媒表面の反応機構を解明する目的で行われた例と有機合成への応用例とが含まれている。

### 2.1 二重結合移行

ブテンの異性化は、有機合成としては興味ある反応とはいえないが、触媒の表面性質、表面反応のメカニズムを理解するには大変有効であり、この反応

を行わせることにより塩基触媒作用を示すことが明らかになった固体も多い。固体塩基触媒上では、次のスキームで進行する<sup>1)</sup>。



すなわち、表面の塩基点によりアリリック水素が $H^+$ として引き抜かれ、アリルアニオンが生成し、金属カチオンにより安定化する。アニオンはcis型のほうがtrans型よりも安定なので生成する2-ブタンはcis-2-ブテンが多い。反応は分子内水素移行で進行する。

ブテン異性化に対する固体塩基の触媒作用の知見を基にして、より複雑な骨格を有するオレフィンの二重結合移行に高活性を示す固体塩基触媒が見いだされている。カレン<sup>2)</sup>、ピネン、イルダジエン、プロトイルデン<sup>3)</sup>などの三員環、四員環を有するオレフィンも、開環することなく選択的に二重結合移行のみが進行する。固体塩基はC-C結合を切断しないという特性とともに高活性であるため、低温で反応が進行し高選択性を示す。

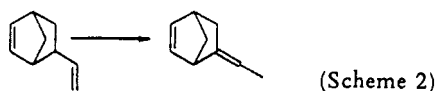
アリル位の水素がアルキル基で置換されるにしたがい、 $H^+$ として引き抜かれ難くなると予想される。したがって、三級アリル位炭素からの $H^+$ 引き抜きで反応が開始される異性化では強い塩基性(超強塩基性)が必要となる。鈴嶋らは5-ビニルビシクロ[2.2.1]ヘプタ-2-エンの異性化を穏和な条件で進行させる固体塩基触媒としてNa-NaOH- $Al_2O_3$ やK-KOH- $Al_2O_3$ を開発した<sup>4)</sup>。後に、CaO<sup>5)</sup>やMgO<sup>6)</sup>も適切な前処理をすればこの反応を進行させることが分かった。CaOやMgOにも3級アリル位

<sup>\*</sup> HIDESHI HATTORI 北海道大学エネルギー先端工学研究センター教授

筆者紹介 (最終学歴) 1968年東京工業大学大学院理工学研究科修了。〔専門〕触媒化学。〔趣味〕河川、山に行くこと、スキー、テニス。〔連絡先〕060札幌市北区北13条西8丁目 Fax. 011-726-0731(勤務先)

<sup>\*\*</sup> HIDETO TSUJI (株)三菱化学横浜総合研究所  
筆者紹介 (最終学歴) 1994年北海道大学大学院理工学研究科修了。〔専門〕触媒化学。〔趣味〕美術鑑賞。〔連絡先〕227 横浜市緑区鴨志田町1000(勤務先)

からの  $H^+$  を引き抜ける程の強い塩基点が存在することがうかがえる。

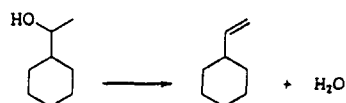


NやOを含む不飽和化合物であるアリルアミンやアリルエーテルの二重結合移行にも固体塩基がよい触媒となる<sup>7,8)</sup>。固体酸を用いると活性点が被毒を受け反応は進行しないが、固体塩基はNやOと相互作用が弱く、反応物から  $H^+$  を引き抜いてアリルアニオンを生成し反応を促進する。反応機構はブテンの異性化と本質的に同じである。アリルアミンやアリルエーテルの場合も、中間体であるアリルアニオンは cis 型のほうが安定なので生成物は cis 型が多くなる。サフロールからイソサフロールへの異性化も  $Na-NaOH-Al_2O_3$  を用いると室温でも効率よく進行する<sup>4)</sup>。

## 2.2 脱水と脱水素

アルコールは酸触媒では脱水が起こりオレフィンとエーテルを、塩基触媒では脱水素が起こりアルデヒドあるいはケトンを生成するのが一般的である。ある種の固体塩基触媒を用いると脱水が起こる。反応機構は、酸触媒の脱水と異なり、生成物の分布も異なる。典型的な例が、2-ブタノールの脱水でみられる。希土類酸化物<sup>9)</sup>、 $ThO_2$ <sup>10,11)</sup>、 $ZrO_2$ <sup>12)</sup>を触媒とすると、1-ブテンがおもに生成し、酸触媒では2-ブテンが生成するのと対照的である。塩基点により引き抜かれる  $H^+$  は1位の炭素からのものであり、アニオン中間体の経路するのに対し、酸触媒ではカルベニウムイオンを経由するからと理解される。

1-シクロヘキシルエタノールの脱水によりビニルシクロヘキサンを生成する反応は  $ZrO_2$  触媒を用いて工業化されている<sup>13)</sup>。1-オレフィンへの選択性は、 $ZrO_2$  に不純物として含まれている Si により酸性点が生成し、低下する。NaOH 処理をすることにより酸性点をなくし選択性を向上させ、工業化に成功した。



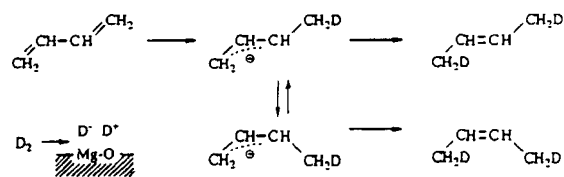
(Scheme 3)

分子内脱水によりモノエタノールアミンからエチレンイミンを生成する反応は、Si、P、およびアルカリを含む酸化物を触媒として工業化された。この

触媒は、弱い酸性和弱い塩基性を有している。反応物は反応性に富む二つの官能基を有しているの、酸性も塩基性も強すぎると副生成物が多くなる。触媒は、Si、Cs、Pの組成を変えることにより酸性・塩基性を調節し、Si/Cs/P/Oの原子比が1/0.1/0.08/2.25のとき選択率が78.8%となった<sup>14)</sup>。

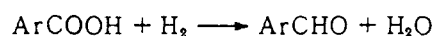
## 2.3 水素化

固体塩基触媒で起こる水素化は、遷移金属やその酸化物による水素化とは様相が異なる。水素分子の不均一な解離吸着により生じた  $H^+$  と  $H^-$  の付加反応である<sup>15~19)</sup>。ブタジエンやイソブレンなどの共役ジエンの水素化はモノオレフィンまでは容易に進行するがアルカンへの水素化は遅い。ブタジエンの水素化ではブテンまで水素化され、ブタンの生成はみられない。共役ジエンがモノオレフィンよりも反応性が格段に高いのは、中間体のアリルアニオンがアルキルアニオンよりはるかに安定であることに因る。1,3-ブタジエンの水素化機構を下に示す。軽水素の代わりに重水素をもちいると、2つの末端炭素にDが1つずつはいった2-ブテンが生成する。



(Scheme 4)

芳香族カルボン酸の直接水素化(還元)で対応するアルデヒドを生成する反応も  $ZrO_2$  を触媒として用い工業化されている<sup>20,21)</sup>。反応機構の詳細は明かではないが、 $ZrO_2$  の塩基性と関連した水素化能および脱水素能がこの反応に重要であることが指摘されている。触媒の結晶化とコーク生成を防ぐため、CrやMnなどが添加されている。



## 2.4 アミノ化

アミンも水素と同じように共役ジエンに1,4付加し、一級、二級のアミンからそれぞれ二級、三級の不飽和アミンが生成する。水素化と本質的に同じ機構で反応が進行する。すなわち、水素化では  $H_2$  が  $H^-$  と  $H^+$  に解離しジエンに付加するが、アミノ化ではアミン( $RNH_2$ )が  $RNH^-$  と  $H^+$  に解離し、付加する。触媒としては、アルカリ土類酸化物が活性を示す<sup>22)</sup>。

## 2.5 Meerwein-Ponndorf-Verley還元

Meerwein-Ponndorf-Verley還元は、アルコールの水素を用いた水素化で、1つの水素移行反応である。アルデヒドとケトンはアルコールと反応し、対応するアルコールを生成する。

柴垣らは、アルデヒド、ケトンのM-P-V還元によるアルコールの生成に含水ジルコニアがよい触媒となることを報告している<sup>23)</sup>。含水ジルコニアは反応条件を変えると、カルボン酸のエステル化<sup>24)</sup>やアミノ化<sup>25)</sup>にも活性を示すようになる。含水ジルコニアの活性点を含めた反応機構は明かではない。

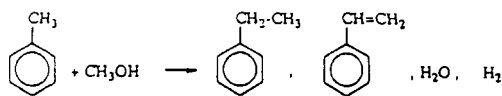
Cs<sup>+</sup>やRb<sup>+</sup>でイオン交換したX型ゼオライトでもアルデヒド、ケトンの2-プロパノールによる還元が進行する<sup>26)</sup>。塩基性点が2-プロパノールからH<sup>+</sup>を引き抜くことにより反応が開始される。塩基点の他にアルデヒド、ケトンをも活性化するためにアルカリカチオンが酸点として作用している。

## 2.6 共役ジエンの環化脱水素二量化

ブタジエンやイソプレンなどをMgOやZrO<sub>2</sub>を触媒として170℃程度で反応させると芳香族が生成する<sup>27, 28)</sup>。ブタジエンを反応物とするZrO<sub>2</sub>ではエチルベンゼン、MgOでは*o*-, *p*-キシレンが主に生成する。ZrO<sub>2</sub>では、Diels-Alderにつづいて二重結合移行・脱水素がおこり、MgOでは、ジエンからのH<sup>+</sup>引き抜きで始まるアニオン機構でそれぞれの生成物を与える。ZrO<sub>2</sub>, MgO以外の固体塩基触媒は、殆ど活性を示さない。

## 2.7 アルキル化

芳香族の核水素化は酸触媒で、側鎖アルキル化は塩基触媒で起こるのが一般的である。トルエンのメタノールによるアルキル化にはCs<sup>+</sup>イオン交換Xゼオライトが活性を示す<sup>29)</sup>。



(Scheme 5)

メタノールの脱水素によりホルムアルデヒドが生成し、それがトルエンとアルドールタイプの反応を起こしスチレンを生成し、エチルベンゼンはスチレンの水素化により生成する。ゼオライトの塩基点はメタノールの脱水素、アルドールタイプの反応の両方に関与している。

アルカリイオン交換ゼオライトの高い活性は細孔内で反応が起こることに起因していると考えられて

いる。コンピューターグラフィックスによると、塩基点とともに酸点の共存が効果的であることが示された<sup>30, 31)</sup>。

アルカリイオンをイオン交換容量を越えて含有するように調製したアルカリイオン添加ゼオライトX, Yは、イオン交換ゼオライトよりも高い活性を示すことが示された<sup>32)</sup>。過剰に存在するアルカリが新たな強い塩基点を発現し活性を向上させている。

イソプロピルベンゼンをエチレンやプロピレンなどのオレフィンでアルキル化するときK-KOH-Al<sub>2</sub>O<sub>3</sub>を用いると室温で反応が進行し、アルキル化は側鎖に起こる<sup>33)</sup>。この触媒の塩基点は非常に強いので、室温でイソプロピルベンゼンからH<sup>+</sup>を引き抜き不安定な三級アニオンを生成できる。

## 2.8 アルドール縮合

アセトンのアルドール縮合にはBa(OH)<sub>2</sub>が古くから知られているが、アルカリ土類酸化物や希土類酸化物も触媒となる。アルカリ土類酸化物のなかでは活性の序列はBaO>SrO>CaO>MgOである<sup>34)</sup>。少量の水の添加で活性が向上することや、重水素のトレーサー実験の結果を考慮すると、活性点は表面のO<sup>2-</sup>ではなくOH<sup>-</sup>であると思われる<sup>35)</sup>。

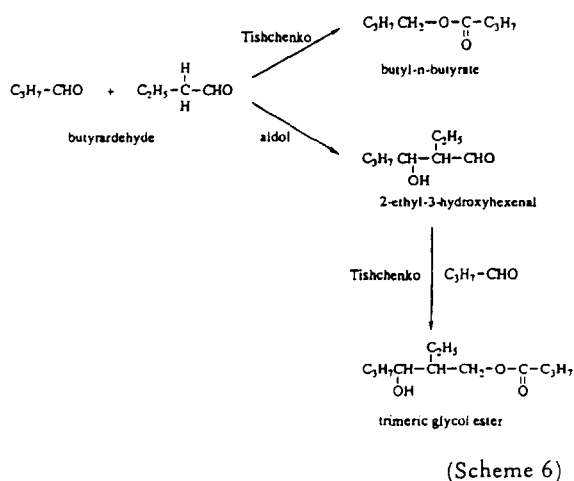
触媒に塩基性と酸性を付与するとジアセトンアルコールの脱水が進行しメシチルオキサイドが生成し、さらに水素化能を付与するとメシチルオキサイドの水素化によりMIBKが生成する。

アルカリメタルクラスターを含有するゼオライトA, X, Y, Lを用い350℃で反応させるとメシチルオキサイドとイソホロンが主生成物となるが、それぞれの生成割合はゼオライトのタイプにより異なる<sup>36)</sup>。細孔の小さいA, Lゼオライトではメシチルオキサイドが、X, Yではイソホロンが多く生成する<sup>37)</sup>。これらゼオライトは塩基点とともに酸点を有しており、細孔径と酸-塩基性の調節で選択性を変えることが出来る。

ハイドロタルサイトMg<sub>6</sub>Al<sub>2</sub>(OH)<sub>16</sub>CO<sub>3</sub>·4H<sub>2</sub>OやクリソタイルMg<sub>3</sub>(OH)<sub>4</sub>Si<sub>2</sub>O<sub>5</sub>もアセトンとホルムアルデヒドのアルドール縮合によるメチルビニルケトン生成のよい触媒となる<sup>38)</sup>。Co<sup>2+</sup>でイオン交換したクリソタイルを用いるとアセトンとメタノールからMVKが生成する。Co<sup>2+</sup>交換により脱水素活性が発現し、メタノールの脱水素によるホルムアルデヒドの生成に続いてアルドール縮合が進行するためである。

*n*-ブチルアルデヒドの液相での自己縮合にアル

カリ土類酸化物を触媒として用いると二量体に加え三量体が生成する<sup>39)</sup>。この反応では *n*-ブチルアルデヒドのアルドール縮合につづいて、生成した二量体と *n*-ブチルアルデヒドの交差エステル化の Tishchenko 反応が起こり三量体が生成する。アルカリイオンで修飾したアルミナでは未修飾のアルミナに比べ活性は著しく向上し、反応は選択的にアルドール縮合した段階で止まる。アルドール縮合には塩基点、交差エステル化の Tishchenko 反応には塩基点と酸点が関与していることが示唆された。



## 2.9 Tishchenko 反応

$\alpha$ -水素のないアルデヒド、例えばベンズアルデヒドやピバルアルデヒドの Tishchenko 反応はアルカリ土類酸化物を用いると容易に進行する<sup>40)</sup>。アルカリ土類酸化物が活性を示すのは、塩基点に加え酸点が存在するためと考えられている。アルカリイオンで修飾したアルミナやシリカは活性を示さない。

$\alpha$ -水素のあるアルデヒドでは、Tishchenko 反応はアルドール縮合との競争反応になる。アルカリ土類酸化物などの代表的な固体塩基を用いた場合、 $\alpha$ -水素のあるアルデヒドの反応はアルドール縮合に傾くようである。

## 2.10 Michael 付加

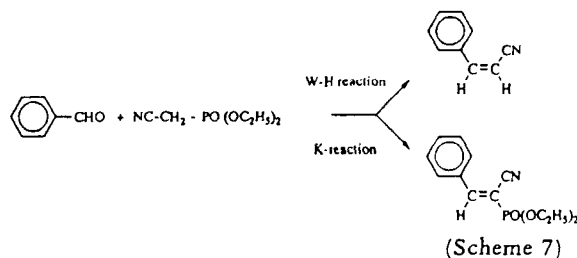
Michael 付加はカルバニオンの共役付加であり、通常、水酸化ナトリウム、ナトリウムエトキシド、ピペリジンなどの塩基存在化で進行する。固体触媒の応用例は少ない。Sinisterra のグループは、活性メチレン基を持つマロン酸エチル、酢酸エチルアセテート、アセチルアセトン、ニトロメタン、アセトフェノンのカルコンへの Michael 付加が部分的に脱水した Ba(OH)<sub>2</sub> を触媒として用いると効率よく進行する事を報告している<sup>41~43)</sup>。また、KF-Al<sub>2</sub>O<sub>3</sub>

もニトロメタンをもちいる Michael 付加を室温で促進する。アルカリ土類酸化物の活性は低い。

我々は、クロトン酸メチルの二量化は Michael 付加で進行し、MgO が固体塩基の中で特異的に高活性を示す事を見いだした<sup>44)</sup>。反応機構的な考察からクロトン酸メチルのアリル位の水素が塩基点により引き抜かれ、もう 1 つのクロトン酸メチルの  $\beta$  位に付加したのち、二重結合移行を経て生成物を与えることが明らかになった。ニトロメタンの Michael 付加に活性を示す KF-Al<sub>2</sub>O<sub>3</sub> はこの反応には活性を示さない。このように同種の Michael 付加でも反応物に含まれる置換基の種類により活性な触媒系が異なる。

## 2.11 Wittig-Horner 反応と Knoevenagel 縮合

アルデヒドとニトリルは塩基触媒存在下で Wittig-Horner 反応と Knoevenagel 縮合を起こす。下記の反応には MgO, ZnO, Ba(OH)<sub>2</sub> が触媒として作用する<sup>46)</sup>。塩基点がニトリルのメチレン基から H<sup>+</sup> を引き抜くことにより反応が開始される。



ベンズアルデヒドと活性メチレン基を持つ化合物の Knoevenagel 縮合に、ハイドロタルサイト、アルカリイオン交換ゼオライト<sup>46)</sup>やセピオライト<sup>47)</sup>が触媒となる。塩基性の弱いゼオライトやセピオライトでは副反応であるアルドール縮合が抑えられ、また、バルキーな生成物を与える逐次的な Michael 付加が細孔の大きさにより抑えられて選択性が高くなる。

Knoevenagel 縮合については、アルミナを触媒とした有機合成の例が報告されている<sup>48)</sup>。

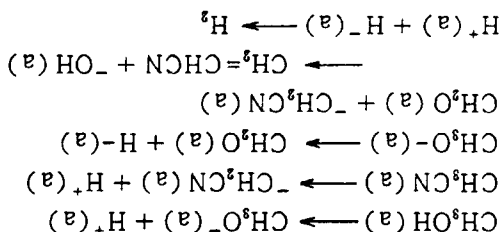
## 2.12 メタノールを用いる $\alpha, \beta$ -不飽和化合物の合成

ケトン、エステル、ニトリルの  $\alpha$  位のメチル基やメチレン基はメタノールと反応しビニル基となる。この反応には MgO を Mn や Cr で修飾した触媒が用いられる。Ueda らは、修飾 MgO を用いアセトニトリルとメタノールを 375°C で反応させるとアクリロニトリルを生成することを見いだした<sup>49~53)</sup>。MgO



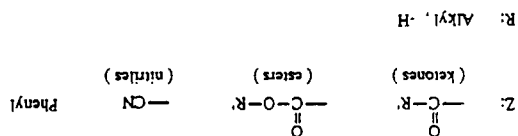
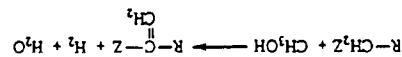
に  $Mg^{2+}$  よりもイオン半径の小さい金属イオンを添加することにより, 塩基性は減少させずに酸点を生成することができ, この様な修飾により活性な触媒が得られる。重水素を用いたトレーサー実験より,

次の反応機構が推定された。



反応は, メタノールの脱水素で生成するホルムアルデヒドとアセトニトリルのアルドールタイプの反応で生成物を与える。まずメタノールは  $H^+$  とメトキシアニオンに解離し, 後者は  $Mg^{2+}$  よりも強いハルゲン酸である添加金属イオンに吸着し, 金属イオンにより  $H^-$  が引き抜かれホルムアルデヒドを生成する。一方, アセトニトリルからは  $H^+$  が引き抜かれ, メチレンアニオンは同様に添加金属イオンに吸着する。

Ueda らは, この反応を一般式で次のように表せる反応に拡張した。



(Scheme 8)

## 2.13 環の変換

環内に酸素を持つ化合物をセオライトを触媒とし  $NH_3$  や  $H_2S$  と反応させ  $O$  を  $N$  や  $S$  と交換させることが出来る<sup>(84~86)</sup>。Hoelderich は, イオン交換したセオライトの酸塩基性と環の変換の活性と選択性を Table 1 のようにまとめた<sup>(86)</sup>。塩基性が増する環の

Table 1 Requirements of acid-base properties of zeolites for O/S- and O/S- transformations.

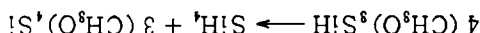
| Reaction                          | basic | acidic |
|-----------------------------------|-------|--------|
| saturated 5 ring + $NH_3$         | -     | +      |
| saturated 6 ring + $NH_3$         | +     | +      |
| saturated 5 ring + $H_2S$         | -     | +      |
| unsaturated 5 ring + $NH_3$       | +     | +      |
| unsaturated 5 ring + $H_2S$       | +     | +      |
| saturated 5 ring lactone + $NH_3$ | +     | +      |
| saturated 5 ring lactone + $H_2S$ | +     | +      |
| saturated 6 ring lactone + $NH_3$ | -     | +      |

$O$  を  $S$  に変換する反応が促進される傾向がみられる。反応機構は明かではないが, セオライトキヤビライ内の塩基点が重要な役割をしていることが示唆される。

## 2.14 オルガノシリコンの反応

最近, オルガノシリコンが関与する反応に対する固体塩基の触媒作用についての報告がなされている。Onaka らは, カルボニル化合物や 2-シクロヘキソンの不飽和ケトンシリル化において,  $MgO$ ,  $CaO$ , を用いたシリル化において,  $MgO$ ,  $CaO$ ,

ヒドロキシアパタイトを触媒として用いると反応が選択的に進行することを見いだしている<sup>(80~82)</sup>。塩基点がシリコン中の  $Si$  と相互作用しシリルアニオン<sup>(83)</sup>の求核性を高める働きをしている。不飽和ケトンのシリル化においては, 塩基触媒を用いると 1.2-付加が起こり, イオン交換モモノロナイト等の酸触媒では 1.4-付加が起こるのと対照的である。トリメトキシシリコンの気相不均化によるシリコン生成に固体塩基が用いられる。活性な触媒として, ハイドロタルサイトと  $KF/Al_2O_3$  が報告されている<sup>(83)</sup>。



## 3. 各種固体塩基触媒の特色

固体塩基触媒の触媒作用は表面塩基点の強度と量に関連することは疑いがなく, これだけが全ての触媒作用を決定する要因とは考えられない。各種固体塩基触媒それぞれに特徴がある。それぞれの特徴について述べる。

### 3.1 単独金属酸化物

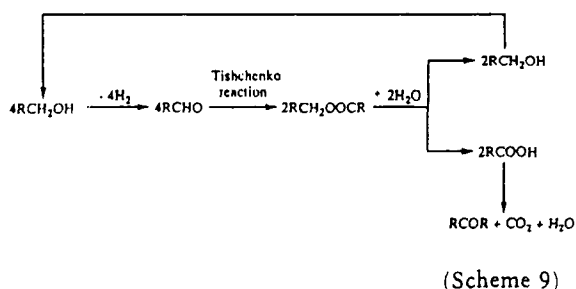
アルカリ土類酸化物は代表的な固体塩基触媒である。塩基性が強いので極く少量の  $CO_2$  や  $H_2O$  の存在で活性点が被毒を受ける。オレフィンから  $H^+$  を引き抜く力は大きく,  $-50^\circ C$  でもメチン異性化を促進する。

希土類酸化物の中でも二三酸化物は強い塩基性を示し, アルカリ土類酸化物と匹敵するが,  $CaO$ ,  $Tb_4O_{11}$ ,  $Pr_6O_{11}$  など高酸化状態で安定な酸化物は塩基性が弱い<sup>(84)</sup>。

$ZrO_2$  と  $ThO_2$  も  $H^+$  引き抜き能力があるが, アルカリ土類酸化物ほどではない。塩基性が弱い代わりには弱い酸性性も示すので, 酸塩基協同作用により特色ある触媒作用を示す。希土類酸化物,  $ZrO_2$ ,  $ThO_2$  に共通にみられる特徴はアルコーンに対して脱水素

ではなく脱水触媒として作用することである。この脱水は酸触媒反応とは異なった機構で進行する。

水、 $\text{CO}_2$ に接触するとすぐに活性点が被毒を受けるので工業プロセスになかなか使用し難いというのが固体塩基触媒の欠点であるが、その中で、 $\text{ZrO}_2$ だけは例外で、最近、相次いで2つの工業プロセスに用いられた。1つは、芳香族カルボン酸の水素化によるアルデヒドの合成であり、もう1つは、1-シクロヘキシルエタンの脱水によるビニルシクロヘキサンの合成である。ところが、20年以上も前からイソブチルアルデヒドからジイソブチルケトンの製造に $\text{ZrO}_2$ が触媒として用いられていた<sup>65, 66)</sup>。下のように Tishchenko 反応を含むスキームで進行し、Tishchenko 反応に $\text{ZrO}_2$ が触媒として作用すると推察される。



### 3.2 ゼオライト

ゼオライトの特色は、カチオン交換性と細孔構造に起因する。酸・塩基性は交換カチオンを変えることにより広い範囲にわたって、また、 $\text{Si}/\text{Al}$ 比を変えることにより狭い範囲で調節できる。イオン交換によって酸・塩基性を変えたゼオライトの触媒作用は Hoelderich により<sup>69)</sup>、また、最近では Dart と Davis によりまとめられている<sup>67)</sup>。塩基性ゼオライトの調製には、イオン交換とイオン添加が行われている。イオン交換だけではどうしても強い塩基点の発現がみられない。Hathaway と Davis は、イオン交換容量以上のアルカリをゼオライトに添加することによって、強い塩基性を示すゼオライトを調製し得ることを報告している<sup>82)</sup>。イオン交換サイト以外のところにアルカリが酸化物として存在し、それが強塩基性を示す<sup>68)</sup>。そこで、塩基性を有する $\text{MgO}$ 粒子や各種アルカリの酸化物をゼオライトのキャピティー内に生成させた触媒の調製が試みられ、いくつかの系では形状選択性塩基触媒反応を示すと報告されている<sup>69)</sup>。

塩基性ゼオライトの目標は、形状選択性であることは明らかであるので、構造の保持が重要である。

構造の崩壊は、高温で水蒸気に触れたり、あるいは、 $\text{Si}/\text{Al}$ 比の大きいゼオライトほどアルカリ溶液に不安定である等が分かってきたが<sup>70)</sup>、塩基性ゼオライト調製法の確立がまず重要な課題であろう。調製法についての報告がいくつか見られるようになったので<sup>71, 72)</sup>、これらの強塩基性ゼオライトの数多くの反応に対する触媒としての応用が期待される。

### 3.3 非酸化物系固体塩基触媒

金属酸化物である固体塩基触媒の塩基性点は表面 $\text{O}^{2-}$ と考えられているが、活性点(塩基点)が $\text{O}^{2-}$ 以外の固体塩基触媒がいくつか報告されている。酸化物系固体塩基とは異なる、特色ある塩基触媒作用が期待される。

1つは、Y型ゼオライトに低原子価の希土類元素を担持した触媒である。YbやEu金属を液体アンモニアに溶解し、ゼオライトに担持し、加熱排気すると固体塩基触媒として作用する<sup>73, 74)</sup>。活性点として $\text{YbNH}$ 、 $\text{EuNH}$ などのイミドが提案されている。調べられた反応は1-ブテンの異性化であり、この反応では金属酸化物との相違が表れていないが、反応物から $\text{H}^+$ を引き抜くのはOではなくNであり、他の反応物に対してNの特異性が表れる事が期待される。

KFを担体に担持すると、フッ素化剤として、また、塩基触媒として作用することはすでに10年以上前に知られていた<sup>75~77)</sup>。担体として特に優れているのが $\text{Al}_2\text{O}_3$ である。 $\text{KF}/\text{Al}_2\text{O}_3$ は多くの有機塩基触媒反応、たとえば Michael 付加、Knoevenagel 反応、Darzens 縮合および類似反応に有効な触媒として作用する<sup>78)</sup>。触媒活性点として、 $\text{F}^-$ アニオンが反応物から $\text{H}^+$ を引き抜くのか、あるいは、水の存在下でKFと $\text{Al}_2\text{O}_3$ の反応で生成するKOHが作用するのかは未だ不明な点である。フッ素化剤として作用するときには、 $\text{F}^-$ アニオンが作用しているに違いないので、塩基触媒として作用するときにも $\text{F}^-$ が活性点となっていることは十分考えられる。もし $\text{O}^{2-}$ アニオン以外の活性点であると、上記希土類化合物と同様に、特異的触媒活性が期待できる。

有機合成に用いられるときには、 $\text{KF}/\text{Al}_2\text{O}_3$ は $200^\circ\text{C}$ 以下の温度での乾燥等の簡単な前処理をして用いられているが、 $300\sim 500^\circ\text{C}$ で真空加熱をすると強い塩基点を必要とする反応にも活性を示すようになる<sup>83)</sup>。

## 4. おわりに

固体塩基触媒の有機合成, ファインケミカルズ合成への応用は, 最近になりやっと多くの報告がなされ始めた。固体塩基でなければ促進されない反応もいくつか見いだされており, 固体塩基の触媒作用は均一系塩基触媒の単なる模倣ではない面もある。本稿では触れなかったが, キャラクタリゼーションとともに量子化学的な計算もなされており<sup>79-84)</sup>, 固体塩基触媒表面の理解も着実に進んで来ている。これらにより反応の種類に応じた必要な機能を明らかにすることは, ファインケミカルズ用触媒の設計にとどまらず, 固体特有な触媒反応を開発するためにも重要となろう。

## 文 献

- 1) H. Hattori, *Heterogeneous Catalysis and Fine Chemicals III*, Elsevier, Amsterdam (1993), p. 35
- 2) Shimizu et al., *J. Catal.*, **45**, 302 (1977)
- 3) H. Hattori, et al., *Chem. Lett.*, **1979**, 133
- 4) G. Suzukamo, et al., *Acid-Base Catalysis*, Kodansha-VCH (1989), p. 405
- 5) T. Baba, et al., *Appl. Catal.*, **97**, L19 (1993)
- 6) H. Kabashima, et al., under submission
- 7) A. Hattori, et al., *J. Catal.*, **65**, 246 (1980)
- 8) H. Matsushashi, et al., *ibid.*, **85**, 457 (1984)
- 9) A. J. Lundeen, R. van Hoozen, *J. Org. Chem.*, **32**, 3386 (1967)
- 10) 戸松ら, *油化学*, **17**, 236 (1986)
- 11) K. Thomke, *Proc. 6th ICC*, London (1976), p. 303
- 12) T. Yamaguchi, et al., *Chem. Lett.*, **1976**, 677
- 13) 高橋ら, *触媒*, **35**, 12 (1993)
- 14) 植嶋ら, *石油学会誌*, **35**, 362 (1992)
- 15) H. Hattori, et al., *J. Am. Chem. Soc.*, **98**, 4652 (1976)
- 16) Y. Tanaka, et al., *Proc. 7th ICC*, Tokyo (1980), p. 1254
- 17) Y. Imizu, et al., *J. Catal.*, **56**, 303 (1979)
- 18) Y. Imizu, et al., *J.C.S. Chem. Commun.*, **1978**, 1091
- 19) Y. Imizu, et al., *J. Catal.*, **76**, 235 (1982)
- 20) T. Yokoyama, et al., *Appl. Catal.*, **A88**, 149 (1992)
- 21) T. Yokoyama, et al., *Acid-Base Catalysis II*, Kodansha-Elsevier (1994), p. 47
- 22) Y. Kakuno, H. Hattori, *J. Catal.*, **85**, 509 (1984)
- 23) M. Shibagaki, et al., *Bull. Chem. Soc. Jpn.*, **61**, 3283 (1988)
- 24) K. Takahashi, et al., *ibid.*, **62**, 2353 (1989)
- 25) K. Takahashi, et al., *ibid.*, **62**, 1333 (1989)
- 26) J. Shabtai, et al., *J. Mol. Catal.*, **27**, 35 (1984)
- 27) H. Suzuka, H. Hattori, *Appl. Catal.*, **48**, L7 (1989)
- 28) H. Suzuka, H. Hattori, *J. Mol. Catal.*, **63**, 371 (1990)
- 29) T. Yashima, et al., *J. Catal.*, **26**, 303 (1972)
- 30) H. Ito, et al., *ibid.*, **64**, 284 (1980)
- 31) A. Miyamoto, et al., *Acid-Base Catalysis*, Kodansha-VCH (1989), p. 497
- 32) P. E. Hathaway, M. E. Davis, *J. Catal.*, **119**, 497 (1989)
- 33) G. Suzukamo, et al., *Chem. Lett.*, **1987**, 585
- 34) G. Zhang, et al., *Appl. Catal.*, **36**, 189 (1988)
- 35) G. Zhang, et al., *ibid.*, **40**, 183 (1988)
- 36) T. Yashima, et al., *J. Catal.*, **33**, 486 (1974)
- 37) P. Chu, et al., U.S. Patent, 4,605,787 (1986)
- 38) E. Suzuki, et al., *Chem. Lett.*, **1987**, 1843
- 39) H. Tsuji, et al., *J. Catal.*, **148**, 759 (1994)
- 40) K. Tanabe, K. Saito, *ibid.*, **35**, 274 (1974)
- 41) A. Garcia-Raso, et al., *Synthesis*, **1982**, 1037
- 42) J. Barrios, et al., *J. Catal.*, **112**, 528 (1988)
- 43) J. Yamawaki, et al., *Bull. Chem. Soc. Jpn.*, **56**, 1885 (1983)
- 44) H. Kabashima, et al., under submission
- 45) J. V. Sinisterra, et al., *J. Col. Inter. Sci.*, **115**, 520 (1987)
- 46) A. Corma, et al., *J. Appl. Catal.*, **59**, 237 (1990)
- 47) A. Corma, et al., *J. Catal.*, **126**, 192 (1990)
- 48) F. Texier-Boullet, A. Foucand, *Tetrahedron Lett.*, **23**, 4937 (1982)
- 49) W. Ueda, *石油学会誌*, **36**, 421 (1993)
- 50) H. Kurokawa, et al., *J. Catal.*, **126**, 199 (1990)
- 51) H. Kurokawa, et al., *ibid.*, **126**, 208 (1991)
- 52) H. Kurokawa, et al., *Acid-Base Catalysis*, Kodansha-VCH (1989), p. 93
- 53) W. Ueda, et al., *Acid-Base Catalysis II*, Kodansha-Elsevier (1994), p. 35
- 54) Y. Ono, *Heterocycle*, **16**, 1755 (1981)
- 55) Y. Ono, *Stud. Surf. Sci. Catal.*, **5**, 19 (1980)
- 56) Y. Ono, et al., *Acta Phys. Chem.*, **24**, 233 (1978)
- 57) P. B. Venuto, P. S. Landis, *Adv. Catal.*, **18**, 259 (1968)
- 58) Y. Ono, et al., *Ind. Eng. Chem. Prod. Res. Dev.*, **5**, 180 (1976)
- 59) W. F. Hoelderich, *Acid-Base Catalysis*, Kodansha-VCH (1989), p. 1
- 60) M. Onaka, et al., *Chem. Lett.*, **1989**, 1393
- 61) K. Higuchi, et al., *J. Chem. Soc. Chem. Commun.*, **1991**, 1035
- 62) K. Sugita, et al., *Chem. Lett.*, **1990**, 481
- 63) Y. Nomoto, et al., *Acid-Base Catalysis II*, Kodansha-Elsevier (1994), p. 447
- 64) H. Hattori, et al., *Proc. 8th Nation. Symp. Catal. India. Sindri* (1987), p. 243
- 65) US Patent, 3,966,822 (1976)
- 66) 古賀, *有機合成化学*, **33**, 702 (1975)
- 67) C. B. Dart, M. E. Davis, *Catal. Today*, **19**, 151 (1994)
- 68) H. Tsuji, et al., *Chem. Lett.*, **1991**, 1881
- 69) H. Tsuji, et al., *Proc. 10th ICC*, Budapest (1992), p. 1171
- 70) F. Yagi, et al., *Acid-Base Catalysis II*, Kodansha-Elsevier (1994), p. 349
- 71) M. Lasperas, et al., *Microporous Mater.*, **1**, 343 (1993)
- 72) I. Rodriguez, et al., *Heterogeneous Catalysis and Fine Chemicals III*, Elsevier (1993), p. 623

- 73) T. Baba, et al., *J. Chem. Soc. Faraday Trans.*, **88**, 891 (1993)  
74) T. Baba, et al., *ibid.*, **89**, 3177 (1993)  
75) J. Yamawaki, T. Ando, *Chem. Lett.*, 45 (1979)  
76) J. H. Clark, *Chem. Rev.*, **80**, 429 (1980)  
77) 安藤, 山脇, 有機合成協会誌, **39**, 14 (1981)  
78) T. Ando, *Acid-Base Catalysis II*, Kodansha-Elsevier (1994), p. 9  
79) H. Kawakami, S. Yoshida, *J. Chem. Soc. Faraday Trans.*, **2**, **80**, 921 (1984)  
80) H. Fujioka, et al., *Surf. Sci.*, **149**, L53 (1985)  
81) H. Kobayashi, et al., *J. Phys. Chem.*, **94**, 7206 (1990)  
82) T. Ito, et al., *ibid.*, **95**, 4477 (1991)  
83) K. Sawabe, et al., *J. Chem. Phys.*, **97**, 6871 (1992)  
84) H. Kobayashi, et al., *Acid-Base Catalysis II*, Kodansha-Elsevier (1994), p. 233

**Fine Chemicals and Solid Base Catalysts.** Hideshi HATTORI and Hideto TSUJI (Center for Advanced Research of Energy Technology, Hokkaido University, Kita-ku, Kita-13, Nishi-8, Sapporo 060, Japan)

Catalysis and applications of solid bases for the organic reactions which are important in fine chemical syntheses are reviewed. The reactions included are double bond migration, dehydration, dehydrogenation, hydrogenation, amination, Meerwein-Ponndorf-Verley reduction, dehydrocyclo-dimerization, alkylation, aldol condensation, Tishchenko reaction, Wittig-Horner reaction, Knoevenagel condensation, synthesis of  $\alpha, \beta$ -unsaturated compounds, ring transformation, and reaction of organosilanes. Characteristic features of different types of solid bases are also summarized.

Key-words: Fine chemicals, Solid bases

(© 1995 Catalysis Society of Japan)

## 《解 説》

塩基性触媒としてのゼオライト  
による新しい反応

服 部 英

北海道大学エネルギー先端工学研究センター

ゼオライトの塩基性を評価する手法として、XPSによる $O_{1s}$ 、吸着ピロールの $N_{1s}$ のBEを測定する方法、IRによる吸着ピロールのN-H伸縮振動波数の測定、TPDによる吸着二酸化炭素の脱離温度の測定を紹介する。

塩基性ゼオライトは、アルカリイオン交換とそれ自身塩基性を示す物質をキャビティー内に包含させることにより調製できる。アルカリイオンの種類を変えることにより、またSi/Al比を変えることにより塩基強度を調節できる。イオン交換だけでは強い塩基点を発現することは出来ないが、アルカリ酸化物等を包含させることにより強塩基性ゼオライトを調製できる。

これら塩基性ゼオライトの固体塩基触媒として有機合成に応用した例を、オレフィン二重結合移行、Meerwein-Ponndorf-Verley還元、アルキレーション、アルドール縮合、Knoevenagel縮合、環の変換について述べた。

## 1. はじめに

ゼオライトはイオン交換することにより酸・塩基性を変えることができる点が固体酸・固体塩基触媒としての特徴と言えよう。ゼオライトの酸性点を触媒活性点として進行する反応は、石油精製のクラッキングをはじめ多々あり、膨大な研究がなされている。一方、塩基性は酸性と対をなす概念であるにもかかわらず、一般の固体塩基触媒の有機合成反応への応用も数少なく、まして塩基性ゼオライトの研究例は少ないのが現状である。しかし、ファインケミカルズへの応用を始め、各所で塩基性ゼオライトを含めた固体塩基触媒の応用が報告され始めてきた。塩基性ゼオライトは塩基性質の調節が容易であることに加え、形状選択性を有するので固体塩基触媒としての応用はこれから重要になってくると思われる。

本稿では、ゼオライトの塩基性のキャラクターゼーション、および、触媒調製について概説したのち、塩基性ゼオライトの各種有機合成反応への応用例を述べる。

## 2. 塩基性ゼオライトのキャラクターゼーション

キャラクターゼーションの手法により得られる情報は異なる。いくつかの手法と得られた情報について述べよう。

## 2.1 XPS

Okamotoら<sup>1)</sup>は、Si/Al比および交換カチオンの異なるゼオライトX、Yの $O_{1s}$ のBEをXPSで測定し、Oの塩基強度とBEのシフトについて報告している。図1に示すように、 $O_{1s}$ のBEは交換カチオンの電気陰性度が增大するにしたがい大きくなり、Oの負電荷が大きくなる。負電荷の大小だけで塩基強度が決まるわけではないが、窒素化合物では、 $N_{1s}$ のBEと塩基強度との間により相関が見られる。Oについても同様に考えると、交換カチオンの電気陰性度が小さくなるほどゼオライト格子のOの塩基

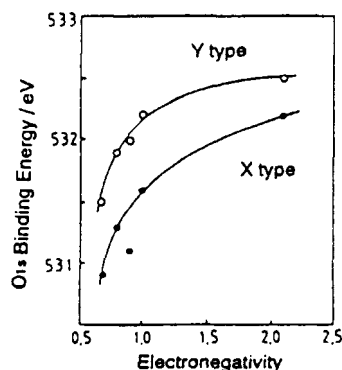


図1  $O_{1s}$ のBEと交換カチオンの電気陰性度との関係

強度は強くなるといえる。Al/Si 比を変えることによって  $O_{1s}$  の BE に影響がある。Al/Si 比を変えることによって  $O_{1s}$  の BE に影響がある。Al/Si 比が大きくなると、格子 O の塩基強度が強くなることが報告されている。

Huang ら<sup>2)</sup>は、アルカリイオン交換した X, Y ゼオライトにピロールを吸着させ  $N_{1s}$  の BE を測定し、塩基強度との関連を報告している。すなわち、塩基強度は交換カチオンを  $Li^+$ ,  $Na^+$ ,  $K^+$ ,  $Rb^+$ ,  $Cs^+$  と変えるにしたがい増大し、 $N_{1s}$  の BE も減小する。

## 2.2 IR

吸着したピロールの N-H 伸縮振動の波数が塩基強度の指標となる。塩基強度が大きいほど、N-H の H との酸塩基相互作用が強く、N-H 伸縮振動の波数が低波数へシフトする。Barthomeuf<sup>3)</sup>は種々のアルカリイオン交換ゼオライトに吸着したピロールの N-H 伸縮振動波数を測定した。カチオンの電気陰性度とともに表 1 に示す。

表 1 ゼオライトに吸着したピロールの N-H 伸縮振動波数のシフト ( $\Delta r_{NH}$ ) と酸素の平均電荷 ( $q_O$ )

| Zeolite  | $\Delta r_{NH}$ | $q_O$  |
|----------|-----------------|--------|
| CsX      | 240             | -0.461 |
| NaX      | 180             | -0.413 |
| KY       | 70              | -0.383 |
| NaY      | 30-40           | -0.352 |
| KL       | 30              | -0.356 |
| Na-MOR   | 30              | -0.278 |
| Na-Beta  | 30              | -0.240 |
| Cs ZSM-5 | 0               | -0.236 |
| Na ZSM-5 | 0               | -0.225 |

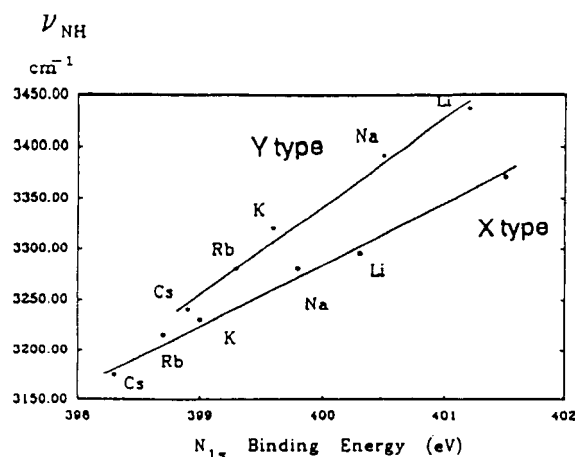


図 2 吸着ピロールの  $N_{1s}$  の BE と N-H 伸縮振動波数との関係

Huang ら<sup>2)</sup>は、吸着ピロールの IR と XPS を測定した。図 2 に示すように、N-H 伸縮振動の吸収波数と  $N_{1s}$  の BE との間により相関関係が見られることを報告している。イオン交換するアルカリを Li, Na, K, Rb, Cs とするにしたがい塩基強度が増大することを示している。

## 2.3 TPD

$CO_2$  の TPD は最も一般的な塩基性測定手法であるが、この方法で、アルカリイオン添加型のゼオライトがイオン交換ゼオライトよりも強い塩基点を発現することが報告されている<sup>4)</sup>。図 3 に示すように、アルカリをイオン交換容量以上にゼオライトに含有させると、 $CO_2$  の脱離ピークは大きく、高温に現れる。アルカリ酸化物がゼオライトキャビティー内に生成し、塩基量・強度が増大したことを示している。

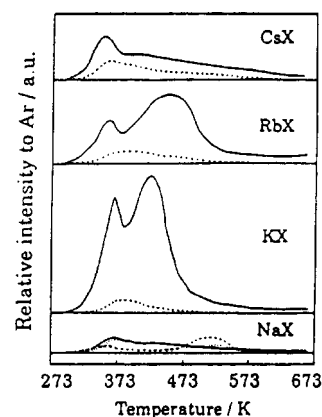


図 3 吸着  $CO_2$  の TPD プロット

.....イオン交換, ——イオン添加

## 3. 塩基性ゼオライトの調製

塩基性ゼオライトの調製として、アルカリイオン交換することと、それ自身塩基性を示す物質をキャビティー内につくることが行われている。また、ゼオライトの Al/Si 比を変えることによって塩基性の調節が可能である。

### 3.1 イオン交換ゼオライト

アルカリ土類や希土類などの多価イオンで交換すると酸性質が発現する。イオン交換で塩基性を発現させるにはアルカリイオンを用いる以外に方法はないといえる。アルカリイオンで交換すると塩基性ゼオライトとなることは、トルエンのメタノールによるアルキル化が側鎖に起こることによって示唆された<sup>5)</sup>。活性はイオン半径の大きい  $Rb^+$  や  $Cs^+$  を用いた方が、また、Al/Si 比の大きい X ゼオライトの方

が高かった。反応の結果より推定された塩基性の強さは、後に測定された前項で述べた塩基性評価の結果と一致した<sup>1)</sup>。イオン交換やAl/Si比を変えるだけでは強い塩基性ゼオライトを調製することは出来ず、強い塩基性を得るためには他の方法によらざるを得ない。

### 3.2 塩基性物質添加ゼオライト

ゼオライトキャビティー内に塩基性物質を導入すると、ゼオライトの特徴である形状選択性を保持した塩基性触媒を調製することが出来る。例えば、X型ゼオライトに酢酸セシウム水溶液を含浸させると、交換容量以上のCs<sup>+</sup>が添加されたゼオライトをつくる事が出来る。

HathawayとDavis<sup>6)</sup>は、この様に調製されたCs添加XやYゼオライトが、イソプロパノールの脱水素やトルエンのアルキル化に対して、イオン交換ゼオライトより格段に高い活性を示すことを報告している。ブテンの二重結合異性化に対しては、イオン交換型のKX, RbX, CsXよりも、イオン添加型のKX, RbX, CsXの方が2桁以上活性が高いことも報告されている<sup>4)</sup>。XゼオライトへのCs添加では、単位セル当り8個の酸化物(Cs<sub>2</sub>O)すなわち、スーパーケージに1個の酸化物までは均等にキャビティー内に分布されるとの報告もある<sup>7)</sup>。また、アルカリイオン添加型のゼオライトは、処理によっては骨格構造を容易に崩壊する。特に、水蒸気存在する条件で高温に加熱すると構造の崩壊が起こり易くなる<sup>8)</sup>。

低原子価の希土類をゼオライトに担持すると塩基触媒となる<sup>9, 10)</sup>。Yb, Euをアンモニアに溶解しゼオライトに含浸させる。加熱排気するとアンモニア、水素、窒素が脱離し、塩基触媒作用を示す。活性種はYbNH, EuNHなどのイミドと考えられている。この場合塩基点はNである。酸化物系の塩基点はOであるので、塩基点がNである特異性が期待されるが、今のところ見られていない。

## 4. ゼオライトの塩基触媒作用

ゼオライトを触媒とする有機合成反応は、ゼオライトの酸性、担持された金属の触媒能に起因するのは多いが、塩基性に起因する反応は少ない。イオン交換のみでは強い塩基点を発現せず、また強い塩基性ゼオライトの調製は、比較的近年行われたものであり、反応への試行例が少なかったことによると思われる。しかし、形状選択性ととも塩基性質を

い範囲にわたって連続的に調節し得るという特徴を持つゼオライトは重要であり、これからは使用される機会は多くなると思われる。ここではゼオライトが塩基触媒反応に用いられた例を述べる。

### 4.1 オレフィン二重結合移行

1-ブテンの異性化は触媒の性能を調べるテスト反応としてよく行われる強い塩基点を必要とする反応である。反応温度0℃では、イオン交換しただけでは活性を示さないが、アルカリ添加型のX, Yゼオライトは活性を示すようになる<sup>4)</sup>。CsXが最も高い活性を示す。反応は、生成する2-ブテンのcis/trans比は高く、1-ブテンのアリル位の水素がH<sup>+</sup>として塩基点によって引き抜かれアリルアニオンを中間体として進行する。

Yb, Euをアンモニアに溶解しNaY, KYゼオライトに含浸し加熱排気した触媒は、加熱温度200℃付近でYbNH, EuNH種がキャビティー内に生成し、ブテンの異性化活性が高くなる<sup>9, 10)</sup>。生成2-ブテンのcis/trans比は9-10であり、塩基触媒反応であることが示唆されている。

代表的な固体塩基触媒であるMgOではアリルベンゼンの異性化は進行するが、ゼオライトキャビティー内にMgO微粒子を生成させた触媒では進行しない<sup>11)</sup>。反応物規制の形状選択性が見られた例である。

### 4.2 Meerwein-Ponndorf-Verley還元

M-P-V還元はアルコールの水素を用いた還元で、1つの水素移行反応である。アルデヒドとケトンアルコールと反応し、対応するアルコールとなる。この反応にCs<sup>+</sup>やRb<sup>+</sup>でイオン交換したXゼオライトが触媒となる<sup>12)</sup>。2-プロパノールを用いたときの提案されている機構を図4に示すが、塩基点が

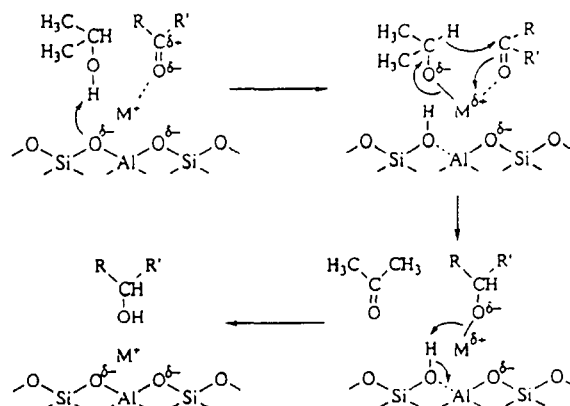
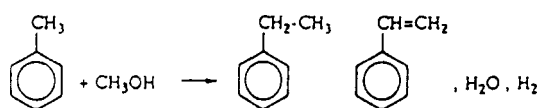


図4 Meerwein-Ponndorf-Verley還元  
のスキーム

2-プロパノールから $H^+$ を引き抜くことにより反応が開始される。塩基点の他にアルデヒド、ケトンを活性化するためにアルカリカチオンが酸点として作用している。

#### 4.3 アルキル化

芳香族の核アルキル化は酸触媒で、側鎖アルキル化は塩基触媒で起こるのが一般的である。トルエンのメタノールによるアルキル化には $Cs^+$ イオン交換Xゼオライトが活性を示す<sup>5)</sup>。メタノールの脱水素によりホルムアルデヒドが生成し、それがトルエンとアルドールタイプの反応によりスチレンを生成する。エチルベンゼンはスチレンの水素化により生成する。ゼオライトの塩基点はメタノールの脱水素、アルドールタイプの反応の両方に関与している。



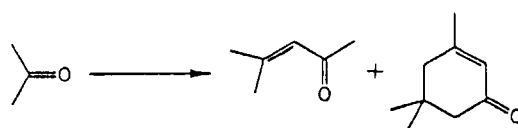
アルカリイオンをイオン交換容量以上含有するイオン添加 X, Y ゼオライトは、イオン交換ゼオライトよりも高い活性を示す<sup>13)</sup>。過剰に存在するアルカリが酸化物としてキャビティー内に存在し、強い塩基点を発現し活性を向上させている。

コンピュータグラフィックスによると、キャビティー内で反応分子が塩基点の他に酸点の作用を受けており、これが高い活性をもたらしていると推測されている<sup>14)</sup>。

最近、炭酸ジメチルをアルキル化剤として用いる反応が固体塩基触媒で進行することが報告されている<sup>15~17)</sup>。フェニルアセトニトリルの $\alpha$ メチル化は、アルカリ交換 X, Y ゼオライトを触媒として、メチル化剤としてメタノール、炭酸ジメチルを用いると進行するが、炭酸ジメチルの方が格段に反応性が高い。NaY ゼオライトが活性低下が少なく、高選択的に $\alpha$ メチルフェニルアセトニトリルを生成する。

#### 4.4 アルドール縮合

アセトンをアルカリメタルクラスターを含有する A, X, Y, L ゼオライトを触媒を用い 350°C で反応させるとメシチルオキサイドとイソホロンが生成するが、生成割合はゼオライトのタイプによって異なる<sup>18)</sup>。細孔径の小さい A, L ゼオライトではアセトン 2 分子から生成するメシチルオキサイドが、X, Y ゼオライトではアセトン 3 分子より生成するイソホロンが多く生成する。



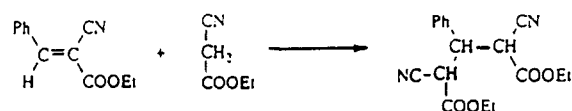
ホルムアルデヒドとプロピオン酸メチルのアルドール縮合でメチルメタクリレートを生成する反応も $K^+$ イオン交換後 KOH 添加 Y ゼオライトを用いると収率よく進行する<sup>19)</sup>。この反応にも酸点と塩基点の共存が必要とされている。アルドール縮合にはアルドール付加に引き続き脱水が起こるので、脱水反応に酸点が必要ではないかと推測される。

#### 4.5 Knoevenagel 縮合

アルデヒドとニトリルの Knoevenagel 縮合は、アルカリイオン交換したゼオライトが触媒となる。次の反応は Knoevenagel 縮合に引続き Michael 付加が起こり得て、両反応とも塩基の存在で進行するが、ゼオライトを用いると生成物規制の形状選択性により、Knoevenagel 縮合だけ起こることが出来る<sup>7)</sup>。この反応にも、Cs をイオン交換容量以上に添加した X 型ゼオライトは、イオン交換ゼオライトより高い活性を示す。



Knoevenagel condensation



Michael addition

#### 4.6 環の変換

5員環、6員環の環内にO原子を有する化合物を $NH_3$ や $H_2O$ と反応させ、OをNやSと交換させる反応にゼオライトが触媒として働く<sup>20~24)</sup>。反応例を下に示す。

Hoelderich<sup>25)</sup>は、ゼオライトの酸塩基性と活性と選択性との関係を表2のようにまとめた。ゼオラ



X = S, NH



表2 環の変換(O/N, O/S)に対する  
ゼオライトの酸塩基性の効果

| Reaction                                    | basic | acidic |
|---------------------------------------------|-------|--------|
| saturated 5 ring + NH <sub>3</sub>          | —     | +      |
| saturated 5 ring + H <sub>2</sub> S         | +     | > +    |
| saturated 6 ring + NH <sub>3</sub>          | —     | ++     |
| unsaturated 5 ring + NH <sub>3</sub>        | +     | —      |
| unsaturated 5 ring + H <sub>2</sub> S       | +     | —      |
| saturated 5 ring lactone + NH <sub>3</sub>  | +     | +      |
| saturated 5 ring lactone + H <sub>2</sub> S | +     | —      |
| saturated 6 ring lactone + NH <sub>3</sub>  | —     | +      |

イトの塩基性が増加するとOをSに変換する反応が促進される傾向が見られる。酸点・塩基点がどの分子にどの様に作用するのかについては明かではないが、それらが重要な役割をしていることは明かである。

#### 5. おわりに

他の固体塩基触媒と比較した場合、ゼオライトの固体塩基触媒としての特質が幾つか挙げられる。まず、塩基強度を広い範囲にわたって変化させることが出来る。塩基性物質をキャビティー内に存在させることにより、強い塩基点を発現させることが可能となり、カバー出来る塩基強度の範囲が一段と広まった。また、ゼオライト骨格 Si-O-Al に由来する酸点の共存が、塩基性ゼオライト触媒の特徴となり、酸・塩基点の共同作用で促進される反応もある。塩基性ゼオライトに最も期待されているのが、形状選択的塩基触媒作用であろう。現在のところ、明確な形状選択性を示す例はほとんど報告されていないが、近い将来にいくつかの例がでてくると予測される。

#### References

- 1) Y. Okamoto, M. Ogawa, A. Maezawa, *J. Catal.*, **112**, 427 (1988).
- 2) M. Huang, A. Adnot, S. Kaliaguine, *J. Catal.*, **137**, 322 (1992).
- 3) D. Barthomeuf, *Stud. Surf. Sci. Catal.*, **65**, 157 (1991).
- 4) H. Tsuji, F. Yagi, H. Hattori, *Chem. Lett.*, **1991**, 1881.
- 5) T. Yashima, K. Sato, T. Hayasaka, N. Hara, *J. Catal.*, **26**, 303 (1972).
- 6) P. H. Hathaway, M. E. Davis, *J. Catal.*, **116**, 263 (1989).
- 7) a) I. Rodriguez, H. Cambon, D. Brunel, M. Lesperas, P. Geneste, *Stud. Surf. Sci. Catal.*, **78**, 623 (1993). b) M. Lasperas, H. Cambon, D. Brunel, I. Rodriguez, P. Geneste, *Microporous Mater.*, **1**, 343 (1993).
- 8) F. Yagi, H. Tsuji, H. Hattori, H. Kita, *Acid-Base Catalysis II*, (1994), p. 349.
- 9) T. Baba, G. J. Kim, Y. Ono, *J. Chem. Soc., Faraday Trans.*, **88**, 891 (1992).
- 10) T. Baba, S. Hikita, R. Koide, Y. Ono, T. Hanada, T. Tanaka, S. Yoshida, *J. Chem. Soc., Faraday Trans.*, **89**, 3177 (1993).
- 11) H. Tsuji, F. Yagi, H. Hattori, H. Kita, *Proc. 10th Intern. Congr. Catal.*, Budapest (1982), p. 1171.
- 12) J. Shabtai, R. Lazer, E. Biron, *J. Mol. Catal.*, **27**, 35 (1984).
- 13) P. E. Hathaway, M. E. Davis, *J. Catal.*, **119**, 497 (1989).
- 14) A. Miyamoto, S. Iwamoto, K. Agusa, T. Inui, *Acid-Base Catalysis*, Kodansha (1989), p. 497.
- 15) Z. H. Fu, Y. Ono, *J. Catal.*, **1994**, 145, 166.
- 16) Z. H. Fu, Y. Ono, *Catal. Lett.*, **1993**, 18, 59.
- 17) Z. H. Fu, Y. Ono, *Catal. Lett.*, **1993**, 21, 43.
- 18) T. Yashima, H. Suzuki, N. Hara, *J. Catal.*, **33**, 486 (1974).
- 19) P. T. Wierzychowski, L. W. Zatorski, *Catal. Lett.*, **9**, 411 (1991).
- 20) Y. Ono, *Heterocycle*, **16**, 1755 (1981).
- 21) Y. Ono, *Stud. Surf. Sci. Catal.*, **5**, 19 (1980).
- 22) Y. Ono, K. Hatada, K. Fujita, A. Halgeri, T. Keii, *J. Catal.*, **41**, 322 (1976).
- 23) Y. Ono, T. Mori, K. Hatada, *Acta Phys. Chem.*, **24**, 233 (1978).
- 24) P. B. Venuto, P. S. Landis, *Adv. Catal.*, **18**, 259 (1968).
- 25) W. F. Hoelderich, *Acid-Base Catalysis* (Ed. K. Tanabe et al.), Kodansha (1989), p. 1.

#### New Reactions Catalyzed by Basic Zeolites

Hideshi HATTORI

Center for Advanced Research of Energy Technology,  
Hokkaido University, Sapporo 060

Zeolites possessing basic properties have been developed for the catalysts for base-catalyzed reactions. The present review describes the methods for characterization of basic properties,

the preparative methods for basic zeolites, and applications of the basic zeolites to organic reactions.

For characterization, the binding energies of  $O_{1s}$  of the frame oxygen and of  $N_{1s}$  of the adsorbed pyrrol measured by XPS reflect the basic properties of the zeolites. The wave numbers of N-H stretching of the adsorbed pyrrol measured by IR correlate with the basic strength of the zeolites. The basic strength is also evaluated by TPD of the adsorbed  $CO_2$ .

The basic properties of the zeolites are able to be adjusted by selecting the alkali ions as exchanged cation and the Si/Al ratio of the zeolite framework. Strongly basic zeolites can be prepared by encapsulation of basic materials such as alkali oxides and imides of rare earth elements.

The applications of basic zeolites to organic reactions are described for the following reactions: double bond migration of olefine, Meerwein-Ponndorf-Verley reduction, alkylation, aldol condensation, Knoevenagel condensation, and ring transformation.

Key words: Base-catalyzed reaction, Basic zeolite, Catalysis, Alkali ion.

**Table 1. Types of Heterogeneous Basic Catalysts**

- 
- |                                                             |
|-------------------------------------------------------------|
| (1) single component metal oxides                           |
| alkaline earth oxides                                       |
| alkali metal oxides                                         |
| rare earth oxides                                           |
| ThO <sub>2</sub> , ZrO <sub>2</sub> , ZnO, TiO <sub>2</sub> |
| (2) zeolites                                                |
| alkali ion-exchanged zeolites                               |
| alkali ion-added zeolites                                   |
| (3) supported alkali metal ions                             |
| alkali metal ions on alumina                                |
| alkali metal ions on silica                                 |
| alkali metal on alkaline earth oxide                        |
| alkali metals and alkali metal hydroxides on alumina        |
| (4) clay minerals                                           |
| hydrotalcite                                                |
| chrysotile                                                  |
| sepiolite                                                   |
| (5) non-oxide                                               |
| KF supported on alumina                                     |
| lanthanide imide and nitride on zeolite                     |
- 

Following the report by Pines et al., certain metal oxides with a single component were found to act as heterogeneous basic catalysts in the absence of such alkali metals as Na and K. In the 1970s, Kokes et al. reported that hydrogen molecules were adsorbed on zinc oxide by acid-base interaction to form proton and hydride on the surface.<sup>2,3</sup> They proved that the heterolytically dissociated hydrogens act as intermediates for alkene hydrogenation. In the same period, Hattori et al. reported that calcium oxide and magnesium oxide exhibited high activities for 1-butene isomerization if the catalysts were pretreated under proper conditions such as high temperature and high vacuum.<sup>4</sup> The 1-butene isomerization over calcium oxide and magnesium oxide was recognized as a base-catalyzed reaction in which the reaction was initiated by abstraction of a proton from 1-butene by the basic site on the catalyst surfaces.

The catalytic activities of basic zeolites were reported also in early 1970s. Yashima et al. reported that side chain alkylation of toluene was catalyzed by alkali ion-exchanged X and Y type zeolites.<sup>5</sup> The reaction is a typical base-catalyzed reaction, and the activity varied with the type of exchanged alkali cation and with type of zeolite, suggesting that the basic properties can be controlled by selecting the exchanged cation and the type of zeolite.

In addition to the above mentioned catalysts, a number of materials have been reported to act as heterogeneous basic catalysts. The types of heterogeneous basic catalysts are listed in Table 1. Except for non-oxide catalysts, the basic sites are believed to be surface O atoms. Oxygen atoms existing on any materials may act as basic sites because any O atoms would be able to interact attractively with a proton. The materials listed in Table 1 act as a base toward most of the reagents and, therefore, are called heterogeneous basic catalysts or solid base catalysts.

Four reasons for recognizing certain materials as heterogeneous basic catalysts are as follows.

(1) Characterization of the surfaces indicates the existence of basic sites: Characterizations of the surfaces by various methods such as color change of the acid-base indicators adsorbed, surface reactions, adsorption of acidic molecules, and spectroscopies

(UV, IR, XPS, ESR, etc.) indicate that basic sites exist on the surfaces.

(2) There is a parallel relation between catalytic activity and the amount and/or strength of the basic sites: The catalytic activities correlate well with the amount of basic sites or with the strength of the basic sites measured by various methods. Also, the active sites are poisoned by acidic molecules such as HCl, H<sub>2</sub>O, and CO<sub>2</sub>.

(3) The material has similar activities to those of homogeneous basic catalysts for "base-catalyzed reactions" well-known in homogeneous systems: There are a number of reactions known as base-catalyzed reactions in homogeneous systems. Certain solid materials also catalyze these reactions to give the same products. The reaction mechanisms occurring on the surfaces are suggested to be essentially the same as those in homogeneous basic solutions.

(4) There are indications of anionic intermediates participating in the reactions: Mechanistic studies of the reactions, product distributions, and spectroscopic observations of the species adsorbed on certain materials indicate that anionic intermediates are involved in the reactions.

The studies of heterogeneous catalysis have been continuous and progressed steadily. They have never been reviewed in the *Chemical Reviews* before. It is more useful and informative to describe the studies of heterogeneous basic catalysis performed for a long period. In the present article, therefore, the cited papers are not restricted to those published recently, but include those published for the last 25 years.

## II. Generation of Basic Sites

One of the reasons why the studies of heterogeneous basic catalysts are not as extensive as those of heterogeneous acidic catalysts seems to be the requirement for severe pretreatment conditions for active basic catalysts. The materials which are now known as strong basic materials used to be regarded as inert catalysts. In the long distant past, the catalysts were pretreated normally at relatively low temperatures of around 723 K. The surfaces should be covered with carbon dioxide, water, oxygen, etc. and showed no activities for base-catalyzed reactions. Generation of basic sites requires high-temperature pretreatment to remove carbon dioxide, water, and, in some cases, oxygen.

This can be understood with the data in Figure 1 in which decomposition pressures are plotted against reciprocal temperature for carbonates and peroxides of alkaline earth elements.<sup>6</sup> In addition to carbonates and peroxides, hydroxides are formed at the surface layers of the oxides. The decomposition pressures are very low at room temperature. On exposure to the atmosphere, alkaline earth oxides adsorb carbon dioxide, water, and oxygen to form carbonates, hydroxides, and peroxides. Removal of the adsorbed species from the surfaces is essential to reveal the oxide surfaces. Therefore, high-temperature pretreatment is required to obtain the metal oxide surfaces.

The evolutions of water, carbon dioxide, and oxygen when Mg(OH)<sub>2</sub> and BaO are heated under vacuum at elevated temperatures are shown in Figures 2 and

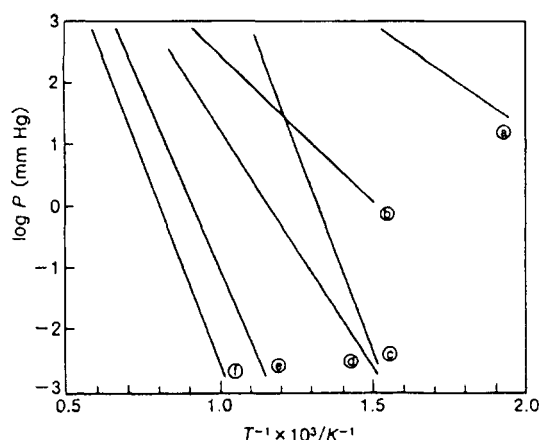


Figure 1. Equilibrium pressure for decomposition:

- (a)  $2\text{SrO}_2 = 2\text{SrO} + \text{O}_2$ , (b)  $2\text{BaO}_2 = 2\text{BaO} + \text{O}_2$ ,  
 (c)  $\text{MgCO}_3 = \text{MgO} + \text{CO}_2$ , (d)  $\text{CaCO}_3 = \text{CaO} + \text{CO}_2$ ,  
 (e)  $\text{SrCO}_3 = \text{SrO} + \text{CO}_2$ , (f)  $\text{BaCO}_3 = \text{BaO} + \text{CO}_2$ .

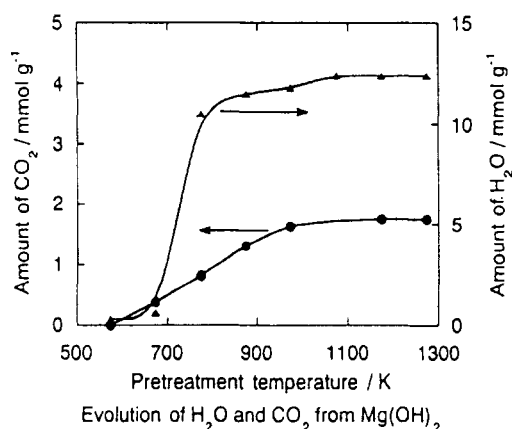


Figure 2. Evolution of  $\text{H}_2\text{O}$  and  $\text{CO}_2$  from  $\text{Mg}(\text{OH})_2$ .

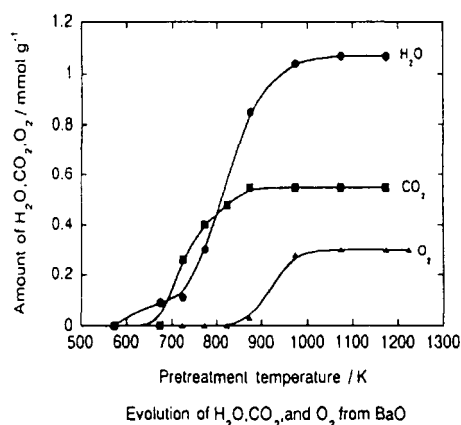


Figure 3. Evolution of  $\text{H}_2\text{O}$ ,  $\text{CO}_2$ , and  $\text{O}_2$  from  $\text{BaO}$ .

3.<sup>4,7</sup> For  $\text{MgO}$ , evolution of water and carbon dioxide continues up to 800 K. For  $\text{BaO}$ , evolution of these gases continues to much higher temperatures. In addition, oxygen evolves above 900 K. Evolution of carbon dioxide, water, and oxygen results in generation of basic sites on the surfaces which act as

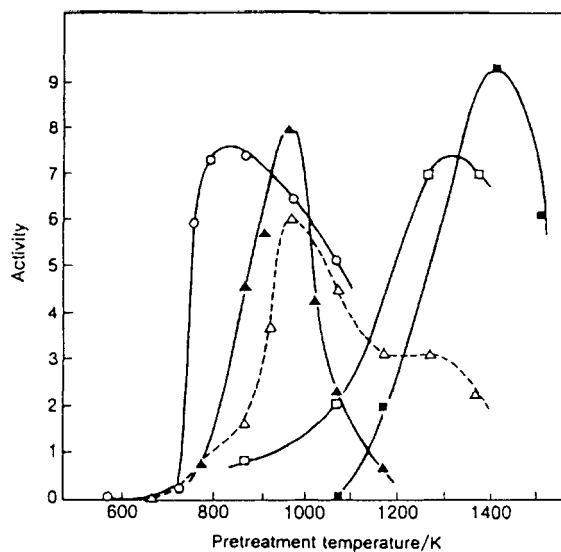


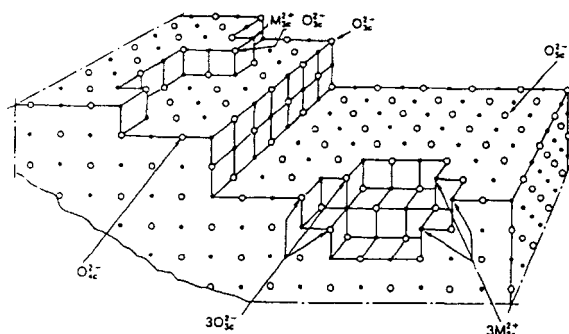
Figure 4. Variations of activity of  $\text{MgO}$  for different types of reactions as a function of pretreatment temperature:  $\circ$ , 1-butene isomerization at 303 K ( $3.5 \times 10^3 \text{ mmHg min}^{-1} \text{ g}^{-1}$ );  $\blacktriangle$ ,  $\text{CH}_4\text{-D}_2$  exchange at 673 K ( $4.3 \times 10^3 \text{ s}^{-1} \text{ g}^{-1}$ );  $\triangle$ , amination of 1,3-butadiene with dimethylamine at 273 K ( $5 \times 10^{17} \text{ molecules min}^{-1} \text{ g}^{-1}$ );  $\square$ , 1,3-butadiene hydrogenation at 273 K ( $2.5 \times 10^6 \text{ min}^{-1} \text{ g}^{-1}$ );  $\blacksquare$ , ethylene hydrogenation at 523 K ( $0.3 \text{ min}^{-1} \text{ g}^{-1}$ ).

catalytically active sites for several reaction types.

The nature of the basic sites generated by removing the molecules covering the surfaces depends on the severity of the pretreatment. The changes in the nature of basic sites are reflected in the variations of the catalytic activities as a function of pretreatment temperature. In many cases, the variations of the activity are dissimilar for different reaction types. The activity variations of  $\text{MgO}$  for different reactions are shown in Figure 4.<sup>8</sup> The activity maxima appear at different catalyst-pretreatment temperatures for different reaction types: 800 K for 1-butene isomerization, 973 K for methane- $\text{D}_2$  exchange and amination of 1,3-butadiene with dimethylamine, 1273 K for hydrogenation of 1,3-butadiene, and 1373 K for hydrogenation of ethylene.

As the pretreatment temperature increases, the molecules covering the surfaces are successively desorbed according to the strength of the interaction with the surface sites. The molecules weakly interacting with the surfaces are desorbed at lower pretreatment temperatures, and those strongly interacting are desorbed at higher temperatures. The sites that appeared on the surfaces by pretreatment at low temperatures are suggested to be different from those that appeared at high temperatures. If simple desorption of molecules occurs during pretreatment, the basic sites that appeared at high temperatures should be strong. However, rearrangement of surface and bulk atoms also occurs during pretreatment in addition to the desorption of the molecules, which is evidenced by a decrease in the surface area with an increase in the pretreatment temperature.

Coluccia and Tench proposed a surface model for  $\text{MgO}$  (Figure 5).<sup>9</sup> There exist several  $\text{Mg-O}$  ion pairs of different coordination numbers. Ion pairs of low



**Figure 5.** Ions in low coordination on the surface of MgO. (Reprinted from ref 9. Copyright 1981 Kodansha.)

coordination numbers exist at corners, edges, or high Miller index surfaces of the (100) plane. Different basic sites generated by increasing the pretreatment temperature appear to correspond to the ion pairs of different coordination numbers. However, the correspondence between the catalytically active sites for different reaction types and the coordination number of the ion pairs is not definite yet.

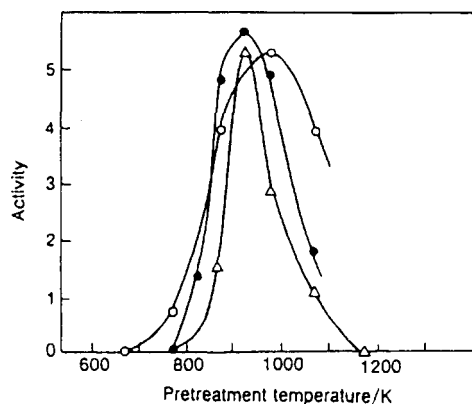
Among the ion pairs of different coordination numbers, the ion pair of 3-fold  $\text{Mg}^{2+}$ –3-fold  $\text{O}^{2-}$  ( $\text{Mg}^{2+}_{3c}\text{--O}^{2-}_{3c}$ ) is most reactive and adsorbs carbon dioxide most strongly. To reveal the ion pair  $\text{Mg}^{2+}_{3c}\text{--O}^{2-}_{3c}$ , the highest pretreatment temperature is required. At the same time, the ion pair  $\text{Mg}^{2+}_{3c}\text{--O}^{2-}_{3c}$  is most unstable. The  $\text{Mg}^{2+}_{3c}$  and  $\text{O}^{2-}_{3c}$  tend to rearrange easily at high temperature. The appearance of such highly unsaturated sites by the removal of carbon dioxide and the elimination by the surface atom rearrangement compete. Such competition results in the activity maxima as the pretreatment temperature is increased.

Although the surface model shown in Figure 5 is proposed for MgO, the other metal oxide heterogeneous bases may be in a situation similar to that of MgO. The nature of basic sites varies with the severity of the pretreatment conditions for most heterogeneous basic catalysts.

The surface sites generated on rare earth oxides, however, behave differently from those of the other heterogeneous base catalysts. The sites of rare earth oxides do not seem to vary in nature with pretreatment temperature. Variations of the activities of  $\text{La}_2\text{O}_3$  as a function of the pretreatment temperature is shown in Figure 6 for 1-butene isomerization, 1,3-butadiene hydrogenation, and methane– $\text{D}_2$  exchange.<sup>10–12</sup> Pretreatment at 923 K results in the maximum activity for all reactions. The surface sites generated by removal of water and carbon dioxide seem to be rather homogeneous in the sense that the same surface sites are relevant to all the reactions mentioned above.

### III. Characterization of Basic Surfaces

The surface properties of the heterogeneous basic catalysts have been studied by various methods by which existence of basic sites has been realized. Different characterization methods give different information about the surface properties. All the properties of basic sites cannot be measured by any



**Figure 6.** Variations of activity of  $\text{La}_2\text{O}_3$  for different types of reaction as a function of pretreatment temperature:  $\circ$ , 1-butene isomerization at 303 K (1 unit:  $6.4 \times 10^{20}$  molecules  $\text{min}^{-1} \text{g}^{-1}$ );  $\triangle$ ,  $\text{CH}_4\text{--D}_2$  exchange at 573 K (1 unit:  $10^{-2}\%$   $\text{s}^{-1} \text{g}^{-1}$ );  $\bullet$ , 1,3-butadiene hydrogenation at 273 K (1 unit:  $1.2 \times 10^{20}$  molecules  $\text{min}^{-1} \text{g}^{-1}$ ).

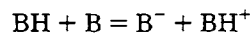
single method. Integration of the results obtained by different characterizations leads us to understand the structures, reactivities, strengths, and amounts of the basic sites on the surfaces. In this section, representative methods for characterization of the surface basic sites are described. It is emphasized what aspect of the basic sites is disclosed by each characterization method.

#### III-1. Indicator Methods

Acid–base indicators change their colors according to the strength of the surface sites and  $\text{p}K_{\text{BH}}$  values of the indicators. The strength of the surface sites are expressed by an acidity function ( $H_-$ ) proposed by Paul and Long. The  $H_-$  function is defined by the following equation:<sup>13,14</sup>

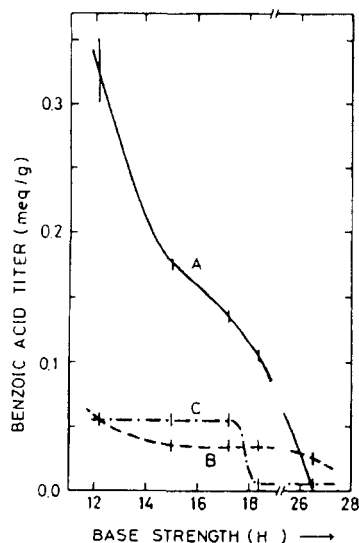
$$H_- = \text{p}K_{\text{BH}} + \log [\text{B}^-]/[\text{BH}]$$

where  $[\text{BH}]$  and  $[\text{B}^-]$  are, respectively, the concentration of the indicator BH and its conjugated base, and  $\text{p}K_{\text{BH}}$  is the logarithm of the dissociation constant of BH. The reaction of the indicator BH with the basic site ( $\text{B}$ ) is



The amount of basic sites of different strengths can be measured by titration with benzoic acid. A sample is suspended in a nonpolar solvent and an indicator is adsorbed on the sample in its conjugated base form. The benzoic acid titer is a measure of the amount of basic sites having a basic strength corresponding to the  $\text{p}K_{\text{BH}}$  value of the indicator used. Using this method, Take et al. measured outgassed samples of MgO, CaO, and SrO. The results are shown in Figure 7.<sup>15</sup> Magnesium oxide and CaO possess basic sites stronger than  $H_- = 26$ .

The indicator method can express the strength of basic sites in a definite scale of  $H_-$ , but this has disadvantages too. Although the color change is assumed to be the result of an acid–base reaction, an indicator may change its color by reactions different from an acid–base reaction. In addition, it



**Figure 7.** Benzoic acid titer vs base strength of (A) MgO, (B) CaO, and (C) SrO. (Reprinted from ref 15. Copyright 1971 Academic.)

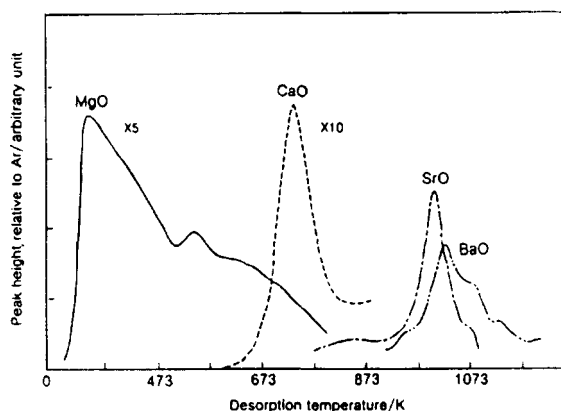
requires a long time for benzoic acid to reach an adsorption equilibrium when titration is carried out in a solution. In some cases, the surface of heterogeneous basic catalysts may dissolve into a titration solution. If this happens, the number of basic sites should be overestimated. Therefore, special care should be taken with the indicator method.

### III-2. Temperature-Programmed Desorption (TPD) of Carbon Dioxide

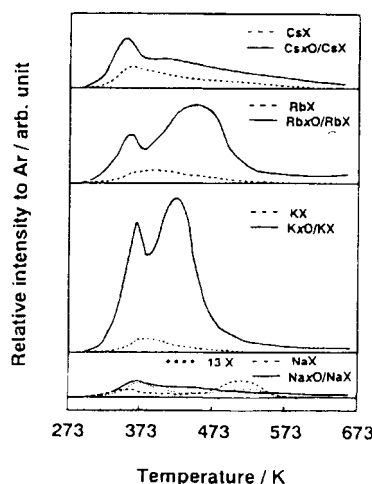
This method is frequently used to measure the number and strength of basic sites. The strength and amount of basic sites are reflected in the desorption temperature and the peak area, respectively, in a TPD plot. However, it is difficult to express the strength in a definite scale and to count the number of sites quantitatively. Relative strengths and relative numbers of basic sites on the different catalysts can be estimated by carrying out the TPD experiments under the same conditions. If the TPD plot gives a sharp peak, the heat of adsorption can be estimated.

TPD plots of carbon dioxide desorbed from alkaline earth oxides are compared in Figure 8 in which adsorption of carbon dioxide and the following treatment before the TPD run were done under the same conditions.<sup>16</sup> The strength of basic sites is in the increasing order of MgO < CaO < SrO < BaO. The number of basic sites per unit weight that can retain carbon dioxide under the adsorption conditions increases in the order BaO < SrO < MgO < CaO.

Enhancement of basic strength by addition of alkali ions to X-zeolite in excess of the ion exchange capacity was demonstrated by TPD plots of carbon dioxide as shown in Figure 9.<sup>17</sup> The peak areas are larger for the alkali ion-added zeolites (solid lines) than for the ion-exchanged zeolites (dotted lines). In particular, desorption of carbon dioxide still continues at the desorption temperature of 673 K for ion-added zeolites.



**Figure 8.** TPD plots of carbon dioxide desorbed from alkaline earth oxides. (Reprinted from ref 16. Copyright 1988 Elsevier.)

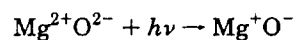


**Figure 9.** TPD plots of CO<sub>2</sub> adsorbed on alkali ion-exchanged and alkali ion-added zeolites.

### III-3. UV Absorption and Luminescence Spectroscopies

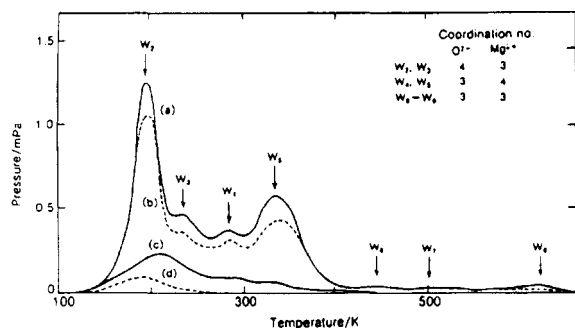
UV absorption and luminescence spectroscopies give information about the coordination states of the surface atoms.

High surface area MgO absorbs UV light and emits luminescence, which is not observed with MgO single crystal. Nelson and Hale first observed the absorption at 5.7 eV, which is lower than the band gap (8.7 eV, 163 nm) for bulk MgO by 3 eV.<sup>18</sup> Tench and Pott observed photoluminescence.<sup>19,20</sup> The UV absorption corresponds to the following electron transfer process involving surface ion pair.<sup>21,22</sup>



Absorption bands were observed at 230 and 274 nm, which are considerably lower in energy than the band at 163 nm for bulk ion pairs. The bands at 230 and 274 nm are assigned to be due to the surface O<sup>2-</sup> ions of coordination numbers 4 and 3, respectively.

Luminescence corresponds to the reverse process of UV absorption, and the shape of the luminescence spectrum varies with the excitation light frequency



**Figure 10.** TPD plots for hydrogen adsorbed on MgO at various pretreatment temperatures/K: (a) 1123, (b) 973, (c) 823, (d) 673.

and with the adsorption of molecules. Emission sites and excitation sites are not necessarily the same. Excitons move on the surface and emit at the ion pair of low coordination numbers where emission efficiency is high.

Ion pairs of low coordination numbers responsible for UV absorption and luminescence exist at corners, edges, or high Miller index surfaces. The surface model for MgO shown in figure 5 was proposed on the basis of UV absorption and luminescence together with the effects of hydrogen adsorption on the luminescence spectrum. The luminescence spectrum excited by the 274 nm light was much more severely influenced by hydrogen adsorption than that excited by the 230 nm light. Hydrogen molecules interact more strongly with the ion pairs of coordination number 3 than with those of coordination number 4. Hydrogen molecules are heterolytically dissociated on these sites.

Although the UV absorption and luminescence spectroscopies give us useful information about the coordination state, it is difficult to count the number of the sites of a certain coordination state.

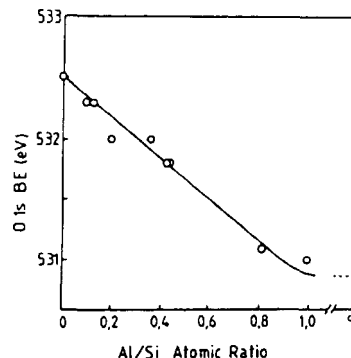
### III-4. Temperature-Programmed Desorption of Hydrogen

This method gives information about the coordination state of the surface ion pairs when combined with the other methods such as UV absorption and luminescence spectroscopies. The number of each ion pair could be counted if TPD is accurately measured with a proper calibration method. This method has been applied only to the MgO surface.

Hydrogen is heterolytically dissociated on the surface of MgO to form H<sup>+</sup> and H<sup>-</sup>, which are adsorbed on the surface O<sup>2-</sup> ion and Mg<sup>2+</sup> ion, respectively. TPD plots of hydrogen adsorbed on MgO pretreated at different temperatures are shown in Figure 10.<sup>23,24</sup> Seven desorption peaks appear in the temperature range 200–650 K, and appearance of the peaks varies with the pretreatment temperature. Appearance of the peaks at different temperatures indicates that several types of ion pairs with different coordination numbers exist on the surface of MgO. The adsorption sites on MgO pretreated at different temperatures and the coordination numbers of each ion pair are assigned as summarized in Table 2. The assignment of the surface ion pairs are based on the surface structure model of MgO (Figure 5).

**Table 2.** Coordination Numbers of Active Sites on MgO and Their Concentration Obtained from TPD for Hydrogen Adsorbed

| active site                       | coordination no. |                  | number of sites/10 <sup>15</sup> m <sup>-2</sup> at pretreatment temperature |       |       |        |
|-----------------------------------|------------------|------------------|------------------------------------------------------------------------------|-------|-------|--------|
|                                   | O <sub>1C</sub>  | Mg <sub>1C</sub> | 673 K                                                                        | 823 K | 973 K | 1123 K |
| W <sub>2</sub> and W <sub>3</sub> | 4                | 3                | 4.0                                                                          | 11.6  | 29.3  | 32.4   |
| W <sub>4</sub> and W <sub>5</sub> | 3                | 4                | 0.0                                                                          | 4.9   | 22.1  | 26.5   |
| W <sub>6</sub> and W <sub>7</sub> | 3                | 3                | 0.0                                                                          | 0.3   | 1.3   | 4.1    |
| W <sub>8</sub>                    | 3                | 3                |                                                                              |       | 1.2   | 4.2    |



**Figure 11.** Correlation between the binding energy of the O<sub>1s</sub> band and the Al/Si atomic ratio. (Reprinted from ref 25. Copyright 1988 Academic.)

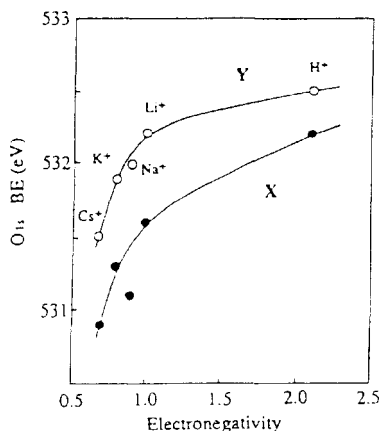
TPD of hydrogen supports the surface model of MgO illustrated.

Heterolytic dissociation of hydrogen on the MgO surface is also demonstrated by IR spectroscopy. The IR bands for O–H and Mg–H stretching vibration were observed.<sup>9</sup>

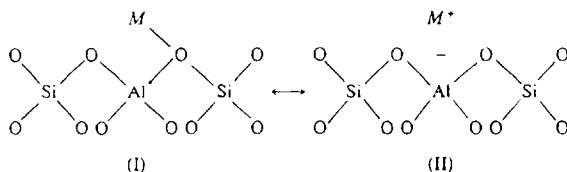
### III-5. XPS

The XPS binding energy (BE) for oxygen reflects the basic strength of the oxygen. As the O<sub>1s</sub> BE decreases, electron pair donation becomes stronger. Okamoto et al. studied the effects of zeolite composition and the type of cation on the BE of the constituent elements for X- and Y-zeolites ion-exchanged with a series of alkali cations as well as H-forms of A, X, Y, and mordenite.<sup>25</sup> The BE values of O<sub>1s</sub> are plotted against the Al/Si atomic ratio in Figure 11. The BE of O<sub>1s</sub> decreases as the Al content increases.

The effect of an ion-exchanged cation on the O<sub>1s</sub> BE is shown in Figure 12 as a function of the electronegativity ( $\chi$ ) of the cation. With increasing  $\chi$ , the O<sub>1s</sub> BE increases. The O<sub>1s</sub> BE of zeolite is directly delineated to the electron density of the framework oxygen. On the basis of XPS features of zeolite, Okamoto et al. proposed a bonding model of zeolite as shown in Figure 13.<sup>25</sup> Configurations I and II are in resonance. In configuration I, extra framework cations form covalent bonds with framework oxygens, while in configuration II, the cations form fully ionic bondings with the negatively charged zeolite lattice. As the electronegativity of the cation increases and approaches that of oxygen, the contribution of configuration I increases to reduce the net charges on the lattice. This explains the dependences of the O<sub>1s</sub> BE on the electronegativity of the cation as shown in Figure 12.



**Figure 12.** Binding energy of the  $O_{1s}$  band for cation exchanged zeolite as a function of the cation electronegativity ( $x$ ): (●) Y-zeolite and (○) X-zeolites. (Reprinted from ref 25. Copyright 1988 Academic.)

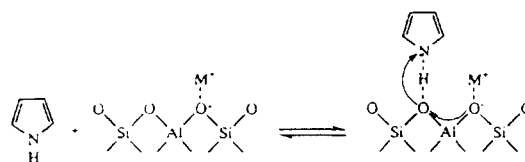


**Figure 13.** Schematic bonding model of zeolite.

Although the relation between electron density and the basic strength of O is not theoretically established, a good correlation between the BE of the  $N_{1s}$  band and basicity is well established for a wide variety of organic compounds containing N. It may be acceptable that the BE of the  $O_{1s}$  band changes monotonously with the basic strength of O when comparison is made within a same series of exchanged cations.

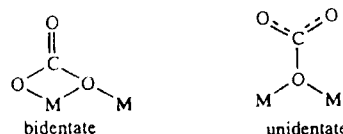
XPS measurement of the probe molecule adsorbed on basic sites gives information about the strength of the basic sites. Huang et al. measured the  $N_{1s}$  BE of the pyrrole adsorbed on alkali cation-exchanged X- and Y-zeolites.<sup>26</sup> The  $N_{1s}$  envelopes were deconvoluted into three peaks. One of the peaks was assigned to pyrrole adsorbed on the framework oxygen adjacent to the alkali cations other than the sodium cation. The BE of the peak varies with the exchanged cation in such a way that the  $N_{1s}$  BE decreases as the basic strength of the zeolite increases as  $Li < Na < K < Rb < Cs$ . The deconvolution of XPS  $N_{1s}$  peaks into three peaks indicates that the basic strength of the framework oxygen is inhomogeneous in the zeolite cage and that the cation exerts an influence only on the adjacent framework atoms. These suggest that electrons are localized significantly on  $M^+(AlO_2)^-$  units. A proposed model for pyrrole chemisorbed on a basic site of alkali cation-exchanged zeolite is shown in Figure 14.

As described later, the basic strength is reflected in the N–H stretching vibration frequency of pyrrole in the IR spectrum.<sup>27</sup> The  $N_{1s}$  BE in XPS correlates linearly with the N–H vibration frequencies of chemisorbed pyrrole. As the exchanged cation changes in the sequence Li, Na, K, Rb, and Cs, both the  $N_{1s}$  BE and the frequency of the N–H stretching vibration decrease for X- and Y-zeolites.<sup>26</sup>



**Figure 14.** Model for pyrrole chemisorbed on a basic site.

**Scheme 1.** Adsorbed Forms of Carbon Dioxide



### III-6. IR of Carbon Dioxide

This method gives information about the adsorbed state of  $CO_2$  on the surface. Carbon dioxide interacts strongly with a basic site and, therefore, the surface structures including basic sites are estimated from the adsorbed state of  $CO_2$ .

Carbon dioxide is adsorbed on heterogeneous basic catalysts in different forms: bidentate carbonate, unidentate carbonate, and bicarbonate (Scheme 1). On the MgO surface, the adsorbed form varies with the coverage of the adsorbed carbon dioxide. Bidentate carbonate is dominant at low coverage, and unidentate carbonate at high coverage.<sup>28</sup> Evans and Whately reported the adsorption of carbon dioxide on MgO.<sup>29</sup> In addition to unidentate and bidentate carbonates, bicarbonate species were also detected. For CaO, carbon dioxide is adsorbed in the form of bidentate carbonate regardless of the coverage.

In the adsorption state of unidentate carbonate, only surface oxygen atoms participate, while the metal ion should participate in the adsorption state of bidentate. In other words, the existence of only a basic site is sufficient for unidentate carbonate, but the existence of both a basic site and a metal cation is required for bidentate carbonate.

### III-7. IR of Pyrrole

Pyrrole is proposed to be a probe molecule for measurement of the strength of basic sites.<sup>17</sup> The IR band ascribed to the N–H stretching vibration shifts to a lower wavenumber on interaction of the H atom in pyrrole with a basic site. Barthomeuf measured the shifts of N–H vibration of pyrrole adsorbed on alkali ion exchanged zeolites.<sup>27,30</sup> The results are given in Table 3. The charges on the oxygen calculated from Sanderson's electronegativities are also listed in Table 3. The shift increases when the negative charge on the oxide ion increases. The negative charge is associated closely with the strength of the basic site. The basic strengths of alkali ion-exchanged zeolites are in the order  $CsX > NaX > KY > NaY$ , KL, Na-mordenite, Na-beta.

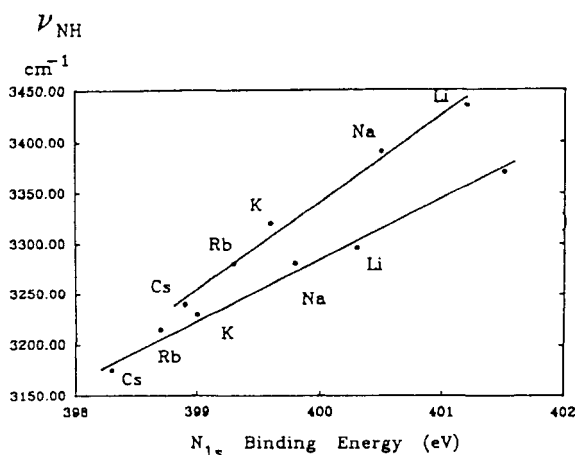
The N–H vibration frequencies observed by IR are plotted against the  $N_{1s}$  BE observed by XPS as shown in Figure 15.<sup>26</sup> For both X- and Y-zeolites, linear relations are observed; strengths of the basic sites



**Table 3. Shifts of N-H Vibration of Pyrrole Adsorbed on Zeolites and Calculated Average Charge on Oxygen**

| zeolite | $\Delta\nu_{\text{NH}}^a$ | $q_{\text{O}}^b$ | zeolite  | $\Delta\nu_{\text{NH}}^a$ | $q_{\text{O}}^b$ |
|---------|---------------------------|------------------|----------|---------------------------|------------------|
| CsX     | 240                       | -0.461           | Na-MOR   | 30                        | -0.278           |
| NaX     | 180                       | -0.413           | Na-beta  | 30                        | -0.240           |
| KY      | 70                        | -0.383           | Cs ZSM-5 | 0                         | -0.236           |
| NaY     | 30-40                     | -0.352           | Na ZSM-5 | 0                         | -0.225           |
| KL      | 30                        | -0.356           |          |                           |                  |

<sup>a</sup> Shift of N-H from the liquid. <sup>b</sup> Charge on oxygen calculated from Sanderson electronegativity.



**Figure 15.** Relationship between  $N_{1s}$  binding energy and N-H stretching vibration frequencies of chemisorbed pyrrole on (○) X-zeolites and (●) Y-zeolites. (Reprinted from ref 26. Copyright 1992 Academic.)

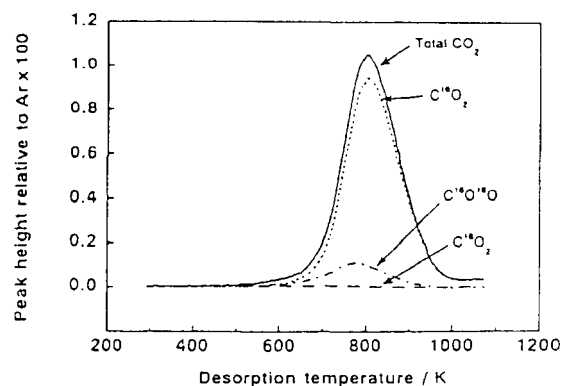
are in the order  $\text{CsX} > \text{RbX} > \text{KKX} > \text{NaX} > \text{LiX}$  and  $\text{CsY} > \text{RbY} > \text{KY} > \text{NaY} > \text{LiY}$ .

### III-8. Oxygen Exchange between Carbon Dioxide and Surface

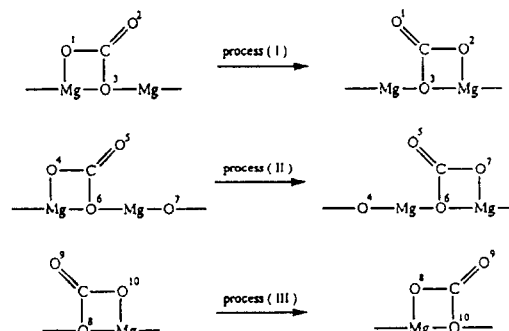
This method gives information about the dynamic nature of interaction of adsorbed  $\text{CO}_2$  with the surface ion pair. As described above, carbon dioxide is used as a probe molecule for the basic properties in IR and TPD. If  $^{18}\text{O}$ -labeled, carbon dioxide is used, additional information about the nature of basic sites is obtained.

Yanagisawa et al. reported that oxygen exchange between adsorbed  $\text{CO}_2$  and the MgO surface takes place to a considerable extent.<sup>31</sup> They observed a TPD desorption peak consisting mainly of  $\text{C}^{16}\text{O}_2$  and  $\text{C}^{16}\text{O}^{18}\text{O}$  after  $\text{C}^{18}\text{O}_2$  adsorption on MgO and suggested that the adsorbed  $\text{C}^{18}\text{O}_2$  interacts with the peroxy ion  $(^{16}\text{O}_2)_2^{2-}$  on a defect in the MgO surface. Essentially the same result was independently reported by Shishido et al.<sup>32</sup> The interpretation of the exchange mechanisms, however, was not the same as that of Yanagisawa et al.

Tsuji et al. reported the oxygen exchange in detail.<sup>33</sup> TPD plots for  $\text{C}^{18}\text{O}_2$  adsorbed on MgO are shown in Figure 16 in which  $41 \times 10^{-6}$  mol  $\text{C}^{18}\text{O}_2$   $\text{g}^{-1}$  (one  $\text{CO}_2$  molecule per  $670 \text{ \AA}^2$ ) was adsorbed. Extensive oxygen exchange was observed; no  $\text{C}^{18}\text{O}_2$  was desorbed. Proposed processes for the mechanism of migration of the surface bidentate carbonate are shown in Figure 17. There are at least two ways,



**Figure 16.** TPD plots for  $\text{C}^{18}\text{O}_2$  adsorbed on MgO.



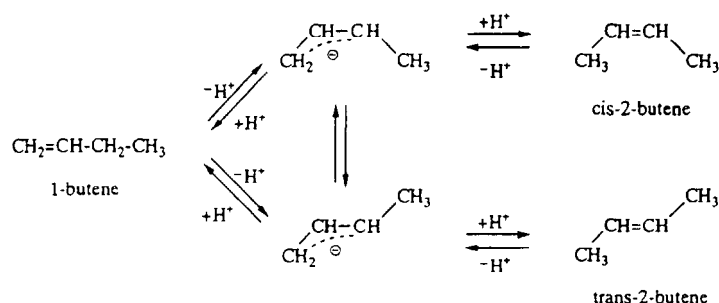
**Figure 17.** Proposed processes for the mechanisms of migration of the surface bidentate carbonate.

processes I and II, for the adsorbed carbonate species to migrate over the surface. In process I, carbon dioxide rolls over the surface in such a way that the free oxygen atom in the bidentate carbonate approaches the adjacent Mg atom on the surface. In process II, the carbon atom approaches the adjacent O atom on the surface.

In process I, the carbonate species always contains two  $^{18}\text{O}$  atoms. Therefore, repetition of process I results in the exchange of one oxygen atom, but not the exchange of two oxygen atoms in the desorbed  $\text{CO}_2$ . The repetition of process II also results in the exchange of one oxygen atom. For evolution of  $\text{C}^{16}\text{O}_2$ , both processes I and II should be involved. In addition to processes I and II, process III is possible. This process is essentially the same as the mechanism proposed for the oxygen exchange between bidentate carbonate and oxide surface. The carbonate species are able to migrate on the surface over a long distance by a combination of process I-III without leaving the surface, if process III exists. IR spectra of the adsorbed  $\text{CO}_2$  changes with increasing temperature. It is suggested that the bidentate carbonate formed on room temperature adsorption of  $\text{CO}_2$  migrates over the surface as the temperature is raised in the TPD run. The migration occurs mostly in the temperature range from room temperature to 473 K.

The results of the oxygen exchange between  $\text{CO}_2$  and MgO surface suggest an important aspect of the nature of surface basic sites. The basic sites are not fixed on the surface but are able to move over the surface when carbon dioxide is adsorbed and de-

Scheme 2. 1-Butene Isomerization



sorbed. The position of the basic site (surface O atom) changes as CO<sub>2</sub> migrate over the basic site. In addition, it became clear that not only O<sup>2-</sup> basic sites but also adjacent Mg<sup>2+</sup> sites participate in CO<sub>2</sub> adsorption. Therefore, it is reasonable to consider that the metal cations adjacent to the basic site participate in the base-catalyzed reactions.

#### IV. Catalysis by Heterogeneous Basic Catalysts

In this section, selected examples of heterogeneous base-catalyzed reactions are described. Some of them aim at elucidating the reaction mechanisms. The others are applications to various organic syntheses to show the potential use of heterogeneous catalysts.

##### IV-1. Double Bond Migration

1-Butene isomerization to 2-butenes has been extensively studied over many heterogeneous basic catalysts to elucidate the reaction mechanisms and to characterize the surface basic properties. The reaction proceeds at room temperature or below over most of heterogeneous basic catalysts. Over MgO, for example, the reaction occurs even at 223 K if the catalyst is properly activated.

The reaction mechanisms for 1-butene isomerization are shown in Scheme 2.<sup>34</sup>

The reaction is initiated by abstraction of allylic H by basic sites to form *cis* or *trans* forms of the allyl anion. In the form of the allyl anion, the *cis* form is more stable than the *trans* form. Therefore, *cis*-2-butene is predominantly formed at the initial stage of the reaction. A high *cis*/*trans* ratio observed for the base-catalyzed isomerization is in contrast to the value close to unity for acid-catalyzed isomerization.

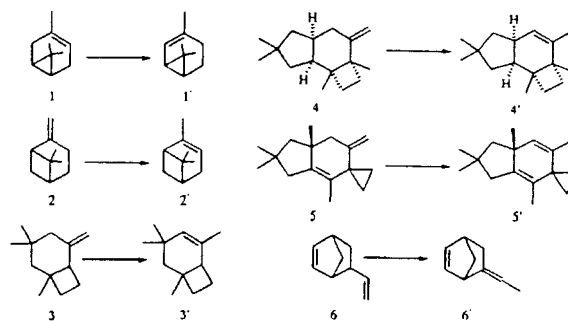
The *cis* to *trans* ratio in 2-butenes produced could be used to judge whether the reaction is a base-catalyzed or acid-catalyzed one. Tsuchiya measured the ratio *cis*/*trans* in 1-butene isomerization, and found a high value for Rb<sub>2</sub>O.<sup>35</sup>

Coisomerization of butene-*d*<sub>0</sub> and -*d*<sub>8</sub> is a useful method to determine the reaction mechanisms.<sup>36</sup> In the coisomerization, a mixture containing equal amounts of nondeuteriobutene (*d*<sub>0</sub>) and perdeuteriobutene (*d*<sub>8</sub>) is allowed to react, and the isotopic distributions in the products and reactant are analyzed. If the reaction proceeds by hydrogen addition–abstraction mechanisms, an intermolecular H (or D) transfer is involved and the products will be composed of *d*<sub>0</sub>, *d*<sub>1</sub>, *d*<sub>7</sub>, and *d*<sub>8</sub> isotopic species. On the other hand, if the reaction proceeds by hydrogen abstraction–addition mechanisms, an intramolecular

H (or D) transfer is involved, and the products will be composed of *d*<sub>0</sub> and *d*<sub>8</sub> isotopic species.

Since an H<sup>+</sup> is abstracted first for base-catalyzed isomerization to form allyl anions to which the H<sup>+</sup> returns at a different C atom, an intramolecular H (or D) transfer is expected. Therefore, an intramolecular H (or D) transfer and a high *cis*/*trans* ratio are characteristic features for 1-butene double bond isomerization over heterogeneous basic catalysts.<sup>37,38</sup>

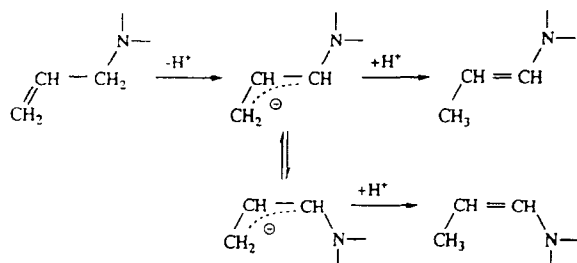
The fundamental studies of 1-butene double bond isomerization over heterogeneous basic catalysts were extended to the double bond migration of olefins having more complex structures such as pinene (1), carene (2), protoilludene (4), illudadiene (5), as shown below.<sup>39–41</sup>



These olefins contain three-membered and four-membered rings. If acidic catalysts were used, the ring-opening reactions would easily occur, and the selectivities for double bond migration should markedly decrease. A characteristic feature of heterogeneous basic catalysts is a lack of C–C bond cleavage ability. The double bond migration selectively occurs without C–C bond cleavages over heterogeneous basic catalysts.

As mentioned above, the heterogeneous basic catalysts are highly active for double bond migration, the reactions proceed at a low temperature. This is advantageous for olefins which are unstable at high temperature. Because of this advantage, the heterogeneous basic catalyst, Na/NaOH/Al<sub>2</sub>O<sub>3</sub>, is used for an industrial process for the selective double bond migration of 5-vinylbicyclo[2.2.1]heptene (6).<sup>41,42</sup> The reaction proceeds at the low temperature of 243 K.

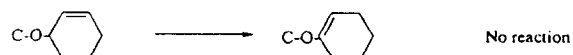
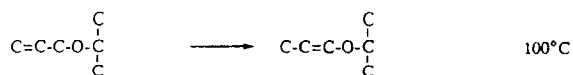
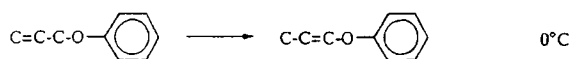
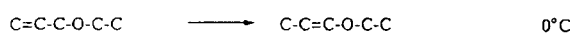
Heterogeneous basic catalysts have another advantage in double bond migration. For the double bond migration of unsaturated compounds containing heteroatoms such as N and O, heterogeneous basic catalysts are more efficient than acidic catalysts.

**Scheme 3. Double Bond Migration of Allylamines to Enamines**

Acidic catalysts interact strongly with heteroatoms, became poisoned, and show no activity. On the other hand, the active sites of heterogeneous basic catalysts interact weakly with heteroatoms and, therefore, act as efficient catalysts.

Allylamines undergo double bond migration to enamines over alkaline earth oxides (Scheme 3).<sup>43</sup> For instance, 1-*N*-pyrrolidino-2-propene isomerizes to 1-*N*-pyrrolidino-1-propene over MgO, CaO, SrO, and BaO at 313 K. The reaction mechanisms are essentially the same as those for 1-butene isomerization. The basic sites abstract an H<sup>+</sup> from the reactant to form allyl anions as an intermediate as shown below. In this scheme too, the *cis*-form of the intermediate of the allyl anion is more stable than the *trans*-form, and the products are mostly in the thermodynamically less stable *cis*-form.

Similarly, 2-propenyl ethers undergo double bond migration to 1-propenyl ethers.<sup>44</sup> The reaction mechanisms are the same as those for 1-butene and allylamines in the sense that the intermediates are allyl anions and mostly in the *cis*-form. Among heterogeneous basic catalysts, CaO exhibits the highest activity, and La<sub>2</sub>O<sub>3</sub>, SrO, and MgO also show high activities. The reaction temperatures required to initiate the reactions are different for each reactant, as shown below. 3-Methoxycyclohexene is unreactive,

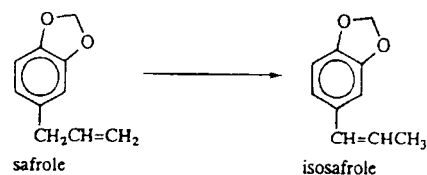


tive, which is explained as being due to the fact that the adsorbed state is such that the allylic H points away from the surface, and cannot be abstracted by the basic sites on the surface.

Double bond migration of safrole to isosafrole was reported to proceed at 300 K over Na/NaOH/Al<sub>2</sub>O<sub>3</sub>.<sup>41</sup>

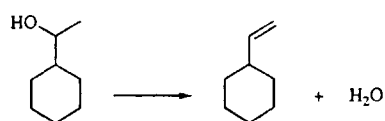
#### IV-2. Dehydration and Dehydrogenation

In general, alcohols undergo dehydration to olefins and ethers over acidic catalysts, and dehydrogenation



to aldehydes or ketones over basic catalysts. In some cases, however, heterogeneous basic catalysts promote dehydration of alcohols in which the mechanisms and product distribution differ from those for acid-catalyzed dehydration. The characteristic features of base-catalyzed dehydration are observed for 2-butanol dehydration. The products consist mainly of 1-butene over the rare earth oxides,<sup>45</sup> ThO<sub>2</sub>,<sup>46,47</sup> and ZrO<sub>2</sub>.<sup>48</sup> This is in contrast to the preferential formation of 2-butenes over acidic catalysts. The initial step in the base-catalyzed dehydration is the abstraction of an H<sup>+</sup> at C-1 and 2-butanol to form anion.

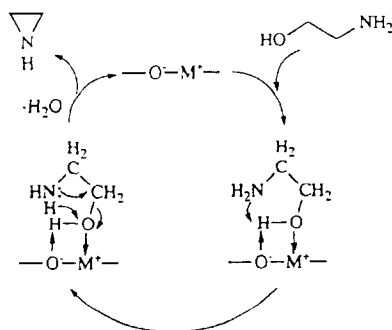
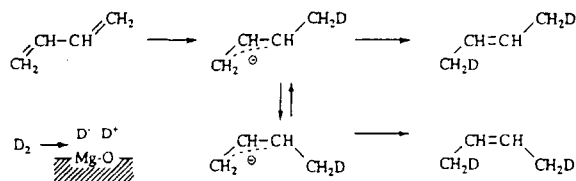
Dehydration of 1-cyclohexylethanol to vinylcyclohexane has been industrialized by use of ZrO<sub>2</sub> as a catalyst.<sup>49</sup> In the dehydration of 2-alcohols to the corresponding 1-olefins over ZrO<sub>2</sub>, the selectivity for 1-olefins depends on the amount of Si contained in ZrO<sub>2</sub> as an impurity. Si contaminants in ZrO<sub>2</sub> generate acidic sites. By treatment of ZrO<sub>2</sub> with NaOH to eliminate the acidic sites, the byproducts of 2-olefins are markedly reduced and the selectivity for 1-olefins is increased. The ZrO<sub>2</sub> treated with NaOH is used for the industrial process for the production of vinylcyclohexane.



Intramolecular dehydration of monoethanolamine to ethylenimine has also been industrialized by use of the mixed oxide catalyst composed of Si, alkali metal, and P. The catalyst possesses both weakly acidic and basic sites.<sup>50</sup> Because monoethanolamine has two strong functional groups, weak sites are sufficient to interact with the reactant. If either acidic sites or basic sites are strong, the reactant interacts too strongly with the sites and forms undesirable byproducts. It is proposed that the acidic and basic sites act cooperatively as shown in Scheme 4. The composition of the catalyst is adjusted to control the surface acidic and basic properties. A selectivity of 78.8% for ethylenimine was obtained for the catalyst composed of Si/Cs/P/O in the atomic ratio 1/0.1/0.08/2.25.

#### IV-3. Hydrogenation

Kokes and his co-workers studied the interaction of olefins with hydrogen on ZnO, and reported heterolytic cleavages of H<sub>2</sub> and C-H bonds.<sup>2,3</sup> The negatively charged  $\pi$ -allyl anions are intermediate for propylene hydrogenation. Participation of heterolytically dissociated H<sup>+</sup> and H<sup>-</sup> in the hydrogenation is generally applicable in base-catalyzed hydrogenation. The observation that MgO pretreated at 1273 K exhibited olefin hydrogenation activities was

**Scheme 4. Intramolecular Dehydration of Monoethanolamine****Scheme 5. Hydrogenation of 1,3-Butadiene**

a clear demonstration of heterogeneous base-catalyzed hydrogenation.<sup>51</sup> The hydrogenation occurring on heterogeneous basic catalysts has characteristic features which distinguish heterogeneous basic catalysts from conventional hydrogenation catalysts such as transition metals and transition metal oxides.

The characteristic features of base-catalyzed hydrogenation are as follows.

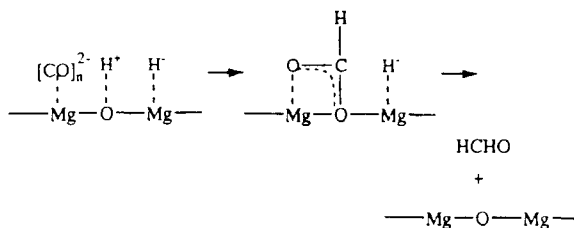
(1) There is a large difference in the hydrogenation rate between monoenes and conjugated dienes: Conjugated dienes undergo hydrogenation much faster than monoenes. For example, 1,3-butadiene undergoes hydrogenation at 273 K over alkaline earth oxides, while butenes need a reaction temperature above 473 K. The products of diene hydrogenation consist exclusively of monoenes, with no alkanes being formed at 273 K.

(2) There is a predominant occurrence of 1,4-addition of H atoms in contrast to 1,2-addition which is commonly observed for conventional hydrogenation catalysts: In 1,3-butadiene hydrogenation, 2-butenes are preferentially formed over heterogeneous basic catalysts, while 1-butene is the main product over conventional hydrogenation catalysts.

(3) There is retention of the molecular identity of H atoms during reaction: While a hydrogen molecule dissociates on the catalyst surface, two H atoms used for hydrogenation of one reactant molecule originate from one hydrogen molecule.

Features 1 and 2 are characteristic of hydrogenation in which anionic intermediates are involved.<sup>52</sup> The reaction (Scheme 5) of 1,3-butadiene hydrogenation is shown below, where H is replaced by D for clarity. The products contain two D atoms at the terminal C atoms if D<sub>2</sub> is used instead of H<sub>2</sub>.

Deuterium 1 is dissociatively adsorbed to form D<sup>+</sup> and D<sup>-</sup>. 1,3-Butadiene consists of 93% *s*-trans conformer and 7% *s*-cis conformer in the gas phase at 273 K. At first, D<sup>-</sup> attacks 1,3-butadiene to form the allyl anion of the *trans* form which undergoes either interconversion to form *cis* allyl anion or addition of

**Scheme 6. Hydrogenation of Carbon Monoxide**

D<sup>+</sup> to form butenes. Since the electron density of the allyl anions is highest on the terminal C atom, the positively charged D<sup>+</sup> selectively adds to the terminal C atom to complete 1,4-addition of D atoms to yield 2-butene.

On alkaline earth oxides, the interconversion between the *trans*-allyl anion and *cis*-allyl anion is faster than the addition of D<sup>+</sup>. As a result, *cis*-2-butene-*d*<sub>2</sub> is preferentially formed. On the other hand, the addition is faster than the interconversion on ThO<sub>2</sub>,<sup>53</sup> ZrO<sub>2</sub>,<sup>54,55</sup> and rare earth oxides,<sup>56</sup> *trans*-2-butene-*d*<sub>2</sub> being a main product.

A large difference in the reactivity between dienes and monoenes is caused by difficulty of alkyl anion formation compared to allyl anion formation. Alkyl anions are less stable than allyl anions; thus, the reactions of monoenes with H<sup>-</sup> to form alkyl anions require high temperature.

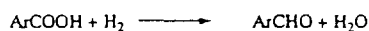
Feature 3 arose from the location of the active sites. Both D<sup>+</sup> and D<sup>-</sup> on one set of active sites are assumed not to migrate to other sites, and each set of active sites is isolated from the others. This happens because the basic hydrogenation catalysts are metal oxides.

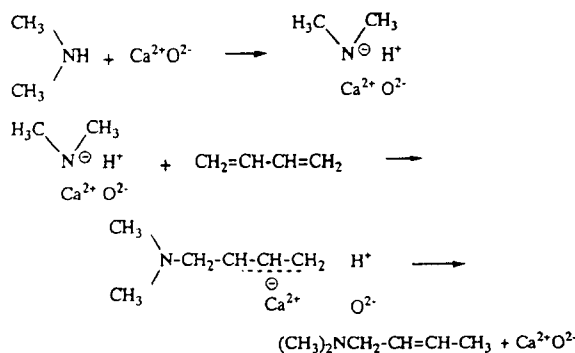
The active sites for hydrogenation on alkaline earth oxides are believed to be metal cation-O<sup>2-</sup> ion pairs of low coordination, as described in the preceding section. In the surface model structure of MgO, it is plausible that the Mg<sup>2+</sup><sub>3c</sub>-O<sup>2-</sup><sub>3c</sub> pairs act as hydrogenation sites.

Dissociatively adsorbed H<sup>+</sup> and H<sup>-</sup> also hydrogenate CO on MgO, La<sub>2</sub>O<sub>3</sub>, ZrO<sub>2</sub>, and ThO<sub>2</sub>.<sup>57,58</sup> TPD study and IR measurement indicate that the reaction proceeds by the following mechanism shown in Scheme 6.

1,3-Butadiene undergoes transfer hydrogenation with 1,3-cyclohexadiene over La<sub>2</sub>O<sub>3</sub>, CaO, ThO<sub>2</sub>, and ZrO<sub>2</sub>.<sup>59,60</sup> The product distributions are similar to those for hydrogenation with H<sub>2</sub> except for ZrO<sub>2</sub>, on which a relatively large amount of 1-butene is formed.

Direct hydrogenation (or reduction) of aromatic carboxylic acids to corresponding aldehydes has been industrialized by use of ZrO<sub>2</sub>.<sup>61,62</sup> Although the reaction mechanism is not clear at present, the hydrogenation and dehydration abilities, which are associated with the basic properties of ZrO<sub>2</sub>, seem to be important for promoting the reaction. The catalytic properties are improved by modification with the metal ions such as Cr<sup>3+</sup> and Mn<sup>4+</sup> ions. Crystallization of ZrO<sub>2</sub> is suppressed and coke formation is avoided by addition of the metal ions.

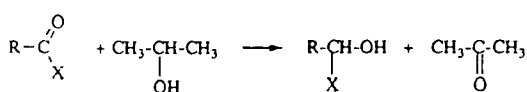


**Scheme 7. Amination of 1,3-Butadiene****IV-4. Amination**

Amines undergo an addition reaction with conjugated dienes over heterogeneous basic catalysts.<sup>63</sup> Primary and secondary amines add to conjugated dienes to form unsaturated secondary and tertiary amines, respectively. Amination with monoamines scarcely proceeds over basic catalysts. The reaction mechanisms for amination with conjugated dienes are essentially the same as those for the hydrogenation in the sense that heterolytic dissociation of hydrogen ( $\text{H}_2 \ll \text{H}^+ + \text{H}^-$ ) and amine ( $\text{RNH}_2 \ll \text{H}^+ + \text{RNH}^-$ ) are involved in the reaction. The sequence that the anion and  $\text{H}^+$  successively add to the 1,4 position of conjugated dienes is common to hydrogenation and amination. As an example, the reaction mechanisms for addition of dimethylamine to 1,3-butadiene are shown in Scheme 7. The reaction over CaO takes place at 273 K.

**IV-5. Meerwein-Ponndorf-Verley Reduction**

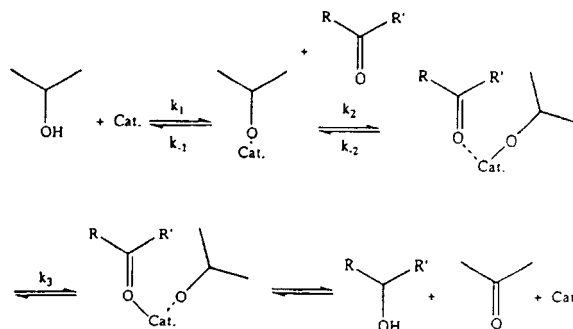
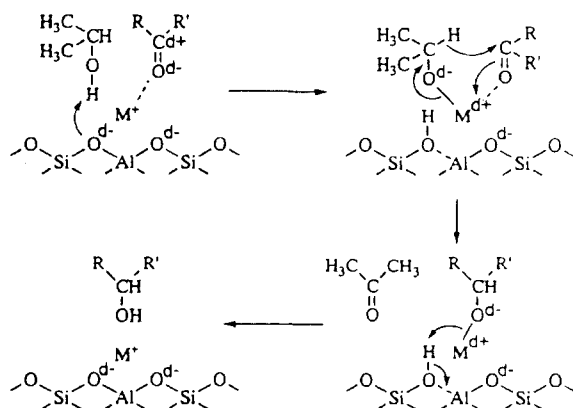
Meerwein-Ponndorf-Verley reduction is the hydrogenation in which alcohols are used as a source of hydrogen and is one of the hydrogen transfer reactions. Aldehyde and ketones react with alcohols to produce corresponding alcohols by Meerwein-Ponndorf-Verley reduction:



Shibagaki et al. studied Meerwein-Ponndorf-Verley reduction of various kinds of aldehydes and ketones in the temperature range 273–473 K.<sup>64</sup> They found hydrous zirconium oxide as a highly active catalyst for the reactions. 2-Propanol was used as a hydrogen source. On the basis of the isotope effect and kinetic analysis, it was suggested that the slow step is hydride transfer from the adsorbed 2-propanol to the adsorbed carbonyl compound (Scheme 8).

The reactions of carboxylic acids with alcohols to form esters are also catalyzed by hydrous zirconium oxide at a reaction temperature above 523 K.<sup>65</sup> Similarly, amidation of carboxylic acids or esters with amines or ammonia proceeds over hydrous zirconium oxide in the temperature range 423–473 K.<sup>66</sup>

Although hydrous zirconium oxide is proposed to be an effective catalyst for the above reactions, the

**Scheme 8. Hydrogen Transfer from 2-Propanol to Aldehydes and Ketones****Scheme 9. Meerwein-Ponndorf-Verley Reduction of Ketones or Aldehydes with 2-Propanol**

nature of the active sites has not been elucidated. The reaction mechanisms involving the active sites are not clear for the hydrous zirconium oxide catalyzed reactions. In particular, the reason why the hydrous form of zirconium oxide is more efficient than the anhydrous form of zirconium oxide is unclear.

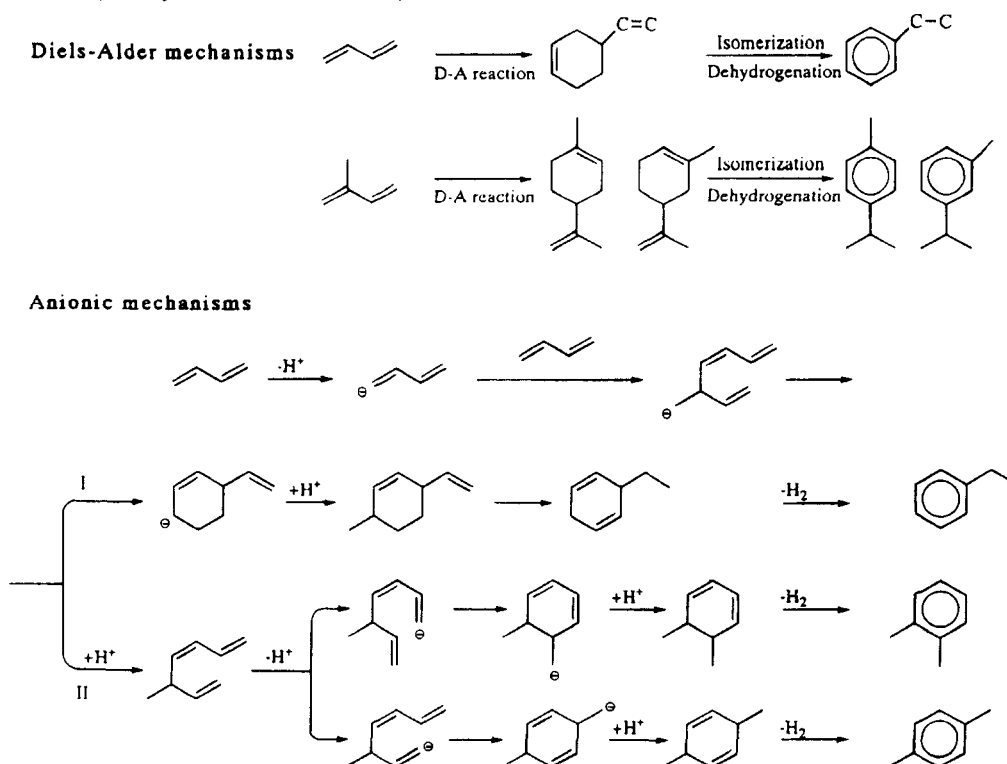
Meerwein-Ponndorf-Verley reduction of ketones or aldehydes with 2-propanol proceeds over x-zeolites ion-exchanged with  $\text{Cs}^+$  and  $\text{Rh}^+$ .<sup>67</sup> The mechanisms proposed for the zeolites are shown in Scheme 9. The reaction is initiated by abstraction of an  $\text{H}^+$  from 2-propanol by the basic sites of the catalyst. In addition to the basic sites, exchanged cations play a role of stabilizing the ketone by the hydride transferring from adsorbed 2-propanol to the ketone.

**IV-6. Dehydrocyclodimerization of Conjugated Dienes**

Conjugated dienes such as 1,3-butadiene and 2-methyl-1,3-butadiene (isoprene) react over  $\text{ZrO}_2$  and  $\text{MgO}$  to yield aromatics at 643 K.<sup>68,69</sup> Heterogeneous basic catalysts other than  $\text{ZrO}_2$  and  $\text{MgO}$  scarcely exhibit appreciable activities. For the formation of aromatics from dienes, two kinds of mechanisms are possible. One involves the Diels-Alder reaction followed by double bond migration and dehydrogenation. The other involves anionic intermediates.

Over  $\text{MgO}$ , 1,3-butadiene mainly produces *o*- and *p*-xylenes, which will not be formed via the Diels-Alder reaction. Over  $\text{ZrO}_2$ , the main product from

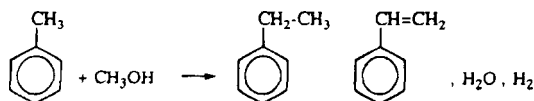
Scheme 10. Dehydrocyclodimerization of 1,3-Butadiene



1,3-butadiene is ethylbenzene which will be formed via the Diels–Alder reaction. Two mechanisms for dehydrocyclodimerization are shown in Scheme 10. The mechanisms involving the Diels–Alder reaction take place over  $\text{ZrO}_2$ , and the anionic mechanisms take place over  $\text{MgO}$ .

#### IV-7. Alkylation

In general, alkylation of aromatics occurs at a ring position over an acidic catalyst, while side chain alkylation takes place over a basic catalyst. Toluene undergoes side chain alkylation with methanol to produce ethylbenzene and styrene over  $\text{Cs}^+$  ion-exchanged X-zeolite.<sup>5</sup>



The first step in this reaction is dehydrogenation of methanol to formaldehyde, which undergoes aldol type reaction with toluene to form styrene. Ethylbenzene is formed by hydrogenation of styrene. The basic sites in the zeolite catalyst participate in both the dehydrogenation of methanol and the aldol type reaction.

Alkylation of toluene was studied by computer graphics on the basis of quantum chemical calculation.<sup>70,71</sup> The calculation also suggests that the high activity results from copresence of acidic and basic sites in a cavity of zeolite.

The zeolites having alkali ions in excess of their ion-exchange capacity exhibit higher activities than

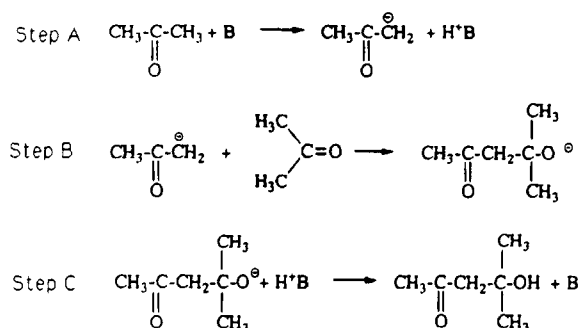
the simple ion-exchanged zeolites.<sup>72</sup> The high activities are caused by the generation of strong basic sites by addition of alkali ions which are located in the zeolite cavities in the form of alkali oxides.

$\text{K/KOH/Al}_2\text{O}_3$  is an efficient catalyst for alkylation of isopropylbenzene with olefins such as ethylene and propylene.<sup>41</sup> The reaction occurs at 300 K. In this reaction, too, alkylation occurs selectively at the side chain. The selective occurrence of the side chain alkylation is due to the anionic mechanisms as proposed by Suzukamo et al. The basic sites of  $\text{K/KOH/Al}_2\text{O}_3$  are sufficiently strong to abstract an  $\text{H}^+$  from isopropylbenzene to form an unstable tertiary anion at a low temperature.

#### IV-8. Aldol Addition and Condensation

Aldol addition of acetone to form diacetone alcohol is well known to be catalyzed by  $\text{Ba}(\text{OH})_2$ . Alkaline earth oxides,  $\text{La}_2\text{O}_3$ , and  $\text{ZrO}_2$  are also active for the reaction in the following order:  $\text{BaO} > \text{SrO} > \text{CaO} > \text{MgO} > \text{La}_2\text{O}_3 > \text{ZrO}_2$ .<sup>73</sup> With  $\text{MgO}$ , addition of a small amount of water increases the activity, indicating that the basic  $\text{OH}^-$  ions either retained on the surface or formed by dehydration of diacetone alcohol are active sites for aldol addition of acetone. By the tracer experiments in which a mixture containing equal amount of acetone- $d_0$  and - $d_8$  was allowed to react, the slow step was elucidated to be step B in Scheme 11.<sup>74</sup>

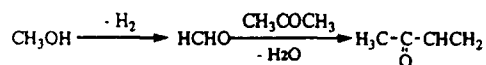
By use of the catalysts possessing both acid and base sites, the product diacetone alcohol undergoes dehydration to mesityl oxide. If hydrogenation ability is further added to the catalyst, mesityl oxide is hydrogenated to methyl isobutyl ketone (MIBK).

**Scheme 11. Aldol Addition of Acetone**

When the aldol condensation of acetone is performed over A-, X-, Y-, or L-zeolites containing alkali metal clusters at 623 K, mesityl oxide and isophorone are produced as main products.<sup>75</sup> The ratio of the two products is dependent on the types of zeolites. A-type zeolites favor the formation of the smaller molecule of mesityl oxide. With X- or Y-zeolite, isophorone is preferentially produced. For the smaller pore sized L-zeolite, the formation of mesityl oxide is about twice as great as that of isophorone.<sup>76</sup> These catalysts possess acidic sites in addition to basic sites. Controlling the acid-base properties and choice of the zeolite pore size results in obtaining each product selectively.

Aldol condensation of formaldehyde with methyl propionate to form methyl methacrylate is catalyzed by X- and Y-zeolites having a basic property. The highest conversion was obtained with the zeolite ion-exchanged with K followed by being impregnated with potassium hydroxide.<sup>77</sup>

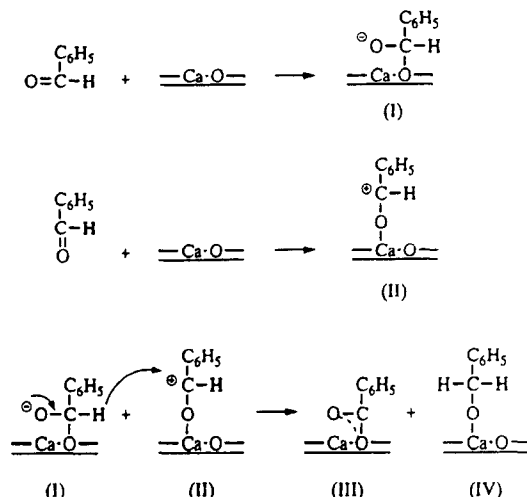
Hydrotalcite ( $\text{Mg}_6\text{Al}_2(\text{OH})_{16}\text{CO}_3\cdot 4\text{H}_2\text{O}$ ) and chrysotile ( $\text{Mg}_3(\text{OH})_4\text{Si}_2\text{O}_5$ ) act as efficient catalysts for the production of methyl vinyl ketone (MVK) through aldol condensation between acetone and formaldehyde at 673 K.<sup>78</sup> Synthetic  $\text{Co}^{2+}$  ion-exchange chrysotile,  $\text{Co}_x\text{Mg}_{3-x}(\text{OH})_4\text{Si}_2\text{O}_5$ , produces methyl vinyl ketone from acetone and methanol. By addition of  $\text{Co}^{2+}$ , dehydrogenation sites are generated. Methanol is dehydrogenated to formaldehyde which undergoes aldol condensation with acetone to produce MVK.

**IV-9. The Tishchenko Reaction**

The Tishchenko reaction is a dimerization of aldehydes to form esters. Since the reaction mechanisms are similar to those of the Cannizzaro reaction, the Tishchenko reaction is thought to be a base-catalyzed reaction.

Benzaldehyde converts to benzylbenzoate over alkaline earth oxides.<sup>79</sup> This reaction proceeds by a Tishchenko type reaction as shown in Scheme 12.

In this reaction, not only basic sites ( $\text{O}^{2-}$  ion) but also acidic sites (metal cation) participate. The slow step is  $\text{H}^-$  transfer from I to II. The activities of the alkaline earth oxides were reported to be in the order  $\text{MgO} < \text{CaO} < \text{SrO} < \text{BaO}$ , indicating that basic strength is important among alkaline earth oxides.

**Scheme 12. Esterification of Benzaldehyde**

For the aldehydes with  $\alpha$ -hydrogen, such as benzaldehyde and pivalaldehyde, Tishchenko reactions take place selectively to produce corresponding esters. For the aldehydes having  $\alpha$ -hydrogen, Tishchenko reactions compete with aldol condensations. This was typically observed in the reaction of butyraldehyde.

In self-condensation of butyraldehyde, the dimers resulting from aldol condensation and the trimers resulting from Tishchenko reaction of the dimer with butyraldehyde were formed by use of alkaline earth oxides as catalysts, as shown in Scheme 13.

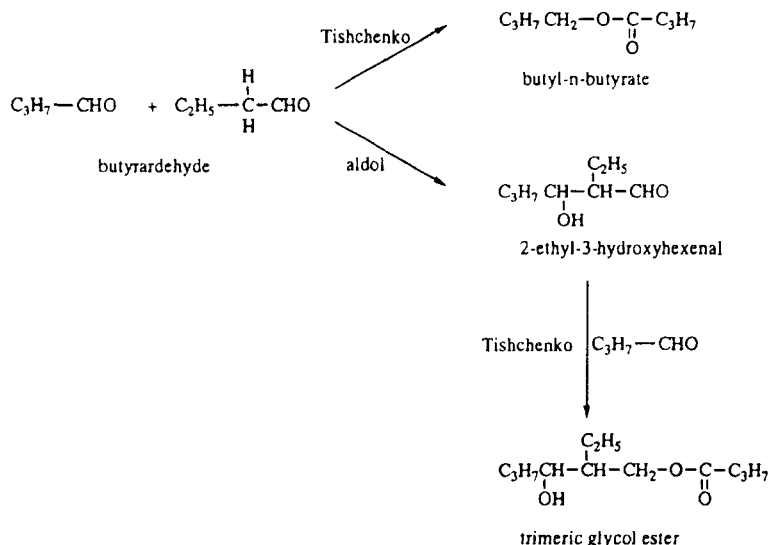
By use of aluminas modified with alkalis as catalysts, the reaction was selective for the formation of dimer by aldol condensation, and the Tishchenko reaction scarcely occurred. For the aldol condensation, the presence of only basic sites is sufficient, but for the Tishchenko reaction, the presence of both basic sites and acidic sites is required. By modification of alumina with alkali ions, basic sites are generated and the acidic sites are suppressed. Therefore, only the aldol condensation takes place. On the other hand, a considerable amount of trimer was formed on alkaline earth oxides. It is suggested that not only basic sites but also acidic sites participate in the reaction taking place on alkaline earth oxides.

**IV-10. Michael Addition**

Michael additions are conjugate additions of carbanions and are catalyzed by bases such as sodium hydroxide, sodium ethoxide, and piperidine. The reactions have special value since they serve to form carbon-carbon bonds. However, only limited types of heterogeneous catalysts have been applied to Michael additions. In heterogeneous system, the basic sites are responsible for forming the carbanion by abstraction of an  $\text{H}^+$  from the molecule having an  $\alpha$ -hydrogen.

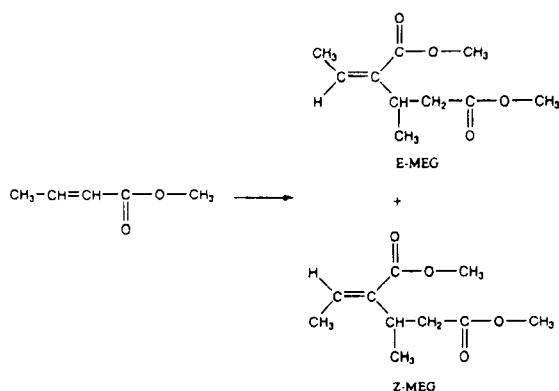
Partially dehydrogenated  $\text{Ba}(\text{OH})_2$  catalyzes Michael additions of chalcones with active methylene compounds such as ethyl malonate, ethyl acetoacetate, acetylacetone, nitromethane, and acetophenone.<sup>80</sup>

Potassium fluoride supported on alumina ( $\text{KF-Al}_2\text{O}_3$ ) is active for the following Michael additions

**Scheme 13. Self-Condensation of Butyraldehyde**

at room temperature: nitromethane with 3-buten-2-one and 1,3-diphenyl-2-propen-1-one,<sup>81</sup> nitroethane with 3-buten-2-one,<sup>82</sup> and dimenone with methyl vinyl ketone.<sup>83</sup>

Dimerization of methyl crotonate proceeds by self-Michael addition to form methyl diesters of (Z)- and (E)-2-ethylidene-3-methylglutalic acid (Z-MEG and E-MEG).<sup>84</sup>

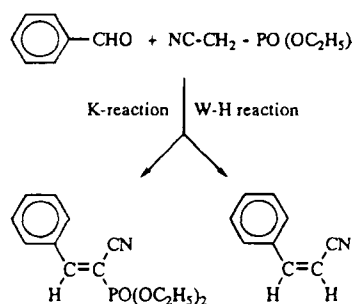


Among various types of basic catalysts, only MgO exhibits a high activity. The reasons why only MgO is active are not clear yet, but the other base catalysts such as CaO, La<sub>2</sub>O<sub>3</sub>, ZrO<sub>2</sub>, KOH/Al<sub>2</sub>O<sub>3</sub>, and KF/Al<sub>2</sub>O<sub>3</sub> show negligible activities as compared to MgO. The reaction is initiated by abstraction of allylic H of methyl crotonate by the basic site to form an allyl carbanion. The carbanion attacks a second methyl crotonate at the β-position to form the methyl diester of 3-methyl-2-vinylglutalic acid, which undergoes double bond migration to form the final product.

**IV-11. The Wittig–Horner Reaction and Knoevenagel Condensation**

Aldehydes react with nitriles over basic catalysts such as MgO, ZnO, and Ba(OH)<sub>2</sub> to yield the Wittig–

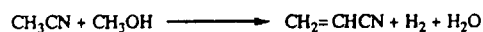
Horner reaction and the Knoevenagel condensation as shown below.<sup>85</sup>



For the Knoevenagel condensation of benzaldehyde with the compounds possessing a methylene group, hydrotalcite and alkali ion-exchange zeolites<sup>86</sup> and alkali ion-exchange sepiolites<sup>87</sup> act as catalysts. For the zeolites and sepiolites, the aldol condensation which would occur as a side reaction is suppressed due to weak basic properties, and Michael addition producing bulky products is also suppressed due to the small space of the cavities where the basic sites are located. The activities of the zeolite are enhanced by replacing framework Si by Ge, which causes a change in the basic properties.<sup>88</sup>

**IV-12. Synthesis of α,β-Unsaturated Compound by Use of Methanol**

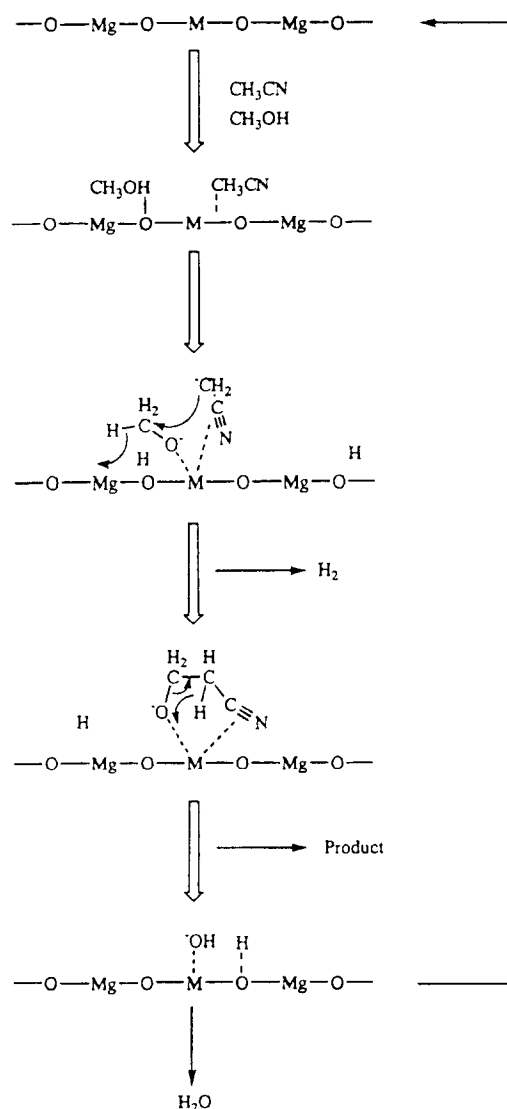
The methyl and methylene groups at the α-position of saturated ketones, esters, and nitriles are converted to vinyl groups by reactions with methanol over MgO modified by Mn ion or Cr ion.<sup>89–93</sup> Ueda et al. reported that acetonitrile reacts with methanol to produce acrylonitrile over Mn–MgO at the reaction temperature of 648 K.



Magnesium oxide is required to be modified by addition of transition metal ions to exhibit high



Scheme 14. Formation of Acrylonitrile



activity and selectivity for the reaction. The addition of a metal ion with an ionic radius larger than  $\text{Mg}^{2+}$  ion increases the amount of basic sites, while the addition of a metal ion with an ionic radius smaller than  $\text{Mg}^{2+}$  ion induces the surface acid sites without any appreciable change in the amount of surface basic sites. The active catalysts are obtained in the latter case.

On the basis of isotopic tracer studies for reaction mechanisms, Scheme 14 is elucidated.

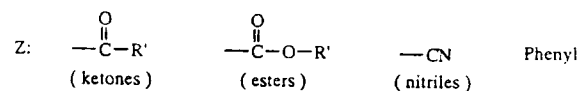
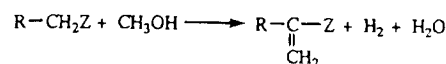
The reaction mechanisms consist essentially of dehydrogenation and aldol type condensation. Methanol is dehydrogenated to form formaldehyde, which undergoes aldol condensation with acetonitrile. At first, methanol is dissociated on the basic site to form  $\text{H}^+$  and  $\text{CH}_3\text{O}^-$ . The methoxy anion ( $\text{CH}_3\text{O}^-$ ) is adsorbed on the added metal ion site because the metal ion is a stronger Lewis acid than  $\text{Mg}^{2+}$  ion. Then, an  $\text{H}^-$  is abstracted from the methoxy anion by the metal ion to form formaldehyde. On the other hand, an  $\text{H}^+$  is abstracted from acetonitrile to form

Table 4. Requirements on Zeolites in O/S and O/S Transformations

| reaction                                               | basic | acidic |
|--------------------------------------------------------|-------|--------|
| saturated 5-member ring + $\text{NH}_3$                | —     | +      |
| saturated 5-member ring + $\text{H}_2\text{S}$         | +     | +      |
| saturated 6-member ring + $\text{NH}_3$                | —     | ++     |
| unsaturated 5-member ring + $\text{NH}_3$              | +     | —      |
| unsaturated 5-member ring + $\text{H}_2\text{S}$       | +     | —      |
| saturated 5-member ring lactone + $\text{NH}_3$        | +     | +      |
| saturated 5-member ring lactone + $\text{H}_2\text{S}$ | +     | —      |
| saturated 6-member ring lactone + $\text{NH}_3$        | —     | +      |

the intermediate methylene anion, which is also adsorbed on the added metal ion.

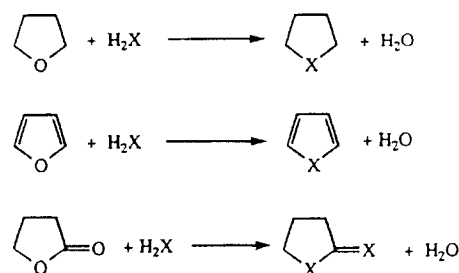
Ueda et al. expanded the reaction of acetonitrile with methanol to the formations of  $\alpha,\beta$ -unsaturated compounds generally expressed as follows:



R: Alkyl, -H

#### IV-13. Ring Transformation

An oxygen atom in a ring position can be replaced by N or S with  $\text{NH}_3$  or  $\text{H}_2\text{S}$  over zeolite catalysts for which the acid and base properties are adjusted by ion exchange.<sup>94-98</sup>



X: S, -NH

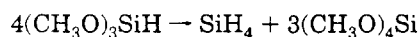
For the reaction of  $\gamma$ -butyrolactone and  $\text{H}_2\text{S}$ , the activity order is  $\text{CsY} > \text{RbY} > \text{KY} > \text{NaY} > \text{LiY}$ , which coincides with the strength of basicity. Hoelderich summarizes the relation between acid-base properties and the selectivities as given in Table 4.<sup>99</sup> The question as to what properties the catalysts should possess, i.e. basicity or acidity, for O/N and O/S exchange of heterocyclic compounds cannot be answered definitely. However, there is a tendency that increasing the basic properties enhances the activity and selectivity for ring transformation of O into S with  $\text{H}_2\text{S}$ . The basic sites that exist in the zeolite cavities should play an important role for the ring transformation reactions.

#### IV-14. Reactions of Organosilanes

Recently, reactions involving organosilanes have been reported to be catalyzed by heterogeneous basic catalysts. Onaka et al. reported that heterogeneous

basic catalyst such as MgO, CaO, and hydroxyapatite catalyze cyanosilylations of carbonyl compounds and unsaturated ketones like 2-cyanohexenone with cyanomethylsilane.<sup>100,102</sup> Basic sites interact strongly with Si in silanes so that the nucleophilicity of the silanes increases. In the cyanosilylation of unsaturated ketones, 1,2-addition products are selectively formed by use of basic catalysts, while 1,4-addition products are obtained by use of acidic catalyst such as ion-exchanged montmorillonites.

For the formation of silane by disproportionation of trimethoxysilane, heterogeneous basic catalysts are used.<sup>103</sup>



High activities were reported for hydrotalcite and alumina-supported fluorides such as KF/Al<sub>2</sub>O<sub>3</sub>.

### V. Characteristic Features of Heterogeneous Basic Catalysts of Different Types

The catalytic properties of heterogeneous basic catalysts are closely associated with the amount and strength of the basic sites existing on the surfaces. However, the amount and strength of the basic sites are not whole measures to determine the catalytic properties. The other factors to be taken into account are not clear at present. It appears that there are characteristic features commonly observed for a certain type of heterogeneous basic catalysts. In this section, catalytic features of different types of heterogeneous catalysts are described.

#### V-1. Single Component Metal Oxides

Alkaline earth oxides such as MgO, CaO, SrO, and BaO are most extensively studied. They possess strong basic sites. The order of the basic strength is BaO > SrO > CaO > MgO. As described in the earlier section, the surfaces are covered with CO<sub>2</sub> and H<sub>2</sub>O before pretreatment. To be active catalysts, they need pretreatment at a high temperature to remove adsorbed CO<sub>2</sub> and H<sub>2</sub>O. In addition, the active sites are easily poisoned by even small amounts of impurities like CO<sub>2</sub> and H<sub>2</sub>O contained in the reactants. To obtain full capabilities of alkaline earth oxides, the reaction system should be kept free of the impurities, which makes the industrial uses of the alkaline earth oxides difficult, especially at low reaction temperatures. At high reaction temperatures, the poisoning effects are reduced, and certain alkaline earth oxides show catalytic activities for the reactions from which poisons like H<sub>2</sub>O are liberated.

One of the features of alkaline earth oxides is a high ability to abstract an H<sup>+</sup> from an allylic position. This feature is revealed in the double bond migration of olefinic compounds. Butene, for instance, undergoes double bond migration even at 223 K.

Rare earth oxides have been studied to a lesser extent as compared to alkaline earth oxides. The reactions for which basic sites of rare earth oxides are relevant are hydrogenation of olefins, double bond migration of olefins, aldol condensation of ketones, and dehydration of alcohols. The activity sequences of a series of rare earth oxides are shown in Figure

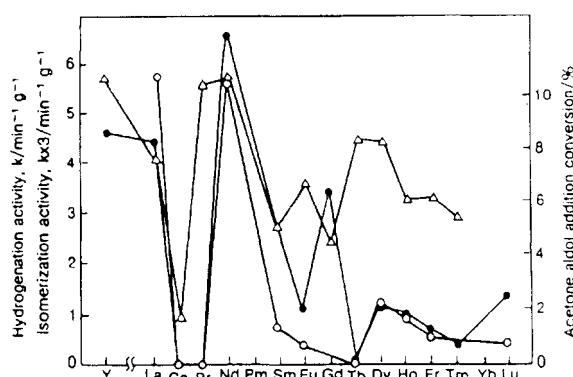


Figure 18. Catalytic activities of rare earth oxides for 1-butene isomerization (○), 1,3-butadiene hydrogenation (●), and aldol addition of acetone (Δ).

18 for 1-butene isomerization, 1,3-butadiene hydrogenation, and acetone aldol condensation.<sup>104</sup> The activity sequence is the same for 1-butene isomerization and 1,3-butadiene hydrogenation, which is different from that of aldol condensation. For the isomerization and the hydrogenation, the oxides of sesquioxide stoichiometry show activity while the oxides with metal cations of higher oxidation states are entirely inactive. The situation is different in acetone aldol condensation. The oxides with high oxidation state, CeO<sub>2</sub>, Tb<sub>4</sub>O<sub>7</sub>, and Pr<sub>6</sub>O<sub>11</sub>, show considerable activity. The oxides with metal cations of oxidation state higher than 3 possess weak basic sites which are sufficient to catalyze the aldol condensation but not strong enough to catalyze hydrogenation and isomerization.

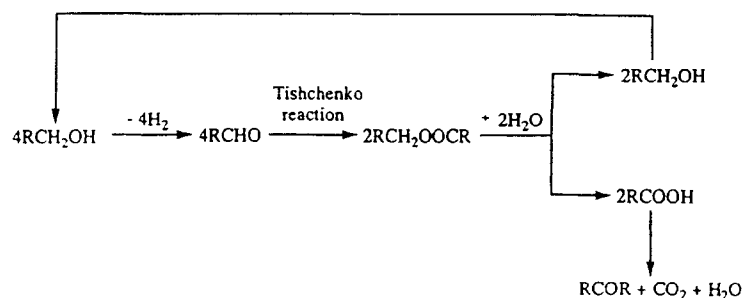
As described in the preceding section, rare earth oxides show characteristic selectivity in dehydration of alcohols. 2-Alcohols undergo dehydration to form 1-olefins. The formation of thermodynamically unstable 1-olefins contrasts with the formation of stable 2-olefins in the dehydration over acidic catalysts. The selectivity is the same as that observed for ZrO<sub>2</sub>.

Zirconium oxide is a unique heterogeneous basic catalyst in the sense that two industrial processes have been established recently that use ZrO<sub>2</sub> as a catalyst. One is reduction of aromatic carboxylic acids with hydrogen to produce aldehydes.<sup>61</sup> The other is dehydration of 1-cyclohexylethanol to vinylcyclohexane.<sup>48</sup> In addition, the production of diisobutyl ketone from isobutyraldehyde has been industrialized for more than 20 years.<sup>105</sup> The reaction scheme for the production of diisobutyl ketone in which the Tishchenko reaction is involved is shown in Scheme 15.

One of the difficulties of most of the heterogeneous basic catalysts for industrial uses arises from rapid poisoning by CO<sub>2</sub> and H<sub>2</sub>O. This is not the case with ZrO<sub>2</sub>. Zirconium oxide retains its activity in the presence of water, which is one of the products for the reactions of carboxylic acid and 1-cyclohexylethanol.

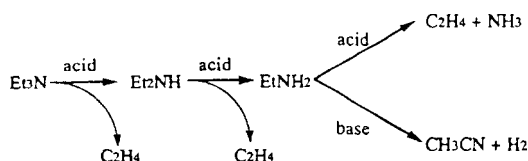
The catalytic features of ZrO<sub>2</sub> are understood in terms of bifunctional acid-base properties.<sup>49,106,107</sup> Although the strengths of the basic and acid sites are low, a cooperative effect makes ZrO<sub>2</sub> function as an efficient catalyst. Because of weakly acidic and basic

## Scheme 15. Formation of Ketone from Aldehyde



sites, the active sites are not poisoned by  $\text{CO}_2$  and water.

Zirconium oxide shows not only basic properties but also acidic properties, depending on the reactant.<sup>106</sup> The acid–base bifunctionality of  $\text{ZrO}_2$  is clearly revealed in the reaction of alkylamine to nitrile.<sup>108</sup> The conversion of secondary amines and tertiary amines to nitriles requires both acidic and basic sites as shown below.



By use of acidic catalyst like  $\text{SiO}_2\text{--Al}_2\text{O}_3$ , ethylene and ammonia are formed. Over  $\text{ZrO}_2$ , dehydrogenation to produce nitrile occurs in preference to the formation of ethylene and ammonia.

Although  $\text{ZrO}_2$  shows interesting catalytic properties, the structure of the active sites is still unclear. Clarification of the active sites is desired.

## V-2. Zeolites

The characteristic features of zeolites result from their ion-exchange ability and specific pore structure. The acid–base properties are controlled by selecting the types of ion-exchanged cations and by the Si/Al ratio of the zeolite framework. Wide variation of acid–base properties can be achieved by ion-exchange and ion-addition, while relatively small change in acid–base properties is yielded by changing the Si/Al ratio.

To prepare basic zeolites, two approaches have been undertaken. One approach is to ion-exchange with alkali metal ions, and the other is to impregnate the zeolite pores with fine particles that can act as bases themselves. The former produces relatively weak basic sites, while the latter results in the strong basic sites.

With alkali ion-exchanged zeolites, the type of alkalis used affects the basic strength of the resulting zeolites. Effects of the alkali ions on basic strength are in the following order:  $\text{Cs}^+ > \text{Rb}^+ > \text{K}^+ > \text{Na}^+ > \text{Li}^+$ . the basic sites are framework oxygen. The bonding of the framework oxygen is rather covalent in nature. This causes the basic sites of ion-exchanged zeolites to be relatively weak as compared to, for example, those of alkaline earth oxides.

Table 5. Activities of Ion-Exchanged and Ion-Added Zeolites for 1-Butene Isomerization

| catalyst <sup>a</sup> | reaction rate/mmole g <sup>-1</sup> min <sup>-1</sup> |                      |
|-----------------------|-------------------------------------------------------|----------------------|
|                       | 273 K                                                 | 423 K                |
| NaX E                 | 0                                                     | 0                    |
| NaX A                 | 0                                                     | $1.1 \times 10^{-2}$ |
| KX E                  | 0                                                     | 0                    |
| KX A                  | $2.4 \times 10^{-2}$                                  | $7.8 \times 10^{-2}$ |
| RbX E                 | 0                                                     | 0                    |
| RbX A                 | $3.2 \times 10^{-2}$                                  | 1.3                  |
| CsX E                 | $8.6 \times 10^{-4}$                                  | $1.3 \times 10^{-1}$ |
| CsX A                 | $1.4 \times 10^{-1}$                                  | 1.1                  |

<sup>a</sup> E, ion-exchanged; A, ion-added.

Preparation of fine particles of alkali oxides inside the cavities of zeolites was developed by Hathaway and Davis.<sup>72,109</sup> They impregnate NaY zeolite with cesium acetate aqueous solution and calcine at 723 K to decompose cesium acetate into cesium oxide placed in the cavities. The resulting zeolite possesses basic sites stronger than those of simple ion-exchanged zeolite.

Tsuji et al. prepared the zeolites containing a series of alkali metal ions in excess of the ion-exchanged capacities and compared their catalytic activities and basic sites with simply ion-exchanged zeolites. TPD plots of adsorbed carbon dioxide are shown in Figure 9. The TPD peaks appear at higher temperatures for “ion-added” zeolites than for ion-exchanged zeolites, indicating generation of new basic sites that are stronger than sites of ion-exchanged zeolites.

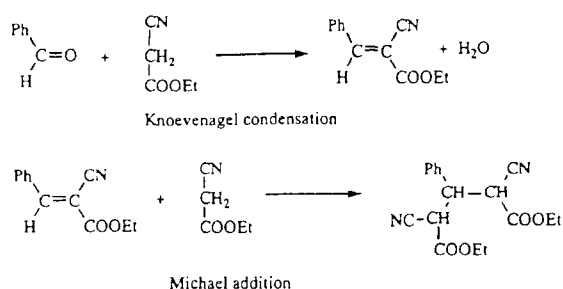
The results of the catalytic activities of the ion-added zeolites and the ion-exchanged zeolites for 1-butene isomerization are summarized in Table 5.<sup>17,110</sup> Except for CsX, ion-exchanged zeolites did not exhibit any activities at 273 K and 423 K. The ion-added zeolites showed considerable activities, and the order of the activities for different alkali ions was  $\text{Cs} > \text{Rb} > \text{K} > \text{Na}$ .

Zeolites often collapse during preparation procedures. Yagi et al. prepared Cs ion-added zeolites to establish the preparative conditions to retain the zeolite framework during preparative procedures.<sup>111</sup> It was found that the crystalline structures of zeolites, in particular alkali ion-added zeolites, are easily destroyed by exposure to water vapor at high temperatures and that zeolites of high Si/Al ratio are unstable to alkali treatment.

Besides alkali metal oxides, the fine particles of MgO were placed in the zeolite cavities.<sup>110</sup> The resulting zeolites also showed strong basic properties, though the basic sites on the fine particles of MgO

are not as strong as those of bulk MgO. The ionicity of the Mg–O bond is reduced for a fine particle of MgO as compared to bulk MgO, and therefore, the basic strength of the  $O^{2-}$  ion is reduced. The dependence of the particle size on the strength of basic site was studied for ultrafine MgO particles by Itoh et al.<sup>112</sup> It was also concluded that smaller particles exhibit weaker basicity.

One of the important objects for preparation of basic zeolites is to realize the shape selectivity in base-catalyzed reactions. Corma et al. reported the shape selectivity of alkali ion-exchanged zeolites in the reaction of benzaldehyde with ethyl cyanoacetate.<sup>113</sup> Lasperas et al. prepared zeolite containing cesium oxide in the cavities by the "postsynthetic method", which is similar to the methods by Harthaway and Davis<sup>72</sup> and Tsuji et al.<sup>17,110</sup> The reaction of benzaldehyde with ethyl cyanoacetate proceeded as shown below.<sup>114,115</sup>



Knoevenagel condensation proceeded, but the product did not undergo the following Michael addition because of the limited space in the zeolite cavities.

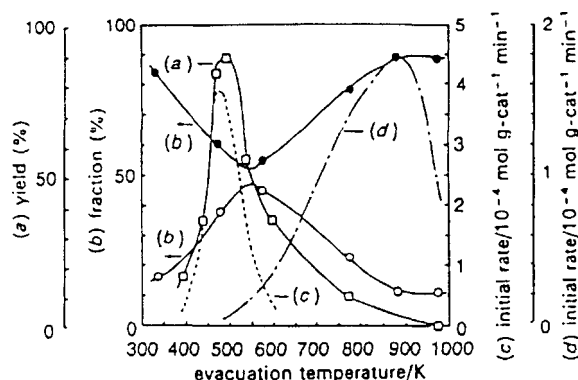
Tsuji et al. reported the shape selectivity of the zeolite containing MgO.<sup>110</sup> Nonsupported MgO catalyzes double bond migrations of both 1-butene and allylbenzene, while the zeolite containing MgO in the cavities catalyzes the former but fails to catalyze the latter.

The studies of basic zeolites, in particular, those of strongly basic zeolites have started quite recently. To reveal the potential of basic zeolites, establishment of preparative methods, identification of basic sites, and application of the basic zeolites to a wide variety of the base-catalyzed reactions are required.

### V-3. Basic Catalysts of the Non-Oxide Type

Most of heterogeneous basic catalysts are in the form of oxides. The basic sites are  $O^{2-}$  ions with different environments depending on their type. If the basic sites are constituted by elements other than  $O^{2-}$ , the catalysts are expected to show catalytic properties different than those of the catalysts of the oxide form.

Potassium fluoride supported on alumina (KF/ $\text{Al}_2\text{O}_3$ ) was introduced by Clark<sup>116</sup> and by Ando and Yamawaki<sup>117,118</sup> as a fluorinating reagent and a base catalyst. As a base catalyst, KF/ $\text{Al}_2\text{O}_3$  has been applied to a number of organic reactions. The reactions for which KF/ $\text{Al}_2\text{O}_3$  acts as a catalyst include Michael additions,<sup>82,83,119,120</sup> Wittig–Honner reactions,<sup>121,122</sup> Knoevenagel condensations,<sup>121,122</sup> Darzen condensations,<sup>81,121</sup> condensation of phenyl acetylene

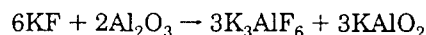
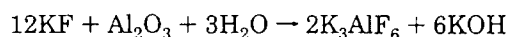


**Figure 19.** Fraction of  $\text{Yb}^{3+}$  (●) and  $\text{Yb}^{2+}$  (○) plotted against evacuation temperature and the catalytic activities of Yb/Na-Y for (---) 1-butene isomerization, (---) ethylene hydrogenation, and (□) Michael reaction of cyclopenten-2-one with dimethyl malonate. 1-Butene isomerization was carried out at 273 K over Yb/NaY. Ethylene hydrogenation was carried out at 273 K over Yb/LY. Michael reaction was carried out at 323 K over Yb/NaY. (Reprinted from 133. Copyright 1993 Chemical Society of London.)

with benzaldehyde,<sup>124</sup> alkylations at C, O, N, and S with aldehydes and dimethyl sulfate,<sup>117,125–127</sup> and disproportionation of alkylsilanes.<sup>103</sup>

In contrast to many applications to organic syntheses as a base catalyst, KF/ $\text{Al}_2\text{O}_3$  has not been studied extensively for the surface properties, and the structures of basic sites have not been clarified yet. At the beginning, the basic sites were considered to be  $\text{F}^-$  ions dispersed on the alumina support. Insufficient coordination only with surface OH groups may result in the formation of active  $\text{F}^-$  ions. This was supported by  $^{19}\text{F}$  MASNMR.<sup>128–130</sup>

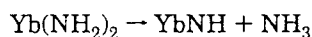
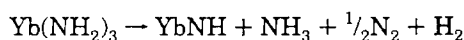
On the other hand, it was proposed on the basis of IR and XRD studies that the basic sites originate from KOH and/or aluminate produced by the following reactions:<sup>129,131</sup>



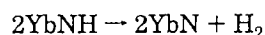
Taking account of the above results and the results of titrating the water soluble base on the surface together with the results of IR study, thermogravimetry, and SEM, Ando et al. concluded that there are three basic species or mechanisms of the appearance of the basicity on the surface of KF/ $\text{Al}_2\text{O}_3$ .<sup>130,132</sup> These are (i) well-dispersed and incompletely coordinated  $\text{F}^-$  ions, (ii)  $[\text{Al}-\text{O}^-]$  ions which generate  $\text{OH}^-$  ions when water is present, and (iii) cooperation of  $\text{F}^-$  and  $[\text{Al}-\text{OH}]$  which can behave as an in situ-generated base during the course of the reaction.

For the other catalysts of the non-oxide type, Baba et al. prepared low-valent lanthanide species introduced into zeolite cavities.<sup>133,134</sup> They impregnated K–Y with Yb and Eu dissolved into liquid ammonia followed by thermal activation. The variations of the catalytic activities of the Yb/K–Y catalyst as a function of the thermal activation temperature are shown in Figure 19 for 1-butene isomerization, ethylene hydrogenation, and Michael addition of cyclopenten-2-one with dimethyl malonate.<sup>133</sup>

The chemical states of Yb were studied by TPD, IR, XAFS, and XPS as a function of evacuation temperature. The states of Yb changed from Yb(II, III) amides, Yb(II, III) imides, to Yb(III) nitride as follows:



and



As for the catalytically active sites, it was concluded that the Yb(II) imide species catalyze 1-butene isomerization and the Michael addition and that the Yb(III) nitride species catalyzes ethylene hydrogenation.

In the above reactions, characteristic features which distinguish the non-oxide catalysts from the metal oxides are not obvious. However, it is expected that the features will become apparent for certain base-catalyzed reactions if the applications of the non-oxide catalysts to various kinds of reactions are expanded.

#### V-4. Heterogeneous Superbasic Catalysts

To activate a reactant under mild conditions, a catalyst possessing very strong basic sites is desired to be prepared. There have been some attempts to prepare those superbasic catalysts.

Suzukamo et al. prepared a superbasic catalyst by addition of alkali hydroxides to alumina followed by further addition of alkali metals.<sup>41</sup> To a calcined alumina, sodium hydroxide was added at 583–593 K with stirring under a nitrogen stream. In 3 h, sodium metal was added and the mixture was stirred for another 1 h at the same temperature to give a pale blue solid. The resulting catalyst possesses basic sites stronger than  $H_- = 37$  and catalyzes various base-catalyzed reactions such as double bond migrations of 5-vinylbicyclo[2.2.1]hept-2-ene to 5-ethylidenebicyclo[2.2.1]hept-2-ene at the reaction temperature 243–373 K, 2,3-dimethylbut-1-ene to 2,3-dimethylbut-2-ene at 293 K, and safrol to isosafrol at 293 K and side chain alkylations of alkylbenzenes at the reaction temperature 293–433 K. The former two reactions are initiated by abstraction of an  $\text{H}^+$  from the tertiary carbon in the molecules to form tertiary carbanions. Because tertiary carbanions are unstable, the abstraction of an  $\text{H}^+$  from a tertiary carbon requires a strong basic site.

Ushikubo et al. prepared a superbasic catalyst by addition of metallic sodium to  $\text{MgO}$ .<sup>135</sup> Magnesium oxide was pretreated at a high temperature and mixed with  $\text{NaN}_3$ . The mixture was heated at 623 K to decompose  $\text{NaN}_3$  to evolve metallic sodium vapor to which  $\text{MgO}$  was exposed. The resulting catalyst acted as an efficient catalyst for decomposition of methyl formate to CO and methanol. The activity was much higher than that of  $\text{MgO}$ . Although the basic strength of Na-added  $\text{MgO}$  was not compared with that of  $\text{MgO}$ , the high activity of Na-added  $\text{MgO}$  for the decomposition of methyl formate appears to

be due to the enhancement of basic strength caused by the addition of Na to  $\text{MgO}$ .

#### VI. Concluding Remarks

Heterogeneous basic catalysts have been investigated for almost 40 years during which a number of reactions have been found to proceed on the basic catalysts. Nevertheless, the reactions for which heterogeneous basic catalysts have been used are only a part of a great number of organic reactions. Use of heterogeneous basic catalysts in organic syntheses has been increasing in recent years. There should be many reactions which heterogeneous basic catalysts can efficiently promote, but have not been used for. One reason for the limited use of heterogeneous basic catalysts arises from a rapid deactivation while being handled under the atmosphere; the catalysts should be pretreated at high temperatures and handled in the absence of air prior to use for the reaction. If this care is taken, heterogeneous catalysts should promote a great number of reactions.

It was found that some of the reactions specifically proceed on the heterogeneous basic catalysts. The catalytic actions of heterogeneous basic catalysts are not simple copies of those of homogeneous basic catalysts, though it is not clearly understood where the features of heterogeneous basic catalysts originate from. To clarify this point, characterizations of the surface sites together with elucidation of the reaction mechanisms occurring on the surfaces should be extended.

Although the theoretical calculations of the surface sites and the reaction mechanisms are not described in this article, there have been efforts on these points.<sup>136–141</sup> The results of the quantum chemical calculations explain well the experimental results, and give us valuable information about the heterogeneous basic catalysis. Unfortunately, the theoretical calculations have been done only for the  $\text{MgO}$  catalyst. An attempt to calculate the other catalyst systems is highly desirable.

The methods of preparing heterogeneous catalysts and the characterizations of the surfaces have been developed. Keen insight into the surface reaction mechanisms and the functions required for the reactions together with the accumulation of the heterogeneous base-catalyzed reactions will enable to design the heterogeneous basic catalysts active for desired reactions.

#### References

- (1) Pines, H.; Veseley, J. A.; Ipatieff, V. N. *J. Am. Chem. Soc.* **1955**, *77*, 6314.
- (2) Kokes, R. J.; Dent, A. L. *Advan. Catal.* **1972**, *22*, 1.
- (3) Kokes, R. J. *Proceedings of the 5th International Congress of Catalysis* Miami Beach, FL, 1972; p 1.
- (4) Hattori, H.; Yoshii, N.; Tanabe, K. *Proceedings of the 5th International Congress on Catalysis*, Miami Beach, FL, 1972; p 233.
- (5) Yashima, T.; Sato, K.; Hayasaka, T.; Hara, N. *J. Catal.* **1972**, *26*, 303.
- (6) Tanabe, K.; Misono, M.; Ono, Y.; Hattori, H. *New Solid Acids and Bases*; Kodansha (Tokyo)–Elsevier (Amsterdam, Oxford, New York, Tokyo), 1989; p 30.
- (7) Hattori, H.; Maruyama, K.; Tanabe, K. *J. Catal.* **1976**, *44*, 50.

- (8) Tanabe, K.; Misono, M.; Ono, Y.; Hattori, H. *New Solid Acids and Bases*; Kodansha (Tokyo)–Elsevier (Amsterdam, Oxford, New York, Tokyo), 1989; p 39.
- (9) Coluccia, S.; Tench, A. J. *Proceedings of the 7th International Congress on Catalysis* Tokyo, Japan, 1980; p 1160.
- (10) Fukuda, Y.; Hattori, H.; Tanabe, K. *Bull. Chem. Soc. Jpn.* **1978**, *51*, 3151.
- (11) Imizu, Y.; Sato, K.; Hattori, H. *J. Catal.* **1981**, *71*, 64.
- (12) Utiyama, M.; Hattori, H.; Tanabe, K. *J. Catal.* **1978**, *4*, 237.
- (13) Hammett, L. P. *Physical Organic Chemistry*; McGraw-Hill: New York, 1940; Chapter IX.
- (14) Paul, M. A.; Long, F. A. *Chem. Rev.* **1957**, *57*, 1.
- (15) Take, J.; Kikuchi, N.; Yoneda, Y. *J. Catal.* **1971**, *21*, 164.
- (16) Zhang, G.; Hattori, H.; Tanabe, K. *Appl. Catal.* **1988**, *36*, 189.
- (17) Tsuji, H.; Yagi, F.; Hattori, H. *Chem. Lett.* **1991**, 1881.
- (18) Nelson, R. L.; Hale, J. W. *Disc. Faraday Soc.* **1958**, *52*, 77.
- (19) Tench, A. J.; Pott, G. T. *Chem. Phys. Lett.* **1974**, *26*, 590.
- (20) Zecchina, A.; Lofthouse, M. G.; Stone, F. S. *J. Chem. Soc. Faraday Trans. 1*, **1975**, *71*, 1476.
- (21) Coluccia, S.; Tench, A. J.; Segall, R. L. *J. Chem. Soc. Faraday 1* **1978**, *75*, 1769.
- (22) Stone, F. S.; Zecchina, A. *proceedings of the 6th International Congress on Catalysis* London, 1976; p 162.
- (23) Ito, T.; Kuramoto, M.; Yoshida, M.; Tokuda, T. *J. Phys. Chem.* **1983**, *87*, 4411.
- (24) Ito, T.; Murakami, T.; Tokuda, T. *J. Chem. Soc. Trans. Faraday 1*, **1983**, *79*, 913.
- (25) Okamoto, Y.; Ogawa, M.; Maezawa, A.; Imanaka, T. *J. Catal.* **1988**, *112*, 427.
- (26) Huang, M.; Adnot, A.; Kaliaguine, S. *J. Catal.* **1992**, *137*, 322.
- (27) Barthomeuf, D. *J. Phys. Chem.* **1978**, *55*, 138.
- (28) Fukuda, Y.; Tanabe, K. *Bull. Chem. Soc. Jpn.* **1973**, *46*, 1616.
- (29) Evans, J. V.; Whaley, T. L. *Trans. Faraday Soc.* **1967**, *63*, 2769.
- (30) Barthomeuf, D. *Stud. Surf. Sci. Catal.* **1991**, *65*, 157.
- (31) Yanagisawa, Y.; Shimodama, H.; Ito, A. *J. Chem. Soc. Chem. Commun.* **1992**, 610.
- (32) Shishido, T.; Tsuji, H.; Gao, Y.; Hattori, H.; Kita, H. *React. Kinet. Catal. Lett.* **1993**, *51*, 75.
- (33) Tuji, H.; Shishido, T.; Okamura, A.; Gao, Y.; Hattori, H.; Kita, H. *J. Chem. Soc. Faraday Trans.* **1994**, *90*, 803.
- (34) Hattori, H. *Stud. Surf. Sci. Catal.* **1993**, *78*, 35.
- (35) Tsuchiya, S. *Acid-Base Catalysis*; Kodansha (Tokyo)–VCH (Basel, Cambridge, New York, Weinheim), 1989; p 169.
- (36) Hightower, J. W.; Hall, K. W. *J. Am. Chem. Soc.* **1967**, *89*, 778.
- (37) Satoh, A.; Hattori, H. *J. Catal.* **1976**, *45*, 36.
- (38) Hattori, H.; Itoh, M.; Tanabe, K. *J. Catal.* **1976**, *41*, 46.
- (39) Hattori, H.; Tanabe, K.; Hayano, K.; Shirahama, H.; Matsumoto, T. *Chem. Lett.* **1979**, 133.
- (40) Shimazu, K.; Tanabe, K.; Hattori, H. *J. Catal.* **1977**, *45*, 302.
- (41) Suzukamo, G.; Fukao, M.; Hibi, T.; Chikaishi, K. *Acid-Base Catalysis*; Kodansha (Tokyo)–VCH (Basel, Cambridge, New York, Weinheim), 1989; p 405.
- (42) Suzukamo, G.; Fukao, M.; Minobe, M. *Chem. Lett.* **1987**, 585.
- (43) Hattori, A.; Hattori, H.; Tanabe, K. *J. Catal.* **1980**, *65*, 246.
- (44) Matsushashi, H.; Hattori, H. *J. Catal.* **1984**, *85*, 457.
- (45) Lundeen, A. J.; van Hoozen, R. J. *Org. Chem.* **1967**, *32*, 3386.
- (46) Tomatsu, T.; Yoneda, H.; Ohtsuka, H. *Yukagaku*, **1968**, *17*, 236.
- (47) Thomke, K. *Proceedings of the 6th International Congress on Catalysis* London, UK, 1976; p 303.
- (48) Yamaguchi, T.; Sasaki, H.; Tanabe, K. *Chem. Lett.* **1976**, 677.
- (49) Takahashi, K.; Hibi, T.; Higashio, Y.; Araki, M. *Shokubai (Catalyst)* **1993**, *35*, 12.
- (50) Ueshima, M.; Yano, H.; Hattori, H. *Sekiyu Gakkai (J. Jpn. Petroleum Inst.)* **1992**, *35*, 362.
- (51) Hattori, H.; Tanaka, Y.; Tanabe, K. *J. Am. Chem. Soc.* **1976**, *98*, 4652.
- (52) Tanaka, Y.; Imizu, Y.; Hattori, H.; Tanabe, K. *Proceedings of the 7th International Congress on Catalysis* Tokyo, Japan 1980; p 1254.
- (53) Imizu, Y.; Hattori, H.; Tanabe, K. *J. Catal.* **1979**, *56*, 303.
- (54) Imizu, Y.; Hattori, H.; Tanabe, K. *J. Chem. Soc. Chem. Commun.* **1978**, 1091.
- (55) Nakano, Y.; Yamaguchi, T.; Tanabe, K. *J. Catal.* **1983**, *80*, 307.
- (56) Imizu, Y.; Sato, K.; Hattori, H. *J. Catal.* **1982**, *76*, 235.
- (57) Hattori, H.; Wang, G. *Proceedings of the 8th International Congress on Catalysis* Berlin, Germany 1984; p III-219.
- (58) Wang, G.; Hattori, H. *J. Chem. Soc. Faraday Trans. 1* **1984**, *80*, 1039.
- (59) Yamaguchi, T.; Hightower, J. W. *J. Am. Chem. Soc.* **1977**, *99*, 4201.
- (60) Shima, H.; Yamaguchi, T. *J. Catal.* **1984**, *90*, 160.
- (61) Yokoyama, T.; Setoyama, T.; Fujita, N.; Nakajima, M.; Maki, T.; Fukui, K. *Appl. Catal. A* **1992**, *88*, 149.
- (62) Yokoyama, T.; Setoyama, T.; Nakajima, M.; Fujita, N.; Maki, T. *Acid-Base Catalysis II*; Kodansha (Tokyo)–Elsevier (Amsterdam, Oxford, New York, Tokyo), 1994; p 47.
- (63) Kakuno, Y.; Hattori, H. *J. Catal.* **1984**, *85*, 509.
- (64) Shibagaki, M.; Takahashi, K.; Matsushita, H. *Bull. Chem. Soc. Jpn.* **1988**, *61*, 3283.
- (65) Takahashi, K.; Shibagaki, M.; Matsushita, H. *Bull. Chem. Soc. Jpn.* **1989**, *62*, 2353.
- (66) Takahashi, K.; Shibagaki, M.; Kuno, H.; Kawakami, H.; Matsushita, H. *Bull. Chem. Soc. Jpn.* **1989**, *62*, 1333.
- (67) Shabtai, J.; Lazer, R.; Biron, E. *J. Mol. Catal.* **1984**, *27*, 35.
- (68) Suzuka, H.; Hattori, H. *Appl. Catal.* **1989**, *48*, L7.
- (69) Suzuka, H.; Hattori, H. *J. Mol. Catal.* **1990**, *63*, 371.
- (70) Ito, H.; Miyamoto, A.; Murakami, Y. *J. Catal.* **1980**, *64*, 284.
- (71) Miyamoto, A.; Iwamoto, S.; Agusa, K.; Inui, T. *Acid-Base Catalysis*; Kodansha (Tokyo)–VCH (Basel, Cambridge, New York, Weinheim), 1989; p 497.
- (72) Hathaway, P. E.; Davis, M. E. *J. Catal.* **1989**, *119*, 497.
- (73) Zhang, G.; Hattori, H.; Tanabe, K. *Appl. Catal.* **1988**, *36*, 189.
- (74) Zhang, G.; Hattori, H.; Tanabe, K. *Appl. Catal.* **1988**, *40*, 183.
- (75) Yashima, T.; Suzuki, H.; Hara, N. *J. Catal.* **1974**, *33*, 486.
- (76) Chu, P.; Kuehl, G. W. US Patent, 4,605,787, 1986.
- (77) Weirzchowski, P. T.; Zatorski, L. W. *Catal. Lett.* **1991**, *9*, 411.
- (78) Suzuki, E.; Idemura, S.; Ono, Y. *Chem. Lett.* **1987**, 1843.
- (79) Tanabe, K.; Saito, K. *J. Catal.* **1974**, *35*, 274.
- (80) Garcia-Raso, A.; Garcia-Raso, J.; Campaner, B.; Mestres, R.; Sinisterra, J. V. *Synthesis* **1982**, 1037.
- (81) Yamawaki, J.; Kawate, T.; Ando, T.; Hanafusa, T. *Bull. Chem. Soc. Jpn.* **1983**, *56*, 1885.
- (82) Campelo, J. M.; Climent, M. S.; Marinas, J. M. *React. Kinet. Catal. Lett.* **1992**, *47*, 7.
- (83) Laszlo, P.; Peuneteau, P. *Tetrahedron Lett.* **1983**, *22*, 2645.
- (84) Kabashima, H.; Tsuji, H.; Hattori, H.; Kita, H. Submitted.
- (85) Sinisterra, J. V.; Mouloungui, Z.; Marinas, M. J. *Colloid Interface Sci.* **1987**, *115*, 520.
- (86) Corma, A.; Fornas, V.; Martin-Aranda, R. H.; Garcia, H.; Promo, J. *Appl. Catal.* **1990**, *59*, 237.
- (87) Corma, A.; Martin-Aranda, Sanchez, F. J. *Catal.* **1990**, *126*, 192.
- (88) Texier-Boullet, F.; Faucand, A. *Tetrahedron Lett.* **1982**, *23*, 4927.
- (89) Ueda, W. *Sekiyu Gakkaishi (J. Jpn. Petroleum Inst.)* **1933**, *36*, 421.
- (90) Kurokawa, H.; Kato, T.; Ueda, W.; Morikawa, Y.; Moro-oka, Y.; Ikawa, T. *J. Catal.* **1990**, *126*, 199.
- (91) Kurokawa, H.; Kato, T.; Kuwabara, T.; Ueda, W.; Morikawa, Y.; Moro-oka, Y.; Ikawa, T. *J. Catal.* **1991**, *126*, 208.
- (92) Kurokawa, H.; Ueda, W.; Morikawa, Y.; Moro-oka, Y.; Ikawa, T. *Acid-Base Catalysis*; Kodansha (Tokyo)–VCH (Basel, Cambridge, New York, Weinheim), 1989; p 93.
- (93) Ueda, W.; Ohwaka, H.; Iwasaki, K.; Kuwabara, T.; Ohshida, T.; Morikawa, Y. *Acid-Base Catalysis II*; Kodansha (Tokyo)–Elsevier (Amsterdam, Oxford, New York, Tokyo) **1994**; p 35.
- (94) Ono, Y. *Heterocycle* **1981**, *16*, 1755.
- (95) Ono, Y. *Stud. Surf. Sci. Catal.* **1980**, *5*, 19.
- (96) Ono, Y.; Mori, T.; Hatada, K. *Acta Phys. Chem.* **1978**, *24*, 233.
- (97) Venuto, P. B.; Landis, P. S. *Adv. Catal.* **1968**, *18*, 259.
- (98) Ono, Y.; Takeyama, Y.; Hatada, K.; Keii, T. *Ind. Eng. Chem. Prod. Res. Dev.* **1976**, *5*, 180.
- (99) Hoelderich, W. F. *Acid-Base Catalysis*; Kodansha (Tokyo)–VCH (Basel, Cambridge, New York, Weinheim), 1989; p 1.
- (100) Onaka, M.; Higuchi, K.; Sugita, K.; Izumi, Y. *Chem. Lett.* **1989**, 1393.
- (101) Higuchi, K.; Onaka, M.; Izumi, Y. *J. Chem. Soc. Chem. Commun.* **1991**, 1035.
- (102) Sugita, K.; Ohta, A.; Onaka, M.; Izumi, Y. *Chem. Lett.* **1990**, 481.
- (103) Nomoto, Y.; Suzuki, E.; Ono, Y. *Acid-Base Catalysis II*; Kodansha (Tokyo)–Elsevier (Amsterdam, Oxford, New York, Tokyo) **1994**; p 447.
- (104) Hattori, H.; Kumai, H.; Tanaka, K.; Zhang, G.; Tanabe, K. *Proc. 8th National Symposium on Catalysis* Sindh, India, 1987; p 243.
- (105) Koga, I. *Yuki Gouseikagaku* **1975**, *33*, 702.
- (106) Yamaguchi, T. *Sekiyu Gakkaishi (J. Jpn. Petroleum Inst.)* **1993**, *36*, 250.
- (107) Tanabe, T. *Proceedings of the 8th International Congress on Catalysis*, Calgary, Canada 1988; Vol. 5, p 85.
- (108) Xu, B.; Yamaguchi, T.; Tanabe, K. *Appl. Catal.* **1990**, *64*, 41.
- (109) Dart, C. B.; Davis, M. E. *Catal. Today* **1994**, *19*, 151.
- (110) Tsuji, H.; Yagi, F.; Hattori, H.; Kita, H. *Proceedings of the 10th International Congress on Catalysis*, Budapest, Hungary, 1992; p 1171.
- (111) Yagi, F.; Tsuji, H.; Hattori, H.; Kita, H. *Acid-Base Catalysis II*; Kodansha (Tokyo)–Elsevier (Amsterdam, Oxford, New York, Tokyo), 1994; p 349.
- (112) Itoh, H.; Utamapanya, S.; Stark, J. V.; Klabunde, K. J.; Schlup, J. *Chem. Mater.* **1993**, *5*, 71.
- (113) Corma, A.; Martin-Aranda, R. M. *J. Catal.* **1990**, *130*, 130.
- (114) Lasperas, M.; Cambon, H.; Brunel, D.; Rodriguez, I.; Geneste, P. *Microporous Mater.* **1993**, *1*, 343.
- (115) Rodriguez, I.; Cambon, H.; Brunel, D.; Lasperas, M.; Geneste, P. *Stud. Surf. Sci. Catal.* **1993**, *78*, 623.
- (116) Clark, J. H. *Chem. Rev.* **1980**, *80*, 429.
- (117) Yamawaki, J.; Ando, T. *Chem. Lett.* **1979**, 45.
- (118) Ando, T.; Yamawaki, J. *Yukigosei Kyokaiishi (J. Org. Syn. Inst.)* **1981**, *39*, 14.
- (119) Clark, J. H.; Cork, D. G.; Robertson, M. S. *Chem. Lett.* **1983**, 1145.

- (120) Villemin, D. *J. Chem. Soc. Chem. Commun.* **1983**, 1092.  
(121) Villemin, D. *Chem. Ind. (London)* **1985**, 166.  
(122) Texier-Bullet, F.; Villemin, D.; Licard, M.; Mison, H.; Foucaud, A. *Tetrahedron* **1985**, *41*, 1259.  
(123) Villemin, D.; Rocha, R. *Tetrahedron* **1986**, *27*, 1789.  
(124) Villemin, D.; Richard, M. *Tetrahedron Lett.* **1984**, *75*, 1059.  
(125) Yamawaki, J.; Ando, T.; Hanafusa, T. *Chem. Lett.* **1981**, 1143.  
(126) Ando, T.; Yamawaki, J.; Kawate, T.; Sumi, S.; Hanafusa, T. *Bull. Chem. Soc. Jpn.* **1982**, *55*, 2504.  
(127) Elisabeth, A. E.; Schmittling, E. A.; Sawyer, J. S. *J. Org. Chem.* **1993**, *58*, 3229.  
(128) Clark, J. H.; Goodman, E. M.; Smith, D. K.; Brown, S. J.; Miller, J. M. *J. Chem. Soc. Chem. Commun.* **1986**, 657.  
(129) Duke, C. V. A.; Miller, J. M.; Clark, J. H.; Kybett, A. P. *J. Mol. Catal.* **1990**, *62*, 233.  
(130) Ando, T.; Clark, J. H.; Cork, D. G.; Hanafusa, T.; Ichihara, J.; Kimura, T. *Tetrahedron Lett.* **1987**, *28*, 1421.  
(131) Weinstock, L. M.; Stevenson, J. M.; Tomeliui, S. A.; Pan, S. H.; Utne, T.; Jobson, R. B.; Reinhold, F. *Tetrahedron Lett.* **1986**, *27*, 3845.  
(132) Ando, T. *Acid-Base Catalysis II*; Kodansha (Tokyo)–Elsevier (Amsterdam, Oxford, New York, Tokyo), 1994; p 9.  
(133) Baba, T.; Kim, G. J.; Ono, Y. *J. Chem. Soc. Faraday Trans.* **1993**, *88*, 891.  
(134) Baba, T.; Hikita, S.; Koide, R.; Ono, Y.; Hanada, T.; Tanaka, T.; Yoshida, S. *J. Chem. Soc. Faraday Trans.* **1993**, *89*, 3177.  
(135) Ushikubo, T.; Hattori, H.; Tanabe, K. *Chem. Lett.* **1984**, 649.  
(136) Kawakami, H.; Yoshida, S. *J. Chem. Soc. Faraday Trans. 2* **1984**, *80*, 921.  
(137) Fujioka, H.; Yamabe, S.; Yanagisawa, Y.; Matsumura, K.; Huzimura, R. *Surf. Sci.* **1985**, *149*, L53.  
(138) Kobayashi, H.; Yamaguchi, M.; Ito, T. *J. Phys. Chem.* **1990**, *94*, 7206.  
(139) Ito, T.; Tashiro, T.; Kawasaki, M.; Toi, T.; Kobayashi, H. *J. Phys. Chem.* **1991**, *95*, 4477.  
(140) Sawabe, K.; Koga, N.; Morokuma, K. *J. Chem. Phys.* **1992**, *97*, 6871.  
(141) Kobayashi, H.; Salahub, D. S.; Ito, T. *Acid-Base Catalysis II*; Kodansha (Tokyo)–Elsevier (Amsterdam, Oxford, New York, Tokyo), 1994; p 207.

CR940033V

典型的な例が、2-ブタノールの脱水でみられる。上記触媒では1-ブテンが主に生成し、酸触媒では2-ブテンが生成するのと対照的である。酸触媒ではカルベニウムイオンを経由するのに対し、塩基触媒では引き抜かれるH<sup>+</sup>は1位の炭素からのものであり、アニオン中間体を経由するからと理解される。

1-シクロヘキシルエタノールの脱水によりビニルシクロヘキサンを生成する反応はZrO<sub>2</sub>触媒を用いて工業化されている<sup>10)</sup>。NaOH処理により副生物を生成する酸性点をなくし選択性を向上させ工業化に成功した。

分子内脱水によりモノエタノールアミンからエチレンイミンを生成する反応は、Si、P、およびアルカリを含む酸化物を触媒として工業化された。この触媒は、弱い酸性と弱い塩基性を有している。反応物は反応性に富む二つの官能基を有しているため、酸性も塩基性も強すぎると副生成物が多くなる。触媒は、Si、Cs、Pの組成を変えることにより酸性・塩基性を調節し、Si/Cs/P/Oの原子比が1/0.1/0.08/2.25のとき選択率が78.8%となった<sup>11)</sup>。



### 2.3 水素化

固体塩基触媒でも水素化が起こるが、反応の挙動は遷移金属やその酸化物による水素化とは異なる。水素分子の不均一な解離吸着により生じたH<sup>+</sup>とH<sup>-</sup>の付加により進行する<sup>12)</sup>。ブタジエンやイソプレンなどの共役ジエンの水素化はモノオレフィンまでは容易に進行するが、アルカンへの水素化は遅い。共役ジエンがモノオレフィンよりも反応性が格段に高いのは、中間体のアリルアニオンがアルキルアニオンよりはるかに安定であることによる。

芳香族カルボン酸の直接水素化（還元）で対応するアルデヒドを生成する反応もZrO<sub>2</sub>を触媒として用い工業化されている<sup>13)</sup>。ZrO<sub>2</sub>の塩基性と関連した水素化能および脱水素能がこの反応に重要であることが指摘されている。

### 2.4 アミノ化

アミンも水素と同じように共役ジエンに1,4付加し、1級、2級のアミンからそれぞれ2級、3

級の不飽和アミンが生成する。水素化と本質的に同じ機構で反応が進行する。すなわち、水素化ではH<sub>2</sub>がH<sup>-</sup>とH<sup>+</sup>に解離するが、アミノ化ではアミン(RNH<sub>2</sub>)がRNH<sup>-</sup>とH<sup>+</sup>に解離し、ジエンに付加する。触媒としては、アルカリ土類酸化物が活性を示す<sup>14)</sup>。

### 2.5 Meerwein-Ponndorf-Verley還元

Meerwein-Ponndorf-Verley還元は、アルコールの水素を用いた水素化で、一つの水素移行反応である。アルデヒドとケトンアルコールと反応し、対応するアルコールを生成する。

柴垣らは、アルデヒド、ケトンのM-P-V還元によるアルコールの生成に含水ジルコニアがよい触媒となることを報告している<sup>15)</sup>。反応条件を変えると、カルボン酸のエステル化やアミノ化にも活性を示すようになる。含水ジルコニアの活性点を含めた反応機構については不明な点があるが、塩基性点が作用しているのは疑いない。

### 2.6 共役ジエンの環化脱水素二量化

ブタジエンやイソプレンなどをMgOやZrO<sub>2</sub>を触媒として170°C程度で反応させると芳香族が生成する<sup>16)</sup>。ブタジエンを反応物とするとZrO<sub>2</sub>ではエチルベンゼン、MgOではo-, p-キシレンが主に生成する。ZrO<sub>2</sub>では、Diels-Alderに続いて二重結合移行・脱水素が起こり、MgOでは、ジエンからのH<sup>+</sup>引き抜きで始まるアニオン機構でそれぞれの生成物を与える。ZrO<sub>2</sub>、MgO以外の固体塩基触媒は、ほとんど活性を示さない。

### 2.7 アルキル化

芳香族の核水素化は酸触媒で、側鎖アルキル化は塩基触媒で起こるのが一般的である。トルエンのメタノールによるアルキル化にはCs<sup>+</sup>イオン交換Xゼオライトが活性を示す<sup>17)</sup>。メタノールの脱水素により生成したホルムアルデヒドがトルエンとアルドールタイプの反応を起こしスチレンを、エチルベンゼンはスチレンの水素化により生成する。ゼオライトの塩基点はメタノールの脱水素、アルドールタイプの反応の両方に関与している。アルカリイオンをイオン交換容量を超えて含有するように調製したアルカリイオン添加ゼオライトX、Yは、イオン交換ゼオライトよりも高い活性を示すことが示された<sup>18)</sup>。過剰に存在するアルカリが新たな強い塩基点を発現し活性を向上させている。



イソプロピルベンゼンをエチレンやプロピレンなどのオレフィンでアルキル化するとき、 $\text{K-KOH-Al}_2\text{O}_3$ を用いると室温で反応が進行し、アルキル化は側鎖に起こる<sup>19)</sup>。この触媒の塩基点は非常に強いので、室温でイソプロピルベンゼンから $\text{H}^+$ を引き抜き、不安定な3級アニオンを生成できる。

## 2.8 アルドール縮合

アセトンのアルドール縮合には $\text{Ba(OH)}_2$ が古くから知られているが、アルカリ土類酸化物や希土類酸化物も触媒となる。アルカリ土類酸化物のなかでは活性の序列は表面積当たり $\text{BaO} > \text{SrO} > \text{CaO} > \text{MgO}$ である<sup>19)</sup>。少量の水の添加で活性が向上することや、重水素のトレーサー実験の結果を考慮すると、活性点は表面の $\text{O}^{2-}$ ではなく $\text{OH}^-$ であると思われる<sup>20)</sup>。

ハイドロタルサイト $\text{Mg}_6\text{Al}_2(\text{OH})_{16}\text{CO}_3 \cdot 4\text{H}_2\text{O}$ やクリソタイル $\text{Mg}_3(\text{OH})_4\text{Si}_2\text{O}_5$ もアセトンとホルムアルデヒドのアルドール縮合によるメチルビニルケトン生成に活性を示す<sup>21)</sup>。 $\text{Co}^{2+}$ でイオン交換したクリソタイルを用いると、アセトンとメタノールからMVKが生成する。 $\text{Co}^{2+}$ 交換により脱水素活性点が発現し、メタノールの脱水素によるホルムアルデヒドの生成に続いてアルドール縮合が進行するためである。

n-ブチルアルデヒドの液相での自己縮合にアルカリ土類酸化物を触媒として用いると、二量体に加え三量体が生成する<sup>22)</sup>。n-ブチルアルデヒドのアルドール縮合に続いて、生成した二量体とn-ブチルアルデヒドの交差エステル化のTishchenko反応が起こり、三量体が生成する。アルカリイオンで修飾したアルミナでは、反応は選択的にアルドール縮合した段階で止まる。アルドール縮合には塩基点、交差エステル化のTishchenko反応には塩基点と酸点が関与していることが示唆された。

## 2.9 Tishchenko 反応

ベンズアルデヒドやピバルアルデヒドなどの $\alpha$ -水素を持たないアルデヒドのTishchenko反応はアルカリ土類酸化物を用いると容易に進行する<sup>23)</sup>。アルカリ土類酸化物が活性を示すのは、塩基点に加え酸点が存在するためと考えられている。アルカリイオンで修飾したアルミナやシリカは活性を示さない。

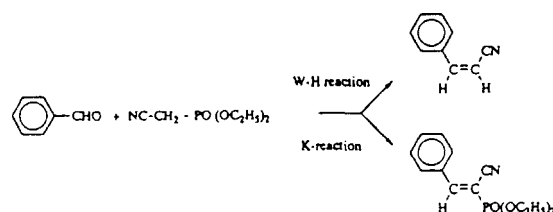
## 2.10 Michael 付加

Michael付加は、水酸化ナトリウム、ナトリウムエトキシド、ピペリジンなどの塩基存在下で進行するが、固体触媒の応用例は少ない。Sinisteraは、活性メチレン基を持つマロン酸エチル、酢酸エチルアセテート、アセチルアセトン、ニトロメタン、アセトフェノンのカルコンへのMichael付加が、部分的に脱水した $\text{Ba(OH)}_2$ を用いると効率よく進行することを報告している<sup>24), 25)</sup>。また、 $\text{KF-Al}_2\text{O}_3$ もニトロメタンを用いるいくつかのMichael付加を室温で促進するが、アルカリ土類酸化物の活性は低い。

クロトン酸メチルの二量化はMichael付加で進行し、固体塩基のなかで $\text{MgO}$ だけが特異的に高活性を示すことが見いだされた<sup>26)</sup>。ニトロメタンのMichael付加に活性を示す $\text{KF-Al}_2\text{O}_3$ はこの反応には活性を示さない。同種のMichael付加でも反応物の種類により活性な触媒系が異なる。

## 2.11 Wittig-Horner 反応と Knoevenagel 縮合

アルデヒドとニトリルは塩基触媒存在下でWittig-Horner反応とKnoevenagel縮合を起こす。下記の反応には $\text{MgO}$ 、 $\text{ZnO}$ 、 $\text{Ba(OH)}_2$ が触媒として作用する<sup>27)</sup>。塩基点がニトリルのメチレン基から $\text{H}^+$ を引き抜くことにより反応が開始される。

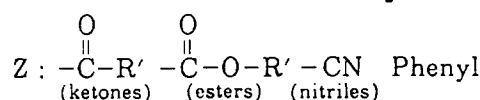
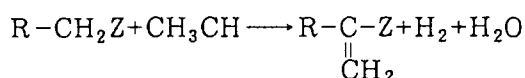


ベンズアルデヒドと活性メチレン基を持つ化合物のKnoevenagel縮合にハイドロタルサイト、アルカリイオン交換したゼオライト<sup>28)</sup>やセピオライト<sup>29)</sup>が触媒となる。塩基性の弱いゼオライトやセピオライトでは副反応であるアルドール縮合が抑えられ、また、バルキーな生成物を与える逐次的なMichael付加が細孔の大きさにより抑えられて選択性が高くなる。

## 2.12 メタノールを用いる $\alpha, \beta$ -不飽和化合物の合成

ケトン、エステル、ニトリルの $\alpha$ 位のメチル基やメチレン基はメタノールと反応しビニル基と

なる。この反応には MgO を Mn や Cr で修飾した触媒が用いられる。Ueda らは、修飾 MgO を用いアセトニトリルとメタノールを 375°C で反応させるとアクリロニトリルを生成することを見いだした<sup>30)</sup>。反応は、メタノールの脱水素で生成するホルムアルデヒドとアセトニトリルのアルドールタイプの反応で生成物を与える。Ueda らは、この反応を一般式で次のように表せる反応に拡張した。



R: Alkyl, -H

### 2.13 環の変換

環内に酸素を持つ化合物をゼオライトを触媒とし NH<sub>3</sub> や H<sub>2</sub>S と反応させ、O を N や S と交換させることができる<sup>31)</sup>。Hoelderich は、イオン交換したゼオライトの酸塩基性と環の変換の活性と選択性をまとめ、塩基性が増すと環の O を S に変換する反応が促進される傾向を指摘した<sup>32)</sup>。反応機構は明らかではないが、ゼオライトキャビティー内の塩基点が重要な役割を果たしていることが示唆される。

### 2.14 オルガノシランの反応

最近、オルガノシランが関与する反応に対する固体塩基の触媒作用についての報告がなされている。Onaka らは、カルボニル化合物や 2-シクロヘキセノンなどの不飽和ケトンのシアノトリメチルシランを用いたシアノシリル化において、MgO, CaO, ヒドロキシアパタイトを触媒として用いると反応が選択的に進行することを見いだしている<sup>33)</sup>。塩基点がシラン中の Si と相互作用しシアノアニオンの求核性を高める働きをしている。不飽和ケトンのシアノシリル化においては、塩基触媒を用いると 1,2-付加が起こり、イオン交換モンモリロナイトなどの酸触媒では 1,4-付加が起こるのと対照的である。

トリメトキシシランの気相不均化に活性な触媒として、ハイドロタルサイトと KF/Al<sub>2</sub>O<sub>3</sub> が報告されている<sup>34)</sup>。

## 3 各種固体塩基触媒の特色

固体塩基触媒の触媒作用は表面塩基点の強度と量に関連するが、これがすべての触媒作用を決定する要因とは考えられない。各種固体塩基触媒それぞれに特徴がある。

### 3.1 単独金属酸化物

アルカリ土類酸化物は代表的な固体塩基触媒である。塩基性が強いので、ごく少量の CO<sub>2</sub> や H<sub>2</sub>O の存在で活性点が被毒を受ける。オレフィンから H<sup>+</sup> を引き抜く力は大きく、-50°C でもブテン異性化を促進する。

希土類酸化物のなかでも二三酸化物は強い塩基性を示し、アルカリ土類酸化物に匹敵するが、CeO<sub>2</sub>, Tb<sub>4</sub>O<sub>7</sub>, Pr<sub>6</sub>O<sub>11</sub> など高酸化状態で安定な酸化物は塩基性が弱い。

ZrO<sub>2</sub> と ThO<sub>2</sub> も H<sup>+</sup> 引き抜き能力があるが、アルカリ土類酸化物ほどではない。塩基性が弱い代わりに弱い酸性も示すので、酸塩基協同作用により特色ある触媒作用を示す。希土類酸化物、ZrO<sub>2</sub>, ThO<sub>2</sub> に共通にみられる特徴は、アルコールに対して脱水素ではなく脱水触媒として作用することである。この脱水は酸触媒反応とは異なった機構で進行する。

水、CO<sub>2</sub> に接触するとすぐに活性点が被毒を受けるので工業プロセスに使用しにくいというのが固体塩基触媒の欠点であるが、ZrO<sub>2</sub> だけは例外で、最近、二つの工業プロセスに用いられた。芳香族カルボン酸の水素化によるアルデヒドの合成と 1-シクロヘキシルエタノールの脱水によるビニルシクロヘキサンの合成である。ところが、20 年以上も前からイソブチルアルデヒドからジイソブチルケトンの製造に ZrO<sub>2</sub> が触媒として用いられていた<sup>35)</sup>。プロセスは Tishchenko 反応を含み、ここに ZrO<sub>2</sub> が触媒として作用すると推察される。

### 3.2 ゼオライト

ゼオライトの特色は、カチオン交換性と細孔構造に起因する。交換カチオンを変えることにより広い範囲で、また、Si/Al 比を変えることにより狭い範囲で酸・塩基性を調節できる。イオン交換によって酸・塩基性を変えたゼオライトの触媒作用は、Hoelderich<sup>32)</sup> や、また最近では Dart と Davis によりまとめられている<sup>36)</sup>。

塩基性ゼオライトの調製には、イオン交換とイオン添加が行われている。イオン交換のみでは強い塩基点の発現がみられない。Hathaway と Davis は、イオン交換容量以上のアルカリをゼオライトに添加することにより、強い塩基性を示すゼオライトを調製し得ることを報告している<sup>18)</sup>。イオン交換サイト以外のところにアルカリが酸化物として存在し、それが強塩基性を示す<sup>37)</sup>。塩基性を有する MgO 粒子や各種アルカリの酸化物をゼオライトのキャビティー内に生成させた触媒の調製が試みられ、いくつかの系では形状選択性塩基触媒反応を示すと報告されている。

塩基性ゼオライトの目標は形状選択性であることは明らかであるので、構造の保持が重要である。高温で水蒸気に触れると、構造の崩壊が起こる、あるいは、Si/Al 比の大きいゼオライトほどアルカリ溶液に不安定であることなどがわかってきたが、塩基性ゼオライト調製法の確立がまず重要な課題であろう。調製法についての報告がいくつか見られるようになったので、強塩基性ゼオライトの各種反応に対する触媒としての応用が期待される。

### 3.3 非酸化物系固体塩基触媒

金属酸化物である固体塩基触媒の塩基性点は表面  $O^{2-}$  と考えられているが、塩基点が  $O^{2-}$  以外の固体塩基触媒がいくつか報告されている。酸化物系固体塩基とは異なる特色ある塩基触媒作用が期待される。

Yb や Eu 金属を液体アンモニアに溶解し、ゼオライトに担持し、加熱排気すると固体塩基触媒として作用する<sup>38)</sup>。活性点として  $YbNH$ 、 $EuNH$  などのイミドが提案されている。報告されたブテンの異性化では金属酸化物との相違が表されていないが、 $H^+$  を引き抜くのは O ではなく N であり、他の反応に対して N の特異性が表れることが期待される。

KF を担体に担持すると、フッ素化剤として、また、塩基触媒として作用する<sup>39)</sup>。担体として優れているのが  $Al_2O_3$  である。 $KF/Al_2O_3$  は Michael 付加、Knoevenagel 反応、Darzens 縮合および類似反応に有効な触媒として作用する。活性点としては、 $F^-$  アニオンが反応物から  $H^+$  を引き抜くのか、あるいは、水の存在下で KF と  $Al_2O_3$  の反応で生成する KOH が作用するのかはまだ不明で

ある。フッ素化剤として作用するときには、 $F^-$  アニオンが作用しているに違いないので、塩基触媒として作用するときにも  $F^-$  が活性点となっていることは十分考えられる。 $O^{2-}$  以外が活性点ならば、上記希土類化合物と同様に特異的触媒活性が期待できる。 $KF/Al_2O_3$  を有機合成に用いられるときには、 $200^\circ C$  以下の温度で乾燥などの前処理をして用いるが、 $300\sim 500^\circ C$  で真空加熱をすると強い塩基点を必要とする反応にも活性を示すようになる。

## 4 おわりに

固体塩基触媒の有機合成への応用は、最近になりやっと多くの報告がなされ始めた。固体塩基でなければ促進されない反応もいくつか見いだされており、固体塩基の触媒作用は均一系塩基触媒の単なる模倣ではない。本稿では触れなかったが、キャラクターゼーションとともに量子化学的な計算もなされており、固体塩基触媒表面の理解も着実に進んできている。反応の種類に応じた必要な機能を明らかにすることは有機合成用触媒を開発するためにも重要となろう。

### 参考文献

- 1) Tanabe, K., Misono, M., Ono, Y., Hattori, H., "New Solid Acids and Bases" (1989) Kodansha.
- 2) Hattori, H.; Tanabe, K.; Hayano, K.; Shirahama, H.; Matsumoto, T. Chem. Lett. 1979, 133.
- 3) Suzukamo, G.; Fukao, M.; Hibi, T.; Chikaishi, K. Acid-Base Catalysis; Kodansha (Tokyo)-VCH (Basel, Cambridge, New York, Weinheim), (1989), p.405.
- 4) Baba, T.; Endou, T.; Hannda, H.; Ono, Y., Appl. Catal., 97, L19 (1993).
- 5) Hattori, A.; Hattori, H.; Tanabe, K.J. Catal., 65, 246 (1980).
- 6) Matsushashi, H.; Hattori, H.J. Catal., 85, 457 (1984).
- 7) Lundeen, A.J.; van Hoozen, R.J. Org. Chem., 32, 3386 (1967).
- 8) 戸松, 米田, 大塚, 油化学, 17, 236 (1968).
- 9) Yamaguchi, T.; Sasaki, H.; Tanabe, K. Chem. Lett., 1976, 677.
- 10) 高橋, 日比, 東尾, 荒木, 触媒誌, 35, 12 (1993).
- 11) 植嶋, 矢野, 服部, 石油誌, 35, 362 (1992).
- 12) Tanaka, Y.; Imizu, Y.; Hattori, H.; Tanabe, K. Proc. 7th Intern. Congr. Catal. Tokyo, (1980), p.1254.
- 13) Yokoyama, T.; Setoyama, T.; Fujita, N.; Nakajima, M.; Maki, T.; Fukui, K. Appl. Catal. A 88, 149 (1992).
- 14) Kakuno, Y.; Hattori, H., J. Catal., 85, 509 (1984).
- 15) Shibagaki, M.; Takahashi, K.; Matsushita, H. Bull.

- Chem. Soc. Jpn., 61, 3283 (1988).
- 16) Suzuka, H.; Hattori, H., J. Mol. Catal., 63, 371 (1990).
  - 17) Yashima, T.; Sato, K.; Hayasaka, T.; Hara, N., J. Catal., 26, 303 (1972).
  - 18) Hathaway, P.E.; Davis, M.E., J. Catal., 119, 497 (1989).
  - 19) Zhang, G.; Hattori, H.; Tanabe, K., Appl. Catal., 36, 189 (1988).
  - 20) Zhang, G.; Hattori, H.; Tanabe, K., Appl. Catal., 40, 183 (1988).
  - 21) Suzuki, E.; Idemura, S.; Ono, Y., Chem. Lett., 1987, 1843.
  - 22) H. Tsuji, F. Yagi, Hattori, H., Kita, H., J. Catal., 148, 759 (1994).
  - 23) Tanabe, K.; Saito, K., J. Catal., 35, 274 (1974).
  - 24) Garcia-Raso, A.; Garcia-Raso, J.; Campaner, B.; Mestres, R.; Sinisterra, J.V., Synthesis 1982, 1037.
  - 25) Barrios, J.; Rojas, R.; Alcanrara, A.R.; Sinisterra, J.V., J. Catal., 112, 528 (1998).
  - 26) Kabasima, H. Tsuji, H., Hattori, H., Kita, H., under submission.
  - 27) Sinisterra, J.V.; Mouloungui, Z.; Marinas, M.J., Col. Inter. Sci., 115, 520 (1987).
  - 28) Corma, A.; Fornas, V.; Martin-Aranda, R.H.; Garcia, H.; Promo, J., Appl. Catal., 59, 237 (1990).
  - 29) Corma, A.; Martin-Aranda, Sanchez, F.J., Catal., 126, 192 (1990).
  - 30) Ueda, W., 石油誌, 36, 421 (1993).
  - 31) Ono, Y., Heterocycle, 16, 1755 (1981).
  - 32) Hoelderich, W.F., Acid-Base Catalysis; Kodansha (Tokyo)-VCH (Basel, Cambridge, New York, Weinheim), (1980), p.1.
  - 33) Onaka, M.; Higuchi, K.; Sugita, K.; Izumi, Y., Chem. Lett., 1989, 1393.
  - 34) Nomoto, Y.; Suzuki, E.; Ono, Y., Acid-Base Catalysis II; Kodansha (Tokyo)-Elsevier (Amsterdam, Oxford, New York, Tokyo) (1994) in press.
  - 35) US Patent, 3 966 822 (1976).
  - 36) Dart, C.B.; Davis, M.E., Catal. Today, 19, 151 (1994).
  - 37) Tsuji, H.; Yagi, F.; Hattori, H., Chem. Lett., 1991, 1881.
  - 38) Baba, T.; Hikita, S.; Koide, R.; Ono, Y.; Hanada, T.; Tanaka, T.; Yoshida, S.J., Chem. Soc. Faraday Trans., 89, 3177 (1993).
  - 39) 安藤, 山脇, 有機合成協会誌, 39, 14 (1981).

## (10) トルエンの側鎖アルキル化

北海道大学エネルギー先端工学研究センター教授

はつとり ひでし  
服部 英

### 1 はじめに

石油精製において、固体酸触媒は FCC をはじめ種々のプロセスに使われている。塩基性は酸性と対をなす概念であるが、固体塩基触媒はバルク製品の生成プロセスに用いられることはなかった。固体塩基触媒の研究は、固体酸触媒の研究にかなり遅れをとっているのは、バルク製品の製造に使われなかったことが大きな理由と思われる。それでも現在は多種多様の固体塩基触媒が知られるようになってきた。固体塩基触媒は、石油精製よりは石油化学工業のプロセスに用いられる可能性が大きいというのが一般的な通念であろう。

固体塩基触媒がバルク製品製造には使えないのか？ “可能性があるとしたら”トルエンの側鎖アルキル化でエチルベンゼン、スチレンを生成する反応であるというのが夢の反応の所以、と筆者は理解している。アルキル置換芳香族のアルキル化は、酸触媒では芳香核に、塩基触媒では側鎖に起こることは知られていたからである。

さて、アルキル化剤としてはオレフィンとアルコールがあり、いずれの場合も塩基触媒反応である。

### 2 オレフィンによるアルキル化

オレフィンによるアルキル化については、1950年代に金属 Na<sup>1)</sup> やカリウムグラファイト (KC<sub>8</sub>)<sup>2)</sup> を触媒としてトルエンのエチレンによるアルキル化の報告がある。いずれもオートクレーブでの反

応であり、200°C、150°C で 30 % を超える収率であった。また、最近では、Al<sub>2</sub>O<sub>3</sub>-KOH-K などの超強塩基触媒を用いてトルエンのプロピレンによるアルキル化を行い、162°C 6 時間で収率 36 % でイソブチルベンゼンを生成したとの報告もなされている<sup>3)</sup>。メカニズムについては、文献 1) では、アルキルナトリウムを中間体とする連鎖反応、文献 3) では、トルエンのメチル基の H を強塩基点が H<sup>+</sup> として引き抜きカルバニオンを生成することを提案している。これらは、いずれもバッチ式反応器で数時間反応を行わせた結果であり、塩基触媒を用いると反応が進行することは明らかになったが、大量生産するために流通式反応器を用いたら、一体どの程度の収率になるのかは不明である。固体塩基触媒について一般に言えることではあるが、触媒の活性点は水や CO<sub>2</sub> により被毒を受けやすい。流通式で反応を行う場合には、特に反応物中に水、CO<sub>2</sub> の混入を避けなければならない。工業プロセスでは、ここが困難な点になることはトルエンのオレフィンによるアルキル化でも例外でない。

### 3 メタノールによるアルキル化

#### 3.1 これまでの研究事例

トルエンのメタノールによるアルキル化については、流通式反応器を用いた研究がいくつか見られるが、いずれも転化率、収率が低い。Sidrenko らは、アルカリイオン交換ゼオライトが活性を示すことを報告し<sup>4)</sup>、Yashima らは、アルカリイオン交換ゼオライト X、Y を用いて詳細に研究を行

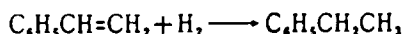
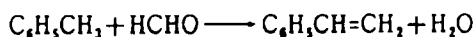
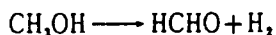
い、K, Rb, Cs で交換すると側鎖アルキル化が進行することを報告した<sup>5)</sup>。Li, Na で交換すると核アルキル化が進行する。最も高い収率を示したのは Rb で交換したゼオライト X であるが、生成するスチレン、エチルベンゼンの合計収率は 15 % 以下であった。反応温度は 425°C が最適で、接触時間を変えてもより高い収率は得られなかった。また、メタノールをホルムアルデヒドに変えても反応性は多少向上するが、反応の傾向は変らなかった。また、一連のリン酸塩を用いて、酸-塩基性により選択性が決定されるとの報告も見られる<sup>6)</sup>。

最近では、アルカリイオンをイオン交換容量以上加えたアルカリ添加ゼオライト、特に Cs 添加ゼオライト X が単純なイオン交換ゼオライトよりも活性が高いとの報告もある<sup>7)</sup>。それでも、反応条件が最適ではなかったと思われるが、収率は 5 % 以下である。また、CO の生成がかなり多い。

### 3.2 反応機構と触媒設計のポイント

側鎖と核アルキル化の選択性、収率など触媒の活性を決めているものは何か、なぜ高収率が得られないのか、また、マグネシアなど他の固体塩基触媒はゼオライトに比べてなぜ活性が低いのか、不明な点が多い。

トルエンのメタノールによるアルキル化では、反応は Sidrenko らが提案したように、次のように進行すると思われる<sup>4)</sup>。まず、メタノールが脱水素しホルムアルデヒドを生成する。ホルムアルデヒドはトルエンとアルドールタイプの縮合反応を起こし、スチレンと水を生成する。一部のスチレンは、メタノールの脱水素あるいはホルムアルデヒドの分解により生じた水素で水素化されエチルベンゼンを生成する。



メタノールの脱水素、アルドールタイプの縮合ともに塩基触媒反応であり、活性点が塩基点であることがうなずける。ただ、塩基点の存在だけではこの反応は効率よく進行しない。触媒を設計する上で考慮すべきは次の点であろう。

#### 1. ホルムアルデヒドの $\text{H}_2$ と CO への分解も

塩基触媒で促進される。

2. 反応温度が低すぎると、生成する水による活性点の被毒が起こる。
3. Li, Na 交換ゼオライト程度の酸性でもあると核アルキル化が進行する。

従って、メタノールをホルムアルデヒドに変換し、トルエンから  $\text{H}^+$  を引き抜き、ホルムアルデヒドは分解せず、しかも水に被毒を受けない塩基点を有する触媒が有効な触媒と成り得る。ゼオライト系触媒が他の固体塩基よりも活性が高いのは、塩基性質だけではなく細孔構造が寄与していると思われる。細孔内で酸点と塩基点の協同作用<sup>8-11)</sup>、電場によりホルムアルデヒドの安定化<sup>12)</sup>、あるいはトルエンの分極、あるいはモビリティの制約<sup>13,14)</sup>がおこり比較的高い活性を示すのであろう。高々 15 % 程度の収率を飛躍的に向上させるには、やはり何らかのブレークスルーがなければならない。それが何であるかがわかったとき“夢の反応”から現実の反応になる。

### 引用文献

- 1) H. Pines, J. A. Vesely, and V. N. Ipatief, 77, 554 (1955).
- 2) H. Podall and W. E. Foster, 23, 401 (1958).
- 3) G. Suzukamo, M. Fukao, T. Hibi, K. Tanaka, and K. Chikaishi, "Acid-Base Catalysis" (1989), Kodansha-VCH, p.405.
- 4) Y. N. Sidrenko, P. N. Galich, V. S. Il'in, and I. E. Neimark, *Dokl. Akad. Nauk SSSR*, 173, 132 (1967).
- 5) T. Yashima, K. Saito, T. Hayasaka, and N. Hara, *J. Catal.*, 26, 303 (1972).
- 6) T. Sodesawa, I. Kimura, and F. Nozaki, *Bull. Chem. Soc. Jpn.*, 52, 2431 (1979).
- 7) P. E. Hathaway and M. E. Davis, *J. Catal.*, 119, 497 (1989).
- 8) H. Itoh, A. Miyamoto, and Y. Murakami, *J. Catal.*, 64, 284 (1980).
- 9) H. Itoh, T. Hattori, K. Suzuki, A. Miyamoto, and Y. Murakami, *J. Catal.*, 72, 170 (1981).
- 10) H. Itoh, T. Hattori, K. Suzuki, and Y. Murakami, *J. Catal.*, 79, 21 (1983).
- 11) A. Miyamoto, S. Iwamoto, K. Agusa, and T. Inui, "Acid-Base Catalysis" (1989), Kodansha-VCH, p.497.
- 12) M. L. Unland, *J. Phys. Chem.*, 82, 580 (1978).
- 13) J. J. Freeman and M. L. Unland, *J. Catal.*, 54, 183 (1978).
- 14) M. D. Sefcik, *J. Am. Chem. Soc.*, 101, 2164 (1979).

# 高エネルギー粒子線照射による 核変換反応を利用した 組成制御と新材料

高橋 平七郎\* 野田 哲二\*\*

## 1. はじめに

原子炉、核融合炉材料において、常に大きな問題となっているのが、照射損傷による材料特性劣化である。最近、さらに中性子照射過程で生ずる核反応生成元素が炉材料の性質に著しく影響することが大きな課題となっている。炉材料において、この核変換元素で最も注目されてきたのが $(n, \alpha)$ 、 $(n, p)$ 反応による核融合炉や高速炉材料へのヘリウム、水素導入である。これら気体元素の他に新たな課題として、核変換で生成した固体元素による材料組成の変化に起因する材料特性変化が指摘されている。核融合炉候補材料を構成している合金成分が中性子照射によりいかなる元素に変換し、どのような材料組成になるかについて既に検討されている<sup>(1)</sup>。また、こうした材料特性に関する課題以外に、加速器を用いて半減期の長い放射性核種を半減期の短い核種にする、いわゆる消滅処理研究<sup>(2)</sup>がある。さらに最近、核変換反応で利用価値の高い安定元素を製造することや<sup>(3)</sup>、通常の合金化プロセスでは実現できない、高性能の合金を製造する研究が注目されている<sup>(4)</sup>。本稿では、これらの一端を紹介する。

## 2. 核変換元素による材料組成変化と合金製造

同位体の核反応特性と粒子線エネルギー、粒子線束を制御することにより、自然界に余り多く存在しない元素を生成することができる。また、通常の方法では製造し難い組成を有

する合金を調整することが可能である。次に、核反応で生成する元素例を示す。

### (1) 核変換生成元素

超硬合金をはじめ多くの材料の合金元素として利用され、また、資源的にも少なく高価であるオスミウム(Os)は、次の核変換で生成される<sup>(5)(6)</sup>。

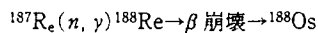
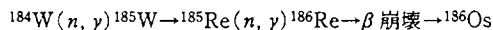


図1に、米国の HFIR(HFIR のフルネーム：高速同位体

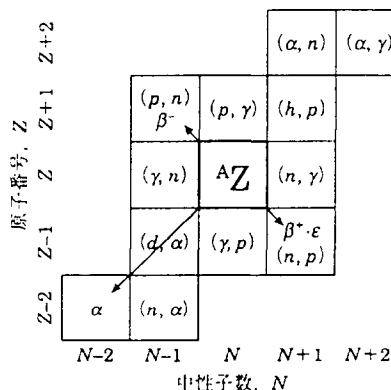


図1 核変換元素生成に関する中性子数と原子番号の関係。枠内は核変換反応を示す。

\* 北海道大学教授；エネルギー先端工学研究センター（〒060 札幌市北区北13条西8丁目）

\*\* 金属材料技術研究所主任研究員

Composition Controlled New Materials Production Using Transmutation Reaction Under Irradiation of High Energy Particles; Heishichiro Takahashi\*, Tetsuji Noda\*\*(\*Center for Advanced Research of Energy Technology, Hokkaido University, Sapporo. \*\*National Research Institute for Metals, Tsukuba)

Keywords: transmutation, neutron irradiation, radioisotope, neutron-induced alloy, semiconductor

1995年4月26日受理

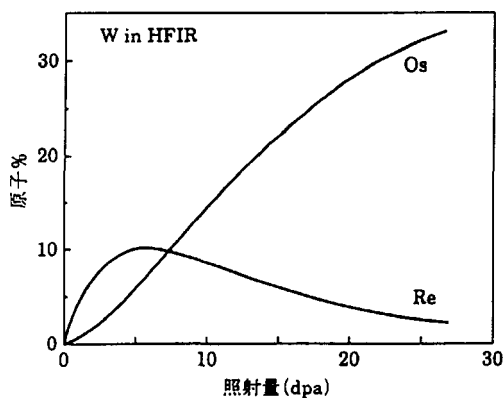
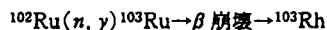


図2 HFIR照射によるWのReおよびOsへの核変換<sup>(5)</sup>.

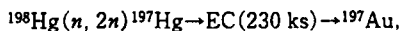
炉)で生成されたOsおよびReの生成量と照射量との関係を示す。

また、同様に高価なロジウム(Rh)は、



の核反応で生成される。

照射を利用した錬金術とも言える金(Au)の生成は、自然界の水銀(Hg)に含まれている $^{198}\text{Hg}$ あるいは $^{200}\text{Hg}$ (各々10%, 20%含有)を高エネルギー中性子で照射することにより、次の核変換反応で生成される。



または、 $^{200}\text{Hg}(n, \alpha)^{197}\text{Pt} \rightarrow ^{197}\text{Au}$

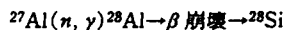
もし、核融合炉が実現した場合、一基による生産能力は年間200 kg程度(Hg原量00 kgの場合)である。水銀からの分離工程があり経済的には引き合わないため、現実的で無いかも知れないが、理論的には可能である<sup>(7)</sup>。

図2に粒子線と同位体との反応における原子番号(Z)と中性子数(N)との関係を示す。図から明らかなように、粒子の種類およびエネルギーの組合せによって種々の元素に変換できる。例えば、図において(p, n)や(n, p)の核反応を起こさせると、質量Aの元素Zは各々矢印で示した枠に相当する元素に変換される。具体的例として、Feに中性子(n)を照射するとCrとMnに、また、プロトン(p)あるいはHe(h)を照射するとCo, Ni等に変換できる。こうした核変換反応を利用した材料合成の可能性の例を以下に示す。

### 3. 金属合金製造への応用

#### (1) Al-Si合金

Alの安定同位体は $^{27}\text{Al}$ であり、熱中性子照射により、



に核変換される。また、熱中性子に対する他の反応はほとんど無視できる程度に小さいので、中性子照射量の制御により、

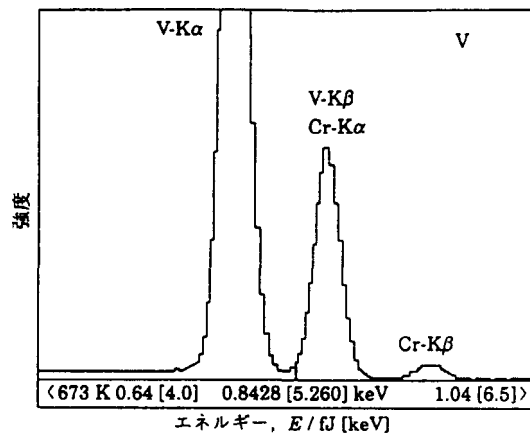
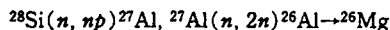


図3 673 Kで17.7 dpaまで純VをHFIR照射後のEDS分析結果<sup>(8)</sup>。核変換でCrが約16原子%生成。

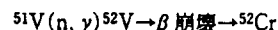
Si濃度を精密に制御できる。また、照射温度を変化させることにより形成析出物の寸法や分布状態の制御も可能である。さらに、



の核変換反応によりMgも生成できるためAl-Si-Mg合金の製造もできる。

#### (2) V-Cr合金

Vは、99.75%の $^{51}\text{V}$ からなるので、熱中性子と次の反応、



によりCrを生成する<sup>(1)(5)</sup>。

この核変換でのCr生成の実証例を図3に示す<sup>(8)</sup>。このように、純VからV-Cr合金が製造できる。

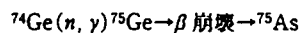
#### (3) その他の合金化

Cuの同位体の核変換により、ZnおよびNiが生成されることが報告されている。長時間の中性子照射をすれば、Cu-Ni-Znの三元系合金が生成される<sup>(9)</sup>。

### 4. 半導体製造への応用

#### (1) GeからGaAsの製造

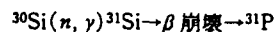
天然のGeは、 $^{70}\text{Ge}$ (20.55%),  $^{72}\text{Ge}$ (27.3%),  $^{73}\text{Ge}$ (7.67%),  $^{74}\text{Ge}$ (36.74%),  $^{76}\text{Ge}$ (7.67%)から構成されている。これらの中で、 $^{70}\text{Ge}$ と $^{74}\text{Ge}$ だけを同位体分離により取り出すことができれば、核変換を利用して、



の反応により直接GeからGaAsを製造できる<sup>(10)</sup>(薄膜デバイスであれば変換量も少なく済む.)。

#### (2) n型Si半導体の製造

Si単結晶を中性子照射すると、次の核変換が起こる。



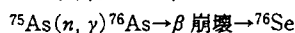
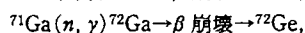
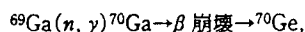


この結果、磷(P)を均一にドーブしたn型半導体となる<sup>(11)</sup>。なお、Pの濃度は、 $N=NO \cdot S \cdot \phi \cdot t$ で与えられる。ここでNは生成した<sup>31</sup>Pの濃度(原子/m<sup>3</sup>)、NOは<sup>30</sup>Siの原子数( $1.53 \times 10^{27}$  原子/m<sup>3</sup>)、Sは核反応断面積( $0.11 \times 10^{-28}$  m<sup>2</sup>)、 $\phi$ は熱中性子束(m<sup>-2</sup> s<sup>-1</sup>)、tは照射時間(s)である。したがって、 $N=0.0168 \phi \cdot t$ となる。一方、n型Si半導体の比抵抗Rは、 $R=5 \times 10^{11}/N$  (Ωm)で与えられるため、比抵抗は中性子照射量に反比例する。この方法で作製された結晶の抵抗率は予めPを添加し帯域溶融結晶に比較して極めて均一な分布となっている<sup>(12)</sup>。

この方法の問題点は<sup>30</sup>Siの自然存在率3.12%と低いため、照射効率が悪いことであるが、<sup>30</sup>Si濃度を高くすることで生産性は向上可能である。

NTD(Neutron Transmutation Doping)は、n型GaAs作製に適用されている<sup>(13)</sup>。<sup>70</sup>Ga、<sup>72</sup>GaからGe、<sup>75</sup>AsからSeが不純物として添加され、 $10^{11}$ 倍までの抵抗率制御が可能である。

中性子核変換によるGaAsへのドナー元素のドーピングには、同位体として含有されている<sup>69</sup>Ga、<sup>71</sup>Gaおよび<sup>75</sup>Asの核変換を利用する。これらを含むGaAsを熱中性子で照射すると、次の核反応により、ドナーとして作用する安定なGeおよびSeが生成する<sup>(13)</sup>。



なお、照射で導入される欠陥は、焼鈍によって除去可能である。

以上に概述したように、実際の材料の基本となる元素のほとんどは単一の質量の核種でなく中性子の数が異なった2

種以上の同位体から構成されている。同位体制御材料の製造には、まず同位体レベルでの材料組成の制御が必要であり、目的に応じて同位体分離をする。さらに核変換の条件を精密に設定すれば、微量の成分調整が可能である。また、加速器などにより各種同位体元素を予め注入し照射条件を適切に設定することにより、これまでの通常の材料合成で得られない種々の未知機能の薄膜合成も可能で今後の発展が期待できる。

## 文 献

- (1) F. M. Mann: HEDL-TME81-37, UC-20C, Hanford Engineering Development Laboratory, (1982).
- (2) 消滅処理研究の現状, 日本原子力学会, (1994).
- (3) 核融合反応の多角的利用を目指して, 日本原子力産業会議, (1988), p. 70.
- (4) 野田哲二: 金属, 7月号, (1993), 32.
- (5) L. R. Greenwood, F. A. Garner: J. Nucl. Mater., 212-215(1994), 635.
- (6) B. A. Engholm, E. T. Cheng and K. R. Schultz: Fusion Technology, 10(1986), 1290.
- (7) K. R. Schultz, B. A. Engholm, R. F. Bourque, E. T. Cheng, M. J. Schaffer and C. P. C. Wang: Fusion Technology, 10(1986), 1279.
- (8) S. Ohnuki, H. Takahashi, K. Shiba, A. Hishinuma, J. E. Pawel and F. A. Garner: J. of Nucl. Mater., 218(1995), 217.
- (9) F. A. Garner, L. R. Greenwood and F. M. Mann: Fusion Reactor Materials, DOE/ER-0313/13, (1993), p. 42.
- (10) A. Tikhomirov: Physics Research, B70(1992), 1.
- (11) M. Tanenbaum and A. D. Mills: J. Electrochem. Soc., 108(1961), 171.
- (12) 滝口蓮一: 半導体結晶材料総合ハンドブック, フジテクノシステム, (1986), p. 79.
- (13) J. Mueller, W. Kellner and H. Kniepkamp: J. Appl. Phys., 51(1980), 3178.

**(平成 7 年度)**

**4. 共同研究者ならびに研究テーマ一覧**

**5. 学生指導研究テーマ一覧**

**6. 科学研究費等一覧**

**7. 国際会議出席一覧**

**8. 学会賞受賞一覧**

## 4. 共同研究者ならびに研究テーマ一覧

### [炭素系資源転換反応分野]

大阪ガス（株）開発研究所

炭素小球体の生成メカニズムに関する研究

興亜石油（株）麻里布精油所

石油コークス製造に関する基礎研究

ジャパンエナジー（株）水島精油所

重質油の構造評価に関する研究

新エネルギー・産業技術総合開発機構（RITE）

Extractive Volatilisation of Minerals from Coal Ashes by Chlorination

日本エネルギー学会（石炭利用基盤技術研究）

加熱に伴う石炭基本物性の変化とプロセス物性の関係

日本エネルギー学会（石炭液化技術商業化基盤としての石炭分子化学試験調査）

石炭中の非共有結合（凝集構造）の評価

### [炭素系資源評価分野]

北海道電力（株）総合研究所

石炭灰利用乾式脱硫・脱硝剤による同時脱硫脱硝反応機構解明に関する研究

大阪ガス（株）開発研究所

固体表面に存在する水素の性質と触媒機能における役割

### [エネルギー転換制御分野]

東芝（株）

W-Y<sub>2</sub>O<sub>3</sub>複合材料のMHD電極への適用性に関する実験評価

日本タングステン（株）

MHD電極用タングステンFGM電極材料の開発

### [極限材料工学分野]

新日本製鉄所（株）室蘭研究所

結晶粒成長におよぼす加工熱処理の影響

日本製鋼所（株）室蘭研究所

鋼の繰返し急速加熱・冷却による表面亀裂発生

中国北京科技大学材料系 教授 胡本芙

Fe-Cr-Ni 基鋼の非平衡偏析機構に関する研究

バッテリー・パシフィック・ノースウエスト研究所

主任研究員 R. A. Garner, D. S. Gelles

核融合炉用低放射化材料に関する基礎研究

## 5. 指導学生研究テーマ一覧

### [炭素系資源転換反応分野]

#### 卒業論文

森山 亮 (金属工学科)  
愛澤 禎典 (応用化学科)  
三浦 滋 (合成化学工学科)

蓑和田 登 (合成化学工学科)  
山下 琢治 (合成化学工学科)

重質炭化水素類の炭化反応の制御  
電子受容体添加による石炭の高次構造変化  
カルシウムシリケートを用いた排煙の乾式  
脱硫・脱硝反応機構の研究  
多環芳香族炭化水素の屈折率  
石灰石による脱硫反応に及ぼす  $\text{CO}_2$  の影響

#### 修士論文

小野 俊哉 (物質工学専攻)

ヘテロ化合物の蒸気圧推算

### [炭素系資源評価分野]

#### 卒業論文

遠藤 浩光 (金属工学科)  
  
澤井 哲也 (金属工学科)  
傳馬 大輔 (金属工学科)  
香西 盛智 (応用化学科)  
山内 豊 (合成化学工学科)

石炭水素化分解反応特性と生成オイル分の  
化学構造  
キノリンの水素化脱窒素触媒の研究  
石炭炭化反応中のガス発生特性  
芳香族化合物の核水素化触媒の研究  
含酸素化合物の分子容推算

#### 修士論文

浅井 哲 (分子化学専攻)  
  
渋谷 忠 (分子化学専攻)  
則永 行庸 (分子化学専攻)  
濱口 光一 (分子化学専攻)  
  
肥後 健太郎 (分子化学専攻)  
  
町田 崇一郎 (分子化学専攻)  
  
松岡 献二郎 (分子化学専攻)

PVC (ポリ塩化ビニル) による炭素表面  
の改質と構造変化  
固体塩基触媒の有機合成への応用  
水の脱離に伴う褐炭の高次構造変化  
メソポーラスマテリアルの高機能触媒化の  
研究  
クラッキング、異性化などの固体酸触媒反  
応における共存水素の効果  
炭酸カルシウムを用いた脱硫・脱硝反応の  
研究  
磁気共鳴法を用いた石炭と溶媒の相互作用

### [エネルギー転換制御分野]

#### 卒業論文

菊地 浩之 (原子工学科)

改良型パルスシーケンスを用いたEPI法に  
よる高速流速測定

長谷部 滋則（原子工学科）

三浦 亨（原子工学科）

村上 和哉（原子工学科）

画像データによるMHDプラズマ物理量の  
2次元解析

MHD発電用W-Y<sub>2</sub>O<sub>3</sub>電極の研究

二波長輻射吸収法によるMHDプラズマ噴流  
の分光解析

#### 修士論文

赤木 憲二（原子工学専攻）

テータピンチにおける磁場－プラズマ共鳴  
現象の解析

大石 茂（原子工学専攻）

高効率MHD－汽力複合発電システムの検討

西山 正人（原子工学専攻）

北大5 MWth MHD発電チャンネル内の3次元  
電磁流体解析

水澤 英男（原子工学専攻）

磁気共鳴映像法によるMHDプラズマ流れ  
可視化に関する検討

#### [極限材料工学分野]

#### 卒業論文

中村 正人（金属工学科）

イオン注入後アニールによる点欠陥及び  
注入原子拡散挙動

新堂 陽介（金属工学科）

Ni-Al合金の照射による組織・組成変化  
電子線／He同時照射した改良型316L鋼の  
損傷組織

本田 孝（金属工学科）

#### 修士論文

相沢 大器（物質工学専攻）

鋼の急速加熱冷却による表面き裂発生と  
表面組織変化

石田 秀幸（物質工学専攻）

高エネルギーイオン注入したSi中の二次  
欠陥分布

坂口 紀史（物質工学専攻）

照射誘起偏析の動的挙動に関する計算機  
シミュレーション

土田 博思（物質工学専攻）

電子線／H及びHeイオン同時照射オース  
テナイト系ステンレス鋼の損傷組織観察

#### 博士課程論文

橋本 直幸（金属工学専攻）

オーステナイト系ステンレス鋼の照射誘起  
粒界移動挙動

## 6. 科学研究費等一覧

### [炭素系資源転換反応分野]

千葉 忠俊 試験研究（分担）

流動層反応電極を用いた二酸化炭素の固定

熊谷 治夫 国際学術研究（分担）

ビクトリア褐炭の化学的特性の解明とそれに基づく機能物質の製造

### [炭素系資源評価分野]

服部 英 一般研究（C）（代表）

分子状水素から触媒活性点が生成する水素化分解用固体酸触媒の開発

服部 英 重点領域研究（1）（分担）

特殊反応場を生かした触媒反応とそのための触媒材料  
－形状選択性固体塩基触媒の開発－

服部 英 研究成果公開促進費「研究成果公开发表（B）」（代表）

環境問題と触媒化学  
－酸性雨と温暖化をなくすために－

### [極限材料工学分野]

高橋平七郎 一般研究（B）（代表）

イオン注入法による接合界面の組成・構造変化と接合特性に関する研究

木下 博嗣 一般研究（C）（代表）

照射損傷組織に及ぼす照射速度および析出物の影響

## 7. 国際会議出席一覧

### [炭素系資源転換反応分野]

- |       |          |                                                               |
|-------|----------|---------------------------------------------------------------|
| 千葉 忠俊 | 1995. 10 | 45th Canadian Chemical Engineering Conference, Quebec, Canada |
| 熊谷 治夫 | 1995. 9  | 8th International Conference on Coal Science, Oviedo, Spain   |

### [炭素系資源評価分野]

- |       |          |                                                                                                  |
|-------|----------|--------------------------------------------------------------------------------------------------|
| 服部 英  | 1995. 3  | 17th Symposium on Efficient Use of Energy and Direct Electrical Power Generation, Sapporo, Japan |
|       | 1995. 3  | The 1995 SO <sub>2</sub> Control Symposium, Miami, Florida, USA                                  |
|       | 1995. 9  | 8th International Conference on Coal Science, Oviedo, Spain                                      |
|       | 1995. 10 | The 27th Seminar on Science and Technology (Catalysis), Sapporo, Japan                           |
|       | 1995. 10 | An International Workshop on Environmental Catalysis Technology, Pohang, Korea                   |
| 佐藤 正昭 | 1995. 9  | 8th International Conference on Coal Science, Oviedo, Spain                                      |

### [エネルギー転換制御分野]

- |       |         |                                                             |
|-------|---------|-------------------------------------------------------------|
| 青木 義昭 | 1995. 6 | The 33rd Symposium on Engineering Aspects of MHD, Tennessee |
|-------|---------|-------------------------------------------------------------|

### [極限材料工学分野]

- |       |          |                                                                                                                                           |
|-------|----------|-------------------------------------------------------------------------------------------------------------------------------------------|
| 高橋平七郎 | 1995. 6  | 7th International Conference Intergranular and Interphase Boundaries in Materials, Lisbon                                                 |
|       | 1995. 9  | The 4th Japan-France Materials Science Seminar on Structural Evolution in Materials: The Dependence on Atomistic Phenomena, Fontainebleau |
|       | 1995. 9  | 7th International Conference on Fusion Reactor Materials, Obninsk                                                                         |
|       | 1995. 10 | The 3rd Sino-Japanese Symposium on Materials for Advanced Energy Systems and Fission and Fusion Engineering, Chengdu                      |
|       | 1995. 12 | The 117th Meeting of JIM on International Symposia on Advanced Materials and Technology for the 21st Century, Honolulu                    |
| 木下 博嗣 | 1995. 12 | The 117th Meeting of JIM on International Symposia on Advanced Materials and Technology for the 21st Century, Honolulu                    |



|       |          |                                                                                                                        |
|-------|----------|------------------------------------------------------------------------------------------------------------------------|
| 渡辺 精一 | 1995. 5  | International Symposium on Plant Aging and Life Prediction of Corrodible Structures, Sapporo                           |
|       | 1995. 7  | US/Japan Workshop on Theory and Modeling of Irradiation Effects in Materials for Fusion Energy System, Livermore       |
|       | 1995. 12 | The 117th Meeting of JIM on International Symposia on Advanced Materials and Technology for the 21st Century, Honolulu |

## 8. 学会賞受賞一覧

[極限材料工学分野]

高橋平七郎 日本電子顕微鏡学会賞（瀬藤賞）

超高压電子顕微鏡法によるイオン・電子照射下における格子欠陥と  
溶質原子の相互作用に関する研究

**9. 平成7年度センター職員名簿**

**10. 平成7年度運営委員会委員名簿**

## 9. 平成7年度センター職員名簿

### センター長

教 授 工学博士 吉田 宏

### [炭素系資源転換反応分野]

教 授 工学博士 千葉 忠俊

助 手 工学博士 熊谷 治夫(兼務)

### [炭素系資源評価分野]

教 授 工学博士 服部 英

助 手 博士(工学) 佐藤 正昭

### [エネルギー転換制御分野]

教 授 工学博士 粥川 尚之

助教授 工学博士 青木 義明

助 手 工学修士 谷津 茂男(兼務)

助 手 博士(工学) 沖中 憲之(兼務)

客員教授 工学博士 大竹 一友(豊橋技術科学大学)

客員助教授 工学博士 石川 元雄(京都大学)

### [極限材料工学分野]

教 授 工学博士 高橋 平七郎

助 手 Ph. D 渡辺 精一

助 手 工学修士 木下 博嗣(兼務)

### [超高压電子顕微鏡研究室]

技 官 望月 進(兼務)

技 官 菅原 健治(兼務)

(兼務)は工学部よりの兼務者を表す

# 10. 平成7年度運営委員会委員名簿

|     |                 |     |        |
|-----|-----------------|-----|--------|
| 委員長 | エネルギー先端工学研究センター | 教授  | 吉田 宏   |
| 委員  | 工学部             | 教授  | 阿部 寛   |
| 委員  | 工学部             | 教授  | 石井 邦宣  |
| 委員  | 理学部             | 教授  | 石川 達雄  |
| 委員  | 電子科学研究所         | 教授  | 野村 一成  |
| 委員  | 触媒化学研究センター      | 教授  | 下澤 楯夫  |
| 委員  | エネルギー先端工学研究センター | 教授  | 岩本 正和  |
| 委員  |                 | 教授  | 粥川 尚之  |
| 委員  |                 | 教授  | 高橋 平七郎 |
| 委員  |                 | 教授  | 千葉 忠俊  |
| 委員  |                 | 教授  | 服部 英   |
| 委員  |                 | 助教授 | 青木 義明  |